

ACS SYMPOSIUM SERIES **608**

Innovations in Supercritical Fluids

Science and Technology

Keith W. Hutchenson, EDITOR
DuPont Company

Neil R. Foster, EDITOR
University of New South Wales

Developed from a symposium held
at the American Institute of Chemical Engineers
Annual Meeting,
San Francisco, California,
November 13–18, 1994



American Chemical Society, Washington, DC 1995

Innovations in supercritical fluids



Library of Congress Cataloging-in-Publication Data

Innovations in supercritical fluids: science and technology / Keith W. Hutchenson, editor, Neil R. Foster, editor.

p. cm.—(ACS symposium series; 608)

“Developed from a symposium sponsored by the American Institute of Chemical Engineers at the American Institute of Chemical Engineers Annual Meeting, San Francisco, California, November 13–18, 1994.”

Includes bibliographical references and indexes.

ISBN 0–8412–3324–1

1. Supercritical fluid extraction—Congresses.

I. Hutchenson, Keith W., 1959— II. Foster, Neil R., 1952— III. American Institute of Chemical Engineers. Meeting (1994: San Francisco, Calif.) IV. Series.

TP156.E8I465 1995
541.3'4—dc20

95–38445
CIP

This book is printed on acid-free, recycled paper.



Copyright © 1995

American Chemical Society

All Rights Reserved. The appearance of the code at the bottom of the first page of each chapter in this volume indicates the copyright owner's consent that reprographic copies of the chapter may be made for personal or internal use or for the personal or internal use of specific clients. This consent is given on the condition, however, that the copier pay the stated per-copy fee through the Copyright Clearance Center, Inc., 222 Rosewood Drive, Danvers, MA 01923, for copying beyond that permitted by Sections 107 or 108 of the U.S. Copyright Law. This consent does not extend to copying or transmission by any means—graphic or electronic—for any other purpose, such as for general distribution, for advertising or promotional purposes, for creating a new collective work, for resale, or for information storage and retrieval systems. The copying fee for each chapter is indicated in the code at the bottom of the first page of the chapter.

The citation of trade names and/or names of manufacturers in this publication is not to be construed as an endorsement or as approval by ACS of the commercial products or services referenced herein; nor should the mere reference herein to any drawing, specification, chemical process, or other data be regarded as a license or as a conveyance of any right or permission to the holder, reader, or any other person or corporation, to manufacture, reproduce, use, or sell any patented invention or copyrighted work that may in any way be related thereto. Registered names, trademarks, etc., used in this publication, even without specific indication thereof, are not to be considered unprotected by law.

PRINTED IN THE UNITED STATES OF AMERICA

**American Chemical Society
Library**

**1155 16th St., N.W.
Washington, D.C. 20036**

1995 Advisory Board

ACS Symposium Series

Robert J. Alaimo
Procter & Gamble Pharmaceuticals

Mark Arnold
University of Iowa

David Baker
University of Tennessee

Arindam Bose
Pfizer Central Research

Robert F. Brady, Jr.
Naval Research Laboratory

Mary E. Castellion
ChemEdit Company

Margaret A. Cavanaugh
National Science Foundation

Arthur B. Ellis
University of Wisconsin at Madison

Gunda I. Georg
University of Kansas

Madeleine M. Joullie
University of Pennsylvania

Lawrence P. Klemann
Nabisco Foods Group

Douglas R. Lloyd
The University of Texas at Austin

Cynthia A. Maryanoff
R. W. Johnson Pharmaceutical
Research Institute

Roger A. Minear
University of Illinois
at Urbana–Champaign

Omkaram Nalamasu
AT&T Bell Laboratories

Vincent Pecoraro
University of Michigan

George W. Roberts
North Carolina State University

John R. Shapley
University of Illinois
at Urbana–Champaign

Douglas A. Smith
Concurrent Technologies Corporation

L. Somasundaram
DuPont

Michael D. Taylor
Parke-Davis Pharmaceutical Research

William C. Walker
DuPont

Peter Willett
University of Sheffield (England)

Foreword

THE ACS SYMPOSIUM SERIES was first published in 1974 to provide a mechanism for publishing symposia quickly in book form. The purpose of this series is to publish comprehensive books developed from symposia, which are usually “snapshots in time” of the current research being done on a topic, plus some review material on the topic. For this reason, it is necessary that the papers be published as quickly as possible.

Before a symposium-based book is put under contract, the proposed table of contents is reviewed for appropriateness to the topic and for comprehensiveness of the collection. Some papers are excluded at this point, and others are added to round out the scope of the volume. In addition, a draft of each paper is peer-reviewed prior to final acceptance or rejection. This anonymous review process is supervised by the organizer(s) of the symposium, who become the editor(s) of the book. The authors then revise their papers according to the recommendations of both the reviewers and the editors, prepare camera-ready copy, and submit the final papers to the editors, who check that all necessary revisions have been made.

As a rule, only original research papers and original review papers are included in the volumes. Verbatim reproductions of previously published papers are not accepted.

Preface

THE UTILIZATION OF SUPERCRITICAL FLUID (SCF) science and technology has changed significantly over the past two decades from an early emphasis on extractions in the petroleum and chemical industries to applications in the food, personal care, and environmental remediation industries. However, only a relatively small number of commercial-scale plants are now in operation, and this fact indicates that the potential of this field has not been fully realized. The focus of much recent research in the SCF area has been of an interdisciplinary nature with emphasis on the measurement of high-quality, fundamental data. As a result, the potential now exists for the development of a variety of innovative applications, as evidenced by the recent scientific literature and conferences in this area.

This volume was developed from a selection of papers presented at one of these recent conferences, the "Symposium on Supercritical Fluid Science and Technology" held as part of the 1994 Annual Meeting of the American Institute of Chemical Engineers in San Francisco, California, in November, 1994. The chapters were selected to represent the breadth of the innovative applications that are currently being investigated within this field, and to reflect the diversity of papers presented at the symposium.

This volume spans the range of research from fundamental aspects of supercritical fluid science to developmental aspects of the technology for commercial applications. The first chapter provides an overview of the field of supercritical fluid science and technology by discussing the significance of accurate fundamental solubility data in the scale-up process and by presenting selected representative examples of recent innovations in the field. This is followed by a section containing chapters that describe both fundamental research on molecular interactions and simulations as well as experimental and theoretical aspects of relevant phase behavior. The second section presents examples of research on chemical and catalytic transformations in supercritical fluid media. The third section includes chapters on various topics and applications of the technology, such as supercritical water oxidation for the total oxidative destruction of hazardous wastes. The final section presents a review of applications in the forest products industry and several chapters representative of innovations in this area.

About the cover

The cover design symbolizes the experiments conducted by L. Cailletet (1891) in which high pressures were generated with a mercury-filled tube extending to the top of the Eiffel Tower. This design is a tribute to the creativity and innovation demonstrated by the early researchers in the field.

Acknowledgments

We thank the authors and speakers for their valuable contributions in presenting papers at the symposium and preparing chapters for this book. We thank the reviewers for their careful evaluations and valuable suggestions for improving the quality of these chapters. We also extend our appreciation to Lori Boock, Joan Brennecke, Pablo Debenedetti, Esin Gulari, Keith Johnston, Erdogan Kiran, Rich Lemert, Kraemer Luks, Mac Radosz, Ted Randolph, Anneke Sengers, Jeff Tester, and David Tomasko for chairing the symposium sessions. Finally, we thank Michelle Althuis, the ACS Books Acquisitions Editor for this volume, who patiently guided us through the process of preparing this book.

KEITH W. HUTCHENSON
DuPont Central Research and Development
Experimental Station
P.O. Box 80304
Wilmington, DE 19880-0304

NEIL R. FOSTER
School of Chemical Engineering and Industrial Chemistry
University of New South Wales
Sydney
New South Wales 2052
Australia

July 24, 1995

Chapter 1

Innovations in Supercritical Fluid Science and Technology

Keith W. Hutchenson¹ and Neil R. Foster²

¹DuPont Central Research and Development, Experimental Station,
P.O. Box 80304, Wilmington, DE 19880-0304

²School of Chemical Engineering and Industrial Chemistry, University
of New South Wales, Sydney, New South Wales 2052, Australia

As is reflected in the contents of this volume, much of the recent research in the field of supercritical fluid science and technology has been devoted to developmental aspects of exciting novel applications. However, to fully realize the potential of these possibilities, due consideration must be given to the quality of the fundamental solubility data upon which they are based. This aspect and the implications on the scale-up process are discussed in detail. Secondly, representative examples of recent innovations in supercritical fluid technology which may well influence future research priorities and have commercial ramifications are described. These include the applications of chemistry and catalysis in supercritical fluids, supercritical water oxidation (SCWO), gas-antisolvent (GAS) extraction, precipitation with a compressed fluid antisolvent (PCA), and rapid expansion from a supercritical solution (RESS).

As is evident from the nature of the papers in this volume, a substantial proportion of research activity in the field of supercritical fluid (SCF) science and technology is now being devoted to developmental aspects of potential commercial applications. Whilst this trend is most encouraging, and there are a number of large commercial supercritical fluid extraction (SCFE) plants in current use, it should be remembered that the design of such plants is a relatively infant technology. One of the major impediments to the wider commercialization of SCF technology in the past has been the lack of sufficient design data required for the reliable scale-up of laboratory-based developments. Consequently, it is appropriate to reflect on relevant aspects of past and present supercritical fluid research, and to speculate on what emphasis is warranted in future work.

A common element of the various applications of SCF technology being considered in current research is that the phase behavior of the solute species in the SCF medium must be known precisely for reliable scaling to commercial processes. The importance of measurement and modeling of solubility data is fundamental to these potential applications. Because of the significance of this important aspect of

0097-6156/95/0608-0001\$14.75/0
© 1995 American Chemical Society

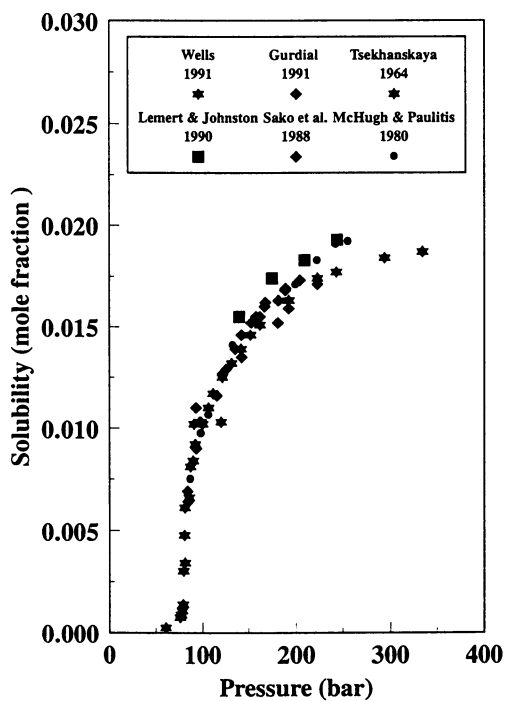


Figure 1. Solubility Data for Naphthalene in SC-CO₂ at 308.1 K (1, 16, 84-87).

SCF technology, a critical review of this topic is presented here along with some common pitfalls that can impact successful commercialization.

Secondly, specific areas of current research and development are presented that build upon this fundamental understanding. Although it is not possible in this limited space to discuss all the novel innovations currently under investigation in this rapidly growing field, the following applications have been selected for this discussion as representative examples: chemistry and catalysis in supercritical fluids, supercritical water oxidation (SCWO), gas–antisolvent (GAS) extraction, precipitation with a compressed fluid antisolvent (PCA), and rapid expansion from a supercritical solution (RESS). A separate review chapter (Chapter 26) is presented that discusses applications in the forest products industry. Finally, individual chapters of this volume are introduced in the discussion to highlight their relevance to current research in the field of supercritical fluid science and technology.

Solubility Measurement and Modeling

Precision and Accuracy. The first step in the technology development process is to establish proof of technical feasibility. In the context of applications involving SCFs, this stage usually involves the determination of the solubility of a single major component of the substrate to be extracted. The enhanced solubility of pure solid solutes in SCFs, compared with that predicted by ideal gas behavior, has been well documented, and there have been literally hundreds of systems for which solubility data have been reported. However, in the context of scale-up, the precision and accuracy of such data must be quantified in order to minimize uncertainty in the scale-up process. The SCF–solute system for which most solubility data have been reported is possibly that of naphthalene in supercritical carbon dioxide (SC-CO₂). The first data reported by Tsekhanskaya et al. (1) have frequently been used as a baseline of experimental reliability for researchers studying the solubility of other solutes in SC-CO₂. In other words, the naphthalene-CO₂ system has been used as a standard for calibrating solubility apparatus and, as is illustrated in Figure 1, the data from several studies demonstrate a high degree of consistency.

An essential component of efficient and successful scale-up is the availability of a model to enable process simulation to be undertaken and thus minimize expensive, real-time pilot plant investigations. This has been, and remains, a major hurdle for the large-scale utilization of the technology. Despite extensive studies, state-of-the-art equations-of-state (EOS) are still not capable of adequately and quantitatively predicting SCF behavior in even the simplest of systems. This problem is illustrated graphically in Figures 2 and 3, in which the naphthalene solubility data of Tsekhanskaya (1) have been correlated with the Peng–Robinson equation of state—one of the simplest and most commonly used EOS. Upon first examination, the EOS appears to provide an excellent correlation of the data over the entire range of solubility and pressure/density as shown in Figure 2. However, the expanded-scale illustration of the same data and model fit in Figure 3 clearly shows that this perception is incorrect. In the vicinity of the critical point, discrepancies between experimental and model values of more than 50% occur—and this, it is important to note, is for one of the most exhaustively studied systems for which data are available. It is also significant, as will be discussed later, that both components in the system (i.e., carbon dioxide and naphthalene) are readily available in high purity, and neither presents any difficulties with respect to chemical analysis.

The difficulties experienced in correlating data are even more pronounced when the chemical characterization of the solutes are not straight-forward, when high purity

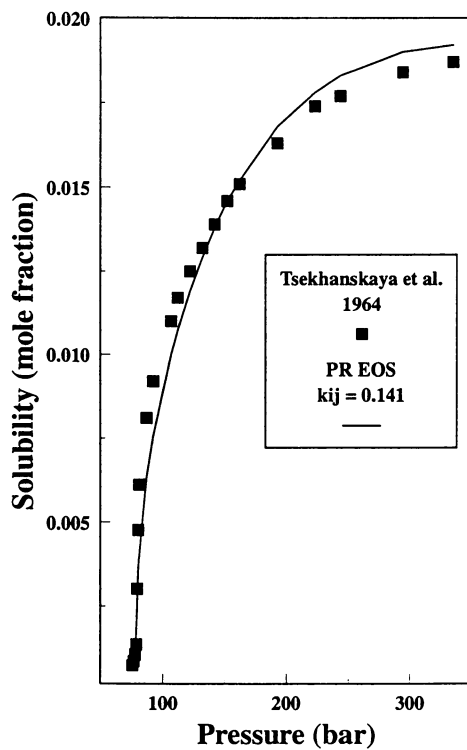


Figure 2. Solubility of Naphthalene in SC-CO₂ at 308.1 K (1) Correlated with the Peng-Robinson EOS.

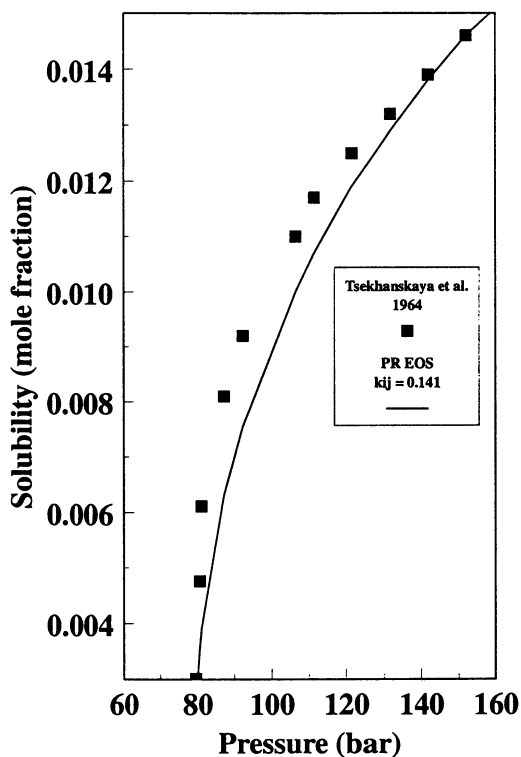


Figure 3. Solubility of Naphthalene in SC-CO₂ at 308.1 K (1) Correlated with the Peng-Robinson EOS with an Expanded Scale Showing Poor Fit in the 80-140 bar Region.

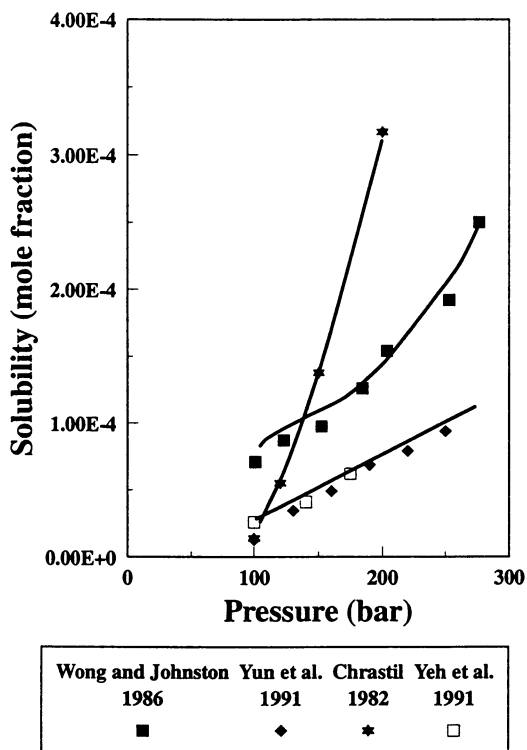


Figure 4. Solubility Data for Cholesterol in SC-CO₂ at 313.1 K (88-91).

material is not readily available, and when the solubility of the solute in the SC-CO₂ is low. The difficulties manifested by such systems are illustrated by example in Figures 4 to 6. The solubility data for cholesterol in SC-CO₂ (Figure 4) demonstrates the enormous discrepancies that exist in the published data, and the impact that such uncertainties would have on the scale-up process should they not be recognized could well be economically and technically catastrophic. The solubility of cholesterol in SC-CO₂ is approximately two orders of magnitude lower than for naphthalene, so calibration of the solubility apparatus with naphthalene would not necessarily provide a valid indication of the precision and accuracy of the cholesterol data. A difficulty also associated with such low solubilities is that gravimetric measurement becomes a very time consuming method for solubility measurement, and analytical techniques become the preferred option. The analysis of cholesterol is not straight-forward, and may require a derivitization step, thus introducing an additional source of error.

Cosolute Effects. The data presented in Figures 5 to 7 illustrate the significance that the presence of impurities in the solute can have on the integrity of solubility data. The oleic acid/SC-CO₂ system (Figure 5) has the additional complicating factor of the solute being liquid, and thus the nature of contacting between the two components to ensure that saturation has occurred is of considerable importance. The level of impurities for all three systems varied between 0.1 and 5 wt%. As is indicated by the data, discrepancies of up to two orders of magnitude exist, and the potential impact of this uncertainty in the quality of fundamental data on the scale-up process cannot be overstated.

The 1,1-bis(4-chlorophenyl)-2,2,2-trichloroethane (p,p'-DDT)/SC-CO₂ system (Figure 6) provides another example of solute impurity effects on the integrity of solubility data—it is clear that more than 60% of the initial solubility measured in this system is due to a “more volatile” component present in the solute at reportedly no greater than 0.1 wt%. It is unlikely that the effects observed as a consequence of the presence of impurities are always enhancements in solute solubility. Further, the impact of this behavior is more significant when considered in the context that most potential applications of SCF extraction technology involve extraction from a substrate consisting of multiple solutes. There have been a number of recent studies involving mixed solutes, that is ternary systems consisting of solute-1, solute-2 and a single SCF (2-9). In some of these systems the solubility of the individual solutes is greater than that observed in the binary systems consisting of the pure solutes and a single SCF. A specific example of this phenomenon has been observed by Kurnik and Reid (5). As is illustrated in Figure 7, a solubility enhancement of 280% was observed for benzoic acid (BA) when extracted with CO₂ from a mixture of BA and naphthalene compared with the equilibrium solubility for pure benzoic acid. This observation has considerable ramifications in the design of a commercial plant and on its capital and operating costs. A further complication is that, in some cases, the presence of a third component can lower the solubilities of each solute. Consequently, one cannot assume that solubility data obtained from binary systems will always provide the worst-case scenario (i.e., lowest solubility, highest solvent:feed ratio) for process design purposes.

The influence of the solute matrix on solubility can be explained in terms of an “entrainer effect” resulting from the modification of the SCF solvent properties by the more soluble solute. Whilst this “cosolvent phenomenon” has been observed in conventional liquids and is reasonably well understood in these systems, it must be remembered that supercritical fluids are not ideal systems and, as has already been demonstrated, the level of fundamental understanding despite over 100 years of

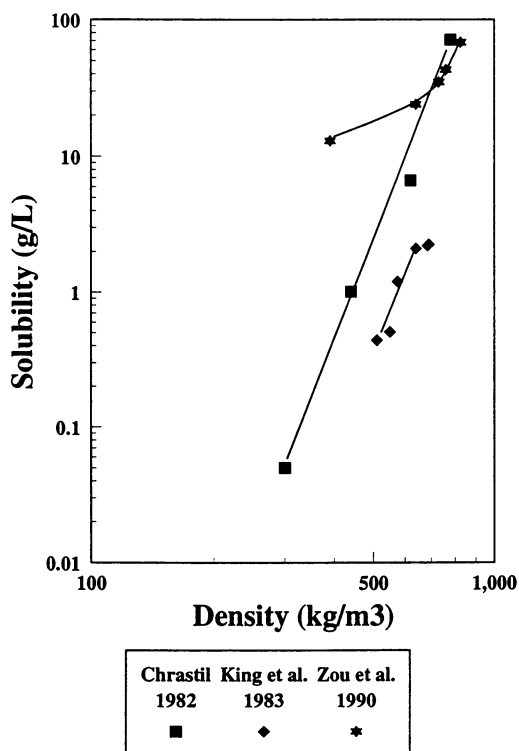


Figure 5. Solubility Data for Oleic Acid in SC-CO₂ at 333.1 K (90, 92-93).

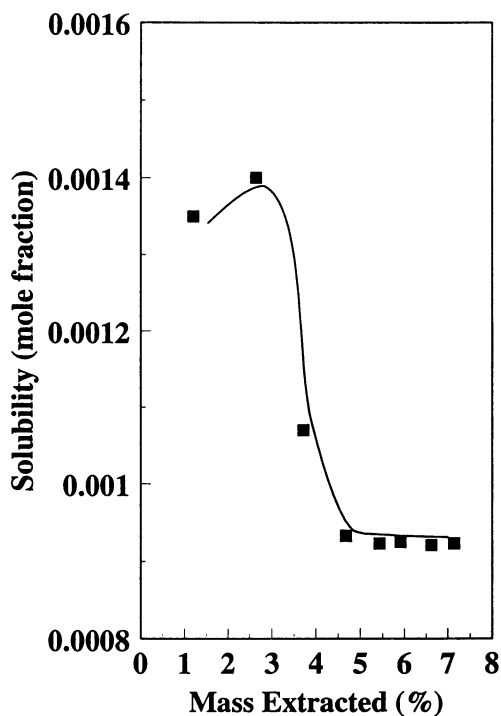


Figure 6. Purification of p,p'-DDT using SC-CO₂ at 333.1 K and 207.5 bar (9).

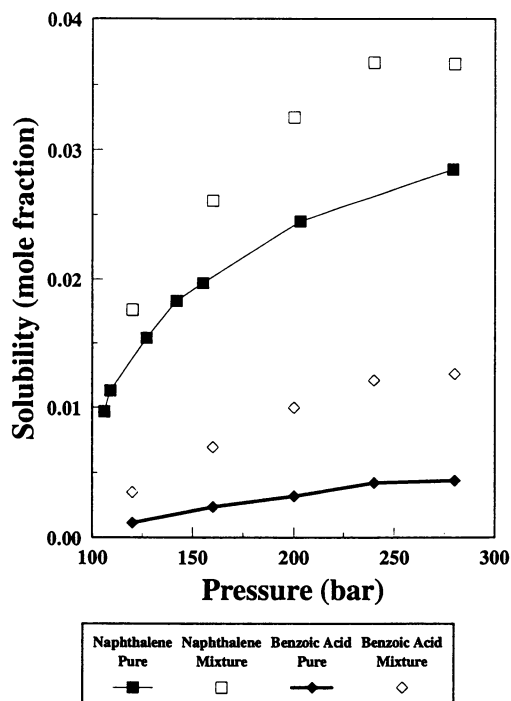


Figure 7. Solubility of Naphthalene, Benzoic Acid, and their Mixtures in SC-CO₂ at 318 K (5). Adapted from Reference 5.

research and development is still not sufficient to enable *a priori* predictions of single component solubility in even a commonly used SCF such as CO₂.

Whilst the continuation of investigations of binary systems is necessary for the development of a fundamental understanding of the behavior of supercritical fluids, it is appropriate that future research involves detailed studies of ternary SCF (solute-1/solute-2/SCF) systems with the objective of addressing the issue of the influence of mixture composition or solute-solute interactions on the solubility behavior of such systems. Bamberger et al. (6) have claimed that substantial changes in the composition of a ternary CO₂-solid triglyceride mixture had no influence on solute solubility or selectivity. However, it is likely that this behavior is a result of the heterogeneous nature of the triglyceride molecule—a characteristic that results in generally poor selectivities when extracting natural triglycerides with SC-CO₂ (10). In possibly the most recent study of ternary systems involving SC-CO₂, Macnaughton and Foster (9) investigated the influence on the mutual solubilities of the pesticide, p,p'-DDT, and the herbicide, (2,4-dichlorophenoxy)acetic acid (2,4-D), as part of an environmental engineering program. A single solubility isotherm was obtained for a 50 mol% mixture of the two solutes. These data are presented in Figure 8. The experimental precision on each data point was 3% and therefore, within the limits of the experiment, the solubility of the p,p'-DDT in the ternary system is not significantly different to the binary system. At the lower pressures, however, the 2,4-D solubilities were depressed by more than 10% which is too large to be a result of experimental error.

In order to develop a more fundamental understanding of the ternary system behavior, Macnaughton (11) used a novel solubility technique which utilized two equilibrium cells arranged in series, each being packed with a different solute. Supercritical CO₂ was passed through the first cell, during which it became saturated with solute 1, and was then passed through the second cell. The solute in the second cell was effectively being contacted with a CO₂-cosolvent mixture—the cosolvent being the solute in the first cell. The experiment was carried out with p,p'-DDT in the first column and 2,4-D in the second column and was then repeated with the order of the columns reversed. One isotherm of solubility data was measured at 313.1 K for both configurations. The data obtained with the first configuration showed that the solubility of 2,4-D was enhanced by up to 60%, whilst the solubility of p,p'-DDT was identical to that obtained for the binary p,p'-DDT-CO₂ system. The results obtained with the second configuration revealed a significant depression in 2,4-D solubility. The experimental consequences of this were quite serious because it meant that some of the 2,4-D in the supercritical phase that entered the second cell actually precipitated or was absorbed on the p,p'-DDT. Consequently, the second cell no longer contained pure p,p'-DDT but rather a mixture of p,p'-DDT and 2,4-D which essentially violated the purpose of the experiments. However, these experiments were repeated to confirm that the behavior observed was not anomalous.

Cosolvent Effects. In order to increase the solute solubility and/or selectivity and to reduce operating costs in continuous extraction processes, small amounts of cosolvents may be added to modify the polarity and solvent strength of the primary supercritical fluid (4, 12-14). The cosolvents, which are usually referred to as entrainers, are commonly polar or non-polar miscible organics.

To date, the solubility data for solid solutes in contact with binary solvent mixtures under supercritical conditions is limited. In addition, most of the currently available experimental data on the solubilities of pure and mixed solutes in SCF-cosolvent mixtures have been obtained at temperatures lower than the critical mixture

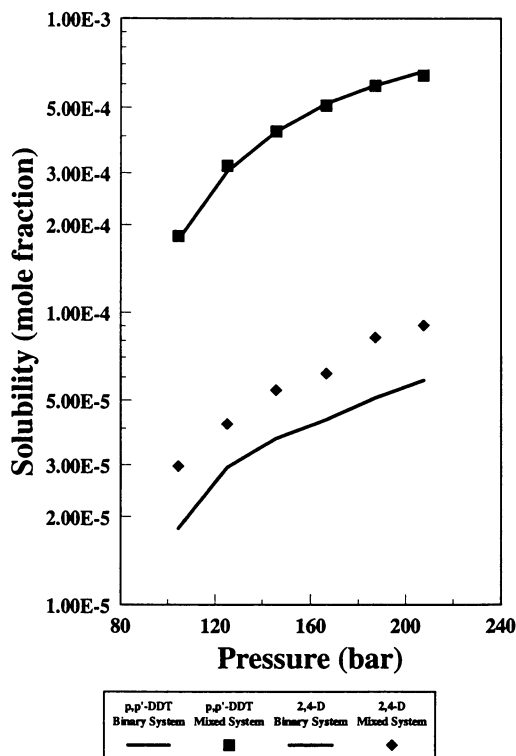


Figure 8. Solubility of p,p'-DDT, 2,4-D, and their Mixtures in SC-CO₂ at 313 K (11).

temperatures. To illustrate the enhanced solubility that can be obtained with the addition of organic cosolvents to a primary supercritical fluid such as carbon dioxide, the data obtained by Ting (15) are presented in Figures 9 and 10. The data demonstrate that cosolvents can enhance the solubility of solids in SCFs by orders of magnitude. This phenomenon is of substantial significance in the design of supercritical fluid processes. The use of cosolvents can enable the severity of operating conditions to be considerably reduced. For example, reductions in operating pressure associated with this approach could provide substantial capital cost savings in the design of a SCF extraction facility.

It has already been noted that the presence of impurities in the solute can induce significant enhancements or depressions in component solubility. A similar effect of cosolvent purity has also been reported, as demonstrated by the data presented in Figure 11 (16).

Correlation of Data. Numerous approaches have been taken in the search for correlative and predictive models of phase behavior in supercritical fluid systems, and there is no question that such investigations should continue in the future. However, the reliability, precision, and accuracy of data being used in model development must always be borne in mind. From the perspective of scale-up, the basis of such models does not need the same degree of fundamental rigor as is the case for molecular-based approaches to describing chemical interactions in supercritical fluid systems. Scale-up is often based on correlations which are valid for a limited range of boundary conditions of operating variables. Provided that the boundary conditions for a specific correlation are not traversed, such an approach can provide a powerful tool in process design. For example, simple semi-log plots of solute solubility as a function of SCF density can provide an excellent correlation of experimental data over a relatively wide range of temperature, as shown in Figure 12 for the cholesterol-ethane system (17). The fact that the solubility isotherms when presented in this manner are almost parallel also provides a high level of surety in interpolating between the extremes of temperature. However, caution should be exercised in using such a correlative technique as a general tool. The possible ramifications of this are illustrated in Figure 13, where it is clear that the solubility of p,p'-DDT in CO₂ does not follow the linear semi-log behavior demonstrated by the cholesterol-ethane system. However, as shown in Figure 14, a very high level of confidence in data correlation for the p,p'-DDT/CO₂ system can be obtained from a log-log regression. Once again, the parallel solubility isotherms obtained facilitate reliable interpolation of data. It is clear from the data presented that the absence of a fundamental, molecular-based model for predicting phase behavior in supercritical fluids does not necessarily prevent reliable scale-up from being achieved.

A number of papers in this volume specifically address the measurement and modeling of solubilities in SCFs, and others depend upon this aspect for actual implementation. For example, Ziegler et al. present a new experimental method for measuring the mixture critical curve for binary mixtures with CO₂ in Chapter 6. Macnaughton et al. report in Chapter 8 both predictive and experimental methods for the selection of cosolvents for the SCFE of pesticides from solid matrices. In Chapter 9, Knudsen et al. compare several classes of equations of state for the prediction of phase equilibria. Dooley et al. report in Chapter 18 results for the SCFE from polymeric matrices. Montero et al. describe the SCFE of hazardous contaminants from soils in Chapter 19, and in Chapter 20, Rahmé et al. describe a kinetic model for extractions. These latter three papers illustrate another physical

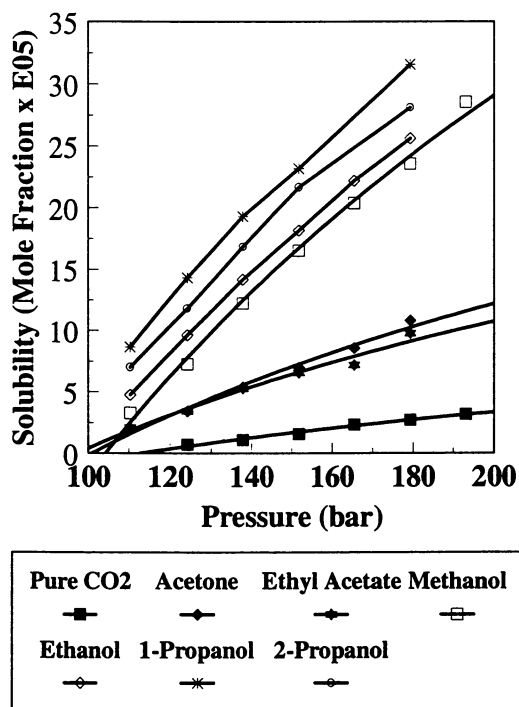


Figure 9. Solubility of Naproxen in Pure and Modified SC-CO₂ at 333.1 K using Various Cosolvents at 3.5 mol% (15).

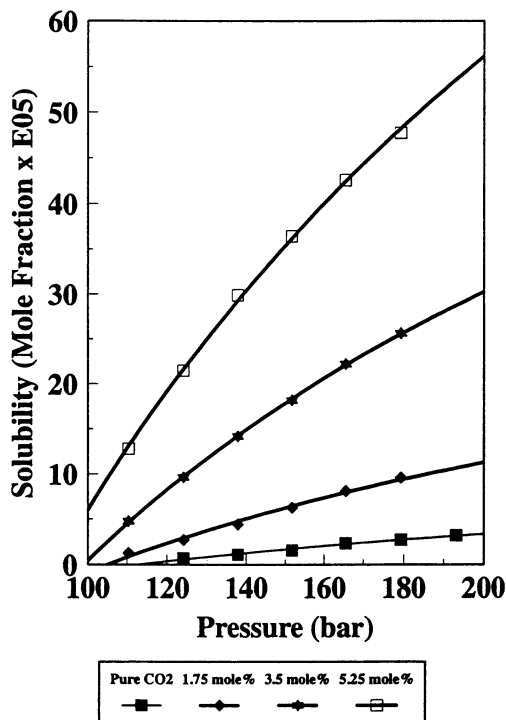


Figure 10. Solubility of Naproxen in Pure and Ethanol-Modified SC-CO₂ at 333.1 K (15).

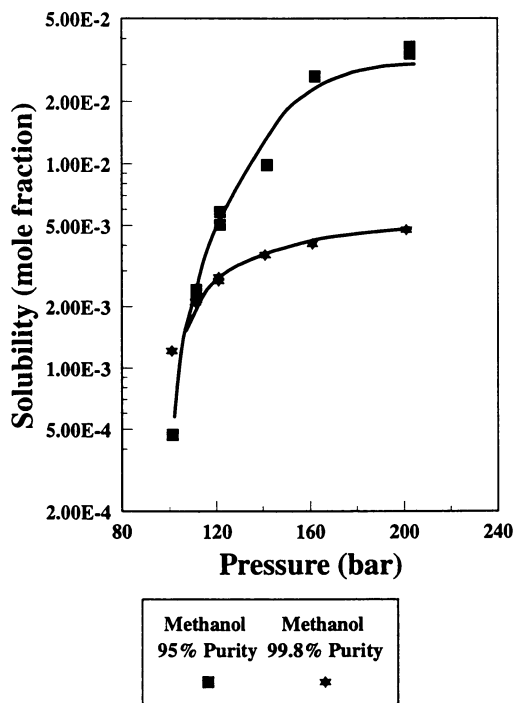


Figure 11. Effect of Cosolvent Purity on *o*-Hydroxybenzoic Acid Solubility at 328 K in SC-CO₂ Modified with 3.5 mol% Methanol (16).

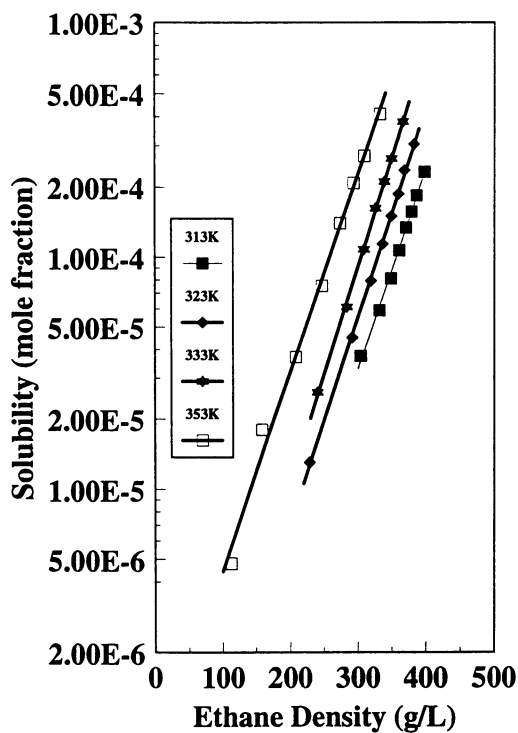


Figure 12. Semi-log Solubility Plot for Cholesterol in SC-Ethane (17).

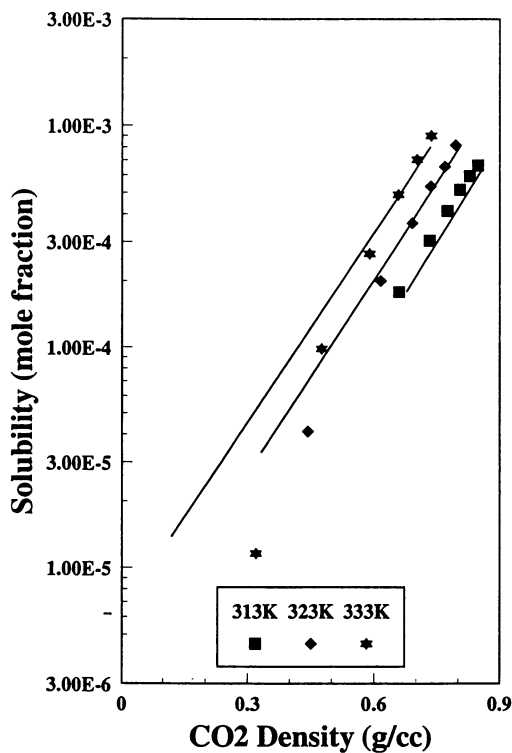


Figure 13. Semi-log Solubility Plot for p,p'-DDT in SC-CO₂.

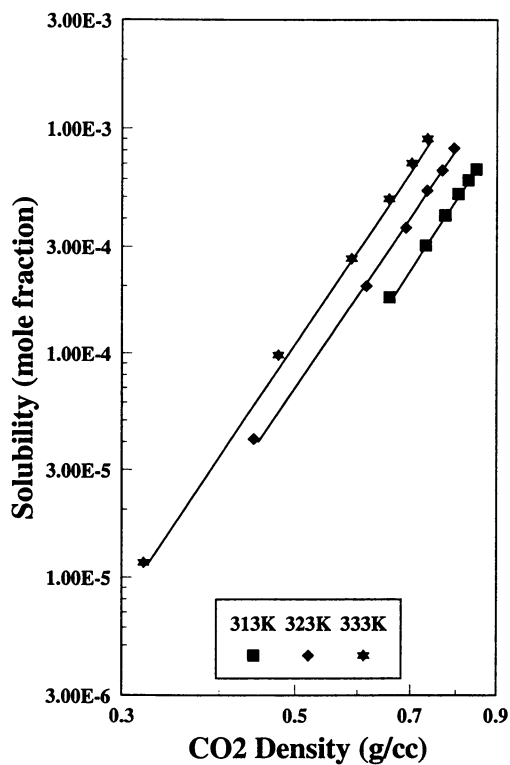


Figure 14. Log-log Solubility Plot for p,p'-DDT in SC-CO₂.

property of fundamental importance for rational design and scale-up—i.e., mass transfer coefficients. The SCFE of solutes from porous matrices such as polymers and soils are often mass transfer limited and require accurate measurements or estimates of transport coefficients for reliable scale-up. Discussion on this aspect of SCF technology is provided by Brunner (18).

Selected Examples of Innovations in SCF Technology

Chemistry and Catalysis in Supercritical Fluid Media. The application of SCF media for separations is now reasonably well established. Conducting chemical transformations in these media has enormous potential, but has thus far received relatively minor commercial implementation (with notable exceptions such as the high-pressure low-density polyethylene process). Growing environmental (and therefore, economic) pressures in waste minimization through source reduction rather than expensive end-of-pipe treatments continues to drive the chemical industry to evaluate alternative processes. Supercritical fluids can potentially address some of these concerns through, for example, solvent replacement with environmentally-benign (and, perhaps, less expensive) alternatives, the development of more efficient processes through enhanced yields and selectivities, the exploitation of enhanced catalyst recovery and prolonged catalyst life, and through the invention of novel reactive separation processes.

The literature in this area has been the subject of several reviews (19-25), the most recent being a comprehensive review by Savage, et al. (26). The research described in these reviews has clearly demonstrated the potential of using SCFs as reaction media for a variety of applications. Some of the potential advantages of conducting chemical reactions in SCF media are presented below, along with a representative sampling of papers from the literature illustrating selected applications and trends suggested by current research.

It is well known that the density-dependent properties of a SCF solvent (e.g., solubility, diffusivity, and viscosity) can be manipulated with relatively small changes in temperature and pressure. Polar solvents have the added feature of an adjustable dielectric constant. In chemical reaction applications, one can potentially exploit the resulting effects of these "tunable" solvent features in a variety of ways; for example, through enhancing component and catalyst solubilities (possibly even homogenizing a previously heterogeneous reaction), influencing kinetic rates through both temperature and pressure effects, shifting equilibrium constants to favor desired products, increasing selectivity and yields, reducing mass transfer limitations in diffusion-limited reactions, minimizing heterogeneous catalyst deactivation (through prevention of coking and extraction of fouling products or contaminants), and facilitating the separation and recovery of reaction products. There is tremendous opportunity for successfully exploiting these potential advantages in economical, commercial processes.

Solvent Replacement. As indicated above, solvent replacement represents an important motivation for exploring SCF reactions. Carbon dioxide and water have been the primary solvent candidates of choice in most of this research because they are both inexpensive and environmentally benign. For example, DeSimone et al. (27) report the replacement of conventional chlorofluorocarbon solvents with SC-CO₂ for the homogeneous free radical polymerization of fluoropolymers. As a more recent example, Tanko and Blackert (28) report the bromination of toluene and ethylbenzene in CO₂ at supercritical conditions using atomic bromide free radicals initiated

photochemically from molecular bromine. They report the production of the corresponding benzylic bromides in high yield with selectivities in SC-CO₂ essentially identical to that observed in the conventional chlorinated organic solvent, carbon tetrachloride.

High-temperature water (both sub- and supercritical) is an interesting reaction media for several additional reasons. For example, reaction chemistries can shift from heterolytic (ionic) to homolytic (free-radical) mechanisms as the density is varied from liquid- to gas-like values under supercritical conditions (29). In addition, the variable dielectric constant (30) and hydrogen bonding strength in the vicinity of the critical point result in some unique solvation properties such as the complete miscibility of most organics (23). As an example of published work, Siskin, Katritzky, and co-workers have presented a series of papers (see for example (31-33)) on reactions of many organic compounds in both sub- and supercritical water. They report enhanced reaction rates, the predominance of ionic reaction pathways at higher temperatures as an alternative to thermolytic, free-radical routes, and that water can function as an effective acid or base catalyst at these conditions.

Solvation in supercritical water is an important component of the application of this solvent as a reaction media. Indeed, this topic has been the subject of a number of recent studies (see for example (34)). Several papers in this book address some of the fundamental issues concerning solvation and hydrogen bonding in high-temperature aqueous environments. In Chapter 3, Savage and co-workers present the results of molecular dynamics simulations of hydrogen bonding in SCF water. Chialvo et al. present in Chapter 4 results of an investigation of solvation, hydrogen bonding, and ion-pairing for dilute NaCl solutions in SCF water. Johnston et al. describe in Chapter 5 the results of simulation and spectroscopic investigations of the solvation of electrolytes and nonelectrolytes in water at conditions ranging from ambient to supercritical conditions.

Homogeneous Catalysis. Several recent publications suggest that SCFs represent a very promising medium for homogeneous catalysis. For example, Poliakoff, Howdle, and co-workers (see for example (35)) have presented several fundamental studies on organometallic reactions, primarily using metal carbonyl complexes as catalysts. Rathke et al. (36, 37) report a method for the cobalt carbonyl catalyzed hydroformylation reaction converting an alkene to an aldehyde by reaction with carbon monoxide and hydrogen under supercritical conditions in CO₂. For their specific application of propylene hydroformylation, they report a significant enhancement of the yield of linear butyraldehyde product (*n:iso* molar ratio of 7.3 versus about 4 for other solvents in the conventional "oxo" process). Noyori and co-workers (38) report an interesting example of solvolytic homogeneous catalysis in SC-CO₂. These researchers show that under supercritical conditions, formic acid can be produced from the hydrogenation of CO₂ in the presence of certain ruthenium(II)-phosphine complex catalysts at substantially higher initial rates than in conventional liquid organic solvents, and about five times as fast as a similar synthesis in water reported recently by Gassner and Leitner (39). More recently, Tumas and co-workers (40) have applied homogeneous transition metal catalysis to selective olefin oxidations with encouraging preliminary results.

Heterogeneous Catalysis. There have been several studies of heterogeneous catalysis in SCF media, but this remains a largely unexplored area, particularly in terms of catalyst screening for specific applications. An early study by Tiltcher et al. (41) evaluated the relative merits of using SCF media in a comparative study on the

catalytic isomerization of 1-hexene and the disproportionation of 1,4-diisopropylbenzene performed under liquid, gaseous, and supercritical conditions. They reported a pronounced effect of temperature and pressure on catalytic activity in the supercritical region. Collins et al. (42) report enhanced *p*-xylene selectivity in the vicinity of the critical point for the disproportionation of toluene over a zeolite catalyst. Yokota, Fujimoto, and co-workers (see for example (43)) present results on a series of studies of the Fischer-Tropsch synthesis reaction to produce liquid hydrocarbons from synthesis gas (CO and H₂) over supported cobalt, iron, and ruthenium catalysts. Relative to gas- and liquid-phase processes, they report good heat transfer rates and the efficient removal of products from the catalyst pores, which effectively suppresses the hydrogenation of the primary olefin products. Partial oxidation applications of heterogeneous catalysis in SCF media is another emerging area, and a couple of examples (44, 45) are presented below.

Phase Transfer Catalysis. Liotta, Eckert, and co-workers (46) have recently reported what is apparently the first published application of phase transfer catalysis using a SCF phase; i.e., the nucleophilic displacement on benzyl chloride by bromide ion in the presence of tetraheptyl ammonium bromide. This study also presents solubility measurements for quaternary ammonium salts and 18-crown-6 ether in SC-CO₂ both with and without various cosolvents. This investigation opens many new possibilities for chemical transformations in SCF media.

Heterogeneous Catalyst Regeneration. Catalyst deactivation is of significant commercial importance in the design and operation of heterogeneous catalytic reactors. Tiltcher and Hofmann (47) discuss the potential advantages of using SCF media for *in situ* catalyst regeneration and present several examples where supercritical fluids have been evaluated for preventing or mitigating the deactivation of heterogeneous catalysts due to coking, fouling, and poisoning. In general, the solvation of deactivating components in a SCF mixture combined with the improved mass transport through catalyst pores (relative to liquid solutions) has shown the potential for improving catalyst activity and the *in situ* regeneration of deactivated catalysts. Much of this work has concentrated on the removal of coke precursors from catalysts before they react to form intractable carbon (26). More recently, Ginosar and Subramaniam (48) have reported the existence of optimum operating conditions in the supercritical region where deactivation rates are minimized in porous catalysts. In Chapter 16, Subramaniam and Jooma extend this previous work to show how the removal of peroxide impurities from olefinic feeds leads to further improvements in the maintenance of catalyst activity at supercritical conditions.

Selective Oxidations. This represents an important class of industrially-relevant reactions that has seen only limited research in SCF media (26). These reactions are often heterogeneously catalyzed in gas- and liquid-phase reactors and are typically characterized by mass transfer limitations, low conversions, and poor selectivities. SCFs are attractive for this class of reactions for many of the potential advantages mentioned previously. For example, in heterogeneous reactions, mass transfer limitations should be greatly reduced relative to the liquid-phase case, and there is a possibility for homogenizing the reaction through the use of soluble organometallic catalysts. Dooley and Knopf (44) present one of the earliest studies of partial oxidation reactions in a SCF media—the partial oxidation of toluene to benzaldehyde, benzyl alcohol, and the cresol isomers in SC-CO₂ in the presence of a supported cobalt oxide catalyst. Although they report low rates and conversions, this example

suggests the technical feasibility of the catalytic partial oxidation of alkyl aromatics in SCF solvents, which are of significant industrial importance. More recent published examples of this general reaction class report the partial oxidation of methane to methanol in both catalytic (45) and uncatalyzed (49) reactions.

Cycloadditions. There have been a number of studies over the last several years of Diels-Alder cycloaddition reactions in SCF media (20, 26). This class of reactions has been used, for example, to study pressure effects on reaction rates (50), stereoselectivity (51), and isomerization (52) in SCFs. In Chapter 11 of this volume, Knutson et al. present the results of a recent study of the Diels-Alder reaction of maleic anhydride and 2,3-dimethyl-1,3-butadiene in supercritical propane with both a reactive and an unreactive cosolvent.

Ionic Reactions. The potential for conducting ionic reactions in SCF media was mentioned previously for hydrothermal reactions. As an additional example, Brennecke, Chateauf, and co-workers present in Chapter 10 a study of solvent effects on intermolecular interactions and reactivity for ionic reactions in SCFs. Specifically, they measure reaction rates for the benzhydryl cation with tetramethylethylene and triethylamine in SCF fluoroform. This paper also represents the first application of a pulse radiolysis technique to monitor SCF reactions.

Enantioselective Synthesis. Asymmetric selectivity is becoming increasingly important in chemical synthesis, particularly in the pharmaceutical industry (53). Burke, Tumas, and co-workers (54) have recently reported the successful use of enantioselective catalysis in a hydrogenation application in SCF CO₂. This opens exciting new possibilities for biologically-active products where stereoselectivity is desired.

Enzymatic Reactions. Another emerging area of importance is that of enzyme-catalyzed reactions in SCFs. Randolph et al. (55), Clifford (25), and Savage et al. (26) provide reviews of the literature in this area, and general overviews are provided by Aaltonen and Rantakylä (56), Russell et al. (57), and Nakamura (58). Results presented in these reviews clearly show that enzymes retain their activity on exposure to SC-CO₂. In addition to the general characteristics of SCF solvents mentioned previously, enzyme-catalyzed reactions exhibit the additional potential advantages of pronounced chemo-, regio- and stereoselectivity for industrially-relevant compounds (57). Much of the work in this area has focused on lipase-catalyzed esterification reactions primarily in SC-CO₂, but also in other non-aqueous solvents. The enantioselective synthesis of chiral pharmaceuticals has also been demonstrated (59). Thus, conducting enzyme-catalyzed reactions in SCF media may provide an alternative process to conventional aqueous routes that results in high value-in-use products. This area will likely see growing attention as industrial interest in enzyme catalysis increases (60).

Polymerizations. Polymerization and polymer modifications in SCF media have seen widespread interest in recent years, and this trend will likely accelerate as industrial motivations such as solvent replacement become increasingly important. An overview of this rapidly growing field is beyond the scope of this summary, so the reader is referred to recent, comprehensive reviews of this area by Scholsky (61) and Kiran (62).

Supercritical Water Oxidation. An emerging technology in the environmental field that represents a more established application of reactions in SCFs is that of the oxidative destruction of organic wastes in supercritical water, a process known as Supercritical Water Oxidation (SCWO). Tester, et al. (63) have recently presented a comprehensive review of ongoing fundamental research in this area as well as the technological issues facing the commercial-scale development of this process. This technology was also the topic of a recent specialized conference sponsored by the U.S. Government Departments of Energy, Defense, and Commerce (64).

In general, the SCWO process is intended to carry out the total oxidative destruction of hazardous organic compounds in aqueous waste streams. Although a commercial SCWO process built by Eco Waste Technologies has recently begun operation (65), this facility is limited to waste streams that minimize the impact of two significant technical challenges facing this technology—scaling and corrosion. The broader challenge limiting widespread commercialization has been to develop a process capable of the efficient separation of inorganic salts to prevent scaling on heated surfaces and to accommodate the complete destruction of halogenated hydrocarbons with their associated corrosion. However, highly-efficient organic destruction has been reported at relatively low reactor residence times (on the order of one minute) for temperatures exceeding 550 °C. Under these conditions, many organic compounds are completely miscible with the water, as are oxidizers such as oxygen, peroxides, and nitrates. NO_x formation is essentially undetectable due to the relatively low temperatures (compared to incineration temperatures). This technology is receiving significant interest for specialized applications such as the destruction of chemical warfare agents, of organics in high-level radioactive wastes, and of highly-toxic specialty pharmaceuticals, but the process has not received broad acceptance by the chemical industry primarily due to concerns about the corrosion and scaling issues and the process economics.

A number of the papers in this volume represent fundamental and applied studies related to this technology. Chapters 3–5 report new fundamental studies of molecular interactions in supercritical water and the resulting effects on solvation and hydrogen bonding. In Chapter 14, Gopalan and Savage present an elementary, free-radical reaction mechanism to model the SCWO of a model aromatic compound (phenol) of fundamental interest. Dell'Orco et al. report in Chapter 12 a study on the use of nitrate and nitrite as oxidizers in the hydrothermal (both sub- and supercritical water) oxidation of model compounds for an important radioactive waste. In Chapter 13, Tester and co-workers describe both SCWO and hydrolysis of a chlorinated model compound in a plug flow reactor. Bourhis, et al. report in Chapter 23 on the effect of adding relatively small amounts of either hydrogen peroxide or nitric acid to the feed stream to enhance initial oxidation rates. Abraham and co-workers discuss in Chapter 15 the use of heterogeneous catalysts in SCWO to enhance complete oxidation at lower operating temperatures. Mitton et al. address in Chapter 22 one of the key technical concerns with commercializing this technology, that of process vessel corrosion. They report both general corrosion as well as pitting and stress corrosion cracking in high-nickel alloys. In Chapter 21, Downey and co-workers present results of another corrosion study as well as results for the SCWO of certain chemical weapon reagents. Blaney et al. describe in Chapter 30 another potential application of this technology: the processing of pulp and paper mill sludge. Chen et al. present in Chapter 24 the results of a simulation study for a concentric-tube reactor design.

Separations and Materials Formation with Compressed Fluid Antisolvents. Two approaches involving the use of compressed fluid antisolvents to effect separations have been investigated in recent years. The first, known as the gas anti-solvent (GAS) process, employs an often overlooked property of supercritical fluids, that is, their ability to dissolve in and expand numerous common organic solvents at moderate pressures. Upon dissolution of the SCF, the expanded organic solvent experiences a substantial decrease in its cohesive energy (solvent strength) enabling the selective precipitation of solutes. This scenario forms the basis for a process that shows great promise and is the object of much current interest. Applications as diverse as citric acid and β -carotene purification, purification and comminution of RDX explosive materials, the comminution of proteins, and the production of biodegradable powders and polymeric microspheres are currently being studied (66-70). The second variation, known as precipitation with a compressed fluid antisolvent (PCA) (71), involves spraying liquid solutions into gas, liquid, or supercritical fluid solvents to induce precipitation. It should be emphasized that the solvent must dissolve in the SCF in the PCA approach, and as such, this process is quite different from the GAS technique.

Several factors contribute to the attractiveness of the GAS process. Unlike the more traditional SCFE processes, the SCF is not the extracting solvent but actually a highly-soluble solute that forces other solutes out of solution (i.e., the SCF is an antisolvent). Many materials of interest in the area of SCFE (e.g., pharmaceutical compounds) possess high melting points and low vapor pressures, and thus have only low solubilities in SCFs, even at high pressures. Whilst such low solubilities make extraction and separation via SCFE unattractive, the low solubilities in the SCF antisolvent can benefit the GAS process. In addition, the solute handling capacity of the GAS process is dictated not by characteristically low SCF solubilities, but instead by the solubility of the solute in the organic solvent, which is normally many orders of magnitude higher.

While avoiding the low capacity problems of more traditional SCFE processes, it is important to note that the GAS process still takes advantage of many of the positive features of SCFs. The beneficial mass transport properties (low viscosity, high diffusivity) are responsible for the rapid dissolution of the SCF into the liquid phase. The sensitivity of the SCF density to changes in pressure and temperature are to some extent passed on to the expanded liquid phase, which also manifests rapid changes in density (and thence solvent power) with changes in temperature and pressure near the critical locus. In some respects, the GAS process can be seen as combining the best features of SCFE and conventional liquid solvent processing.

Another attractive feature of the GAS process is the degree of control that is possible over the crystallization process. The degree of dissolution of the SCF into the liquid phase, and hence its subsequent expansion, are primarily governed by the system pressure. As a result the yield of precipitate and its composition have been shown to be strong functions of pressure, a process variable which can be reproducibly achieved and much more rapidly manipulated than, for instance, the system temperature. Control of crystal morphology, particle size, and the size distribution of the resultant crystal population can also be exercised by control of the rate of addition of the SCF antisolvent.

Despite the obvious potential of the GAS process, very little is known of the effect of operating conditions on the resulting separation efficiencies and crystal morphologies. Quantitative findings are especially rare. Previous studies into the GAS process (66, 67, 72) have primarily concentrated on the purification of complex and difficult-to-characterize mixtures, while few (68, 73) have dealt with simplified

systems from which a fundamental understanding of the process can be acquired. In even fewer cases has a methodical study of single-solute GAS systems been linked to more complex systems involving the expansion of solutions containing multiple solutes (73). The consequent lack of basic understanding of the GAS process is a major hindrance to its commercialization. Part of the difficulty lies in the fact that the GAS process generally involves multiple solutes, a liquid solvent and a SCF antisolvent. In order to develop a fundamental understanding of the GAS process, it is necessary not only to examine the process itself, but also the interactions between the various components (solute + SCF, SCF + solvent, solute-1 + solute-2 + SCF, solute + SCF + solvent, and finally solute-1 + solute-2 + solvent + SCF).

In the PCA method, the solvent must dissolve in the SCF or undesired material is formed. The goal of the process is not to expand the liquid, but rather to achieve rapid two-way mass transfer to dry the materials being formed. The antisolvent is usually a liquid or a SCF rather than a gas, but the term "compressed fluid" is used to include all three states. The liquid is sprayed into the fluid through a nozzle, and the morphology is strongly influenced by the nature of the resulting jet. Because of orientation in this jet, a variety of morphologies may be made with PCA that cannot be achieved with the GAS technique, although both processes have interesting and practical potential applications. The PCA process has been used to form microspheres, microporous fibers, hollow microporous fibers, asymmetric membranes, highly oriented fibrils ($< 1 \mu\text{m}$), and microcellular foams (see for example (74)).

Rapid Expansion of Supercritical Fluid Solutions—the RESS Process. The manufacture of highly-uniform fine powders and microspheres using the RESS process has been demonstrated at bench and pilot scale. The principle of this exciting new technique exploits the unusual properties of supercritical fluids. The solubility of many organic compounds in SCFs are often enhanced to levels more than 10^6 times higher than the solubilities predicted from ideal gas considerations. If a SCF containing a dissolved solute is rapidly expanded to atmospheric pressure, then the supersaturation of the solute reaches very high levels, resulting in very rapid nucleation and, consequently, the production of a uniform fine powder. Results of the first serious study of RESS were published in 1984 (75), and numerous investigations have been reported since. The solute-SCF combinations that have been used include germanium oxide and water (76), polycaprolactone and CO_2 (77), and polycarbosilane and pentane (78). The application of RESS technology to the field of encapsulation was investigated in a recent study by Tom et al. (79). The production of composite drug-polymer (poly-L-lactic acid and lovastatin) microspheres using supercritical CO_2 was examined. The results indicate that whilst the concept may be technically feasible, a complete understanding of the mechanics of the process has not been achieved.

Many industries are replacing existing solvent extraction processes with SCFE plants because this eliminates the use of organic solvents and the associated waste treatment and handling problems. An area of considerable significance in this respect is the microencapsulation of active fragrance and flavor agents within a coating of a protective material. This technique is widely used in the food processing industry with more than 15,000 tons of encapsulated flavoring products being used within the United States each year (80). Many of the chemicals that are used in the flavor and fragrance industry are volatile, thermally labile, sensitive to oxidation, and relatively expensive. Microencapsulation is used to reduce the reactivity between the active agent and the outside environment, to enhance materials handling, and to achieve

controlled release of the active ingredient. The results of microencapsulation include extended shelf life of products, the prevention of loss of valuable components, the ability to utilize sensitive materials, and the capability of incorporating time-release mechanisms into products. Typical applications of microencapsulation are listed in Table I.

Table I. Typical Applications of Microencapsulation (81,82)

Achieving the gradual release of flavors during microwaving and fragrances in emollients.
The protection of aspartame during cooking.
Oxidation protection for sensitive oils and essences.
Protection during freeze/thaw cycles
Masking the taste of potassium chloride.
Reducing undesirable interactions between chemicals within a mixture—e.g., choline chloride and vitamins.

The basic process involves extracting both the flavor agent as well as the encapsulation material (usually starches or carbohydrates) and then expanding this solution through a small orifice to produce microspheres containing the active agent coated with the encapsulation material. The advantages of RESS are best illustrated with reference to existing microencapsulation technology.

A range of conventional techniques exist for achieving microencapsulation in the food and fragrance industries. Spray drying is the most common method of microencapsulation, and it is also the simplest. The active agent as well as the encapsulation material are combined in an emulsion and then atomized through a nozzle into a drying chamber where hot air evaporation leads to the formation of an impervious surface film. Although widely used and relatively simple, the major drawbacks of this technique are the elevated temperatures (> 100 °C), which can degrade sensitive materials, and the potential for oxidation of the active agent. The overall loss of active ingredient within the drier can be as high as 50% and is a function of the feed composition (81). Another important technique is the extrusion of the active ingredient and the coating material. Although low temperature extrusion processes have been developed, typical temperatures are still in the range of 85 to 130 °C which prohibits the processing of volatile and temperature-sensitive materials. Alternative techniques used for achieving microencapsulation include spray chilling, fluidized bed coating, centrifugal extrusion, coacervation, and cocrystallization. Two potential disadvantages of many of these processes include the difficulty of processing thermally-sensitive compounds and the potential for product contamination if additional chemicals such as surfactants are used in the treatment. In addition, the composition of the encapsulated particles is often constrained to undesirable levels of below 10-15% active agent by the processing technique. Generally, the production of particles with higher concentrations is accompanied with unacceptable losses of the valuable ingredient.

The RESS process has the potential to eliminate some of these problems. The processing temperature can be as low as 40 °C which would eliminate problems of chemical decomposition or loss of activity caused by the elevated temperature processes listed above. The production of composite particles of poly-L-lactic and lovastatin with lovastatin concentrations of 20 to 37% has been reported (79), which indicates that the composition of the encapsulated product can be varied as a function

of the supercritical solution composition. A further advantage of this technique is that the only chemicals necessary for treatment would be the encapsulation material, the active agent, and CO₂, thus eliminating all potential for contamination of the final product with residual solvent. The potential exists to develop a processing technology that can yield tailor-made particles that have extended shelf life and can be used for a range of applications, in particular facilitating the microencapsulation of substances that are currently difficult or impossible to treat with existing techniques.

Supercritical Fluids in the Forest Products Industry. Another interesting application area for supercritical fluid technology is found in the forest products industry, including pulp and paper processing. Kiran presents an overview of this area in Chapter 26 as well as some new results for polymer impregnation in wood. This review chapter is followed by several additional chapters describing particular applications of SCF technology of interest in the industry. Hassan, et al. describe in Chapter 27 experimental phase behavior measurements for several wood preservatives in SC-CO₂. In Chapter 28, Sahle-Demessie et al. present results on impregnation of such chemical preservatives into wood using SCFs. In Chapter 29, Vandana and Teja present results on the extraction of the promising cancer drug taxol from the bark of yew trees using SC-CO₂. And finally, Blaney, et al. present in Chapter 30 results of an application of SCWO for the treatment of pulp and paper mill sludge. Although not specifically included in the discussion in these chapters, another interesting extension of this natural products area is the SCFE of other medicinally-active compounds and of natural flavors from plant sources (see for example (83)). In Chapter 25, Hortacsu et al. present results on the mathematical modeling of release mechanisms of such extractable compounds from plant matrices during SCFE.

Acknowledgments

We would like to acknowledge DuPont for providing the time and resources for one of us (KWH) to edit this volume and to organize the symposium upon which the book is based.

References

1. Tsekhanskaya, Y. V.; Iomtev, M. B.; Mushkina, E. V. *Russ. J. Phys. Chem.* **1964**, *38*, 1173.
2. Pennisi, K. J.; Chimowitz, E. H. *J. Chem. Eng. Data* **1986**, *31*, 285.
3. Chang, H.; Morrell, D. G. *J. Chem. Eng. Data* **1985**, *30*, 74.
4. Dobbs, J. M.; Johnston, K. P. *Ind. Eng. Chem. Res.* **1987**, *26*, 1476.
5. Kurnik, R. T.; Reid, R. C. *Fluid Phase Equilib.* **1982**, *8*, 93.
6. Bamberger, T.; Erickson, J. C.; Cooney, C. L.; Kumar, S. K. *J. Chem. Eng. Data* **1988**, *33*, 327.
7. Tan, C. S.; Weng, J. Y. *Fluid Phase Equilib.* **1987**, *34*, 37.
8. Gopal, J. S.; Holder, G. D.; Kosal, E. *Ind. Eng. Chem. Process Des. Dev.* **1985**, *24*, 697.
9. Macnaughton, S. J.; Foster, N. R. *Ind. Eng. Chem. Res.* **1994**, *33*, 2757.
10. Tilly, K. D.; Chaplin, R. P.; Foster, N. R. *Sep. Sci. Tech.* **1990**, *25*, 357.
11. Macnaughton, S. J. PhD Thesis, University of New South Wales, Australia, 1994.
12. Schmitt, W. J.; Reid, R. C. *J. Chem. Eng. Data* **1986**, *31*, 204.

13. Dobbs, J. M.; Wong, J. M.; Johnston, K. P. *J. Chem. Eng. Data* **1986**, *31*, 303.
14. Dobbs, J. M.; Wong, J. M.; Lahiere, R. J.; Johnstone, K. P. *Ind. Eng. Chem. Res.* **1987**, *26*, 56.
15. Ting, S. S. T.; Macnaughton, S. J.; Tomasko, D. L.; Foster, N. R. *Ind. Eng. Chem. Res.* **1993**, *32*, 1471.
16. Gurdial, G. S. PhD Thesis, University of New South Wales, Australia, 1992.
17. Singh, H.; Yun, S. L. J.; Macnaughton, S. J.; Tomasko, D. L.; Foster, N. R. *Ind. Eng. Chem. Res.* **1993**, *32*, 2841.
18. Brunner, G. *Gas Extraction: An Introduction to Fundamentals of Supercritical Fluids and the Application to Separation Processes*; Topics in Physical Chemistry; Steinkopff: Darmstadt, Germany, 1994, Vol. 4.
19. Subramaniam, B.; McHugh, M. A. *Ind. Eng. Chem. Res.* **1986**, *25*, 1.
20. Catalytica Study No. 4189 NM; Catalytica, Inc.; Mountain View, CA, 1990.
21. Wu, B. C.; Paspek, S. C.; Klein, M. T.; LaMarca, C. In *Supercritical Fluid Technology: Reviews in Modern Theory and Applications*; T. J. Bruno and J. F. Ely, Eds.; CRC Press: Boca Raton, FL, 1991; p 511.
22. Caralp, M. H. M.; Clifford, A. A.; Coleby, S. E. In *Extraction of Natural Products Using Near-Critical Solvents*; M. B. King and T. R. Bott, Eds.; Chapman & Hall: Glasgow, UK, 1993; p. 50.
23. Shaw, R. W.; Brill, T. B.; Clifford, A. A.; Eckert, C. A.; Franck, E. U. *Chem. Eng. News* **1991**, *69(51)*, 26.
24. Brennecke, J. F. In *Supercritical Fluid Engineering Science*; E. Kiran and J. F. Brennecke, Eds.; ACS Symposium Series No. 514; American Chemical Society: Washington, D.C., 1993; p 201.
25. Clifford, A. A. In *Supercritical Fluids: Fundamentals for Application*; NATO ASI Series. Series E: Applied Sciences; E. Kiran and J. M. H. Levelt Sengers, Eds.; Kluwer Academic: Dordrecht, 1994; Vol. 273; p 449.
26. Savage, P. E.; Gopalan, S.; Mizan, T. I.; Martino, C. J.; Brock, E. E. *AIChE J.* **1995**, *41*, 1723.
27. DeSimone, J. M.; Guan, Z.; Eisbernd, C. S. *Science* **1992**, *257*, 945.
28. Tanko, J. M.; Blackert, J. F. *Science* **1994**, *263*, 203.
29. Xu, X.; De Almeida, C.; Antal, M. J., Jr. *J. Supercrit. Fluids* **1990**, *3*, 228.
30. Franck, E. U. In *Organic Liquids: Structure, Dynamics, and Chemical Properties*; A. D. Buckingham, E. Lippert and S. Bratos, Eds.; Wiley: New York, 1978; p 181.
31. Siskin, M.; Katritzky, A. R. *Science* **1991**, *254*, 231.
32. Kuhlmann, B.; Arnett, E. M.; Siskin, M. *J. Org. Chem.* **1994**, *59*, 3098.
33. Katritzky, A. R.; Barcock, R. A. *Energy & Fuels* **1994**, *8*, 990.
34. Cochran, H.D.; Cummings, P.T.; Karaborni, S. *Fluid Phase Equilib.* **1992**, *71*, 1.
35. Howdle, S. M.; Jobling, M.; Poliakoff, M. In *Supercritical Fluid Technology: Theoretical and Applied Approaches to Analytical Chemistry*; F. V. Bright and M. E. P. McNally, Eds.; ACS Symposium Series No. 488; American Chemical Society: Washington, D.C., 1992; p 121.
36. Rathke, J. W.; Klingler, R. J.; Krause, T. R. *Organometallics* **1991**, *10*, 1350.
37. Rathke, J. W.; Klingler, R. J. U.S. Patent 5,198,589, 1993.
38. Jessop, P. G.; Ikariya, T.; Noyori, R. *Nature* **1994**, *368*, 231.
39. Gassner, F.; Leitner, W. *J. Chem. Soc., Chem. Commun.* **1993**, *19*, 1465.
40. Feng, S.; Le Lacheur, R. M.; Morgenstern, D. A.; Buelow, S.; Mitchell, M.; Burns, C. J.; Tumas, W. Presented at the 1994 Annual A.I.Ch.E. Meeting, San Francisco, CA, November, 1994; paper 120c.

41. Tiltscher, H.; Wolf, H.; Schelchshorn, J. *Ber. Bunsenges. Phys. Chem.* **1984**, *88*, 897.
42. Collins, N. A.; Debenedetti, P. G.; Sundaresan, S. *AIChE J.* **1988**, *34*, 1211.
43. Fan, L.; Yokota, K.; Fujimoto, K. *AIChE J.* **1992**, *38*, 1639.
44. Dooley, K. M.; Knopf, F. C. *Ind. Eng. Chem. Res.* **1987**, *26*, 1910.
45. Dixon, C. N.; Abraham, M. A. *J. Supercrit. Fluids* **1992**, *5*, 269.
46. Suleiman, D.; Boatright, D. L.; Dillow, A. K.; Liotta, C. L.; Eckert, C. A., submitted for publication in *Tetrahedron Lett.*, 1995.
47. Tiltscher, H.; Hofmann, H. *Chem. Eng. Sci.* **1987**, *42*, 959.
48. Ginosar, D. M.; Subramaniam, B. In *Catalyst Deactivation 1994*; Studies in Surface Science and Catalysis; B. Delmon and G. F. Froment, Eds.; Elsevier: Amsterdam, 1994; Vol. 88; p 327.
49. Savage, P. E.; Li, R.; Santini, J. T., Jr. *J. Supercrit. Fluids* **1994**, *7*, 135.
50. Paulaitis, M. E.; Alexander, G. C. *Pure & Appl. Chem.* **1987**, *59*, 61.
51. Kim, S.; Johnston, K. P. *Chem. Eng. Comm.* **1988**, *63*, 49.
52. Ikushima, Y.; Saito, N.; Arai, M. *J. Phys. Chem.* **1992**, *96*, 2293.
53. Stinson, S. C. *Chem. Eng. News* **1994**, *72(38)*, 38.
54. Burke, M. J.; Gross, M. F.; Feng, S.; Tumas, W. submitted for publication in *Science*, 1995.
55. Randolph, T. W.; Blanch, H. W.; Clark, D. S. In *Biocatalysis in Industry*; J. S. Dordick, Ed.; Plenum: New York, 1991; p 219.
56. Aaltonen, O.; Rantakylä, M. *CHEMTECH* **1991**, *21*, 240.
57. Russell, A. J.; Beckman, E. J.; Chaudhary, A. K. *CHEMTECH* **1994**, *24*, 33.
58. Nakamura, K. In *Proceedings of the 3rd International Symposium on Supercritical Fluids*; G. Brunner and M. Perrut, Eds.; Strasbourg, France, 1994; Vol. 3; p 121.
59. Aaltonen, O.; Rantakylä, M. In *Proceedings of the 2nd International Symposium on Supercritical Fluids*; M. A. McHugh, Ed.; Boston, MA, 1991; p 146.
60. Gerhartz, W. *Enzymes in Industry*; VCH Publishers: New York, 1990.
61. Scholsky, K. M. *J. Supercrit. Fluids* **1993**, *6*, 103.
62. Kiran, E. In *Supercritical Fluids: Fundamentals for Application*; NATO ASI Series. Series E: Applied Sciences; E. Kiran and J. M. H. Levelt Sengers, Eds.; Kluwer Academic: Dordrecht, 1994; Vol. 273; p 541.
63. Tester, J. W.; Holgate, H. R.; Armellini, F. J.; Webley, P. A.; Killilea, W. R.; Hong, G. T.; Barner, H. E. In *Emerging Technologies in Hazardous Waste Management III*; D. W. Tedder and F. G. Pohland, Eds.; ACS Symposium Series No. 518; American Chemical Society: Washington, D.C., 1993; p 35.
64. *First International Workshop on Supercritical Water Oxidation*; Jacksonville, FL, February 6-9, 1995.
65. McBrayer, R. Presented at the 1995 Spring National A.I.Ch.E. Meeting, Houston, TX, 1995; paper 69b.
66. Shishikura, A.; Takahashi, H.; Arai, K. In *Proceedings of the 2nd International Symposium on Supercritical Fluids*; M. A. McHugh, Ed.; Boston, MA, 1991; p 299.
67. Chang, C. J.; Randolph, A. D. *Biotech. Prog.* **1991**, *7*, 275.
68. Gallagher, P. M.; Krukonis, V. J. In *Proceedings of the 2nd International Symposium on Supercritical Fluids*; M. A. McHugh, Ed.; Boston, MA, 1991; p 45.
69. Yeo, S.-D.; Lim, G.-B.; Debenedetti, P. G.; Bernstein, H. *Biotech. & Bioeng.* **1993**, *41*, 341.

70. Randolph, T. W.; Randolph, A. D.; Mebes, M.; Yeung, S. *Biotech. Prog.* **1993**, *9*, 429.
71. Dixon, J. D.; Johnston, K. P.; Bodmeier, R. A. *AIChE J.* **1993**, *39*, 127.
72. Liou, Y.; Chang, C. J. *Sep. Sci. Tech.* **1992**, *27*, 1277.
73. Chang, C. J.; Liou, Y. *J. Chem. Eng. Jap.* **1993**, *26*, 517.
74. Dixon, D. J.; Luna-Barcenas, G.; Johnston, K. P. *Polymer* **1994**, *35*, 3998.
75. Krukonis, V. Presented at the 1984 National A.I.Ch.E. Meeting, Houston, TX, 1984; paper 140f.
76. Petersen, R. C.; Matson, D. W.; Smith, R. D. *J. Am. Chem. Soc.* **1986**, *108*, 2100.
77. Lele, A. K.; Shine, A. D. *Polymer Preprints (ACS)* **1990**, *31(1)*, 677.
78. Matson, D. W.; Petersen, R. C.; Smith, R. D. *Mater. Lett.* **1986**, *4*, 429.
79. Tom, J. W.; Lim, G.-B.; Debenedetti, P. G.; Prud'homme, R. K. In *Supercritical Fluid Engineering Science*; E. Kiran and J. F. Brennecke, Eds.; ACS Symposium Series No. 514; American Chemical Society: Washington, D.C., 1993; p 238.
80. Brannon-Peppas, L. In *Polymeric Delivery Systems*; M. A. El-Nokay, D. M. Piatt, and B. A. Charpentier, Eds.; ACS Symposium Series No. 520; American Chemical Society: Washington, D.C., 1993; p 42.
81. Shahadi, F.; Han, X.-Q. *Crit. Rev. in Food Sci. and Nutr.* **1993**, *33*, 501.
82. Greenblatt, H.; Dombroski, M.; Klishevich, W.; Kirkpatrick, J.; Bajwa, I.; Garrison, W.; Redding, B. K. In *Encapsulation and Controlled Release*; Royal Society of Chemistry: Cambridge, UK, 1993; p 148.
83. *Extraction of Natural Products Using Near-Critical Solvents*; King, M. B.; Bott, T. R., Eds.; Chapman & Hall: Glasgow, UK, 1993.
84. Wells, P. A. PhD Thesis, University of New South Wales, Australia, 1991.
85. Lemert, R. M.; Johnston, K. P. *Fluid Phase Equilib.* **1990**, *59*, 31.
86. Sako, S.; Ohgahki, K.; Katayama, T. J. *J. Supercrit. Fluids* **1988**, *1*, 1.
87. McHugh, M. A.; Paulitis, M. E. *J. Chem. Eng. Data* **1980**, *25*, 326.
88. Wong, J. M.; Johnston, K. P. *Biotech. Prog.* **1986**, *2*, 29.
89. Yun, S. L. J.; Liang, K. K.; Gurdial, G. S.; Foster, N. R. *Ind. Eng. Chem. Res.* **1991**, *30*, 2476.
90. Chrastil, J. *J. Phys. Chem.* **1982**, *86*, 3016.
91. Yeh, A.-I.; Liang, J. H.; Hwang, L. S. *J. Am. Chem. Soc.* **1991**, *68*, 224.
92. King, M. B.; Alderson, D. A.; Fallah, F. H.; Kassim, D. M.; Kassim, K. M.; Sheldon, J. R.; Mahmud, R. S. In *Chemical Engineering at Supercritical Fluid Conditions*; M. E. Paulaitis, J. M. L. Penninger, R. D. Gray, Jr. and P. Davidson, Eds.; Ann Arbor Science: Ann Arbor, MI, 1983; p 31.
93. Zou, M.; Yu, Z.-R.; Kashulines, P.; Rizvi, S. S. H. *J. Supercrit. Fluids* **1990**, *3*, 23.

RECEIVED July 24, 1995

Chapter 2

Molecular-Based Approach to Gas Solubility at Near-Critical Conditions

A. A. Chialvo^{1,2}, Yu. V. Kalyuzhnyi^{1,3}, and P. T. Cummings^{1,2}

¹Department of Chemical Engineering, University of Tennessee,
Knoxville, TN 37996-2200

²Chemical Technology Division, Oak Ridge National Laboratory,
Oak Ridge, TN 37831-6268

Exact expressions for Henry's constant, the solute distribution factor, and Ostwald coefficient along the solvent's orthobaric curve are derived through the statistical mechanical interpretation of the second derivative of the system's Helmholtz free energy at infinite dilution $A_{vx}^\infty = -(\partial P/\partial x_2)_{T,p}^\infty$. This quantity, whose critical value — Krichevskii's parameter — defines the asymptotic behavior of several important solvation properties at criticality, allows a natural splitting of the system's thermodynamic properties into solute-induced (finite) and compressibility driven (diverging) contributions. The observed disparity between the critical and the fitted asymptotic behavior as well as the density³ dependencies of Henry's constant and the solute distribution factor along the coexistence curve are then statistical mechanically interpreted. In addition, the linearity (or lack thereof) in the orthobaric density dependencies of coefficients away from the solvent's critical point is rationalized. Finally, the formalism is illustrated with integral equation calculations for infinitely dilute binary solutions of hard core Yukawa fluids.

Despite more than twenty years of intense activity in the field of gas solubility and its importance in several application-oriented topics of interest such as biomedical technology (the enhanced oxygen solubility in perfluorinated hydrocarbons as blood substitutes and gas carriers in liquid breathing (1)), anesthesia (2), environmental pollution control (oxygen and ozone in water for waste water treatment), geochemistry (undersea gas hydrates (3)), and chemical process design (enhanced oil recovery, gas sweetening, sludge oxidation), accurate high-temperature gas solubility data are still scarce. The extrapolation of low-temperature behavior to higher

³Permanent address: Institute for Condensed Matter Physics, 290011 Lviv, Ukraine

0097-6156/95/0608-0034\$12.00/0
© 1995 American Chemical Society

temperatures is not an appropriate approach because the solubility of gases along the saturation curve decreases with temperature, goes through a minimum, and then increases steadily as the system approaches the solvent's critical point (4). This behavior, which appears to be a universal feature for aqueous and non-aqueous near-critical solvents (5) prompted some authors to seek some phenomenological justification (5-7).

In particular, Japas and Levelt Sengers (7) derived the limiting temperature dependence of Henry's constant and the solute distribution factor K^∞ and presented two useful linear correlations for these quantities in terms of the so called Krichevskii's parameter and the solvent's orthobaric density around the solvent's critical point. Later, Wilhelm (8) suggested an alternative asymptotically linear relation involving the Ostwald's coefficient L^∞ , rather than of the K^∞ , arguing that this quantity might show a wider linear range than that for K^∞ .

Although more insightful than the phenomenological approach, the elucidation of the molecular mechanism underlying the solubility of gases in liquids represents a formidable challenge and has eluded chemical engineers searching for better macroscopic correlations to properly describe the temperature dependence of gas solubility. The solvation process has usually been portrayed as the transfer of a solute molecule from a fixed point in an ideal gas phase to a fixed point in a condensed phase composed of a solvent at constant pressure (or volume), temperature, and composition (9). Therefore, this microscopic interpretation characterizes the solvation phenomenon as a solvent effect in that the final state involves solute-solvent interactions which are absent in the initial state. Although there is nothing wrong with this approach, we find more convenient for our purposes to interpret solvation as the local rearrangement (perturbation) of the solvent structure around the solute molecule with respect to that around any solvent molecule at the same temperature and density, i.e., the perturbation from the structure of the ideal solution. It becomes immediately clear that this perturbation is the result of the solute-solvent molecular asymmetry (nonideality), i.e., a solute-induced effect (10).

As the infinitely dilute system approaches the solvent's critical condition, the solvation quantities may be obscured by the diverging critical quantities so that it is imperative to be able separate the two contributions. We have recently pointed out that the coexistence of both short- (solvation) and long-ranged (compressibility driven) effects makes supercritical solutions challenging to model, but, at the same time, this feature suggests a natural way to characterize their thermodynamic properties in terms of solvation and compressibility driven contributions (10). This characterization allows us to evaluate the impact of molecular asymmetry on the system's thermodynamic properties by discriminating between the effects due to the perturbation (solvation) and those due to its propagation (compressibility driven). Based on this idea we have recently developed a rigorous molecular-based formalism to establish the microscopic basis of supercritical solvation in terms of well-defined molecular correlation function integrals (10).

The main question we will address in this paper is how such a characterization can be used to shed some light on the solvation of gases in near-critical solvents from a statistical mechanical rather than a phenomenological viewpoint. In this paper we briefly review an extension of the previous solvation formalism for dilute mixtures based entirely on the statistical mechanical interpretation of the second derivative of the system's Helmholtz free energy at infinite dilution, $A_{vx}^\infty = -(\partial P / \partial x_2)_{T,p}^\infty$. First, we derive rigorous statistical mechanical expressions for the temperature dependence of Henry's constant and the distribution coefficient (and consequently Ostwald coefficient) along the vapor-liquid coexistence curve in terms of the volumetric and entropic solute-induced effects. Then, we discuss the rationale behind the observed linearity of the orthobaric density dependence of these coefficients in the vicinity of

the solvent's critical point. Finally, we present some integral equation calculations to illustrate our formalism for infinitely dilute binary solutions of hard core Yukawa fluids.

Theoretical Background

Let us consider a system composed of N molecules interacting with the same intermolecular potential, i.e., an *ideal solution* of $(N-1)$ molecules labelled solvent and one molecule labelled solute in a volume V , at temperature T , and total pressure P . The infinitely dilute solution can be formed in a "thought solvation process" in which a solvent molecule (labelled solute in the ideal solution) *mutates* into a true solute molecule. This hypothetical process, the realization of Kirkwood's coupling parameter charging (see (11) for details), involves an isothermal-isobaric coupling work equal to the difference of residual chemical potential between the infinitely dilute solute and the pure solvent at constant temperature and either constant volume or pressure (10)

$$\mu_2^{\infty}(T,P) - \mu_1^{r0}(T,P) = \int_0^{\rho(P)} \left(\frac{\partial P}{\partial x_2} \right)_{T,\rho}^{\infty} \frac{d\rho}{\rho^2} \quad (1)$$

where superscripts r , o , and ∞ indicate a residual property, a pure component, and an infinitely dilute solution, respectively. We have recently derived several equivalent statistical mechanical expressions which depict this derivative as the isothermal-isochoric finite pressure change induced by the microscopic rearrangement of the solvent structure around the infinitely dilute solute relative to that in the corresponding ideal solution (pure solvent) (12). Consequently, from a microscopic viewpoint this derivative measures the amplitude of the solute-induced perturbation of the solvent structure, whose effect propagates out a distance proportional to the solvent's correlation length. Since the latter is proportional to the solvent's isothermal compressibility, the propagation distance diverges at the solvent's critical point even though the amplitude of the perturbation, and consequently $(\partial P/\partial x_2)_{T,\rho}^{\infty}$, remain finite (13). In particular, at the solvent's critical point, $(\partial P/\partial x_2)_{T_c,\rho_c}^{\infty}$ defines Krichevskii's parameter (for a detailed discussion see (10,12-14)).

According to the statistical mechanical interpretation of $(\partial P/\partial x_2)_{T,\rho}^{\infty}$ and its finiteness we can point out that the species residual chemical potentials are finite and involve short-ranged interactions, e.g., those associated with the rearrangement of the solvent structure around the solute. Accordingly, we can also define the short-ranged (SR) enthalpic and entropic counterpart of equation (1), i.e., the enthalpic and entropic solute-induced effects in terms of $(\partial P/\partial x_2)_{T,\rho}^{\infty}$ and/or its temperature derivative (10). Here we simply quote the resulting expressions (Chialvo *et al.*, submitted to *AICHE J.*)

$$\bar{v}_2^{\infty}(\text{SR}) - \bar{v}_1^0 = (\beta/\rho^2)(\partial P/\partial x_2)_{T,\rho}^{\infty} \quad (2)$$

for the *volumetric solute-induced effect*,

$$\begin{aligned} \left[\bar{h}_2^{\text{r}\infty}(\text{SR}) - h_1^{\text{r}0} \right]_{\text{T,P}} &= \int_0^{\rho(\text{P})} \left(\frac{\partial \text{P}}{\partial x_2} \right)_{\text{T},\rho}^{\infty} \frac{d\rho}{\rho^2} + \beta \int_0^{\rho(\text{P})} \left(\frac{\partial(\partial \text{P}/\partial x_2)_{\text{T},\rho}^{\infty}}{\partial \beta} \right)_{\rho,x} \frac{d\rho}{\rho^2} \\ &\quad - \left(\frac{\beta}{\rho} \right)^2 \left(\frac{\partial \text{P}}{\partial \beta} \right)_{\rho} \left(\frac{\partial \text{P}}{\partial x_2} \right)_{\text{T},\rho}^{\infty} \end{aligned} \quad (3)$$

for the *enthalpic solute-induced effect* and,

$$\begin{aligned} \left[\bar{s}_2^{\text{r}\infty}(\text{SR}) - s_1^{\text{r}0} \right]_{\text{T,P}} &= - \left(\frac{k\beta^3}{\rho^2} \right) \left(\frac{\partial \text{P}}{\partial x_2} \right)_{\text{T},\rho}^{\infty} \left(\frac{\partial \text{P}}{\partial \beta} \right)_{\rho}^{\infty} \\ &\quad + k\beta^2 \int_0^{\rho(\text{P})} \left(\frac{\partial(\partial \text{P}/\partial x_2)_{\text{T},\rho}^{\infty}}{\partial \beta} \right)_{\rho,x} \frac{d\rho}{\rho^2} \end{aligned} \quad (4)$$

corresponding to the *entropic solute-induced effect*, where \bar{v}_2^{∞} is the solute partial molar volume at infinite dilution, $\bar{v}_1^0 = \rho^{-1}$, $\beta = 1/kT$, k is Boltzmann's constant, and the first integral in the right-hand-side of equation (3) is just $(\mu_2^{\text{r}\infty}(\text{T},\rho) - \mu_1^{\text{r}0}(\text{T},\rho))$. Note also that by substituting equation (2) into equations (3)-(4) and recalling the definition of a residual property at constant density and temperature, we also have that,

$$\left[\bar{h}_2^{\text{r}\infty}(\text{SR}) - h_1^{\text{r}0} \right]_{\text{T,P}} = \left[\bar{u}_2^{\text{r}\infty}(\text{SR}) - u_1^{\text{r}0} \right]_{\text{T},\rho} - \beta \left(\frac{\partial \text{P}}{\partial \beta} \right)_{\rho} \left[\bar{v}_2^{\infty}(\text{SR}) - v_1^0 \right]_{\text{T},\rho} \quad (5)$$

where $[...]_{\alpha,\beta}$ indicates that the residual properties between brackets are defined at fixed values of the variables (α,β) , u denotes internal energy and,

$$\left[\bar{s}_2^{\text{r}\infty}(\text{SR}) - s_1^{\text{r}0} \right]_{\text{T,P}} = \left[\bar{s}_2^{\text{r}\infty}(\text{SR}) - s_1^{\text{r}0} \right]_{\text{T},\rho} - \beta \left(\frac{\partial \text{P}}{\partial \beta} \right)_{\rho} \left[\bar{v}_2^{\infty}(\text{SR}) - v_1^0 \right]_{\text{T},\rho} \quad (6)$$

Therefore, from equations (3)-(6) the change of Gibbs free energy for the solvation process of an infinitely dilute solute in a pure solvent can be recast as,

$$\begin{aligned} \Delta G_{\text{solvation}} &= \left[\bar{h}_2^{\text{r}\infty}(\text{SR}) - h_1^{\text{r}0} \right]_{\text{T,P}} - T \left[\bar{s}_2^{\text{r}\infty}(\text{SR}) - s_1^{\text{r}0} \right]_{\text{T,P}} \\ &= \left[\bar{u}_2^{\text{r}\infty}(\text{SR}) - u_1^{\text{r}0} \right]_{\text{T},\rho} - T \left[\bar{s}_2^{\text{r}\infty}(\text{SR}) - s_1^{\text{r}0} \right]_{\text{T},\rho} \end{aligned} \quad (7)$$

which indicates that the solvation can be entirely characterized by the finite perturbation of the solvent structure due to the presence of the solute, i.e., compressibility driven effects play no explicit role in this process.

Gas solvation in particular involves systems with $(\partial P/\partial x_2)_{T,p}^{\infty} > 0$, i.e., volatile solutes (13) or weakly attractive and repulsive systems in the classification of Debenedetti and Mohamed (15). The volumetric solute-induced effect, according to equation (2), translates as a short-ranged contribution of the solute partial molar volume at infinite dilution being smaller than the pure solvent molar volume. In microscopic terms this means that the solvation shell around the solute is solvent-depleted. This behavior suggests at least a pair of obvious questions: What is the role played by the solute-induced effects in the solvation of gases? Is there any molecular (statistical mechanical) connection between the temperature dependence of the gas solubility coefficients and the thermal solute-induced effects? In the next section we address these questions in relation to the gas solubility at near critical conditions.

Temperature Dependence of Henry's Constant and Solute Distribution Factor

The derived expressions for the volumetric and thermal solute-induced effects are now applied to study the orthobaric temperature dependence of Henry's constant, $H_{2,1}(T)$, and the solute distribution coefficient, $K^{\infty}(T)$. Along the orthobaric curve σ these two quantities can be written as (7)

$$\ln[H_{2,1}(T)/f_1^{\circ}(T)] = \beta a_x^{r\infty} \quad (8)$$

and,

$$\begin{aligned} \ln K^{\infty}(T) &= \lim_{x_2 \rightarrow 0} \ln(y_2/x_2) \\ &= \beta(a_x^{r\infty} - a_y^{r\infty}) \end{aligned} \quad (9)$$

where x_2 and y_2 denote the solute mole fractions in the liquid and vapor phases, respectively, $a^r = A^r/N$ is the residual Helmholtz free energy per molecule, $a_{\alpha}^{r\infty} = (\partial a^r/\partial \alpha)_{T,p}^{\infty}$, superscript ∞ indicates infinite dilution, and α denotes the solute's mole fraction in either phase. For the sake of completeness we also mention Ostwald's coefficient, L^{∞} , which is related to K^{∞} as follows,

$$L^{\infty} = (K^{\infty})^{-1}(\rho_{\sigma}^l/\rho_{\sigma}^v) \quad (10)$$

Note also that the composition derivative, $a_{\alpha}^{r\infty}$, is given by the integral

$$a_{\alpha}^{r\infty} = \int_0^{p(P_{\sigma})} \left(\frac{\partial P}{\partial \alpha_2} \right)_{T,p}^{\infty} \frac{dp}{\rho^2} \quad (11)$$

Therefore, according to equations (8)-(10), the temperature dependence $H_{2,1}(T)$ and $K^\infty(T)$ are directly associated to the temperature dependence of the integral (11) along the saturation line, i.e.,

$$\left(\frac{da_\alpha^{\text{r}\infty}}{dT}\right)_\sigma = \left(\frac{\partial a_\alpha^{\text{r}\infty}}{\partial T}\right)_\rho + \left(\frac{\partial a_\alpha^{\text{r}\infty}}{\partial \rho}\right)_T \left(\frac{d\rho}{dT}\right)_\sigma \quad (12)$$

where the partial derivatives of $a_\alpha^{\text{r}\infty}$ are simply the phase's *volumetric solute-induced effect*,

$$\left(\frac{\partial a_\alpha^{\text{r}\infty}}{\partial \rho}\right)_T = \beta^{-1} \left[\bar{v}_2^\infty(\text{SR}) - v_1^0 \right]_{T,\rho}^{\sigma(\alpha)}, \quad \alpha = x, y \text{ and } \sigma(\alpha) = l, v \quad (13)$$

and the phase's *entropic solute-induced effect*,

$$\left(\frac{\partial a_\alpha^{\text{r}\infty}}{\partial T}\right)_\rho = - \left[\bar{s}_2^{\text{r}\infty}(\text{SR}) - s_1^{\text{r}0} \right]_{T,\rho}^{\sigma(\alpha)}, \quad \alpha = x, y \text{ and } \sigma(\alpha) = l, v \quad (14)$$

with $s^{\text{r}}(T, \rho)$ being the residual entropy per molecule (7). Therefore, according to equation (8), the orthobaric temperature dependence of $\ln(H_{2,1}/f_1^0)$ is directly linked to the behavior of the *solute-induced effects* on the properties of the condensed phase, i.e.,

$$\begin{aligned} \ln[H_{2,1}(T)/f_1^0(T)] = & (T_c/T) \ln[H_{2,1}(T_c)/f_1^0(T_c)] \\ & - \beta \int_{T_c}^T \left(\bar{s}_2^{\text{r}\infty}(\text{SR}) - s_1^{\text{r}0} \right)_{T,\rho^l} dT + T^{-1} \int_{\rho_c}^{\rho^l} T_\sigma \left(\bar{v}_2^\infty(\text{SR}) - v_1^0 \right)_{T,\rho^l} d\rho^l \end{aligned} \quad (15)$$

Analogously from equation (9), the orthobaric temperature dependence of $\ln K^\infty(T)$ is linked to the difference in *solute-induced effects* between the two phases in vapor-liquid equilibrium, i.e.,

$$\begin{aligned} \ln K^\infty(T) = & -\beta \int_{T_c}^T \left[\left(\bar{s}_2^{\text{r}\infty}(\text{SR}) - s_1^{\text{r}0} \right)_{T,\rho^l} - \left(\bar{s}_2^{\text{r}\infty}(\text{SR}) - s_1^{\text{r}0} \right)_{T,\rho^v} \right] dT \\ & + T^{-1} \left[\int_{\rho_c}^{\rho^l} T_\sigma \left(\bar{v}_2^\infty(\text{SR}) - v_1^0 \right)_{T,\rho^l} d\rho^l - \int_{\rho_c}^{\rho^v} T_\sigma \left(\bar{v}_2^\infty(\text{SR}) - v_1^0 \right)_{T,\rho^v} d\rho^v \right] \end{aligned} \quad (16)$$

where $K^\infty(T_c)=1$. Note that, for the sake of clarity in our analysis, we have used the "macroscopic" forms (as opposed to the statistical mechanical interpretation) of the solute-induced effects. A detailed analysis of the statistical mechanical counterpart of these effects are given elsewhere (10).

In what follows, we seek an interpretation of the conditions that the solute-induced effects should satisfy, in the vicinity of the solvent's critical point, in order for $H_{2,1}(T)$ and $K^\infty(T)$ to follow the linear behavior depicted by the asymptotic expressions proposed by Japas and Levelt Sengers (7), i.e.,

$$T \ln(H_{2,1}/f_1^0) = A + \left(\frac{1}{k\rho_c^2} \right) \left(\frac{\partial P}{\partial x_2} \right)_{T_c, \rho_c}^\infty (\rho^1 - \rho_c) \quad (17)$$

and,

$$T \ln K^\infty = \left(\frac{2}{k\rho_c^2} \right) \left(\frac{\partial P}{\partial x_2} \right)_{T_c, \rho_c}^\infty (\rho^1 - \rho_c) \quad (18)$$

where the constant $A \equiv T_c \ln[H_{2,1}(T_c)/f_1^0(T_c)]$ (16) and ρ^1 is the orthobaric liquid density with a critical value ρ_c .

The asymptotic expression (17) implies, according to equation (15), that the integral of the entropic solute-induced effect in the condensed phase must be negligibly small in comparison with the other two terms in equation (15). Likewise, the asymptotic expression (18) implies that the solute-induced effects in both phases are of similar sizes in the neighborhood of the solvent's critical point, so that the first integral in equation (16) cancels out while the second can be replaced by a density-averaged value, i.e., $\rho_c^{-2}(\partial P/\partial x_2)_{T_c, \rho_c}^\infty \equiv \overline{\rho^{-2}(\partial P/\partial x_2)_{T_c, \rho_c}^\infty}$. A more complete interpretation of the validity and the rationale behind the success of these asymptotic equations is discussed elsewhere (Chialvo *et al.*, submitted to *AICHE J.*).

Integral Equation Calculations

In this section we illustrate the thermodynamic behavior of an infinitely dilute solution of neon (Ne) along the coexistence curve of the solvent, xenon (Xe), and extract some important information about the orthobaric density dependence of $(\partial P/\partial x_2)_{T_c, \rho}^\infty$ in the vicinity of the solvent's critical point. The system is modeled as a two-component hard core Yukawa fluid (HCYF) (17), for which the intermolecular potential $\phi_{ij}(r)$ is,

$$\phi_{ij}(r) = \begin{cases} \infty & \text{if } r < \sigma_{ij} \\ \omega_{ij}(r) & \text{if } r > \sigma_{ij} \end{cases} \quad (19)$$

where σ_{ij} is hard-sphere diameter for the ij -interaction, and

$$\omega_{ij}(r) = -\frac{\epsilon_{ij}\sigma_{ij}}{r} \exp(-\alpha_{ij}(r - \sigma_{ij})) \quad (20)$$

Although real fluids do not follow this behavior, they can be qualitatively described by this simple model. In particular, the parameters σ_{ij} and ϵ_{ij} can be identified with the corresponding size and energy Lennard-Jones parameters, and the unlike interactions follow the Lorentz-Berthelot combining rules. Following Henderson *et al.* (17) we choose $\alpha_{ij}\sigma_{ij}=1.8$ for all ij -pairs.

The rationale behind this choice is twofold: despite its simplicity this model shows a vapor-liquid phase transition and, within the mean spherical approximation (MSA) closure, this model offers an analytical solution to the Ornstein-Zernike equation (18). According to the analysis of the previous sections, the integral equations calculations must be carried out using a theory which is able to provide a consistent description of both the structure and the thermodynamics in the vicinity of the solvent's critical point. By consistency we mean that the critical point of the liquid-vapor coexisting curve, obtained from the condition of equal chemical potentials and pressure in both phases, should coincide with the critical point of the spinodal line defined by the condition $\beta(\partial P/\partial \rho)_T = 1 - \rho \hat{c}(\mathbf{0}) = 0$.

To achieve this consistency we have chosen the generalized MSA (GMSA), which for the present two-component system reads,

$$\begin{cases} c_{ij}(r) = -\beta\omega_{ij}(r) + r^{-1} \sum_{n=1}^N A_{ij}^{(n)} \exp(-z_{ij}^{(n)}r) & \text{if } r > \sigma_{ij} \\ h_{ij}(r) = -1 & \text{if } r < \sigma_{ij} \end{cases} \quad (21)$$

where the Yukawa terms are introduced to correct the regular MSA for thermodynamic self-consistency. If the contact values of the radial distribution functions $g_{ij}(r)$ are known, then the method of Høye and Stell (19) can be used to determine the Yukawa coefficients in equation (21) which will enforce thermodynamic consistency.

In the present study we consider an infinitely dilute solution, which means that the correction is only done for the solvent-solvent correlation, and for simplicity, we truncate the summation of Yukawa terms at $N=2$, with $\sigma_{11}z_{11}^{(1)}=9$ and $\sigma_{11}z_{11}^{(2)}=16$.

The parameters $A_{11}^{(n)}$ ($n=1,2$) follow from the solution of the constraints imposed on the contact values of the pair correlation functions and the isothermal compressibility, i.e., the condition of thermodynamic consistency. One way to do this is by means of an equation of state derived via the MSA energy route (19) which yields quite accurate thermodynamics. However, for the sake of simplicity, here we used the thermodynamic results from a perturbation theory presented elsewhere (17). In addition, the solute-solvent interactions must be chosen such that the solvent and solute chemical potentials become equal for the limiting condition in which the solute potential parameters become identically the same as those for the solvent. To satisfy this condition we assume the convenient though arbitrary relation for the Yukawa parameters,

$$\begin{aligned} \sigma_{ij}z_{ij}^{(n)} &= \sigma_{11}z_{11}^{(n)} \\ A_{ij}^{(n)} &= \frac{\epsilon_{ij}\sigma_{ij}}{\epsilon_{11}\sigma_{11}} A_{11}^{(n)} \end{aligned} \quad (22)$$

The solution of the GMSA with the Yukawa coefficients as defined in equation (22) is obtained by the Baxter factorization method (20). The general scheme of the solution is similar to that presented elsewhere (21,22). In the present case the analytical solution results in a set of non-linear algebraical equations for the Yukawa parameters, $A_{11}^{(n)}$, together with the parameters related to the Baxter factorization functions. We solve this set of equations by an iterative approach as described by Kalyuzhnyi and Holovko (23). In summary, this formalism gives a self-consistent description of both thermodynamics and microstructure for the model in the entire region of state conditions of interest.

In Figure 1 we show the vapor-liquid coexistence curve for the pure solvent, described as a hard sphere Yukawa fluid. Note that the binodal and spinodal curves meet at the critical conditions, i.e., $kT_c/\epsilon_{11} = 1.2561$ and $\rho_c \sigma_{11}^3 = 0.3129$ where σ_{11} and ϵ_{11} are the solvent's size and energy parameters.

In what follows we study an infinitely dilute solute 2 in a solvent 1 characterized by a ratio of size parameters $(\sigma_{22}/\sigma_{11}) = 0.697$ and a ratio of energy parameters $(\epsilon_{22}/\epsilon_{11}) = 0.142$. These ratios correspond to the system Ne(2)-Xe(1) if described as Lennard-Jones spheres (10).

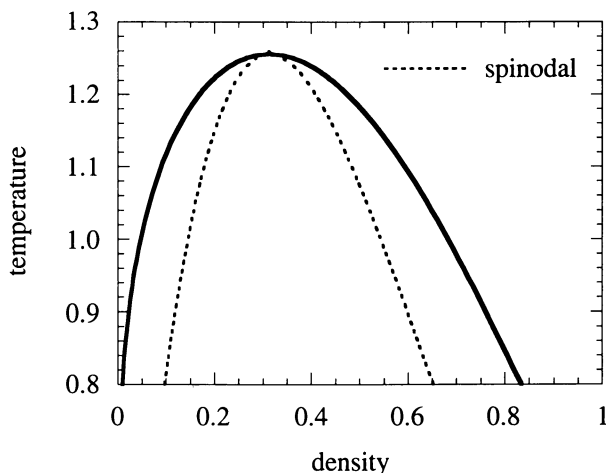


Figure 1. Phase envelope of a hard core Yukawa fluid with $\alpha_{11}\sigma_{11}=1.8$ as predicted by the integral equation calculations. Temperature and density in units of ϵ_{11} and σ_{11} .

Figure 2 shows the comparison between the behavior of the infinitely dilute solute partial molar volume, \bar{v}_2^∞ , and its corresponding short-range (SR) contribution, $\bar{v}_2^\infty(\text{SR})$, along the coexistence curve of pure solvent as predicted by the integral equation calculations. In Figure 3 we show the behavior of $\bar{v}_2^\infty(\text{SR})$ in more detail.

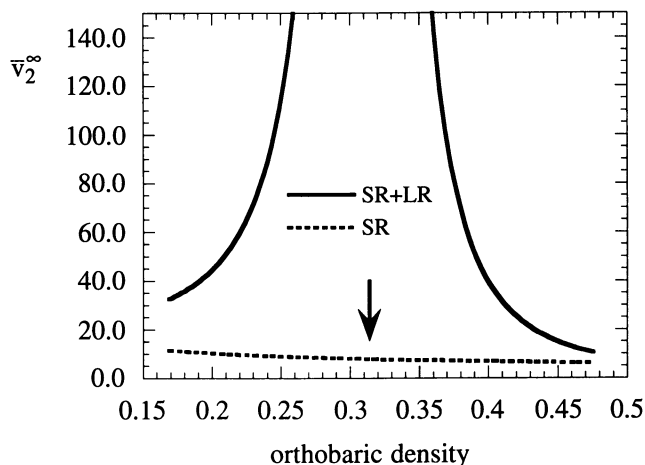


Figure 2. Orthobaric density dependence of the infinite dilute solute partial molar volume for the hard core Yukawa solution with $\alpha_{11}\sigma_{11}=1.8$. Comparison between the total (SR+LR) and the short-range (SR) contributions. Volume and density in units of σ_{11} .

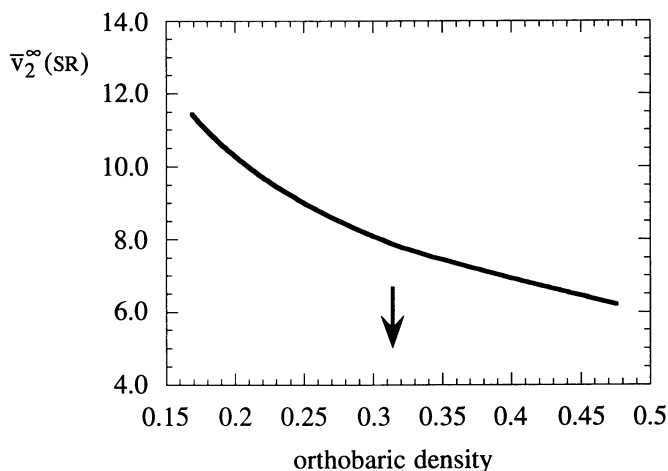


Figure 3. Orthobaric density dependence of the short-ranged contribution to the infinite dilute solute partial molar volume for the hard core Yukawa solution with $\alpha_{11}\sigma_{11}=1.8$. Arrow indicates the location of the solvent's critical density. Volume and density in units of σ_{11} .

The orthobaric density dependence of $(\partial P/\partial x_2)_{T,\rho}^\infty$ for this type of mixture is shown in Figure 4 in comparison with two special cases; one in which $\sigma_{22} = \sigma_{11}$ and $\epsilon_{22} = 0.142\epsilon_{11}$, and the other in which $\sigma_{22} = 0.697\sigma_{11}$ and $\epsilon_{22} = \epsilon_{11}$.

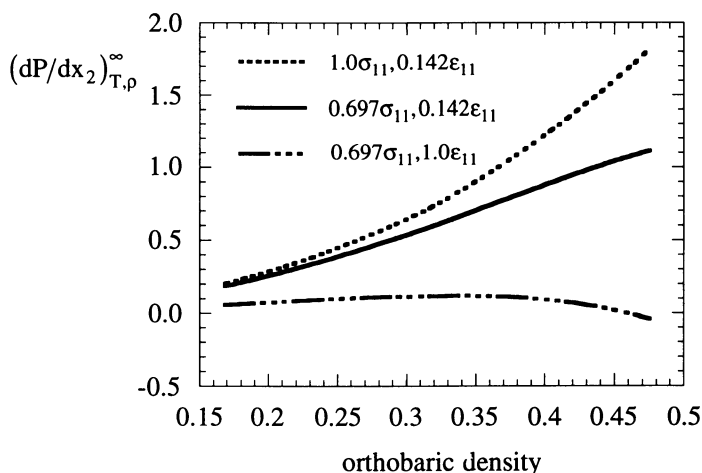


Figure 4. Comparison between the orthobaric density dependence of $(\partial P/\partial x_2)_{T,\rho}^\infty$ for three repulsive infinitely dilute hard core Yukawa fluid mixtures with $\alpha_{11}\sigma_{11}=1.8$. The coefficients indicate the relative sizes of σ_{22} and ϵ_{22} with respect to the solvent's parameters. Pressure and density in units of in units of ϵ_{11} and σ_{11} .

Note that the change in the solute's size and energy parameters, σ_{22} and ϵ_{22} , shows opposite effects on $(\partial P/\partial x_2)_{T,\rho}^\infty$. This behavior may explain the quasi-linearity on the orthobaric density dependence of $(\partial P/\partial x_2)_{T,\rho}^\infty$. In Figure 5 we show that as the size of the solute's potential parameters approaches those of the solvent, $(\partial P/\partial x_2)_{T,\rho}^\infty$ becomes negligibly small, i.e., the solution becomes ideal. From Figures 4 and 5 we find that within the density range ($0.74 \leq \rho_r \leq 1.28$), the average value of $(\partial P/\partial x_2)_{T,\rho}^\infty$ along the orthobaric curve, i.e.,

$$\overline{\rho^{-2}(\partial P/\partial x_2)_{T,\rho}^\infty} = (1/2\Delta) \int_{\rho_c - \Delta}^{\rho_c + \Delta} (\partial P/\partial x_2)_{T,\rho}^\infty \frac{d\rho}{\rho^2}$$

departs less than 0.04% from the corresponding value at criticality, i.e.,

$$\rho_c^{-2}(\partial P/\partial x_2)_{T_c,\rho_c}^\infty \equiv \overline{\rho^{-2}(\partial P/\partial x_2)_{T,\rho}^\infty}$$

which is one of the conditions discussed at the end of the previous section.

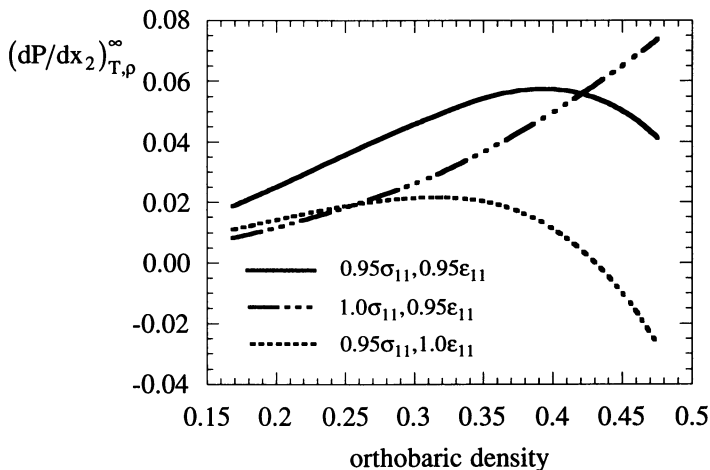


Figure 5. Comparison between the orthobaric density dependence of $(\partial P/\partial x_2)_{T,p}^{\infty}$ for three repulsive infinitely dilute hard core Yukawa fluid mixtures with $\alpha_{11}\sigma_{11}=1.8$. The coefficients indicate the relative sizes of σ_{22} and ϵ_{22} with respect to the solvent's parameters. Pressure and density in units of in units of ϵ_{11} and σ_{11} . Note the change in scale.

Final Remarks

In this paper we have briefly reviewed a generalization of our previous solvation formalism to fluid mixtures involving any type of molecular asymmetry. The current analysis provides a clear statistical mechanical interpretation of the splitting between solvation (finite) and compressibility driven (diverging) contributions to thermodynamic properties of supercritical solutions. Specifically, the formalism connects the changes of the solvent's local environment around an infinitely dilute solute (solute-induced effects $\sim (\partial P/\partial x_2)_{T,p}^{\infty}$) with the solvation contribution to the infinite dilution solute partial molar properties. Moreover, the statistical mechanical interpretation of solvation in terms of solute-induced effects offers some insight into the molecular mechanism behind the orthobaric temperature dependence of Henry's constant and the solute distribution factor. Using integral equation calculations for hard core Yukawa fluids we were able to give some microscopic support to our statistical mechanical interpretation of the agreement between the asymptotic expressions for the solubility coefficients and their actual behavior beyond the asymptotic region. The complete microscopic picture of this interpretation must include the analysis of the entropic solute-induced effects. This part of the study is in progress.

Acknowledgements

This work was supported by the Division of Chemical Sciences, Office of Basic Energy Sciences, U.S. Department of Energy.

References

- (1) Riess, J. G.; Blanc, M. L. *Angew. Chem.* **1978**, *90*, 654.
- (2) Schnoy, N.; Pfannkuch, F.; Beisbarth, H. *Anaesthetist* **1979**, *28*, 503.
- (3) Appenzeller, T. *Science* **1991**, *252*, 1790.
- (4) Wilhelm, E.; Battino, R.; Wilcock, R. J. *Chem. Rev.* **1977**, *77*, 219.
- (5) Beutier, D.; Renon, H. *AICHE J.* **1978**, *24*, 1122.
- (6) Schotte, W. *AICHE J.* **1985**, *31*, 154.
- (7) Japas, M. L.; Levelt Sengers, J. M. H. *AICHE J.* **1989**, *35*, 705.
- (8) Wilhelm, W. In *Molecular Liquids: New Perspectives in Physics and Chemistry*; J. J. C. Teixeira-Dias, Ed.; Kluwer Academic Publishers: 1992; pp 175-206.
- (9) Ben-Naim, A. *Solvation Thermodynamics*; Plenum Press: New York, 1987.
- (10) Chialvo, A. A.; Cummings, P. T. *AICHe J.* **1994**, *40*, 1558.
- (11) Chialvo, A. A. *J. Phys. Chem.* **1991**, *95*, 6683.
- (12) Chialvo, A. A.; Cummings, P. T. *Molec. Phys.* **1995**, *84*, 41.
- (13) Levelt Sengers, J. M. H. In *Supercritical Fluid Technology*; T. J. Bruno and J. F. Ely, Eds., CRC Press: Boca Raton, 1991; pp 1-56.
- (14) Levelt Sengers, J. M. H. *J. Supercrit. Fluids* **1991**, *4*, 215.
- (15) Debenedetti, P. G.; Mohamed, R. S. *J. Chem. Phys.* **1989**, *90*, 4528.
- (16) Harvey, A. H.; Levelt Sengers, J. M. H. *AICHE J.* **1990**, *36*, 539.
- (17) Henderson, D.; Waisman, E.; Lebowitz, J. L.; Blum, L. *Molec. Phys.* **1978**, *35*, 241.
- (18) Ornstein, L. S.; Zernike, F. *Proc. Akad. Sci. (Amsterdam)* **1914**, *17*, 793.
- (19) Høye, J. S.; Stell, G. *J. Chem. Phys.* **1977**, *67*, 439.
- (20) Baxter, R. J. *J. Chem. Phys.* **1970**, *52*, 4559.
- (21) Høye, J. S.; Waisman, E.; Stell, G. *Molec. Phys.* **1976**, *32*, 209.
- (22) Høye, J. S.; Blum, L. *J. Stat. Phys.* **1977**, *16*, 399.
- (23) Kalyuzhnyi, Yu.V.; Holovko, M.F. *Molec. Phys.* **1993**, *80*, 1165.

RECEIVED April 24, 1995

Chapter 3

A Molecular Dynamics Investigation of Hydrogen Bonding in Supercritical Water

Tahmid I. Mizan, Phillip E. Savage, and Robert M. Ziff

Department of Chemical Engineering, University of Michigan,
Ann Arbor, MI 48109-2136

The extent, distribution, and temporal and structural aspects of hydrogen bonding in supercritical water were investigated through molecular dynamics simulations at 773 K and densities between 115 and 659 kg/m³ using a flexible water potential. Pair energy distributions in supercritical water do not have the bimodal nature of liquid water distributions. Supercritical water molecular pairs are energetically disposed towards parallel alignment of dipoles in the first solvation shell whereas liquid water pairs favor a near-orthogonal orientation. An energetic criterion was used to identify hydrogen bonded molecular pairs. The number of hydrogen bonds per water molecule in supercritical water is one-sixth to one-half of that present in ambient water. Unlike in ambient water in which almost all the molecules belong to a hydrogen bonded gel, hydrogen bonded clusters in supercritical water typically consist of fewer than five members. The persistence time constant for hydrogen bonds is 0.1 ps in supercritical water in contrast to 0.6 ps in ambient water.

Hydrogen bonding in ambient liquid water has been extensively studied (1). Many of the interesting and indeed, chemically and biologically significant properties of liquid water can be attributed to hydrogen bonding. Of late however, supercritical water (SCW) has shown potential as a medium for chemical processes (2). It is particularly attractive as a solvent because many of its properties can be tuned by adjusting the temperature or pressure. Pyrolysis (3), hydrolysis (4), oxidation (5) and electrochemical reactions (6) are examples of the range and variety of reactions possible in SCW. There is, however, an incomplete understanding of the nature of SCW and the role it plays in the progress of these reactions. Whether hydrogen bonding exists in SCW to a significant degree is still a matter of study. The influence of hydrogen bonding on any medium is evident not only in the strength of interactions between molecules but also in the dynamics. Hydrogen bonding manifests itself in the pair correlation functions, dimer energy distributions, dielectric constant, and in molecular relaxation processes. Clearly, information on the nature and extent of hydrogen bonding in SCW and the underlying molecular phenomena would advance understanding about the solvent behavior of SCW.

There have been only a few previously published computer simulation studies of

0097-6156/95/0608-0047\$12.00/0
© 1995 American Chemical Society

hydrogen bonding in SCW, although some studies (7) have alluded to hydrogen bonding in describing structural and other phenomena observed in SCW. As discussed more fully later, simulation studies use either a geometric definition or an energetic definition of hydrogen bonding. Cochran et al. (8) examined hydrogen bonding in SCW using a rigid simple point charge (SPC) water model (9). Using the geometric definition, Cochran et al. found that the number of hydrogen bonds per water molecule in SCW was about one-third that in ambient water. They observed that the identity of the central particle, whether it was a water molecule, an ion, or a polar or non-polar molecule, had little influence on the number of hydrogen bonds per water molecule. The absolute number of hydrogen bonds around the solute was, however, influenced by its nature because of the enhanced (or depressed) local density effect. It was also found that the degree of hydrogen bonding in the supercritical region decreased with density. In a follow-up study Cummings et al. (10) examined hydrogen bonding in SCW for a number of new solutes. Little additional insight was obtained, however, except for the observation that highly polar aromatic solutes such as benzonitrile may increase the degree of hydrogen bonding in SCW.

Mountain (11) investigated hydrogen bonding in SCW using 108 molecules interacting via the TIP4P (12) pair potential which models the water molecule as a rigid rotor with four interaction sites. His simulations were of only 3.32 ps duration, but covered temperatures and densities from the vapor-liquid coexistence curve to 1100 K and from 100 kg/m³ to 1000 kg/m³. Mountain also used a geometric definition of hydrogen bonding and found that the average number of intermolecular hydrogen bonds per water molecule, n_{HB} , decreased with an increase in temperature. Moreover, a definite temperature scaling trend was observed for the ratio n_{HB}/n , where n is the number density, except at supercritical densities below 450 kg/m³.

Experimental results from neutron diffraction with isotopic substitution (NDIS) studies seem to show almost no evidence of hydrogen bonding at the supercritical temperature of 673 K and density of 660 kg/m³ (13). This assertion is based on the absence of a peak in the oxygen-hydrogen pair correlation function, g_{OH} , at 1.8 Å which typically appears whenever hydrogen bonding exists. These experiments are very difficult (14) and additional independent confirmation of these results is awaited.

On the other hand, infra-red absorption studies for the O-D stretch in dilute mixtures of HDO in H₂O, by Franck and Roth (15) have provided contrary information. At 673 K and a very low density of 16.5 kg/m³ they observed distinct R-, Q- and P- branches of the O-D vibrations. These branches are in agreement with the corresponding vibration-rotation structures observed for the free HDO molecule. At densities above 100 kg/m³ the Q branch was no longer observable, however, an absorption maximum is clearly visible. This peak is said to be indicative of hydrogen bonding, and its frequency increased with decreasing density. Since no separate absorption frequency at 2700 cm⁻¹, the characteristic frequency for free O-D groups, was noticed above 100 kg/m³, it follows that above this density some form of hydrogen bonding exists. Thus, while neutron diffraction experiments seem to indicate an absence of hydrogen bonding even at high densities, spectroscopic evidence suggests otherwise.

Recently, Chialvo and Cummings (16) compared molecular dynamics (MD) simulations using the extended simple point charge (SPCE) water model (17) and the simple point charge with gas phase dipole moment (SPCG) water model (18) to the NDIS data (13). The SPCE model produced a distinct g_{OH} , first peak, whereas the SPCG model, which has a smaller dipole moment, performed somewhat better by producing a flat shoulder instead of the pronounced peak. Neither of these models, however, reproduced the NDIS result of a complete absence of the first g_{OH} , peak.

There are two criteria in vogue for determining whether hydrogen bonding exists between a pair of molecules. Rahman and Stillinger (19) used the energetic definition that a hydrogen bond exists if the pair interaction energy between the molecules is

less than a negative threshold value, $E_{\text{HB,cut}}$. An alternative geometric criterion is that a hydrogen bond exists if O...H and O...O distances, as well as the O..H-O angle are within a specified range of values (1). In this work, we have relied on the first definition. There is some arbitrariness about how to assign the threshold value. Usually, this value is determined from studying the pair energy distribution. For liquid water, this distribution is bimodal. Thus, the minimum between the two peaks may be taken as the threshold value. This convention was adhered to in our analysis, although other conventions are possible (20). Cochran et al. (8) used the minimal geometric criterion of Beveridge et al. (14), while Mountain (11) used a more liberal version of the geometric criterion in which no angle specification was required and only the O..H distance specification was considered sufficient for determining the presence of a hydrogen bond. Kalinichev (7) has pointed out that the diffuseness of the g_{OH} hydrogen bonding peak observed at supercritical conditions as well as the fact that the first two coordination spheres exhibit a considerable degree of overlap, would suggest that a simple geometric criterion such as the one used by Mountain (11) may not be totally adequate. In addition, Chialvo and Cummings (16) found that even for a hypothetical water molecule with almost zero dipole moment, the geometrically defined hydrogen bonding component to g_{OH} was relatively strong, suggesting that a definition for hydrogen bonding based solely on geometric criteria is insufficient. In an illuminating comparison of the energetic criterion versus the simple geometric criterion for hydrogen bonding, Kalinichev found that the energetic definition was more appropriate for distinguishing between hydrogen bonded and non-hydrogen bonded molecular pairs (21). His Monte Carlo studies of hydrogen bonding in SCW using the TIP4P model indicated further that a combined criterion might be preferable at densities above 700 kg/m^3 .

Our work is distinct from the previous molecular simulation studies of hydrogen bonding in SCW in several ways. Firstly, we have used the energetic criterion to establish the existence of hydrogen bonding in contrast to other MD studies which have used various geometric criteria. Moreover, we provide the first report of the dynamics of hydrogen bonding (specifically, hydrogen bond persistence times) under supercritical conditions, although Rapaport (22) has examined hydrogen bond persistence autocorrelation functions for liquid water. In addition, no work has been reported on hydrogen bond cluster size distributions in SCW prior to our work. Finally, we have used a flexible water potential, whereas all previous investigations (8,11,16,21) have used rigid water models.

Simulation studies of solutes in ambient liquid water have found that flexibility in the water model may increase the stability and residence times of water molecules clustering around a solute (23). Some dynamic properties such as orientational correlation times for liquid water have been found to be more faithfully reproduced by flexible water models than by rigid water models (24). Flexibility allows the HOH angle, and thus, the dipole moment to respond to the molecular environment. Mizan et al. (25) have observed the mean dipole moment of SCW to decrease with density when a flexible water model is used for simulations. Zhu et al. (26) suggest that this response of molecular geometry and hence dipole moment to the surroundings constitutes a sort of many-body interaction. Thus, flexibility in a water potential introduces some many-body effects into the water potential. The inclusion of flexibility in the water model may, therefore, be important in SCW also, particularly for dynamic properties.

Details of Simulations

A brief description of the simulation methodology used in this study is given below. The model system consisted of 256 water molecules in a constant volume cubic cell subject to toroidal boundary conditions. Standard MD techniques (27) were used for the simulations. A multiple time step method, the reversible reference system

propagator algorithm (r-RESPA) (28), was used to integrate the equations of motion. The long time step was set at 2 fs (femtosecond) while the short time step was set at 0.25 fs. We applied separate temperature scaling to the translational, rotational and internal degrees of freedom (24) at every long time step using an adaptation of the method of Berendsen et al. (29) in order to maintain the temperature at around the desired value. The flexible simple point charge water potential of Teleman et al. (30) was used. The intermolecular potential used was

$$u_{\text{inter}} = \sum_{i=1}^{N-1} \sum_{j=i+1}^N \left\{ 4\epsilon \left[\left(\frac{\sigma}{r_{ij}} \right)^{12} - \left(\frac{\sigma}{r_{ij}} \right)^6 \right] + \sum_{l,k} \frac{1}{4\pi\epsilon_0} \frac{q_{il}q_{jk}}{r_{ijk}} \left[1 + \frac{\epsilon_{\text{RF}} - 1}{2\epsilon_{\text{RF}} + 1} \left(\frac{r_{ijk}}{R_{\text{cut}}} \right)^3 \right] \right\} \quad (1)$$

The Lennard-Jones interaction between the oxygen atoms is represented by the first term while the second term represents the reaction field corrected Coulomb interaction between all pairs of charges on different molecules. The indices i and j refer to the molecules, whereas the subscripts l and k represent the oxygen or hydrogen atom sites. A cutoff, R_{cut} , based on molecular center of mass distance was used in order to ensure neutrality of charge. The neighbor list was updated automatically. The external dielectric constant defining the reaction field, ϵ_{RF} , was set at 80. The intramolecular potential consisted of harmonic bond and angle terms

$$u_{\text{intra}} = \sum_{\text{all bonds}} \frac{1}{2} k_b (r - r_0)^2 + \sum_{\text{all angles}} \frac{1}{2} k_\theta (\theta - \theta_0)^2 \quad (2)$$

Parameter values for the water model are given elsewhere (30). Atomic coordinates were saved every 50 fs. All systems were equilibrated for at least 100 ps (picosecond) prior to production runs. The total length of production runs was 100 ps (except where otherwise stated). Dimer energies for each pair of molecules were calculated for each configuration of the 100 ps trajectory. These were then used to establish a connectivity matrix based on whether or not the dimer energy was below the threshold energy, $E_{\text{HB,cut}}$. Each element of this matrix corresponds to a molecular pair and has a logical value of true if the pair is hydrogen bonded and false otherwise. The connectivity matrix was used for determining hydrogen bond cluster size distributions and persistence times.

Liquid water was simulated at 300 K and 997 kg/m³. The size of the simulation box was 19.73 Å, and a 9.5 Å cutoff was used. Supercritical water was simulated at a temperature of 773 K and densities in the range 115–659 kg/m³. While the phase envelope of the water model we used is not known, qualitative comparison of the structural, thermodynamic, dielectric and other properties of this model at the above conditions (25) with results for water models for which the critical point is exactly known, leads us to conclude that the simulation conditions are in the one phase region. The state points with densities of 115 kg/m³ and 257 kg/m³ represent conditions used for oxidation studies in SCW.

The supercritical temperature used in our simulations was sufficiently distant from the critical temperature, T_c , that the length of the simulation cell was larger than the correlation length, ξ , which is given by (31)

$$\xi = \xi_0 (\Delta\tilde{T})^{-\nu} [1 + \xi_1 (\Delta\tilde{T})^{\Delta_1} + \dots] \quad (3)$$

where the values of the universal exponents are $\nu = 0.63$ and $\Delta_1 = 0.51$. The dimensionless temperature difference is defined as $\Delta\tilde{T} = (T - T_c) / T$ where the

specific constants ξ_0 and ξ_1 have values of 1.3 Å and 2.16 respectively, for water. At 773 K, ξ is 7.6 Å, based on the experimental T_c of water. This ξ is smaller than the largest and smallest simulation box sizes of 40.5 Å and 22.6 Å, respectively.

Results and Discussion

The dimer energy distributions, hydrogen bond cluster size distribution and persistence times of simulated water were calculated at saturated liquid and supercritical conditions. Liquid water simulations provided a reference point for comparison with both results from the literature and with our simulation results for supercritical conditions. The results are discussed below.

Dimer Energies. Dimer energies or pair energies are the energies of interaction experienced by any two molecules in the system. A clear understanding of pair energies is essential to a meaningful interpretation of our results because we employ a pair energy cutoff criterion to identify hydrogen bonded pairs. Figure 1 shows the distribution of pair energies for the flexible SPC water model at ambient liquid and four supercritical states. The characteristic bimodal nature of the curve for liquid water is evident in the figure. The smaller second peak is indicative of hydrogen bonding. At supercritical conditions the smaller of the two maxima found in the ambient water dimer energy distribution disappears leaving only a remnant in the shape of a broad, sloping shoulder. This suggests that the extent of hydrogen bonding is considerably reduced in SCW. Since, at supercritical conditions there is no minimum on which to base a threshold value, we use the ambient water threshold value, $E_{\text{HB,cut}} = -13.2$ kJ/mol, for all calculations. The high density supercritical states have a larger slope in the hydrogen bonding or attractive branch of the pair energy distribution curve. The corresponding larger area under the hydrogen bonding branch of the curves results in a greater degree of hydrogen bonding at higher supercritical densities. The shape of the dimer energy distributions and the trends observed are in complete accord with the distributions obtained by Kalinichev in Monte Carlo simulations of supercritical TIP4P water (7).

Since we use an energetic criterion to determine hydrogen bonding, the energetic environment that a reference molecule experiences is germane to our investigation. The energetic environment around a molecule may be described by the trajectory-averaged dimer energies as a function of molecular separation, $E_{\text{pair}}(r)$. These are plotted for liquid and supercritical water in Figure 2. The figure shows two distinct minima in the ambient water curve corresponding to the first two solvation shells. The shallow minimum corresponding to the second solvation shell is indicative of the tetrahedral structuring in the liquid. The curves for supercritical states do not have distinct minima in the second solvation shell region. The pair energies in this region are still negative, however, and hence energetically favorable. These energetic considerations are reflected in the atom-atom pair correlation functions discussed later. The well depth of the $E_{\text{pair}}(r)$ curves for SCW decreases with increasing density. This trend has also been observed by Kalinichev (7). The well is deeper for liquid water than for SCW by more than 5 kJ/mol. This would suggest that water molecules are more strongly hydrogen bonded in the liquid phase. The positions of the $E_{\text{pair}}(r)$ minima are the same for both SCW and liquid water. This observation is in apparent conflict with the fact that the first g_{OO} peak is shifted to greater separations for SCW when compared to the liquid water peak at around 2.8 Å (as is evident from Figure 6). However, the distal branch of the potential well has a more gentle slope for SCW than for ambient water and this results in a wider, though shallower, potential well. This energetic trend manifests itself structurally as a broader first g_{OO} peak which is shifted to larger separations. It may be pointed out that $E_{\text{pair}}(r)$ consists of Lennard-Jones and Coulombic parts. While the Lennard-Jones

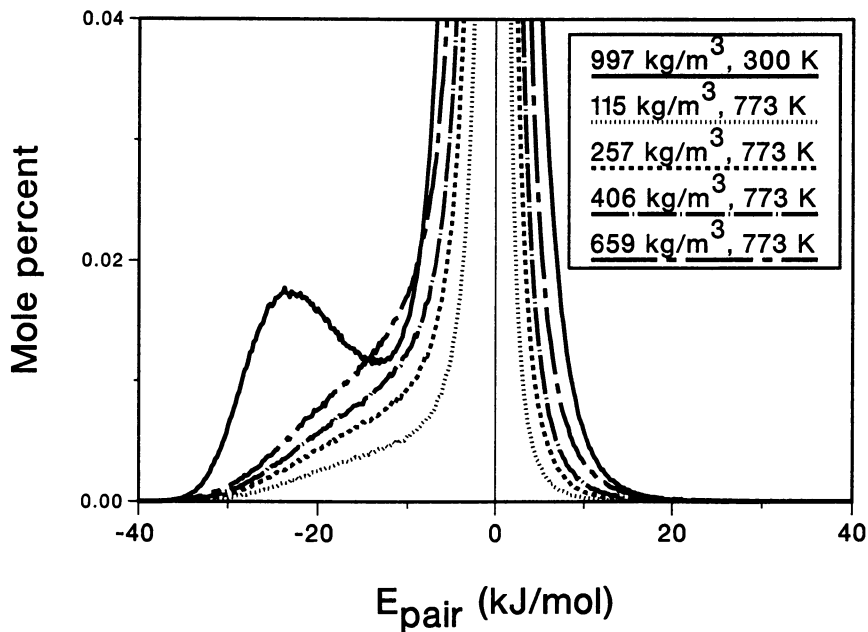


Figure 1. Pair energy distributions of liquid and supercritical water.

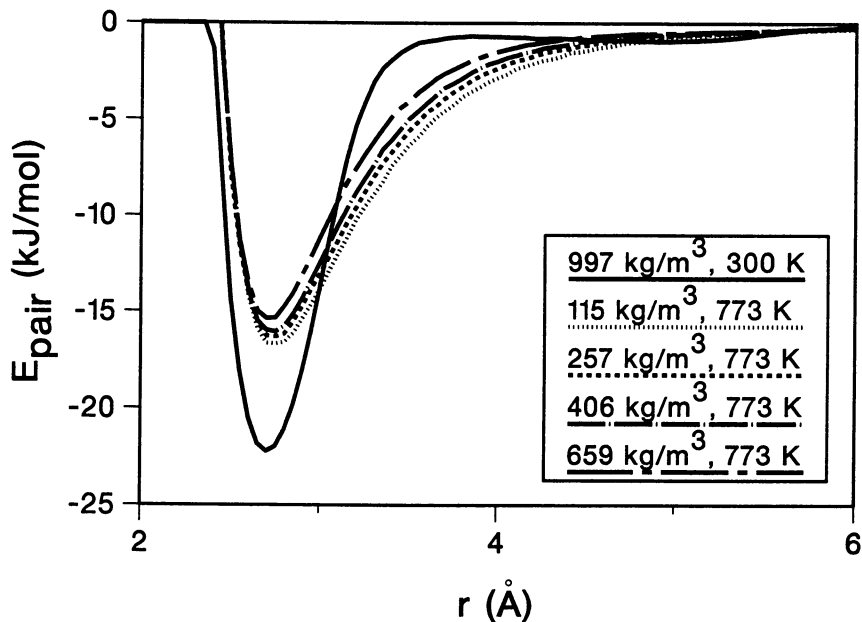


Figure 2. Pair energy as a function of molecular separation.

part, which is spherically symmetric, is independent of both temperature (7) and density, the Coulombic part is not because it depends upon the orientations of the pairs and because $E_{\text{pair}}(r)$ is averaged over orientations. The HOH angle and hence the dipole moment of the monomer changes with density (25). Moreover, at higher temperatures, each molecular pair possesses the energy to visit a larger variety of orientational configurations. Both the change in dipole moment and the greater variety of orientations visited by the pairs contribute to the change in the Coulombic part of $E_{\text{pair}}(r)$ with changes in temperature and density for the flexible water model used in this study. We note that only the latter phenomenon would contribute to a variation in $E_{\text{pair}}(r)$ with changes in temperature or density for a rigid water model.

To examine the energetic environment of a water molecule further we explored how molecular orientations influenced the trajectory-averaged pair interaction energies. The angle between molecular dipoles gives an indication of the orientation of molecular pairs (see Figure 3). The dimer energies, E_{pair} for the nearest neighbor interactions are plotted as a function of dipole-dipole angle, $\theta_{\mu\mu}$ in Figure 4. In this context it should be recalled that as Figure 1 shows, a large majority of the pairs are at such great separations that they have nearly zero energy of interaction. Since there is little or no energy of interaction between them, these pairs do not have a strong energetically preferred orientation with respect to each other. Thus, averaging the pair energies of molecules with a particular dipolar angle for all separations would yield little information because the zero energy pairs would contribute overwhelmingly to the average, and a very flat profile would result. In view of this consideration we chose to average over the first solvation shell only. This region consists of molecules separated by 3.4 Å or less for liquid water and 4.4 Å or less for SCW. A number of interesting features are evident in the curves in Figure 4. Liquid water molecular pairs are more orientationally sensitive than SCW pairs. This is clear from the deep well of the liquid water curve represented by the solid line. The liquid water curve shows a minimum at around 80°. The shallow SCW curves seem to have a minimum at around 0°. Thus, while SCW pairs in the first solvation shell prefer a parallel dipolar alignment, liquid water pairs tend to remain orthogonal. We believe that this fundamental difference in preferred dipolar orientations is a distinguishing feature of SCW and one of the most interesting findings of our work. The near-orthogonal orientations of ambient water molecular pairs correspond to minimum energy or near-minimum energy structures such as the one depicted in Figure 3. While such minimum energy configurations are accessible to SCW molecular pairs, they are counterbalanced by configurations with highly repulsive (positive) pair energies, corresponding to a close approach of like charges made possible by the high rotational and transitional kinetic energies associated with the high temperature of the supercritical state. Another noticeable trend in SCW is that the higher the density the more positive the pair energy becomes at all dipolar orientations. In contrast, liquid water, which has a greater density than all the supercritical states shown in Figure 4, has more negative pair energies.

We also examined E_{pair} as a function of the dipolar angle for non-nearest neighbor pairs, separated by more than 3.4 Å for liquid water and more than 4.4 Å for SCW. These functionalities are depicted in Figure 5. The energy variation for these pairs is less than 1 kJ/mol. At all conditions a parallel orientation is more favorable, more so at greater densities. Clearly, liquid water and SCW are very distinct from the point of view of the molecular energetic environment that they create.

Degree of Hydrogen Bonding. Hydrogen bonds may be enumerated simply by counting the number of pairs of molecules that have dimer energies below the cutoff value, $E_{\text{HB,cut}}$, and then averaging over configurations. Table I gives the number of hydrogen bonds per water molecule, n_{HB} , calculated for each state point. At 300 K, liquid water was found to have 3.13 hydrogen bonds per molecule for the flexible

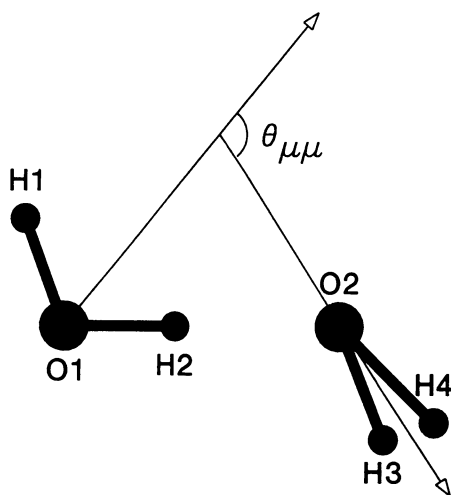


Figure 3. Water dimer.

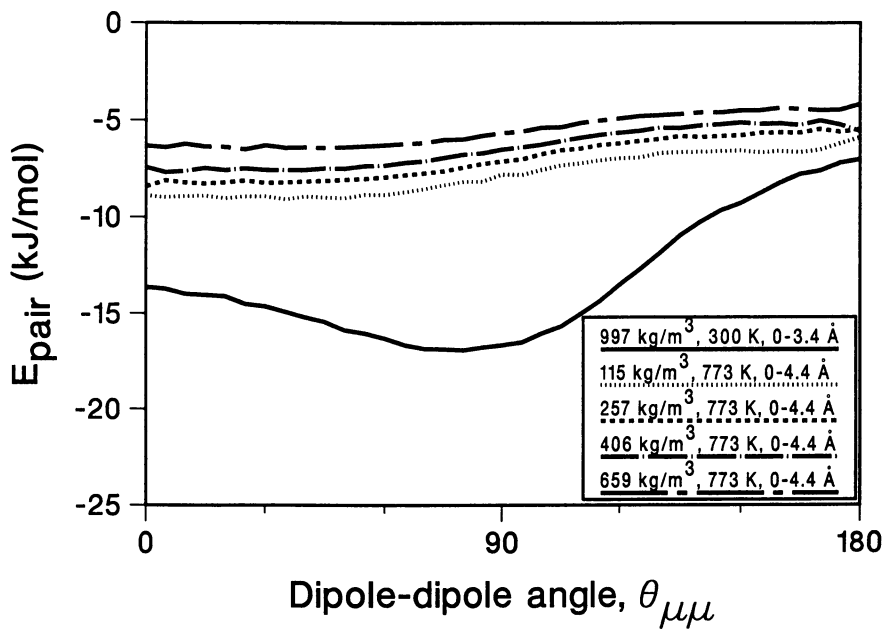


Figure 4. Pair energy as a function of dipole-dipole angle for nearest neighbor pairs.

SPC model used in this study. Using the TIP4P water model, Jorgensen and Madura (32) calculated this value to be 3.59 at 298 K. Their dimer energy distribution had a minimum at -9.4 kJ/mol, however, so that their threshold value was less negative than ours. Jorgensen and Madura calculated the average hydrogen bonding energy of TIP4P liquid water at 298 K to be -17.2 kJ/mol whereas we obtained the value -21.95 kJ/mol. This difference in hydrogen bonding energies is consistent with the potential energy observed for the flexible SPC model (25) being more negative than those obtained with rigid models such as the TIP4P at similar conditions. The hydrogen bonding energy reported by Jorgensen and Madura (32) had a -22.8 kJ/mol contribution from Coulomb interactions and a 5.6 kJ/mol contribution from Lennard-Jones interactions. As Table I shows, our values for these quantities are -28.79 kJ/mol and 6.84 kJ/mol, respectively.

Table I. Hydrogen bond analyses

Property	Units	State 0	State 1	State 2	State 3	State 4
T	K	300	773	773	773	773
ρ	kg/m ³	996.48	115.26	257	405.8	659.3
n_{HB}		3.13	0.46	0.80	1.06	1.44
$\langle E_{\text{HB,Coul}} \rangle$	kJ/mol	-28.79	-23.22	-23.48	-23.73	-24.12
$\langle E_{\text{HB,LJ}} \rangle$	kJ/mol	6.84	4.08	4.22	4.36	4.65
$\langle E_{\text{HB}} \rangle$	kJ/mol	-21.95	-19.14	-19.27	-19.37	-19.47
τ_{HB}	ps	0.6	0.2	0.1	0.1	0.1

At the 257 kg/m³ density supercritical state, n_{HB} was 0.8, a value about one-fourth that found in ambient water. This observation is in general agreement with the results obtained by Cochran et al. (8) who reported an n_{HB} of 0.8 at a near-critical state point (270 kg/m³, 616 K). At a higher density of 406 kg/m³, we observed 1.06 hydrogen bonds per water molecule. Cochran et al. (8) obtained a value of about 1.0 at similar density (405 kg/m³) but lower temperature (578 K). While Cochran et al. used a different water model and the geometric definition of hydrogen bonding, a comparison of our results with their results is, none the less, instructive. The decrease in the degree of hydrogen bonding in SCW as compared to ambient water was a result of both a decrease in density and an increase in the orientational disorder facilitated by higher kinetic energy at the higher temperature. At the lowest density supercritical state, n_{HB} was only 0.46. It is clear from Table I that, in the supercritical regime, hydrogen bonding decreases with density. These observations are consistent with the results of both Cochran et al. (8) and Mountain (11). At the supercritical state 115 kg/m³, 773 K, the hydrogen bonding energy is -19.14 kJ/mol compared to the ambient water value of -21.95 kJ/mol. A number of factors contribute to this increase on going from the liquid to the supercritical state. Firstly, a decrease in Coulombic attraction results from less orientational order (because of the higher temperature), lower densities (greater separations) and smaller dipole moments (25). This is reflected in the more positive Coulombic contributions to the hydrogen bonding energies, $\langle E_{\text{HB,Coul}} \rangle$, as is evident from Table I. Secondly, the Lennard-Jones component of the hydrogen bonding energy, $\langle E_{\text{HB,LJ}} \rangle$, decreases because of the lower density. Thus, the trend towards more positive hydrogen bonding energies on going from liquid to supercritical water caused by the more positive Coulombic hydrogen bonding energies in SCW are somewhat offset by the smaller Lennard-Jones hydrogen bonding energies in SCW. The density effect is observed to continue on going from denser to less dense supercritical states as is clear from the consistent decrease in $\langle E_{\text{HB,LJ}} \rangle$ with decrease in density. The change in the Coulombic contribution, $\langle E_{\text{HB,Coul}} \rangle$, with density is influenced not only by the density directly because of the change in average molecular separations, but also indirectly through

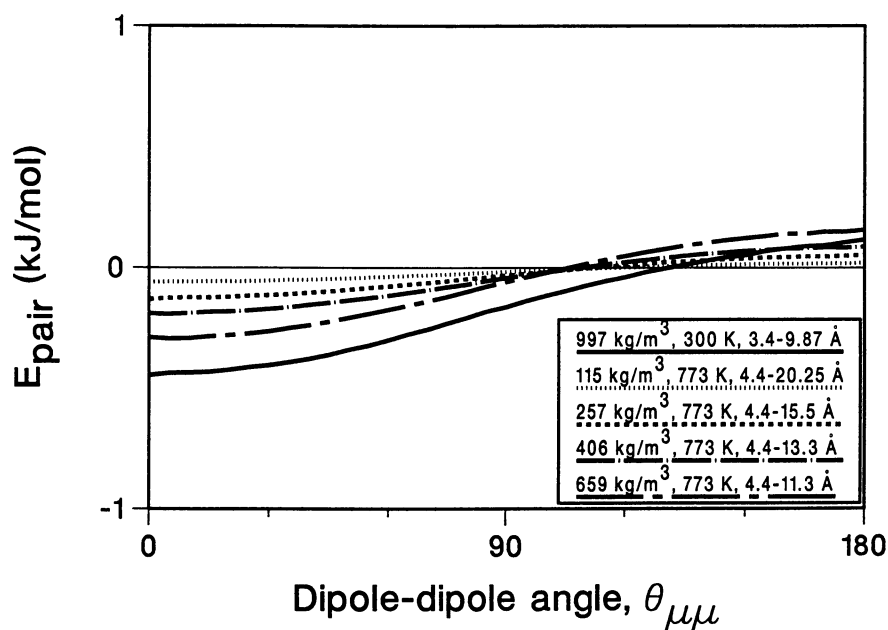


Figure 5. Pair energy as a function of dipole-dipole angle for non-nearest neighbor pairs.

the decrease in average dipole moment with decrease in density. It is interesting to note that while the pair energies for less dense SCW are more negative than for denser states both for the same separations and orientations (see Figures 2 and 4), the hydrogen bonding energies are slightly more positive at lower densities.

Fluid Structure and Hydrogen Bonding. Hydrogen bonding expresses itself most dramatically in the structure of a fluid. Fluid structure can succinctly be represented by atom-atom pair correlation functions. Figures 6 and 7 depict the oxygen-oxygen and oxygen-hydrogen pair correlation functions for liquid water and SCW. The figures, taken from Mizan et al. (25), are reproduced here for convenience. The oxygen-oxygen pair correlation function, g_{OO} , for liquid water shows two distinct peaks. The second peak situated at around 4.5 Å is indicative of the tetrahedral ordering and hence is evidence of hydrogen bonding. The lowest density supercritical state g_{OO} shows no second peak, indicating the absence of significant hydrogen bonding. The higher density supercritical states have a shifted and very faint second peak. The g_{OH} curve for liquid water shows the characteristic peak at 1.8 Å which is considered to be a very strong indication of hydrogen bonding. This peak may be interpreted with reference to Figure 3, which shows the disposition of a water dimer in a minimum energy configuration. The first g_{OH} peak corresponds to the H2-O2 distance on this figure, whereas the second peak at around 3.3 Å represents a distance such as H1-O2. Clearly, a sharp first peak implies that for a greater portion of the time, the adjacent O and H atoms of neighboring molecules (such as H2 and O2) are localized in close proximity to each other. This is an attractive interaction from an electrostatic perspective, and results in the very negative dimer energies characteristic of hydrogen bonds. Large amplitude libration or even free rotation would reduce the portion of the time that such atoms would spend in this energetically favorable condition and hence result in diffuse g_{OH} peaks. Both the high and low density supercritical states exhibited some degree of hydrogen bonding as indicated by the g_{OH} peak at around 1.8 Å. However, the trough at around 2.4 Å clearly rises higher at the supercritical states than in the ambient state. This behavior together with the broadening of the 1.8 Å peak is indicative of orientational disorder and hence a decrease in the extent of hydrogen bonding.

Orientational Correlations and Hydrogen Bonding. It is difficult to extract information about the relative orientations of molecules from only the atom-atom pair correlations functions. The cosine of the dipole-dipole angle as a function of molecular separations provides more insight into the orientation of molecules in each hydration shell. This quantity will be referred to in this study as simply the dipole correlation function, $\cos\theta_{\mu\mu}(r)$, and is defined as

$$\cos\theta_{\mu\mu}(r) = \left\langle \left[\hat{\mu}_i(\vec{r}_i) \cdot \hat{\mu}_j(\vec{r}_j) \right] \delta(r - r_{ij}) \right\rangle \quad (4)$$

where $\hat{\mu}_i$ is the dipole unit vector defined as, $\hat{\mu}_i = \vec{\mu}_i/\mu_i$. The angular brackets indicate averaging over all the molecular pairs as well as over the entire length of the trajectory. Figure 8 shows the dipole correlation functions for ambient water and for the four supercritical states. To obtain good resolution for the curves in this figure, longer trajectories had to be used than were used for the other data presented in this work. An 800 ps trajectory was used for generating the liquid water curve, whereas 200 ps trajectories were used for the SCW curves. If a dipole is parallel with the reference dipole it will contribute positively to the dipole correlation function. On the other hand, antiparallel orientations contribute negatively. The curve for ambient water indicates parallel orientations in the first solvation shell. Interestingly, the peak is situated at 2.5 Å, a smaller separation than the position of the first g_{OO} maximum

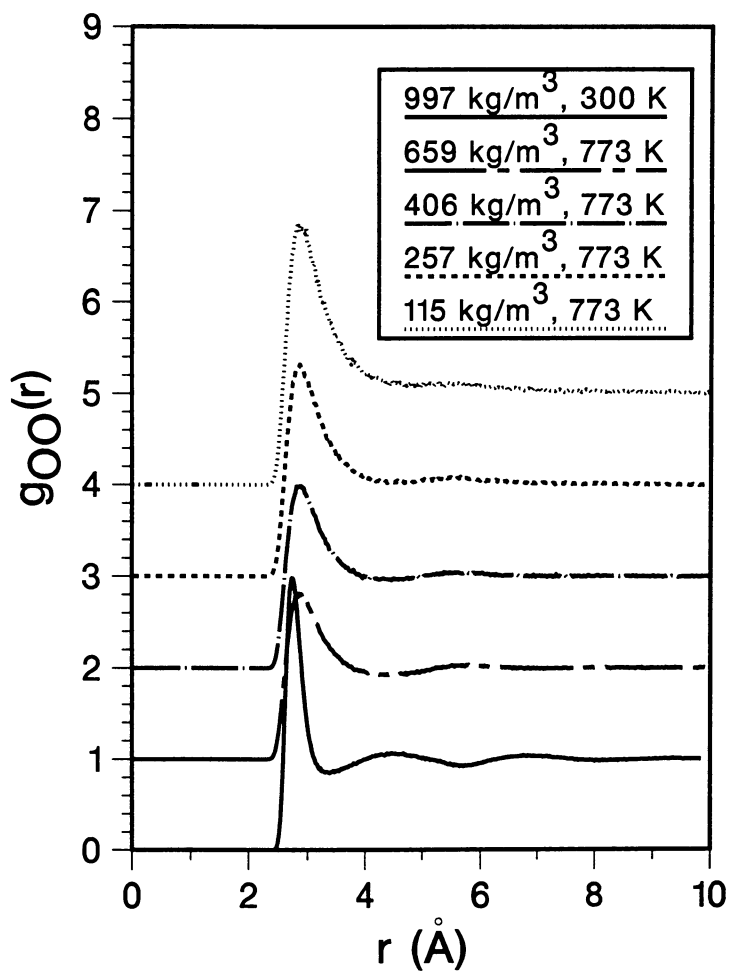


Figure 6. Oxygen-oxygen pair correlation functions of liquid and supercritical water (From ref. 25). The ordinates have been shifted for clarity.

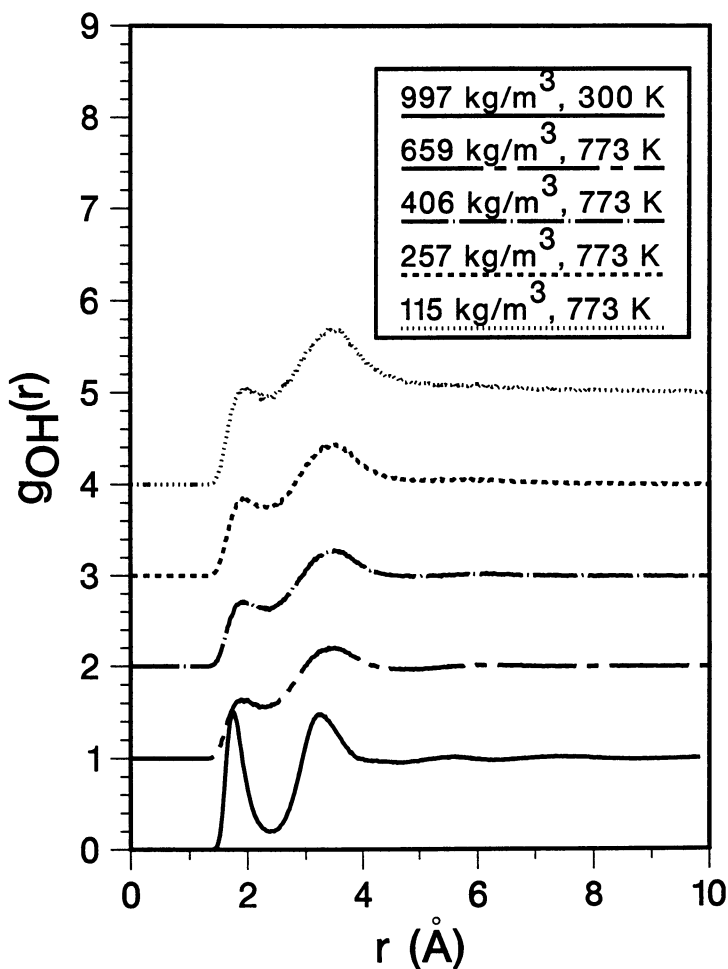


Figure 7. Oxygen-hydrogen pair correlation functions of liquid and supercritical water (From ref. 25). The ordinates have been shifted for clarity.

at 2.8 Å. Although the separations for $\cos\theta_{\mu\mu}(r)$ are the center of mass distances and not oxygen-oxygen distances as in g_{OO} , this distinction is not sufficient to explain the difference between the peak position of the former correlation with respect to the latter. Dipole correlation functions reported by Belhadj et al. (33) and Alper and Levy (34) show the same feature. It may be recalled that Figure 4 shows that for liquid water orthogonal orientations are more favorable than parallel orientations. Thus, there may indeed be a preponderance of orthogonally oriented dipoles in the region of the first g_{OO} peak. Since orthogonal orientations have a vanishing cosine value, however, they do not contribute to the dipole correlation function. Nearest-neighbor dipoles that are non-orthogonal appear to occur overwhelmingly at distances smaller than the first g_{OO} maximum position. This explains the nature of the liquid water $\cos\theta_{\mu\mu}(r)$ curve. Figure 8 shows a region of antiparallel dipolar orientations corresponding to the second solvation shell, followed again by parallel orientations at separations slightly smaller than the position of the third solvation shell peak of g_{OO} .

The dipole correlation functions for the supercritical states are in sharp contrast to the behavior of this function for liquid water. Under supercritical conditions, a broader, though distinctly parallel orientation is observed for the first solvation shell. Parallel orientations are energetically more favorable as is evident in Figure 4. There is very little orientational correlation beyond the nearest neighbor separations. This is consistent with the structural and energetic picture of SCW that we have obtained so far, as a fluid with very little long-range correlation. It is noteworthy that the dipolar correlations for SCW are less intense at lower densities. On the other hand, $E_{\text{pair}}(r)$ and $E_{\text{pair}}(\theta_{\mu\mu})$ functionalities of Figures 2 and 4 clearly indicate that the low density states are energetically more favorable. Thus, it may be surmised that the density dependence of the dipolar correlations is influenced more by entropic than energetic considerations. The orientational disorder alluded to earlier, which was suggested as a possible cause of the diffuseness of the hydrogen bonding g_{OH} peak of SCW in contrast to liquid water, is apparent in Figure 8. The dipole correlation functions for SCW are broader and less intense than that for liquid water. This indicates a wider variation of nearest neighbor molecular orientations in SCW.

Figure 8 also shows some unconnected data points at very small separations for the supercritical states. At these supercritical temperatures molecules have sufficient kinetic energies to make extremely close approaches to one another. The number of molecules over which $\cos\theta_{\mu\mu}(r)$ is averaged is proportional to r^2 so that at the smallest separations the statistics are poorest. Moreover, for the lowest density states, fewer molecules are available per unit volume, resulting in even poorer statistics. Thus, we believe that these stray points are probably statistical noise, so we have elected not to connect them to the curves for each state point.

The dipoles do not act independently of one another. There is a collective aspect to their reorientations. This is reflected in the dielectric constant. Hydrogen bonding also manifests itself in the dielectric constant of the fluid. The dielectric constant of flexible SPC water at ambient conditions has been calculated to be 84 (25), whereas at the lowest and highest density supercritical states this quantity has values of 1.68 and 12.92 (25), respectively. Since this quantity is intimately connected to collective orientational rearrangements in the fluid and since these rearrangements are more difficult in the presence of hydrogen bonding, the low dielectric constants of SCW are indicative of the lesser significance of hydrogen bonding compared to ambient water.

Cluster Size Distribution. When the interaction energy of a pair of molecules is less than the threshold value, $E_{\text{HB,cut}}$, a hydrogen bond is said to exist. A molecule can be hydrogen bonded to several other molecules, which, in turn, can be hydrogen bonded to yet other molecules. In this way a network or cluster of hydrogen bonded molecules may exist in a fluid. In this subsection we examine the characteristics of

hydrogen bonded clusters. Table II lists the cluster size distributions at all the state conditions simulated. The number fractions of clusters with N water molecules, W_N are listed against the cluster size, S_N . It is clear from the table that at ambient conditions the majority of the water molecules are predisposed to belong to a large, sometimes spanning cluster. There is about a 30% chance of water molecules occurring as unbound entities. At supercritical conditions, however, we are clearly below the percolation threshold. There is a strong probability that water molecules will not be hydrogen bonded, and this probability increases with decreasing density. When hydrogen bonded clusters do exist they are small in size, usually having five or fewer members. At state 1, there is an 80% probability of the molecules not being hydrogen bonded at all. In state 4, the highest density state, this probability decreases to less than 60%. Our results, indicating an overwhelming incidence of free (non-hydrogen bonded) molecules, seem to be at odds with the observation made by Franck and Roth (15) that no characteristic absorption frequency for free O-D groups was noticed above 100 kg/m³. These two results may, however, be reconciled if a more positive $E_{\text{HB,cut}}$ were used in our analysis.

Hydrogen Bond Persistence Times. The temporal nature of hydrogen bonding is characterized by the persistence time or life time of a hydrogen bond. If a hydrogen bond is present at time 0 and exists continuously (within the resolution of the data sampling period) until time t it is said to persist at time t . Figure 9 shows hydrogen bond persistence curves for liquid water and the four supercritical states. The ordinate gives the ratio of the number of hydrogen bonds still present at any time t , $N_{\text{HB}}(t)$, to the number of hydrogen bonds initially present at time 0, $N_{\text{HB}}(0)$. The decay of hydrogen bonds appears to be exponential.

$$N_{\text{HB}}(t) = N_{\text{HB}}(0)\exp(-t / \tau_{\text{HB}}) \quad (5)$$

The hydrogen bond decay constant, τ_{HB} , for each of the state points is given in Table I. Liquid water has a very large decay time. The decay constants for SCW are about one-sixth that of ambient water. This is understandable since at a higher temperature, the higher kinetic energy allows for more frequent disruption of hydrogen bonds. On the other hand, the high density supercritical states have a lower decay constant than the lowest density state. This might be attributable to a smaller mean free path and more frequent collisions in the high density states.

Summary and Conclusions

We investigated hydrogen bonding and the underlying energetic environment in SCW through MD simulations using a flexible SPC water model. Data were obtained at ambient conditions and four supercritical state points that are typical of conditions of interest in SCW reaction studies. Pair energy distributions were reported for liquid and supercritical water. The bimodal character of the liquid water pair energy distribution was absent in SCW. At supercritical conditions a parallel alignment of the dipoles of molecular pairs is energetically more favorable in the first solvation shell, whereas in liquid water a near-orthogonal alignment represents more negative pair energies. We employed an energetic criterion for determining the existence of a hydrogen bond between a pair of molecules. Only 1.44 hydrogen bonds per water molecule were observed at a density of 659 kg/m³ and temperature of 773 K, while about 0.46 hydrogen bonds per molecule were found to be present at the same temperature but a lower density of 115 kg/m³. In contrast, ambient liquid water was found to have 3.13 hydrogen bonds per molecule. Hydrogen bonded water molecules are known to form clusters. In ambient water, most molecules belong to a single cluster known as the gel. At the supercritical conditions we investigated, water

Table II. Hydrogen bond cluster size distribution

S_N	W_N				
	State 0	State 1	State 2	State 3	State 4
1	0.287	0.805	0.689	0.624	0.578
2	0.027	0.133	0.167	0.171	0.165
3	0.002	0.039	0.067	0.076	0.076
4		0.014	0.032	0.042	0.043
5		0.006	0.017	0.025	0.027
6		0.002	0.010	0.016	0.018
7			0.006	0.011	0.014
8			0.004	0.008	0.010
9			0.003	0.006	0.008
10			0.002	0.004	0.006
11			0.001	0.003	0.006
12				0.003	0.005
13				0.002	0.004
14				0.002	0.003
15				0.001	0.003
16				0.001	0.002
17				0.001	0.002
18				0.001	0.002
19				0.001	0.002
20				0.001	0.001
21					0.001
22					0.001
23					0.001
24					0.001
25					0.001
26					0.001
27					0.001
28					0.001
29					0.001
30					0.001
31					0.001
32					0.001
33					0.001
35					0.001
36					0.001
37					0.001
41					0.001
251	0.001				
252	0.003				
253	0.013				
254	0.055				
255	0.180				
256	0.431				

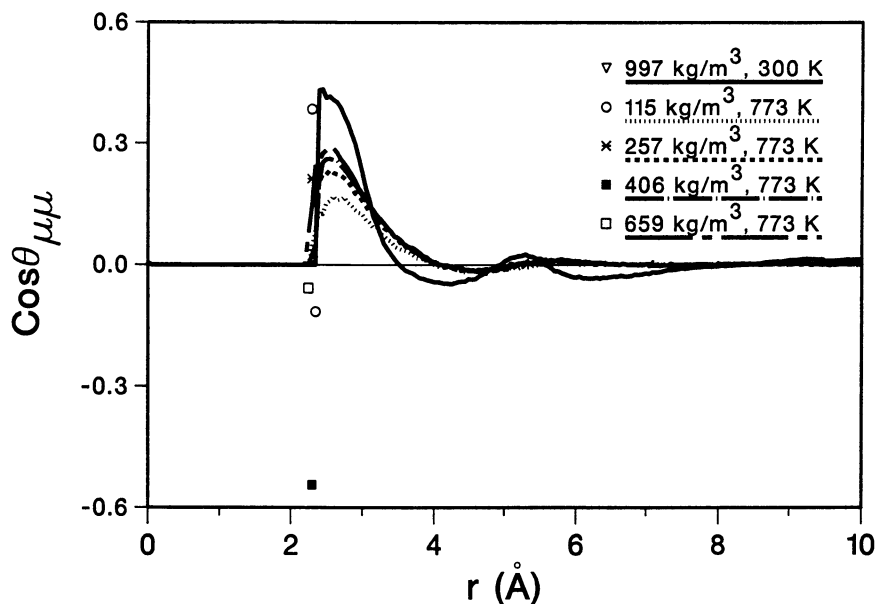


Figure 8. Cosine of dipole-dipole angle as a function of molecular separation.

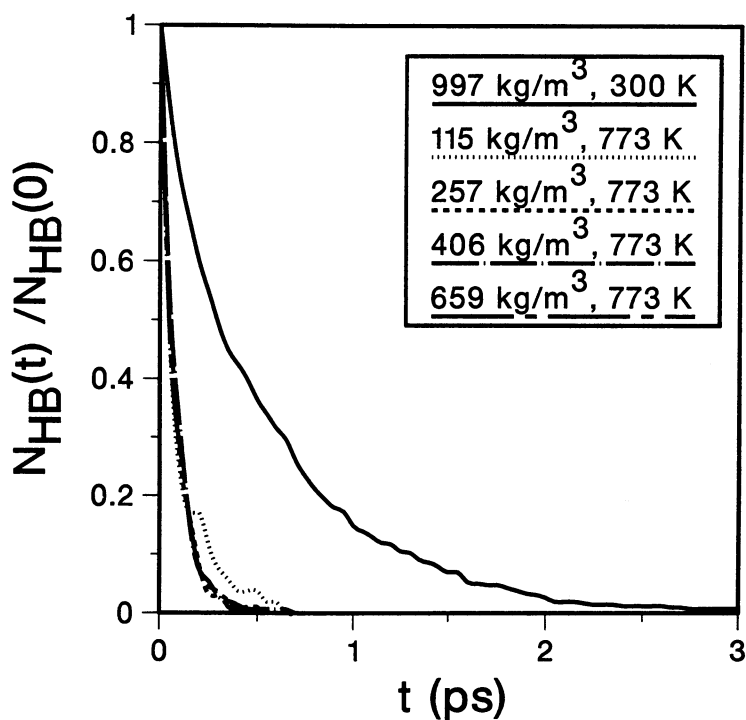


Figure 9. Hydrogen bond persistence times.

molecules exist largely as single entities or small clusters of five or fewer members. Similar contrasting behavior has been observed for the persistence of hydrogen bonds. In SCW, hydrogen bonds have a continuous survival time constant of 0.1 ps. In ambient water this time constant is 0.6 ps. In summary, SCW is only weakly hydrogen bonded, although the effect becomes stronger with increasing density. Our work is the first study of hydrogen bonding in SCW which uses a flexible water model. We also present hydrogen bond analysis based on an energetic criterion as opposed to geometric criteria used by previous studies. Another novel aspect of our work is a study of hydrogen bond dynamics. Finally, ours is the only study to date to report hydrogen bond cluster size distributions for SCW.

Literature Cited

1. Ladanyi, B.; Skaf, M. *Annu. Rev. Phys. Chem.* **1993**, *44*, 335.
2. Savage, P.; Gopalan, S.; Mizan, T.; Martino, C.; Brock, E. *Reactions at supercritical conditions: Applications and fundamentals*, in press *AIChE J.* 1995.
3. West, M.; Gray, M. *Can. J. Chem. Eng.* **1987**, *65*, 645.
4. Klein, M.; Mentha, Y.; Torry, L. *Ind. Eng. Chem. Res.* **1992**, *31*, 182.
5. Li, R.; Savage, P.E.; Szmukler, D. *AIChE J.* **1993**, *39*, 178.
6. Flarsheim, W.; Bard, A.; Johnston, K. *J. Phys. Chem.* **1989**, *93*, 4234.
7. Kalinichev, A. *Z. Naturforsch.* **1991**, *46a*, 433.
8. Cochran, H.; Cummings, P.; Karaborni, S. *Fluid Phase Equilib.* **1992**, *71*, 1.
9. Berendsen, H.; Potsma, J.; van Gunsteren W.; Hermans, J. In *Intermolecular Forces*; Pullman, B., Ed.; Reidel, Dordrecht, Netherlands, 1981, pp. 331-342
10. Cummings, P.; Chialvo, A.; Cochran, H. *Chem. Eng. Sci.* **1994**, *49*, 2735.
11. Mountain, R. *J. Chem. Phys.* **1989**, *90*, 1866.
12. Jorgensen, W.; Chandrasekhar, J.; Madura, J.; Impey, R.; Klein, M. *J. Chem. Phys.* **1983**, *79*, 926.
13. Postorino, P.; Tromp, R.; Ricci, M.-A.; Soper, A.; Neilson, G. *Nature* **1993**, *366*, 668.
14. Beveridge, D.; Mezei, M.; Mehrotra, P.; Marchese, F.; Ravi-Shanker, G.; Vasu, T.; Swaminathan, S. In *Molecular-Based Study of Fluids*; Haile, J.M.; Mansoori, G.A., Ed.; ACS Symp. Series 204; ACS: Washington, DC, 1983; pp. 281-351.
15. Franck, E.; Roth, K. *Faraday Discuss. Chem. Soc.* **1967**, *43*, 108.
16. Chialvo, A.; Cummings, P. *J. Chem. Phys.* **1994**, *101*, 4466.
17. Berendsen, H.; Grigera, J.; Straatsma, T. *J. Phys. Chem.* **1987**, *91*, 6269.
18. Strauch, H.; Cummings, P. *J. Chem. Phys.* **1992**, *96*, 864.
19. Rahman, A.; Stillinger, F. *J. Chem. Phys.* **1971**, *55*, 3336.
20. Stillinger, F.; Rahman, A. *J. Chem. Phys.* **1972**, *57*, 1281.
21. Kalinichev, A.; Bass, J. *Chem. Phys. Lett.* **1994**, *231*, 301.
22. Rapaport, D.C. *Mol. Phys.* **1983**, *50*, 1151.
23. Guardia, E.; Padro J. *J. Phys. Chem.* **1990**, *94*, 6049.
24. Wallqvist, A.; Teleman, O. *Mol. Phys.* **1991**, *74*, 515.
25. Mizan, T.; Savage, P.; Ziff, R. *J. Phys. Chem.*, **1994**, *98*, 13067.
26. Zhu, S.-B.; Singh, S.; Robinson, G. *J. Chem. Phys.* **1991**, *95*, 2791.
27. Allen, M.P.; Tildesley, D.J. *Computer Simulation of Liquids*; Oxford University Press: Oxford, UK, 1987.
28. Tuckerman, M.; Berne, B.; Martyna, G. *J. Chem. Phys.* **1992**, *97*, 1990.
29. Berendsen, H.; Potsma, J.; van Gunsteren, W.; DiNola, A.; Haak, J. *J. Chem. Phys.* **1984**, *81*, 3684.
30. Teleman, O.; Jonsson, B.; Engstrom, S. *Mol. Phys.* **1987**, *60*, 193.
31. Sengers, J.V.; Levelt Sengers, J.M.H. *Annu. Rev. Phys. Chem.* **1986**, *37*, 189.
32. Jorgensen, W.; Madura, J. *Mol. Phys.* **1985**, *56*, 1381.
33. Belhadj, M.; Alper, H.; Levy, R. *Chem. Phys. Lett.* **1991**, *179*, 13.
34. Alper, H.; Levy, R. *J. Chem. Phys.* **1989**, *91*, 1242.

RECEIVED April 24, 1995

Chapter 4

Solvation, Hydrogen Bonding, and Ion Pairing in Supercritical Aqueous Solutions

Simulation and Experiments

A. A. Chialvo^{1,2}, P. T. Cummings^{1,2}, H. D. Cochran², J. M. Simonson³,
and R. E. Mesmer³

¹Department of Chemical Engineering, University of Tennessee,
Knoxville, TN 37996-2200

²Chemical Technology Division and ³Chemical and Analytical Science
Division, Oak Ridge National Laboratory, Oak Ridge, TN 37831-6224

Molecular dynamics of highly dilute aqueous NaCl solutions are performed to study the microstructure, the anion-cation potential of mean-force, and the water-water hydrogen bonding, as well as to characterize the ionic solvation in the vicinity of the solvent's critical point. The association constant for the ion pair Na^+/Cl^- and the constant of equilibrium between the contact-ion-pairs and the solvent-separated-ion-pairs are determined for a water-NaCl model at a near critical state condition. Simulation results are compared with experimental conductance measurements and the prediction of a simple continuum model.

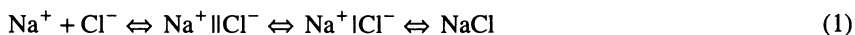
The wide-ranging interest in the properties of aqueous solutions hinges upon several important factors such as the role that ionic association plays in chemical and biochemical reactions in solution (1), and its effect on determining their critical behavior (2). Tremendous progress has been achieved in the last quarter of century in the understanding of the microstructure and thermodynamics of water and aqueous electrolyte solutions at ambient conditions (3). Unfortunately, this knowledge cannot always be extrapolated to aqueous systems at more extreme conditions, such as those in highly compressible regions, which are currently of great scientific and practical interest (4,5).

Near critical properties of dilute aqueous electrolyte solutions are extremely difficult to determine with precision due to the simultaneous existence of long-ranged

0097-6156/95/0608-0065\$12.00/0
© 1995 American Chemical Society

density/composition fluctuations and long-ranged Coulombic interactions. For the particular case of highly dilute NaCl in water, this situation translates into a rapid change in the slope of the T-x and P-x critical lines (2). In the highly compressible near-critical region, the solvent's dielectric constant changes dramatically affecting the screening of the Coulombic interactions, and consequently, the degree of ionic association. This feature makes the modeling of dilute aqueous electrolyte systems very challenging (2,6).

The aqueous Na⁺/Cl⁻ association process can be envisioned as follows,



where NaCl is the product of the "reaction" between the Na⁺ and Cl⁻ ions, and Na⁺||Cl⁻ and Na⁺|Cl⁻ represent the solvent separated ion pair (SSIP) and contact ion pair (CIP) states, respectively. Some evidence indicates that these two ion-paired states, whose relative concentrations have been determined experimentally by Raman spectroscopy for a variety of salts (7-9), might act as reaction intermediates (10,11).

A practical way to study this phenomenon is through the determination of the anion-cation potential of mean-force by molecular simulation of model aqueous electrolyte systems. Several studies have been reported on the evaluation of potentials of mean-force between like and unlike ions in water, usually at normal conditions (12-14). However, little is known about the detailed structural, energetic and dynamic nature of ion pairing in aqueous solutions at supercritical conditions (15,16).

In this paper we use molecular dynamics to determine the association and equilibrium constants for aqueous Na⁺/Cl⁻ at a supercritical state condition. In addition we analyze the water microstructure around each ion and calculate the number of water molecules hydrogen-bonded to each other around the ions. Simulation results for the association constant are then compared to those determined from conductance measurements performed at Oak Ridge National Laboratory. Finally we comment on some limitations of the present calculations regarding the constant of integration for the determination of the potential of mean-force and the corresponding effect on the value of the association constant.

Intermolecular Potentials and Simulation Details

Water-water interactions were described by the Simple Point Charge (SPC) model given by (17)

$$\phi_{\text{WW}}(\mathbf{r}_{12}, \boldsymbol{\omega}_1, \boldsymbol{\omega}_2) = \sum_{\alpha=1}^3 \sum_{\beta=1}^3 \frac{q_1^\alpha q_2^\beta}{r_{12}^{\alpha\beta}} + 4\epsilon_{\text{OO}} \left[\left(\frac{\sigma_{\text{OO}}}{r_{\text{OO}}} \right)^{12} - \left(\frac{\sigma_{\text{OO}}}{r_{\text{OO}}} \right)^6 \right] \quad (2)$$

where the subscript OO denotes oxygen-oxygen interactions, \mathbf{r}_{12} is the vector joining the centers of molecules 1 and 2, $\boldsymbol{\omega}_i$ represents the orientational vector of molecule *i*, q_i^α is the charge on site α on molecule *i*, $r_{12}^{\alpha\beta}$ is the distance between site α on molecule 1 and site β on molecule 2, and ϵ and σ are the Lennard-Jones energy and size parameters, respectively. The rationale behind this choice has been given elsewhere (18).

For ion-water interactions we have used the Pettitt-Rosky model (19) which describes each ion-water interaction as the sum of a Lennard-Jones and a Coulombic term. Therefore, the ion-water potential involves an ion-oxygen and two ion-hydrogen interactions,

$$\phi_{1W}(r_{1W}\omega_W) = \sum_{\beta=1}^3 \left\{ \frac{q_1 q_W^\beta}{r_{1W}} + 4\epsilon_{1\beta} \left[\left(\frac{\sigma_{1\beta}}{r_{1\beta}} \right)^{12} - \left(\frac{\sigma_{1\beta}}{r_{1\beta}} \right)^6 \right] \right\} \quad (3)$$

where $\epsilon_{1\beta}$ and $\sigma_{1\beta}$ are given by the Lorentz-Berthelot combining rules (20). Even though the Pettitt-Rosicky ion-water potential was derived from *ab initio* calculations of a slightly different water model, we expect the refitting of this potential using the SPC model to differ negligibly from the original values of $\epsilon_{1\beta}$ and $\sigma_{1\beta}$. In a forthcoming publication we analyze two other ion-water models (Chialvo, *et al.*, submitted to *J. Chem. Phys.*). For the ion-ion interaction, we use the Huggins-Mayer-Fumi-Tosi model for alkali-halide interactions, given by (21,22)

$$\phi_{ij}(r) = \frac{q_i q_j}{r} + B_{ij} e^{-r/\rho_{ij}} - \frac{C_{ij}}{r^6} \quad (4)$$

where B_{ij} , ρ_{ij} and C_{ij} are ion-pair specific constants.

All simulations were performed in the canonical-isokinetic (NVT) ensemble, with $N=256$ particles — $N-2$ water molecules plus an anion and a cation — at a system density of $\rho=0.27$ g/cm³ and an absolute temperature of $T=616$ K. The state condition corresponds to $T_r=1.05$, $\rho_r=1.0$ based on the critical conditions for the SPC water model (23). Standard periodic boundary conditions were used along with the minimum image criterion and a spherical cutoff for the truncated intermolecular interactions (24). Long-ranged Coulombic interactions were corrected by a molecular (center-to-center) and a site-to-site reaction field with a dielectric constant $\epsilon_{RF}=20$ (25) for the water-water and the ion-water interaction respectively. The accuracy of the reaction field was assessed by performing Ewald summation calculations (26) for a few typical constrained configurations. A complete analysis of the effect of truncation and reaction field strength on these calculations is presented elsewhere (Chialvo, *et al.*, submitted to *J. Chem. Phys.*) The production runs for thermodynamic and structural properties comprised 3×10^4 time steps (30 psecs) while those for mean-force calculations were extended to 10^5 time-steps for each constrained ion-pair distance.

Hydrogen bonding. As in our previous work (18,27), we use the minimal geometric criterion of Mezei and Beveridge (26) to study the radial dependence of the number of neighboring water molecules which are H-bonded to a central water molecule, i.e., we report the average number of water molecules to which a water molecule located at a distance r from a central molecule (either solvent or solute) is hydrogen bonded (see Chialvo *et al.*, *Intl. J. Thermophys.*, in press, and (18) for more details).

Association and equilibrium constants. Here we provide some detail about the rationale behind the calculation of the mean-force potential as the route to the determination of the thermodynamic association K_a and equilibrium K_e constants. A complete derivation of the working expressions for these two quantities in terms of the infinitely dilute anion-cation radial distribution function $g_{AC}^\infty(r)$ is given in detail elsewhere (Chialvo, *et al.*, submitted to *J. Chem. Phys.*).

The potential of mean-force $W_{AC}(r)$, which gives the solvent-averaged structural effect on the anion-cation interactions, is related to the anion-cation radial distribution function by (29),

$$g_{AC}(r) = \exp(-\beta W_{AC}(r)) \quad (5)$$

where $\beta = (kT)^{-1}$. In principle there are at least three alternative routes to the determination of $g_{AC}(r)$, and therefore, of $W_{AC}(r)$. The usual one based on counting pairs as a function of their relative distances is inapplicable when only one pair of ions is involved, due to the extremely poor sampling statistics. For highly dilute systems, the practical routes are given by the direct determination of $W_{AC}(r)$ by means of either a free energy (30) or a mean-force approach (31). The advantages of either method are discussed elsewhere (Chialvo, *et al.*, submitted to *J. Chem. Phys.*).

Here we use the mean-force calculation based on the constraint approach proposed by Ciccotti *et al.* (31). During the simulation run the mean-force exerted on the ions by the solvent, \mathbf{F}_{WA} and \mathbf{F}_{WC} where WA and WC denote water-anion and water-cation interactions, respectively, are evaluated as time averages, so that the solvent contribution to the anion-cation mean force becomes,

$$\Delta F(r) = 0.5 \langle \hat{r}_{AC} \cdot (\mathbf{F}_{WA} - \mathbf{F}_{WC}) \rangle \quad (6)$$

where \hat{r}_{AC} is the unit vector along the direction of the anion-cation interactions. The total anion-cation mean-force, $F(r) = -dW_{AC}(r)/dr$, is given by

$$F(r) = F_{AC}^d(r) + \Delta F(r) \quad (7)$$

where $F_{AC}^d(r)$ is the direct anion-cation Coulombic and non-Coulombic contributions. The integration of the total anion-cation mean-force $F(r)$ finally gives the desired potential of mean force $W_{AC}(r)$, provided we can determine the integration constant $W_{AC}(r_0)$, i.e.,

$$W_{AC}(r) = W_{AC}(r_0) - \int_{r_0}^r F(r) dr \quad (8)$$

Even though the ideal choice for this constant would be $W_{AC}(r_0 \rightarrow \infty) = 0$, it is not practical because simulations can only be performed on finite sized systems. In practice we choose $r_0 \approx 8.1 \text{ \AA}$ so that the integration constant can be taken as given by the continuum limiting behavior $W_{AC}(r_0) \approx (q_A q_C / \epsilon r_0)$ (32) where ϵ is the dielectric constant of the pure SPC water as obtained by simulation at the same state conditions (27).

The expression for the association constant in terms of the infinitely dilute anion-cation radial distribution function $g_{AC}^\infty(r)$ is given by (Chialvo, *et al.*, submitted to *J. Chem. Phys.*),

$$K_a = 4\pi \int_0^{r_{\min}} g_{AC}^\infty(r) r^2 dr \quad (9)$$

and the corresponding equilibrium constant between the CIP and SSIP species,

$$K_e = \int_{r_{\min}}^{r_{\max}} g_{AC}^{\infty}(r) r^2 dr / \int_0^{r_{\min}} g_{AC}^{\infty}(r) r^2 dr \quad (10)$$

or alternatively,

$$K_e = 4\pi K_a^{-1} \int_0^{r_{\max}} g_{AC}^{\infty}(r) r^2 dr - 1 \quad (11)$$

where r_{\min} and r_{\max} indicate the position of the first and second valley in $g_{AC}^{\infty}(r)$, respectively. Note that the calculation of $g_{AC}^{\infty}(r)$ in the range ($1\text{ \AA} < r < 8.1\text{ \AA}$) involves a set of 35-40 simulation runs, each of them covering 150 psecs of phase-space trajectory.

Simulation Results for NaCl-Water

According to Figure 1, the average number of water molecules hydrogen-bonded to each other appears independent of the identity of the ion, a behavior already seen for a variety of molecular solutes in water at near critical conditions (18,23). The fact that this number is approximately unity suggests that, at this extreme condition, the only surviving hydrogen bonds are those involving water molecules capable of rotating along the hydrogen bonds. The departure observed at short water-solute distances ($r < 1$) may be due to a less efficient sampling at short distances because the number of molecules in the solvation shell becomes smaller (see Figure 11 of Ref. 18).

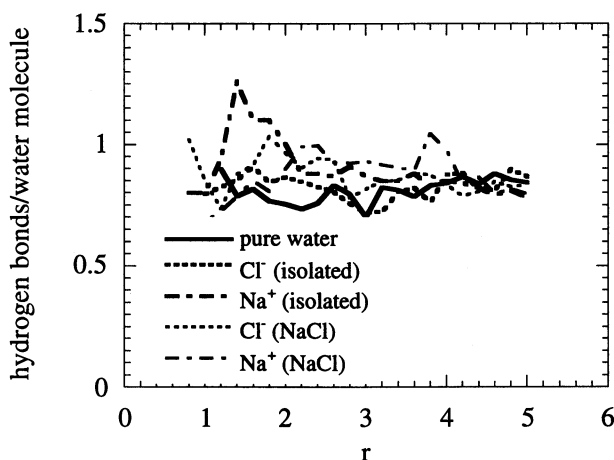


Figure 1. The average number of water molecules hydrogen bonded to a water molecule at distance r (in σ_{OO} units) from the center of the solute surrounding a Na^+ or Cl^- solute at $T_r=1.05$, $\rho_r=1.0$.

In Figure 2 we present the calculated potential of mean-force from constraint dynamics simulation in comparison with the prediction of a continuum model in which the anion-cation interactions are attenuated by the dielectric screening. The simulated potential of mean-force shows clearly two minima, at 2.7 Å and 5.3 Å, corresponding to the CIP and SSIP configurations, respectively.

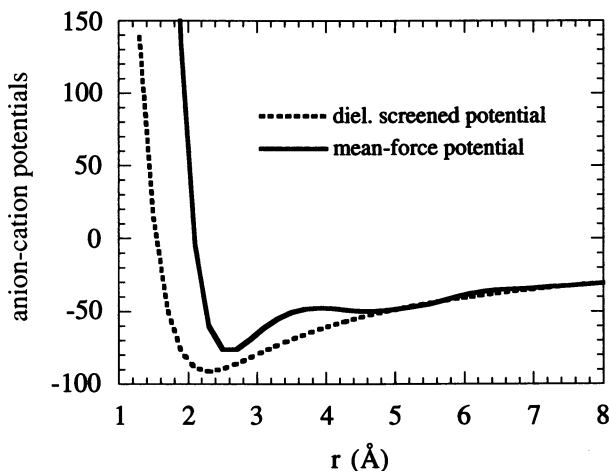


Figure 2. The $\text{Na}^+\text{-Cl}^-$ potential of mean-force in comparison with the bare $\text{Na}^+\text{-Cl}^-$ potential at $T_r=1.05$, $\rho_r=1.0$ (in units of ϵ_{00}).

The continuum model predicts a more negative value for the potential of mean-force with a minimum at 2.4 Å, coinciding with the minimum of the anion-cation bare potential. This model fails to predict the second minimum because it does not take into account the solvent's microstructure around the ions, i.e., it does not account explicitly for solute-solvent interactions, even though it becomes quite accurate for $r \geq 5$ Å. By replotting the dielectric screened and mean-force potential data as anion-cation radial distribution functions, Figure 3, we find that the continuum model not only overpredicts the first peak of $g_{\text{NaCl}}^\infty(r)$ — corresponding to CIP — by approximately an order of magnitude, but also shifts its position to the left from the simulated one (Note the difference between the left and right axes in Figure 3). As expected, the continuum model does not predict the peak associated with the SSIP configuration. Finally, by using equations (9) and (10) with $r_{\text{min}} = 3.8\text{-}4.0$ Å and $r_{\text{max}} = 6.5$ Å, our potential of mean-force calculation gives a $\log K_a^M = 2.70 \pm 0.3$ and a $K_e \approx 0.32$ (where superscript M denotes units of liter/mole). The quoted error in $\log K_a^M$ is related to the uncertainty of the solvent's dielectric constant involved in the calculation of $W_{AC}(r_0)$.

It is instructive to analyze the change of the solvent structure around either ion as the constrained ionic distance changes from the configuration of a CIP to that of a SSIP, i.e., those corresponding to the first two valleys of the $g_{AC}^\infty(r)$. With that purpose we define the following function, equation (12), as the change in the number of water molecules around either ion with respect to what we would find on average around any water molecule, i.e.,

$$N_{I-W}^{\text{ex}}(r) = 4\pi\rho_w \int_0^r (g_{IW}^{\infty}(s) - g_{WW}^0(s))s^2 ds \quad (12)$$

In Figures 4 and 5 we compare the behavior of this function for either ion when the pair is at the CIP and SSIP configuration, respectively. Note also that the strength of the ionic solvation, represented here by $N_{I-W}^{\text{ex}}(r \approx 3.5) > 10$ water molecules, is large regardless of the ion-pair configuration.

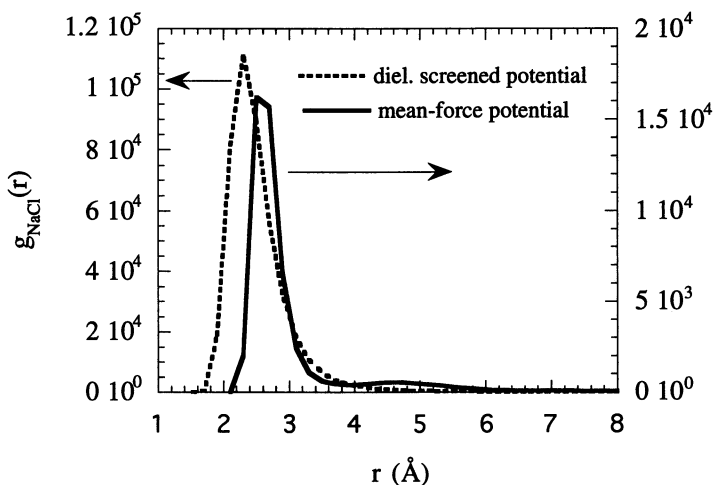


Figure 3. The $\text{Na}^+\text{-Cl}^-$ radial distribution function at $T_r=1.05$, $\rho_r=1.0$. A comparison between PMF calculations and the prediction of a continuum model.

Experimental Results for NaCl-Water

Various experimental techniques, including measurements of electrochemical potentials, calorimetric and solubility measurements, spectroscopic studies, and measurements of electrical conductance, have been applied to the determination of the thermodynamics of reactions in aqueous solutions. The application of these techniques at elevated temperatures and pressures has been reviewed recently (5). Although limitations may be encountered in measurements of equilibrium constants when the fractional concentration of one species over another is too high for meaningful measurements, experimental studies can provide reliable values of ion-association constants in high-temperature aqueous solutions provided the values fall within the range corresponding to resolvable species distributions.

For simple electrolytes such as NaCl, measurements of electrical conductance of dilute aqueous solutions at high temperatures and pressures provide the most direct experimental approach to the determination of equilibrium constants for the ion association reaction at near-critical conditions. The relation between the molar conductance Λ , the limiting conductance Λ_0 , and the equilibrium constant in molar units K_a^M , is often expressed through the Shedlovsky equation (34),

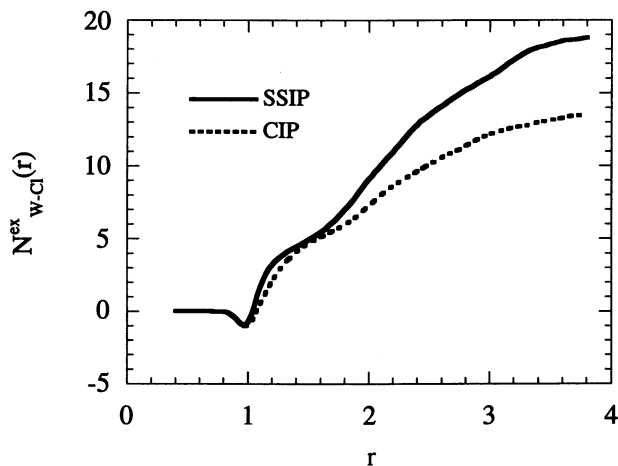


Figure 4. The average number of water molecules around a Cl^- ion in excess of that found around any water molecule, as a function of distance r (in units of σ_{O0}), for the CIP and SSIP configurations at $T_{\text{r}}=1.05$, $\rho_{\text{r}}=1.0$.

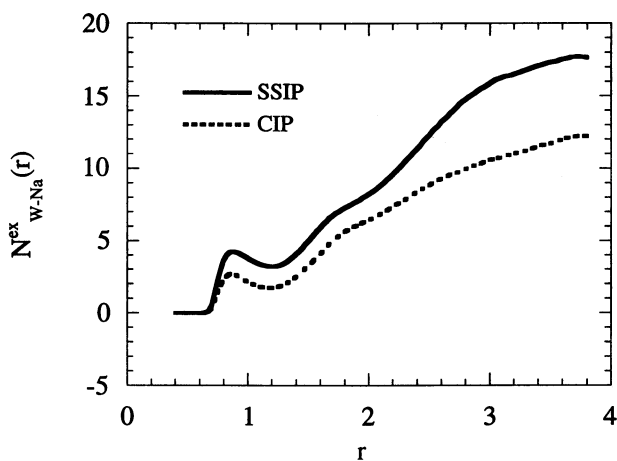


Figure 5. The average number of water molecules around a Na^+ ion in excess of that found around any water molecule, as a function of distance r (in units of σ_{O0}), for the CIP and SSIP configurations at $T_{\text{r}}=1.05$, $\rho_{\text{r}}=1.0$.

$$\frac{1}{\Lambda S(z)} = \frac{1}{\Lambda_0} + \frac{MS(z)\Lambda\gamma_{\pm}^2}{K_a^M \Lambda_0^2} \quad (13)$$

where M is the molarity, γ_{\pm} is the mean-ionic activity coefficient of the electrolyte in molar units, and $S(z)$ is an empirical coefficient dependent on M , Λ_0 , and the limiting Onsager slope. Thus measurements of the molar conductance over a range of molarities give the association constant through nonlinear least-square fitting of the data to equation (13).

Equilibrium constants for ion-association of NaCl in aqueous solutions have been determined from conductance measurements by Fogo *et al.* (35), Quist and Marshall (36), and Ho *et al.* (37) in the temperature and density region appropriate for comparison with the simulation results quoted above. Relatively simple functions of temperature and solvent density are sufficient to reproduce the experimental values with good accuracy. Ho *et al.* used the function,

$$\log K_a^m = 0.997 - 650.07T^{-1} - (10.420 - 2600.5T^{-1})\log \rho \quad (14)$$

where ρ is the solvent density in units of g/cc and superscript m denotes molality. In addition to the representation of the results of Ho *et al.*, values of K_a^m calculated from equation (14) are in good agreement with those determined from the high-pressure conductance measurement of Zimmerman (38) at relatively low pressure and near-critical temperatures.

For water, at the state point treated in the simulation — $T_f=1.05$, $\rho_f=1.0$, i.e., $T=679.5K$, $\rho=0.322g/cc$ — equation (14) predicts $\log K_a^m=3.285$, or $\log K_a^M = \log(K_a^m/\rho)=3.777$ with an experimental uncertainty of $\delta \log K_a^m \approx \pm 0.2$ (37). An equation for $\log K_a^m$ similar to equation (14) is given by Mesmer *et al.* (39) based on the earlier results of Quist and Marshall (36). This representation predicts at this state point a value about 0.6 log units larger than that from equation (14).

Discussion and Final Remarks

Our potential of mean-force calculation indicates that under the near-critical, highly-compressible, and low-dielectrically-screened conditions studied here, water is still a moderate solvent. According to the value of the constant of equilibrium between CIP and SSIP species, K_e , approximately 77% of ion-pairs in this near critical solution are CIP, in contrast to only 2.6% at ambient conditions (13). This difference is largely the result of the additional stabilization of SSIP species at ambient conditions due to the solvent's dielectric screening that suppresses the strong anion-cation Coulombic attraction.

In order to make a fair comparison between the simulation and experimental values of the association constant, we must first analyze the sources of uncertainties and the assumptions involved in the working expressions. The most obvious, and one which has a significant effect, is the constant of integration $W_{AC}(\tau_0)$ in equation (8) based on the continuum model, i.e.,

$$g_{AC}^{\infty}(r) = \exp(-\beta q_A q_C / r_0 \epsilon) \vartheta_{AC}(r) \quad , \quad 0 < r < r_0 \quad (15)$$

where $\vartheta_{AC}(r) = \exp\{\beta(q_A q_C / r_0 \epsilon - W_{AC}(r))\}$. Because the solvent's dielectric constant appears in an exponential, any small change (say a few percent) will have a large impact on the value of the association constant. (Note that this will not be the case for the constant of equilibrium K_e). This can be clearly seen by introducing equation (15) into equation (9) as,

$$K_a = 4\pi \exp(-\beta q_A q_C / r_0 \epsilon) \int_0^{r_{\min}} \vartheta_{AC}(r) r^2 dr \quad (16)$$

One way to minimize the effect of the uncertainties in ϵ in the comparison between simulation and experiment is to compare the values of the *integral* in equation (16) from simulation and experiment rather than the values of the corresponding K_a 's, i.e.,

$$I_a = K_a \exp(\beta q_A q_C / r_0 \epsilon) = 4\pi \int_0^{r_{\min}} \vartheta_{AC}(r) r^2 dr \quad (17)$$

This integral is a very sensitive function of the state conditions. For example, for an infinitely dilute supercritical aqueous solution of NaCl, the simulation results of Cui and Harris (15) indicate that $\log I_a \approx 4.3 \pm 0.13$ at $\rho = 0.1252 \text{ g/cc}$ and $T = 700 \text{ K}$ and $\log I_a \approx 5.6 \pm 0.13$ at $\rho = 0.0832 \text{ g/cc}$ and $T = 800 \text{ K}$. The Guàrdia *et al.* simulation results for ambient water (13) give $\log I_a \approx -1.38$. Moreover, because of its microscopic meaning, I_a will be also very sensitive to the microscopic details of the intermolecular forces involved.

To take advantage of the way the data uncertainties are quoted we present the comparison between our simulation and experimental results in a logarithmic scale, i.e., as $\log I_a$. According to the experimental data of the previous section $\log K_a^M = 3.77 \pm 0.2$, and assuming $r_0 = 8.1 \text{ \AA}$, $\epsilon \approx 5.1$ and the corresponding critical conditions for real water from the NBS/NRC Steam Tables (40), we obtain $\log I_a \approx 1.23 \pm 0.2$. Likewise, taking the simulation result $\log K_a^M = 2.70 \pm 0.3$, $\epsilon = 8.8 \pm 0.9$ for SPC water at $\rho = 0.27 \text{ g/cc}$ and $T = 616 \text{ K}$ (27), we obtain $\log I_a \approx 1.07 \pm 0.3$ where the quoted error comes from the uncertainty in the determination of the solvent's dielectric constant. This comparison clearly indicates that the aqueous electrolyte model used in our simulation describes quite reasonably the ion-pairing at the near-critical condition.

The good agreement between the simulation and experimental values of I_a suggests that care must be exercised in choosing the property used to test the realism with which our ion-water model describes the ion-pairing and related solvation phenomena. The above discussion shows that a direct comparison of the K_a^M values from experiment and simulation is not appropriate because the uncertainties introduced by the constant of integration overshadow the accuracy of the mean-force calculation. For example, if we use the dielectric constant of real water, $\epsilon \approx 5.1$, as is usually done in the literature (13,41,42), we will obtain $\log K_a^M \approx 3.93$ which agrees with the experimental value within the uncertainty of the calculation. This agreement in the values of $\log K_a^M$ contrasts with the order of magnitude difference, $\log K_a^M = 2.70 \pm 0.3$, obtained when using the SPC value of $\epsilon \approx 8.8 \pm 0.9$.

Acknowledgments

This work was supported by the Division of Chemical Sciences, Office of Basic Energy Sciences, U.S. Department of Energy. The work of HDC, JMS and REM has been supported by the Division of Chemical Sciences of the U. S. Department of Energy under Contract No. DE-AC-84OR21400 with Martin Marietta Energy Systems, Inc.

References

- (1) Conway, B. E. *Ionic Hydration in Chemistry and Biophysics*; Elsevier: Amsterdam, 1981.
- (2) Pitzer, K. S. *J. Phys. Chem.* **1986**, *90*, 1502.
- (3) *Recent Advances*; Franks, F., Ed.; Plenum: New York, 1979; Vol. 6.
- (4) Postorino, P.; Tromp, R. H.; Ricci, M. A.; Soper, A. K.; Neilson, G. W. *Nature* **1993**, *366*, 668.
- (5) Mesmer, R. E.; Palmer, D. A.; Simonson, J. M. In *Activity Coefficients in Electrolyte Solutions*; 2nd Edition ed.; K. S. Pitzer, Ed.; CRC Press: Boca Raton, 1991; pp 491-529.
- (6) Levelt Sengers, J. M. H.; Everhart, C. M.; Morrison, G.; Pitzer, K. S. *Chem. Eng. Commun.* **1986**, *47*, 315.
- (7) Fleissner, G.; Hallbrucker, A.; Mayer, E. *J. Phys. Chem.* **1993**, *97*, 4806.
- (8) Hage, W.; Hallbrucker, A.; Mayer, E. *J. Phys. Chem.* **1992**, *96*, 6488.
- (9) Spohn, P. D.; Brill, T. B. *J. Phys. Chem.* **1989**, *93*, 6224.
- (10) Winstein, S.; Clippinger, E.; Fainberg, A. H.; Robinson, G. C. *J. Amer. Chem. Soc.* **1954**, *76*, 2597.
- (11) Sadek, H.; Fuoss, R. M. *J. Amer. Chem. Soc.* **1954**, *76*, 5905.
- (12) Dang, L. X.; Rice, J. E.; Kollman, P. A. *J. Chem. Phys.* **1990**, *93*, 7528.
- (13) Guàrdia, E.; Rey, R.; Padró, J. A. *Chem. Phys.* **1991**, *155*, 187.
- (14) Rey, R.; Guàrdia, E. *J. Phys. Chem.* **1992**, *96*, 4712.
- (15) Cui, S. T.; Harris, J. G. *Chem. Eng. Sci.* **1994**, *49*, 2749.
- (16) Gao, J. *J. Phys. Chem.* **1994**, *98*, 6049.
- (17) Berendsen, H. J. C.; Postma, J. P. M.; von Gunsteren, W. F.; Hermans, J. In *Intermolecular Forces: Proceedings of the Fourteenth Jerusalem Symposium on Quantum Chemistry and Biochemistry*; B. Pullman, Ed.; Reidel: Dordrecht, 1981; pp 331.
- (18) Cummings, P. T.; Chialvo, A. A.; Cochran, H. D. *Chem. Eng. Sci.* **1994**, *49*, 2735.
- (19) Pettitt, B. M.; Rossky, P. J. *J. Chem. Phys.* **1986**, *84*, 5836.
- (20) Hansen, J. P.; McDonald, I. R. *Theory of Simple Liquids*; Second ed.; Academic Press: New York, 1986.
- (21) Fumi, F. G.; Tosi, M. P. *J. Phys. Chem. Solids* **1964**, *25*, 31.
- (22) Tosi, M. P.; Fumi, F. G. *J. Phys. Chem. Solids* **1964**, *25*, 45.
- (23) de Pablo, J. J.; Prausnitz, J. M.; Strauch, H. J.; Cummings, P. T. *J. Chem. Phys.* **1991**, *93*, 7355.
- (24) Allen, M. P.; Tildesley, D. J. *Computer Simulation of Liquids*; Oxford University Press: Oxford, 1987.
- (25) Steinhauser, O. *Molecular Physics* **1982**, *45*, 335.
- (26) de Leeuw, S. W.; Perram, J. W.; Smith, E. R. *Proc. Royal Soc. London*, **1980**, *A373*, 27.
- (27) Cummings, P. T.; Cochran, H. D.; Simonson, J. M.; Mesmer, R. E.; Karaborni, S. *J. Chem. Phys.* **1991**, *94*, 5606.
- (28) Mezei, M.; Beveridge, D. L. *J. Chem. Phys.* **1981**, *74*, 622.

- (29) McQuarrie, D. A. *Statistical Mechanics*; Harper and Row, New York: 1976.
- (30) Jorgensen, W. L.; Ravimohan, C. J. *J. Chem. Phys.* **1985**, *83*, 3050.
- (31) Ciccotti, G.; Ferrario, M.; Hynes, J. T.; Kapral, R. *Chem. Phys.* **1989**, *129*, 241.
- (32) Høye, J. S.; Stell, G. *Faraday Disc. Chem. Soc.* **1977**, *64*, 16-21.
- (33) Cochran, H. D.; Cummings, P. T.; Karaborni, S. *Fluid Ph. Equil.* **1992**, *71*, 1.
- (34) Shedlovsky, T. *J. Franflin Inst.* **1938**, *225*, 739.
- (35) Fogo, J. K.; Benson, S. W.; Copeland, C. S. *J. Chem. Phys.* **1954**, *22*, 212.
- (36) Quist, A. S.; Marshall, W. L. *J. Phys. Chem.* **1968**, *72*, 684-703.
- (37) Ho, P. C.; Palmer, D. A.; Mesmer, R. E. *J. Sol. Chem.* **1994**, *23*, 997.
- (38) Zimmerman, G. H. Ph.D. Thesis, University of Delaware, 1993.
- (39) Mesmer, R. E.; Marshall, W. L.; Palmer, D. A.; Simonson, J. M.; Holmes, H. F. *J. Sol. Chem.* **1988**, *17*, 699.
- (40) Haar, L.; Gallagher, J. S.; Kell, G. S. *Steam Tables*; Hemisphere Publishing Corporation: 1984.
- (41) Guàrdia, E.; Robinson, A.; Padró, J. A. *J. Chem. Phys.* **1993**, *99*, 4229.
- (42) Madhusoodanan, M.; Tembe, B. L. *J. Phys. Chem.* **1994**, *98*, 7090.

RECEIVED April 24, 1995

Chapter 5

Simulation and Spectroscopy of Solvation in Water from Ambient to Supercritical Conditions

Keith P. Johnston¹, Perla B. Balbuena¹, Tao Xiang¹,
and Peter J. Rossky²

¹Department of Chemical Engineering and ²Department of Chemistry
and Biochemistry, University of Texas, Austin, TX 78712

A review is presented of recent computer simulation and UV-visible spectroscopic studies of the solvation of nonelectrolytes and electrolytes in ambient and supercritical water. In addition, new simulation and fluorescence results are presented to focus on subcritical water solutions at temperatures from 298 to 573 K at densities on the coexistence curve of pure liquid water. The solvation of Cl^- is examined with molecular dynamics computer simulation and that of pyrene is probed with fluorescence spectroscopy. For Cl^- there is little loss in the coordination number from ambient to 523 K; this behavior continues up to the critical temperature (647.13 K) due to the strong attractive nature of the chloride-water interaction. Furthermore the negative heat and entropy of hydration are relatively constant up to about 573 K. In contrast, the solvation of pyrene decreases significantly with temperature. For nonelectrolytes such as Xe, the enthalpy of hydration changes from exothermic to endothermic as the coordination number decreases. The corresponding entropy changes from negative to positive as the hydrophobic effect dissipates, and the Gibbs free energy goes through a maximum.

To develop hydrothermal technology, a better understanding is needed of molecular interactions in high temperature aqueous solutions and how they influence thermodynamic properties and chemical kinetics. Although a number of simulation studies have investigated ambient water (AW) (i.e. 298 K and 1 bar) and supercritical water (SCW) ($T_c = 647.13$ K, $\rho_c = 0.322$ g/cc, $P_c = 220$ bar) solutions, far less attention has been given to subcritical liquid water in the interesting temperature regime of 373 to 573 K where the structure changes so dramatically. In many cases, organics are orders of magnitude more soluble in liquid water at 573 K than 298 K. Thus subcritical water may be used as a substitute for organic solvents without the need to go all the way to supercritical temperatures and pressures.

The objective of the new simulation and spectroscopic studies reported in this work is to examine changes in solvation of nonelectrolytes and electrolytes in liquid subcritical water from 298 to 647 K. In order to put the new studies into

0097-6156/95/0608-0077\$12.00/0
© 1995 American Chemical Society

perspective, the following section provides a review of the current state of the art for simulations of pure water and dilute solutions of nonelectrolytes and electrolytes. Thermodynamic properties of hydration are analyzed in terms of solvation structure over this wide range in temperature. The next section is a review of very recent UV-vis spectroscopic studies of organic solutes. After providing these reviews of simulation and spectroscopy, we present a new experimental study of solvation of pyrene in sub- and supercritical water by fluorescence spectroscopy. In the final section, we examine chloride solvation with molecular dynamics simulation at subcritical temperatures not considered previously. The conclusions section synthesizes the results for solvation of nonelectrolytes and electrolytes from both simulation and spectroscopy.

Review of Computer Simulation Studies.

Pure Water. As liquid water is heated from 298 to 673 K, the hydrogen bonded tetrahedral structure dissipates. Based on simulations with the SPCE (Simple Point Charge Extended) model (1), Guissani and Guillot (2) observed that the coordination number of pure saturated liquid water (Figure 1) increases with temperature from a value of about 4.5 at 300 K to a maximum value of 5.9 around 473 K and then decreases towards the critical point. The tetrahedral structure of liquid water causes the coordination number to be about 4.5 at ambient conditions, instead of a value of 12 for a typical Lennard-Jones liquid. Furthermore, molecules beyond the first shell also participate in a very large connected H-bond network. As the temperature is increased, the H-bond network gradually collapses, and molecules in the first shell become much more free to reorient, leaving room for other water molecules. This collapse increases the coordination number. At temperatures larger than about 500 K, the coordination number decreases due to the decrease in density.

The most striking change in structure takes place between 373 and 473 K (2). Here the second peak in the oxygen-oxygen distribution function g_{OO} shifts progressively from 4.5 to 5.5 Å. Furthermore, at 473 K there are very few angular correlations beyond the first shell of neighbors, indicating the extended hydrogen bond network is largely destroyed. Nevertheless, the remaining hydrogen bonds persist up to the critical temperature (3), as is also observed in predictions of a lattice fluid hydrogen bonding model (4), which utilized energy, entropy, and volume of hydrogen bonding parameters obtained from spectroscopic data at subcritical conditions (5).

There is some controversy regarding the degree of hydrogen bonding in SCW. Recent neutron diffraction studies (6,7) indicate that the degree of hydrogen bonding in pure SCW is lower than the values from simulations based on rigid models (such as SPC (Simple Point Charge)(8) and SPCE). This disagreement was confirmed by new simulations with the SPC model(9) done at conditions matched to the experiments. However, significant challenges are present in interpreting the above neutron diffraction data (9,10). The neutron diffraction results agree quantitatively with ab-initio computer simulation(10) for the total structure factor, but the agreement for the spatial radial distribution functions is substantially less satisfying. Further support for an SPC-like model even in SCW comes from the fact that the ab-initio simulated molecular dipole moment is close to that of the SPC model rather than to the gas phase result. The persistence of significant hydrogen bonding among water molecules would not be surprising considering that the hydrogen bond energy considerably exceeds kT even at the critical temperature. Furthermore, previous and new experimental results by Gorbaty et al. (11-13) using IR spectroscopy and X-ray diffraction techniques indicate the presence of hydrogen bonds in supercritical water at temperatures up to 800 K. Thus the degree of

hydrogen bonding in pure SCW is an open question and represents an interesting theoretical and experimental challenge.

Nonelectrolytes in Water. For non-polar solutes, the mechanism of hydration to explain the minimum in the solubility of rare gases and other small solutes in saturated liquid water versus temperature has been proposed by several authors (14,15). For an apolar solute such as a rare gas at low temperatures, the solvation structure is characteristic of so-called hydrophobic hydration. The hydrogen bonding groups straddle the nonpolar surface in order to maintain the hydrogen bonding available to the bulk water. This highly oriented solvent structure resembles clathrate hydrate structures locally. As shown in Figure 1, at ambient conditions the coordination number is much higher for water about Ne than about water. In contrast with the behavior of pure water, there is a pronounced decrease in the coordination number of these hydrophobic solutes as water densities are reduced and temperatures increased along the liquid branch of the coexistence curve. This observation is the first entry in Table I, which will serve as a summary of all the important results throughout this study. Guillot and Guissani (16) simulated the solvation of hydrophobic solutes. At low temperatures, a polyhedral cage of water molecules is formed around a hydrophobic solute that is favored by the highly connected H-bond network. At temperatures higher than about 400 K, for liquid densities on the coexistence curve, the decrease in density favors the occurrence of cavities in the H-bond network that increases the solubility.

Table I. Effect of temperature on the hydration of solutes in the subcritical region from 300 to 573 K along the saturation curve.

Property	Nonelectrolyte	Electrolyte
Coord. number	large decrease	very small decrease
ΔH	- to +	- (small change)
$-\Delta S$	+ to -	+ (small change)
ΔG	(maximum)	- (small change)

To illustrate these concepts we show in Figure 2 computer simulation (16) and experimental data (17,18) for thermodynamic properties of hydration of Xe in liquid water on the coexistence curve for the SPCE model. Extensive discussions about the choice of an appropriate reference state have been presented (19,20). Here we use the excess Gibbs free energy ΔG^0 defined as the change in free energy in transferring the solute from pure ideal gas state to a state at infinite dilution in the solvent at the same temperature T and pressure P. It is related to the solubility of the gas in the liquid through k_H , the Henry's constant, by

$$\Delta G^0 = RT \ln k_H \quad (1)$$

$$\text{where } k_H = \lim_{x_2 \rightarrow 0} \frac{f_2}{x_2} \quad (2)$$

and f_2 and x_2 are the fugacity and liquid mole fraction of the solute, respectively.

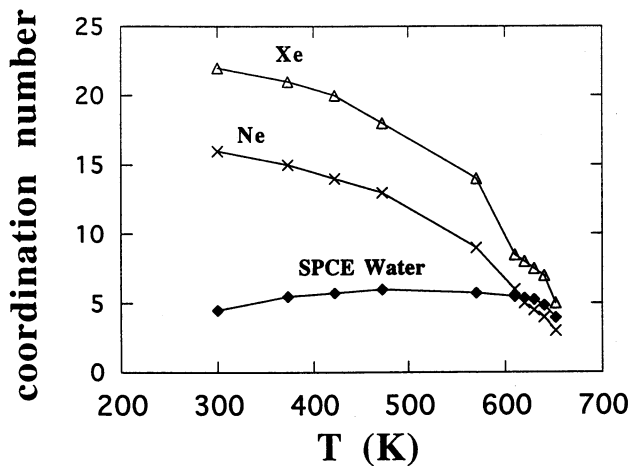


Figure 1. Variation of the coordination number of pure water and Xe and Ne at infinite dilution in liquid SPCE water at densities on the coexistence curve according to MD simulation data (2,16).

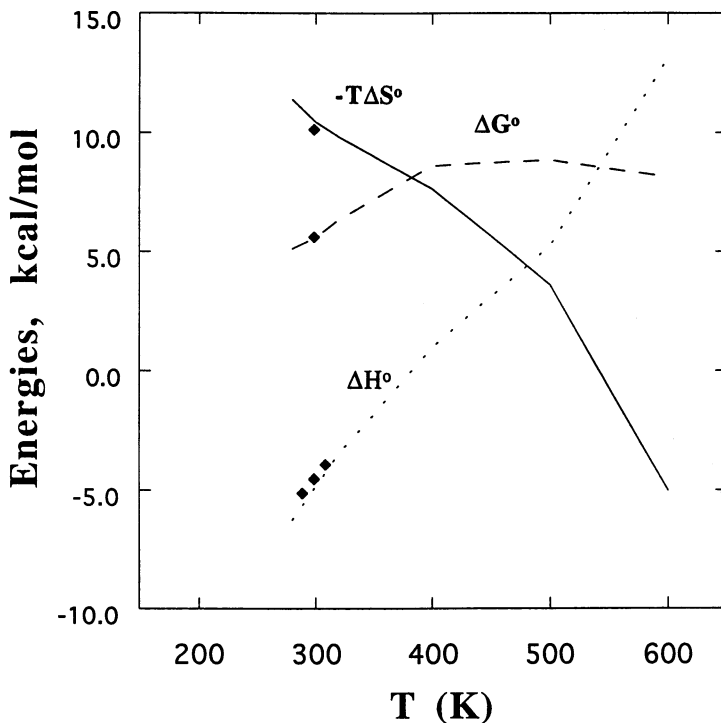


Figure 2. Thermodynamic properties for Xe in water (same densities as Figure 1). Continuum curves are computer simulation data from Ref. 16. Points are experimental data from Refs. 17 and 18.

The positive ΔG° near ambient conditions is caused by ordering of the water, as is evident in the negative $\Delta S^\circ(21)$ while the energy of hydration is slightly exothermic. As the temperature is increased, the tetrahedral extended hydrogen bonding network of water is disrupted, so that there is less tendency for water to orient itself about the solute. Consequently ΔS° decreases in magnitude and becomes positive. Also, ΔH° becomes smaller in magnitude, until it changes sign and becomes endothermic, reflecting the energy needed to create a cavity in the solution. Here the contribution of the attractive solute-solvent interactions becomes progressively smaller relative to the repulsive forces. Since at low temperatures ΔH° is found to change more rapidly than $-T\Delta S^\circ$, the sum, ΔG° , increases with temperature passing through a maximum (that corresponds to a minimum in gas solubility) at temperatures near 400 K (Table I). Afterwards ΔG° decreases causing the solubility to increase reaching values higher than at ambient conditions.

Electrolytes in Water. A systematic investigation of the qualitative behavior of solutes of different charge at infinite dilution in ambient water has been carried out by Geiger (22). The nature of the structure breaking effect has been investigated using molecular dynamics (MD). Static and dynamic properties have been compared for the interactions of water with otherwise equivalent spherical solutes carrying charges ranging from 0 (non-polar, Xe type) to +2 (several cations) and -1 (model anion). An increase in charge causes the first peak in the solute-oxygen pair distribution function (designated as $g_{\text{IO}}(r)$) to become much higher and more narrow reflecting the growth in structure in the first solvation shell due to the increasingly attractive electrostatic interaction. Also, an increment of about 30 K does not change the first peak in $g_{\text{IO}}(r)$ for the case of a monovalent cation, although the structure beyond the first shell is flattened out. For a given charge, the first peak of $g_{\text{IO}}(r)$ is comparable for an anion and a cation, while more structure is found in the second shell of the anion. The effect of solutes on water structure (for example on $g_{\text{OO}}(r)$) has also been analyzed. The addition of a nonelectrolyte increases the first peak of $g_{\text{OO}}(r)$ slightly, while ions partially destroy the water structure. A similar loss in structure occurs in pure water with an increase in temperature. Recently, MD simulations have been used to determine the equilibrium structure of water molecules about Na^+ and Cl^- ions at ambient conditions and at two states near the critical point (23,24). The SPC model was used for water. It has been found that the local density of water in the first solvation shell of the ions decreases only slightly from AW to SCW conditions. The first measurements of ion hydration in SCW have been reported recently (25) using X-ray absorption fine structure. Radial distribution functions have been determined for 0.2M solutions of Sr^{++} in SCW, and also for solutions of Kr in SCW. The decrease in coordination number from AW to SCW for Sr^{++} is much larger than that for Cl^- in simulations. Because of this profound difference in desolvation behavior, further work is required to understand ion solvation as was the case above for pure water.

The system NaCl at infinite dilution in water has been the subject of several publications (26,27). In particular, Cui and Harris (26) studied this ion pair system over a wide range of temperature and density, and also considered ion association. At 800 K and a density of 0.083 g/cm^3 , the ion association is driven by a gain in the entropic contribution to the potential of mean force (pmf) due to the loss of electrostriction upon ion pairing. The energetics oppose ion pairing as water strongly solvates the isolated ions. The results follow the same trends by continuum theory (28) at ambient conditions, but the actual values are much larger

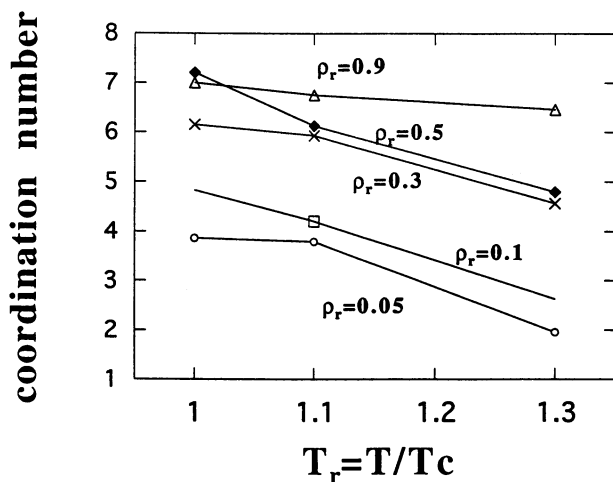


Figure 3. Variation of the coordination number of Cl^- versus temperature in SCW according to MD simulations (29-31), SPC model. Density and temperature reduced with the model critical properties.

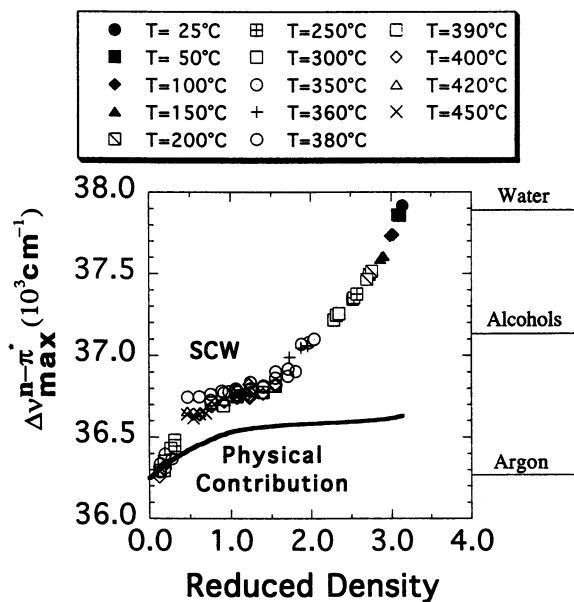


Figure 4. Solvatochromic data for acetone in SCW (35).

in magnitude in SCW. On the other hand, the presence of oscillations caused by the molecular nature of the solvent in the pmf, as given by molecular theory in AW (28), is absent at SCW conditions.

Recently, we examined the solvation of species of varying polarity along the reaction coordinate for the S_N2 reaction of Cl^- and CH_3Cl from ambient water to SCW (29-31). The SPC model was used for water. In the collinear transition state, the negative charge is distributed equally between the two chlorines. For $T_r = 1$ and $\rho_r = 1.5$ (temperature and density reduced with respect to the critical properties of the SPC model (32) corresponding to $T = 587$ K and $\rho = 0.405$ g/cc), the free energy barrier at the transition state is nearly as high as in ambient water, corresponding to the small reduction in the coordination number about Cl^- which keeps the reactants well-stabilized (Table I). At 758 K and 0.11 g/cc, the coordination number of water about Cl^- is 4.6 according to our simulations (31), compared to a value of 4.5 obtained by using a lattice model that incorporates hydrogen bonding (4), while the corresponding simulated value at ambient conditions is 8. In Figure 3 the coordination number about the chloride ion n_{Cl} are presented over a wide range in temperature and density for the ion-dipole complex between Cl^- and CH_3Cl . Extreme conditions (e.g., reduced densities of 0.05 and 0.3 for reduced temperatures of 1.0 and 1.3, respectively) are found to be necessary to remove half of the water molecules in the first solvation shell about the chloride ion. In addition, much of the hydrogen bonding in AW is still present down to $\rho_r = 0.5$, despite the fact that the majority of the weaker water-water hydrogen bonds have dissipated (30,31).

A compilation of experimental hydration properties for ionic solutions has been presented (33) along with a discussion of several models. At subcritical conditions, from 300 K to about 573 K, both experimental measurements and predictions of a semicontinuum model (34) show a small change in ΔG , ΔH and $-T\Delta S$ as a function of temperature (Table I). Solvation is highly exothermic, as indicated by ΔH . The change in entropy is always negative but remains relatively small within this range of temperatures. However, both ΔH and $-T\Delta S$ change markedly above 573 K as the liquid expands to a much greater degree with temperature on approach to the critical density.

Review of UV-visible Spectroscopy.

UV-visible spectra of organic solutes in SCW have become available only recently. In both supercritical fluids and conventional liquids, solvent-solute interactions are often characterized by spectral shifts for solvatochromic probes. Solvatochromic data are shown for acetone in SCW in Figure 4 (35). The value $\Delta\nu$ (max) is the energy of the maximum in the $n-\pi^*$ absorbance band. It is corrected for temperature effects, based on measurements of ν (max) in argon. The $\Delta\nu$ (max) of water mimics that of many organic solvents as the temperature increases. This parallelism suggests it could be used as a substitute for various organic solvents.

Three distinct density regions are observed, as were observed previously for fluorescent probes in CO_2 and fluoroform (36). In the liquid ($1.5 < \rho_r < 3.5$) and gaseous regions ($\rho_r < 0.5$), $\Delta\nu$ (max) changes significantly with density, whereas it changes much less in the near critical region ($0.5 < \rho_r < 1.5$). The degree of

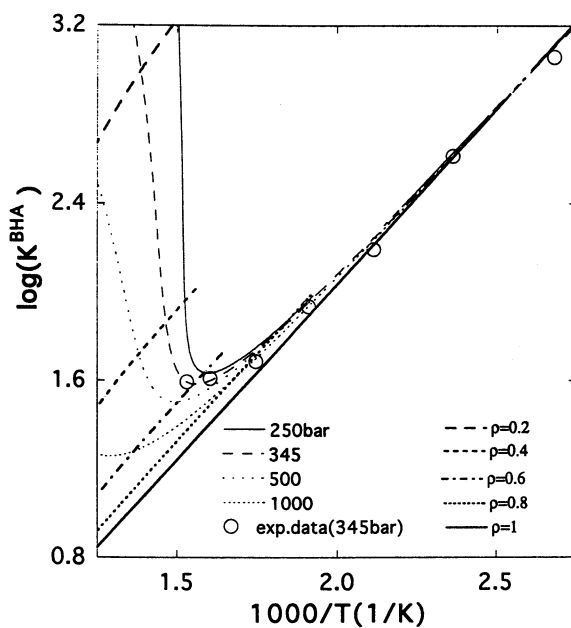
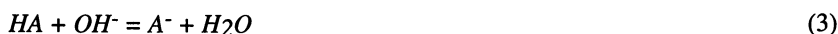


Figure 5. Temperature dependence of K_{BHA} for the reaction of β -naphthol + OH^- (39).

hydrogen bonding between acetone and water may be estimated from the difference between the experimental Δv (max) and the calculated so-called physical contribution, due to dipole-dipole and induction forces. Based on this, the hydrogen bonding persists to densities as low as 0.1 g/mL. At 653 K, it is well established at $\rho_r = 0.5$ and changes little with an increase in density. At the critical point about 1/3 of the hydrogen bonds between acetone and water at ambient temperature are still present, which is analogous to the behavior of hydrogen bonding in pure water based on IR spectra (37) and computer simulation data (3,38).

In a second example of UV-visible spectroscopy of organic solutes in supercritical water, we examine Bronsted acid-base behavior (39). The objective is to develop in-situ pH indicators for SCW. The equilibrium constant, K_{BHA} , for a reaction between an organic acid (β -naphthol) and a base (OH^- ion) may be written as



with an equilibrium constant defined by

$$K_{BHA} = \frac{m_{A^-}}{m_{HA} \cdot m_{OH^-}} \quad (4)$$

where the infinite dilution activity coefficient of each species is defined as unity, and the mole fraction of water is essentially unity.

Experimental results for the temperature dependence of K_{BHA} are shown in Figure 5 for a constant pressure of 345 bar (39). The lines are extrapolations of the data with a modified Born model which includes the water of hydration in the Born radius for OH^- . Over most of the temperature range this acid-base reaction is exothermic (at a constant pressure of 345 bar); however, it becomes endothermic at the highest temperatures. At high temperatures, the results are complicated by the large decrease in ρ with an increase in T . The change in slope of $\log K_{BHA}$ vs $1/T$ at constant pressure may be understood in terms of the following thermodynamic relationship:

$$\Delta H^0/RT^2 = (\partial \ln K / \partial T)_P = (\partial \ln K / \partial T)_\rho - \rho \alpha (\partial \ln K / \partial \rho)_T \quad (5)$$

where α is the volume expansivity $(-1/\rho)(\partial \rho / \partial T)_P$. At lower temperatures, the isothermal compressibility and volume expansivity are relatively small and the second term may be neglected. Here, the reaction is exothermic for K_{BHA} since the acidity and basicity of the products are less than that of the reactants. However, at higher temperatures, the volume expansivity becomes large and the second term becomes dominant. Because $\partial \ln K / \partial \rho$ is relatively constant, the shape of the isotherms at high temperature follows the volume expansivity. The isobars become endothermic at high temperatures, since $\partial \ln K / \partial \rho$ is negative and the volume expansivity is positive. The decrease in K with an increase in ρ is due to the greater stabilization of the smaller OH^- ion relative to the naphtholate anion as the dielectric constant increases.

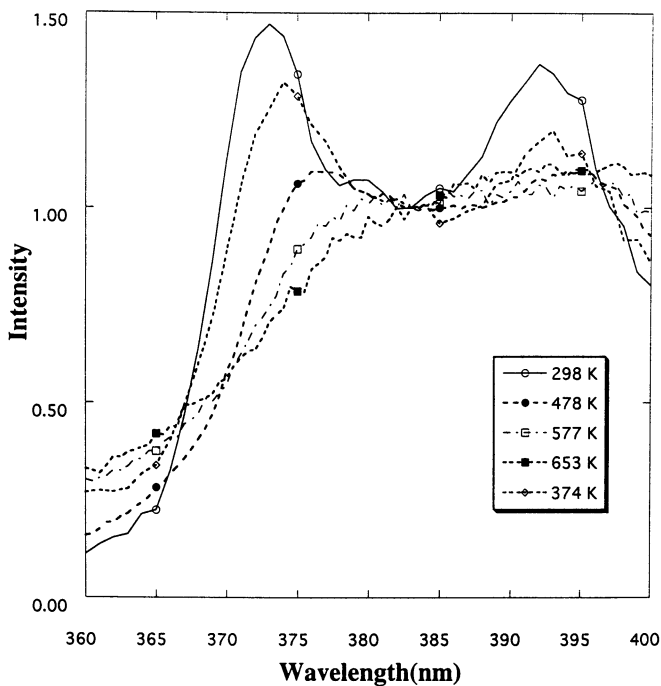


Figure 6. Fluorescence spectra of pyrene in liquid water at densities on the coexistence curve.

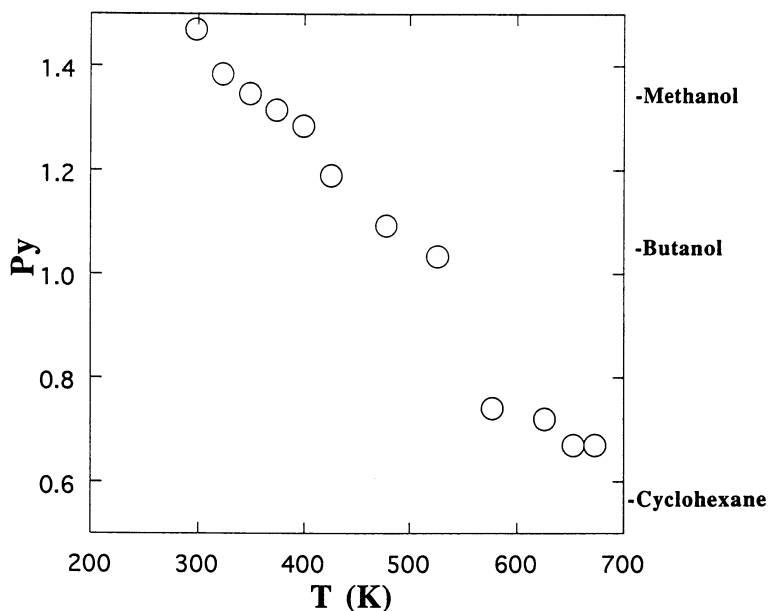


Figure 7. I/III intensity ratio vs. temperature for pyrene in water.

Results and Discussion.

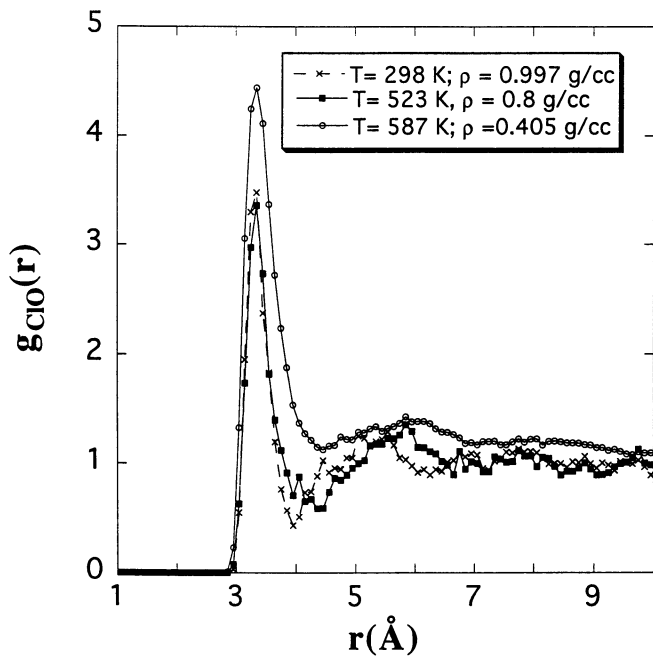
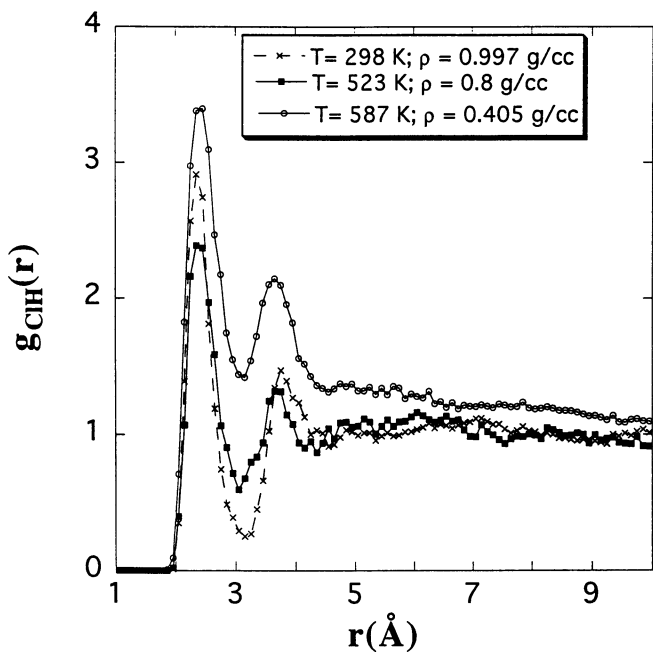
Fluorescence Spectroscopy. Because we are not aware of previous fluorescence experiments of organics in water at elevated temperature, we present a brief description of the experiments. Ultra-filtered water (Millipore) was used for experiments. Pyrene (Aldrich) was purified by vacuum sublimation at about 423 K. Fresh solutions (10^{-7} - 10^{-6} M) were prepared and filtered for each experiment. The stability of pyrene in pure water was tested in batch stainless steel reactors, which consisted of Swagelock 1/4" tees. The solutions first were purged with nitrogen for 30 min., then the reactors were sealed at room temperature in a nitrogen atmosphere and immersed in a constant-temperature (673 K) sand bath for 2 hours. The products were analyzed by gas chromatography. Pyrene was stable in pure water for at least 2 hours at 673 K and 345 bar.

Steady state fluorescence spectra were obtained with an SLM Aminco 500 fluorometer and a high pressure optical cell with three sapphire windows. The cell was similar to a previous design (35). The excitation wavelength was 338nm. Emission and excitation slit widths were 5 nm and 7 nm, respectively, because of the decrease in quantum yield at high temperature. The pressure was controlled electronically with a Beckman Model 100 A HPLC pump and was measured to within 1% with a Heise 710A digital pressure gauge. During a spectral scan, the pressure varied less than 0.345 bar. The solutions were first deoxygenated with N_2 for 30 min.

The Py scale of solvent polarity is based on the photophysical properties of pyrene in solution. The emission spectrum of the monomer consists of five vibronic bands labeled I-V in progressive order, i.e. the 0 - 0 bands being labeled I, etc. The intensity of various bands are strongly dependent on solvent environment. Significant enhancement is observed in the 0 - 0 vibronic band intensity in the presence of polar solvents. The ratio of emission intensities for bands I and III (Py=I/III) serves as a measure of solvent polarity and structure (40,41). Figure 6 shows steady state fluorescence spectra of pyrene in pure water at different temperatures. Py changes with temperature as water density decreases along the coexistence curve as shown in Figure 7. The peaks (Figure 6) become broader as temperature increases. The intensities of emission at 373 nm and 383 nm have been chosen to determine the ratio I/III. At 293 K, the Py value determined in this work is about 10% lower than that reported by Street and Acree(40). They used a 3-nm emission slit width at 294 K. The difference may come from the difference of emission slit width (42,43).

For temperatures from 300 to 520 K, Py decreases fairly linearly with temperature. The III band is small, since the polarity of water is high. Above 473 K, the I band becomes small as well. At 520 K, there is a sharp decrease in Py. It is interesting that this discontinuity takes place in the region where the coordination number of pure water (Figure 1) goes through a maximum. This temperature is approximately in the region where the tetrahedral structure of water has vanished. This sharp decrease is also observed for the coordination number of water about Xe and CH_4 (Figure 1), except that it takes place at 570 K. However, a large change was not observed in this region for the Δv (max) of acetone or the hydration of Cl^- . It appears that this large change in solvation is present for hydrophobic solutes and does not occur for highly polar and ionic solutes. For temperatures above 577 K, Py is quite small, near that of cyclohexane, and changes little as the temperature is further increased.

Structural Results from MD Simulations. In this section we focus on solvation properties for ions in subcritical liquid water and at one supercritical condition.

Figure 8. Radial distribution function $g_{ClO}(r)$.Figure 9. Radial distribution function $g_{ClH}(r)$ at the same conditions as Figure 8.

Radial distribution functions of the chloride ion in water are compared at three states: 1) ambient liquid conditions: $T = 298.15$ K and $\rho = 0.997$ g/cc; 2) an intermediate subcritical temperature and liquid density: $T = 523$ K and $\rho = 0.8$ g/cc; and 3) a supercritical condition: $T = T_c$ and $\rho = 1.5 \rho_c$ ($T = 587$ K and $\rho = 0.405$ g/cc). The SPC model was used for water; details are given in our previous publications (29-31). We consider the solute-oxygen and solute-hydrogen pair correlation functions, in order to obtain information about the effect of temperature and density on the structural arrangements of water near the solute.

Figure 8 shows the chloride-oxygen pair correlation function. The results at liquid subcritical conditions are from new simulations. At room temperature, water molecules distribute near the chloride ion in a first shell with a maximum at 3.5 Å, followed by a deep minimum at 4 Å, and a second shell that peaks at about 5.5 Å. When the temperature is raised to 523 K, the first peak broadens slightly remaining centered in the same position. The first minimum and the second peak shift outwards to approximately 4.4 and 5.8 Å, respectively. The shift of the position of the second oxygen peak (Figure 8) to further distances at the higher temperatures is due to the higher kinetic energy and lower bulk density. At supercritical conditions, the first peak is even broader and the second peak is substantially diminished. The coordination number calculated according to a geometric definition (30, 31) remains constant, within the statistical error, ranging from an ambient value of about 8 to 7.6 at 523 K to 7.7 in SCW.

The solvent structure is further understood upon examination of the solute-hydrogen distribution function. The first two peaks in $g_{ClH}(r)$, shown in Figure 9, correspond to the two hydrogen atoms belonging to water molecules in the first coordination shell that form H-bonds with the chloride ion. At the three states they peak at about 2.5 Å. The magnitude of the first peak has a minimum value at the intermediate temperature, however the number of chloride-water H-bonds does not pass through a minimum at that condition, but decreases from a value of 7.2 at ambient water to 6.3 at the intermediate temperature and a lower value of 4.2 at the supercritical condition. The difference between the behavior of $g(r)$ and that of the number of hydrogen bonds is just due to a factor of the density absent in $g(r)$.

The decrease in the number of chloride-water hydrogen bonds is also seen in Figure 10, that shows the chloride-water pair energy distribution. The ordinate represents the number of water molecules interacting with the chloride with the energy given in the abscissa. The highest peak, centered near zero, is indicative of the water molecules located far away from the solute. The other peak, centered at about -12 kcal/mol, corresponds to molecules forming hydrogen bonds with the chloride, and a clear decrease is observed as a function of temperature. Nevertheless, the number of strong interactions remains high, as indicated by the persistence of the AW coordination number at the intermediate and supercritical temperatures. As pointed out in Table I, this determines one of the main differences in behavior of electrolytes as opposed to nonelectrolytes.

Summary.

The main features of hydration in the subcritical region are summarized in Table I along the liquid branch of the coexistence curve from 300 to 573 K. The coordination number of nonelectrolytes decreases significantly as the temperature is increased to the critical point, according to both simulations of rare gases and fluorescence studies of pyrene. For gas solutes such as Xe, the enthalpy of hydration changes from exothermic to endothermic as the coordination number decreases. Also, the entropy changes from negative to positive as the hydrophobic

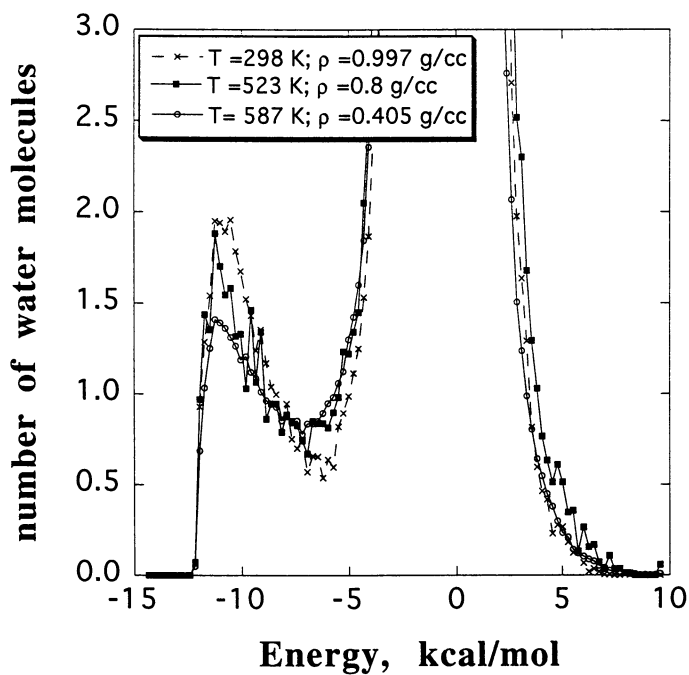


Figure 10. Pair energy distribution for the water molecules about the chloride ion.

effect dissipates, and the Gibbs free energy goes through a maximum. The entropy of hydration is strongly influenced by the hydrogen bonds between the water molecules surrounding the nonelectrolyte.

In contrast with the behavior for nonelectrolytes, there is little change within this temperature range in the coordination number and each of the thermodynamic properties of hydration for electrolytes with temperature. The strongly attractive nature of the chloride-water interaction versus the weaker nonelectrolyte-water interaction explains the difference in the temperature effects. It also explains the fact that the water-water interactions have a much smaller influence on the coordination number of electrolytes versus nonelectrolytes.

Acknowledgments are made to the US Army Research Office for University Research Initiative Grant N° DAAL 03-92-6-0174 and to the Separations Research Program at The University of Texas. Computation support came from The University of Texas System Center for High Performance Computing, Cray Research Inc., the Army Research Office under contract number DAALO3-89-C-0038 with the University of Minnesota, the Army High Performance Computing Research Center (AHPCRC) and the DoD Shared Resource Center at the AHPCR. Partial support of this work by a grant from the R. A. Welch Foundation (F-0761) to P. J. R. is also acknowledged.

Literature Cited.

- Berendsen, H. J. C.; Grigera, J. R.; Straatsma, T. P., *J. Phys. Chem.* **1987**, *91*, 6269-6271.
- Guissani, Y.; Guillot, B., *J. Chem. Phys.* **1993**, *98*, 8221-8235.
- Mountain, R. D., *J. Chem. Phys.* **1989**, *90*, 1866-1870.
- Gupta, R. B.; Johnston, K. P., *Ind. Eng. Chem. Res.* **1994**, *33*, 2819-2829.
- Smits, P. J.; Economou, I. G.; Peters, C. J.; de Swaan Arons, J., *J. Phys. Chem.* **1994**, *98*, 12080-12085.
- Postorino, P.; Tromp, R. H.; Ricci, M.-A.; Soper, A. K.; Neilson, G. W., *Nature* **1993**, *366*, 668-670.
- Tromp, R. H.; Postorino, P.; Neilson, G. W.; Ricci, M.-A.; Soper, A. K., *J. Chem. Phys.* **1994**, *101*, 6210-6215.
- Berendsen, H. J. C.; Postma, J. P. M.; Van Gunsteren, W. F.; Hermans, J. *Intermolecular Forces*; Reidel: Dordrecht, 1981.
- Chialvo, A. A.; Cummings, P. T., *J. Chem. Phys.* **1994**, *101*, 4466-4469.
- Fois, E. S.; Sprik, M.; Parrinello, M., *Chem. Phys. Lett.* **1994**, *223*, 411-415.
- Gorbaty, Y. E.; Demianets, Y. N., *Chem. Phys. Lett.* **1983**, *100*, 450-454.
- Gorbaty, Y. E.; Demianets, Y. N., *Mol. Phys.* **1985**, *55*, 571-588.
- Gorbaty, Y. E.; Kalinichev, A. G., submitted to *J. Phys. Chem.* **1995**.
- Franks, F., *Far. Symp. Chem. Soc.* **1982**, *17*, 7-10.
- Ben-Naim, A. *Water and aqueous solutions. Introduction to a molecular theory.*; Plenum Press: New York, NY, 1974.
- Guillot, B.; Guissani, Y., *J. Chem. Phys.* **1993**, *99*, 8075-8094.
- Olofsson, G.; Oshodj, A. A.; Qvarnstrom, E.; Wadso, I., *J. Chem. Therm.* **1984**, *16*, 1041-1052.
- Dec, S. F.; Gill, S. J., *J. Sol. Chem.* **1985**, *14*, 417-429.
- Guillot, B.; Guissani, Y., *Mol. Phys.* **1993**, *79*, 53-75.
- Ben-Naim, A., *J. Phys. Chem.* **1978**, *82*, 792-803.
- Rossky, P. J. In *Computer simulation of chemical and biomolecular systems*; Beveridge, D. L. and Jorgensen, W. L., Ed.; Ann. of the NY Acad. of Sci.; New York Acad. of Sci.: New York, NY, 1986; Vol. 482, pp 115-126.
- Geiger, A., *Ber. Bunsenges. Phys. Chem.* **1981**, *85*, 52-63.

- 23 Cummings, P. T.; Cochran, H. D.; Simonson, J. M.; Mesmer, R. E.; Karaborni, S., *J. Chem. Phys.* **1991**, *94*, 5606-5621.
- 24 Cochran, H. D.; Cummings, P. T.; Karaborni, S., *Fluid Phase Equilibria* **1992**, *71*, 1-16.
- 25 Pfund, D. M.; Darab, J. G.; Fulton, J. L.; Ma, Y., *J. Phys. Chem.* **1994**, *98*, 13102-13107.
- 26 Cui, S. T.; Harris, J. G., *Chem. Eng. Sci.* **1994**, *49*, 2749-2763.
- 27 Gao, J., *J. Phys. Chem.* **1994**, *98*, 6049-6053.
- 28 Pettitt, B. M.; Rossky, P. J., *J. Chem. Phys.* **1986**, *84*, 5836-5844.
- 29 Balbuena, P. B.; Johnston, K. P.; Rossky, P. J., *J. Am. Chem. Soc.* **1994**, *116*, 2689-2690.
- 30 Balbuena, P. B.; Johnston, K. P.; Rossky, P. J., *J. Phys. Chem.* **1995**, *99*, 1554-1565.
- 31 Flanagin, L. W.; Balbuena, P. B.; Johnston, K. P.; Rossky, P. J., *J. Phys. Chem.* **1995**, in press.
- 32 de Pablo, J. J.; Prausnitz, J. M.; Strauch, H. J.; Cummings, P. T., *J. Chem. Phys.* **1990**, *93*, 7355-7359.
- 33 Fernández-Prini, R. J.; Corti, H. R.; Japas, M. L. *High-Temperature Aqueous Solutions: Thermodynamic Properties*; CRC Press: Boca Raton, FL, 1992.
- 34 Tanger IV, J. C.; Pitzer, K. S., *J. Phys. Chem.* **1989**, *93*, 4941-4951.
- 35 Bennett, G. E.; Johnston, K. P., *J. Phys. Chem.* **1994**, *98*, 441-447.
- 36 Sun, Y.-P.; Fox, M. A.; Johnston, K. P., *J. Am. Chem. Soc.* **1992**, *114*, 1187-1194.
- 37 Buback, M.; Crerar, D.; Koplitz, L. M. In *Hydrothermal Experimental Techniques*; Ulmer, G.; Barnes, H. L., Ed.; Wiley: New York, NY, 1987, pp 333.
- 38 Kalinichev, A. G.; Heinzinger, K. *Computer Simulations of Aqueous Fluids at High Temperatures and Pressures*; Springer-Verlag: New York, NY, 1992.
- 39 Xiang, T.; Johnston, K. P., *J. Phys. Chem.* **1994**, *98*, 7915-7922.
- 40 Street, K. W.; Acree, W. E., *J. of Liq. Chromatogr.* **1986**, *9*, 2799-2808.
- 41 Brenecke, J. F.; Tomasko, D. L.; Peshkin, J.; Eckert, C. A., *Ind. Eng. Chem. Res.* **1990**, *29*, 1682-1690.
- 42 Street, K. W.; Acree, W. E., *Analyst* **1986**, *111*, 1197-1201.
- 43 Waris, R.; Acree, W. E.; Street, K. W., *Analyst* **1988**, *113*, 1465-1467.

RECEIVED May 1, 1995

Chapter 6

Supercritical Fluid Flow Injection Method for Mapping Liquid–Vapor Critical Loci of Binary Mixtures Containing CO₂

James W. Ziegler¹, Thomas L. Chester^{2,4}, David P. Innis²,
Steven H. Page^{3,5}, and John G. Dorsey^{1,6}

¹Department of Chemistry, University of Cincinnati, Mail Location 172,
Cincinnati, OH 45221–0172

²Miami Valley Laboratories, Procter & Gamble Company,
P.O. Box 538707, Cincinnati, OH 45253–8707

³Organic Analytical Research Division, National Institute of Standards
and Technology, Gaithersburg, MD 20899

A simple peak-shape method⁽¹⁾ was used to estimate liquid-vapor critical loci of 13 binary mixtures, yielding accurate results when compared to limited available data. The technique is a flow-injection method performed with chromatographic equipment, a flame-ionization detector, and subcritical and supercritical fluids. Each analysis is performed under isobaric and isothermal conditions. The resulting detector signal indicates the phase state. Twelve to fifteen mixture critical points can be determined in about 1 - 1.5 days.

The binary mixtures studied were CO₂ combined with: acetone, acetonitrile, 1-butanol, chloroform, ethanol, hexane, methanol, octane, 1-octanol, 1-propanol, 2-propanol, tetrahydrofuran, and toluene. Mixture critical points were determined within 1 °C and 1 atm (0.1 MPa). The maximum deviation between mixture critical pressures for CO₂-toluene and CO₂-methanol determined by the peak-shape method and data reported from view-cell techniques was 3%.

With the exception of a few cases, phase equilibrium data that have been reported to date are far from adequate for supercritical fluid chromatography (SFC) and supercritical fluid extraction (SFE) purposes. In many cases no data exist at all. Due to the non-polar nature of CO₂, it is common to add a modifier in both SFC and SFE to enhance the performance of the system. In SFC, even when a modifier is not added, the solvent used to dissolve and introduce the sample forms a binary mixture with the CO₂ mobile phase. In a binary mixture, the phase state depends on the composition of the mixture and on the local temperature and pressure.

⁴Corresponding author

⁵Current address: Procter & Gamble Company, 11050 York Road,
Hunt Valley, MD 21030–2098

⁶Current address: Department of Chemistry, Florida State University,
Tallahassee, FL 32306–3006

0097–6156/95/0608–0093\$12.00/0
© 1995 American Chemical Society

Knowledge of the phase behavior of CO₂ combined with typical laboratory solvents would be very useful in setting parameters for SFC, SFE, and other applications of supercritical fluids. However, in 1994, Page et al. reported that only 8 of 38 common CO₂-solvent binary mixtures have been adequately investigated for SFC and SFE purposes(2). These are CO₂ combined with: acetone, benzene, ethanol, hexane, methanol, toluene, tributylphosphate and water.

The literature contains several references describing phase behavior investigations of various CO₂-solvent binary mixtures. For example, Gurdial et al. provide discussions concerning binary mixtures of CO₂-acetone, CO₂-isopropanol, CO₂-(C₁ - C₆) n-alcohols, and CO₂-(C₅ - C₁₀) n-alkanes(3). Jennings et al. provide a thorough review along with their own work for CO₂-1-alkanol systems(4). Typically these studies do not exceed 60 °C and 10 mol % solvent in CO₂. Thus a lot of data exist for the low-temperature end of various liquid-vapor (l-v) critical loci, while little data exist from 60 °C to the critical point of pure co-solvent. Of the mixtures studied in the present work, sufficient previously reported data to permit estimation of the entire l-v critical locus exist only for CO₂ combined with acetone, ethanol, methanol, and toluene.

The limited amount of available phase behavior data stems from the difficulty of acquiring data with the methodology and equipment used in the past. Most previous studies have been performed using high-pressure view cells and either visual observation or light-scattering detection. This permits investigation of phase equilibria in terms of pressure, temperature, and composition (P-T-x). However, these techniques require a considerable amount of time and equipment not commonly available in most analytical chemistry laboratories.

In 1993, a simple and relatively fast solvent-peak-shape method was described for estimating l-v critical loci of CO₂-solvent binary mixtures(1). This work is capable of being performed with SFC equipment, but only determines the temperature and pressure coordinates of points on the l-v critical locus. A single l-v critical locus can be mapped in about 1 - 1.5 days. So far we have estimated thirteen CO₂-solvent l-v critical loci using this method.

In this manuscript, "critical point," "critical pressure," and "critical temperature" will be used when a single component is being discussed. "Mixture critical point," "mixture critical pressure," and "mixture critical temperature" will be used to discuss phase behavior of a binary mixture(5). The identification of different types of binary mixtures (i.e. Type I - Type VI) will be that originally described by van Konynenburg and Scott(6).

Background

The peak-shape method(1) is based on the process of dynamic liquid film formation and removal. A small volume of test solvent is injected into a capillary tube. This tube then passes into a temperature-controlled oven. The outlet is connected to a flow restrictor interfacing the tube with a flame-ionization detector (FID). A pressure-controlled stream of CO₂ continuously flows through the apparatus. The test solvent is injected at room temperature, where only a single liquid phase exists over the full range of composition of the resulting binary mixture. The test solvent is then transported to the oven by the flowing CO₂. A loss in the definition of the solvent plug edges will occur due to longitudinal diffusion, Taylor dispersion, and other dispersion phenomena during transport. For these reasons, the injection volume must be large enough to ensure delivery of a portion of pure solvent to the heated region of the capillary tube.

If the oven temperature is between the critical temperatures of the two components, and the pressure is below the l-v critical locus, phase separation is thermodynamically possible. Let us consider what happens at an observation point near the injector end of the thermostatted portion of the capillary tube while the

system is maintained at pressure P_1 (see Figure 1). As the center of the solvent plug approaches the observation point, the concentration of solvent in the CO_2 mobile phase begins to rise. When the local solvent concentration crosses the dew-point curve, the fluid divides into separate liquid and vapor phases. The compositions of these phases (solvent-saturated vapor and CO_2 -saturated liquid) are fixed for a given pressure. As the overall concentration of solvent continues to increase, the ratio of liquid to vapor increases at the observation point. When the solvent concentration passes through the bubble-point curve, the last bubble of vapor disappears forming a single-phase "plug" of liquid. The concentration of solvent in the liquid phase is now free to rise to unity as the heart of the liquid plug approaches the observation point. Thus, as the liquid plug moves past the observation point, the mole fraction of solvent varies from zero to essentially unity and then eventually back to zero as the liquid plug is swept away.

As the experiment is repeated at progressively higher pressures, the compositions of the liquid and vapor phases approach each other and merge at the mixture critical point. This occurs when the pressure is at the mixture critical pressure corresponding to the mixture critical temperature that is equal to the oven temperature. At pressures greater than the mixture critical pressure, no phase separation occurs. This is somewhat analogous to the procedure used by Ng and Robinson(7) in which the compositions of the two phases were determined and were observed to merge at the mixture critical pressure. However, as we will explain later, the peak-shape method avoids the need of determining the compositions of the two phases, when only the mixture critical pressure and temperature are desired.

If a liquid plug is formed, it will be propelled down the tube by the continuous application of "dry" CO_2 at the inlet end. If the solvent wets the walls of the capillary tube, a liquid film will remain behind the plug on the walls. The plug volume is consumed by this process of dynamic liquid film formation, if the tube is long enough for the solvent volume injected.

As soon as film formation begins, so does its removal. "Dry" CO_2 enters from the inlet end of the tube, passes over the liquid film, and evaporates solvent until becoming saturated. Thus, the film disappears from the inlet end as shown in Figure 2. The dynamic film formation and removal process in a tube is analogous to that occurring in the retention gap injection procedure in gas chromatography (GC)(8-11) and in the dynamic coating procedure used to deposit stationary phases in open-tubular GC columns(12-16). The rate of solvent removal depends on its saturation concentration in CO_2 vapor under the applied pressure and temperature, and on the flow rate of the CO_2 vapor.

Following injection, only a normal baseline signal is recorded until one tube volume passes through the system. The first solvent to reach the detector is in the saturated vapor phase (the edge of which has been somewhat softened by transit through the column, connector, and restrictor). Thus the detector signal changes rather abruptly from background to a current corresponding to the delivery rate of solvent-saturated CO_2 vapor. Since the mobile phase is saturated with solvent, the detector signal remains flat as long as this composition is delivered to the detector. Because each analysis is performed under isothermal and isobaric conditions, the composition should remain constant. The detector signal remains flat until the last of the liquid evaporates and is transported to the detector, after which the signal reverts back to the background level. Thus the normal solvent peak is rectangular in shape when a liquid film is formed.

The height of the rectangular peak is determined by the removal rate and subsequent delivery rate of solvent vapor to the FID. As pressure is increased and nears the mixture critical pressure, the saturation concentration of solvent in the vapor phase increases, causing the solvent film to be more quickly removed. This increases the height of the rectangular detector signal. Upon increasing pressure, a slight increase in mass flow rate will occur through the (passive) flow restrictor. This will also contribute to a slight increase in the height of the detector signal.

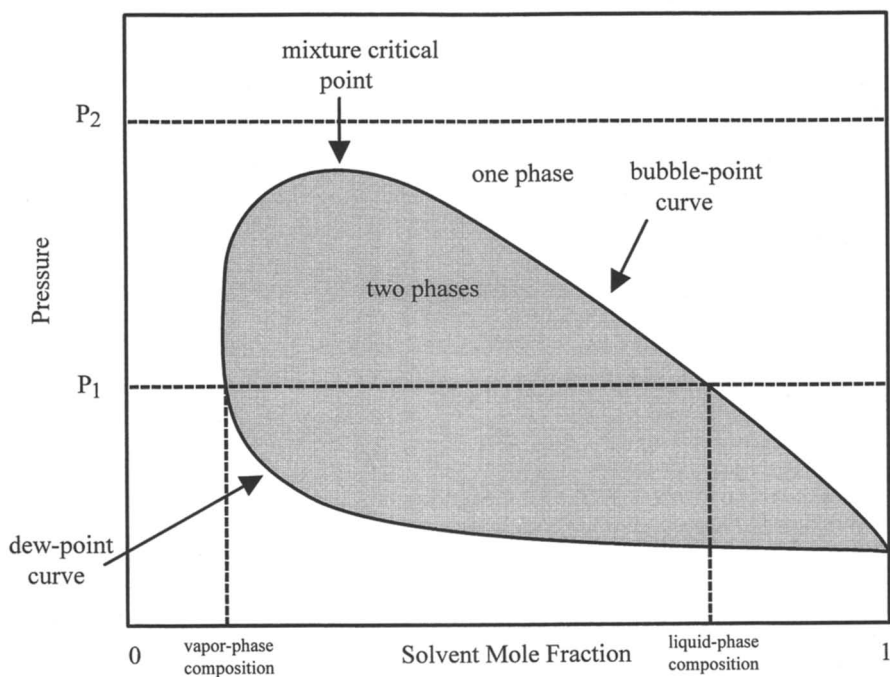


Figure 1. Isotherm for a Type I binary mixture.

Increasing temperature has a similar effect on the peak height, as the saturation concentration of solvent in CO₂ vapor increases. The area of the detector peak reflects the total mass of solvent injected and should be constant for a given injection volume. Under constant temperature, pressure, and flow rate conditions, increasing injection volume will cause a longer film to form in the capillary tube. Thus the time required for removal will increase, yielding longer detector signals. However, the height of the peaks should not change as the saturation concentration and flow rate are not affected by injection volume.

If the oven temperature is between the critical temperatures of the two components, and the pressure is above the l-v critical locus (P₂ of Figure 1), only a single phase will be present. Phase separation does not exist, so the process of dynamic film formation cannot occur. Under these conditions, the injected solvent simply experiences the characteristic longitudinal diffusion and dispersion band broadening mechanisms as it travels down the tube to the FID. The resulting detector signal is a skewed Gaussian peak. By observing the peak shape, the phenomena occurring in the tube can be monitored, and hence the phase behavior of the mixture under the controlled temperature and pressure conditions can be determined.

Another important consideration is the temperature of the FID. Figure 3 shows the temperatures experienced by the injected solvent over an entire analysis under two-phase conditions. Initially, injection is performed at room temperature (T₁), and only a single liquid phase exists. Upon entering the thermostatted oven (T₂), phase separation will occur. To avoid potential problems with phase behavior upon expansion through the restrictor into the FID, the FID temperature (T₃) should be maintained above the critical temperature of the least volatile component of the mixture. This results in the delivery of a single phase to the detector, and avoids unwanted additional phase changes.

To successfully apply the peak-shape method, the column must be long enough for sufficient film formation and removal to occur. The required injection volume is dependent on the mixture being studied, and the pressure and temperature applied. If too small an injection volume is used, film formation and removal will not occur to the extent that the resulting detector signal is distinguishable as either rectangular or skewed Gaussian. This is because not enough solvent is present to saturate a significant amount of the CO₂ vapor phase. Under one-phase conditions, if too large an injection volume is used in a short tube, the resulting peak shape may appear to be rectangular. This results because there is insufficient time for dispersion phenomena sufficient to produce a skewed Gaussian appearance to occur. Thus, it may be necessary to change the injection volume in the course of a set of observations to verify that rectangular peaks are caused by saturation, and that skewed Gaussian peaks are not due to an insufficient injection volume. In addition, relatively small injection volumes are required at low temperatures. However, at higher temperatures the injection volume must be increased because the concentration of injected solvent increases in the saturated vapor phase. The temperature where the injection volume must be increased varies among solvents and must be experimentally determined.

A third peak shape might be observed when applying the peak-shape method. This is a stepped peak. It will be observed when the pressure and temperature are in a two-phase region of the phase diagram, and the injection volume is too large for the length of tube being employed. When this occurs, the liquid plug will not be completely exhausted by dynamic film formation prior to reaching the detector. Thus, liquid solvent is initially delivered to the detector, and produces a very large signal. After all of the excess liquid plug reaches the detector, only solvent-saturated vapor will be left to be delivered. The signal drops to a level corresponding to the delivery rate of the vapor phase and remains at this level until all of the injected solvent has been evaporated and swept into the detector. Stepped peaks can be avoided by employing a tube long enough (with respect to the injection

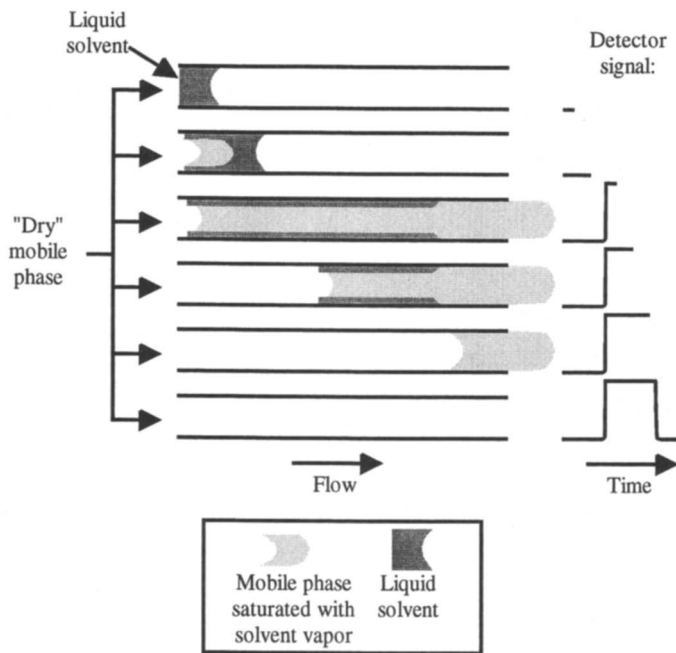


Figure 2. Dynamic liquid film formation and removal, showing the resulting detector signal. (Reproduced with permission from ref. 1. Copyright 1993 *J. Microcol. Sep.*).

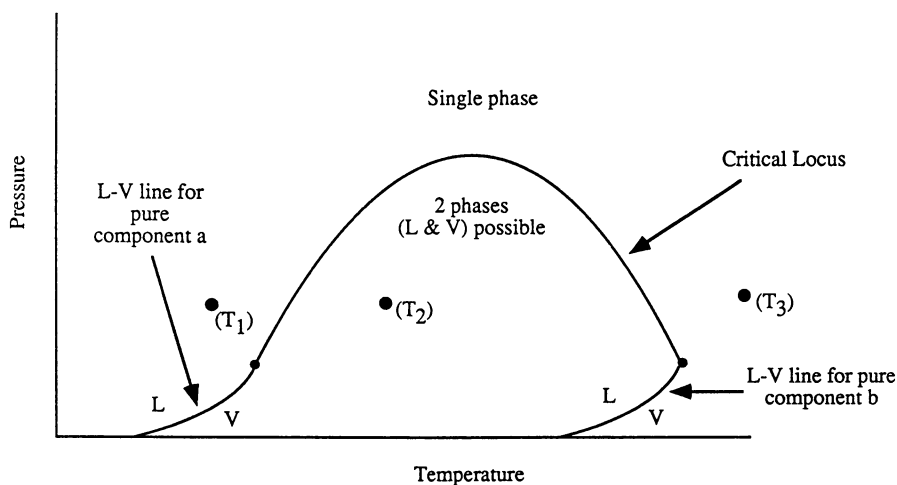


Figure 3. Phase diagram for a Type I binary mixture compressed into pressure and temperature dimensions.

volume) to allow the entire liquid plug to be consumed by the process of dynamic film formation.

Experimental

Solvents. All solvents were used as received without further purification. Acetone, 1-butanol, chloroform, octane, 1-octanol, 1-propanol, 2-propanol, and toluene were Reagent Grade. Acetonitrile, hexane, and methanol were HPLC Grade. Ethanol was USP-Absolute 200 Proof, and tetrahydrofuran was High Purity, UV Grade.

Apparatus. Two systems were used. A general schematic of system 1 is shown in Figure 4. System 1 could be set to the nearest 1 °C and 0.1 MPa, and was used to estimate the 13 l-v critical loci. System 2, controllable to 0.1 °C and 0.01MPa, was used for more thorough investigations into the performance of the peak-shape method by studying CO₂-methanol.

For system 1, a modified(17, 18) Varian Analytical Instruments (Palo Alto, CA) syringe pump provided the pressure-controlled CO₂ stream for all studies. Solvents were injected by means of a Valco Instruments Company, Inc. (Houston, TX) ECI4W internal loop injector valve, with varying sample loop sizes of 60, 100, 200, and 500 nL. A Hewlett- Packard Company (Wilmington, DE) 5830A GC was used for both the oven and the FID. The FID was maintained at 350 °C. Polyimide-coated fused-silica capillary (50- μ m i.d.), Polymicro Technologies (Phoenix, AZ) was used. The capillary tube lengths ranged from 2 to 6 m. Most of the studies were performed using approximately 6-m lengths. All fused-silica capillary connections made outside the oven employed PEEK tubing sleeves with stainless steel ferrules and nuts. All fused-silica capillary connections made inside the oven employed stainless steel fittings with graphite fused-silica adapters.

SFC-grade CO₂, Matheson Gas Products, Inc. (Secaucus, NJ), was used for all studies. Stainless steel tubing, 0.05-cm. i.d., ran from the pump and was attached to approximately 25 cm of fused-silica capillary, 50- μ m i.d., by a Valco ZU1 union. The capillary tube was then connected to the Valco injector. Placing a short section of 50- μ m i.d. fused-silica capillary between the injector and the pump's supply tube helped to minimize back flow of solvent upon injection. The injector was placed on top of the GC, under room temperature conditions. Injection was performed using the waste-port-restrictor technique(19). A short piece of fused-silica capillary, 25- μ m i.d., served as the waste port restrictor. The capillary tube used for the phase behavior studies was mounted on a wire GC-style column cage, and hung in the oven. The inlet end was pushed through a septum in the unused injector port of the GC, and connected to the external Valco injector. Depending on the injector loop size, between 25 cm and 75 cm of capillary tube was left at room temperature from the injector to the oven. This is necessary to dampen the flow recoil when the valve is actuated, and thus prevents contaminating the CO₂ supply tube and fitting (20). The other end of the capillary tube was connected via a Valco ZU.5 union to a frit restrictor, Dionex Corp. (Salt Lake City, UT), which was attached to the FID. Each solvent injection was made under isobaric and isothermal conditions. Detector attenuation was kept high in order to observe the solvent peaks.

System 2 was a Dionex Corporation Supercritical Fluid Chromatograph, Model 501. It consisted of a syringe pump, pneumatic actuated injector, oven, and FID. Deactivated fused-silica capillary tubing (Polymicro Technologies), 50 μ m i.d., and 20 m in length was used. The capillary tube was connected to a frit restrictor (Dionex Corp.) using the column coupler supplied with the instrument. The FID was maintained at 250 °C.

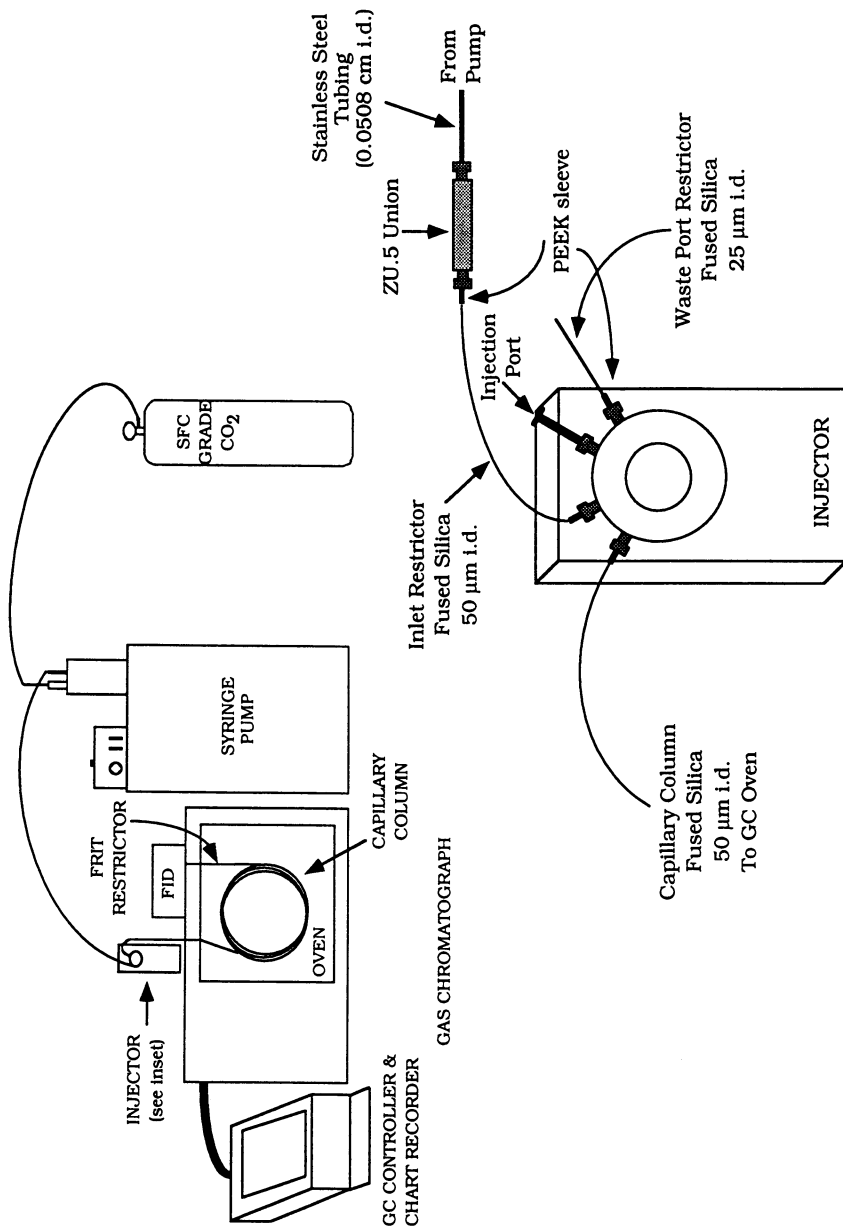


Figure 4. Schematic of system 1.

Calibration. A two-point pressure calibration was performed on system 1. The system "zero" was set to 1 atm when the pump was in the "empty" position and the outlet line was open to the atmosphere. The output was monitored with a voltmeter, and the "zero adjustment" on the pump pressure monitor board was set so the voltmeter gave a reading of 0.010V (1V = 100 atm). (Note: All pressures were experimentally determined in units of atmospheres, and have been converted here to MPa.) The pump's outlet line was then connected to a lecture bottle of CO₂, submerged in a room-temperature water bath. Again, a voltmeter was used to monitor the output of the pressure transducer. The "gain adjustment" on the pump pressure monitor board was set to give the calculated vapor pressure for CO₂ at the temperature of the water bath. The pressure drop that exists in the system was ignored because it should be small in a short, open tube. The programmed temperature of the GC oven was calibrated using a data logger and a thermocouple. Temperatures to the nearest degree Celsius were obtained from the calibration curve.

System 2 was capable of being operated at 0.01 MPa increments. The system was calibrated by a one point calibration procedure. The peak-shape method was used to determine the phase transition for CO₂-methanol at 60.0 °C, and this value was compared to that reported by Brunner (21). The difference between the two values was 0.21 MPa. This was taken as the pressure drop of the system. Because the programmed pressure of the instrument is the applied pressure at the inlet of the tube, and not the pressure at the outlet, 0.21 MPa was subtracted from all pressures in future studies. The oven temperature was monitored using a thermocouple, which was calibrated to the nearest 0.1 °C by determining melting points and boiling points of standard substances.

Results and Discussion

Figure 5 shows a series of detector signals obtained using the peak-shape method for the study of CO₂-methanol at 150 °C. The change in peak shape can be observed over the pressure range of 16.1 MPa to 16.3 MPa. The peak at 16.1 MPa has a flat-top or rectangular characteristic. The peak at 16.3 MPa appears to be skewed Gaussian. The phase transition occurs somewhere between these two pressures. The peak at 16.2 MPa shows a transitional peak, one that is a cross between rectangular and skewed Gaussian. Based on this, the mixture critical pressure is estimated to be 16.2 MPa.

Plotting Peak Height vs. Pressure. As can be seen in Figure 5, observing the peak shape allows a rough estimate of the mixture critical pressure to be made. However, this is a very qualitative and subjective determination. It was found that objectivity could be added to the determination of the mixture critical pressure by plotting peak height vs. pressure. Over a small pressure range, the CO₂ mass flow rate is approximately constant, and thus the output signal is proportional to the vapor phase concentration of the solvent. Under isothermal conditions, the solvent concentration in the vapor phase remains relatively constant with increasing pressure except when very near the mixture critical pressure. There the solvent concentration in the vapor phase rapidly changes with pressure.

A study was performed with system 2 using methanol as the solvent, a temperature of 80.0 °C, and various pressures in the range of 8 - 20 MPa. Figure 6a is a plot of the observed peak heights at various pressures. When large increments of pressure values are used (0.1 MPa or larger), the plot resembles a sigmoidal curve. The mixture critical pressure exists near the apparent inflection. At low pressures, the plot is relatively flat indicating approximately constant vapor phase composition. Near the mixture critical pressure, the vapor phase concentration of

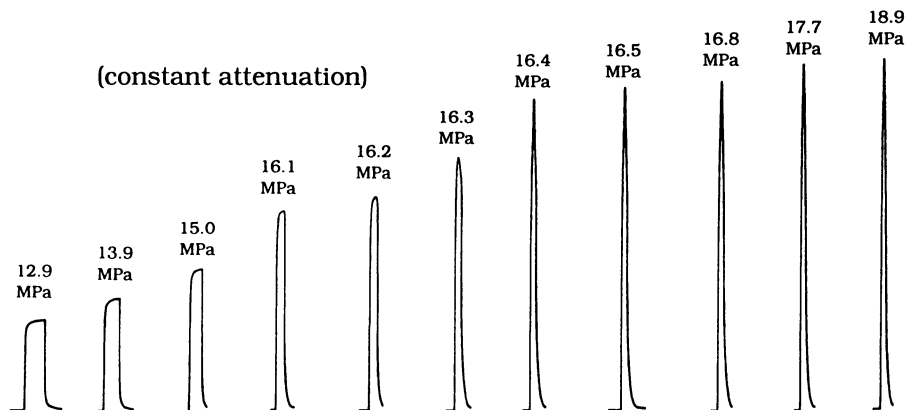


Figure 5. A series of peaks from studies of CO₂-methanol at 150°C.

Table I. Comparison Of Carbon Dioxide-Methanol Data

Temperature (°C)	Mixture Critical Pressure (MPa)		
	E. Brunner Ref's 21, 22	This Work System 1	This Work System 2
46.5	9.01		
48		9.5	
48.4	9.29		
50	9.6	9.8	
60	11.14	11.4	11.15
70	12.56	12.7	
71		12.8	
80	13.74	13.9	13.74
81		14.0	
90		14.8	
100	15.42	15.5	15.39
110	16.03	16.1	
120		16.4	16.48
130		16.5	
140	16.41	16.4	16.42
150	16.13	16.2	
160		15.8	15.74
169	15.36		
170		15.3	
180		14.7	14.58
190		13.9	
198.5	13.06		
200	12.93	13.0	
218.5	10.86		

solvent increases considerably, as indicated by the increase in peak height. Above the mixture critical pressure, only a single phase exists. The peak heights should again be relatively constant. Because the height of the peak is dependent on the rate of delivery of solvent to the detector, which will increase slightly with increasing flow rate caused by increasing pressure, a slight positive slope should be observed in the "flat lines" before and after the inflection point.

Another experiment was performed under the same conditions (80.0 °C for CO₂-methanol), except that the pressure was varied in 0.01 MPa increments in the immediate vicinity of the apparent inflection shown in Figure 6a. The results of this study are shown in Figure 6b. The apparent inflection is actually a discontinuity in the plot. This discontinuity can be used to more objectively determine the mixture critical pressure at a given temperature. The mixture critical pressure at 80.0 °C was determined to be 13.74 MPa with this method. Using system 1 and simply observing the change in peak shapes resulted in an estimated value of 13.9 MPa at 80 °C for the mixture critical pressure.

Although the method of plotting peak height vs. pressure yields more precise values for mixture critical pressures, it is more time consuming than simply observing the peak shape change at the 0.1 MPa level. With system 1 we ignored pressure drop, and used a simple calibration procedure. This allowed for a rapid survey of a wide pressure range at 0.1 MPa increments. To obtain more precise data, as is acquired with system 2, more tedious calibration procedures and analyses must be used. A quick survey over a wide range of pressures must still be performed to determine the location of the apparent inflection. Then several studies must be performed by increasing pressure in 0.01 MPa increments to determine the location of the discontinuity. Table I lists data obtained for CO₂-methanol with both systems 1 and 2, system 1 using the change in peak shape to determine the mixture critical pressure and system 2 plotting peak height vs. pressure and observing the discontinuity to determine the mixture critical pressure. Very small deviations exist between the data from the two systems. The method of choice is a function of the needs of the user, and depends on both the required precision of mixture critical pressure values and the time available to perform such investigations. Either method provides a significant advantage over view-cell techniques in simplicity and time, and eliminates the need to use equations of state for the prediction of phase behavior along the l-v critical locus.

Comparison to Existing Data for CO₂-Toluene and CO₂-Methanol. The data obtained with system 1 for CO₂-toluene were compared to the phase behavior data reported by Ng and Robinson from a high-pressure view-cell study (7). The comparison is graphically represented in Figure 7. Data obtained with system 1 for CO₂-methanol was compared to the work of Brunner, et al. (21, 22). This comparison is represented in Figure 8, and Table I. Even at the lower precision obtainable with system 1, no more than a 3% deviation in mixture critical pressures exists between data from the peak-shape method and that previously reported. Some deviation is expected due to the pressure drop which was ignored in system 1.

System 2 was used to perform a more precise comparison between data obtained with the peak-shape method, and that obtained by Brunner using high-pressure view-cells. These data are also listed in Table I. Four of the mixture critical points were determined at the same temperature in our work and Brunner's. These are 60.0 °C, 80.0 °C, 100.0 °C and 140.0 °C. The mixture critical pressure reported at 60.0 °C was used to initially estimate the pressure drop correction of the system, and will thus be ignored for comparison purposes. Based on the other three temperatures, the average deviation in mixture critical pressure values between the data obtained with the two different techniques is 0.013 MPa. Excellent agreement is observed across the entire l-v critical locus when this pressure-drop compensation

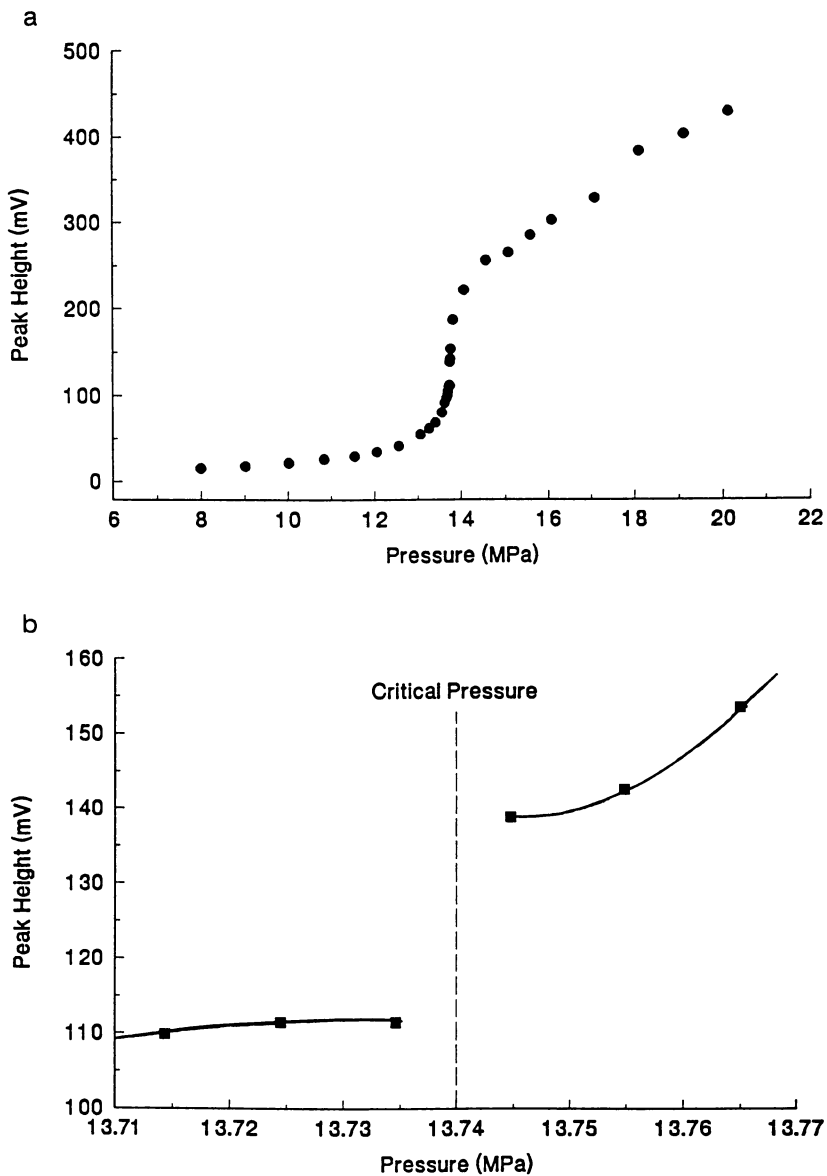


Figure 6. (a) A plot of Peak Height vs. Pressure for a series of CO₂-methanol studies at 80.0°C. (b) The apparent inflection of the plot in (a) bracketed by data points at the 0.01 MPa increment level.

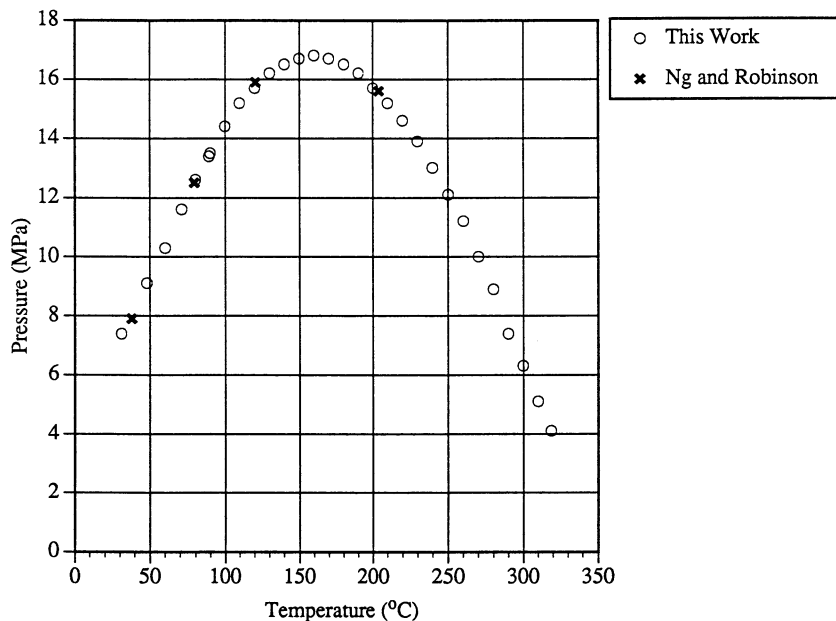


Figure 7. Comparison of data obtained in this work with that of ref. 7 for CO₂-toluene. (Adapted from ref. 25).

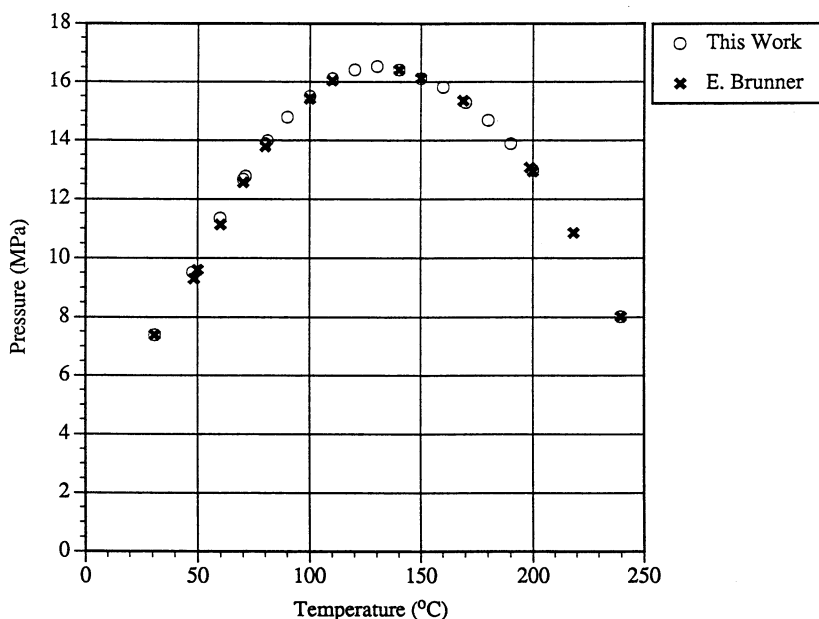


Figure 8. Comparison of data obtained in this work with that of references 21 and 22 for CO₂-methanol. (Adapted from ref. 25).

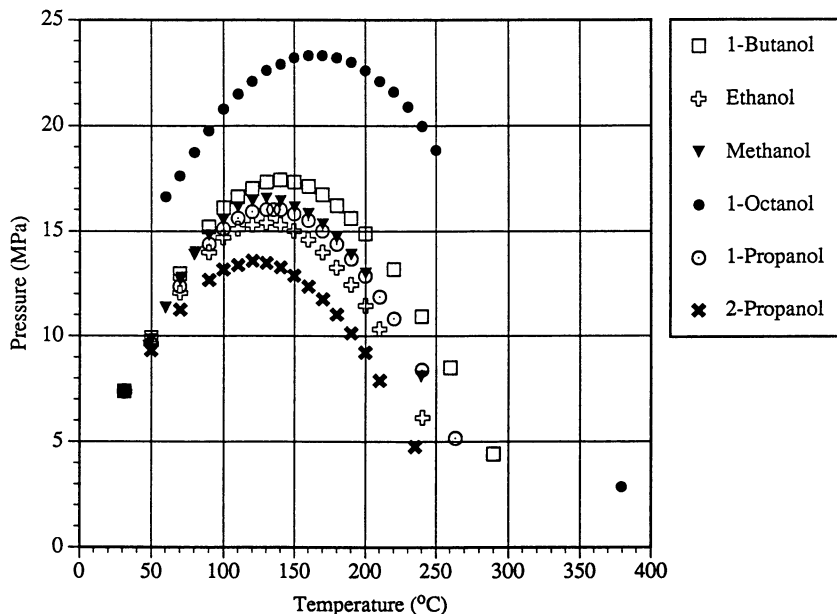


Figure 9. Critical loci for CO₂ combined with different alcohols determined by the peak-shape method. (Adapted from ref. 25).

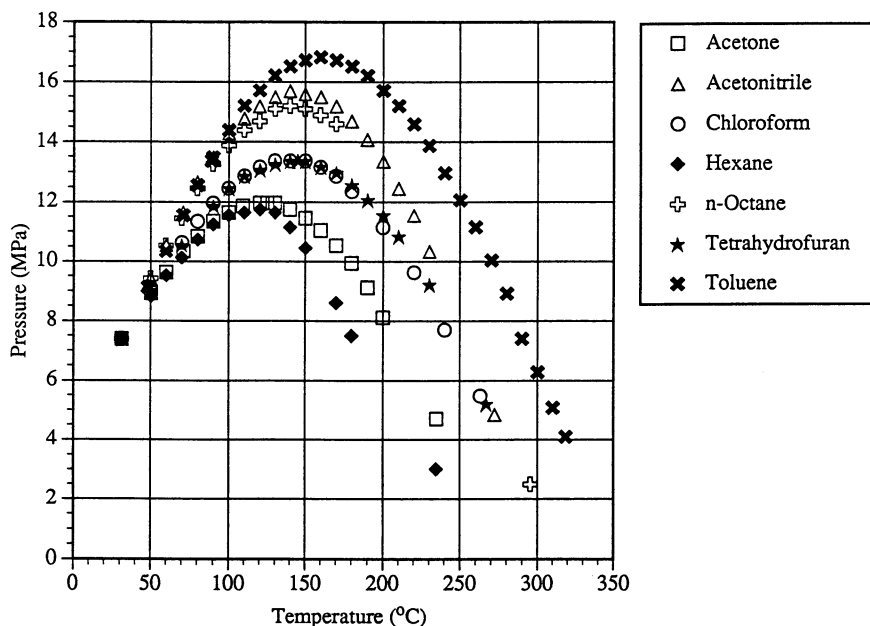


Figure 10. Critical loci for CO₂ combined with various solvents determined by the peak-shape method. (Adapted from ref. 25).

is applied. This suggests that the accuracy of the peak-shape method is limited by the pressure drop of the capillary tube used, and the attainable pressure and temperature precision of the equipment. All of our work was performed with 50- μm i.d. tubes, but larger i.d. tubes should produce even more accurate results as the pressure drop will be reduced.

Critical Loci for Eleven Additional Binary Mixtures. The l-v critical loci for eleven additional CO_2 -solvent binary mixtures were generated by the peak-shape method. These are CO_2 combined with acetone, acetonitrile, 1-butanol, chloroform, ethanol, hexane, octane, 1-octanol, 1-propanol, 2-propanol, and tetrahydrofuran. The l-v critical loci for all 13 binary mixtures studied in this work are plotted in Figures 9 and 10. The raw data used to generate these l-v critical loci are provided in Table II, along with the critical points for the pure solvents reported from References 23 and 24.

Several of the curves have gaps due to difficulties encountered in trying to distinguish peaks as either rectangular or skewed Gaussian (25). Indistinguishable peak shapes could be a result of abnormal flow profiles in the tube, the inability to successfully transfer a portion of pure liquid solvent, problems related to wetting of the walls of the capillary tube or, for 1-octanol on the low-temperature end, different mass transfer behavior. (The curvature of the critical locus for CO_2 -1-octanol suggests that the binary mixture is other than Type I or Type II). Restrictor variations to control flow, different tube inner diameters, and deactivating the tubing might solve some of these problems. Despite these gaps, using the reported critical point of pure solvent and the determined mixture critical points, an approximate l-v critical locus can be interpolated for all of the binary mixtures studied in this work.

Conclusion

Investigation of the peak-shape method for estimating the l-v critical loci of binary mixtures containing CO_2 as one of the components has shown favorable results. The technique is very straightforward and simple, requiring much less time and special equipment compared to other methods previously employed to study phase behavior. The precision of the technique appears to be limited by the equipment, and subsequent calibration procedures, and not by the fundamental processes of phase separation and dynamic film formation and removal.

For fast, but low-precision data, a simple head space calibration procedure is used, and the peak shapes are monitored subjectively to provide an estimation of the mixture critical pressure within 0.1 MPa. For more precise data, better equipment and more rigorous calibration procedures can be applied. Plotting peak height vs. pressure at 0.01-MPa increments gives a more objective estimate of the mixture critical pressure. The difference in mixture critical pressures obtained by these two techniques was no more than about 0.2 MPa when comparing CO_2 -methanol studies. Increasing the precision from 0.1MPa to 0.01MPa requires additional time, and thus the benefits of the slightly better precision compared to the time required must be considered.

Comparison of data from the peak-shape method with that previously reported from high-pressure view-cell techniques for CO_2 -toluene and CO_2 -methanol showed excellent agreement. None of the binary mixtures studied have l-v critical loci reported in the literature to the extent that was determined in this work. The peak-shape method was found to be a good technique for estimating the phase behavior of binary mixtures containing CO_2 , requiring very little time and producing accurate data.

Table II. Mixture Critical Pressures (MPa) Obtained by the Peak-Shape Method

Temp. (°C)	Acetone	Aceto-nitrile	1-Butanol	Chloro-form	Ethanol	Hexane	Methanol
31.1	7.39*	7.39*	7.39*	7.39*	7.39*	7.39*	7.39*
48		9.2					9.5
50	8.9	9.4	9.9	9.1	9.6	8.8	9.8
60	9.6	10.5				9.5	11.4
70			13.0	10.6	12.1	10.1	12.7
71	10.3	11.7					12.8
80	10.8	12.7		11.4		10.7	13.9
81							14.0
90	11.4	13.5	15.2	12.0	14.0	11.3	14.8
100	11.7	14.3	16.1	12.5	14.7	11.6	15.5
109	11.9						
110		14.8	16.6	12.9	15.1	11.7	16.1
120	12.0	15.2	17.0	13.2	15.3	11.8	16.4
125	12.0						
130	12.0	15.5	17.3	13.4	15.4	11.7	16.5
140	11.8	15.7	17.4	13.4	15.3	11.2	16.4
150	11.5	15.6	17.3	13.4	15.0	10.4	16.2
160	11.0	15.5	17.1	13.2	14.6		15.8
170	10.5	15.2	16.7	12.9	14.0	8.6	15.3
180	9.9	14.7	16.2	12.4	13.3	7.5	14.7
190	9.1	14.1	15.6		12.5		13.9
200	8.1	13.4	14.9	11.2	11.5		13.0
210		12.5			10.3		
220		11.6	13.2	9.6			
230		10.3					
234.5						3.0*	
234.9	4.7*						
239.4							8.1*
240			10.9	7.7			
240.7					6.1*		
260			8.5				
263.2				5.5*			
272.3		4.9*					
289.8			4.4*				

*The first entry in each column is the critical point of CO₂. The last entry in each column is the critical point for the pure solvent (from references 23 and 24).

Table II. (Continued)

Temp. (°C)	n-Octane	1-Octanol	1-Propanol	2-Propanol	Tetrahydrofuran	Toluene
31.1	7.39*	7.39*	7.39*	7.39*	7.39*	7.39*
48						9.1
50	9.4		9.6	9.3	9.0	
60	10.5	16.6				10.3
70	11.5	17.6	12.4	11.3	10.5	
71						11.6
80	12.5	18.8				12.6
89						13.4
90	13.3	19.8	14.4	12.7	11.9	13.5
100	13.9	20.8	15.1	13.2	12.5	14.4
110	14.4	21.5	15.6	13.4	12.9	15.2
120	14.7	22.1	15.9	13.6	13.1	15.7
130	15.1	22.6	16.0	13.5	13.3	16.2
135			16.0			
140	15.2	22.9	16.0	13.3	13.4	16.5
145					13.4	
150	15.1	23.2	15.8	12.9	13.4	16.7
160	14.9	23.3	15.5	12.4	13.2	16.8
170	14.6	23.3	15.0	11.8	13.0	16.7
180		23.2	14.4	11.0	12.6	16.5
190		23.0	13.7	10.1	12.1	16.2
200		22.6	12.9	9.2	11.6	15.7
210		22.1	11.9	7.9	10.8	15.2
220		21.6	10.8			14.6
230		20.9			9.2	13.9
235				4.8*		
240		20.0	8.4			13.0
250		18.9				12.1
260						11.2
263.6			5.2*			
266.9					5.2*	
270						10.0
280						8.9
290						7.4
295.7	2.5*					
300						6.3
310						5.1
318.6						4.1*
379.3		2.9*				

Acknowledgments

J.G.D. would like to thank NIEHS and The Procter and Gamble Company for support of this work. S.H.P. would like to thank NIST and the National Research Council (NRC) Postdoctoral Research Associateship Program.

Disclaimer: Suppliers of the commercial equipment, instruments, and materials listed in this chapter were identified to specify adequately the experimental procedure. Such identification should not be construed as endorsement or recommendation by the National Institute of Standards and Technology, nor does it imply that the best available equipment or materials were used.

Literature Cited

1. Chester, T.L. and Innis, D.P., *J. Microcol. Sep.*, **1993**, *5*, 261.
2. Page, S.H. and Morrison, J.F. in *The 5th International Symposium on Supercritical Fluid Chromatography and Extraction*. 1994. Baltimore, MD.
3. Gurdial, G. S.; Foster, N. R.; Yun, S. L. J.; Tilly, K. D. in *Supercritical Fluid Engineering Science*, E.K.a.J.F. Brennecke, Editor. 1993, American Chemical Society: Chapt. 3.
4. Jennings, D.W., Gude, M.T., and Teja, A.S., in *Supercritical Fluid Engineering Science*, E. Kiran and J.F. Brennecke, Editor. 1993, American Chemical Society: Chapter 2.
5. McHugh, M.A. and Krukonis, V.J., in *Supercritical Fluid Extraction Principles and Practice*. 1986, Butterworths: Stoneham, MA. p. 23.
6. van Konynenburg, P.H. and Scott, R.L., *Phil. Trans. R. Soc. of London, A.*, **1980**, *298*, 495.
7. Ng, H.-J. and Robinson, D.B., *J. Chem. Eng. Data*, **1978**, *23*, 325.
8. Grob, K.J. and Muller, R., *J. Chromatogr.*, **1982**, *244*, 185.
9. Grob, K.J., *J. Chromatogr.*, **1982**, *237*, 15.
10. Grob, K.J., Karper, G., and Riekkola, M.L., *J. Chromatogr.*, **1985**, *334*, 129.
11. Grob, K. and Schilling, B., *J. Chromatogr.*, **1987**, *391*, 3.
12. Novotny, M., Bartle, K.D., and Blomberg, L., *J. Chromatogr.*, **1969**, *45*, 469.
13. Novotny, M., Blomberg, L., and Bartle, K.D., *J. Chromatogr. Sci.*, **1970**, *8*, 390.
14. Tesarik, K. and Necasova, M., *J. Chromatogr.*, **1972**, *65*, 39.
15. Boogaerts, T., Verstappe, M., and Verzele, M., *J. Chromatogr. Sci.*, **1972**, *10*, 217.
16. Bartle, K.D., *Anal. Chem.*, **1973**, *45*, 1831.
17. Chester, T.L., in *Analytical Instrumentation Handbook*, G.W. Ewing, Editor. 1990, Marcel & Dekker, Inc.: New York. p. 843.
18. Van Lenten, F.J. and Rothman, L.D., *Anal. Chem.*, **1976**, *48*, 1430.
19. Chester, T.L. and Innis, D.P., *J. Microcol. Sep.*, **1989**, *1*, 230.
20. Chester, T.L. and Innis, D.P., *Submitted to Anal. Chem.*
21. Brunner, E., *J. Chem. Thermodyn.*, **1985**, *17*, 671.
22. Brunner, E., Hultenschmidt, W., and Schlichtharle, G., *J. Chem. Thermodyn.*, **1987**, *19*, 273.
23. Lide, D.R., ed. *CRC Handbook of Chemistry and Physics*. 71st ed. 1990 - 1991, CRC Press, Inc.
24. Lide, D.R., ed. *CRC Handbook of Chemistry and Physics*. 72nd ed. 1991 - 1992, CRC Press, Inc.
25. Ziegler, J. W.; Dorsey, J. G.; Chester, T. L.; Innis, D. P. *Anal. Chem.*, **1995**, *67*, 456.

RECEIVED June 20, 1995

Chapter 7

Dramatic Density-Induced Structural Changes in Microemulsions Formed in Near-Critical and Supercritical Solvents

J. Zhang and J. L. Fulton

Chemical Sciences Department, Pacific Northwest Laboratory,
Battelle Memorial Institute, P.O. Box 999, 902 Battelle Boulevard,
Richland, WA 99352

We demonstrate that the secondary structure of a microemulsion can be altered by changing the density of the continuous phase solvent. These changes in the microemulsion structure lead to dramatic changes in the physical properties of the system, such as the solution viscosity or electrical conductivity. For giant, rod-like micelles formed using the surfactant L- α -phosphatidylcholine (L- α -lecithin) in propylene, the system viscosity changes by three orders-of-magnitude with small changes in the system pressure. For the system of spherical micelles formed with didodecyldimethylammonium bromide (DDAB), the micelle clustering at low density increases electrical conductivity of the solution by three orders-of-magnitude.

The microemulsion systems in near- or supercritical fluids are of importance for understanding reaction mechanisms and for modelling polymers. We also report results for a sodium dodecyl sulfate (SDS) aqueous solution forming normal micelles that can incorporate a small amount of fluid in the micellar core. For this system, changes in the primary structure can be induced by altering the amount of supercritical fluid in the microemulsion core by changing the fluid density. We establish correlations between the measured physical properties and the spectroscopic results.

Many studies over the last eight years (1-3) have explored the properties of microemulsions formed in near- and supercritical solvents of the short chain alkanes (e.g., ethane, propylene). The existence of these phases in CO₂ systems has also been reported (4-6). These microemulsions generally consist of ultra-small droplets of water surrounded by a shell of surfactant molecules. These structures are generally spherical and have sizes in the range from 10 to 100 nanometers. More recent studies have demonstrated that other aggregate geometries (e.g., rods and ellipses) are possible and have also shown how the microemulsion secondary

0097-6156/95/0608-0111\$12.00/0
© 1995 American Chemical Society

structure (the spatial distribution of droplets) can be changed by altering the density of the supercritical fluid phase (3c,3d).

Generally, the primary structure, that is the size and shape of the droplet, is not affected by the properties of the continuous phase solvent. For the systems where the bending energy of the interfacial film (7) is dominant, changes in fluid density have little effect on the primary structure. In this paper, we demonstrate that the secondary structure of the microemulsion can change appreciably in response to small changes in the near- or supercritical fluid density. These structural changes can lead to quite dramatic changes in the microemulsion physical properties, such as the solution viscosity and the electrical conductivity. These changes are attributed to the changes in the inter-aggregate attractive interactions that are controlled by the density of the continuous phase solvent. Thus, a remaining challenging problem is to derive details of the mechanisms of these density-induced changes in the microemulsion structures and to show how they manifest the dramatic changes in the system physical properties.

In this article, we also present our results for a sodium dodecyl sulfate (SDS)/ethylene/water normal micelle system where changes in the fluid density do affect the primary structure. In contrast to the reverse microemulsions (3c,3d), for this normal micelle system, ethylene is incorporated into the cores of the micelle as the fluid density is increased. The primary structure of the microemulsion droplets is altered in response to a change in the overall volume fraction of the "oil" (ethylene) microphase.

Because of the unique characteristics of supercritical fluids, changes in pressure induce large changes in fluid density, giving rise to changes in solvating strength of the fluid. As a result, one can control the interactions between microemulsion droplets and fluid environments by simply changing the fluid pressure. We also describe systems employing near-critical fluids. A near-critical fluid is herein defined as a liquid that is at a temperature above a reduced temperature ($T_r = T/T_c$) of approximately 0.75 and below its critical temperature, T_c . Due to the proximity of the critical point, a near-critical fluid is still somewhat compressible in contrast to a normal liquid that has very low compressibility.

An earlier small-angle neutron scattering (SANS) study (8) showed evidence of strong attractive interactions between AOT/water microemulsion droplets dispersed in liquid propane, and the magnitude of these interdroplet attractive interactions can be greatly increased by decreasing the pressure. In the present paper, we summarize our studies in three different surfactant-based near- or supercritical fluid systems. From both physical property measurements and spectroscopic information, we illustrate how the pressure-induced density change can affect the microstructure.

Experimental

The surfactant, didodecyldimethylammonium bromide (99%, DDAB) was purchased from Eastman Kodak Inc. and was used as received. Sodium dodecyl sulfate (>99%, SDS) was purchased from Fluka BioChemika and used without purification. L- α -phosphatidylcholine (soy-bean lecithin) was purchased from

Calbiochem with a reported purity >97%. This product contains about 62-65% of linoleic acid branches and 15-17% of palmitic acid esters branches. The remainder of the product is a mixture of shorter chain lipids. Its average molecular weight is approximately 796 dalton. Lecithin is a zwitterionic surfactant at pH=7.0. Formation of a lecithin gel is very dependent on the purity of lecithin (9). We have tested the gel formation in three liquid solvents (n-octane, cyclohexane, and n-dodecane) and found that the critical water concentrations (W_c , water-to-surfactant molar ratio at which the gel is initially formed) for gelation are similar to those reported by others in these solvents (9). Propane, propylene and ethylene were all obtained from Scott Specialty Gases (c.p. grade).

Various techniques were used for the solution preparation and property measurements. For the DDAB and lecithin systems, a pre-weighed amount of surfactant was loaded into a high pressure spectroscopy cell. Distilled-deionized water was directly injected into the cell using a microsyringe yielding a desired water-to-surfactant molar ratio. The system was then filled with a near-critical fluid and allowed to stir overnight for complete solubilization and equilibration. All experiments were performed in the one phase region. Experiments were done at 26.5°C for the DDAB/propane systems, 30°C for the lecithin/propylene systems, and 40°C for the SDS aqueous solutions. Measurements of the conductivity, viscosity, and spectroscopic properties were made by reducing the pressure through discharging small amounts of the microemulsion solutions (maintaining a constant mole fraction of surfactant and water). Details of the high-pressure conductivity (10) and viscosity techniques (3d) are described elsewhere.

FT-IR experiments were performed after purging the instrument (Nicolet 740 FT-IR spectrometer) for at least 48 hours to eliminate interferences of air and moisture. Details about the high pressure FT-IR instrument, the cell design and solvent subtraction method are given in an earlier publication (11).

For measurements of the SDS microemulsion, a different strategy was used. An SDS aqueous solution (170 mM) was loaded into a high pressure view cell for solubility measurements. Solubility of ethylene in pure water and 170 mM SDS aqueous solutions were both measured at 40°C. In contrast to the DDAB and lecithin systems, the SDS microemulsion is prepared as a two-phase system in the measurement cells: an upper supercritical ethylene phase is in contact with the lower aqueous microemulsion phase. All measurements of the SDS system were conducted on the lower microemulsion phase.

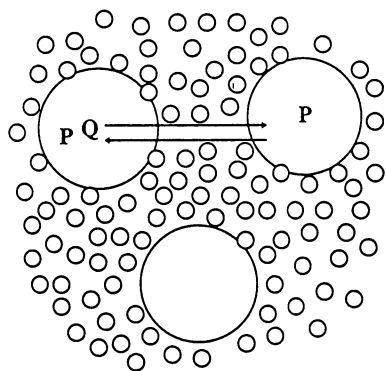
The saturation concentration of the ethylene in the predominately-aqueous microemulsion was measured using a liquid/fluid saturation cell. Through vigorous stirring the aqueous phase would become saturated with ethylene in about 30 min. The ethylene-saturated microemulsion was discharged through a metering valve into a trap at ambient pressure. The quantity of evolved ethylene gas was measured volumetrically.

For fluorescence lifetime measurements, pyrene (Molecular Probe) was used to study changes in the microemulsion environment as a function of pressure. Due to the dynamic quenching of pyrene fluorescence by oxygen, it is essential that oxygen be eliminated from the SDS aqueous solution by placing the solution under vacuum momentarily prior to measurement. Instrumentation for fluorescence measurements has been previously described (3c).

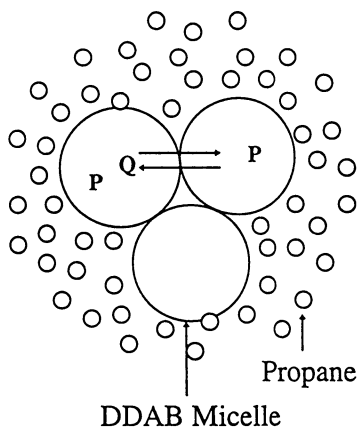
Results and Discussion

Electrical Conductivity in a DDAB/Propane Microemulsion. Measurement of electrical conductivity is a simple and an effective method for studying certain aspects of microemulsion structure. Variables which induce conductivity changes in

Pressure-Induced, Microemulsion Droplet Clustering:



At higher density, increased interactions between solvent and micelles reduce the exchange process



At lower density, strong micelle clustering enhances the exchange process

Scheme I

microemulsions include volume fraction (12,13), temperature (14), and pressure (10). In the systems that are predominately oil ($\phi_{oil} > 0.70$), a remarkable increase in conductivity is sometimes observed corresponding to what has been called a percolation threshold. However, the precise percolation mechanism is not always clear and this behavior has been described by both static and dynamic percolation models. The static percolation model is consistent with micelle coalescence in a precursor to a bicontinuous phase, whilst percolation clusters from the dynamic percolation model are associated with "sticky encounters" due to attractive interactions.

Figure 1 shows the conductivity of a propane/DDAB (0.326M)/water microemulsion ($s/o=0.42$) as a function of pressure. The conductivity of the single-phase system is reduced by almost three orders of magnitude when the pressure is increased from 100 to 450 bar. The systems become two-phase below 100 bar, so that reducing the pressure has the effect of bringing the system closer to a phase boundary. The increase in the electrical conductivity as a function of pressure was attributed to either a structural transition to a bicontinuous phase or micelle clustering due to attractive micelle interactions. The latter mechanism was favored in a detailed study (3c), applying fluorescence quenching techniques to this high pressure microemulsion solution. In that study, we clearly showed that the sharp decrease in conductivity with increasing pressure is attributed to the disappearance of percolative conduction. The mechanism of conduction above the percolation threshold is thought to be one of the surfactant ions hopping from droplet to droplet within the droplet clusters but no micelle coalescence occurring because the DDAB micelle size is uniform over the entire pressure range (100-450 bar) from our fluorescence quenching measurements. This supports the dynamic percolation model that is represented by Scheme I. That is, the overall shape of the micelles in the clusters is little changed from the micelles that are individually dispersed. However, strong interdroplet attractive interactions will enhance the solute exchange rates. The correlation between electrical conductivity and solute exchange rates between micelle droplets is in a good agreement with literature reports in the liquid microemulsion systems (15-18).

Viscosity Measurements and FT-IR Spectroscopy of the L- α -Lecithin Microemulsion. For a lecithin/propylene/water system, we observed a dramatic transition from a solid-like gel to a low viscosity fluid as the pressure of the system is increased. Similar to the electrical conductivity changes observed in a DDAB microemulsion, the viscosity change in the lecithin system with changing pressure is another indication that the extent of interactions between aggregates is changed as a function of pressure.

Unlike the DDAB/propane microemulsion system, soy-bean lecithin is a zwitterionic surfactant. In the lecithin/propylene microemulsion, the very small changes in the electrical conductivity observed with changing pressure are ascribed to a lack of appreciable amounts of ions in the aqueous microphase.

It is known that addition of water to a liquid organic solvent containing the lecithin surfactant induces large viscosity changes (9). This phenomenon was also observed in the lecithin/near-critical propylene microemulsion at 30°C. In addition,

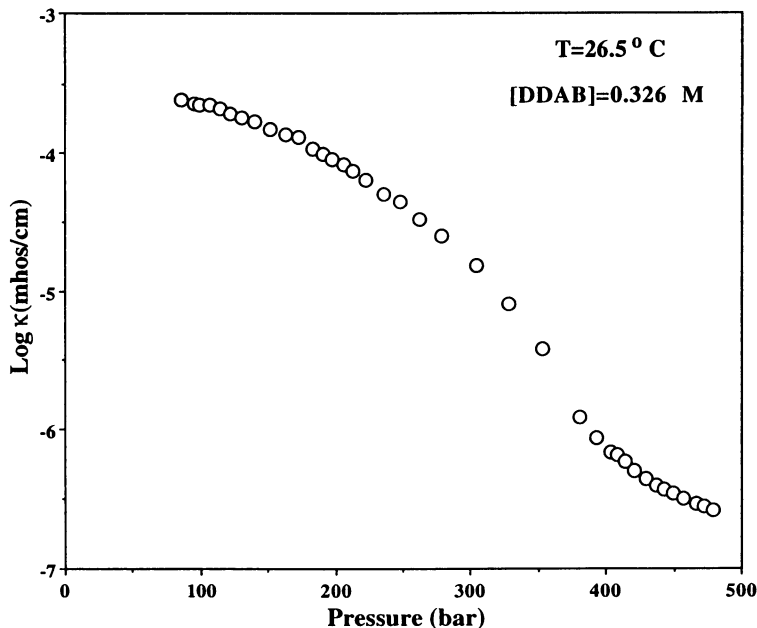


Figure 1. Conductivity of a DDAB/propane (W=24) microemulsion at 26.5°C.

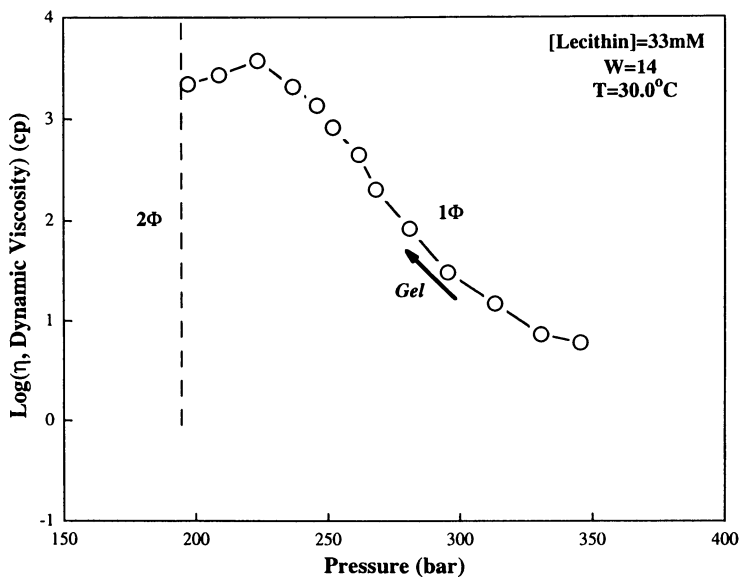


Figure 2. Dynamic viscosity (log-scale) of the lecithin/propylene microemulsion (W=14) as a function of pressure at 30°C.

we found that a phase transition from non-gel to gel occurs when pressure is varied from high to low at a constant water concentration. Figure 2 shows the effect of pressure on the dynamic viscosity (log-scale) for the lecithin/propylene microemulsion with $W=14$ at 30°C . The system viscosity at $W=14$ undergoes an increase of almost three orders-of-magnitude as the pressure is reduced to 225 bar. However, over this pressure range, propylene density only drops about 4% from 0.56 to 0.54 g/mL. The viscosity appears to reach a maximum and then decreases slightly just before reaching the phase boundary of the system. In order to get a clear understanding of the mechanisms for both water- and pressure-induced lecithin gel formations, we applied FT-IR spectroscopy to look at the phosphate ($\text{P}=\text{O}$) vibrational band. Earlier NMR studies (19,20) showed that the water-induced gel formation in a conventional liquid was attributed to a strong stiffening near the phosphorus atom and on the adjacent triglyceride. Figure 3 shows plots of the $\text{P}=\text{O}$ band frequency vs. W -value at 210 bar (the bottom axis) and vs. pressure at $W=14$ (the top axis), both at 30°C . We observed a continuous red shift in the $\text{P}=\text{O}$ stretching frequency and band broadening as W values were increased from 0 to about 8 but little change in the vibrational mode for W values above 8. In comparison, we observed no pressure effect on the $\text{P}=\text{O}$ vibrational frequency although the system viscosity changes by almost three orders-of-magnitude over this pressure range. The water-induced $\text{P}=\text{O}$ band shift and broadening are due to hydration *or/and* H-bonding of the phosphate group. The H-bonding causes changes in the electron distribution on the phosphate group, affecting the $\text{P}=\text{O}$ force constant thus lowering the vibrational frequency, as well as broadening the band. Changing the system pressure does not affect the local solvent environment of the interfacial regions since no change in the $\text{P}=\text{O}$ stretching frequency is observed. Rather, varying the system pressure changes the lecithin structure through the changes in the inter-rod interactions.

Scheme II depicts the two mechanisms for the gel formation induced by either water content (scheme II (A)) or pressure (scheme II (B)). Addition of water into the lecithin microemulsion induces one-dimensional growth of the aggregates into long tubular rods. By continuously increasing the water content at or above a threshold lecithin volume fraction ($0.014 < \phi < 0.145$), the long tubular rods reach a critical length where the rods interact with one another, forming a transient, polymer-like network, resulting in a large macroscopic viscosity. In contrast, changing the pressure of the system does not alter the polar environment of the head groups of the surfactants determined from the IR measurements. Since the hydrogen bond and electrostatic interactions are dominant factors affecting the geometry of the rods it is unlikely that pressure is inducing a large structural change. Rather the pressure effect on viscosity is most likely caused by altering the strong interaction between the rods leading to entanglement at lower pressures. An alternative explanation is that changes in the fluid density induce small changes in the rigidity of the rods. Higher rigidity alters the coiling of these giant rods by increasing the persistence length leading to much larger coil diameters and eventual entanglement.

Solubility Measurements of Ethylene in SDS Aqueous Solutions. As we discussed above, if the continuous phase solvent is a near- or supercritical fluid phase, one can adjust the magnitude of interdroplet interactions by simply tuning the

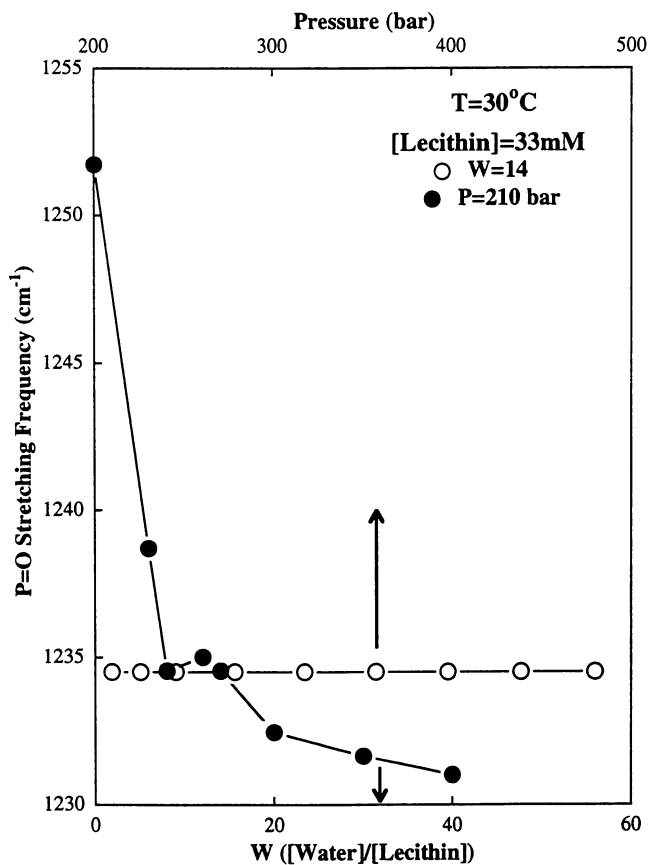
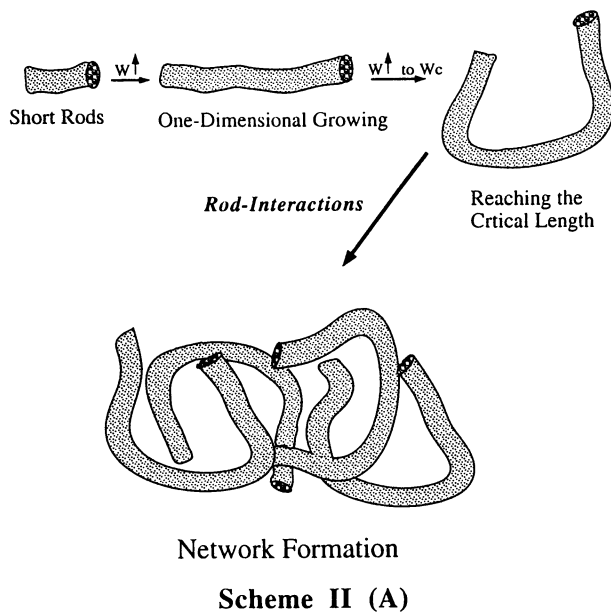
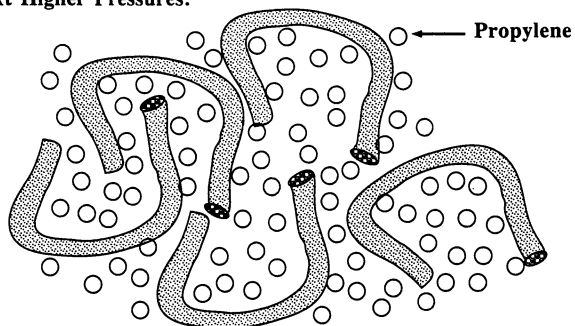
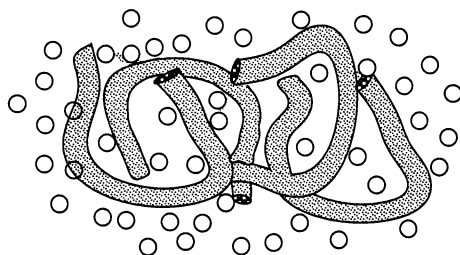
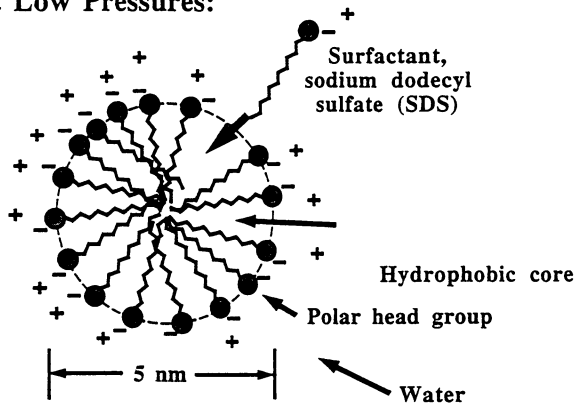


Figure 3. Peak frequency of P=O stretching band in 33 mM lecithin/propylene microemulsions (30°C) as a function of W at 210 bar (the bottom axis) and of pressure at W=14 (the top axis).

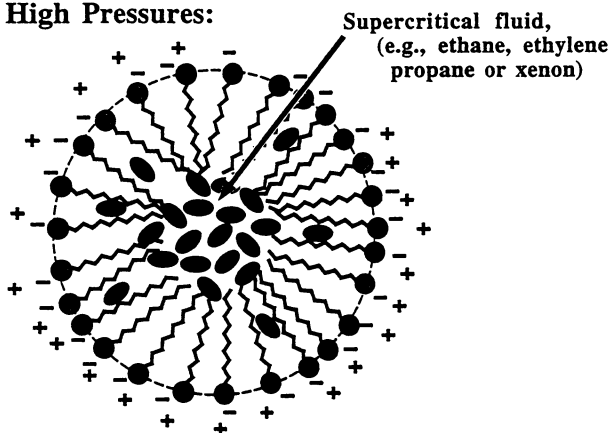
Water-Induced Lecithin Gel Formation:*Pressure-Induced Lecithin Gel Formation:*(a) **At Higher Pressures:**(b) **At Lower Pressures:****Scheme II (B)**

*Pressure-Induced Swelling of
Normal Micelle Cores*

(a) At Low Pressures:



(b) At High Pressures:



Scheme III

continuous phase pressure. These continuously- adjustable microemulsion solutions display drastic changes in their physical properties such as electrical conductivity and viscosity. What happens if this adjustable solvent is added to the micelle core regions in a system where the continuous phase is water? How do density changes of the internal supercritical fluid phase affect the microemulsion structure?

To answer these questions we chose a SDS/water normal-micelle system because it is one of the most widely studied microemulsions. Scheme III illustrates the structures of an SDS micelle with and without supercritical fluid incorporated into the cores. A continuous size increase with increasing system pressure was found in recent x-ray scattering studies (21). To gain a more detailed understanding of this system, we first investigated the solubility of ethylene in both pure water and 170 mM SDS aqueous solution. Figure 4 shows the measured solubility of ethylene in both neat water and 170 mM SDS aqueous solution (in units of grams(ethylene)/mL(solution)). If we consider only the ethylene dissolved in the cores of the SDS micelles, we observed a well-behaved curve of ethylene solubility vs. pressure given in Figure 5. In this study, we choose to define the ethylene micelle solubility in terms of an ethylene mole fraction given by the ratio of ethylene in the micelle core to the total moles of ethylene and SDS in the solution. Above a pressure of about 150 bar, the SDS micelles are essentially saturated with ethylene. This observation is in good agreement with our earlier study of a SDS/Xe system using x-ray scattering technique (21).

To further explore this structural change, we applied fluorescence spectroscopy to determine how the solvent environment of the SDS core region changes as a function of pressure. Pyrene is a good candidate for this study because of its sensitivity to the local solvent environment and its hydrophobicity. Figure 5 also shows the fluorescence lifetime data as a function of pressure. At the ambient pressure, pyrene experiences a more dodecane-like environment in the micelle cores because the measured lifetime ($\tau=335$ ns) is closer to that in neat dodecane solvent ($\tau=385$ ns), but much longer than that in water ($\tau=210$ ns). The difference in fluorescence lifetimes in the dodecane and the SDS solution at $P=1$ bar may be attributed to a small amount of water penetrating into the core region that slightly changes the micropolarity around the pyrene molecules. Increasing pressure from 1 to 130 bar results in *longer* fluorescence lifetimes due to uptake of ethylene in the core region. At pressures above 130 bar, the fluorescence lifetimes are no longer changing with increasing pressure. This is another indication of complete solubilization of ethylene in the SDS core region. Above a pressure of 130 bar, increasing pressure mainly compresses the micelle core which slightly decreases the pyrene lifetime. From this study, we can see that changing the fluid pressure dramatically alters the environment of the core region, presumably due to the micellar growth through incorporation of the fluid.

For this normal micelle system, we increase the overall volume fraction of the oil-like phase through addition of supercritical ethylene to the cores of the micelles. In this case, a change in the primary structure of the micelle is observed where the micelle swells to accept the fluid. The mole fractions of the fluid in the core are quite high, approaching a molar ratio of about 1:2, ethylene to SDS. This is still much lower than the saturation concentration of ethylene in a comparable liquid alkane such as dodecane. Thus the factors limiting the further uptake of ethylene into the

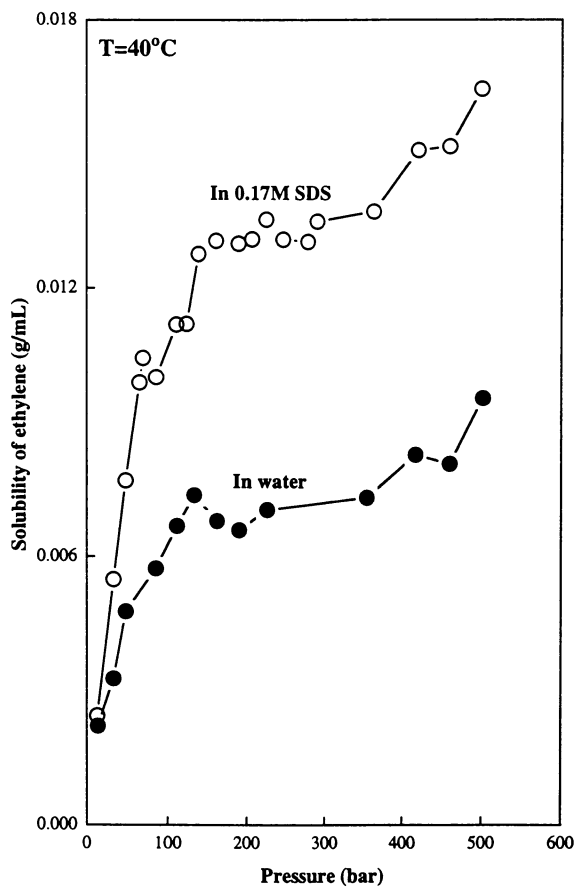


Figure 4. Solubility of ethylene in water (●) and in 170 mM SDS aqueous solution (○) as a function of pressure at 40°C.

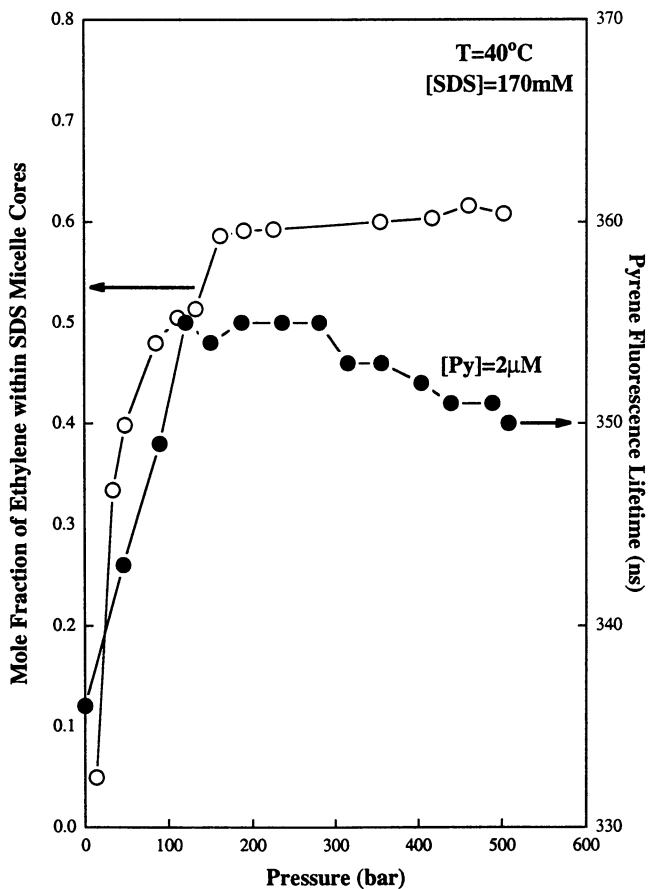


Figure 5. Solubility of ethylene in the core region of 170 mM SDS micelles (after subtraction) (○) and pyrene fluorescence lifetime within 170 mM SDS micelles (●) as a function of pressure both at 40°C.

cores of the micelles are probably related to properties of the interfacial film such as the changes in the surface tension, bending radius and/or the total interfacial area.

Conclusions

In this paper, we present a systematic study of three different surfactant-based fluid systems. We show that the continuous phase density for *reverse* microemulsions has a large effect on the degree of inter-droplet attractive interactions which can directly affect the secondary structure of the microemulsion. These changes in the secondary structure can induce large changes in physical properties, e.g., electrical conductivity and dynamic viscosity. For these reverse microemulsions, the volume fraction of the fluid and water microphases remains constant as the density of the continuous phase increases. In comparison, for a SDS normal-micelle system, the primary structure of the micelle is changing by swelling or growth of the micelles upon incorporation of ethylene into the hydrophobic cores. This change in primary structure is in response to a change in the volume fractions of the oil-like phase (ethylene) that occurs upon pressurization with the fluid.

Acknowledgement. This research was supported by the Director, Office of Energy Research, Office of Basic Energy Science, Chemical Science Division of the U. S. Department of Energy, under contract DE-AC06-76RLO 1830.

Literature Cited

- (a). Gale, R. W.; Fulton, J. L.; Smith, R. D. *J. Am. Chem. Soc.* **1987**, *109*, 920.
(b). Smith, R. D.; Fulton, J. L.; Blitz, J. P.; Tingey, J. M. *J. Phys. Chem.* **1990**, *94*, 781.
(c). Fulton, J. L.; Blitz, J. P.; Tingey, J. M.; Smith, R. D. *J. Phys. Chem.* **1989**, *93*, 4198.
(d). Tingey, J. M.; Fulton, J. L.; Smith, R. D. *J. Phys. Chem.* **1990**, *94*, 1997.
- (a). Lemert, R. M.; Fuller, R. A.; Johnston, K. P. *J. Phys. Chem.* **1990**, *94*, 6021.
(b). McFann, G. J.; Johnston, K. P. *J. Phys. Chem.* **1991**, *95*, 4889.
- (a). Zhang, J.; Bright, F. V. *J. Phys. Chem.* **1992**, *96*, 5633.
(b). Zhang, J.; Bright, F. V. *J. Phys. Chem.* **1992**, *96*, 9608.
(c). Zhang, J.; Fulton, J. L.; Smith, R. D. *J. Phys. Chem.* **1993**, *97*, 12331.
(d). Zhang, J.; White, G. L.; Fulton, J. L. *J. Phys. Chem.* **1995**, *97*, 5540.
- McFann, G. J.; Johnston, K. P.; Howdle, S. M. *AIChE J.* **1994**, *40* (3), 543.
- Hoefling, T. A.; Beitle, R. R.; Enick, R. M.; Beckman, E. J. *Fluid Phase Equilib.* **1993**, *83*, 203.
- DeSimone, J. M.; Maury, E. E.; Menciloglu, Y. Z.; McClain, J. B.; Romack, T. J.; Combes, J. R. *Science* **1994**, *265*, 356.
- Beckman, E. J.; Fulton, J. L.; Smith, R. D. *"Supercritical Fluid Technology: Reviews in Modern Theory and Applications"*, Bruno, T. J.; Ely, J. F., Eds., CRC Press, **1991**, 405.

8. Kaler, E. W.; Billman, J. F.; Fulton, J. L.; Smith, R. D. *J. Phys. Chem.* **1991**, *95*, 458.
9. Schurtenberger, P.; Scartazzini, R.; Luisi, P. L. *Rheol. Acta.* **1989**, *28*, 372.
10. Tingey, J. M.; Fulton, J. L.; Matson, D. W.; Smith, R. D. *J. Phys. Chem.* **1991**, *95*, 1445.
11. Fulton, J. L.; Yee, G. G.; Smith, R. D. *J. Am. Chem. Soc.* **1991**, *113*, 8327.
12. Lagues, M.; Ober, R.; Taupin, C. *J. Phys. (Paris) Lett.* **1978**, *39*, 487.
13. Dijk, M. A. van *Phys. Chem. Lett.* **1985**, *55*, 1003.
14. Eicke, H. -F.; Borkovec, M.; Das-Gupta, B. *J. Phys. Chem.* **1989**, *93*, 314.
15. Jada, A.; Lang, J.; Zana, R. *J. Phys. Chem.* **1989**, *93*, 10.
16. Lang, J.; Lalem, N.; Zana, R. *J. Phys. Chem.* **1992**, *96*, 4667.
17. Jada, A.; Lang, J.; Zana, R.; Makhloufi, R.; Hirsch, E.; Candau, S. J. *J. Phys. Chem.* **1990**, *94*, 387.
18. Lang, J.; Lalem, N.; Zana, R. *Colloids and Surfaces.* **1992**, *68*, 199.
19. Capitani, D.; Segre, A. L.; Haering, G.; Luisi, P. L. *J. Phys. Chem.* **1988**, *92*, 3500.
20. Daum, U.; Wei, G.; Luisi, P. L. *Colloid Polym. Sci.* **1988**, *266*, 657.
21. Fulton, J. L.; Pfund, D. in preparation.

RECEIVED May 19, 1995

Chapter 8

Predictive and Experimental Methods for the Choice of Cosolvent in the Supercritical Fluid Extraction of Pesticides

S. J. Macnaughton¹, P. Alessi², A. Cortesi², I. Kikic², and Neil R. Foster¹

¹School of Chemical Engineering and Industrial Chemistry, University of New South Wales, Sydney, New South Wales 2052, Australia

²Dipartimento di Ingegneria Chimica, dell' Ambiente e delle Materie Prime, Università di Trieste, Piazzale Europa 1, 34127 Trieste, Italy

The extraction of pesticides from soils and other solids using supercritical fluids can be significantly improved through the use of cosolvents. The difficulty in predicting which cosolvents will produce the largest solubility enhancements with individual pesticides is due in part to the lack of physical and chemical data available for most pesticides.

Solubility data for lindane in supercritical fluid CO₂-cosolvent mixtures are reported at 313.1K. These data have been correlated directly with the Peng-Robinson equation of state. In order to predict the effect of cosolvents on the solubility of lindane in supercritical CO₂ the interactions between lindane and each cosolvent must be known. One technique, that has been successfully used to predict the vapour liquid equilibria of many binary systems, utilises relevant Henry's constant data to calculate interaction parameters for equations of state. This technique has been extended to ternary solid-supercritical fluid-cosolvent systems. Appropriate Henry's constant data describing the equilibrium between the pure cosolvents and lindane have been measured and subsequently used to predict the ternary system solubility data. These predicted data have been directly compared with the measured solubility data.

Remediation of contaminated soils using supercritical fluid extraction has been shown to be technically feasible. Several laboratory studies have extracted chlorinated pesticides and other chlorinated pollutants from soils - DDT, Toxaphene and Arochlor (a polychlorinated biphenyl) (1,2,3,4,5). The addition of cosolvents to a primary supercritical fluid has been shown many times to enhance the solubility of solute and it has also been shown to improve the behaviour of soil

extractions. Dooley et al. (1) found that the addition of 5% methanol to CO₂ significantly enhanced the total extraction of DDT from soils. With the cosolvent, approximately 95% of the pesticide could be removed compared to only 70% removal without the cosolvent. Recently Markowz and Subklew (5) also found that the extraction of PCBs from soils was improved when methanol was used as a cosolvent. Several other studies have also reported enhanced extraction results when cosolvents have been used (6,7).

The solubility of pollutant species in supercritical fluids has been examined as part of a program investigating the supercritical remediation of soils. The solubility of several pesticides has been determined in supercritical CO₂ (DDT and 2,4-D (8) and lindane, endrin and methoxychlor (9)). In this work the solubility of lindane (γ -1,2,3,4,5,6,hexachlorocyclohexane) has been determined in supercritical CO₂ -cosolvent mixtures. The focus of the study was to examine several cosolvents in order to establish which one causes the largest enhancement of the solubility of lindane. Lindane was selected as part of an ongoing investigation of pesticide extraction with supercritical fluids. The determination of the solubility of lindane in CO₂-cosolvent mixtures is time consuming and therefore an indirect technique was also used to predict the solubility behaviour. The Henry's constants of each cosolvent at infinite dilution were measured in lindane at 390.9 K (melting point approx. 385 K) and these data correlated with the Peng-Robinson equation of state (PR EOS) which was then used to predict the solubility of lindane in the CO₂-cosolvent mixtures.

Background

In a previous study (10,11), Henry's constant data were correlated with the Boublick-Mansoori-van der Waals and the PR EOS and these equations were subsequently used to predict binary vapour-liquid equilibria (VLE). The advantage of this technique is that it is considerably easier to measure Henry's constants than VLE data. The basis of this technique is that the Henry's constants can be used to evaluate interaction parameters for equations of state and then the equations of state can be used to predict phase equilibria. Although the original study considered only binary liquid systems this approach has been extended to ternary systems for this study. The aim of the work is to predict the solubility of solids in supercritical fluid-cosolvent mixtures using Henry's constants for the cosolvent-solid systems combined with binary solid-supercritical fluid solubility data.

Initially, the applicability of this technique to ternary liquid systems was examined. A literature search revealed a suitable system (CO₂ - toluene - 1-methylnaphthalene (1-MN)) for which the appropriate VLE data (12) as well as Henry's constant data (13,14) had been measured. Henry's constant data were used to calculate interaction parameters for the PR EOS. The PR EOS, with the calculated interaction parameters, was then used to calculate VLE data. The results of this work are shown in Figure 1 in which the binary CO₂ -toluene system is investigated. The calculated vapour phase compositions at 353K are in good

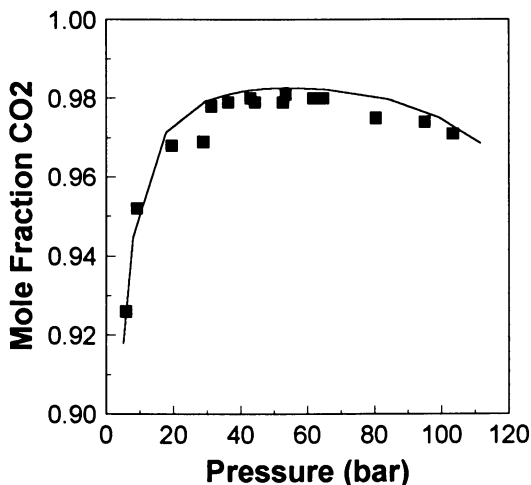


Figure 1. The vapour phase composition for the system CO₂-toluene at 353 K. (■ experimental data, (12), — prediction using PR EOS and Henry's constant data.)

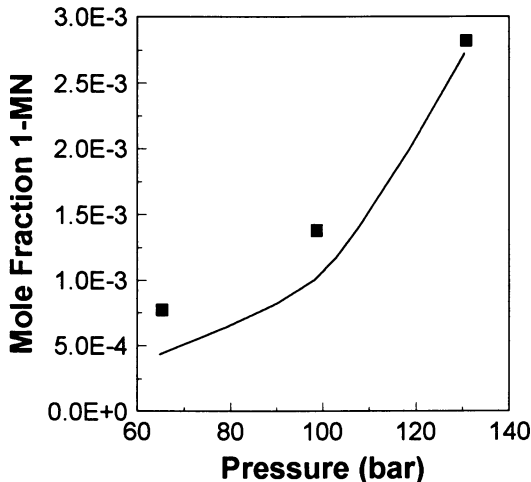


Figure 2. The vapour phase composition for the system CO₂-toluene-1-MN at 353 K. (■ experimental data, (12), — prediction using PR EOS and Henry's constant data.). Note; 1-MN:Toluene ratio fixed at 9:1.

agreement with the experimental data. A satisfactory result was also obtained for the ternary system (see Figure 2). In this case, three interaction parameters were needed to perform the calculation. Two of these parameters (CO_2 - toluene (k_{12}) and CO_2 -1-MN (k_{13})) were fitted to binary experimental data and the third parameter (k_{23}) was obtained from Henry's constant data for the toluene-1-MN system.

The calculation technique used for this ternary system mirrors the situation that exists when trying to calculate cosolvent solubility behaviour in supercritical fluid systems. If the PR EOS is to be used to calculate these solubilities then three separate interaction parameters are needed;

- (1) k_{12} between the supercritical solvent and the cosolvent. This parameter can be evaluated from VLE data if available.
- (2) k_{13} between the supercritical solvent and the solute. This parameter can be evaluated from binary solute-supercritical solvent solubility data - if available.
- (3) k_{23} between the cosolvent and the solute. This parameter can be evaluated either by fitting it to experimental ternary solubility data or else from cosolvent-solute Henry's constants.

These two alternative methods for obtaining k_{23} have been examined in this study for the system CO_2 -cosolvent-lindane. Six different cosolvents were examined. Both the Henry's constants for each cosolvent in lindane and the experimental solubilities of lindane in the CO_2 -cosolvent mixtures were measured for these systems. The two methods have been compared for the purpose of establishing whether the lindane solubilities could be predicted using Henry's constant data to calculate k_{23} .

Experimental

Materials. The source and purities of the chemicals used in this study are listed in Table I. The lindane originally contained a small percentage of impurities which were removed in an earlier study as described elsewhere (Macnaughton et al., 1994).

Table I The source and purity of the materials used.

Material	Source	Purity
CO_2	SIAD	99.98%
Lindane	Aldrich	97%
Acetonitrile	Carlo Erba	99.8%
Ethanol	Fluka	99.8%
Acetone	Chromanorm	99.8%
Ethyl Acetate	Sigma	99.8%
Heptane	Aldrich	99+%
Chloroform	Sigma	99.9%

(1) Solubility Measurements. The solubilities of lindane and two other pesticides in supercritical CO₂ have been measured at 313.1 K and 333.1 K (9) using a continuous flow apparatus similar to that described previously (15,16). This same apparatus was used in a slightly modified form to measure the solubility of lindane in CO₂ containing small amounts (2 mol %) of cosolvents. The only differences in the solubility measurement technique to that described elsewhere concern the preparation of the cosolvent-CO₂ mixture and the handling of the solute collected during each experiment. The experimental pressures and temperatures were chosen on the basis of available critical locus data to ensure that each CO₂-cosolvent mixture was indeed supercritical.

The cosolvent preparation technique was identical to that used by Ting et al., (17) and Gurdial et al., (18). The barrel of the ISCO syringe pump was used as a mixing bomb for the CO₂ and the cosolvent. Initially a metered dose of cosolvent was introduced into the empty barrel of the syringe pump and then liquid CO₂ was added until the desired pressure (typically 50 - 60 bar) was achieved. The temperature of the barrel of the syringe pump was maintained at a constant temperature of 274.1K to ensure that only liquid CO₂ entered the pump. The dosage of cosolvent required to achieve a composition of 2 mol% cosolvent was determined from the molar volumes of each component and assuming negligible volume change upon mixing (18). Mixing of the cosolvent and CO₂ was achieved by cycling the temperature of the syringe from 273K to 313K and back to 273K four times over a period of two hours.

The determination of solubility was based on the weight of solute trapped in a valve and filter and the corresponding volume of CO₂. The gas volume was measured with a precision of 0.01L using a wet test meter (SIM Brunt) that was calibrated to an accuracy of $\pm 0.4\%$. Prior to weighing, the valve and filter were dried to a constant weight at 50°C to remove any traces of cosolvent in the precipitated solute. The mass of solute was determined to $\pm 0.2\text{mg}$ using a Mettler H31 balance. The typical mass of solute that was collected in each experiment was greater than 100mg giving a potential error due to weighing of less than 0.2%.

During each experiment the system pressure was maintained to within $\pm 0.2\%$ of the desired value by adjusting the regulating valve and the pump flowrate. The system pressure was measured using a Druck pressure transducer (DPI 260) accurate to $\pm 0.1\%$. The system temperature was controlled to within $\pm 0.1\text{K}$ using an immersion circulator (Haake N3) and monitored using an RTD platinum probe accurate to $\pm 0.1\text{K}$.

Six different cosolvents were investigated in this study and cross-contamination with cosolvents was a potential problem. The entire apparatus was purged for 16 hours with nitrogen between experiments. In this way all traces of the previous cosolvent were eliminated from the system before a new cosolvent mixture was prepared.

(2) **Measurement of Henry's Constants.** The Henry's constants of the six cosolvents in lindane were determined using gas-liquid chromatography which is a good means of studying interactions in dilute solutions. The theory on which this technique is based is briefly described below.

The relationship which correlates the specific retention volume, $V_{g,i}$, with gas chromatographic quantities is the following:

$$V_{g,i} = \frac{F}{W_s} j \frac{P_o - P_w^\circ}{760} \frac{273}{T_o} (t_r - t_a) \quad (1)$$

$$j = \frac{3(P_i - P_o)^2 - 1}{2(P_i - P_o)^3 - 1} \quad (2)$$

where F is the carrier gas flow rate (cm^3/s), W_s is the weight of the stationary phase in the column (g), j is the James-Martin factor, P_o is the outlet column pressure (mmHg), P_i is the inlet column pressure (mmHg), P_w° is the vapour pressure of water at flow-meter temperature (mmHg), T_o is the flow-meter temperature (K), t_r and t_a are the retention time and dead time (s), respectively. Henry's constants, H_i , are calculated by means of the following equation:

$$\ln H_i = \ln \frac{RT}{V_{g,i} M w_s} Z_g \phi_i \quad (3)$$

where R is the gas constant, $M w_s$ is the molecular weight of the stationary phase, T is the column temperature (K), and $Z_g \phi_i$ is the compressibility factor multiplied by the fugacity coefficient of the phase gas (close to unity; in this work considered equal to one).

In this study, a gas chromatograph (Fractovap Model B - Carlo Erba) with a thermal conductivity detector was used. The column (1m long, 4-mm internal diameter) was packed with about 20% lindane on Chromosorb 100/120 mesh. The flow of carrier gas, helium, as measured by a bubble flowmeter was about 30 cm^3/min , the inlet pressure was measured with a mercury manometer, the outlet pressure was atmospheric and monitored with a barometer. Between 0.1 to 0.5 μl of each sample was injected using a 5- μl Hamilton syringe. The error on the measurements has been estimated as 3 to 5%. The measurements were carried out at 390.9K which is above the melting point of the lindane. At this temperature lindane has a significant vapour pressure that cannot be neglected (approx 0.5 kPa). To account for any potential losses of lindane during the experiment the column was weighed before and after the test. The weight loss was considered linear during the experiment and the real weight of the stationary phase (i.e. W_s in equation 1) was calculated for each solute injection (Note: the total weight loss was less than 1%).

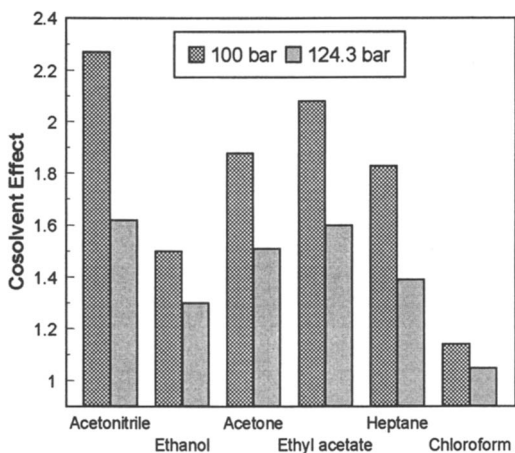


Figure 3 Cosolvent Effect for Lindane in Supercritical CO₂ at 313.1 K.

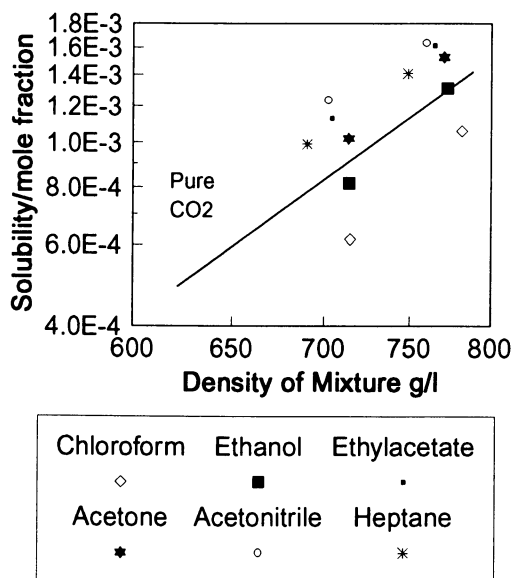


Figure 4 Lindane Solubility in CO₂-Cosolvent Mixtures as a Function of Mixture Density.

Results

The solubilities of lindane in the various cosolvent mixtures are listed in Table II. Each measurement was the average of at least three determinations and the standard deviation of each measurement is also listed. These data are shown in Figure 3 which illustrates the cosolvent effect (defined as the ratio of the ternary system solubility to the binary system solubility - y_3/y_2). The relative effects of each cosolvent are clearly visible with acetonitrile providing the largest solubility enhancement and chloroform the smallest.

Table II Solubility of Lindane in Supercritical CO₂ - Cosolvent Systems.

Cosolvent (2 mole %)	313.1 K and 100 bar			313.1 K and 124.3 bar		
	$y_3 \times 10^4$	y_3/y_2	Std Dev. (%)	$y_3 \times 10^4$	y_3/y_2	Std Dev. (%)
Acetone	10.5	1.88	2.38	15.3	1.51	0.56
Ethanol	8.16	1.50	0.98	13.1	1.30	0.59
Ethyl Acetate	11.3	2.08	1.98	16.2	1.60	1.12
Acetonitrile	12.4	2.27	2.01	16.4	1.62	1.76
Chloroform	6.17	1.14	0.76	10.6	1.05	2.52
Heptane	9.92	1.83	1.23	14.1	1.39	1.93

The differing effect of each cosolvent can be explained in terms of the different interactions with the solute. In order to do this the influence of density must be removed from the cosolvent effect. This has been done by plotting the solubility data as a function of the supercritical mixture density. The supercritical mixture density (ρ_{MIX}) has been calculated according to Equation 4;

$$\rho_{MIX} = \rho_{CO_2} \frac{\rho_{TERNARY}^{EOS}}{\rho_{BINARY}^{EOS}} \quad (4)$$

where $\rho_{TERNARY}^{EOS}$ refers to the density of the lindane-cosolvent-CO₂ system calculated using the PR EOS and ρ_{BINARY}^{EOS} refers to the density of the binary CO₂-lindane mixture calculated using the PR EOS and ρ_{CO_2} is the density of pure CO₂ (19). As has been described elsewhere (20) this estimation assumes that the errors in the two densities calculated using the PR EOS will be similar. In Figure 4, the solubility data have been plotted as a function of mixture density and the binary system solubility-density dependence has been included for reference. The data for ethanol are close to the solubility-density line for lindane in pure CO₂ which indicates that the cosolvent effect can be directly attributed to density enhancements. The solubility data for chloroform-CO₂ are significantly below the solubility-density behaviour of pure CO₂ which is difficult to explain unless interactions between chloroform and CO₂ or self association of the chloroform in the supercritical CO₂

are contributing to the result. The solubility enhancements for the other four cosolvents exceed those predicted from density considerations alone which indicates the significance of specific lindane-cosolvent interactions in these systems.

The best cosolvent was acetonitrile which also has the lowest molecular weight and the highest polarity (3.5 debye). The polarity of the cosolvent should be significant because lindane has a polarity of 2.51 - 3.08 debye (21) however the next most polar cosolvent - acetone (2.9 debye) - did not produce such a large cosolvent effect. Ethanol and chloroform produced the lowest cosolvent effects and these two molecules are the only cosolvents studied that possess a significant ability to donate hydrogen bonds. The relationship between this property and their performance as cosolvents is difficult to establish from this small solubility data base.

The experimental Henry's constants for 10 cosolvents in lindane at 390.9 K are listed in Table III. The Henry's constant for both normal alkanes and normal alcohols decreases with increasing chain length. Originally, the data were to be measured at several conditions in order to establish the temperature dependence of these constants. However, the potential interference caused by the high estimated vapour pressure of lindane at temperatures above 390.9 K prevented this and below 385 K lindane is no longer a liquid.

Table III Experimental Henry's Constants for Cosolvents in Lindane at 390.9 K.

Cosolvent	H (bar)	Cosolvent	H (bar)
n-Pentane	48.7	Methanol	24.7
n-Heptane	8.45	Ethanol	13.9
Benzene	3.05	n-Propanol	5.62
Acetone	8.67	Acetonitrile	4.39
Ethyl acetate	3.73	Chloroform	5.52

Correlation

CO₂ - Lindane Solubility. The solubility data for lindane in supercritical CO₂ (Macnaughton et al., 1994) were correlated using the PR EOS with van der Waals mixing rules. A single temperature dependent interaction parameter - k_{ij} - was fitted to the data. The major difficulty in correlating these type of data with a cubic equation of state is the lack of physical property data available for pesticides. In order to use the PR EOS the following data are needed for the pesticide lindane - the critical temperature (T_c), the critical pressure (P_c), the acentric factor (ω), the saturated vapour pressure (P^{SAT}) and the molar volume (v^S). All these properties were estimated using the methods listed in Table IV. The boiling point (T_b) is included in Table IV because it was used in the determination of T_c . The estimation of the vapour pressure utilised an existing vapour pressure data point reported at 293.1 K (5.6×10^{-08} bar) (22) whereas all the other techniques relied solely on group contributions based on the structure of the molecule.

The data were successfully correlated with the PR EOS. A single interaction parameter was fitted to each isotherm of data and optimised by minimising the average absolute relative deviation (AARD) between the experimental data and the solubilities calculated with the PR EOS. The interaction parameter at 313.1 K was 0.007 with a corresponding AARD of 5.3% and at 333.1 K -0.040 with a corresponding AARD of 7.7%. The results of this correlation are shown in Figure 5.

Table IV Property Estimation for Lindane.

Physical Property	Value	Estimation Method
T_c	733 K	Somayajulu (23)
P_c	26.1 bar	Somayajulu (23)
ω	0.36	Reid et al. (24)
P^{SAT}		
313.1K	3.64×10^{-07} bar	Modified Watson correlation (25)
333.1K	1.17×10^{-06} bar	
v^S	159 cm ³ /mol	Immirzi and Perini (26)
T_b	506 K	Meissner's method (25)

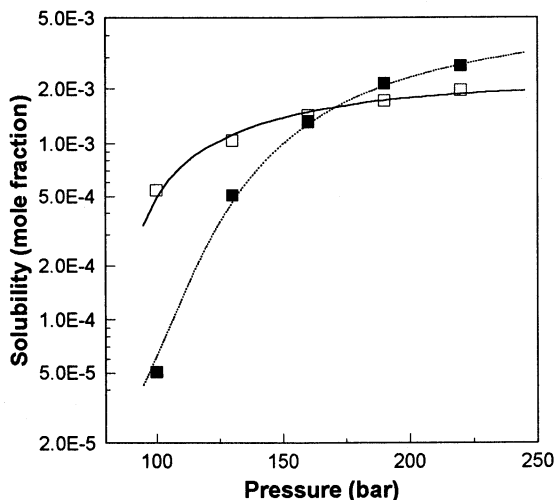


Figure 5 Solubility of Lindane in CO₂ and Correlation with the PR EOS (□ 313.1K experimental; —313.1K correlated with PR EOS; ■ 333.1 K experimental; --- 333.1 K correlated with PR EOS)

CO₂ - Cosolvent - Lindane Solubilities. The ternary solubility data were also correlated with the PR EOS. In this case three interaction parameters were needed;

- (1) k_{12} between the CO₂ and the cosolvent - this parameter was evaluated from VLE data if they were available and otherwise set to zero. The values of k_{12} that were used are listed in Table V;
- (2) k_{13} between CO₂ and lindane - this parameter was taken from the value optimised when the binary data were correlated at 313.1 K ($k_{13} = 0.007$);
- (3) k_{23} between the cosolvent and the lindane - this parameter was fitted to the experimental data.

The results of this correlation were excellent (see Table V) however this was not surprising because the interaction parameter was fitted to only two data points. This correlation will be further tested when more experimental data, at different solvent concentrations and temperatures, are measured for these systems.

In addition to the direct correlation of the ternary system solubility data using the PR EOS, the data were predicted from the experimental Henry's constants using the technique described earlier. The interaction parameters between lindane and the cosolvents (k_{23}) were evaluated using the Henry's constant data and assuming that k_{23} is independent of temperature. The method is briefly described below and has been described more completely elsewhere (10,11). The Henry's constant of component 2 in a liquid^(L) mixture is defined as:

$$H_2^L = \lim_{x_2 \rightarrow 0} \frac{f_2^L}{x_2} = \lim_{x_2 \rightarrow 0} P \phi_2^L \quad (5)$$

where f_2 is the fugacity of component 2. For a binary system, the Henry's constant of cosolvent (2) in lindane (1) is expressed by the following relationship:

$$H_{21}(P_1^s) = P_1^s \phi_2(T, P, x_2 = 0) \quad (6)$$

where P_1^s is the lindane vapour pressure and ϕ_2 is the fugacity coefficient calculated from the PR EOS. Consequently, from experimental data of Henry's constants it is possible to determine the k_{23} values for each cosolvent - lindane pair. The vapour pressure of lindane and critical properties of lindane that were used for this work are those listed in Table IV.

Table V Correlation and Prediction of the Solubility of Lindane in CO₂-Cosolvent Mixtures.

Cosolvent	Solubility Data			Henry's constant	
	k_{12}	k_{23}	AARD	k_{23}	AARD
Acetonitrile	0.0 ^a	-0.130	4.0	0.047	17.3
Ethyl acetate	0.0 ^b	-0.117	0.6	0.021	14.3
Heptane	0.100 ^c	-0.056	5.2	0.124	25.2
Acetone	0.014 ^d	-0.109	2.1	0.058	15.0
Ethanol	0.086 ^e	0.189	3.7	0.143	5.2
Chloroform	0.055 ^f	0.381	7.1	0.024	39.0

^{a,b} set to zero due to a lack of VLE data; ^c (24); ^d (27); ^e (28); ^f (29).

The values of k_{23} determined in this way were then used to calculate the solubility of lindane in the CO₂-cosolvent mixtures. The results of these calculations are shown in Table V. The predictions are excellent for ethanol however they are considerably worse for the other five cosolvents, although acetonitrile was correctly predicted to be the best cosolvent. This can be partially explained by the effect in temperature on the interaction parameter ie. the Henry's constants were determined at 390.9 K whereas the solubility data were predicted at 313.1 K. Another explanation for the poor results is that the PR EOS cannot be used to describe data at low pressures and infinite dilution as well as supercritical phase equilibria using the same interaction parameters. A more detailed conclusion can be made when a larger database is examined.

Conclusion

Solubility data for lindane in six supercritical CO₂-cosolvent mixtures (2 mol%) have been determined at 313.1K using a dynamic solubility technique. The largest cosolvent effect was achieved with acetonitrile and the least effective cosolvent was chloroform. Solubility data for the binary lindane-CO₂ system were successfully correlated using the PR EOS and this was then extended to incorporate the cosolvent systems. The correlation of the data was good however, with the limited number of data for each ternary system, this was expected. The ternary system solubilities were also predicted using experimental Henry's constants to calculate the lindane-cosolvent interaction coefficient for the PR EOS. This prediction was always worse than the direct correlation of the data and it does not appear to fully account for the lindane-cosolvent interaction. The significance of this technique lies in the potential to replace time consuming high pressure experiments on supercritical cosolvent systems with low pressure infinite dilution experiments that are easier to perform.

Acknowledgements

The authors wish to acknowledge financial support from ARC Fellowship No. F4934066, ARC Collaborative Research Grant with BVR PTY LTD (Ref. No. C29380035) as well as CNR (Progetto Finalizzato Chimica Fine).

References

- 1 Dooley, K.M.; Kao, C-P. C.; Gambrell, R.P.; Knopf, F.C., *Ind. Eng. Chem. Res.* **1987a**, 26, 2058.
- 2 Dooley, K.M.; Gambrell, R.; Knopf, F.C., Proceedings from *Int. Conf. on New Frontiers for Haz. Waste Mgt.*, Pittsburg, **1987b**, 383.
- 3 Dooley, K.M.; Ghonasgi, D.; Knopf, F.C.; Gambrell, R.P., *Env. Prog.* **1990**, 9(4), 197.
- 4 Brady, B.O., Dooley, K.M., Knopf, F.C., Gambrell, R.P., *Ind. Eng. Chem. Res.* **1987**, 26, 261.
- 5 Markowz, G.; Subklew, G., "SFE of Polychlorinated Biphenyls from Soils", Proceedings of the 3rd International Symposium on Supercritical Fluids, Strasbourg, **1994**, Tome 2, 505.
- 6 Hess, R.K.; Erkey, C.; Akgerman, A., *J. Supercrit. Fluids*, **1991**, 4, 47.
- 7 Andrews, A.T.; Ahlert, R.C.; Kosson, D.S., *Environ. Prog.* **1990**, 9(4), 204.
- 8 Macnaughton, S.J.; Foster, N.R., *Ind. Eng. Chem. Res.*, **1994**, 33, 2757.
- 9 Macnaughton, S.J.; Kikic, I.; Rovedo, G.; Foster, N.R.; Alessi, P., "The Solubility of Chlorinated Pesticides in Supercritical Carbon Dioxide", *J. Chem. Eng. Data.*, **1995**, in press.
- 10 Neau E.; Alessi P.; Fermeglia M.; Kikic I., *Chem. Eng. Sci.*, **1990**, 45(4), 795-808.
- 11 Kikic I.; Alessi P.; Fermeglia M., *Fluid Phase Equilibria*, **1983**, 14, 363-372.
- 12 Morris, W.O.; Donohue, M.D., *J. Chem. Eng. Data.*, **1985**, 30(3),259.
- 13 Turek, E.A.; Arnold, D.W.; Greenhorn, R.A.; Chao, K.C., *Ind. Eng. Chem. Fundam.*, **1979**, 18, 426.
- 14 Field, L.; Battino, R.; Wilhelm, E., *J. Chem. Thermodynamics*, **1974**, 6, 297.
- 15 Yun, S.L.; Liong, K.K.; Gurdial, G.S.; Foster, N.R., *Ind. Eng. Chem. Res.*, **1991**, 30, 2476.
- 16 Gurdial, G.S.; Foster, N.R., *Ind. Eng. Chem. Res.* **1991**, 30, 575.
- 17 Ting, S. S.T.; Macnaughton, S. J.; Tomasko, D. L.; Foster, N. R., *Ind. Eng. Chem. Res.* **1993**, 32, 1471.
- 18 Gurdial, G.S.; Macnaughton, S.J.; Tomasko, D.L.; Foster, N.R., *Ind. Eng. Chem. Res.* **1993**, 32(7), 1488
- 19 Angus, S.; Armstrong, B.; de Reuck, K.M., *IUPAC International Tables of the Fluid State - Carbon Dioxide*, Pergamon Press, New York, NY, **1976**.
- 20 Foster, N.R.; Singh, H.; Yun, S.L.J.; Tomasko, D.L.; Macnaughton, S.J., *Ind. Eng. Chem. Res.*, **1993**, 32, 2849.

- 21 McClellan, A.L., *Tables of Experimental Dipole Moments Volume 2*, Rahara Enterprises, El Cerrito, Cal. 1974.
- 22 Worthing, C. R., *The Pesticide Manual*. 9th ed., The British Crop Protection Council, 1991.
- 23 Somayajulu, G.R., *J. Chem. Eng. Data.*, 1989, 34, 106.
- 24 Reid, R.C.; Prausnitz, J.M.; Poling, B.E., *The Properties of Gases and Liquids*, McGraw-Hill, New York, 1986.
- 25 Lyman, W. J.; Reehl, W. F.; Rosenblatt, D. H., *Handbook of Chemical Property Estimation Methods*, McGraw-Hill Book Co., New York, NY, 1982.
- 26 Immirzi, A.; Perini, B., *Acta. Cryst.* 1977, A33, 216.
- 27 Katayama, T; Ohgaki, K.; Maekawa, G.; Goto, M.; Nagano, T., *J. Chem. Eng. Japan*, 1975, 8, 89.
- 28 Jennings, D.W.; Lee, R-J., Teja, A.S., *J. Chem. Eng. Data.*, 1991, 42, 76.
- 29 Florusse, L.J.; Peters, C.J., "Experimental Determination of Vapor-Liquid Equilibria in Binary Mixtures of Carbon Dioxide - Chloroform", *J. Chem. Eng. Data*, in preparation, 1994.

RECEIVED May 31, 1995

Chapter 9

Correlation and Prediction of Phase Equilibria of Mixtures with Supercritical Compounds for a Class of Equations of State

Kim Knudsen¹, Lucie Coniglio², and Rafiqul Gani^{1,3}

¹Department of Chemical Engineering, Technical University of Denmark, 2800 Lyngby, Denmark

²Ecole Nationale Supérieure en Génie des Technologies Industrielles, University of Pau, 64000 Pau, France

The correlative and predictive capabilities of a class of equation of state (EOS) models have been compared and evaluated for a range of binary and ternary mixtures involving supercritical fluids (such as CO₂ and propane) at high pressures. The recently proposed models such as the MHV2 model, the LCVN model and the WS (Wong-Sandler) model are among the models evaluated. The performance evaluation has been made in terms of comparisons of the computed values (correlated and predicted) with experimental values as well as computational times needed for a typical point in a P-x,y diagram. Based on the performance evaluation, the MHV2 model and the LCVN model appear to be the most promising.

Separations with a supercritical solvent such as carbon dioxide have been receiving increasing attention in diverse fields such as food and oil processing, biotechnology and environmental control (1). An important step in the computer aided design and analysis of these processes is the correct and consistent estimation of phase equilibrium related properties. This is, however, not an easy task considering the conditions of operation (involving high pressure phase equilibrium) and the non-ideality of the mixture. As a result, thermodynamic models such as the cubic equations of state or the G^E-based models cannot be applied without modifications.

Developments in the last decade related to new mixing rules for the a-parameter (or a/b-parameter) and the b-parameter in the cubic equation of state have focussed on correlation and prediction of high pressure phase equilibria. Currently, there exist several (2-4) methods which appear to be promising. An evaluation of these methods is needed, since for any application intended to design and/or analysis of a process, only one estimated value can be used (considering use of computer aided systems). Also, very few currently available computer aided systems such as process simulators are applicable to supercritical extraction based separation processes (5). Consequently,

³Corresponding author

even though the number of applications using supercritical fluids is increasing, their commercial significance is still limited.

The objective of this paper is to compare the performance of a class of cubic equations of state with respect to correlation and prediction of phase equilibria for mixtures containing supercritical fluids. Since one of the applications of these models is going to be in process design and analysis, the comparison of the performance of the models should also take into account their use in computer aided systems. Therefore, in addition to accuracy and consistency, computational times are also considered to be an important factor. It should be noted that in this paper, the selected models for comparison are used as they are found in the open literature. If parameters for a model are not available, they have been estimated. Another procedure, which was not followed in this work, would have been to fit the parameters of a selected excess free energy model for all the mixing rules and systems considered in this work to evaluate the correlative capabilities of each mixing rule. This approach, however, is beyond the scope of the present paper, and there is no general consensus of which specific model one should use. Neither would this procedure allow us to evaluate the predictive capabilities of the models, which is one of the objectives of this paper. Therefore, we have chosen to take the models as they are reported in the open literature.

This paper compares the ability of the models to correlate and/or predict binary mixture data and ternary mixture data for a range of supercritical fluid-solute systems. The supercritical fluid is either carbon dioxide or propane while the solutes include low molecular weight compounds (such as methanol and isopropanol) as well as high molecular weight compounds (such as free fatty acids and esters from the fish oil). For all the mixtures, experimental data have been compared with the correlated or predicted values. All the models (methods) compared have different ways of determining the mixture *a*-parameter (or *a/b*-parameter) and the mixture *b*-parameter.

THERMODYNAMIC MODELS

The main equations of the various mixing rules studied are given here, together with the abbreviations used in the comparisons. The SRK EOS (6) and the PR EOS (7) are used as base models for the various mixing rules. The reason for not using the same cubic EOS is that parameters have already been estimated for two of the mixing rules incorporating a predictive G^E -model into the mixture *a*-parameter, and in order to use the existing parameters, the base model should not be changed. For the temperature dependent part of the pure component *a*-parameter, the equation of Mathias and Copeman (8) is used. Most of the pure component parameters used in this work can be found in the literature (2, 3, 9-11), whereas the rest have been estimated, and they can be obtained from the authors. The critical properties of the pure components are obtained from the DIPPR data bank (12).

In the vdW model the SRK EOS is used together with quadratic mixing rules for both the *a*- and *b*-parameter. Since temperature dependence can be incorporated into each of the binary interaction coefficients, there are possibilities of a two parameter model (vdW2) without temperature dependent parameters, and a four parameter model (vdW4) with temperature dependent parameters.

$$\begin{aligned}
 a &= \sum_{i=1}^N \sum_{j=1}^N x_i x_j a_{ij} ; a_{ij} = \sqrt{a_{ii} a_{jj}} (1 - k_{ij}) ; k_{ij} = k_{ij}^0 + k_{ij}^T \left(\frac{T}{T^0} - 1 \right) \\
 b &= \sum_{i=1}^N \sum_{j=1}^N x_i x_j b_{ij} ; b_{ij} = \frac{b_{ii} + b_{jj}}{2} (1 - l_{ij}) ; l_{ij} = l_{ij}^0 + l_{ij}^T \left(\frac{T}{T^0} - 1 \right)
 \end{aligned} \quad (1)$$

The random - non random model by Mollerup (13, 14) is used in this paper together with the SRK EOS and a quadratic mixing rule for the b-parameter. As shown in equation (2), none of the three binary interaction coefficients are considered to be temperature dependent in this work.

$$\begin{aligned}
 a^{eff} &= \sum_{i=1}^N x_i \left(\sum_{j=1}^N x_j a_{ji} + \frac{\sum_{k=1}^N x_k E_{ki} (-k_{ki}^0 a_{ki}^0)}{\sum_{i=1}^N x_i E_{ii}} \right) ; a_{ki}^0 = \sqrt{a_{ii} a_{kk}} \\
 E_{ki} &= \exp \left[\left(\frac{-a_{ki}^0 k_{ki}^0}{R T b} \right) \ln \left(1 + \frac{b}{v} \right) \right] ; a_{ki} = a_{ki}^0 (1 - k_{ki})
 \end{aligned} \quad (2)$$

As this model is also known as a density-dependent local composition model, the abbreviation (DDL) is used.

The local composition model of Schwartzentruber, Galivel-Solastiouk and Renon (SGR) is used in this paper together with the SRK EOS.

$$\begin{aligned}
 a &= \sum_{i=1}^N \sum_{j=1}^N x_i x_j a_{ij} ; a_{ij} = \sqrt{a_{ii} a_{jj}} \left(1 - k_{ij} - l_{ij} \frac{m_{ij} x_i - m_{ji} x_j}{m_{ij} x_i + m_{ji} x_j} \right) \\
 k_{ij} &= k_{ji} ; l_{ij} = -l_{ji} ; m_{ij} = 1 - m_{ji}
 \end{aligned} \quad (3)$$

For the b-parameter, a linear mixing rule represented by equation (4) is employed (15).

$$b = \sum_{i=1}^N x_i b_i \quad (4)$$

Huron and Vidal (16) proposed a new mixing rule for the a-parameter (HV) in the SRK EOS given by equation (5).

$$\begin{aligned}
 a &= b \left[\sum_{i=1}^N x_i \frac{a_{ii}}{b_{ii}} - \frac{G^E}{\ln(2)} \right] ; \frac{G^E}{RT} = \sum_{i=1}^N x_i \frac{\sum_{j=1}^N x_j G_{ji} \tau_{ji}}{\sum_{k=1}^N x_k G_{kj}} \\
 G_{ji} &= b_{jj} \exp(-\alpha_{ji} \tau_{ji}) ; \tau_{ji} = \tau_{ji}^0 + \tau_{ji}^T \left(1 - \frac{T^0}{T} \right)
 \end{aligned} \quad (5)$$

The above mixing rule has been derived by combining the EOS with a slightly modified NRTL G^E -model (17) and assuming that $G^{E, EOS} = G^{E, act}$ at infinite pressure. A linear mixing rule (Eq. (4)) is used for the b-parameter.

The mixing rule of Michelsen (18, 19) is used together with original UNIFAC with a linear temperature dependence of the interaction parameter (20). In this work MHV2 is used with a linear mixing rule for the b-parameter, and the mixing rule for the EOS a-parameter is given by equation (6).

$$q_1(\alpha - \sum_{i=1}^N x_i \alpha_{ii}) + q_2(\alpha^2 - \sum_{i=1}^N x_i \alpha_{ii}^2) = \frac{G^E}{RT} + \sum_{i=1}^N x_i \ln\left(\frac{b}{b_{ii}}\right) \quad (6)$$

$$a = \alpha b RT; \quad G^E = G_{UNIFAC}^E; \quad a_{ij} = a_{ij,1} + a_{ij,2} (T - T^0)$$

For MHV1, a quadratic mixing rule for the b-parameter is used and the mixing rule for the EOS a-parameter is given by equation (7).

$$q_1(\alpha - \sum_{i=1}^N x_i \alpha_{ii}) = \frac{G^E}{RT} + \sum_{i=1}^N x_i \ln\left(\frac{b}{b_{ii}}\right) \quad (7)$$

$$a = \alpha b RT; \quad G^E = G_{UNIFAC}^E; \quad a_{ij} = a_{ij,1} + a_{ij,2} (T - T^0)$$

The LCVM mixing rule for the a-parameter (3) is a Linear Combination of the Vidal and Michelsen mixing rules. It is used together with the PR EOS, original UNIFAC (20, 21), and a linear mixing rule for the b-parameter.

$$\alpha = \frac{a}{bRT} = \frac{1-\lambda}{A_m} \left[\frac{G^E}{RT} + \sum_{i=1}^N x_i \ln \frac{b}{b_{ii}} \right] + \frac{\lambda}{A_v} \frac{G^E}{RT} + \sum_{i=1}^N x_i \alpha_{ii} \quad (8)$$

$$G^E = G_{UNIFAC}^E; \quad a_{ij} = a_{ij,1} + a_{ij,2} (T - T^0); \quad \lambda = 0.36$$

In the WS mixing rule (4) the expression for b and a for the mixture are given by equation (9).

$$b = \frac{\sum_{i=1}^N \sum_{j=1}^N x_i x_j \left(b_i + b_j - \frac{a_i + a_j}{RT} \right) \left(\frac{1 - k_{ij}}{2} \right)}{1 + \frac{G^E}{A_v RT} - \sum_{i=1}^N x_i \left(\frac{a_i}{b_i RT} \right)}; \quad a = b \left[\sum_{i=1}^N x_i \frac{a_{ii}}{b_{ii}} - \frac{G^E}{A_v} \right] \quad (9)$$

Original UNIFAC with a linear temperature dependence of the interaction parameter (20) is used as the G^E -model. If UNIFAC parameters exist, the binary interaction coefficient (k_{ij}) is calculated/adjusted (22, 23) in order to reproduce the G^E of UNIFAC (experimental data).

In all, eight different mixing rules/models/methods including the MHV1, MHV2, LCVM, WS, HV, DDLC, SGR, and VdW have been considered (two different numbers of parameters in the VdW mixing rule have also been considered).

MIXTURE DETAILS

Table I gives the details of the binary and ternary mixtures whose computed data are given in this paper. It should be noted that in the actual performance evaluation, larger data sets (whose details can be obtained from the authors) have been considered. The first set of data involves the three binary pair data and the ternary mixture data for the system $\text{CO}_2\text{-CH}_3\text{OH-H}_2\text{O}$. The second set of data involves two of the binary pair data and the ternary mixture data for the system $\text{C}_3\text{H}_8\text{-H}_2\text{O-isopropanol}$. The third system is a non-supercritical fluid system at low pressure (1 atm) involving water and pentanol. This system is included to evaluate the performance of the models for predictions at low pressure. The fourth set of data involve binary mixtures of supercritical fluid and aromatic compounds. The fifth and final set of data involve binary and ternary mixtures of a supercritical fluid and fatty esters and fatty acids (derived from fish oils). The references for the experimental data are also given in Table I.

Table I. Details of the experimental data

System	Mixture	Reference number
A	$\text{CO}_2\text{-CH}_3\text{OH}$	24, 25, 26
B	$\text{CO}_2\text{-H}_2\text{O}$	27, 28
C	$\text{CH}_3\text{OH-H}_2\text{O}$	29
D	$\text{CO}_2\text{-CH}_3\text{OH-H}_2\text{O}$	30
E	$\text{C}_3\text{H}_8\text{-H}_2\text{O}$	31
F	isopropanol- H_2O	32
G	$\text{C}_3\text{H}_8\text{-H}_2\text{O-isopropanol}$	33
H	$\text{H}_2\text{O-pentanol}$	32
I	$\text{CO}_2\text{-acetophenone}$	1
J	$\text{CO}_2\text{-propylbenzene}$	1
K	$\text{CO}_2\text{-ethyl oleate}$	34
L	$\text{CO}_2\text{-ethyl linoleate}$	34
M	$\text{CO}_2\text{-methyl oleate-oleic acid}$	35

COMPUTATIONAL DETAILS

Except for systems F and H, the phase equilibrium calculation involved the computation of P-x,y diagrams. For systems F and H, T-x,y diagrams have been computed. For the binary systems A and B, except for the mixing rules MHV2 and LCVM, all other model parameters have been estimated. For the binary system E, all model parameters have been estimated and the results have been compared with the results of the existing parameters with the MHV2 mixing rule. For system C, the parameters in the mixing rules HV, DDLC, SGR and vdW have been estimated, while the binary interaction coefficient (k_{ij} in eq. 8) in the WS mixing rule has been calculated in order to reproduce the G^E of the experimental data (22 and 23). This procedure has been found to work extremely well for symmetric systems, even though it is claimed in the literature that the WS mixing rule (procedure) has some problems for highly asymmetric systems (36). The same procedure has also been employed to estimate the WS model parameters for systems F and H. For systems D and G no parameters were fitted. As experimental data were not available (for this paper) for the

system C₃H₈-isopropanol and in order to perform a proper calculation of system G, it was necessary for the WS mixing rule to determine the extra WS-parameter (k_{ij} in eq. 8) by use of the MHV2-UNIFAC parameters while for the vdW2 mixing rule both binary interaction coefficients were set equal to zero. The number of model parameters (estimated) for each model is given in Table II together with information on the mixing rule models.

Table II. Information of the different mixing rules

Model	G ^E -model	EOS	Model parameters	Parameters estimated
MHV2	Lin-UNIFAC	SRK	4	0 (4)
MHV1	Lin-UNIFAC	SRK	4	0
LCVM	UNIFAC	PR	4	0 (4)
WS	Lin-UNIFAC	SRK	5	5
HV	NRTL	SRK	6	4
DDLC	-	SRK	3	3
SGR	-	SRK	3	3
vdW2	-	SRK	2	2
vdW4	-	SRK	4	4

Note that for the MHV2 and the LCVM mixing rules, the four model parameters were only estimated for system E. In all cases where the model parameters have not been estimated, they have been taken from the model reference papers: For systems A, B, E, I, and J, the MHV2 parameters are from (37); for systems K, L and M, the MHV1 model parameters are from (9); for systems A, B, E, I, and J, the LCVM parameters are from (3); for systems K and L, the LCVM model parameters are from (10). All the parameters obtained in this work can be obtained from the authors.

In terms of computational time, the vdW2 and vdW4 are the fastest, followed by HV, MHV2, LCVM, SGR, and WS and the slowest is the DDLC model (of the models considered in this paper). The test problem involved the computation of a single point of a P-x,y diagram. The GCEOS model (38), due to its very lengthy computational time, has not been considered in this work.

DISCUSSION OF RESULTS

Table III lists the mixture systems studied and the models that have been compared for each mixture system. Models such as HV, DDLC, SGR, and vdW4 were discarded after mixture system D, mainly because they are non-predictive in nature, meaning that experimental data are necessary in order to estimate the binary parameters in the models. For the mixing rules (MHV2, LCVM, and WS) which can utilize the UNIFAC parameter tables, this is not a problem once the UNIFAC parameters have been obtained. Furthermore, the vdW2 mixing rule can be predictive but not necessarily accurate if both interaction coefficients are set to zero. The mixing rules of the same type as SGR all suffer from the Michelsen-Kistenmacher syndrome (39),

and it has been shown that the predictive capability of the SGR and DDLC mixing rules are somewhat lower than that of the MHV2 and HV mixing rules.

Table III. The models compared for all investigated mixtures

System	Mixture	Models compared
A	CO ₂ -CH ₃ OH	MHV2,LCVM,WS,HV,DDLC,SGR, vdw2,vdW4
B	CO ₂ -H ₂ O	same as above
C	CH ₃ OH-H ₂ O	same as above
D	CO ₂ -CH ₃ OH-H ₂ O	same as above
E	C ₃ H ₈ -H ₂ O	MHV2,LCVM,WS,vdW2
F	isopropanol-H ₂ O	MHV2,LCVM,WS,vdW2
G	C ₃ H ₈ -H ₂ O-Isopropanol	MHV2,LCVM,WS,vdw2
H	H ₂ O-pentanol	MHV2,LCVM,WS,vdW2
I	CO ₂ -acetophenone	MHV2,LCVM
J	CO ₂ -propylbenzene	MHV2,LCVM
K	CO ₂ -ethyl oleate	MHV1,LCVM
L	CO ₂ -ethyl linoleate	MHV1,LCVM,SGR,vdW2
M	CO ₂ -methyl oleate-oleic acid	MHV1

Prediction of phase equilibria for CO₂-CH₃OH-H₂O system.

First the three binary pairs for the ternary system CO₂-CH₃OH-H₂O are considered. As listed in Table III, all the models are evaluated for this system. In Figures 1 and 2, the computed P-x,y diagrams for the binary system, CO₂-CH₃OH, are shown for the eight models. In Figures 3 and 4, the P-x,y diagrams for the binary system, CH₃OH-H₂O, are shown for the eight models. It can be noted that for the CO₂-CH₃OH system, the LCVM and DDLC do not perform as well as the others while for the CH₃OH-H₂O system, all the models perform equally well. The same is true for the system CO₂-H₂O, and this system is therefore not depicted. Note that except for the MHV2 and LCVM models, the computed values for all other models are from correlations (not predictions).

When the ternary mixture phase equilibrium is predicted (this is prediction since the parameters obtained from the binary mixtures are employed), as shown in Figures 5 and 6, with the exception of DDLC and SGR, all other models perform quite well. The MHV2-model starts to deviate at the higher pressure end because the linear UNIFAC-model parameters did not include the corresponding high pressure end. It should be noted that modified UNIFAC introduces additional parameters and that the accuracy of the other models when combined with modified UNIFAC may also be affected in a positive way. Bubble points calculations have been performed to produce these Figures (the composition of water and carbon dioxide is given in ref. 30)

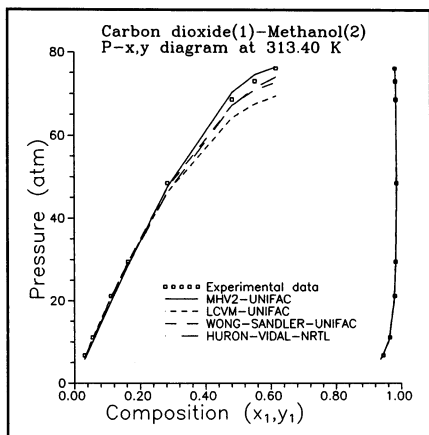


Figure 1 P-x,y diagram at 313.4 K for $\text{CO}_2\text{-CH}_3\text{OH}$

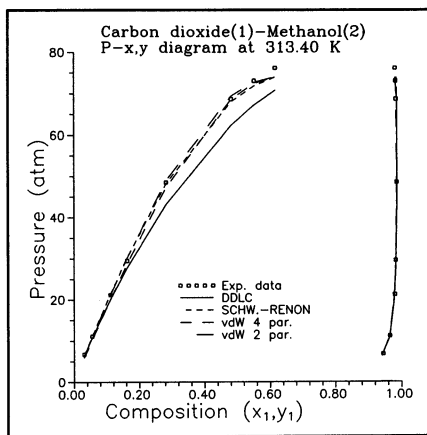


Figure 2 P-x,y diagram at 313.4 K for $\text{CO}_2\text{-CH}_3\text{OH}$

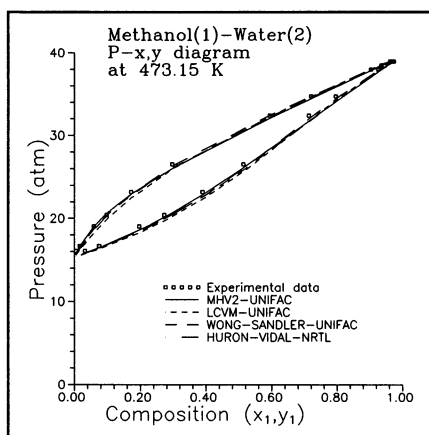


Figure 3 P-x,y diagram at 473.15 K for $\text{CH}_3\text{OH-H}_2\text{O}$

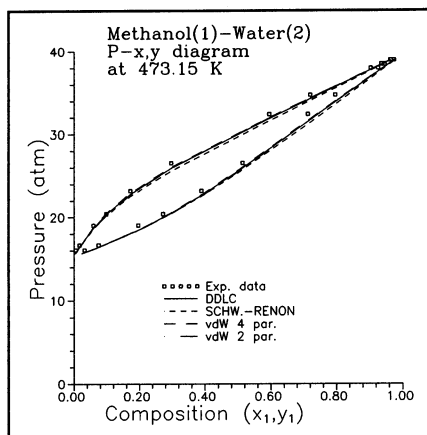


Figure 4 P-x,y diagram at 473.15 K for $\text{CH}_3\text{OH-H}_2\text{O}$

Prediction of phase equilibria for the system $\text{C}_3\text{H}_8\text{-H}_2\text{O}$ -isopropanol

For this system, the main employed class of models are (besides the vdW2 mixing rule) those which combine a G^E -model with an EOS in order to derive an expression for the mixing rule of the a/b -parameter. The following models belong to this class: MHV2, LCVN, WS and HV. The HV mixing rule is not employed since it cannot be used as a predictive model. It can be noted that most of the models have difficulties with the propane-water data (Figures 7 and 8), especially the VDW2 mixing rule for the compositions in the liquid phase, x . At 377.59 K some errors in the vapor phase

compositions, y , are observed for some of the mixing rules. In order to produce these Figures, flash calculations have been performed. It has been shown previously (40) that both the MHV2 and the HV mixing rules (parameters correlated with experimental data) give very accurate equilibrium constants for this system. It is clear that the MHV2 (old and new parameters), LCVM, and WS mixing rules are not bad at all. For the MHV2 mixing rule, the results are shown for both the existing parameter set and the newly estimated parameters, and as for system D it can again be noted that the high pressure data probably did not enter into the original parameter estimation (37).

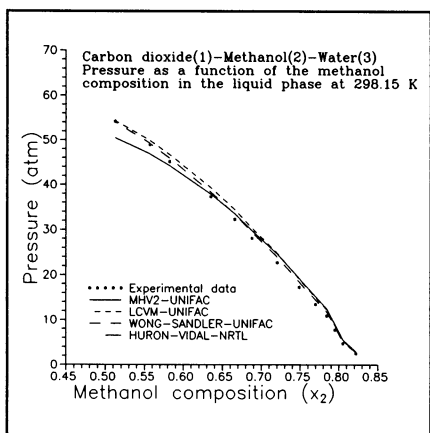


Figure 5 P- x_2 diagram for $\text{CO}_2(1)$ - $\text{CH}_3\text{OH}(2)$ - $\text{H}_2\text{O}(3)$ at 298.15 K

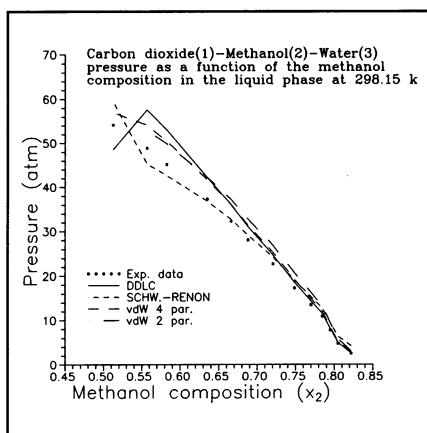


Figure 6 P- x_2 diagram for $\text{CO}_2(1)$ - $\text{CH}_3\text{OH}(2)$ - $\text{H}_2\text{O}(3)$ at 298.15 K

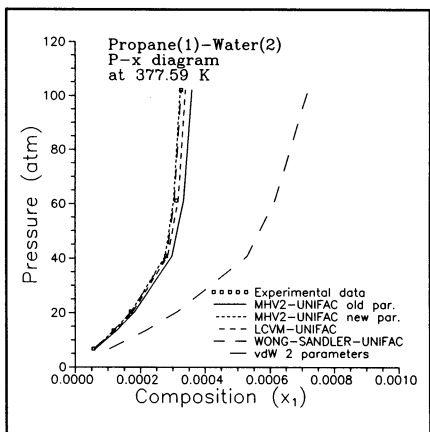


Figure 7 P- x diagram for $\text{C}_3\text{H}_8\text{-H}_2\text{O}$ at 377.59 K

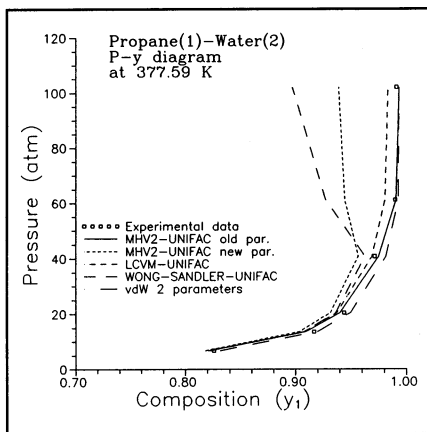


Figure 8 P- y diagram for $\text{C}_3\text{H}_8\text{-H}_2\text{O}$ at 377.59 K

For the H₂O-isopropanol data set (Figure 9) very good agreement is obtained in the prediction with the MHV2 and the correlation with the vdW2 mixing rules, whereas the prediction of the azeotropic point with LCVM is not very good, and the WS mixing rule predicts a false liquid-liquid split. All the models perform rather poorly for the ternary system (Figure 10). The models MHV2 and LCVM at least show the correct trend. Note that the MHV2 model with new parameters (estimated in this paper) over-predicts the experimental values while the original parameters (37) under-predicts the experimental values.

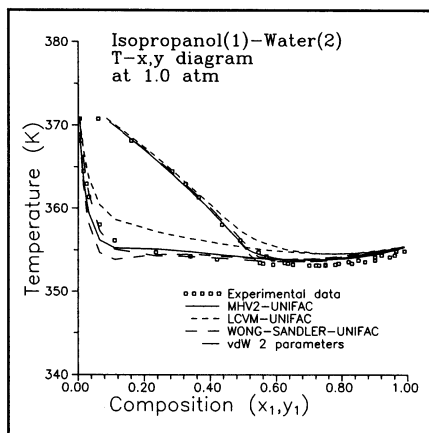


Figure 9 T-x,y diagram for isopropanol - H₂O at 1.0 atm

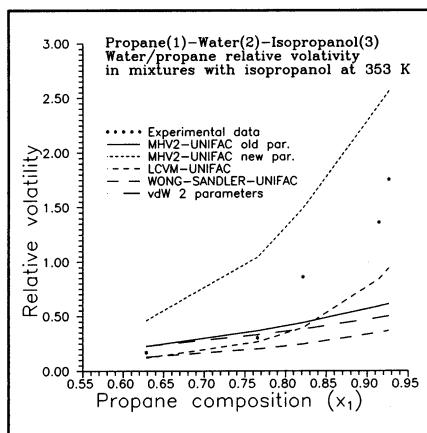


Figure 10 H₂O/C₃H₈ relative volatility at 353 K in C₃H₈-H₂O-isopropanol

Prediction of phase equilibria for systems H, I and J

The computed values for the low pressure binary system water-pentanol is shown in Figure 11. Only the vdW2 model parameters were estimated. Surprisingly, the LCVM model does not perform as well as the other models. The binary systems CO₂-acetophenone and CO₂-propylbenzene are considered next. The LCVM model appears to perform much better than the MHV2 model (especially for system I, see Figures 12 and 13).

It should be noted that the GCEOS model has been found to correlate this data set satisfactorily (1). In this paper, however, neither the parameters of the MHV2 model nor the LCVM model has been correlated to these data, but the result of such a correlation would probably be that these two mixing rules would perform equally well or better than the GCEOS.

Prediction of phase equilibria for systems K, L and M

These systems involve the computation of high pressure phase equilibrium for binary and ternary mixtures with CO₂ and high molecular weight fatty esters and acids derived from fish oil. It should be noted that the data for CO₂-ethyl oleate were not included

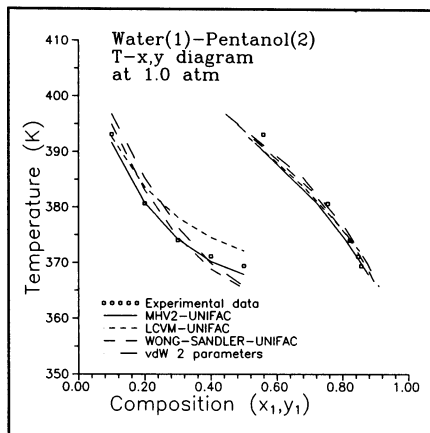


Figure 11 T-x,y diagram for H₂O-pentanol at 1.0 atm

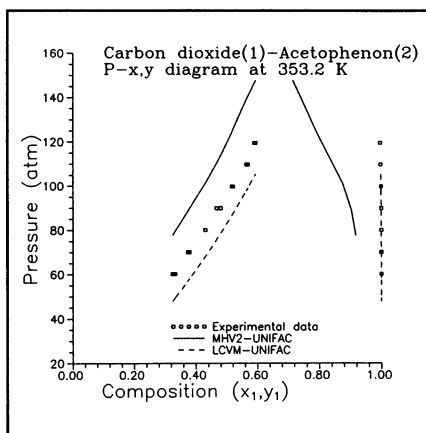


Figure 12 P-x,y diagram for CO₂-acetophenone at 353.2 K

in the estimation of the model parameters for the LCVM mixing rule, and the data for CO₂-ethyl linoleate were not included in the estimation of the model parameters for the MHV1 mixing rule. Figure 14 depicts the experimental data for the binary system CO₂-ethyl oleate, and the calculated P-x,y diagrams with the prediction of the LCVM model and the correlation of the MHV1 model, while Figure 15 depicts the experimental data for the binary system CO₂-ethyl linoleate, and the calculated P-x,y diagrams with the prediction of the MHV1 model and the correlations of the LCVM, SGR and vdW2 models. The results for the CO₂-ethyl oleate system are expected, because the model (MHV1) for which this system went into the parameter estimation performs somewhat better than the model (LCVM) for which this system was not

incorporated in the parameter estimation. For CO₂-ethyl linoleate the correlations of SGR and vdW2 do not unexpectedly appear to perform best, since the LCVM model is based on a group-contribution concept (UNIFAC) and the result with MHV1 is predictions, or more correctly extrapolations, because the same type of components were involved in the parameter estimation. The unexpected result is that the "prediction" with MHV1 is better than the "correlation" with LCVM, which very surprisingly does not perform as well as expected. It is clear from these two figures that the MHV1 model is somewhat more reliable than the LCVM model for fluid-liquid

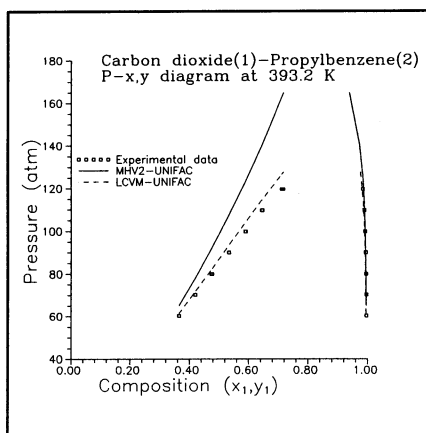


Figure 13 P-x,y diagram for CO₂-propylbenzene at 393.2 K

equilibrium between CO₂ and fish oil related compounds. With respect to the ternary system, only the MHV1 model predictions are given in Table IV since the LCVM model did not perform that well for system L. Bubble point calculations are performed to produce Table IV.

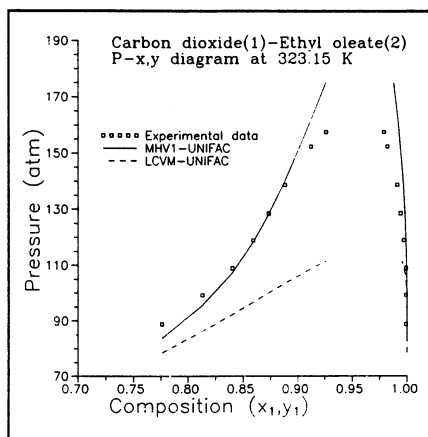


Figure 14 P-x,y diagram for CO₂-Ethyl oleate at 323.15 K

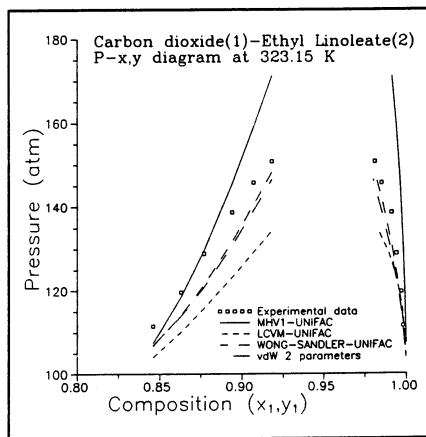


Figure 15 P-x,y diagram for CO₂-Ethyl linoleate at 323 K

Table IV. Fluid-liquid equilibrium at 313.15 K for CO₂ - methyl oleate (MO) - oleic acid (OA), experimentally and calculated with MHV1

Mole fraction in liquid phase		Pressure (atm)		Mole fraction in fluid phase			
CO ₂ exp.	MO exp.	exp.	calc.	CO ₂ exp.	CO ₂ calc.	MO exp.	MO calc.
0.614	0.093	64.64	57.44	1.000	1.000	0.000	0.000
0.771	0.055	122.08	110.43	0.997	0.999	0.002	0.001
0.835	0.041	195.61	186.84	0.995	0.993	0.003	0.004
0.888	0.027	258.28	288.31	0.993	0.983	0.003	0.007
0.627	0.190	58.72	52.70	1.000	1.000	0.000	0.000
0.788	0.110	98.79	89.23	0.997	1.000	0.003	0.000
0.830	0.089	115.57	120.48	0.995	0.997	0.004	0.002
0.859	0.071	148.53	157.74	0.992	0.993	0.006	0.006
0.527	0.356	44.12	35.09	0.999	1.000	0.001	0.000
0.777	0.134	91.19	80.53	0.997	1.000	0.003	0.000
0.868	0.100	120.11	120.81	0.991	0.996	0.007	0.004
0.913	0.065	165.51	173.05	0.984	0.984	0.013	0.014

CONCLUSIONS

The correlative and predictive capabilities for a class of equation of state models have been evaluated. From the results, it is not possible to recommend a single model for all systems studied. It is recommended, however, whichever model is selected, that the correlational as well as predictive capabilities be carefully evaluated before their application related to process design and/or analysis. Also, for some systems, such as CO₂-fatty acids (and/or esters), it is difficult to obtain a good representation of the phase behavior for the entire range of data. Therefore, in these applications, "fine-tuning" of the model parameters is recommended. "Fine-tuning" or re-estimation of model parameters may also be needed for other systems since in some cases the binary mixture data (involving the same groups or molecules) have not been represented adequately. Finally, the mixing rules combining the G^E-model and an EOS to obtain the a-parameter (or the a/b-parameter) and the b-parameter appear to be the best available option to tackle the difficult task of representing phase equilibria involving supercritical fluids. The WS mixing rule has a very nice feature in the way it is ensured that the excess Gibbs energy of the EOS equals that of the experimental data, but in order to make it really useful for prediction of supercritical processes, a parameter estimation of gas-solvent interactions with a group-contribution G_E-model (for example, UNIFAC) is necessary.

LITERATURE CITED

- (1) Bamberger, A.; Maurer, G. *J. Supercrit. Fluids* 1994, 7, 115-127.
- (2) Dahl, S.; Fredenslund, Aa.; Rasmussen, P. *Ind. Eng. Chem. Res.* 1991, 30, 1936-1945.
- (3) Boukoulas, C.; Spiliotis, N.; Coutosikou, P.; Tzouvaras, N.; Tassios, D. *Fluid Phase Equil.* 1994, 92, 75-106.
- (4) Wong, D. S. H.; Sandler, S. I. *AIChE Journal* 1992, 38, 671-680.
- (5) Hytoft, G.; Coniglio, L.; Knudsen, K.; Gani, R. *Proceedings FOCAPD'94*, Editors: M. Doherty and L. Biegler, CACHE Publications, USA, 1994, (in Press).
- (6) Soave, G. *Chem. Eng. Sci.* 1972, 27, 1197-1203.
- (7) Peng, D.-Y.; Robinson D.B. *Ind. Eng. Chem. Fundam.* 1976, 15, 59-64.
- (8) Mathias, P. M.; and Copeman, T. W. *Fluid Phase Equil.* 1983, 13, 91-108.
- (9) Coniglio, L.; Knudsen, K.; Gani, R. *Submitted to Ind. Eng. Chem. Res.* 1994.
- (10) Vlahos, C.; Kalospiros, N.; Kolisis, F.; Tassios, D. *TTPL-9411, Tech. Univ. of Athens, Greece* 1994.
- (11) Apostolou, D.; Kalospiros, N.; Tassios, D. *TTPL-9412, Tech. Univ. of Athens, Greece* 1994.
- (12) Daubert, T. E.; Danner, R. P. *DIPPR Data Compilation*, AIChE, New York, 1986.
- (13) Mollerup, J. *Fluid Phase Equil.* 1983, 15, 189-207.
- (14) Mollerup, J. *Fluid Phase Equil.* 1985, 22, 139-154.
- (15) Schwartzentruber, J.; Galivel-Solastiouk, F.; Renon, H. *Fluid Phase Equil.* 1987, 38, 217-226.

- (16) Huron, M.-J.; Vidal, J. *Fluid Phase Equil.* 1979, 3, 255-271.
- (17) Renon, H.; Prausnitz, J. M. *AIChE Journal* 1968, 14, 135-144.
- (18) Michelsen, M. L. *Fluid Phase Equil.* 1990, 60, 47-58.
- (19) Michelsen, M. L. *Fluid Phase Equil.* 1990, 60, 213-219.
- (20) Hansen, H. K.; Coto, B.; Kuhlmann, B. *SEP-9212, Tech. Univ. of Denmark, Lyngby* 1992.
- (21) Hansen, H. K.; Rasmussen, P.; Fredenslund, Aa.; Schiller, M.; Gmehling, J. *Ind. Eng. Chem. Res.* 1991, 30, 2352.
- (22) Orbey, H.; Sandler, S. I.; Wong, D. S. H. *Fluid Phase Equil.* 1993, 85, 41-54.
- (23) Wong, D. S. H.; Orbey, H.; Sandler, S. I. *Ind. Eng. Chem. Res.* 1992, 31, 2033-2039.
- (24) Ohgaki, K.; Katayama, T. *J. Chem. Eng. Data* 1976, 21, p. 53-55, 1976.
- (25) Suzuki, K.; Sue, H.; Itou, M.; Inomata, H.; Arai, K.; Saito, S. *J. Chem. Eng. Data*, 1990, 35, 63-66.
- (26) Katayama, T.; Ohgaki, K.; Maekeve, G.; Goto, M.; Nagano, T. *J. Chem. Eng. Jap.* 1975, 8, 89-92.
- (27) Takenouchi, S.; Kennedy, G. C. *American Journal of Science* 1964, 262, 445-454.
- (28) Gillespie, P. C.; Wilson, G. M. *Gas Processors Association Research Report, RR-41*, 1980.
- (29) Griswold, J.; Wong, S. Y. *Chem. Eng. Progr. Symp. Ser.* 1952, 48(3), 18-34.
- (30) Chang, T.; Rousseau, R. W. *Fluid Phase Equil.* 1985, 23, 243-258.
- (31) Kobayashi, R.; Katz, D. L.; *Ind. Eng. Chem.* 1953, 45, 440-446.
- (32) Gmehling, J.; Onken, U. *DECHEMA Chemistry Data Series, VOL I*, Frankfurt, 1977.
- (33) Zabaloy, M.; Mabe, G.; Bottini, S. B.; Brignole, E. A. *J. Supercrit. Fluids* 1992, 5, 186-191.
- (34) Bharath, R.; Inomata, H.; Arai, K.; Shoji, K.; Noguchi, Y. *Fluid Phase Equil.* 1989, 50, 315-327.
- (35) Yu, Z.-R.; Zou, M.; Bhaskar, A. R.; Rizvi, S. S. H.; Zollweg, J. A. *J. Supercrit. Fluids* 1993, 6, 63-68.
- (36) Coutsikos, P.; Kalospiros, N.; Tassios, D. *TTPL-9406, Tech. Univ. of Athens, Greece* 1994.
- (37) Schmelzer J. *SEP-9124, Tech. Univ. of Denmark, Lyngby* 1991.
- (38) Skjold-Jørgensen, S. *Ind. Eng. Chem. Res.* 1988, 27, 110-118.
- (39) Michelsen, M. L.; Kistenmacher, H. *Fluid Phase Equil.* 1990, 58, 229-230.
- (40) Knudsen, K. *Ph.D. Dissertation, Tech. Univ. of Denmark, Lyngby.* 1992.

RECEIVED May 3, 1995

Chapter 10

Pulse Radiolysis To Study Intermolecular Interactions and Reactivity in Supercritical Fluids

Jianwei Zhang¹, Karen A. Connery¹, John E. Chateaufneuf²,
and Joan F. Brennecke¹

¹Department of Chemical Engineering and ²Radiation Laboratory,
University of Notre Dame, Notre Dame, IN 46556

SUMMARY

The rates of homogeneous reactions in supercritical fluids (SCFs) can be affected by bulk properties of the system, as well as the strength of solvation. The purpose of the work described in this paper is to extend our previous studies of the solvent effect on reactions in SCFs to ionic reactions. We have used pulse radiolysis to measure the rate of reaction of benzhydryl cation (Ph_2CH^+) with two cosolvents (tetramethylethylene ($(\text{CH}_3)_2\text{C}=\text{C}(\text{CH}_3)_2$) and triethylamine ($(\text{C}_2\text{H}_5)_3\text{N}$)) in SC CHF_3 . These results indicate that the rate constants decrease with increasing pressure, which is in agreement with predictions from three different approximation methods. The pressure effect on the ionic reaction of Ph_2CH^+ with $(\text{CH}_3)_2\text{C}=\text{C}(\text{CH}_3)_2$ can be adequately described by relatively simple solution models and there is no indication of preferential solvation of the ion influencing this reaction. However, for the ionic reaction of Ph_2CH^+ with $(\text{C}_2\text{H}_5)_3\text{N}$, a deviation from the prediction occurring at low pressures at 35°C suggests that Ph_2CH^+ may be preferentially solvated by $(\text{C}_2\text{H}_5)_3\text{N}$ at the lower temperature, indicating that preferential solvation may be cosolvent specific.

INTRODUCTION

Supercritical fluids (SCFs) show potential as attractive media for reactions [1] in addition to the more conventional applications in extractions and separations [2]. Reaction rates in supercritical fluids can be influenced dramatically by widely varying bulk physical properties and the thermodynamic pressure effect on the rate constant [1]. More recently, there have been indications that preferential solvation in SCF mixtures can also affect reaction rates[3,4]. Our objective is to study the effect of pressure and preferential solvation on a variety of reactions in SCFs in order to gain a full understanding of the supercritical solvent effect on reaction rates. In this paper we extend our previous studies to include a charged species in a kinetically-controlled reaction.

The thermodynamic pressure effect on the reaction rate constant and potential changes in reaction rates with changing bulk properties has been investigated for some time. Conversely, interest in the effect of solvation in SCFs and preferential solvation in SCF mixtures is a more recent result of spectroscopic investigations that

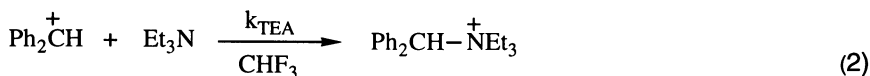
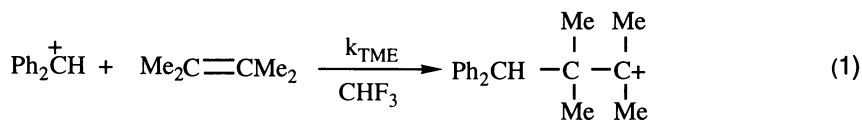
0097-6156/95/0608-0156\$12.00/0
© 1995 American Chemical Society

suggest that the local environment can be significantly different than the bulk [5-9]. These investigations showed that the local density can be as much as twice the bulk density, especially at pressures well below the critical point, and that the local composition can be as much as seven times the bulk composition when a dilute cosolvent is added to a SCF. These experimental results have been corroborated by theoretical integral equation calculations [10], as well as molecular simulations [7, 11].

Previously, we have shown by studying the triplet-triplet annihilation reaction of benzophenone and the benzyl radical recombination reaction in SC CO₂, C₂H₆, CHF₃ and a CO₂/acetonitrile mixture, that normally diffusion controlled reactions of neutral species occur at the expected diffusion controlled limit in SCFs under all conditions [12,13]. This suggests that increased local densities and local compositions do not in any way impede or enhance reaction rates. This was in contrast to other published results [14-16] but it should be noted that subsequent analysis of the pyrene excimer fluorescence data [14, 15, 17] shows that the pyrene excimer is actually formed at the expected diffusion controlled limit under all conditions [18], in agreement with our studies. While they do behave in a predictable fashion, the rates of diffusion controlled reactions can be varied dramatically in the SCF region because the diffusion coefficients of the solutes change substantially in this region.

Conversely, it appears that kinetically controlled reactions can be influenced by solvation. We have studied the hydrogen abstraction reaction of benzophenone triplet with 1,4-cyclohexadiene and isopropanol in SC CO₂, C₂H₆ and CHF₃ [3, 19]. Comparison of the measured reaction rates with predictions of the pressure effect on the rate constant from transition state theory, provides good evidence that the preferential solvation of the triplet by the second reactant substantially increases the reaction rate. This is further supported by a study of the esterification reaction of phthalic anhydride with methanol in SC CO₂, which shows that same trend [4]. In contrast, in the reaction of benzophenone triplet with molecular oxygen in SC CO₂, which might not exhibit preferential solvation due to the relative similarity of O₂ and CO₂, the measured reaction rates are as expected, showing no indication of the effect of preferential solvation [20].

In this report, we will present preliminary results of the reaction of benzhydryl cation (Ph₂CH⁺) with tetramethylethylene (TME) at 35°C and the reaction of benzhydryl cation (Ph₂CH⁺) with triethylamine (TEA) at 35°C and 70°C in SC CHF₃. The benzhydryl cation is formed by the dissociative oxidation of benzhydrol (Ph₂CHOH), which occurs in a reaction with solvent-derived cations that are formed as a result of pulse radiolysis of the solution. We believe this is the first use of pulse radiolysis, which has been a powerful tool to study reactions and solvation in both the gas phase and liquid solutions, to study supercritical fluids. The dilute cation solute reacts in a bimolecular reaction with the quencher (TME or TEA cosolvent), which is present in vast excess. The reaction schemes are shown below.



EXPERIMENTAL

Materials. Benzhydrol (Ph_2CHOH) (Aldrich, 99%) was recrystallized from ethanol. Tetramethylethylene (2,3-dimethyl-2-butene) (Aldrich, 99+%) was purified by bulb-to-bulb distillation. Triethylamine ($(\text{C}_2\text{H}_5)_3\text{N}$) (Aldrich, 99%) was stored over potassium hydroxide pellets and distilled prior to use. Fluoroform (CHF_3) (DuPont Freon-23, 98% purity) was sequentially passed through two high-pressure oxy-traps (Alltech) and two high-pressure charcoal traps (Alltech) to remove oxygen and trace impurities, respectively.

Sample Preparation. Sample mixtures ($\text{Ph}_2\text{CHOH}/\text{TME}/\text{CHF}_3$ or $\text{Ph}_2\text{CHOH}/\text{TEA}/\text{CHF}_3$) were prepared using two Isco Model 260D high pressure syringe pumps, a Rheodyne HPLC injection loop for injection of the cosolvent (quencher), and an injection port for the solid solute. Samples were prepared using a syringe pump containing pure CHF_3 to fill a pre-evacuated sample syringe pump with subcooled CHF_3 through the liquid and solid injection ports containing desired amounts of the quencher (TME or TEA) and the precursor (Ph_2CHOH), respectively. The sample was then heated well above T_c to produce a one phase homogeneous solution. Ph_2CHOH concentrations were on the order of millimolar, which produced micromolar concentrations of Ph_2CH^+ following pulse radiolysis. TME mole fractions ranged from 1×10^{-3} to 7.6×10^{-3} and TEA mole fractions ranged from 3.1×10^{-6} to 5.3×10^{-5} .

Method. Pulse radiolysis was performed using a 10-50 ns pulse of 8 MeV electrons from the Notre Dame Radiation Laboratory linear accelerator (LINAC) (L band, 1.3 GHz). The Pulse Radiolysis apparatus has been described in detail elsewhere [21]. The high-energy pulse of electrons was directed toward the high-pressure cell to irradiate the solution inside and produce solvent-derived cations which in turn undergo dissociative oxidation of benzhydrol, leading to the desired cationic species (Ph_2CH^+). The transient cationic species was monitored using a pulsed 1000 W xenon lamp source, and transient absorption signals were digitized with a LaCroy 7200A Precision Digital Oscilloscope. A Gateway 2000 4DX2-66V computer was used for experimental control.

The pulse radiolysis experiments were performed using a high-pressure optical cell (~ 3 mL capacity) fitted with a customized stainless steel port for incidence of the electron pulse and two Suprasil quartz windows for monitoring the transient absorption signal. The Suprasil quartz windows had mechanical seals composed of lead and copper packing. Pressure in the cell was monitored to ± 0.24 bar with a Heise (Model 901A) pressure gauge. The desired temperature was maintained to $\pm 0.1^\circ\text{C}$ with an Omega (Model CN-6070 A) temperature controller equipped with a Watlow Firerod cartridge heater and a platinum resistance thermometer which made direct contact with the fluid.

Pulse radiolysis experiments require continuous replenishing of the solution to avoid product accumulation. This was accomplished using a flow system consisting of either a high-pressure syringe pump containing the sample and a metering valve or two high-pressure syringe pumps. Experiments were performed using a constant flow rate of ~ 0.8 ml/min.

The optical cell is loaded in a well-ventilated exhaust hood. There is a rupture disc in-line in the flow system in case of overpressurization. In addition, the two syringe pump method described above was developed in order to capture all solvents downstream and to eliminate plugging that would periodically occur when the mixture was rapidly expanded with the metering valve. Finally, the experiments were run remotely from a control room physically separated from the linear accelerator. The

optical cell was monitored with a video camera to ensure appropriate temperature, pressure and flowrate.

RESULTS AND DISCUSSION

Reaction of Ph_2CH^+ with TME. As mentioned above, the reactions were carried out in a vast excess of TME (the quencher) so that the observed rate constants were pseudo-first-order. The bimolecular rate constants were obtained by conducting the experiments at several different quencher concentrations. The bimolecular rate constant (k_{bi}) is the slope of a plot of the observed pseudo-first-order rate constant (k_{obs}) as a function of quencher concentration, as shown in Figure 1 for several different pressures for the reaction of benzhydryl cation with TME in fluoroform. The bimolecular rate constants obtained by this procedure at 35°C at pressures from 63 to 150 bar are shown in Figure 2. These values are, of course, based on bulk concentrations of the cosolvent. The bimolecular rate constants decrease from about $2.2 \times 10^7 \text{ M}^{-1}\text{s}^{-1}$ at 63 bar to about $1.2 \times 10^7 \text{ M}^{-1}\text{s}^{-1}$ at 150 bar. These values are well below the diffusion control limit, so this reaction is clearly fully kinetically controlled. The critical temperature and pressure of pure fluoroform are 25.9°C and 48.4 bar, respectively.

There are several factors that may influence reaction rates in compressed fluids. These include changing bulk physical properties (like the dielectric constant), the thermodynamic pressure effect on the rate constant and, potentially, other short-range solvation effects. We attempted to analyze the data on the reaction of Ph_2CH^+ with TME in SC CHF_3 in three ways. First, we compared the results with trends that have been observed for reactions of neutral molecules with ions in normal incompressible liquid solutions [22]. Next, we calculated the expected pressure effect on the rate constant from a combination of the electrostriction volume from the Drude-Nernst equation [23, 24] with that from the Peng-Robinson equation [25]. Finally, we calculated the expected pressure effect on the rate constant from the model set forth by Wood and coworkers [26, 27] for the partial molar volume of an ion in a supercritical fluid.

Various expressions have been developed for the influence of the solvent on the reaction rate between a neutral molecule and an ion in liquid solvents. They are based on the application of transition state theory to the Gibbs free energy change of inserting ions and dipoles into liquid solvents of zero ionic strength and a given dielectric constant. The various expressions predict that $\ln(k_{\text{bi}})$ versus $1/\epsilon$ (the inverse of the dielectric constant) should be linear with a positive slope [22]. Reaction rates should be somewhat greater in media of lower dielectric constant and this is what we observe in fluoroform. The dielectric constant of fluoroform varies significantly over the range of pressures investigated [28], and a plot of $\ln(k_{\text{bi}})$ versus $1/\epsilon$ is shown in Figure 3. The plot is remarkably linear, suggesting that the reaction is being affected by the solvent in a manner similar to that observed in ordinary liquid solvents.

In the second method of analysis, we have estimated the anticipated pressure effect on the rate constant from transition state theory (i.e., essentially the activation volume, which is the difference in the partial molar volume of the transition state and the reactants) as having two contributions [22]. One comes from the electrostriction of the dielectric solvent around the ion and is given by the Drude-Nernst equation [23, 24], and the other is the contribution to the partial molar volume of each species that comes from simple nonionic forces which can be roughly predicted from an equation of state like the Peng-Robinson equation [25]. The nonionic contribution from Peng-Robinson predicts that the rate constants should actually increase slightly with increasing pressure, in contrast to observations. However, the ionic contribution,

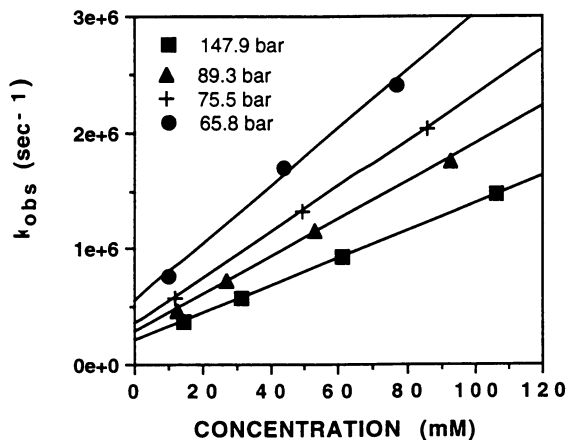


Figure 1: Determination of the bimolecular rate constants (the slopes) from observed rate constants at various pressures.

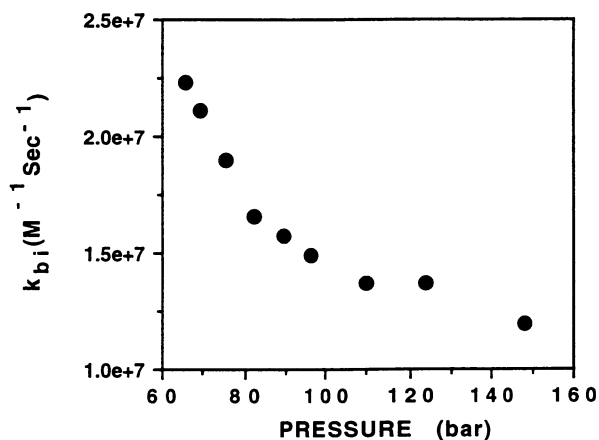


Figure 2: Bimolecular rate constants for the reaction of TME with Ph_2CH^+ in CHF_3 at 35°C at various pressures.

which is based on the pressure derivative of the dielectric constant, decidedly predicts that the rates should decrease with increasing pressure and the combined effect is well in line with the measured values, as shown in Figure 4. At any given temperature and pressure the magnitude of the contribution to the activation volume from electrostriction is roughly twice that from the nonionic forces. However, the exact values of the estimated pressure effect on the rate constant depend on the values chosen as the radius of the cation and transition state. Using reasonable values of 2.45 Å [29] and 7.5 Å, respectively, we obtain the values shown as triangles in Figure 4. Based on these estimates, it appears that the measured reaction rates are quite reasonable and behave as expected when one includes the electrostriction about the ion.

The third method of analysis is quite similar to the second except that the partial molar volumes of the ions due to electrostriction are calculated by the method developed by Wood and coworkers [26, 27], which explicitly includes the compressibility of the dielectric fluid. Their model predicts a dramatic local density enhancement close to the ion and negative partial molar volumes that are much larger in magnitude for the ions than predicted by the Drude-Nernst equation for the same molecular radii. This method also predicts a decrease in the rate constant with increasing pressure but suggests that the change should be somewhat less dramatic in the low pressure region. These estimates are shown as the crosses in Figure 4, which is the plot comparing the experimental and estimated pressure derivatives of the rate constants.

Thus, the trend of the measured reaction rates can be modeled reasonably well by any of the above methods, including the very simple liquid solution based correlation that predicts that $\ln(k_{bi})$ should vary linearly with the inverse of the bulk dielectric constant. There is no indication of preferential solvation, which appears to play a significant role in kinetically controlled reactions of some neutral species, influencing this reaction. This may be due to the fact that the cation is not preferentially solvated by the TME. This would not be unreasonable since the cosolvent (TME) is nonpolar and the solvent (fluoroform) is polar. Another possibility is that the preferential solvation is hidden by the uncertainty in the estimates of the electrostriction, which dominates the pressure effect on the reaction rates.

Reaction of Ph_2CH^+ with $(\text{C}_2\text{H}_5)_3\text{N}$. This ionic reaction was carried out in fluoroform at 35°C and 70°C at pressures from 63 to 150 bar. The bimolecular rate constants, obtained in a similar way to the above reaction, decrease from about 1.87×10^{10} at 63 bar to about $9.29 \times 10^9 \text{ M}^{-1}\text{s}^{-1}$ at 150 bar at 35°C and decrease from 5.32×10^{10} at 77 bar to $1.39 \times 10^{10} \text{ M}^{-1}\text{s}^{-1}$ at 150 bar at 70°C.

A plot of $\ln(k_{bi})$ versus $1/\epsilon$ (the inverse of the dielectric constant) is shown in Figure 5 for the experimental rate constants at both temperatures (35°C and 70°C). The dielectric constants for 70°C were obtained from linear extrapolation of literature dielectric constant data [28]. The dielectric continuum model predicts that $\ln(k_{bi})$ varies linearly with $1/\epsilon$. Our experimental data show remarkable linearity over all the pressure range studied at 70°C. At 35°C $\ln(k_{bi})$ also shows linearity with $1/\epsilon$ for high pressures, but an upward deviation from linearity occurs at lower pressures.

The pressure derivatives of the experimental rate constants at both temperatures are compared in Figure 6 with the predicted values from the method in which the partial molar volumes were calculated from the Peng-Robinson equation of state and the electrostriction term was calculated from the Drude-Nernst equation, with a radius of 2.45 Å for Ph_2CH^+ and a radius of 7.5 Å for the transition state. As we can see, the predicted pressure derivatives of the rate constants match the pressure derivatives of the experimental rate constants very well at 70°C. There is

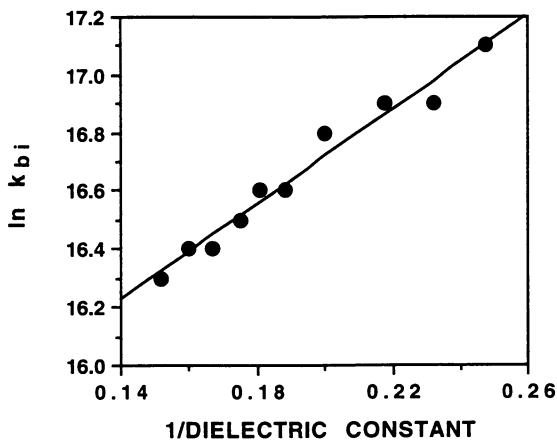


Figure 3: Experimental rate constants for reaction of TME with Ph_2CH^+ in CHF_3 at 35°C as a function of the inverse of the dielectric constant.

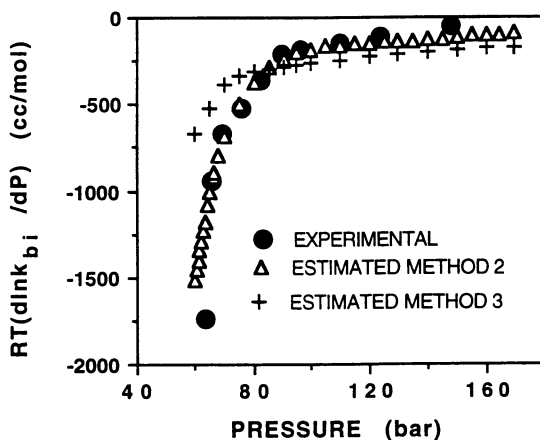


Figure 4: Comparison of the pressure effect on the experimental rate constants to estimated values (see text) for reaction of TME with Ph_2CH^+ in CHF_3 at 35°C .

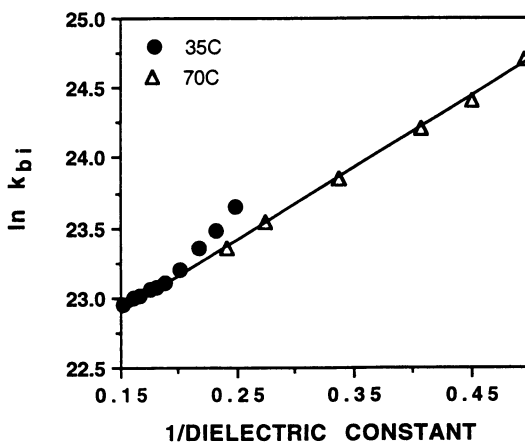


Figure 5: Experimental rate constants for reaction of $(C_2H_5)_3N$ with Ph_2CH^+ in CHF_3 at 35 and 70°C as a function of the inverse of the dielectric constant.

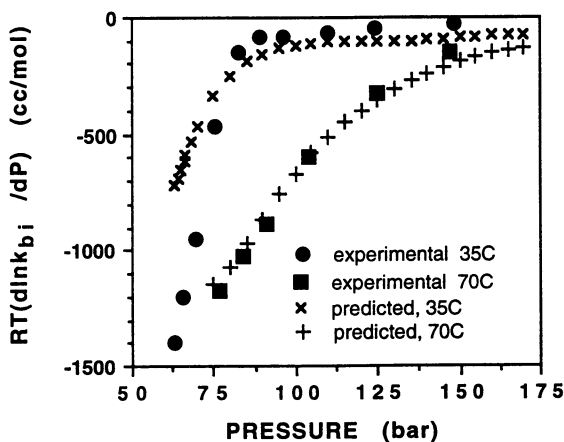


Figure 6: Comparison of the pressure effect on the experimental rate constants with estimated values (see text) for reaction of $(C_2H_5)_3N$ with Ph_2CH^+ in CHF_3 at 35 and 70°C.

some deviation between the prediction and the experimental values at low pressures at 35°C. While the thermodynamic pressure effect on this kinetically controlled ionic reaction can be predicted fairly well by simple models, the slight discrepancy between the model prediction and the experimental values at 35°C may suggest that the cationic species (Ph_2CH^+) is preferentially solvated by $(\text{C}_2\text{H}_5)_3\text{N}$, a strong nucleophile, at lower pressures and the lower temperature. This is not observed for the reaction of Ph_2CH^+ with TME in fluoroform.

CONCLUSIONS

We have presented results, obtained by pulse radiolysis, of two ionic reactions in fluoroform at two temperatures. The rate constants decrease with increasing pressure, which is in qualitative agreement with predictions from three different approximate methods. These methods include 1) correlation from solution theory that predicts that $\ln(k_{\text{bi}})$ should increase linearly with the inverse of the bulk dielectric constant, 2) the thermodynamic pressure effect on the rate constant predicted from the Drude-Nernst equation and 3) the thermodynamic pressure effect on the rate constant predicted from the compressible model developed by Wood and coworkers [26, 27]. The pressure effect on the ionic reaction of Ph_2CH^+ with TME can be adequately described by relatively simple solution models, and the preliminary results indicate that there is no evidence of preferential solvation of the ion influencing this reaction. However, a comparison between the model predicted values and the experimental values for the reaction of Ph_2CH^+ with $(\text{C}_2\text{H}_5)_3\text{N}$ in fluoroform suggest that preferential solvation of cationic species may be occurring at lower pressures on the lower isotherm. It should be noted that the electrostriction term dominates in determining the thermodynamic pressure effects on both ionic reactions investigated in this research.

ACKNOWLEDGMENTS

The work described herein was supported by the National Science Foundation; BP Research; the Exxon Education Foundation (J. Z., K. C., J.F.B.) and the Office of Basic Energy Sciences of the U. S. Department of Energy (J.E.C.), Notre Dame Radiation Laboratory Contribution No. NDRL-3779. Also, we would like to thank DuPont for the generous donation of the CHF_3 .

REFERENCES

- [1] SAVAGE, P. E., GOPALAN, S., NIZAN, T. I., MARTINO, C. J. and BROCK, E. E., submitted to *AIChe J.*, 1994.
- [2] BRENNECKE, J.F. and ECKERT, C. A., *AIChe J.*, Vol. 35, 1989, p. 1409.
- [3] ROBERTS, C. B., CHATEAUNEUF, J. E. and BRENNECKE, J. F., *J. Am. Chem. Soc.*, Vol. 114, 1992, p. 8455.
- [4] ELLINGTON, J. B., PARK, K. M. and BRENNECKE, J. F., *Ind. Eng. Chem. Res.*, Vol. 33, 1994, p. 965.
- [5] KIM, S. and JOHNSTON, K. P., *AIChe J.*, Vol. 33, 1987, p. 1603.
- [6] KIM, S. and JOHNSTON, K. P., *Ind. Eng. Chem. Res.*, Vol. 26, 1987, p. 1206.
- [7] KNUTSEN, B. L., TOMASKO, D. L., ECKERT, C. A., DEBENEDETTI, P. G. and CHIALVO, A. A., In *Supercritical Fluid Technology*, Bright, F. V., McNally, M. E. P., Eds.; ACS Symposium Series 488, American Chemical Society: Washington, DC, 1992.
- [8] YONKER, C. R. and SMITH, R. D., *J. Phys. Chem.*, Vol. 92, 1988, p. 2374.
- [9] CARLIER, C. and RANDOLPH, T. W., *AIChe J.*, Vol. 39, 1993, p. 876.

- [10] WU, R.-S., LEE, L. L. and COCHRAN, H. D., *Ind. Eng. Chem. Res.*, Vol. 29, 1990, p. 977.
- [11] PETSCHKE, I. B. and DEBENEDETTI, P. G., *J. Chem. Phys.*, Vol. 91, 1989, p. 7075.
- [12] ROBERTS, C. B., ZHANG, J., BRENNECKE, J. F. and CHATEAUNEUF, J. E., *J. Phys. Chem.*, Vol. 97, 1993, p.5618.
- [13] ROBERTS, C. B., ZHANG, J., CHATEAUNEUF, J. E. and BRENNECKE, J. F. , *J. Am. Chem. Soc.*, Vol. 115, 1993, p.9576.
- [14] ZAGROBELNY, J. and BRIGHT, F. V., *J. Am. Chem. Soc.*, Vol. 114, 1992, p. 7821.
- [15] ZAGROBELNY, J. and BRIGHT, F. V., *J. Am. Chem. Soc.*, Vol. 115, 1993, p. 701.
- [16] RANDOLPH, T. W. and CARLIER, C., *J. Phys. Chem.*, Vol. 96, 1992, p. 5146.
- [17] ZAGROBELNY, J., BETTS, T. A. and BRIGHT, F. V., *J. Am. Chem. Soc.*, Vol. 114, 1992, p. 5249.
- [18] BRIGHT, F. V., personal communication
- [19] ROBERTS, C. B., CHATEAUNEUF, J. E. and BRENNECKE, J. F. , *AIChE J.*, in press, 1995.
- [20] ROBERTS, C. B., CHATEAUNEUF, J. E. and BRENNECKE, J. F., manuscript in preparation.
- [21] JANATA, E. and SCHULER, R. H., *J. Phys. Chem.*, Vol. 86, 1982, p. 2078.
- [22] REICHARDT, C. *Solvent and Solvent Effects in Organic Chemistry*, 2nd ed., VCH Verlagsgesellschaft mbH, D-6940 Weinheim, FRG, 1988.
- [23] BOTTCHER, C. J. F., VAN BELLE, O. C., BORDEWIJK, P. and RIP, A., *Theory of Electric Polarization*, 2nd ed., Elsevier, Amsterdam, 1973.
- [24] DRUDE, P. and NERNST, W., *Z. Phys. Chem.*, Vol. 1, 1894, p. 79.
- [25] PENG, D. Y. and ROBINSON, D. B., *Ind. Eng. Chem. Fund.*, Vol. 15 , 1976, p. 59.
- [26] WOOD, R. H., QUINT, J. R. and GROLLER, J.-P. E., *J. Phys. Chem.*, Vol. 85, 1981, p. 3944.
- [27] QUINT, J. R. and WOOD, R. H., *J. Phys. Chem.*, Vol. 89, 1985, p. 380.
- [28] MAKITA, R., JUBOTA, H., TANAKA, Y. and KASHIWAGI, H., *Refrigeration*, Vol. 52, 1977, p. 543.
- [29] CHARTON, M., *J. Am. Chem. Soc.*, Vol. 97, 1975, p. 1552.

RECEIVED May 17, 1995

Chapter 11

Kinetics of a Diels–Alder Reaction in Supercritical Propane

Barbara L. Knutson, Angela K. Dillow, Charles L. Liotta,
and Charles A. Eckert¹

Schools of Chemical Engineering and Chemistry
and Specialty Separations Center, Georgia Institute of Technology,
Atlanta, GA 30332–0100

The kinetics of the Diels–Alder reaction of maleic anhydride (MA) and 2,3-dimethyl-1,3-butadiene (DMB) were studied in supercritical fluid propane solutions in the temperature range of 100–140°C and at densities of 6–10 moles/liter, both in excess DMB (a reactive cosolvent) and also in the presence of an unreactive cosolvent (2–10 mole% 2,2,2-trifluoroethanol (TFE)). In the reactive cosolvent systems, low density results at 100°C and 120°C were not in agreement with activation volumes estimated from a cubic equation of state. The effect of unreactive cosolvent on the reaction rate was minimal. Anomalies observed may be the result of a reactive cosolvent-enhanced solute environment in near-critical solutions or enhanced secondary interactions in the transition state.

Supercritical fluids (SCF's) offer many advantages as solvents for reactions as well as for separations. Investigations in near-critical solutions have shown the ability to control reaction rate (*1–7*) selectivity (*8–10*) and chemical equilibria (*11*) with small changes in pressure and temperature. The detoxification of waste streams by supercritical water oxidation is a particularly promising application of SCF technology (see, for example, (*12*)). In spite of this potential as a reaction media, knowledge of the unique solvent properties of SCF's has been applied primarily to enhancing separation selectivities and loadings. Specifically, the effect of local reactant environment and cosolvent addition on reaction rates in near-critical solutions is relatively uncharacterized.

¹Corresponding author

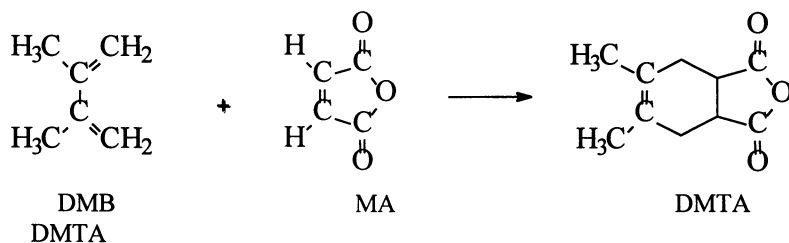
0097–6156/95/0608–0166\$12.00/0
© 1995 American Chemical Society

Cosolvents afford a powerful tool for tuning solvent properties for specific applications (13-18). The often dramatic change in solute solubility upon the addition of cosolvent is attributed to specific cosolvent/solute interactions. Cosolvent effects are also interpreted in light of evidence that the bulk and local solvent environment about a solute in a near critical solution may differ in density and composition (19, 25-28). Although these enhancements are not strictly a critical phenomenon, they appear to be a strong function of density in the highly compressible near-critical region (24-26, 28-30).

Some kinetic investigations have served as probes of the local environment of reactant molecules in near-critical solutions. These investigations have generally been limited to diffusion-controlled reactions, in which the reaction rate was related to the structure of the local environment at various near-critical conditions (5, 31-33). However, Brennecke and coworkers (6, 7) have observed near-critical effects on the rate constant consistent with local solvent enhancements for kinetically-controlled hydrogen abstraction of benzophenone triplet by cyclohexadiene and isopropanol in SCF CO₂ and C₂H₆ (6), and the esterification of phthalic anhydride with methanol in SCF CO₂ (7). In the near-critical region, the rate constants for both reaction systems were significantly larger than predicted. These differences in the experimental and predicted rates were consistent with differences in the local and bulk concentration of the excess reactant in the vicinity of the dilute reactant.

Thus, reactive and unreactive cosolvent effects have a variety of implications in tailoring SCF solvent systems for reactions. In the case of bimolecular reactions, the existence of local enhancements suggest that apparent rate constants are a function of a local solvent environment enriched in the reactive cosolvent. The effective rate constant may also be influenced by the solvent strength associated with the composition-enhanced local environment about the dilute reactant. An unreactive cosolvent species may modify the solvating power and physical properties of SCF/reactant systems and may be used to control reaction rates.

Presented here are results for the reaction of DMB and MA to form 4,5-dimethyl-*cis*-1,2,3,6-tetrahydrophthalic anhydride (DMTA), shown below.



This reaction was investigated in SCF propane in the presence of reactive cosolvent (excess DMB) and unreactive cosolvent TFE over a range of temperatures (100 - 140°C) and pressures (46 - 141 bar). The near-critical effects and cosolvent effects on reaction rate were analyzed from transition state theory, the known solvent effects

on this well-characterized reaction, and the current understanding of the local solute environment in SCF solutions.

Background

The Diels-Alder reaction is a clean, well-characterized bimolecular reaction, generally proceeding in a single step through a pseudo-aromatic transition state. In liquids, it is known to exhibit modest rate increases with solvent polarity (34,35) and to be accelerated by pressure (36). There is some evidence that it may also be accelerated by protic solvents (37). Most Diels-Alder reactions proceed in the gas phase by the same mechanism and with similar activation energies to those observed in liquids.

The reaction of DMB and MA in SCF propane was chosen based on several criteria: the rate is suitable for our flow technique, the diene is a liquid at ambient conditions, and the analysis is not complicated by stereochemical isomers. The critical properties of propane ($T_c = 96.7^\circ\text{C}$, $P_c = 42.5$ bar) allow us to maintain convenient rates at near-critical temperatures. Additionally, propane cannot be involved in specific interactions with the reactants or cosolvent, thus simplifying the interpretation of solvation effects. Also, a series of liquid and SCF experiments indicate that there are no significant side or reverse reactions at the temperatures investigated here. The miscibility of all concentrations of reactants and cosolvents with SCF propane were checked in a visual cell at reaction conditions to ensure that all experiments were carried out in the single phase region.

The cosolvent TFE was chosen in an attempt to maximize the observable cosolvent effect. TFE is a strong hydrogen bond donor, but as a poor base it does not associate appreciably. It also has relatively large solvent polarity/polarizability effect, as measured by its Kamlet-Taft parameters (38). Moreover, TFE will not react with any species present, as confirmed from liquid experiments in which DMB and MA were refluxed in neat TFE ($T_b = 79^\circ\text{C}$) for 12 hours.

Experimental

Apparatus. The flow reactor, shown in Figure 1, has been described in detail elsewhere (39). Isco Model 260D and 500D syringe pumps were used to introduce the reactant mixtures (MA/propane and DMB/propane or DMB/TFE/propane) into the system and maintain pulse-free, constant pressure flow throughout the reactor. The reactor was housed in a shatter-proof vessel as an additional safety precaution. The reactant mixtures flowed from the pumps to preheating coils and were brought together in a static mixer (Koflo Corporation, 17 elements in 3/16" tubing). The reactor consisted of 1/8" o.d. high pressure tubing (High Pressure Equipment) with a volume of 10.8 ml. This coiled tubular reactor, as well as the preheating coil and tubular static mixer, were located in a temperature bath. Temperature was measured using a calibrated thermocouple and digital display (Omega Model HH21) to $\pm 0.3^\circ\text{C}$ and controlled using a three-mode controller (Bayley Instrument Company, Model 123). Pressure was monitored in the reactant lines and at the reactor inlet with

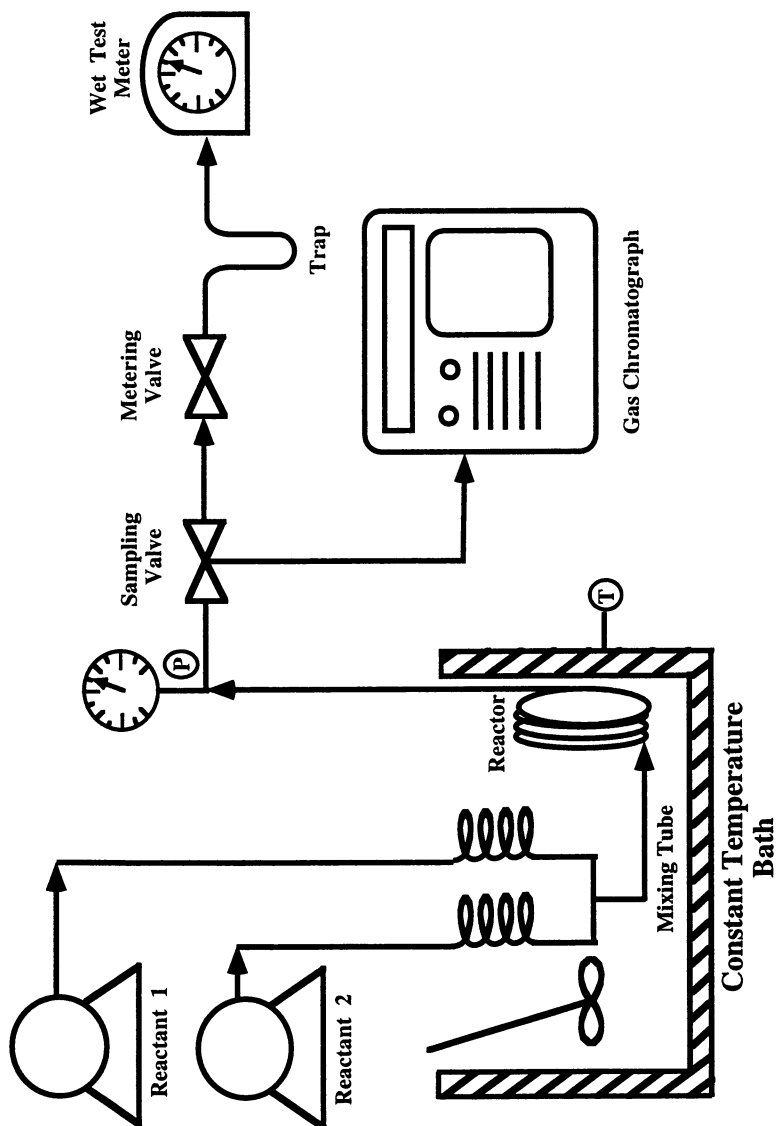


Figure 1. Schematic of flow reactor.

transducers accurate to ± 0.5 bar (Druck Model DPI 420). All pressurized lines external to the temperature bath were heated with heating tape. Flow rate was controlled by a heated micrometering valve (Autoclave Engineers Inc., Model 10VRMM). After the reactor outlet stream was depressurized at the micrometering valve, non-volatiles were precipitated in a trap. The stream was then passed through a water saturator before entering a wet test meter (Precision Scientific Inc., Model 63126) and finally exhausted into a safety hood.

Samples of the pressurized reactor outlet stream were taken using a six-port, external loop sampling valve (Valco Instruments Model C6UW) located before the micrometering valve. Each 250 μl sample was depressurized into a cold liquid solvent, the sample loop was rinsed with this solvent, the total volume of the solvent was determined, and the sample was subsequently analyzed by gas chromatography (Varian 3400) with FID detection.

Procedure. The reaction rate constant was determined for a given temperature and pressure from several flowrates with multiple samples taken at each flowrate. Preheated solutions of DMB/propane and MA/propane were brought together by a standard mixing tee at the reactor inlet in constant volumetric ratios through "cosolvent mode" operation of the Isco syringe pumps.

At the start of each run, 3 to 4 reactor volumes of mixture were flushed through the system at a constant flowrate before sampling the reactor outlet stream. Three samples were taken at each reaction condition and then the flowrate was varied. After changing the flowrate or perturbing the reactor system in any way, sampling did not proceed until a solution volume greater than the reactor volume was flushed through the system at the new conditions. The propane flowrate at STP conditions was measured from wet test meter readings.

The reaction of DMB and MA in SCF propane was investigated at 100, 120, and 140°C at pressures ranging from 46 to 141 bars. This corresponds to reactor solution densities of 6.5 to 9.6 moles/liter, where the critical density of pure propane is 4.9 moles/liter. At the reactor inlet the ratio of the mole fraction of DMB to MA, $y_{\text{DMB}}/y_{\text{MA}}$, was approximately fifteen. The reactive cosolvent, DMB, was present at $1.8 \times 10^{-2} < y_{\text{DMB}} < 2.9 \times 10^{-2}$.

Materials. Acetone (99.9+ %, HPLC grade), dimethylsulfoxide (99.9+ %, HPLC grade), TFE (99.5+ %), and DMB (98%) were obtained from Aldrich Chemical Company and used as received. C.P.-grade propane (99+ %) was purchased from Matheson Gas Products. MA (99+ %) was obtained from Fluka Chemicals, sublimed, and stored in a nitrogen environment.

DMTA was produced by refluxing MA neat in excess DMB for 8 hours in a nitrogen environment. The DMB was then removed by evaporation. Traces of DMB and MA were not detectable in the product when analyzed by gas chromatography with FID detection.

Data Analysis. The composition of the reactor inlet stream was determined from the composition of the pre-reaction mixtures in the respective syringe pumps, the

volumetric ratio of these mixtures fed to the reactor in the syringe pump cosolvent mode, and the density of these feed mixtures. The Soave-Redlich-Kwong (SRK) equation of state was used to determine the composition and density of the pre-reaction mixtures based on gas chromatography analysis of the mixture samples. The pure component properties needed for this calculation were determined by Lydersen's group contribution method for the estimation of critical properties and Lee and Kessler's method for acentric factors (40) [(DMB: $T_c = 526$ K; $P_c = 34.6$ bar; $\omega = 0.22$); MA: $T_c = 720$ K; $P_c = 59.5$ bar; $\omega = 0.45$), (TFE: $T_c = 501$ K; $P_c = 48.6$ bar; $\omega = 0.64$)]. The binary interaction parameters (k_{ij} 's) in these systems were set equal to 0.1, for lack of further information. Mixture densities were calculated by multiplying the known density of pure SCF propane (41) by a ratio of mixture density to the pure propane density as determined from the SRK equation of state.

The volumetric flowrate at reactor conditions was determined from the reactor stream density and the propane flowrate measured at room conditions using the wet-test meter. From this volumetric flowrate, the average time a volume or plug of fluid spent in the reactor was evaluated.

Outlet samples were analyzed by gas chromatography for DMB and product. The consistency of y_{DMB} served as a check of the sampling technique. These values were used to evaluate the bimolecular rate constant from the pseudo-first order rate measured in excess DMB. The reported bimolecular rate constants, given in mole fraction units (min^{-1}), were corrected from the pseudo-first order rate constants divided by the mole fraction of DMB (y_{DMB}) in each sample.

The reactor flow was well within the laminar regime at all flowrates investigated. Several reactor models were employed in this analysis: a plug flow reactor (PFR), a continuous stirred tank reactor (CSTR), and a laminar flow reactor (LFR). Details of the LFR model are given by Carberry (42). Relative to the ideal PFR and CSTR models, the LFR model represents an intermediate effect of mixing on conversion, although the CSTR model was much closer than the PFR model in predicting the mixing effect in this case. Rate constants reported here are based on the LFR model. The PFR model provided rate constants which were, on average, 8.5% below the LFR model, while the CSTR model provided rate constants which were only 1.5% above the LFR model.

The activation volume was predicted from SRK estimates of the partial molal volumes of the transition state and the reactants in supercritical propane/ reactant mixtures. For lack of further information, the transition state parameters were modeled as those of the product and estimated by group contribution methods (40) [DMTA: $T_c = 874$ K; $P_c = 31.7$ bar; $\omega = 0.62$].

Results and Discussion

The rate constants for the reactive cosolvent system at 100, 120, and 140°C are shown in Figure 2. The effect of pressure on rate is in contrast to the trend observed by other investigators for Diels-Alder reactions in SCF CO_2 , in which a significant increase of the rate was observed with small increases in pressure in the

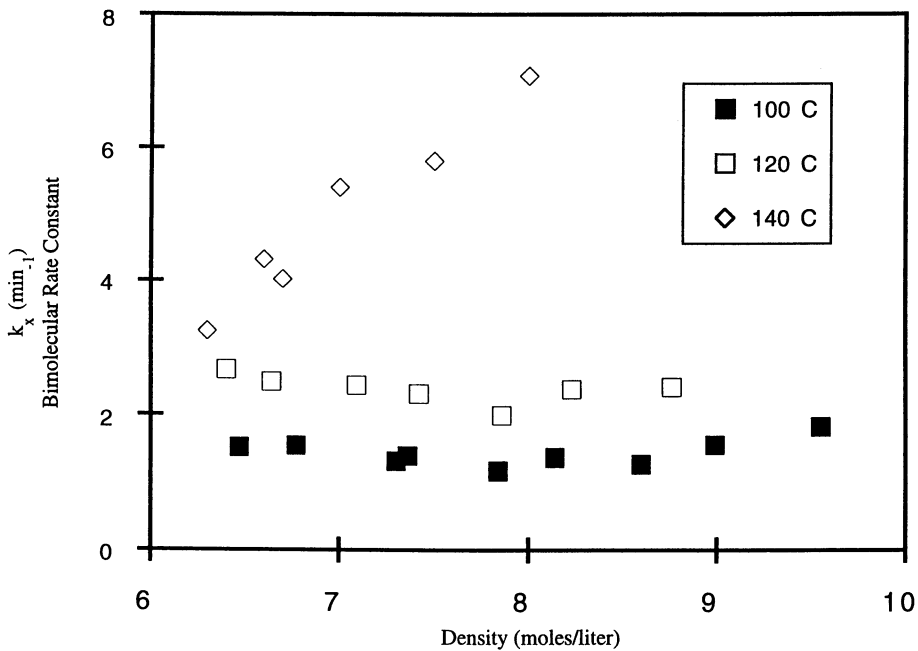


Figure 2. Experimental bimolecular reaction rate constants.

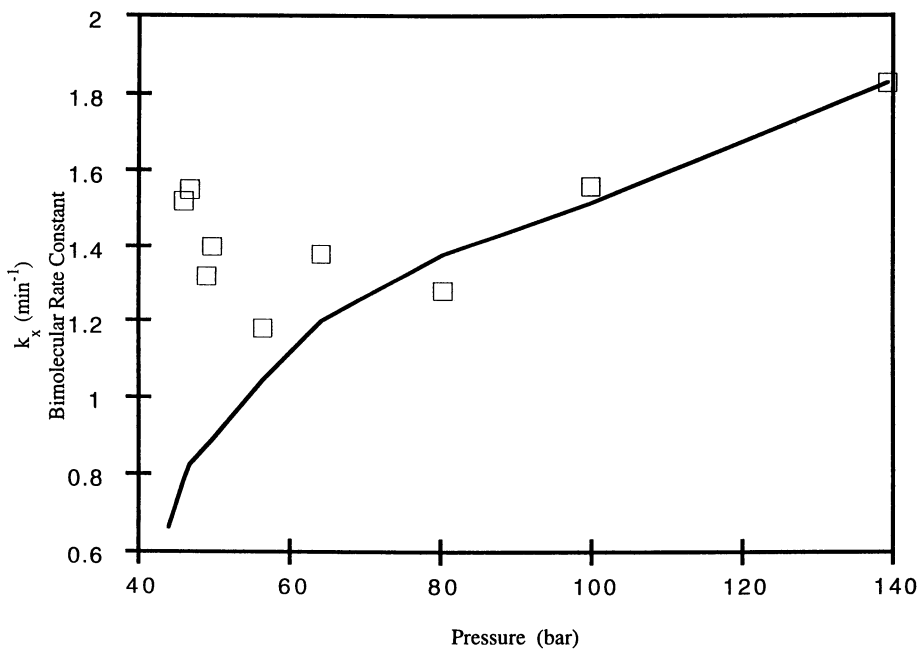


Figure 3. Estimated and experimental rate constants at 100°C.

near-critical region (2,4,43). Unlike the reactive cosolvent environment of this investigation in SCF propane, rates in SCF CO₂ were determined for dilute systems in which the composition of the reactants was of similar magnitude.

The pressure effect on reaction rates is the activation volume, which in liquids is typically ± 0 -40 cc/mole, with structural and solvation contributions equal in size (44). In SCF's, Δv^\ddagger represents primarily a difference in the solvation of the transition state and reactants; the corresponding partial molal volumes of the transition state and substrate in SCF's are large and negative, scaling with the isothermal compressibility of the near-critical fluid (19). Paulaitis and Alexander (2) and Ikushima et al. (4) have reported large negative volumes of activation for Diels-Alder reactions in SCF CO₂. At 50°C in SCF CO₂, a Δv^\ddagger of -750 cc/mole is reported for the methyl acrylate/isoprene reaction (4). Kim and Johnston (45) have predicted values of Δv^\ddagger for the Diels-Alder reaction of maleic anhydride and isoprene in SCF CO₂ as great as -4000 cc/mol, demonstrating the considerable effect of pressure on reaction rate anticipated in near-critical solutions. In view of the other data available, the minimal pressure effects observed in near-critical propane are surprising.

Values of Δv^\ddagger calculated from the SRK equation of state at experimental conditions are shown in Table I. At low densities, the pressure-dependence of the experimental rates in SCF propane at 100 °C and 120 °C differ in size and sign from the predicted values. An activation volume of -480 cc/mole was determined for the experimental data at 140 °C. This value was approximately constant over the range of pressures investigated here and compares favorably with the predicted values. The average predicted activation volume was -400 cc/mole at 140°C.

Table I. Estimated Activation Volumes Corresponding to the Measured Reaction Rates of MA and DMB in SCF Propane.

100 C		140 C	
Pressure (Bars)	Δv^\ddagger (cc/mol)	Pressure (Bars)	Δv^\ddagger (cc/mol)
46.0	-1500		
46.8	-1300	90.6	-570
49.0	-840	96.5	-470
49.7	-780	99.0	-450
56.4	-540	106.1	-380
64.2	-400	119.8	-300
80.3	-260	140.8	-220
99.9	-190		
139.3	-120		

The estimated and experimental rate constants versus pressure are plotted in Figure 3 for the reaction system at 100°C, using the highest density data point as the

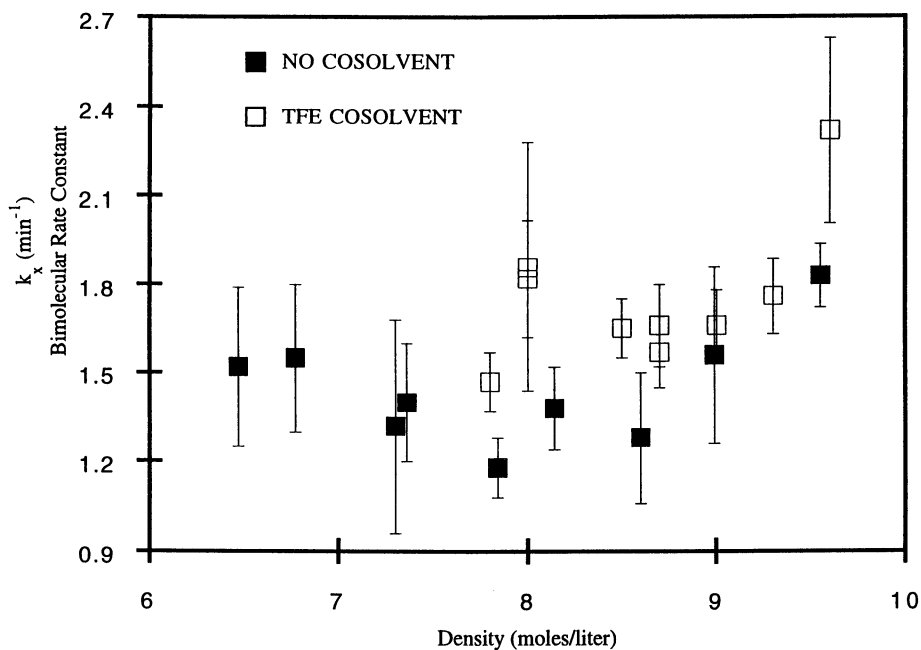
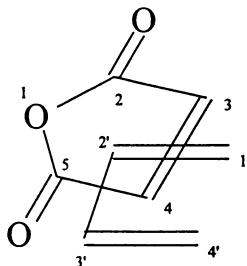


Figure 4. Rate constants at 100°C with and without unreactive cosolvent, 2,2,2-trifluoroethanol.

reference point. The predicted and experimental rate constant differ by a factor of approximately two in the near-critical region.

The unusual density effects reported here are consistent with the measurement of an observed rate constant. The deviation of the well-established pressure, temperature, and solvent effects on Diels–Alder rate constants support this speculation. The measurement of an apparent rate constant could result from an appreciable difference in bulk and local concentration of one reactant in the vicinity of the other reactant. Such local enhancements around a solute or probe molecule have been postulated in ternary SCF solutions from thermodynamic, spectroscopic, kinetic, and computational techniques (see, for example, (46)). These enhancements, though not strictly a critical phenomena, are significant in near-critical solutions. Analysis of rate information based on bulk composition, and not the enhanced local composition, would overestimate the rate constant.

The degree of association of the reactants in the activated complex might also contribute to the minimal effect of pressure on the reaction rates in near-critical propane. Secondary π -interactions between non-bonding sites in the transition state are postulated to enhance the partial transfer of charge from the diene to the electron-deficient dienophile in some Diels–Alder reactions (47). With MA as the dienophile, secondary π -interactions can occur between the non-bonding centers of the 2 and 2' atoms and between the 5 and 3' atoms, as shown below,



This electron transfer is analogous to that of charge-transfer complex formation, which involves partial electron transfer from the highest occupied orbital of an electron donor to the lowest unoccupied orbital of the electron-deficient molecule (48,49). In many cases, Diels–Alder reactions are accompanied by a transient color, which is characteristic of the formation of such complexes (50). Although charge-transfer complex formation may or may not be on the reaction coordinate, it is conceivable that the same interactions which affect the degree of charge-transfer complexes would influence Diels–Alder reaction rates. This degree of association of the reactants may be a function of solvation of the activated complex in the DMB cosolvent/propane environment.

The addition of 2–10% TFE cosolvent at 100 °C caused a slight but measurable rate increase, as shown in Figure 4. Every rate measured in the TFE cosolvent system was higher, and the average increase was 20%. However, the uncertainty of the data due to the sampling technique coupled with the fact that TFE changes the critical point of the mixture precludes analysis of this rate augmentation based on TFE composition.

This slight cosolvent effect on the rate constant is in agreement with measured solvent effects on Diels-Alder reactions. For the reaction of maleic anhydride and isoprene the rate constant varies by only a factor of 13 in ten solvents of widely varying dielectric constants (51). The cosolvent choice of TFE attempted to take advantage of rate-enhancing solvent effects attributed to solvent polarity/polarizability and hydroxylic solvents for the Diels-Alder reaction. The significance of these contributions cannot be established from this experiment. However, at these temperatures, solvent effects attributed to hydrogen bonding interactions are less extensive than at room temperature.

Conclusions

Bimolecular rate constants were measured for the reaction of MA in reactive cosolvent DMB/SCF propane mixtures at 100°C, 120°C and 140°C. At 140°C, rate constants increased with increasing pressure. However, pressure had limited effect on the rate constants measured at 100°C and 120°C at near-critical densities. This minimal effect of pressure had not been observed previously in investigations of Diels-Alder reactions in supercritical fluid CO₂ in which the reactants were at approximately equal and dilute concentrations. Similarly, transition state theory predicts a larger pressure-dependence of the reaction rate in these near-critical solutions.

The addition of unreactive cosolvent (2 to 10 mole% TFE), produced a limited rate increase in the relatively solvent-insensitive Diels-Alder reaction.

The overall solvent insensitivity of this reaction suggest that the observed pressure effect on the reaction rate constants could result from measuring an apparent rate constant. If local composition enhancements of DMB in the vicinity of MA exist, $y_{\text{DMB,bulk}}$ would not be the appropriate value in calculating the bimolecular rate constant from the apparent unimolecular rate constant measured in excess DMB. Use of $y_{\text{DMB,bulk}}$ in local composition-enhanced solutions would result in an apparent rate constant which is greater than the true rate constant. Such local composition enhancements of a cosolvent in the vicinity of a solute are associated with near-critical ternary solutions.

Results of this investigation suggest that the local reactant composition, as well as pressure, temperature, and cosolvent, can be used to manipulate the reaction rate in the near critical region. In reactions with more pronounced solvent effects, the reaction rate may also reflect the increased solvent strength of a composition-enhanced environment.

Acknowledgments

The authors gratefully acknowledge funding support for this work from the Air Force Office of Scientific Research under grant number F49620-93-1-0214 as well as support from E.I. Du Pont de Nemours Co. Additionally, Joe Coppom, Michael

Davis, Alison Williams, and James Wright are acknowledged for their contributions to this project.

Literature Cited

1. Lee, M.; Holtom, G.R.; Hochstrasser, R.M. *Chem. Phys. Lett.* **1985**, *118*, 359.
2. Paulaitis, M.E.; Alexander, G.C. *Pure & Appl. Chem.*, **1987** *59*, 61.
3. Johnston, K.P.; Haynes, C. *AIChE J.* **1987**, *33*, 2017.
4. Ikushima, Y.; Saito, N.; Arai, M. *J. Phys. Chem.* **1992**, *96*, 2293.
5. Randolph, T.W.; Carlier, C. *J. Phys. Chem.* **1992**, *96*, 5146.
6. Roberts, C.B.; Chateaufneuf, J.E.; Brennecke, J.F. *J. Am. Chem. Soc.* **1992**, *114*, 8455.
7. Ellington, J.B.; Park, K.M.; Brennecke, J.F. *Ind. Eng. Chem. Res.* **1994**, *33*, 965.
8. Hyatt, J.A. *J. Org. Chem.* **1984**, *49*, 5097.
9. Kim, S.; Johnston, K.P. *Chem. Eng. Comm.* **1988**, *63*, 49.
10. Collins, N.A.; Debenedetti, P.G.; Sundaresan, S. *AIChE J.* **1988**, *34*, 1121.
11. Kimura, Y.; Yoshimura, Y.; Nakahara, M. *J. Chem. Phys.* **1989**, *90*, 5679.
12. Shaw, R.W.; Brill, T.B.; Clifford, A.A.; Eckert, C.A.; Franck, E. U. *Chemical & Engineering News* **1991**, Dec. 23, 26.
13. Lemert, R.M.; Johnston, K.P. *Ind. Eng. Chem. Res.* **1991**, *30*, 1222.
14. Dobbs, J.M.; and Johnston, K.P. *Ind. Eng. Chem. Res.* **1987**, *26*, 1467.
15. Brennecke, J.F.; Eckert, C.A. *AIChE J.* **1989**, *35*, 1411.
16. Ekart, M.P.; Bennett, K.L.; Ekart, S.M.; Gurdial, G.S.; Liotta, C.L.; Eckert, C.A., *AIChE J.* **1993**, *39*, 235.
17. Tomasko, D.L.; Knutson, B.L.; Pouillot, F.L.L.; Liotta, C.L.; Eckert, C.A., *J. Phys. Chem.* **1993**, *97*, 11823.
18. Gupta, R.M.; Combes, J.R.; Johnston, K.P. *J. Phys. Chem.* **1993**, *97*, 707.
19. Eckert, C.A.; Ziger, D.H.; Johnston, K.P.; Kim, S. *J. Phys. Chem.* **1986**, *90*, 2378.
20. Kim, S.; Johnston, K.P. *Ind. Eng. Chem. Res.* **1987**, *26*, 1206.
21. Kim, S.; Johnston, K.P. *AIChE J.* **1987**, *33*, 1603.
22. Yonker, C.R.; Smith, R.D., *J. Phys. Chem.* **1988**, *92*, 2374.
23. Brennecke, J.F.; Tomasko, D.L.; Peshkin, J.; Eckert, C.A. *Ind. Eng. Chem. Res.* **1990**, *29*, 1682.
24. O'Brien, J.A.; Randolph, T.W.; Carlier, C.; Ganapathy, S. *AIChE J.* **1993**, *39*, 1061.
25. Knutson, B.L.; Tomasko, D.L.; Eckert, C.A.; Debenedetti, P.G.; Chialvo, A.A. In *Recent Advances in Supercritical Fluid Technology: Applications and Fundamental Studies*; Bright, F.V.; McNally M.E.P., Eds.; ACS Symp. Ser. 488; American Chemical Society: Washington D.C., 1992; Chapter 5.
26. Cochran, H.D.; Lee, L.L.; Pfund, D.M. *Proc. Int. Symp. Supercritical Fluids* **1988**, 245.
27. Petsche, I.B.; Debenedetti, P.G. *J. Phys. Chem.* **1989**, *9*, 7075.
28. Wu, R.S.; Lee, L.L.; Cochran, H.D. *Ind. Eng. Chem. Res.* **1990**, *29*, 977.

29. Sun, Y.P.; Fox, M.A.; Johnston, K.P. *J. Am. Chem. Soc.* **1992**, *114*, 1187.
30. Phillips, D.J.; Brennecke, J.F. *Ind. Eng. Chem. Res.*, **1993**, *32*, 943.
31. Schroeder, J.; Schwarzer, D.; Troe, J.; and Voß, F. *J. Chem. Phys.* **1990**, *93*, 2393.
32. Zagrobelny, J.; Bright, F.V. *J. Am. Chem. Soc.* **1993**, *115*, 701.
33. Roberts, C.B.; Zhang, J.; Brennecke, J.F.; Chateaufneuf, J.E. *J. Phys. Chem.*, **1993**, *97*, 5618.
34. March, J. *Advanced Organic Chemistry: Reactions, Mechanisms, and Structure*; John Wiley & Sons: New York, NY, 1992.
35. Reichardt, C. *Solvents and Solvent Effects in Organic Chemistry*; 2nd ed., VCH Verlagsgesellschaft: Weinheim, Germany, 1988.
36. McCabe, J.R.; Eckert, C.A. *Ind Eng. Chem., Fundam.* **1974**, *13*, 168.
37. Beltrame, P. In *Chemical Kinetics*; Bamford, C.H.; Tipper, C.F.H., Eds.; Elsevier Scientific Publishing Company: New York, NY, 1973, vol 9; Chapter 2.
38. Kamlet, M.J.; Abboud, J.-L. M.; Abraham, M.H.; Taft, R.W. *J. Org. Chem.* **1983**, *48*, 2877.
39. Knutson, B.L., Ph.D. Thesis; Georgia Institute of Technology, **1994**.
40. Reid, R.C.; Prausnitz, J.M.; Poling, B.E. *The Properties of Gases and Liquids*; 4th ed., McGraw-Hill: New York, NY, **1987**.
41. Younglove, B.A.; Ely, J.F., *J. Phys. Chem. Ref. Data* **1987**, *16(4)*, 577.
42. Carberry, J.J. *Chemical and Catalytic Reaction Engineering*; McGraw-Hill: New York, NY, **1976**.
43. Worley, G.; Weinstein, R.; Harris, J.G.; Danheiser, R.; Tester, J.W. Presented at AIChE Annual Meeting, San Francisco, CA, 1994, paper 118e.
44. Abraham, M.H., *Progress in Physical Organic Chemistry* **1974**, *11*, 2.
45. Kim, S. Johnston, K.P. In *Supercritical Fluids: Chemical Engineering Principles and Applications*; Squires, T.G.; Paulaitis, M.E., Eds.; ACS Symp. Ser. 329; American Chemical Society: Washington D.C., 1987; Chapter 4.
46. Eckert, C.A.; Knutson, B.L. *Fluid Phase Equilibria* **1993**, *83*, 93.
47. Grieger, R.A.; Eckert, C.A. *J. Am. Chem. Soc.* **1970**, *92*, 7149.
48. McGlynn, S.P. *Chem. Rev.* **1958**, *58*, 1113.
49. Kuroda, H.; Amano, T.; Ikemoto, I.; Akamatu, H. *J. Am. Chem. Soc.* **1967**, *89*, 6056.
50. Kloetzel, M.C. *Org. React.* **1948**, *4*, 1.
51. Dewar, M.J.S.; and Pyron, R.S. *J. Am. Chem. Soc.* **1970**, *92*, 3098.

RECEIVED July 23, 1995

Chapter 12

Hydrothermal Oxidation of Organic Compounds by Nitrate and Nitrite

P. Dell'Orco¹, B. Foy², E. Wilmanns², L. Le², J. Ely², K. Patterson²,
and S. Buelow²

¹Dynamic Experimentation Division and ²Chemical Science
and Technology Division, Los Alamos National Laboratory,
Los Alamos, NM 87545

Reactions of nitrite and nitrate with EDTA (ethylenediamine tetraacetic acid) and acetic acid were studied in hydrothermal systems. Reactions with EDTA were targeted at providing a treatment solution for Hanford Tank Wastes; nitrate/nitrite/EDTA reactions were studied in concentrations pertinent to the Hanford tank problem, to systematically infer the effect of cumulative additions of tank waste constituents on hydrothermal reaction chemistry. Reaction intermediates and products are discussed, and simplified mechanisms for organic oxidation via nitrate/nitrite are presented. Reaction kinetics for organic destruction in Na₄EDTA/NaNO₃/NaNO₂/NaOH systems were developed using a small bench-scale reactor, and applied to a small pilot-scale reactor. Acetic acid oxidation via sodium nitrate was investigated to determine pressure effects of reactions in supercritical water.

The hydrothermal processing of wastes to destroy organic components has long been recognized as an effective method for converting organic constituents in waste streams into carbon dioxide or into simple organic compounds which are amenable to biological treatment (1,2). Subsets of hydrothermal waste treatment include both supercritical water oxidation (SCWO) and wet air oxidation (WAO). SCWO refers to a regime of hydrothermal treatment where the waste stream is raised to temperature-pressure (T-P) parameters above the critical values for water, 374°C and 221 bar. WAO is defined by T-P parameters generally less than 325°C and 175 bar. In both these processes, either pure oxygen or oxygen in air is used to oxidize the organic matter in the waste stream.

Hydrothermal treatment is a more general term than either SCWO or WAO, inclusive of T-P regimes utilized by both processes, while also referring more generally to redox reactions caused by a variety of oxidants: air, oxygen, nitrate, sulfate, and organics included. In addition, the term "hydrothermal" makes no

0097-6156/95/0608-0179\$12.00/0
© 1995 American Chemical Society

reference to solution critical points, which can be significantly different for complex waste streams than for pure water.

For several years, the focus of the hydrothermal processing program at Los Alamos National Laboratory has been to investigate the redox behavior of nitrate and nitrite salts in hydrothermal systems. This interest has arisen from studies involving the destruction of organics in high explosive/propellant waste streams (3), and in Hanford tank wastes (4), which in most cases have sufficient oxidant (in the form of $\text{NO}_3^-/\text{NO}_2^-$) to completely oxidize the organic component in the waste stream.

The work presented here focuses on organic destruction kinetics, using nitrate and nitrite as oxidants, in matrices pertinent to the Hanford tank waste problem. Underground storage tanks at Hanford contain mixed organic-oxidizer-radionuclide wastes resulting from nuclear materials production since the 1940's. The composition of 3:1 diluted Hanford tank 101-SY was used as a baseline for these studies. Tank 101-SY has received notoriety as a "burping" tank at the Hanford reservation. Burping episodes result in gaseous releases highly concentrated in both hydrogen and nitrous oxide. These gases result from redox reactions between nitrate/nitrite and organics present in the tank. The Tank Waste Remediation Systems Program (TWRS) had set organic destruction as a pretreatment priority for tank 101-SY, and other so-called complexant concentrate tanks, to alleviate the burping episodes and to present a waste stream which could be further processed without interference from organic complexants. Hydrothermal processing was initially selected as a primary remediation technology to achieve organic destruction goals for tank safety issues; organic destruction may also be necessary as a treatment to destroy complexants which may interfere with downstream radionuclide separation by ion exchange.

Because of the complex nature of Hanford tank wastes as a whole, simulant 101-SY was studied in a sequential fashion; constituents were added cumulatively in their molar concentration in the full 101-SY simulant, to assess the effects of variations in feed concentrations on the kinetics of organic carbon destruction. The major components of 3:1 diluted simulant 101-SY are shown in Table I. The first six components were studied by cumulative addition, in the order shown. As observed in this table, the molar concentrations studied for simple mixtures were nearly the same as the molar concentrations in the full simulant. Although the project also involved processing the full simulant, these results are provided elsewhere (5).

The processing of the reaction mixtures shown in Table I required the use of pressures (~ 1 kbar) not normally encountered in SCWO or WAO processes; these elevated pressures were required to ensure that simulant mixtures existed as one phase solutions (i.e., no fluid-solid separation) throughout the reaction zone (7). Because these pressures were well beyond conditions normally encountered in hydrothermal treatment processes, the effect of pressure on acetic acid conversion kinetics (a reaction by-product of ethylenediaminetetraacetic acid [EDTA]/nitrate reactions) was also investigated.

Experimental

Two separate apparatuses were used to assess organic reaction kinetics. These will be referred to as the bench-scale reactor (BSR) and small pilot-scale reactor (SPSR) in the ensuing discussions. The BSR had a flow capacity of approximately 20 g/min,

while the SPSR had a flow capacity near 200 g/min. The purpose of using both reactors was to assess whether kinetic behavior observed on the BSR would scale successfully to the SPSR.

Table I. Approximate Molar Concentrations of Major Constituents in 3:1 Diluted Hanford Tank 101-SY Simulant (Adapted from Ref. 6).

Component	Molar Concentration (mol/L soln.)	Concentration Used In This Work* (mol/L soln.)
Total Organic Carbon (TOC, as Na ₄ EDTA, Na ₄ C ₁₀ H ₁₂ N ₂ O ₈)	0.572	0.60
Sodium Nitrate (NaNO ₃)	0.690	0.70
Sodium Nitrite (NaNO ₂)	1.025	1.00
Sodium Hydroxide (NaOH)	0.773	0.80
Sodium Carbonate (Na ₂ CO ₃)	0.236	0.25
Sodium Aluminate (NaAlO ₂)	0.537	0.50
Sodium Chloride (NaCl)	0.100	0.10
Potassium Nitrate (KNO ₃)	0.038	0.04
Chromium Nitrate (Cr(NO ₃) ₃)	0.035	0.04
Sodium Phosphate (Na ₃ PO ₄)	0.030	0.03
Sodium Sulfate (Na ₂ SO ₄)	0.019	0.02
Sodium Fluoride (NaF)	0.007	0.01

*Indicates concentrations used in kinetic studies. Concentrations are provided here at ambient conditions. The balance of the composition is primarily water.

BSR Experimental. A schematic of the BSR, on which all data for kinetic models were collected, is shown in Figure 1. The reactor consisted of 2.32 m of 2.1 mm ID nickel alloy 625 tubing. An air-driven Haskell HSF-300 pump was used to introduce feed solutions to the reactor. The reactor was immersed in a fluidized sandbath, which served to rapidly heat the feed stream and keep the reaction mixtures isothermal. Upon exiting the reactor, the process stream was rapidly quenched with a tube-in-shell heat exchanger, using chilled water as the heat exchange fluid. Approximately 45 m of 0.025 cm ID capillary tubing, preceding a 350-400 bar relief valve (adjustable), was used as a back-pressure regulator. For safety purposes, the entire apparatus was enclosed in a steel framed box with 1/2" Lexan enclosing the frame. Check valves were placed after the feed pump to prevent backflow; relief valves and manually controlled bleed valves were placed at the reactor entrance and exit to avert unwanted pressure increases in the reactor.

The temperature profile of the reactions was determined using nine surface thermocouples, appropriately placed at different distances on the reactor tube. These were disproportionately placed in the first 30 cm and last 30 cm of the reactor tube, to accurately record heat-up and cool-down regions. Typical temperature profiles, shown in Figure 2, indicate that the heat-up zone for the reactor is about 22 cm long,

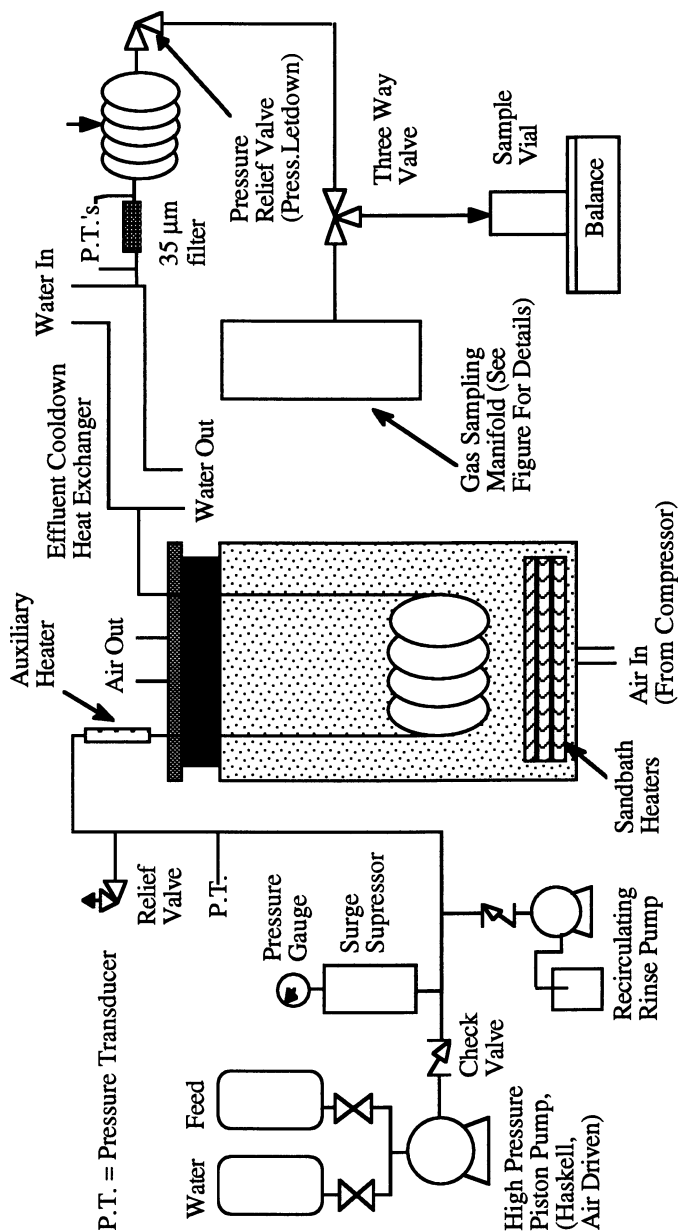


Figure 1. Schematic diagram of bench-scale tubular flow reactor (BSR).

while the remainder of the reactor prior to the heat exchanger quench was relatively isothermal. For the purpose of these studies, an isothermal reactor section was estimated to consist of 135 cm of reactor tubing, resulting in an effective volume of 7.39 cm³. This was the region of the reactor for which all thermocouples were within 10°C of the maximum temperature, which was used as the temperature of the experiment in the kinetic analyses. Because temperature profiles exhibited nearly the same heat-up and cool-down behavior regardless of the sandbath setpoint temperature or mass flow rate, this volume was considered constant for all temperature profiles. There is some uncertainty in the heat-up and cool-down regions of the reactor, which contribute an estimated ±10% error to the effective volume used in these studies.

The mean residence time of the fluid in the high-temperature portion of the reactor was calculated from equation 1:

$$\tau = \frac{V\rho}{m'} \quad (1)$$

where V is the reactor volume in cm³, ρ the fluid density in g/cm³, and m' the mass flow rate in g/s. For complex mixtures above the critical temperature of water, the fluid density is generally not known. In the absence of this information, the density of pure water, ρ_w was used. Recent density measurements indicate that the density of concentrated NaNO₃/NaOH solutions is more than 30-50% higher than ρ_w , so Equation (1) underestimates τ by that amount (7). The residence times included here for concentrated salt mixtures should be viewed as effective values until more extensive density determinations are available.

Gas sampling of the reactor effluent was accomplished by means of a simple gas-liquid separator, depicted in Figure 3. An empty stainless-steel container with volume of 150 mL was joined to a vacuum-tight manifold. A 0.159 cm OD tube fed the effluent into this chamber, and gases evolved from the liquid filled the manifold. The pressure of evolved gases was measured with a capacitance manometer (Baratron) with a range of 1-1000 Torr. Air was removed down to 0.1 Torr by means of a vacuum pump prior to the introduction of effluent. A background gas sample was collected over deionized water to subtract nitrogen and oxygen dissolved in the feed make-up water from concentrations obtained in experimental samples.

Liquid flow rates through the reactor were measured at the outlet with a balance and stopwatch. Typical operation of the reactor began by heating from room temperature while pumping water at the desired flow rate and pressure. The flow rate was varied from 5-20 g/min to achieve various residence times in the reactor. Once at the desired temperature and pressure, the feed to the pump was switched to the reactant solution. After the feed solution had flowed for a minimum of ten reactor volumes, sampling was begun. Aqueous samples were collected in quantities of four 40 mL glass vials with teflon-lined caps. The vials were filled to prevent volatilization before analysis. For each temperature/pressure condition, three sets of quadruplicate samples were taken. A gas sample was collected after the three sets of liquid samples.

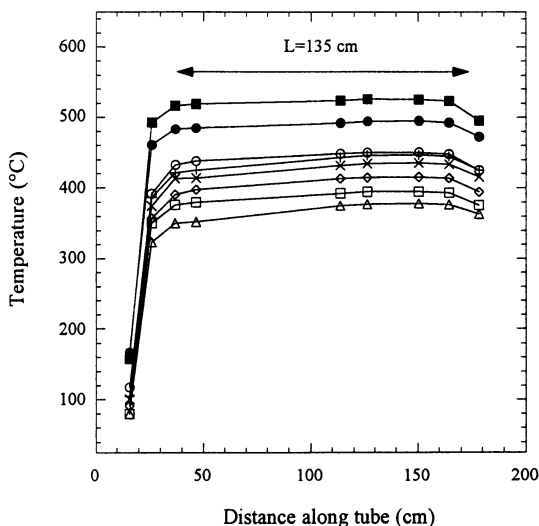


Figure 2. Typical temperature profiles in the bench-scale reactor. Temperatures were registered with K-type thermocouples attached to the outside of the reactor tubing. The profiles were recorded with 3:1 dil. simulant 101-SY pumped through the reactor at flow rates in the range 8-15 g/min. at 1.0 kbar. Note that the first ~10 cm of the tube is unheated.

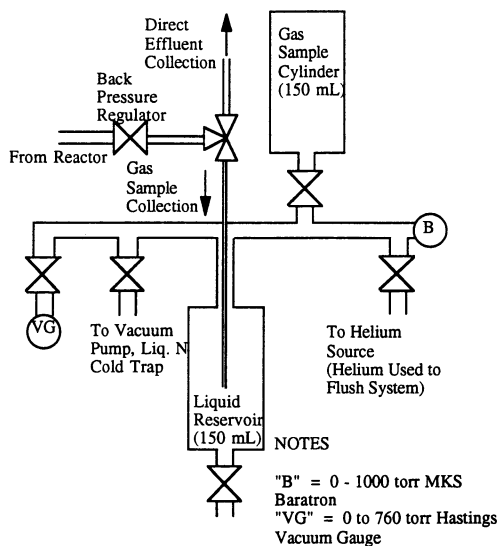


Figure 3. Schematic of Gas Sampling Apparatus for BSR

SPSR Experimental. The SPSR consisted of 8.2 m of 0.478 cm ID nickel alloy 625 tubing, heated resistively with DC power supplies. Heating tapes regulated with controllers and solid-state relays were wrapped on the last 4 m of the reactor tube, to offset heat losses and keep the reactor tube relatively isothermal. Twenty-seven thermocouples, uniformly spaced along the length of the reactor, monitored temperature profiles. A pneumatically-actuated Hydropac piston pump, with a flow capacity of 36 L/hr, introduced feed solutions to the reactor. In practice, the maximum flow rate utilized was 8 L/hr. Gas/liquid samples were obtained using remotely actuated solenoid switching valves, which could divert the cooled reactor effluent to stainless steel sample cylinders. Effluent stream flow rates were measured with a balance and a stopwatch. All reactor operations were controlled remotely, using a LabView program. Relief valves were placed at the reactor entrance and exit to prevent reactor pressurization over design values. Because of the larger volume of this reactor, no personnel were permitted in the reactor room during an experiment. A more detailed description of this reactor has been provided elsewhere (8).

Analytical Methods. Gas products were analyzed by gas chromatography, using an HP 5890A Series II. The GC was fitted with a Chrompack CarboPLOT column (30 m X 0.53 mm ID) with carbon molecular sieve adsorbent, helium carrier gas, and a thermal conductivity detector. The detectable gases were N₂, N₂O, O₂, H₂, CH₄, CO, CO₂, C₂H₆, and C₂H₄. Water was removed by a cold trap on the GC manifold. Although other gas products could have been produced, they would have been in much smaller quantities, since carbon and nitrogen mass recoveries were generally between 90% and 110%. Infrared absorption was attempted with a few selected gas samples, and no other products were detected. In particular, no NO or NO₂ was detected. Ammonia was detected in amounts far less than in the liquid effluent, consistent with its high solubility even at high pH. Gases were calibrated against samples of pure components or analyzed mixtures obtained from Scott Specialty Gases. Liquid samples were analyzed by ion chromatography (IC) for anions and cations, inductively coupled plasma spectroscopy (ICP) for metals, total organic carbon (TOC) and total inorganic carbon (TIC), and by a pH meter. The IC anion analysis determined EDTA, acetate, formate, nitrite, nitrate, oxalate, and glycolate. Cations measured were ammonia and methylamine.

Results and Discussion

Reactions of Simple Mixtures Relating to Simulant 101-SY. Conditions for this series of experiments are outlined in Table II. Nitrate, nitrite, and hydroxide were added cumulatively to the reaction mixture. Reactant and product concentration profiles typical of simple mixtures are shown in Figure 4 for a Na₄EDTA/NaNO₃/NaNO₂/NaOH (reaction mixture 4) experiment conducted at 440°C and 1.0 kbar. Concentrations of these reactants are the same as in the 3:1 diluted 101-SY simulant, as shown in Table I. Figure 4 shows that organic carbon is largely oxidized in 20 seconds reaction time. EDTA was not detected in the effluent, indicating that it decomposed rapidly (and possibly in the heat-up zone of the reactor) to other organics. The TOC component was converted to inorganic carbon (TIC) quantitatively: the carbon mass balances were in the range 90-110%. Nitrate and

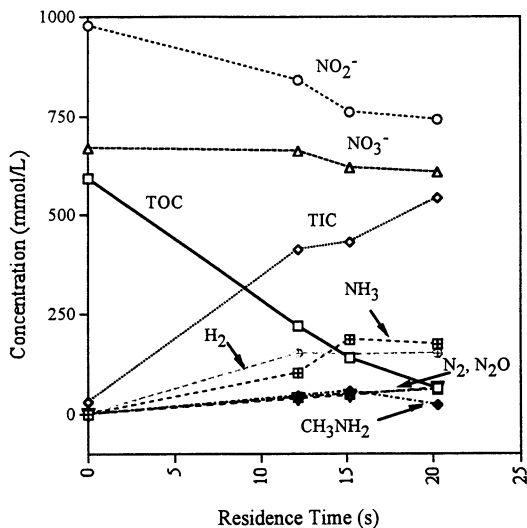


Figure 4. Reaction products for a mixture of Na_4EDTA , NaNO_2 , NaNO_3 and NaOH at 440°C and 1 kbar (14800 psi). Reactant concentrations are shown at ambient conditions. Feed concentrations are shown in Table II.

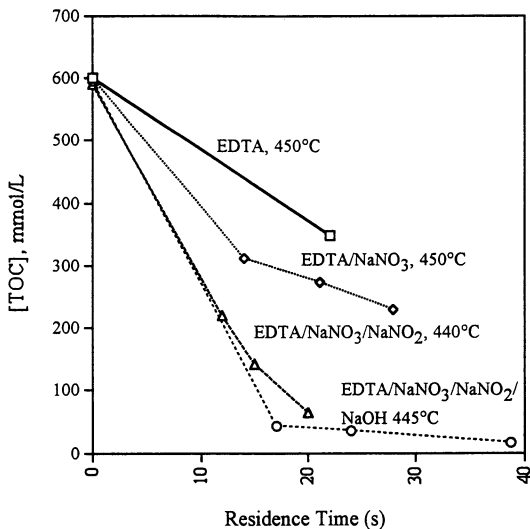


Figure 5. TOC removal as a function of residence time in the oxidation of EDTA at 440°C - 450°C . The data for EDTA alone were taken at 668 bar; other data are for 1.0-1.1 kbar. Concentrations used were 0.6 M TOC (as shown), 0.7 M sodium nitrate, 1 M sodium nitrite, and 0.7 M sodium hydroxide. Concentrations are at ambient conditions.

nitrite disappearance both occur with organic oxidation; considerably more nitrite is reacted than nitrate. The principal nitrogen-containing products were nitrogen gas, nitrite, and ammonia. Trace amounts of methylamine were detected, amounting to less than 1% of the total nitrogen recovered. Hydrogen was also produced in significant quantities. Hydrogen, ammonia, and methylamine are intermediate products of the oxidation-reduction reaction. Other experiments have demonstrated that these products are not present when reactions are carried out above 475°C at residence times greater than 20 seconds. Another feature shown in Figure 4 is that the TIC product is recovered in the effluent while the reactor is at experimental temperature and pressure. If sodium carbonate/bicarbonate exceeded their solubility at reaction temperature (465°C), they would have precipitated in the reactor and lowered the TIC detected in the effluent. The amount that is precipitated on the reactor walls is negligible. The pH in these experiments (mixtures 1-3) dropped slightly, from a feed value of 10.7 to an effluent value of 9.6, indicating only slight changes in the hydroxide concentration.

Table II. Reaction Mixtures Investigated. All mixtures are subsets of 3:1 diluted Hanford 101-SY waste simulant, as shown in Table I. Concentrations provided are at ambient conditions.

Reaction Mixture --->	1	2	3	4
[Na ₄ EDTA] ₀ (mole/L)*	0.06	0.06	0.06	0.06
[NaNO ₃] ₀ (mole/L)	0	0.7	0.7	0.7
[NaNO ₂] ₀ (mole/L)	0	0	1.0	1.0
[NaOH] ₀ (mole/L)	0	0	0	0.7
avg. P(bar)	700	1035	1040	1030
pH(feed)	10.9	10.7	10.6	13.0
Temp range (°C)	298-450	350-467	350-465	350-440

* This addition of Na₄EDTA corresponds to an ambient [TOC]₀ = 0.6 mol/L.

Figure 5 shows the rate of removal of organic for four different reaction mixtures, and demonstrates the effects of different components on the reaction. With a mixture of EDTA and water alone (no added oxidizer), there is ~40% TOC conversion in 30 seconds at 690 bar and 450°C. In this plot, TOC is displayed rather than EDTA specifically because EDTA quickly reacts to form other organics (including acetate, formate, methanol, ethanol, ethylene, methylamine, and others not identified). The fact that EDTA reacts without any added oxidizer implies that hydrolysis is a significant reaction pathway. The observed reaction products, especially the predominant products of HCO₃⁻/CO₃⁼ and formate, suggest that the carboxylic acid moieties hydrolyzed directly to carbonate. When nitrate is added to the EDTA, organic removal rates increase. When nitrite is added to the NaNO₃ and EDTA, nearly complete oxidation of the TOC occurs in 40 seconds reaction time at

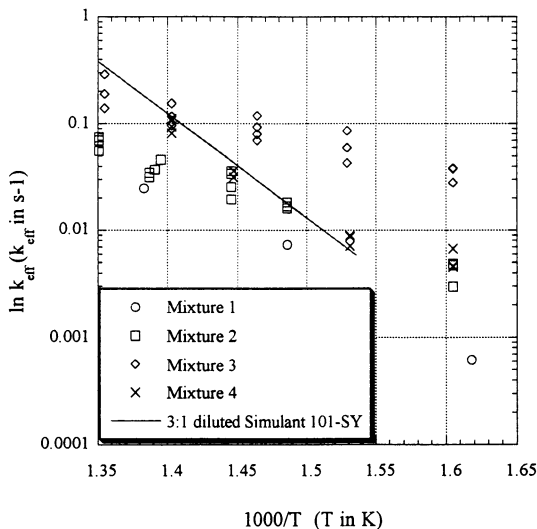


Figure 6. Effective first-order rates for TOC removal in the oxidation of EDTA. Data are shown for four different reaction mixtures, as indicated. The line is a fit obtained for the full 3:1 diluted simulant 101-SY (9). The effective rate constants for the full simulant lie approximately on the mixture 4 data set, at temperatures down to 380°C. All data are shown at 1.0 ± 0.1 kbar, except mixture 1 data which is taken at 0.67 ± 0.05 kbar.

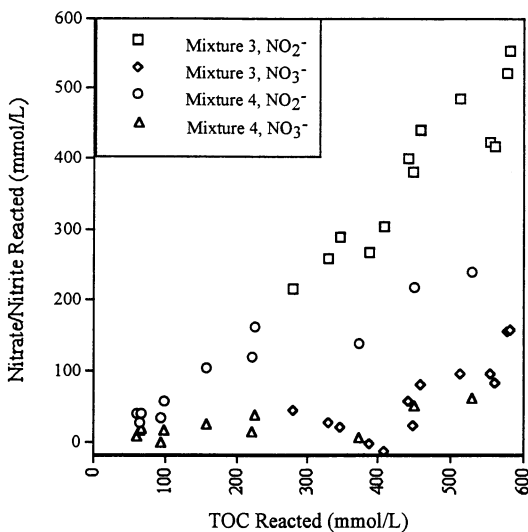


Figure 7. Nitrate and nitrite consumption, shown separately, in the oxidation of EDTA. Concentrations are at ambient conditions. See Table II for experimental conditions.

450°C. The addition of NaOH to the EDTA/NaNO₂/NaNO₃ reaction mixture causes the overall rate to decrease slightly. Each component shown in Figure 5 is present at the level found in for 3:1 diluted simulant 101-SY: EDTA at 0.06 M (TOC at 0.6 M), nitrate at 0.7 M, nitrite at 1 M, and hydroxide at 0.7 M.

The temperature dependence on organic destruction for the four simple mixtures is shown in the form of an Arrhenius plot in Figure 6. The effective first-order rate constants (k_{eff}) used in this plot were calculated from equation 2, which is analytically derived from the equation of continuity for a reacting mixture, assuming that isothermal, constant density, steady-state, and plug flow conditions apply.

$$k_{\text{eff}}(\text{sec}^{-1}) = \left(\frac{1}{\tau}\right) \ln \left(\frac{[\text{TOC}]_0}{[\text{TOC}]_{\tau}}\right) \quad (2)$$

In Figure 6, a k_{eff} value of 0.035 represents 50% organic conversion at a 30 second residence time. It is apparent from this plot that the rate for TOC removal increases when nitrate is added, increases further when nitrite is added to the nitrate, and then decreases when hydroxide is added to the mixture. The "inhibition" by sodium hydroxide decreases with increasing temperature; that is, at high temperatures the rate is the same with or without base. The figure demonstrates that this rate is strongly temperature-dependent, increasing from 0.004 sec⁻¹ at 350°C to 0.02 sec⁻¹ at 465°C. Although there is no reason *a priori* to expect Arrhenius temperature dependence for this simplified kinetic analysis, Figure 6 shows that this behavior is observed within the experimental scatter. In addition, a kinetic model obtained for the full 3:1 diluted 101-SY simulant is shown in Figure 6. These data lie near the data for the simple Na₄EDTA/NaNO₂/NaNO₃/NaOH reaction mixture, indicating that the addition of the other components shown in Table I do not substantially affect reaction kinetics.

Reaction Intermediate Production and Disappearance. As indicated in the previous discussion, the hydrothermal conversion of EDTA in the presence of nitrate/nitrite result in reaction products including H₂, N₂, N₂O, and NH₃. Due to the presence of intermediate product side-reactions and competing oxidation/hydrolysis pathways, an integrated rate expression of the form shown in equation 2 is not a completely accurate description of this complex reactive system.

Figure 7 shows the consumption of nitrate and nitrite in all experiments as a function of organic conversion. In the reaction of EDTA with nitrate, little nitrate is consumed until about 40% of the organic has disappeared. As previously suggested, the EDTA rapidly hydrolyzes before temperatures are high enough to support oxidation by NO₃⁻. With both nitrate and nitrite in the presence of hydroxide, however, the oxidizers (mainly nitrite) are consumed early in the reaction, suggesting that nitrite oxidation competes with EDTA hydrolysis at lower temperatures. The data shown in Figure 7 suggests that nitrite is a more powerful oxidizer for the EDTA hydrolyzed fragments than nitrate. The nitrite consumption is roughly a factor of five greater than the nitrate consumption.

A somewhat surprising result of these experiments was the formation of significant levels of hydrogen in the effluent. Figure 8 shows the amounts of hydrogen formed in the experiments using reaction mixtures 3 and 4. The initial EDTA concentration was 0.06 M; if all of the hydrogen bound to EDTA was

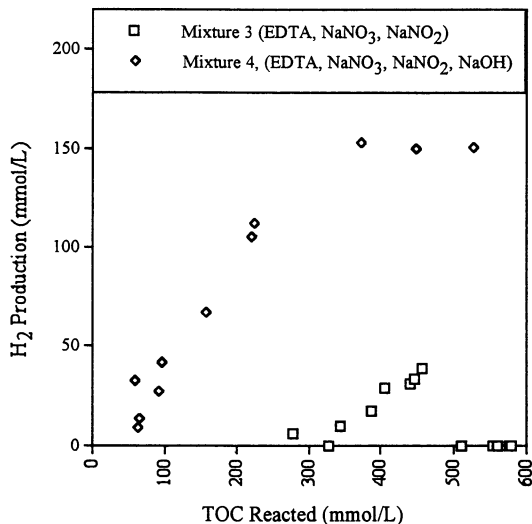


Figure 8. Hydrogen production in EDTA oxidation, with and without hydroxide. The initial TOC concentration was about 600 mmole/L, so points at the right side correspond to complete organic conversion. Hydrogen production is higher with added hydroxide, indicating a possible enhancement of EDTA hydrolysis with base. Concentrations are provided at ambient conditions.

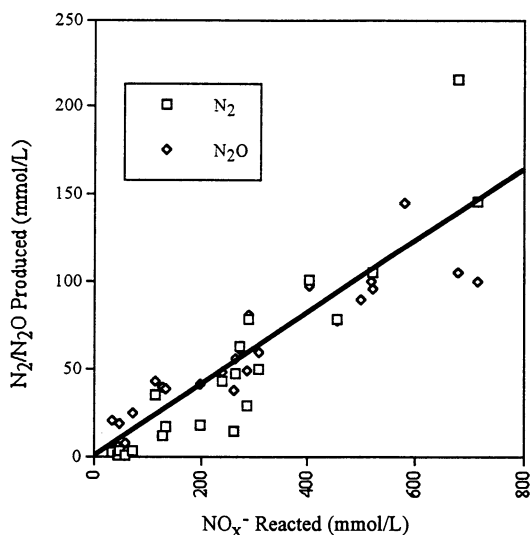
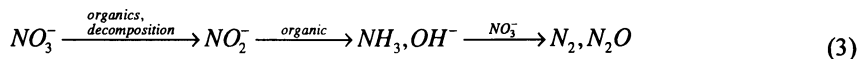


Figure 9. Nitrogen and N₂O formation in the Na₄EDTA/NaNO₂/NaNO₃ reactions. Gas concentrations are plotted versus the amount of nitrate/nitrite reacted, with both values given at ambient conditions. The line is provided to show the general trend of the data.

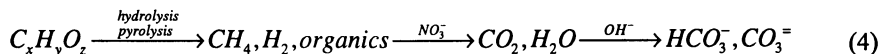
converted to H₂, the effluent concentration would be 0.36 M H₂, since the molecular formula of EDTA is C₁₀H₁₂N₂O₈⁴⁻. The figure shows that a substantial fraction of the hydrogen, up to 0.15 M, was converted to H₂. It appears likely that there is an additional source of hydrogen besides EDTA, and it must be water. If hydrolysis of the organic occurs, hydrogen is "added" to the system and can explain the high yields of H₂. Hydrogen production increases with temperature and degree of organic conversion, reaching a peak near 450°C. At higher temperatures and greater organic conversion, less hydrogen was observed, and in the absence of NaOH, all of the hydrogen produced is subsequently oxidized. The slower oxidation rate of organic matter in the presence of hydroxide conceivably results in pyrolysis/hydrolysis reaction rates eclipsing redox reaction rates, and resulting in higher H₂ production levels observed for this mixture. The H₂ production trends provide further evidence that hydrolysis is a significant reaction pathway for EDTA in hydrothermal systems.

The principal nitrogen products of nitrate/nitrite reduction are N₂ and N₂O. Data from experiments using nitrate and nitrate/nitrite as the oxidizers are shown together in Figure 9. There is a wide variability in the gas concentrations. The data appear to cluster about a line in the plot with slope of about 0.2. Thus, for every five moles of nitrate/nitrite reacted, one mole of N₂ and one mole of N₂O are formed. Other studies on similar mixtures have shown that N₂O can also be reduced at elevated temperatures to form N₂ (9). Most of the remaining nitrogen forms ammonia. Figure 10 shows effluent NH₃ concentrations as a function of the amount of organic reacted. Ammonia is volatile in solution; although zero-headspace sample vials minimized exposure to air, some volatilization loss could have occurred before analysis. Ammonia can be formed either from EDTA-bound nitrogen or hydrogenation of nitrate/nitrite, and it reacts with nitrate/nitrite to form N₂ and N₂O (10). When viewed as a function organic conversion, it appears that NH₃ increases with the amount of TOC oxidized. At elevated TOC conversions, NH₃ conversion decreases, likely due to reaction with nitrate/nitrite. At the lower TOC conversions, the data indicate a production rate of roughly 0.3 moles NH₃ per mole of NO₃⁻/NO₂⁻ consumed, with possibly higher values in the presence of hydroxide.

Nitrogen/Organic Reaction Pathways for these Simple Mixtures. The results presented here are in accord with previous nitrate reduction experiments. In studies of the nitrate/methanol reaction (4), NO₂⁻, NH₃, N₂, and N₂O were observed as reaction products. Similar reaction products have been observed with using acetic acid as a reducing agent (11). The nitrogen chemistry appears to behave according to the following scheme:



This is only schematic; nitrate could be transformed to ammonia in a single step. The reaction of ammonia with nitrate to form N₂ has been discussed thoroughly elsewhere (12). Organic nitrogen may form organic amines (i.e., methylamine, detected in trace amounts) and ammonia, before conversion to N₂. The carbon chemistry appears to be as follows:



The first step in the organic decomposition involves the breakdown of complex organic compounds through pyrolysis or hydrolysis, and could result in a variety of smaller organic fragments. These fragments might include alcohols, carboxylic acids, and others. As temperature increases in the reaction mixtures, nitrite and nitrate oxidation compete with hydrolysis pathways, to form oxygenated organic intermediates and carbon dioxide; carbon dioxide is converted via proton transfer reactions to carbonate/bicarbonate upon reaction quenching.

Kinetics of Simple Mixtures: Scaling to the SPSR. One important question regarding the kinetics of bench-scale systems is their applicability to higher capacity, differently dimensioned, non-isothermal reactors, which are more apt to be used industrially. Several experiments were performed on the small pilot-scale reactor (SPSR) to determine if the bench-scale reactor kinetics were observed using this system. The SPSR had a flow throughput approximately 10 times greater than the BSR, was not isothermal over its 8.23 meter length, and had an inner diameter 2.25 times greater than the BSR.

Comparison between the two reactors first required the development of a kinetic model to apply to the SPSR. Because of the complexity of these "simple" mixtures, rigorous mechanistic based modeling is not justifiable. However, it has been found that several different approaches can be used to provide an empirical data fit which is valid over the range of experimental conditions studied. One such approach, as implied by Figure 6, is an estimation of Arrhenius rate constants using a pseudo-first order (in TOC conversion) rate constant. This and other methods for modeling these data sets are discussed elsewhere (9).

One approach that has given reasonable results is to lump the oxidants (NO_3^- and NO_2^-) as an NO_x^- oxidant, and assume a reaction which is first order in both TOC and NO_x^- . The analytical form of this solved rate equation ($d[\text{TOC}]/dt = -k[\text{TOC}][\text{NO}_x^-]$) is shown by equation 5:

$$X_{\text{TOC}} = \frac{1 - \exp(-k\tau[\text{TOC}]_o(\theta - b))}{1 - b/\theta * \exp(-k\tau[\text{TOC}]_o(\theta - b))} \quad (5)$$

In this equation, k is the Arrhenius rate constant in $\text{L/mol}\cdot\text{s}$, τ is the residence time in seconds, θ is the ratio of $[\text{NO}_x^-]$ to $[\text{TOC}]$ in the feed solution, and b is the stoichiometric coefficient relating the conversion of TOC (X_{TOC}) to the conversion of NO_x^- ($X_{\text{NO}_x^-}$). Equation 4 can be used to fit experimental data by varying the Arrhenius parameters A and E_a and the stoichiometric coefficient for NO_x^- , b , so that the normal χ^2 variable is minimized. To optimize the model for both TOC and NO_x^- conversions, the sum of χ^2 variables for TOC and NO_x^- data sets are minimized. The χ^2 variable is defined by equation 6.

$$\chi^2 = \sum_{i=1\text{to}N} \frac{[X_{\text{model}} - X_{\text{expt}}]^2}{N - K - 1} \quad (6)$$

In equation 6, N is the number of experiments and K is the number of variables optimized, 3. The χ^2 statistic shown in equation 6 is unitless. Performing this

analysis on the Na₄EDTA/NaNO₃/NaNO₂/NaOH data set (all BSR data) results in a rate equation shown by equation 7, which produced χ^2 values of 0.0044 and 0.0006 for NO_x⁻ and TOC conversion data, respectively.

$$-\frac{d[TOC]}{dt} = -0.68 \frac{d[NO_x^-]}{dt} = 1.51 \times 10^{10} \frac{L}{mol * s} \exp\left[-\frac{154.0kJ}{RT}\right] [TOC][NO_x^-] \quad (7)$$

Using this model, temperature profiles from several SPSR experiments were used to predict TOC and NO_x⁻ conversions. Due to the non-isothermal nature of the SPSR, the reactor was modeled as twenty-seven isothermal (one segment per linear foot), plug-flow reactors in series. Average temperatures over each foot of the reactor were used as the reaction temperatures in the plug-flow reactor sections. Figure 11 shows experimentally measured TOC conversions as a function of model-predicted conversions for both reactors. The figure demonstrates that the model developed on the bench-scale reactor accurately predicts TOC conversions for a tenfold increase in reactor scale. In addition, the model developed using the Na₄EDTA/NaNO₃/NaNO₂/NaOH mixture represented mixtures with cumulative additions of Na₂CO₃ and NaAlO₂, in the concentrations shown in Table I. Simulant TOC conversions were also predicted reasonably well using this simple mixture model. Although not shown here, NO_x⁻ conversion trends show good agreement between model and experiment. The ability to correlate bench-scale results with those of a non-isothermal reactor with different flow velocities and different tubing dimensions demonstrates the predictive value of this simple kinetic model. In addition, cumulative additions of other simulant components did not appear to change reaction kinetics in the SPSR, indicating that the simple mixture would suffice for determining kinetic parameters for the purpose of treating 3:1 diluted simulant 101-SY.

Pressure Effect on Organic/Nitrate Reactions. Because these experiments have been performed at pressures not commonly encountered in the hydrothermal processing literature, some simple studies were performed to compare the effect of pressure on NO_x⁻/organic reactions. For these studies, a simple reaction mixture of NaNO₃/CH₃COOH was studied in dilute concentrations (< 0.01 M). These concentrations provided conditions where NaNO₃ has been demonstrated to be soluble (12). Figure 12 shows preliminary results from these experiments. As observed in the figure, there appears to be little or no pressure effect on this reaction in the 400 to 1000 bar range; the reaction is observed to increase in rate at a pressure of 282 bar. The fact that the lower pressure leads to increased reaction rates indicates a possible mass transfer rate limitation, caused by decreased molecular diffusion coefficients, at the higher pressures. Another possible explanation is that the volume of activation for the reaction changes dramatically between 282 and 427 bar, but remains relatively constant from 427 bar to 999 bar, where conversions are nearly indistinguishable.

In addition, a comparison is shown in Figure 12 between nitrate oxidation of acetic acid and hydrogen peroxide oxidation, adopted from the first order acetic acid model suggested by Lee (14). The Lee model was developed at temperatures from 415°C to 525°C at pressures up to 315 bar. As shown in the figure, nitrate appears to

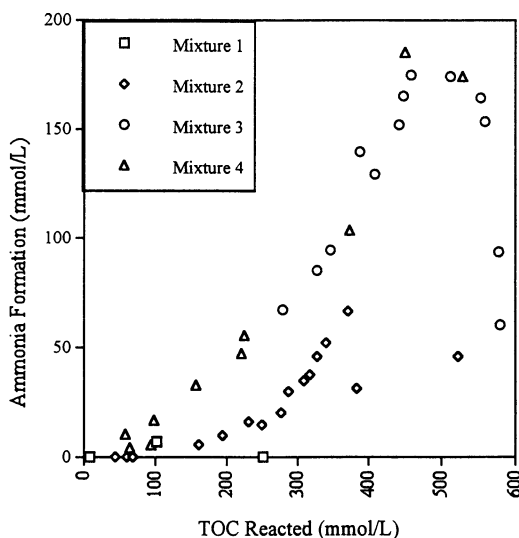


Figure 10. Ammonia formation in the oxidation of EDTA. Experimental conditions provided in Table II. Concentrations are at ambient conditions.

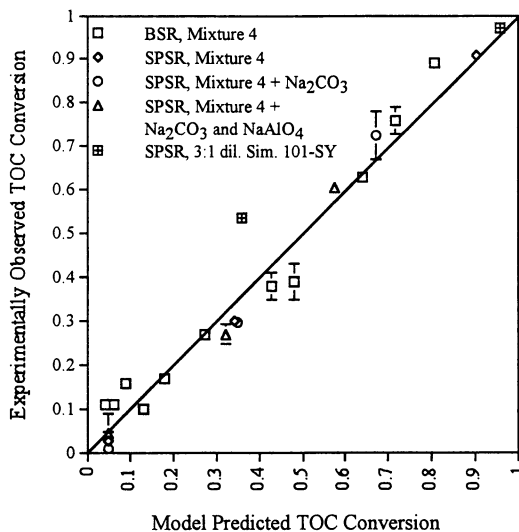


Figure 11. Experimentally Observed versus Model Predicted TOC Conversions for BSR and SPSR data. Error bars represent standard deviations of conversions; model developed for $\text{Na}_4\text{EDTA}/\text{NaNO}_3/\text{NaNO}_2/\text{NaOH}$ data set (Mixture 4) on the BSR.

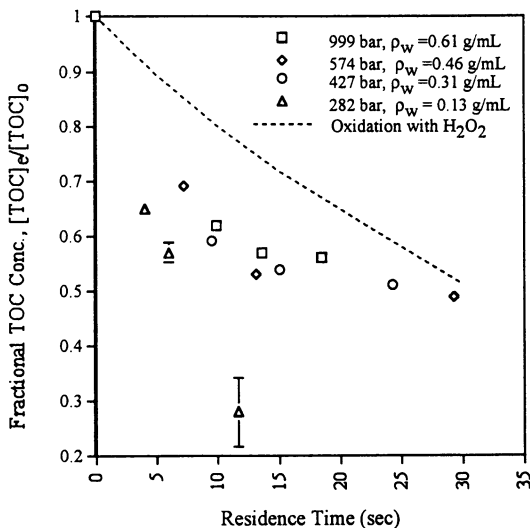


Figure 12. Pressure Effects on Acetic Acid/ NaNO_3 Reaction Mixtures.

The temperature for these experiments was $450 \pm 1^\circ\text{C}$; feed concentrations were 50 ± 2 and 100 ± 5 mM for NaNO_3 and TOC, respectively (~ 1 mol $\text{NaNO}_3/1$ mol CH_3COOH). The line shows the model predicted conversion for acetic acid conversion using H_2O_2 as an oxidant (14). Error bars are 95% confidence intervals.

oxidize acetic acid at a more rapid rate than hydrogen peroxide; although the rate predicted by the H_2O_2 oxidation model is for acetic acid disappearance (as opposed to TOC), it was found in both studies that greater than 95% of the organic carbon recovered was in the form of acetic acid.

Conclusions

This research illustrates reaction pathways for organic oxidation using nitrate and nitrite in simple mixtures. Results indicate that nitrite/nitrate are efficient oxidizers for EDTA in mixtures relevant to the Hanford Tank Waste problem. Reaction by-products are generally benign, including N_2 and N_2O gases and $\text{HCO}_3^-/\text{CO}_3^{2-}$. Some undesirable reaction intermediates are produced at low temperature, short residence time conditions (CH_3NH_2 , H_2 , NH_3), but are reacted to benign products at higher temperature, longer residence time conditions. Nitrite was shown to be a more efficient oxidizer for EDTA and EDTA hydrolysis products than nitrate; the presence of added sodium hydroxide was shown to impede the oxidation rate of both constituents. Hydrolysis/pyrolysis reaction paths were shown to be major conversion mechanisms for the EDTA; these reactions resulted in the formation of reduced products, such as H_2 and CH_4 . Results obtained on the bench-scale reactor for the $\text{Na}_4\text{EDTA}/\text{NaNO}_3/\text{NaNO}_2/\text{NaOH}$ mixture were modeled using a simple 2nd order rate expression, which accurately predicted conversions obtained on a non-

isothermal, small pilot-scale reactor. It was also demonstrated that reaction kinetics observed for this simple mixture were essentially the same as observed for more complex mixtures up to the full 3:1 diluted tank waste simulant. Finally, pressure effects of a simple reaction mixture, $\text{NaNO}_3/\text{CH}_3\text{COOH}$ were investigated. Preliminary results indicate no substantial pressure effect on the reactions above 400 bar. Thus, the sensitivity of reaction kinetics to pressure fluctuations in nitrate oxidation systems is expected to be small in the 400 bar to 1.1 kbar range.

Acknowledgements. The authors would like to acknowledge the Hanford Tank Waste Remediation Systems Program (TWRS) for research funding. Dale Counce, Rhonda McInroy, Pat Trujillo, Mike Sedillo and Carol Monaghan provided analytical and technical support for this work. K. Patterson would like to acknowledge the Chemistry Department at Furman University, for providing her the opportunity for summer research at LANL.

Literature Cited

1. Tester, J.W., et al. in *Emerging Technologies in Hazardous Waste Treatment* Ed. W. Tedder. ACS Symp. Ser. 514, ACS: Washington D.C.: 1992.
2. Shanableh, A., and Gloyna, E.F., Wat. Sci. Tech. **1991**, *23*, 389.
3. Harradine, D.M., Buelow, S.J., Dell'Orco, P. et al. Haz. Waste/Haz. Mat., **1993**, *10*, 233.
4. Dell'Orco, P.C., Foy, B.F., Robinson, J.R., and Buelow, S.J. Haz.Waste/Haz. Mat., **1993**, *10*, 221.
5. Foy, B.R., Dell'Orco, P.C., Wilmanns, E., et al. in Proc. 12th Int'l Conf. on the Prop. of Water and Steam, September, 1994.
6. T.M. Hohl, Westinghouse Hanford Corp. Report, WHC-SD-WM-TI-549 Rev. 0, March, 1993.
7. Anderson, G.K., D. Allen, T. Butenhoff, M. Goemans, and K. Knutsen, Los Alamos Unclassified Report, LA-UR-94:3352, September, 1994.
8. Dell'Orco, P.C. Los Alamos Unclassified Report, LA-UR-94-1989, May, 1994b.
9. Foy, B.R., Dell'Orco, P.C., Breshears, D., et al. Los Alamos Unclassified Report, LA-UR-94:3174, September, 1994.
10. Robinson, J., B. Foy, P. Dell'Orco, et al. Los Alamos Unclassified Report, LA-UR-93-456, February, 1993.
11. Foy, B.R. et al. Los Alamos Unclassified Report, LA-UR-93-3147, September, 1993.
12. Dell'Orco, P.C. Ph.D. Thesis, Dept. of Civil Eng., The Univ. of Texas at Austin, 1994.
13. Dell'Orco, P.C., et al. Los Alamos Unclassified Report, LA-UR-92-3359, September, 1992.
14. Lee, D.S. Ph.D Thesis, Dept. of Civil Eng., The Univ. of Texas at Austin, 1990.

RECEIVED July 17, 1995

Chapter 13

Methylene Chloride Oxidation and Hydrolysis in Supercritical Water

Philip A. Marrone¹, Russell P. Lachance¹, Joanna L. DiNaro¹,
Brian D. Phenix¹, Jerry C. Meyer^{1,3}, Jefferson W. Tester¹,
William A. Peters¹, and K. C. Swallow²

¹Chemical Engineering Department and Energy Laboratory,
Massachusetts Institute of Technology, 77 Massachusetts Avenue,
Room E40-455, Cambridge, MA 02139

²Department of Chemistry, Merrimack College, 315 Turnpike Street,
North Andover, MA 01845

Hydrolysis and oxidation of methylene chloride (CH_2Cl_2) in supercritical water were carried out in a tubular plug flow reactor over the range of 450 - 600°C, 4 - 9 seconds reactor residence time, and sub- to superstoichiometric $\text{O}_2/\text{CH}_2\text{Cl}_2$ feed ratios, all at a pressure of 246 bar. Major products of both hydrolysis and oxidation were carbon monoxide (CO), carbon dioxide (CO_2), formaldehyde (HCHO), methanol (CH_3OH), hydrochloric acid (HCl), and molecular hydrogen (H_2), with small amounts of methane (CH_4) above 562°C. Trace quantities of one and two carbon chlorinated hydrocarbons were also detected. CH_2Cl_2 conversions ranged from 26±9% to 99.9±0.1% over the conditions explored. Conversion under hydrolysis conditions was very close to that under oxidation conditions. The primary effect of O_2 was only to change the product distribution to more CO and CO_2 and less HCHO, CH_3OH , and H_2 relative to that observed under hydrolysis. Significant corrosion of the Hastelloy C-276 preheater tubing was observed, most likely caused by the presence of aggressive Cl^- ions. The experimental evidence suggests a reaction network for CH_2Cl_2 oxidation that involves reaction with water as a first step to produce primarily HCl and HCHO (and CH_3OH at higher temperatures), which are then in turn further oxidized to CO and CO_2 .

Supercritical water oxidation (SCWO) is a promising technology proposed for the destruction of hazardous organic wastes. Above its critical point (374°C, 221 bar), water exhibits properties similar to those of a nonpolar rather than polar solvent, primarily due to the effect of decreases in hydrogen bonding and density that occur

³Current address: U.S. Military Academy, West Point, NY 10996

0097-6156/95/0608-0197\$12.00/0
© 1995 American Chemical Society

near and above the critical point (1). The result is that nonpolar organic compounds and oxygen exhibit complete miscibility in supercritical water, while many polar inorganic salts are virtually insoluble. In the single homogeneous phase formed, oxidation of organic compounds with oxygen is generally rapid and complete to CO_2 and H_2O . Organic heteroatoms such as halogens, sulfur, or phosphorus are converted to their corresponding mineral acids, while nitrogen is converted primarily to N_2 with small amounts of N_2O . A more detailed description of the SCWO process can be found in the reviews by Modell (1), Thomason et al. (2), and Tester et al. (3).

The high stability and toxicity characteristic of many chlorinated organic compounds has led to much recent interest in developing effective means for both their disposal and the cleanup of natural waters and soils contaminated with these compounds. Although landfill and incineration have been used in the past, landfill regulations are becoming increasingly more stringent and incineration can result in equally toxic byproducts such as dioxins (4). SCWO, however, has been shown to be effective at destroying chemically stable compounds such as polychlorinated aromatics and other lower molecular weight compounds, with greater than 99.99% destruction achieved at temperatures of 550-650°C and a residence time of 1 minute or less. (3, 2, 5). Examples of compounds successfully destroyed under these conditions include polychlorinated biphenyls (PCBs), pesticides, chlorinated dioxins, chlorobenzenes, trichloroethylene, and chlorinated methanes.

Although destruction efficiency studies are useful, they typically give little or no quantitative information about the rate of organic destruction or any mechanistic information. Kinetic studies under well defined conditions of temperature, pressure, and composition provide data and correlations useful for the design and optimization of effective commercial-scale SCWO processes. Thus far, however, kinetic studies on the oxidation of chlorinated organic compounds in supercritical water have focused mainly on chlorinated aromatics. Examples include p-chlorophenol, in a flow reactor at 310-400°C and 5-60 s residence times (6); 1,4-dichlorobenzene, with a V_2O_5 catalyst in a batch reactor at 343-412°C and up to 60 min. residence times (7); 2,4-dichlorophenol, using both O_2 and H_2O_2 as oxidants (8); and 2-chlorophenol in a plug flow reactor at 300-420°C and 4-70 s residence times (9).

The present paper provides results of recent experimental determinations of conversion, product spectrum and yields, and global reaction pathways for hydrolysis and oxidation of methylene chloride (CH_2Cl_2) in supercritical water. Because of its nonflammable nature, low boiling point, and excellent solvent power for nonpolar compounds, methylene chloride has been widely used commercially in the past, such as in metal cleaning and degreasing, liquid extraction, manufacture of paint strippers and adhesives, as a foaming or aerosol agent, and as a process solvent in the manufacture of pharmaceuticals and fine organic chemicals (10). Today its use is becoming increasingly restricted because of concern over its health and environmental effects. Nevertheless, CH_2Cl_2 remains an excellent choice for study as a representative chlorinated waste. Further, its chemical structure contains only one chlorine functionality - two indistinguishable C-Cl bonds. Thus CH_2Cl_2 is also a good model compound for study of the chemistry of the C-Cl bond in supercritical water.

We are unaware of any prior kinetic studies of methylene chloride in supercritical water. While MODAR, Inc. (2) and Sandia National Laboratories (11) have experimentally studied SCWO of a number of chemicals including CH_2Cl_2 , their focus was on obtaining high destruction and removal efficiencies, not kinetic data. There have been studies, however, of both catalytic combustion and of hydrolysis of CH_2Cl_2 in high temperature (but subcritical) water. Catalytic combustion of CH_2Cl_2 in air has been performed by a number of researchers using a variety of catalysts (12-15). Each study determined conversions and resulting product distributions as

affected by the specific catalyst used. In a classic study more pertinent to the work in this paper, Fells and Moelwyn-Hughes (16) investigated the kinetics of CH₂Cl₂ hydrolysis in water under acidic and alkaline conditions for temperatures from 80 to 150°C. They found that reaction of CH₂Cl₂ with water under acidic conditions followed first order kinetics in CH₂Cl₂, and resulted in the formation of formaldehyde and hydrochloric acid. Under alkaline conditions, CH₂Cl₂ was found to react not only with water but also with hydroxide ion, which in turn resulted in a number of additional reactions. The reaction of CH₂Cl₂ with OH⁻ was found to be first order in each reactant and second order overall. In similar studies, Chuang and Bozzelli (17) have investigated the vapor phase hydrolysis of chloroform at 611 to 1050°C and 1 atm; Gaisinovich and Ketov (18) investigated hydrolysis of carbon tetrachloride at 350-550°C; and Jeffers et al. (19) have examined hydrolysis of a number of chlorinated methanes, ethanes, ethenes, and propanes over the range of 0-180°C and pH values of 3-14.

Earlier MIT work on SCWO of CH₂Cl₂ was reported by Meyer (20). Because of various experimental difficulties encountered, this early study led to significant improvements in sampling techniques and analytical capabilities. These developments have in turn led to an enhanced overall understanding of the reaction of CH₂Cl₂ in supercritical water, as presented in this current paper.

Experimental and Analytical Methods

The experimental system used in this study is shown in Figure 1 and is described in greater detail by Meyer (20). A brief summary of experimental procedures used for CH₂Cl₂ experiments follows. A dilute feed solution of oxygen dissolved in ambient temperature water was prepared by mixing O₂ gas under a fixed pressure with deionized water in a 3 L, high pressure saturator until equilibrium was achieved. Mixing was accomplished by pumped recirculation of the saturator liquid. The methylene chloride feed solution was prepared in a fume hood by adding pure CH₂Cl₂ by syringe to a 2 L volumetric flask of deionized water. Following vigorous mixing to solubilize the CH₂Cl₂ (the amount added was always an order of magnitude below its solubility limit in water at STP), the resulting single phase, dilute solution was then loaded into a reservoir similar to that containing the oxygen feed (denoted as the organic saturator in Figure 1) and pressurized with 10 psi of helium. The organic and oxygen feed solutions were pumped separately up to approximately 246 bar through a high pressure feed pump. For hydrolysis experiments, pure deionized water was pumped in place of the oxygen solution. The only physical change to the system compared to previous studies was the installation of a low pressure valve on the organic feed line just before the feed pump to sample the aqueous CH₂Cl₂ feed as close to the reactor as possible for accurate determination of CH₂Cl₂ feed concentrations. All pressurized components of the reactor system at ambient temperature were contained behind 1 - 1.3 cm thick Lexan shields.

The preheater fluidized sandbath was not turned on for these experiments to help minimize the time spent by the CH₂Cl₂ at high temperature before entering the reactor. Thus both feeds entered the main reactor fluidized sandbath at ambient temperature and passed through separate lengths of Hastelloy C-276 preheater coils of approximately 3 m length and 0.159 cm O.D. x 0.108 cm I.D., where they were heated to reaction temperature. The preheated feeds were then combined in a Hastelloy C-276 mixing tee at the reactor inlet. The reactor consisted of 4.71 m of coiled Inconel 625 tubing of dimensions 0.635 cm O.D. x 0.171 cm I.D. The operating conditions were always chosen to ensure isothermal, plug flow behavior in the reactor (the measured temperature difference between reactor inlet and exit was usually ≤ 3°C and never > 6°C). Both sandbaths were contained within a fume hood. After exiting the reactor, the effluent passed through a countercurrent shell and tube

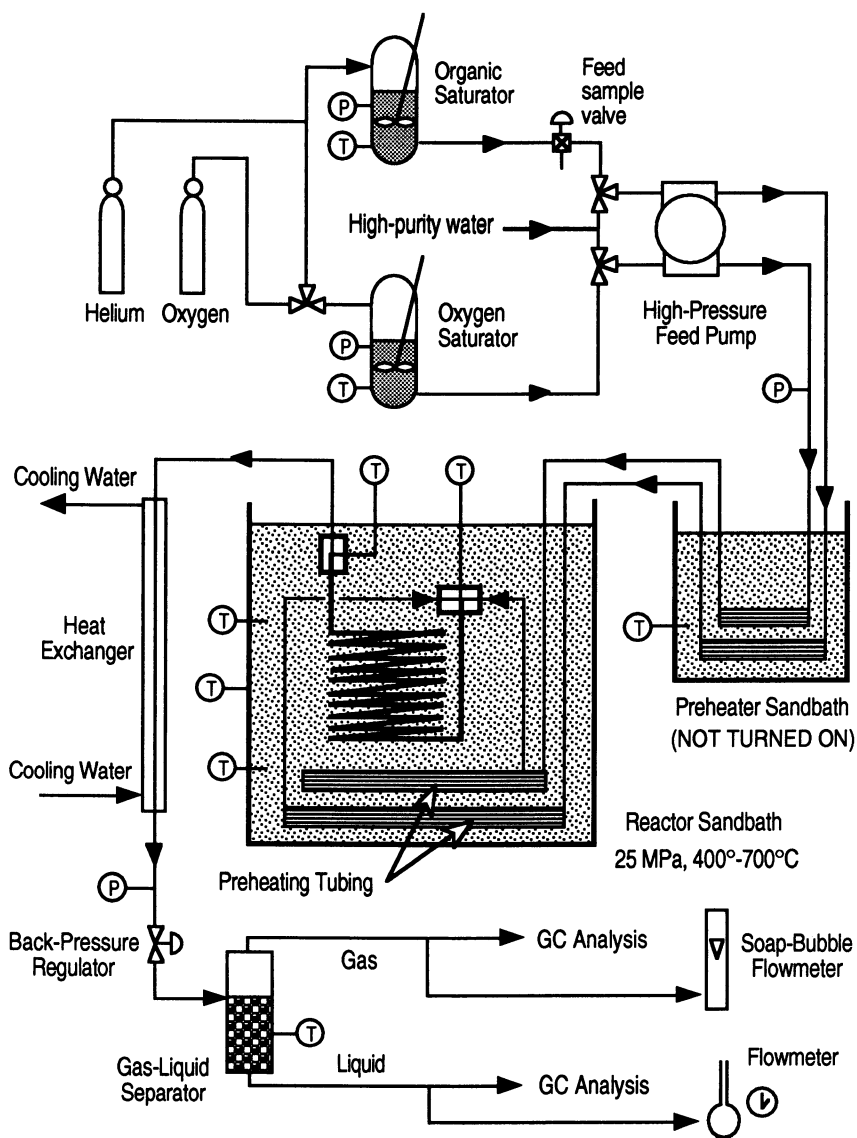


Figure 1. Schematic of experimental plug flow reactor system.

heat exchanger followed by a back pressure regulator valve to reduce temperature and pressure to ambient conditions. The resulting two-phase effluent then passed through a gas-liquid separator column. Liquid and gaseous effluent flows were each measured and sampled for product analysis. The gaseous effluent was ultimately vented to a fume hood. At the end of every experiment, each saturator was vented directly to the fume hood separately and slowly, so as not to mix any O₂ and CH₂Cl₂ vapor.

Gaseous effluent compositions were determined primarily by gas chromatography (GC). A Hewlett Packard 5890 Series II GC with a thermal conductivity detector (TCD) and helium carrier gas was used to detect, identify, and quantify O₂, N₂, CO, CO₂, CH₄, C₂H₆, C₂H₄, and C₂H₂. Two packed columns, 80/100 mesh Porapak T and 60/80 mesh molecular sieve 5A, were used together to provide reliable and clean separations of components. The columns were connected in series through an air actuated switching valve that allowed reversal of column order. A Perkin Elmer Sigma 1B GC also with a TCD detector but nitrogen carrier gas was used to detect and quantify H₂ and He. Chlorinated hydrocarbons in the vapor phase, including CH₂Cl₂, were analyzed using a second Hewlett Packard GC with an electron capture detector (ECD) and a DB-624 capillary column from J&W Scientific Inc. The carrier gas was helium, with nitrogen used as makeup gas to the detector. The presence of any formaldehyde (HCHO), methanol (CH₃OH), or chlorine gas (Cl₂) in the vapor phase was checked by allowing the gaseous effluent to flow through a glass impinger into a vial of water of known volume for a fixed period of time. The water solution was then analyzed for HCHO and CH₃OH as detailed below. Cl₂ was analyzed for by using the o-toluidine colorimetric test.

A variety of analytical techniques were employed for analysis of liquid phase products. Methylene chloride concentrations in feed and effluent samples were determined by GC using either an electrolytic conductivity (Hall) detector (ELCD) in a Tracor 585 GC or by a flame ionization detector (FID) in one of the Hewlett Packard GCs (both HP GCs were also equipped with FID detectors). A DB-624 capillary column with helium carrier gas was used in the Tracor GC, while a DB-1 capillary column (also from J&W Scientific) and helium carrier gas with nitrogen makeup was used in the Hewlett Packard GC. Methanol was also analyzed by FID detection in the other Hewlett Packard GC using an SPB-1 capillary column (Supelco, Inc.) with helium carrier gas and nitrogen makeup. A colorimetric test known as the chromotropic acid method (21-23) was used to detect formaldehyde. Addition of a 1% solution of chromotropic acid in concentrated sulfuric acid to aqueous formaldehyde, in the presence of excess sulfuric acid, gives a violet color. The intensity of color is proportional to the original formaldehyde concentration, which can be quantified by a calibrated spectrophotometer. A Shimadzu UV160U spectrophotometer was used for this purpose at a wavelength of 580 nm. HCl concentrations were determined with a chloride specific ion electrode (Orion Research, Inc.). No ions that would be expected to interfere with the electrode's operation were present in effluent samples. All GCs and other analytical equipment were calibrated regularly using appropriate gaseous or liquid solution standards.

Experiments Performed

A total of 66 experiments were performed in this study, with 23 being under hydrolysis (no added oxygen) conditions. The experiments were all carried out at a fixed pressure of 246 bar, and can be divided into two categories: temperature variation runs, and reactor residence time and concentration variation runs. For the temperature variation runs, experiments were conducted over a temperature range of 450 - 600°C (each one isothermal) at a fixed reactor residence time of 6.0 s and fixed CH₂Cl₂ feed concentration between 0.7 - 1.0x10⁻³ mol/L (under reaction conditions)

Table I. Conditions for Reactor Residence Time and Concentration Variation Experiments (all at 550°C, 246 bar)

Group #	Experimental Runs in Group	[O ₂] ^a (10 ⁻³ mol/L)	[CH ₂ Cl ₂] ^b (10 ⁻³ mol/L)	Feed Ratio ^c	Feed Conditions	Reactor Residence Time Spanned (sec.)
1	6	1.08	0.84	1.3	stoichiometric	4 - 9
2	6	0.58	0.49	1.2	stoichiometric	4 - 9
3	3	2.08	0.80	2.6	superstoichiometric	4,6,8
4	3	0.56	0.24	2.3	superstoichiometric	4,6,8
5	6	0.56	0.84	0.7	substoichiometric	4 - 9

^a Average inlet O₂ concentration; ^b Average inlet CH₂Cl₂ concentration; ^c Feed ratio = [O₂]₀/[CH₂Cl₂]₀

for both hydrolysis and oxidation. Calculated feed ratios (O_2/CH_2Cl_2) for oxidation runs were just above stoichiometric (based on complete oxidation of CH_2Cl_2 to CO_2), ranging from 1.1 to 1.5. Feed ratios for hydrolysis runs were two orders of magnitude less at values of 0.02 - 0.04, which unfortunately were not zero due to residual O_2 in the deionized water used in our experiments. To measure the amount of CH_2Cl_2 breakdown in the organic feed preheater coil, two hydrolysis runs, at 450°C and 575°C, were performed with the reactor replaced by a 0.4 m length of stainless steel tubing. All other run operating conditions were kept the same as that for the corresponding run with the reactor in place.

Five groups of reactor residence time and concentration variation runs, shown in Table I, were performed under oxidation conditions only. Reactor residence times ranged from 4.0 to 9.0 s at a fixed temperature of 550°C. Reactant concentrations were varied both proportionally (to maintain a constant feed ratio) and independently in these runs to explore effects of relative and absolute amounts of each reactant on the reaction rate. Conditions for these runs ranged from sub- to superstoichiometric, with O_2 concentrations ranging from $0.5\text{--}2.1 \times 10^{-3}$ mol/L and CH_2Cl_2 concentrations ranging from $0.24\text{--}0.9 \times 10^{-3}$ mol/L under reaction conditions.

Kinetics Results

Effects of Temperature Variation. From 450 to 600°C, CH_2Cl_2 conversions varied between $26 \pm 9\%$ and $91 \pm 1\%$ under hydrolysis conditions, and between $30 \pm 9\%$ and $99.9 \pm 0.1\%$ (complete conversion) under oxidation conditions (see Figure 2). Complete conversion for oxidation occurred by 563°C. Noteworthy is the observation that hydrolysis and oxidation conversions are the same to within experimental error, except at a few of the high temperatures. This behavior is unusual compared to that observed for most other model compounds studied such as H_2 , CO , CH_3OH , and CH_3COOH , where the presence of oxygen resulted in much greater conversions than that observed in its absence (24-30, 8).

This close agreement of hydrolysis and oxidation conversions suggests that oxygen does not play a significant role in the initial breakdown of methylene chloride in supercritical water. Thus the global kinetics for CH_2Cl_2 destruction should be zero order in O_2 concentration. This lack of oxygen dependence is consistent with behavior frequently observed for the oxidation of other model compounds in supercritical water, although for different reasons. In those cases, O_2 does not participate directly in any rate limiting steps of the elementary reaction network, even though it must be present for the reaction to occur. In the case of CH_2Cl_2 , however, a zero order O_2 dependence apparently results because O_2 is not needed at all for the initial breakdown of CH_2Cl_2 to HCl.

Effects of Residence Time and Feed Concentration Variation. Over the complete range of reactor residence times, reactant concentrations, and feed ratios studied, conversions ranged from a minimum of $55 \pm 5\%$ to a maximum of $97 \pm 2\%$. Note that experimental run groups 1, 3, and 5 (Table I) together correspond to runs where the methylene chloride feed concentration was held constant while oxygen feed concentration was varied from sub- to superstoichiometric conditions. Figure 3 shows a plot of conversion versus reactor residence time for these groups of runs. Also included for comparison is one hydrolysis data point at 6 seconds reactor residence time and 550°C, which had the same CH_2Cl_2 feed concentration as the other points and can be considered the limiting case of substoichiometric conditions. As one might expect, conversion increases with increasing reactor residence time in all cases. Most data points for the same reactor residence time fall well within experimental error of each other, indicating again that conversion is essentially the same regardless of the relative amount of O_2 initially present.

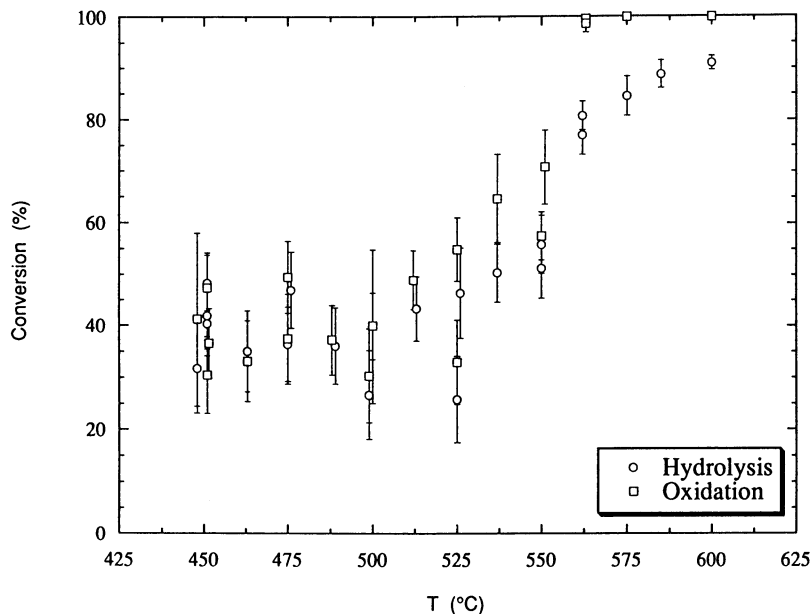


Figure 2. Graph of CH_2Cl_2 conversion vs. temperature for hydrolysis and oxidation. All data at 246 bar and 6 seconds reactor residence time. Error bars indicate 95% confidence intervals.

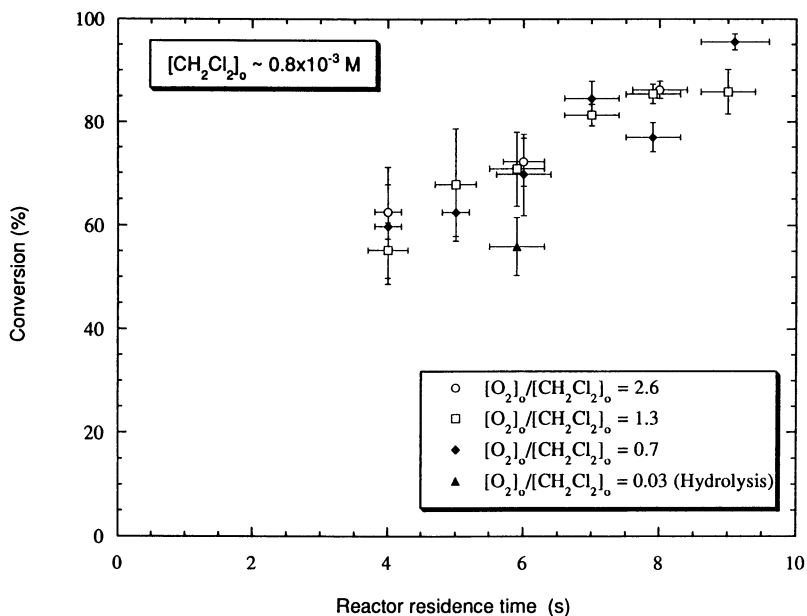


Figure 3. Graph of CH_2Cl_2 conversion vs. reactor residence time at constant CH_2Cl_2 feed concentration. All data at 246 bar and 550°C.

Experimental run groups 2, 4, and 5 correspond to runs where the oxygen feed concentration was held constant while methylene chloride feed concentration was varied from sub- to superstoichiometric conditions. Figure 4 shows a graph of conversion versus reactor residence time for these run groups. In contrast to Figure 3, there appears to be a greater difference between the superstoichiometric and stoichiometric data points, which practically overlap each other, and the substoichiometric data points, which all exhibit consistently lower conversions. Comparison to Figure 3 also shows that the superstoichiometric and stoichiometric conversion values achieved by lowering the CH₂Cl₂ feed concentration (Figure 4 runs) are higher than those achieved by raising the O₂ feed concentration (Figure 3 runs).

Figure 5 is a plot of data from experimental run groups 1 and 2. Both groups were at stoichiometric conditions but reflect different CH₂Cl₂ and O₂ concentrations. As in Figure 4, this plot shows consistently higher conversion values at the same reactor residence times for the runs with lower O₂ and CH₂Cl₂ feed concentrations. Since Figure 3 and the temperature variation runs (Figure 2) show that changing the O₂ concentration has little effect on conversion, however, the results in Figures 4 and 5 must be due in large part to the magnitude of the CH₂Cl₂ feed concentration. Thus it appears that lower CH₂Cl₂ feed concentrations result in a higher overall conversion.

Extent of Reaction in the Organic Feed Preheater Coil. If significant breakdown of CH₂Cl₂ can occur without the need for O₂, then it is possible that breakdown of the CH₂Cl₂ feed may have actually begun before it entered the reactor, i.e. while in the preheater coil. There are two sources of experimental evidence that suggest that this is in fact the case. First, significant corrosion was observed in the organic feed preheater tubing presumably from the presence of HCl, one of the products of CH₂Cl₂ breakdown (see section on corrosion). Second, results from the two hydrolysis runs with the reactor removed show the same conversion within experimental error without the reactor as with the reactor present. The conversions without the reactor for 450°C and 575°C were 36±10% and 82±2% respectively, while the corresponding hydrolysis conversion with the reactor in place for the same two temperatures was 41±13% (average of four separate 450°C runs) and 85±4%. Although only two experiments with the reactor removed were performed, the results do imply that most CH₂Cl₂ breakdown does occur in the preheater coil.

The residence time in the preheater coil depends on the density, which changes considerably as the feed heats from ambient temperature up to 450-600°C. Preheater coil residence times are estimated to range from about 9 to 20 seconds depending on the flow rate and sandbath temperature, which indicates that there was considerably more time for reaction than just the six seconds provided by the isothermal reactor itself. The fact that the temperature variation runs did not all have the same total residence time may account for both some of the scatter and shape of the complete conversion - temperature history observed in Figure 2. For example, a longer time in the preheater coil at temperatures below 500°C and/or a shift to a mechanism more ionic rather than free radical in nature may explain why conversion appears to plateau rather than continue to decrease with decreasing temperature. In any event, a reliable kinetics analysis must take into account not only the isothermal, fixed residence time reactor but also the nonisothermal, variable residence time preheater coil. This determination of the time - temperature history of the organic feed in the preheater under all run conditions and its subsequent use in determining kinetic parameters for the breakdown of CH₂Cl₂ in the complete reactor system is currently under study.

Product Spectrum and Distribution

The following major products were conclusively detected in both hydrolysis and oxidation of CH₂Cl₂ in supercritical water: CO, CO₂, HCHO, CH₃OH, H₂, and HCl.

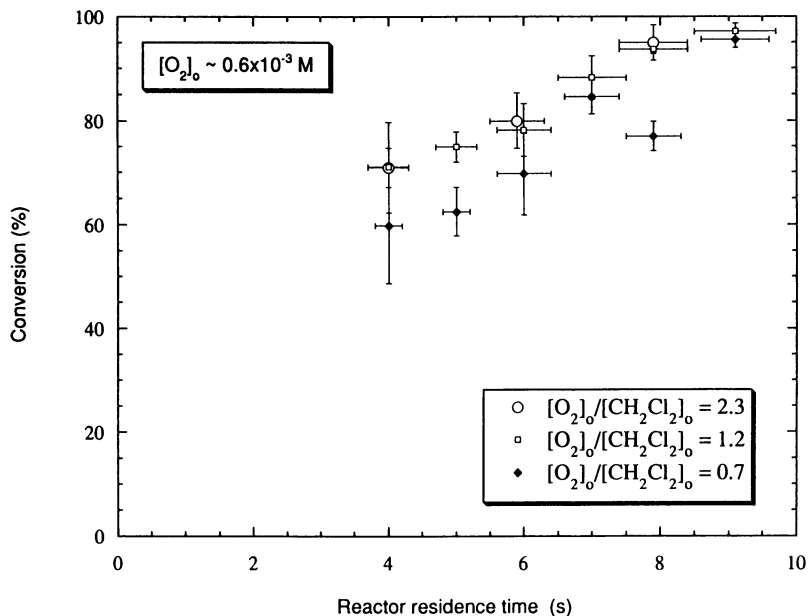


Figure 4. Graph of CH_2Cl_2 conversion vs. reactor residence time at constant O_2 feed concentration. All data at 246 bar and 550°C .

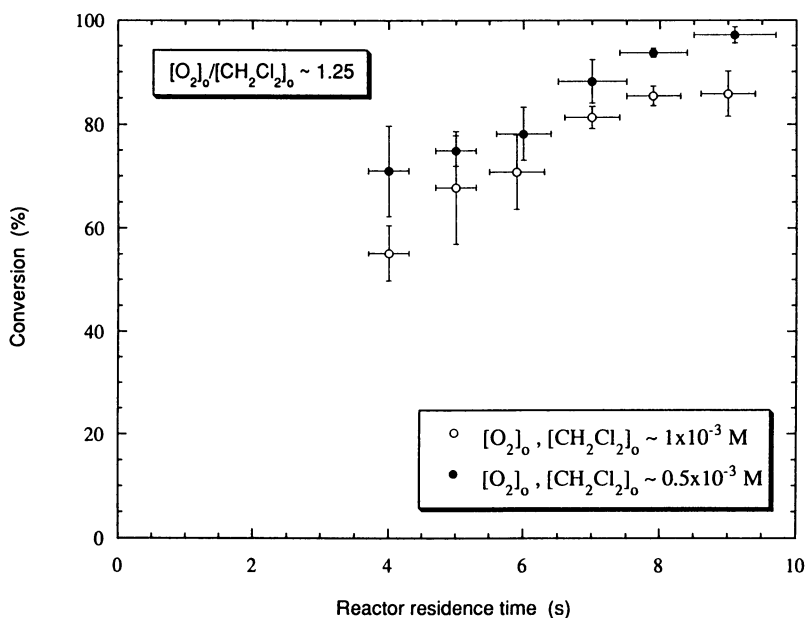


Figure 5. Graph of CH_2Cl_2 conversion vs. reactor residence time at constant $\text{O}_2/\text{CH}_2\text{Cl}_2$ stoichiometric feed ratio. All data at 246 bar and 550°C .

CH₄ was also detected, but only under the following conditions: 562°C and above at 6 seconds reactor residence time, and from 7 to 9 seconds reactor residence time at 550°C. Only small amounts of CH₄ were detected, however ($\leq 1.5\%$ of total mass fed on a carbon basis in each case). In addition to these products, there were trace amounts of the following chlorinated hydrocarbons detected in the vapor phase: chloromethane (CH₃Cl), chloroform (CHCl₃), 1,1-dichloroethylene (C₂H₂Cl₂), cis-1,2-dichloroethylene, trans-1,2-dichloroethylene, and trichloroethylene (C₂HCl₃). Of the total mass balance (carbon basis), CH₃Cl accounted for $< 3\%$, C₂HCl₃ accounted for $< 0.7\%$, and the remaining chlorinated hydrocarbons accounted for $< 0.1\%$ together. Atomic absorption tests on liquid effluent samples indicated ppm levels of soluble nickel ions (presumably from corrosion of Hastelloy C-276 preheater tubing). Equilibrium calculations indicated that the formation of NiCl_x soluble complexes was unlikely at the concentrations of soluble nickel observed in effluent samples. No presence of Cl₂, C₂H₆, C₂H₄, or C₂H₂ was detected. There was $\geq 87\%$ closure on carbon and on chlorine mass balances for all runs, with all but 3 out of the 66 total runs having $\geq 90\%$ closure.

Although the same types of products were observed under both hydrolysis and oxidation conditions, the relative amounts of each product was affected by the presence of O₂, and by temperature. Figure 6 illustrates the relative amounts of carbon-based products formed at the two experimental temperature extremes for hydrolysis and oxidation at a 6 second reactor residence time. The percentages of each product shown represent the fraction of total carbon in the CH₂Cl₂ feed recovered in that product. Thus the percentages of all products shown add up to the total carbon balance for that run. A similar illustration for chlorine-based species would consistently show HCl as the only major product, and is therefore not included. At 450°C, the dominant product is formaldehyde for both hydrolysis and oxidation. At 600°C under hydrolysis conditions, the product spectrum is more diverse. The dominant product now is CO, followed by significant amounts of CO₂ and CH₃OH, but much less HCHO. At 600°C under oxidation conditions, where complete conversion was achieved, practically all of the carbon is in the form of CO₂. Thus 550°C, at which all of the subsequent residence time and concentration variation runs were conducted, was selected to illustrate the high temperature oxidation spectrum. At this temperature, the dominant product is CO, with a significant amount of CO₂ but little HCHO and hardly any CH₃OH. As one can see, the percentage of gaseous products and the variety of total products increases with increasing temperature.

The graphs in Figures 7 and 8 show how major product distributions vary over the complete temperature range explored in these experiments for hydrolysis and oxidation, respectively. All graphs plot molar yield of product versus temperature. As used here, molar yield is defined as the moles of product formed divided by the moles of CH₂Cl₂ feed that reacted. Thus the total molar yield for the carbon products at any given temperature should sum to 1, while the molar yield for chlorinated products should sum to 2. CO, CO₂, and HCHO are shown in Figures 7a and 8a, while H₂, CH₃OH, and HCl are shown in Figures 7b and 8b. These figures show that the molar yield or relative amount formed of HCHO always decreases with increasing temperature under hydrolysis and oxidation. The molar yield of all other products (except HCl) increases with increasing temperature under hydrolysis. Under oxidation, however, CO₂ is the only product that continually increases with increasing temperature. As the major chlorinated product, HCl remains near 2 under both hydrolysis and oxidation.

A comparison of Figures 7a and 8a shows that the amount of HCHO present under oxidation conditions is always less than that under hydrolysis conditions at any given temperature. The amount of CO (up to 550°C) and CO₂ under oxidation conditions, however, is always more than that under hydrolysis conditions. CO exhibits a maximum concentration under oxidation conditions at 550°C, above which

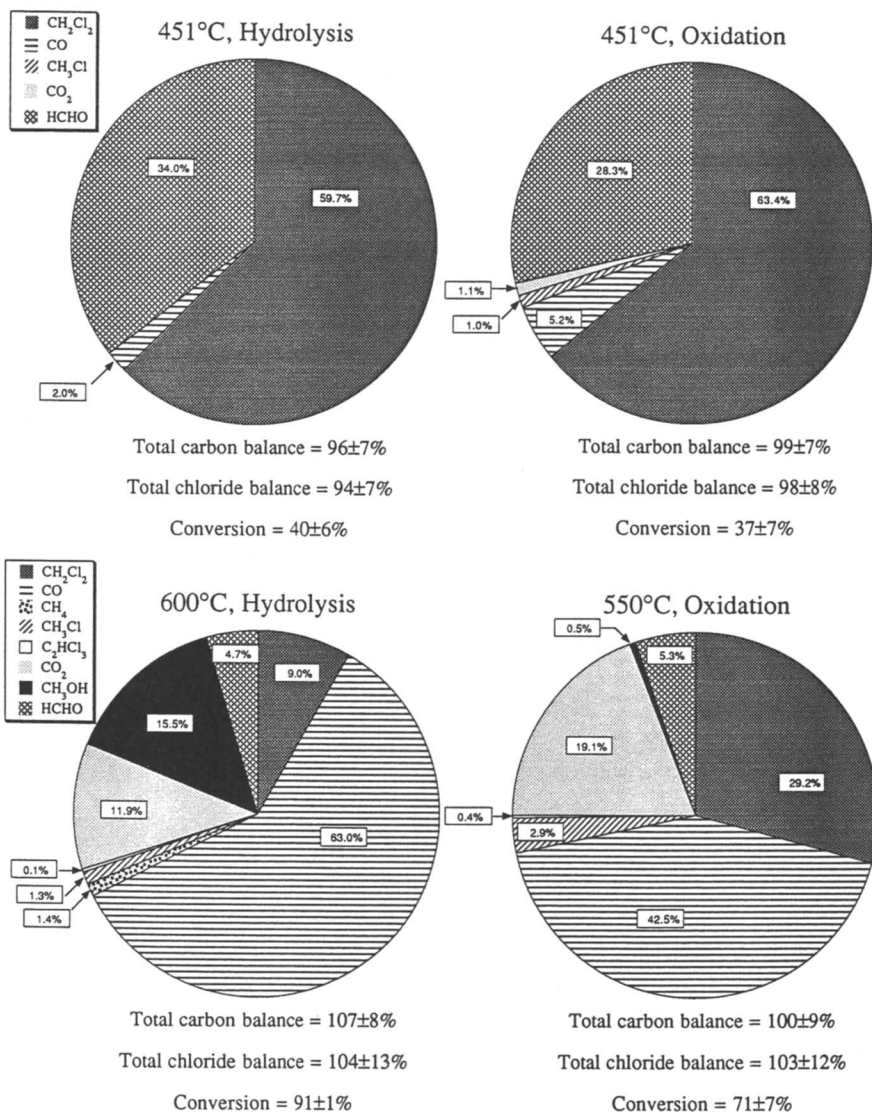


Figure 6. Distribution of carbon-containing products. Units: percent of total amount of carbon fed. All data at 246 bar and 6 seconds reactor residence time.

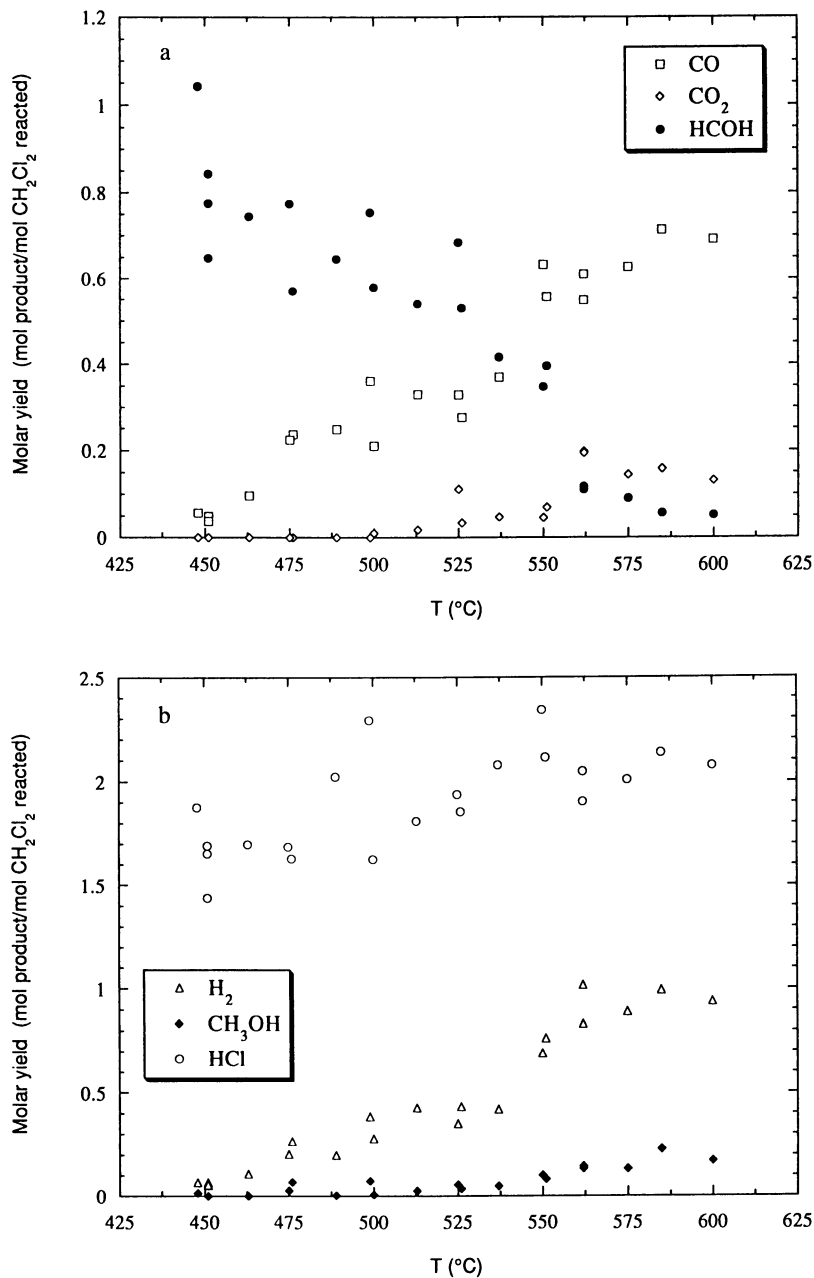


Figure 7. Graph of molar yield of products vs. temperature under hydrolysis conditions a) for CO, CO₂, and HCHO; b) for H₂, CH₃OH, and HCl. All data at 246 bar and 6 seconds reactor residence time.

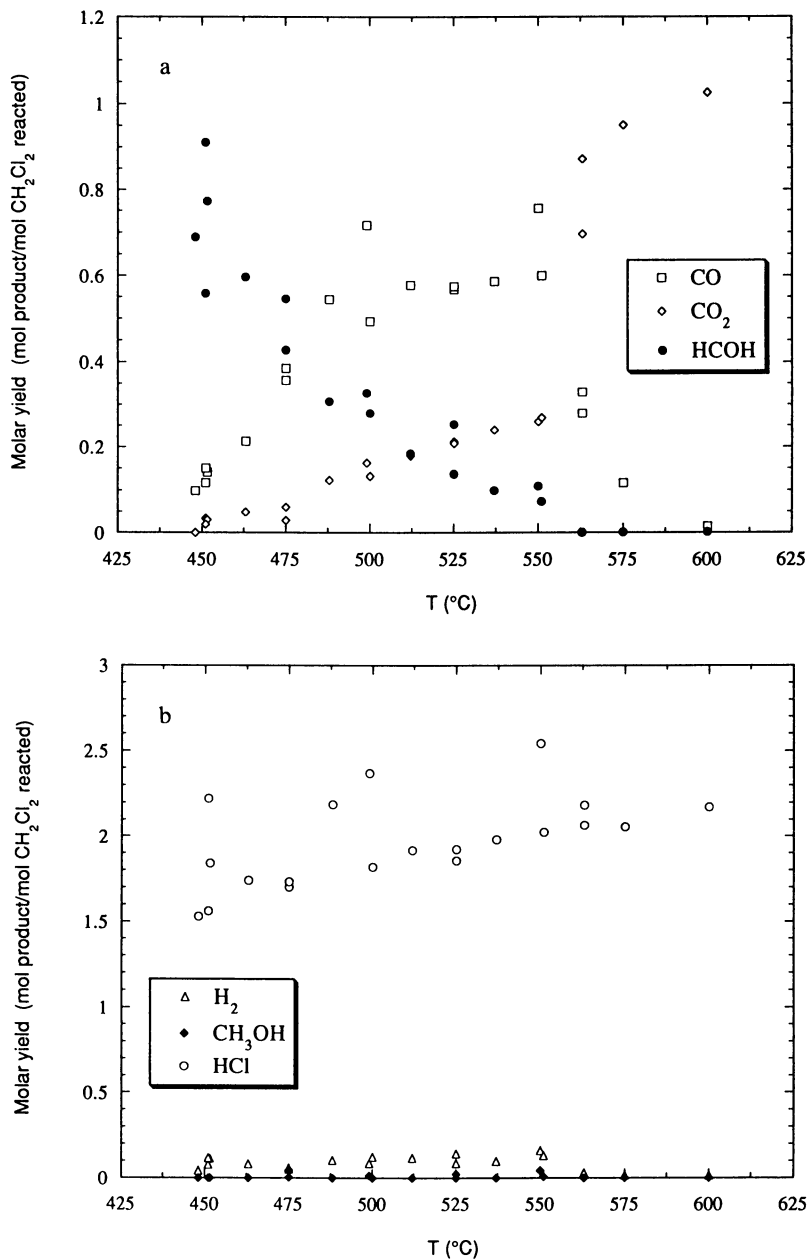


Figure 8. Graph of molar yield of products vs. temperature under oxidation conditions a) for CO, CO₂, and HCHO; b) for H₂, CH₃OH, and HCl. All data at 246 bar and 6 seconds reactor residence time.

its molar yield decreases essentially to zero by 600°C. Comparing Figures 7b and 8b shows that the amount of H₂ and CH₃OH increases with temperature under hydrolysis conditions, but remains close to or at zero for all temperatures under oxidation conditions. The fact that very little CH₃OH remains under oxidation conditions compared to hydrolysis conditions is consistent with an earlier study in CH₃OH oxidation (26, 30), which found less than 3% conversion under hydrolysis conditions but more than 98% conversion under oxidation conditions by 550°C at reactor residence times longer than 6 seconds. Similar trends of no significant hydrolysis conversion but > 98% oxidation conversion were also observed for H₂ at 600°C and 5 s reactor residence times in another earlier study (24). In summary, the presence of O₂ increases the amount of CO and CO₂ formed while reducing the yield of HCHO and also suppressing the buildup of CH₃OH and H₂.

One further point to note from Figure 7b is that under hydrolysis conditions above about 560°C, the number of hydrogen atoms in HCl and H₂ per mole of CH₂Cl₂ converted sums to about 3. This clearly exceeds the number of H atoms that can be generated from CH₂Cl₂ and is strongly indicative of direct chemical reaction of H₂O with CH₂Cl₂.

The concentration of trace chlorinated hydrocarbons in the vapor phase increased with increasing temperature under hydrolysis conditions. Higher amounts were observed under oxidation conditions up to a maximum at 550°C, above which concentrations quickly dropped to < 0.2% of the total mass fed on a carbon basis by 600°C. Highest concentrations were noted at 550°C for the runs with the highest O₂ feed concentrations (superstoichiometric conditions). Although these chlorinated hydrocarbons in general accounted for only a very small amount of the total feed, their presence and increase or decrease with temperature does give information about possible mechanisms and side reactions that could be occurring.

Product distributions overall did not change much with reactor residence time variation under oxidation conditions. The only effect was a relatively greater amount of CO₂ and HCl, and smaller amount of CO produced as residence time increased.

Corrosion

Corrosion was observed in the Hastelloy C-276 organic preheater coil during both hydrolysis and oxidation experiments. Failure of four separate preheater coils occurred after about 104, 44, 54, and 65 hours of operation with CH₂Cl₂ feed. Each tube rupture occurred within a zone from 0.5 to 1.5 ft downstream of where the preheater coil enters the sandbath. Although the exact temperature of the fluid in this region of the preheater coils is unknown, it is unlikely that temperatures of 450 - 600°C could be reached that quickly. It is more likely that the temperature was high but subcritical - giving exactly the conditions (a moderately hot but subcritical, ionic environment) where corrosion is predicted to be particularly aggressive (31).

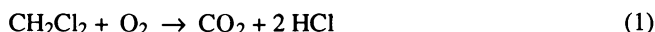
Consistent with this theory, post-failure analysis currently being performed at MIT has found that corrosion appears to be confined to the region around the rupture point on the preheater coils (32,33; see also paper in this ACS volume). Negligible corrosion has been detected at both the entrance (cold) and exit (supercritical temperatures) of the preheater coil. Although the exact type of corrosion has yet to be confirmed, there does appear to be a selective dissolution of nickel in the corroded region of the preheater tubing. Atomic absorption tests performed on liquid effluent samples in the lab of one of the authors (Dr. K.C. Swallow) support these conclusions. Concentrations of soluble nickel were found on the order of 3 to 16 ppm in samples tested, with the higher concentrations found for experiments performed near the time of failure of a preheater coil. Similar atomic absorption tests to determine concentrations of chromium in the effluent samples indicated levels near the detection limit (≤ 0.6 ppm). Rice et al. (11) report similar problems with

corrosion observed during SCWO of CH_2Cl_2 and other chlorinated organics. Concentrations of nickel and chromium in their effluent were comparable to those found in this study, at values of 30.7 ppm and 0.02 ppm respectively.

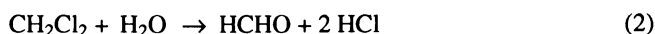
The presence of aggressive corrosion strongly suggests that there was significant breakdown of methylene chloride in the organic preheater coil to HCl - enough to result in failure of the tube in a relatively short amount of exposure time. In addition, it is also possible that the corroding metal wall surface of the preheater coil and/or the presence of HCl may have influenced the rate of CH_2Cl_2 destruction in a catalytic manner. Houser (34) presents evidence that the reactivity of chlorinated hydrocarbons in supercritical water, and the products formed, can be affected significantly by the metal walls of the reactor. No specific attempts were made in this work, however, to determine the extent, if any, of catalytic effects due to the above mentioned sources.

Mechanistic Insights from Experimental Results

The stoichiometry of complete oxidation of CH_2Cl_2 to CO_2 and HCl can be written as:



The kinetics, product spectrum and distribution, and corrosion evidence gathered in this study, however, suggest that the oxidation of CH_2Cl_2 in supercritical water does not proceed directly as written in equation 1. Based on this experimental evidence obtained, a network of possible reaction pathways can be proposed. The fact that 1) conversions were similar under hydrolysis and oxidation conditions, 2) conversion already occurs in the preheater, and 3) the presence of O_2 only shifts the distribution of products to more CO and CO_2 and less HCHO suggests that breakdown of CH_2Cl_2 itself probably occurs by reaction with water, not O_2 . The main products of this first reaction appear to be HCl and HCHO:



Formaldehyde is essentially the only carbon product at 450°C. The same two products were reported by Fells and Moelwyn-Hughes (16) for CH_2Cl_2 hydrolysis under acidic conditions at subcritical temperatures between 80-150°C. As temperature increases above 450°C, another pathway for CH_2Cl_2 breakdown (or possibly HCHO reduction under hydrolysis conditions) to form CH_3OH seems to become significant. Side reactions involving the production of chlorinated hydrocarbons must also increase with temperature, with their formation probably resulting from recombination of free radical fragments derived from CH_2Cl_2 , since only trace amounts of chlorinated hydrocarbons are produced. Once formed, the first intermediate compounds of HCHO and CH_3OH can then be further oxidized to CO, which in turn is oxidized to CO_2 . Figure 9 shows a diagram of this proposed reaction network.

Note that when the individual reactions in this proposed reaction network are added up, the net reaction is the same as that in equation 1. The important distinction, however, is that O_2 is not involved in the initial breakdown of CH_2Cl_2 itself, which proceeds by a hydrolysis pathway. This network is consistent, then, with the observations that O_2 has little effect on the kinetics of CH_2Cl_2 destruction.

Summary and Conclusions

Hydrolysis and oxidation of methylene chloride in supercritical water was studied over the temperature range of 450 to 600°C and 4 to 9 seconds reactor residence time

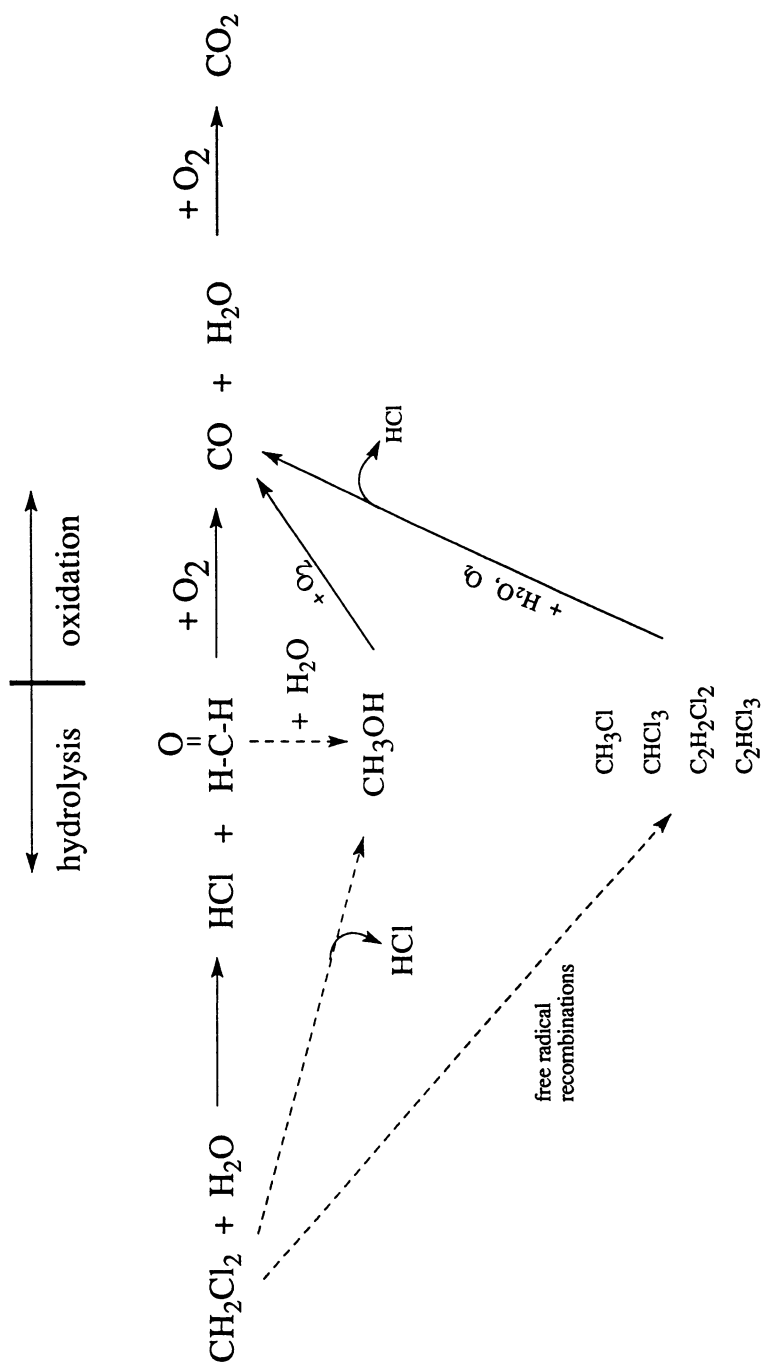


Figure 9. Plausible reaction network for CH_2Cl_2 oxidation in supercritical water.

at feed ratios ranging from sub- to superstoichiometric and a pressure of 246 bar. CH_2Cl_2 concentrations ranged from $0.24\text{--}0.9 \times 10^{-3}$ mol/L, while O_2 concentrations ranged from $0.5\text{--}2.1 \times 10^{-3}$ mol/L.

Conversion of CH_2Cl_2 under hydrolysis conditions was very similar to that under oxidation conditions, usually to within a few percent, at a reactor residence time of 6 seconds. Conversion ranged from $26 \pm 9\%$ to $99.9 \pm 0.1\%$ over the conditions explored. Most of the CH_2Cl_2 breakdown occurred in the organic feed preheater coil, where hydrolysis conditions existed. Significant corrosion was observed within the organic preheater coil in a hot but subcritical region, resulting in the failure and replacement of the tubing on four occasions after exposure times ranging from 44 to 104 hours. The rate of CH_2Cl_2 destruction does not appear to be affected by the concentration of O_2 , although it may be affected by the concentration of CH_2Cl_2 .

Major products of both hydrolysis and oxidation are CO , CO_2 , HCHO , CH_3OH , HCl , and H_2 , with small amounts of CH_4 above 562°C . Trace amounts of chloromethane, 1,1-dichloroethylene, cis-1,2-dichloroethylene, trans-1,2-dichloroethylene, chloroform, and trichloroethylene were detected in the vapor phase effluent. The presence of O_2 resulted in a shift in the product distribution to more CO and CO_2 with less HCHO , CH_3OH , and H_2 . At lower temperatures, HCHO and HCl are the only major products. A greater percentage of gaseous products and a greater variety of products were observed as temperature increased up to 550°C . By 600°C , however, the effluent was mostly CO_2 under oxidation conditions.

The collective evidence from the hydrolysis and oxidation experiments, including kinetics, product spectra and distributions, and corrosion behavior, suggests a possible network of reaction pathways for CH_2Cl_2 oxidation. The major steps include: $\text{CH}_2\text{Cl}_2 + \text{H}_2\text{O} \rightarrow \text{HCHO}$ (or CH_3OH) + $\text{HCl} \rightarrow \text{CO} + \text{H}_2\text{O} \rightarrow \text{CO}_2$; the last two steps involving reaction with O_2 .

Acknowledgments

Both the Army Research Office (grant DAAL03-92-G-0177; project # 30345-CH-URI), under the supervision of Dr. Robert Shaw, and the National Institute of Environmental Health Sciences (NIEHS) are gratefully acknowledged by the authors for their partial support of the research. Full support for two of the authors (CPT. R.P. Lachance and MAJ. J.C. Meyer) was provided by the United States Army. Dr. A. LaFleur and J. LoRuso of the MIT Core Analytical Laboratory and Prof. W. Thilly of the Center for Environmental Health Sciences provided much appreciated analytical equipment loans and technical advice. We wish to thank Prof. P. M. Gschwend and Prof. H. F. Hemond of the Department of Civil and Environmental Engineering at MIT for providing insight in evaluating the reaction network and for other helpful suggestions. In addition, special thanks goes to Dr. D.B. Mitton, Cmdr. J.C. Orzalli, and Prof. R.M. Latanision of the H.H. Uhlig Corrosion Laboratory at MIT for their work in analyzing corrosion in the preheater tubing. Finally, the authors wish to thank Prof. J. B. Howard, Prof. K. A. Smith, and other members of the MIT SCWO research group for helpful insights and suggestions offered in interpreting these results.

Literature Cited

1. Modell, M. "Supercritical Water Oxidation"; In *Standard Handbook of Hazardous Waste Treatment and Disposal*; Freeman, H.M., Ed.; McGraw Hill: New York, NY, 1989; pp. 8.153-8.168.
2. Thomason, T.B.; Hong, G.T.; Swallow, K.C.; Killilea, W.R. "The MODAR Supercritical Water Oxidation Process"; In *Innovative Hazardous Waste Treatment Technology Series, Volume 1: Thermal Processes*; Freeman, H.M., Ed.; Technomic Publishing Co.: Lancaster, PA, 1990; pp. 31-42.

3. Tester, J.W.; Holgate, H.R.; Armellini, F.J.; Webley, P.A.; Killilea, W.R.; Hong, G.T.; Barner, H.E. "Oxidation of Hazardous Organic Wastes in Supercritical Water: A Review of Process Development and Fundamental Research"; In *Emerging Technologies in Hazardous Waste Management III*; Tedder D.W., and Pohland, F.G., Eds.; ACS Symposium Series 518; American Chemical Society: Washington, D.C., 1993; pp. 35-76.
4. Hoke, J.B.; Gramiccioni, G.A.; Balko, E.N. "Catalytic Hydrodechlorination of Chlorophenols"; *Applied Catalysis B: Environmental* 1992, 1(4), 285.
5. Staszak, C.N.; Malinowski, K.C.; Killilea, W.R. "The Pilot-Scale Demonstration of the MODAR Oxidation Process for the Destruction of Hazardous Organic Waste Materials"; *Environ. Prog.* 1987, 6(1), 39.
6. Yang, H.H.; Eckert, C.A. "Homogeneous Catalysis in the Oxidation of p-Chlorophenol in Supercritical Water"; *Ind. Eng. Chem. Res.* 1988, 27, 2009.
7. Jin, L.; Shah, Y.T.; Abraham, M.A. "The Effect of Supercritical Water on the Catalytic Oxidation of 1,4-Dichlorobenzene"; *J. Supercritical Fluids* 1990, 3, 233.
8. Lee, D.S.; Gloyna, E.F.; Li, L. "Efficiency of H₂O₂ and O₂ in Supercritical Water Oxidation of 2,4-Dichlorophenol and Acetic Acid"; *J. Supercritical Fluids* 1990, 3(4), 249.
9. Li, R.; Savage, P.E.; Szmukler, D. "2-Chlorophenol Oxidation in Supercritical Water: Global Kinetics and Reaction Products"; *AIChE J.* 1993, 39(1), 178.
10. Edwards, P.R.; Campbell, I.; Milne, G.S. "The Impact of Chloromethanes on the Environment: Part 2 Methyl Chloride and Methylene Chloride"; *Chemistry & Industry* 1982, 17, pp. 619.
11. Rice, S.F.; Steeper, R.R.; Lajeunesse, C.A. "Destruction of Representative Navy Wastes Using Supercritical Water Oxidation"; Report No. SAND 94-8203 UC-402; Sandia National Laboratories, Livermore, CA, 1993.
12. Young, P.C. "A Kinetic Study of the Catalytic Oxidation of Dichloromethane"; Masters Thesis in the Department of Chemical Engineering, Massachusetts Institute of Technology, Cambridge, MA, 1982.
13. Liepa, M.A. "A Kinetic Study of the Oxidation of Model Chlorinated Hydrocarbons Catalyzed by Chromia Supported on γ -Alumina" Doctoral Thesis in the Department of Chemical Engineering, Massachusetts Institute of Technology, Cambridge, MA, 1988.
14. Hung, S.L.; Pfefferle, L.D. "Methyl Chloride and Methylene Chloride Incineration in a Catalytically Stabilized Thermal Combuster"; *Environ. Sci. Technol.* 1989, 23(9), 1085.
15. Shaw, H.; Wang, Y.; Yu, T.; Cerkanowicz, A.E. "Catalytic Oxidation of Trichloroethylene and Methylene Chloride"; In *Emerging Technologies in Hazardous Waste Management III*; Tedder D.W., and Pohland, F.G., Eds.; ACS Symposium Series 518; American Chemical Society: Washington, D.C., 1993; pp. 358-379.
16. Fells, I.; Moelwyn-Hughes, E.A. "The Kinetics of the Hydrolysis of Methylene Dichloride"; *J. Chem. Soc.* 1958, 1326.
17. Chuang, S.C.; Bozzelli, J.W. "Conversion of Chloroform to HCl by Reaction with Hydrogen and Water Vapor"; *Environ. Sci. Technol.* 1986, 20, 568.
18. Gaisinovich, M.S.; Ketov, A.N. "High-temperature Hydrolysis of Carbon Tetrachloride and Phosgene in the Gaseous Phase"; *Russ. J. Inorg. Chem.* 1969, 14(9), 1218.
19. Jeffers, P.M.; Ward, L.M.; Woytowitch, L.M.; Wolfe, N.L. "Homogeneous Hydrolysis Rate Constants for Selected Chlorinated Methanes, Ethanes, Ethenes, and Propanes"; *Environ. Sci. Technol.* 1989, 23(8), 965.

20. Meyer, J.C. "Oxidation Chemistry and Kinetics of Model Compounds in Supercritical Water: Glucose, Acetic Acid, and Methylene Chloride"; Masters Thesis in the Department of Chemical Engineering, Massachusetts Institute of Technology, Cambridge, MA, **1993**.
21. Bricker, C.E.; Vail, W.A. "Microdetermination of Formaldehyde with Chromotropic Acid"; *Analytical Chemistry* **1950**, *22*(5), 720.
22. West, P.W.; Sen, B. "Spectrophotometric Determination of Traces of Formaldehyde"; *Z. Anal. Chem.* **1956**, *153*, 177.
23. Altshuller, A.P.; Miller, D.L.; Sleva, S.F. "Determination of Formaldehyde in Gas Mixtures by the Chromotropic Acid Method"; *Analytical Chemistry* **1961**, *33*(4), 621.
24. Holgate, H.R.; Tester, J.W. "Fundamental Kinetics and Mechanisms of Hydrogen Oxidation in Supercritical Water"; *Combust. Sci. and Tech.* **1993**, *88*, 369.
25. Holgate, H.R.; Webley, P.A.; Helling, R.K.; Tester, J.W. "Carbon Monoxide Oxidation in Supercritical Water: Effects of Heat Transfer and the Water-Gas Shift Reaction on Observed Kinetics"; *Energy & Fuels* **1992**, *6*, 586.
26. Webley, P.A.; Holgate, H.R.; Stevenson, D.M.; Tester, J.W. "Oxidation Kinetics of Model Compounds of Human Metabolic Waste in Supercritical Water"; Presented at the 20th Intersociety Conference on Environmental Systems, Williamsburg, VA, July 9-12, **1990**; SAE Technical Paper Series No. 901333.
27. Frisch, M.A. "Supercritical Water Oxidation of Acetic Acid Catalyzed by CeO₂/MnO₂"; Masters Thesis, University of Texas at Austin, Austin, TX, **1992**.
28. Boock, L.T.; Klein, M.T. "A Lumping Strategy for Modeling the Oxidation of C₁-C₃ Alcohols and Acetic Acid in High Temperature Water"; *I&EC Research* **1993**, *32*, 2464.
29. Meyer, J.C.; Marrone, P.A.; Tester, J.W. "Acetic Acid Oxidation and Hydrolysis in Supercritical Water"; accepted for publication in *AIChE J.* **1995**.
30. Tester, J.W.; Webley, P.A.; Holgate, H.R. "Revised Global Kinetic Measurements of Methanol Oxidation in Supercritical Water"; *Ind. Eng. Chem. Res.* **1992**, *32*, 236.
31. Huang, S.; Daehling, K.; Carleson, T.E.; Abdel-Latif, M.; Taylor, P.; Wai, C.; Propp, A. "Electrochemical Measurements of Corrosion of Iron Alloys in Supercritical Water"; In *Supercritical Fluid Science and Technology*; Johnston, K.P., and Penninger, J.M.M., Eds.; ACS Symposium Series 406; American Chemical Society: Washington, D.C., **1989**; pp. 287-300.
32. Mitton, D.B.; Orzalli, J.C.; Latanision, R.M. "Corrosion in Supercritical Water Oxidation Systems"; Presented at the 12th International Conference on the Properties of Water and Steam (ICPWS), Orlando, FL, September 11-16, **1994**.
33. Mitton, D.B.; Orzalli, J.C.; Latanision, R.M. "Corrosion Phenomena Associated with SCWO Systems"; *Proceedings of the 3rd International Symposium on Supercritical Fluids* **1994**, *3*, 43.
34. Houser, T.J.; Liu, X. "The Removal of Organic Heteroatoms by Supercritical Water"; *Proceedings of the 3rd International Symposium on Supercritical Fluids* **1994**, *3*, 75.

RECEIVED May 1, 1995

Chapter 14

Phenol Oxidation in Supercritical Water From Global Kinetics and Product Identities to an Elementary Reaction Model

Sudhama Gopalan and Phillip E. Savage

Department of Chemical Engineering, University of Michigan,
Ann Arbor, MI 48109–2136

We developed a detailed free-radical mechanism based on gas-phase chemistry to model the supercritical water oxidation of phenol. The mechanism accounts for the parallel primary paths of ring-opening and dimerization of phenol, the consumption of the phenol dimers as the reaction progresses, and the ultimate formation of carbon oxides as elucidated in earlier experimental studies. Quantitative modeling using the detailed mechanism predicts product yields that are qualitatively consistent with experimental observations. Phenol disappearance rates are predicted to within a factor of 5 of the experimental rates observed between 420 and 480°C. The activation energy and oxygen reaction order predicted by the model are higher than those determined experimentally. Sensitivity analysis reveals that degenerate chain-branching by decomposition of an aromatic hydroperoxide and bimolecular initiation are the elementary steps that influence the phenol oxidation kinetics the most. Areas of improvement are pinpointed to aid future modeling efforts.

Supercritical water oxidation (1), or the oxidation of organic pollutants in aqueous streams at conditions beyond the critical point of water ($T_c = 374^\circ\text{C}$, $P_c = 218$ atm), is an emerging advanced oxidation process for waste treatment. Water above its critical point affords high solubility to both organics and gases. Supercritical water oxidation (SCWO) thus occurs in a homogeneous single phase with the advantage of high intrinsic reaction rates.

Our research on the kinetics of supercritical water oxidation has focused on phenol as a model pollutant. We reported global rate laws for the kinetics of phenol disappearance (2,3) and CO_2 formation (4). We identified reaction products (5,6) and determined that the reaction network featured parallel oxidation paths of dimerization of phenol and ring-opening (3). Using thermochemical and kinetic principles to discriminate between several candidate mechanisms, we postulated a mechanism for these parallel primary paths (7). Now, we use this wealth of experimental data and chemical insight to extend the mechanism and use it as a basis for a quantitative model. In this paper, we present a more complete mechanism for phenol SCWO that accounts for both dimer formation and destruction, and for the ultimate conversion of

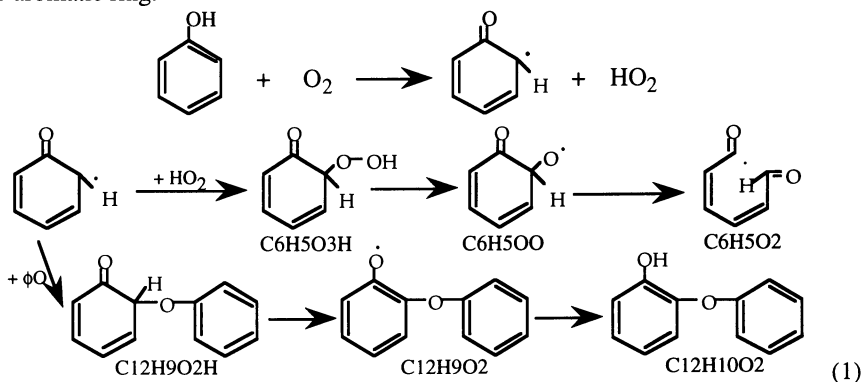
0097-6156/95/0608-0217\$12.00/0
© 1995 American Chemical Society

phenol to CO and CO₂. We analyze the results of detailed kinetic modeling and identify the key elementary steps.

Previous research on reaction mechanisms for SCWO has been largely restricted to elementary reaction models for simple molecules like H₂, CO, CH₄, and CH₃OH. Tester and coworkers published several papers on the fundamental kinetics of these simple compounds (8-11) with increasing degrees of sophistication in the detailed mechanisms. Recently, Brock and Savage (12) developed a single reaction mechanism for the SCWO of C₁ compounds and H₂. Boock and Klein (13) proposed detailed mechanisms for the oxidation of ethanol, 1- and 2-propanol, and acetic acid in near-critical and supercritical water. They did not estimate the rate constants for each step of their mechanisms *a priori*. Rather, they classified each of the reactions into one of eight reaction families and used experimental data to determine Evans-Polanyi parameters for each reaction family. Yang and Eckert (14) suggested abbreviated schemes to explain the SCWO of *p*-chlorophenol. Their mechanistic speculation was largely qualitative.

Mechanism Development

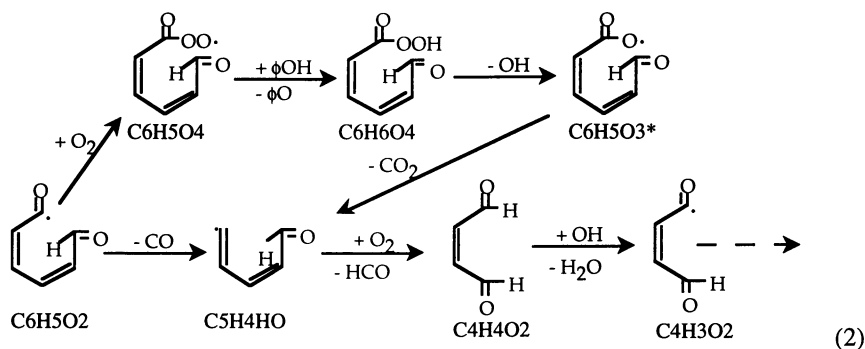
Primary Pathways. An earlier publication (7) presents our proposed free-radical mechanism for the primary paths of phenol oxidation, and the key steps appear in reaction scheme 1. We briefly outline the main features here. The oxidation commences due to bimolecular initiation; viz., abstraction of the phenolic H by O₂ to form the phenoxy radical and HO₂. The phenoxy radical is resonance-stabilized and hence the addition of O₂, a common autoxidation step, is not favored thermodynamically at SCWO conditions. Consequently, the phenoxy radical concentration would build, thereby making radical-radical reactions involving the phenoxy radical important processes for the consumption of phenol. The primary paths of phenol oxidation, which form ring-opening products and phenol dimers, are a result of initial radical-radical reactions. The combination of two phenoxy radical isomers followed by tautomerization forms dimers like 2- and 4-phenoxyphenol, and 2,2'-biphenol as major primary products from phenol SCWO (3). Reaction scheme 1 also shows a sequence of elementary steps that results in ring-opening. The initial step is a combination of HO₂ and a phenoxy radical to form a cyclic α -keto hydroperoxide. Unimolecular homolytic dissociation of the weak O-O bond in the hydroperoxide followed by β -scission of the resulting oxy-radical leads to cleavage of the aromatic ring.



In this paper, the previously reported mechanism (7) for the primary pathways will be extended to describe both the primary and secondary pathways for phenol

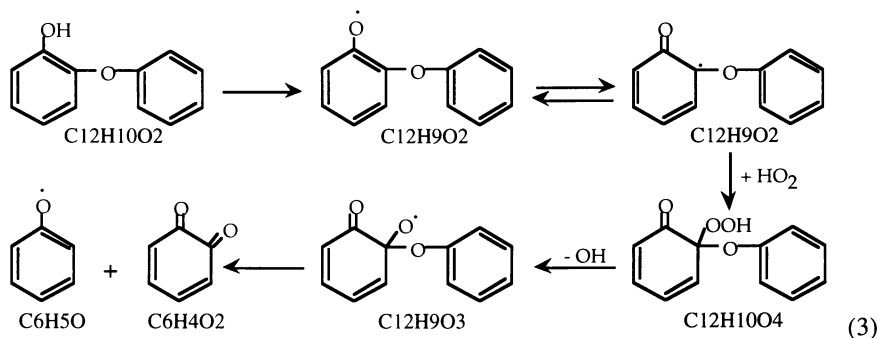
oxidation in supercritical water. In keeping with our previous work, we consider only free-radical reactions. We now include the oxidative degradation process that follows ring-opening and produces CO and CO₂. We also include dimer destruction reactions. Including these secondary reactions leads to a more complete mechanism and model for phenol oxidation in supercritical water.

Production of CO and CO₂. Reaction scheme 2 shows the elementary steps that could occur upon ring-opening and lead to the ultimate formation of CO and CO₂. The acyl radical C₆H₅O₂ formed upon ring-opening can readily add molecular oxygen to form an acylperoxy radical (C₆H₅O₄). We expect no electron-delocalized stabilization in C₆H₅O₂ since Alfassi and Golden (15) found no allylic stabilization in the acyl radical, C₂H₃CO. The acylperoxy radical C₆H₅O₄ can abstract hydrogen either from phenol, or internally from the aldehydic H. The O-H bond in the resulting peracid (BDE ~ 91.2 kcal/mol) is stronger than both the O-H bond in phenol (BDE ~ 86.5 kcal/mol) and the aldehydic C-H bond (BDE ~ 87 kcal/mol). The peracid C₆H₅O₄H can decompose by homolytic dissociation of its weak O-O bond (BDE RCO₂-OH = 40.7 kcal/mol) followed by CO₂ elimination by β-scission, resulting in the formation of a vinyl radical (C₅H₄HO). The vinyl radical can also be formed from the acyl radical C₆H₅O₂ in a parallel path by unimolecular elimination of CO. Vinyl radicals could be expected to react rapidly with molecular oxygen and form HCO and an aldehyde (16). The resulting aldehyde (C₄H₄O₂) could lose the aldehydic H (via hydrogen abstraction by OH) to form another acyl radical (C₄H₃O₂). This acyl radical could react through the same type of steps just described for C₆H₅O₂. Thus, the whole sequence of elementary steps described thus far in this section could occur recursively and ultimately yield CO and CO₂ as the carbon-containing products.



Dimer Decomposition. Experimental results for SCWO of phenol showed that the yield of dimers reached a maximum value and then decreased with increasing phenol conversion (3,6,17). This behavior indicates that dimers are destroyed as the reaction progresses. To account for the destruction of dimers, which are essentially substituted phenols, we use the same elementary processes put forth for the primary pathways for phenol. Reaction scheme 3 shows these elementary steps. The radical C₁₂H₉O₂, formed during the tautomerization necessary to form the dimer (see reaction scheme 1), is essentially a phenoxy radical with a phenoxy substituent. It should therefore undergo the same reactions as the phenoxy radical; viz., radical-radical reactions. We did not include the addition of phenoxy radicals to C₁₂H₉O₂ to form trimers in our model because only traces of trimers were detected in some SCWO experiments. We did include the combination of C₁₂H₉O₂ with HO₂, however. Homolytic dissociation of the O-O bond in the resultant hydroperoxide C₁₂H₁₀O₄ followed by β-scission of

the aryl-O linkage forms a phenoxy radical and quinone. It must be noted that β -scission of a C-C bond to open an aromatic ring is also likely. While the activation energy of this β -scission should be less than that of the aryloxy linkage by a few kcal/mol, it would be compensated for by a lower pre-exponential factor. (Cleavage of the aryl-O bond forms two fragments, which would be expected to involve a higher ΔS^\ddagger as compared to the opening of one of the aromatic rings.) β -scission leading to the opening of one of the aromatic rings in the dimer could account for the formation of single-ring products like 2,3-dihydro-1H-inden-1-one that were detected in our experiments (3). For this initial modeling exercise, we opted to consider only one path for dimer destruction; viz., that leading to the formation of quinone, just as we have considered only one form of coupling of phenoxy radical isomers to form the dimers.



The ring-opening process of quinone has been dealt with in our earlier publication (7). The elementary processes described in the section on CO and CO₂ production are applicable to species formed from the ring-opening of quinone.

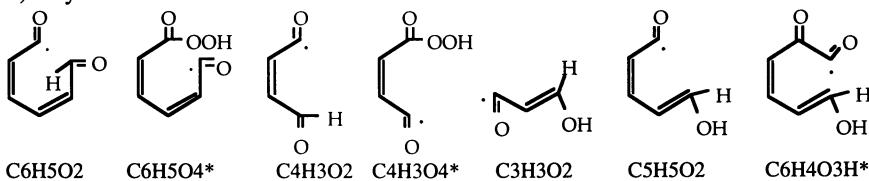
Detailed Kinetic Modeling

The previous section described the new elementary steps appended to our previous mechanism for phenol SCWO. We now use this mechanism as the foundation for a quantitative kinetics model. Figure 1 provides the structures of the various species involved in our proposed mechanism. Isomers are considered as separate species only when the interconversion requires the breaking of a bond and the migration of a group. A detailed chemical kinetic model requires rate data for each reaction in the mechanism and thermochemical data for each species to determine the equilibrium constant for each reaction. Thermochemical properties (H_f , S_f , C_p) for each of these were taken from literature when available (18,19). For a majority of the species, however, we estimated the thermochemical properties (20) using Benson's group additivity rules (21) as implemented by THERM (18). Properties for radicals were estimated from those of the corresponding molecules.

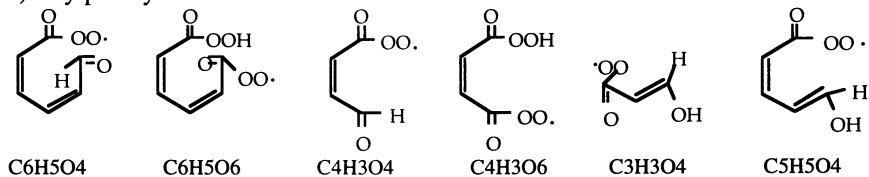
The detailed mechanism is listed in Table I with kinetic parameters in the form $k = AT^n \exp(-E_a/RT)$. Rate parameters for several reactions have been estimated, and the basis for estimation is provided in the footnotes. We used CHEMKIN-II (36) for simulation and SENKIN (37) for sensitivity analysis of the detailed kinetic model. The rate parameters listed in Table I are those for the forward reactions, k_f . Reverse rate coefficients, k_r , in the mechanism were calculated from the forward rate constants, k_f , using the equilibrium constants in concentration units, K_c ;

$$k_r = \frac{k_f}{K_c} \quad (4)$$

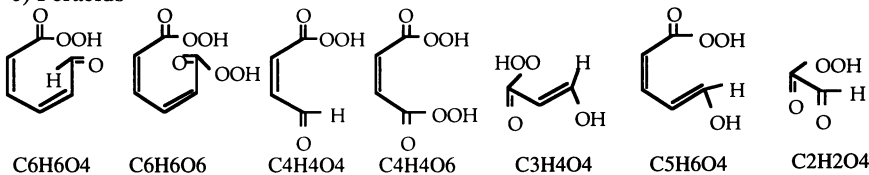
a) Acyl Radicals



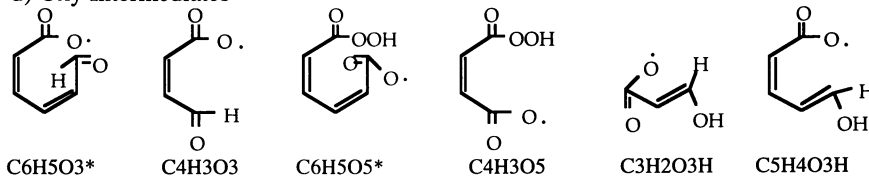
b) Acylperoxy Radicals



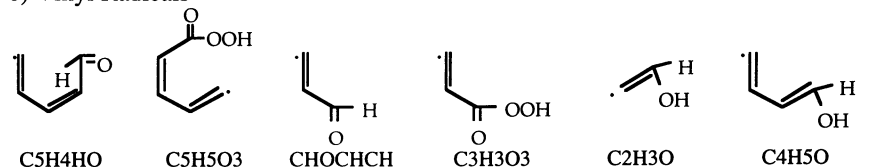
c) Peracids



d) Oxy Intermediates



e) Vinyl Radicals



f) Aldehydes

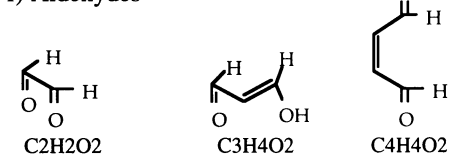


Figure 1. Structures of species in detailed mechanism of Table I (structures of single and multi-ring species provided in reaction schemes 1 and 2)

Table I. Detailed mechanism for phenol SCWO (Units of cm³, s, mol, K).

REACTIONS CONSIDERED	k = A T ⁿ exp(-E/RT)			Ref.
	A	n	E _a	
1. H ₂ O ₂ (+M)=OH+OH(+M)	3.00E+14	0.0	48488	22
Low pressure limit:	1.21E+17	0.0	45507	22
2. H ₂ O ₂ +OH=H ₂ O+HO ₂	7.83E+12	0.0	1331	22
3. HO ₂ +HO ₂ =H ₂ O ₂ +O ₂	4.20E+14	0.0	6030	23
second exponential (a)	1.30E+11	0.0	820	23
4. H+O ₂ (+M)=HO ₂ (+M)	1.63E+13	0.0	761	24
Low pressure limit:	1.56E+18	-0.8	0	22
5. OH+HO ₂ =H ₂ O+O ₂	2.89E+13	0.0	-497	22
6. H+HO ₂ =OH+OH	1.50E+14	0.0	1004	22
7. H+H(+M)=H ₂ (+M)	1.40E+12	0.5	0	b
Low pressure limit:	9.78E+16	-0.6	0	22
8. H+OH(+M)=H ₂ O(+M)	1.62E+14	0.0	149	24
Low pressure limit:	1.41E+23	-2.0	0	22
9. O+O(+M)=O ₂ (+M)	5.39E+12	0.5	0	b
Low pressure limit:	1.89E+13	0.0	-1788	25
10. H+HO ₂ =H ₂ +O ₂	4.28E+13	0.0	1411	22
11. H ₂ O ₂ +H=HO ₂ +H ₂	1.69E+12	0.0	3756	22
12. H ₂ O ₂ +H=H ₂ O+OH	1.02E+13	0.0	3577	22
13. H ₂ O ₂ +O=OH+HO ₂	9.63E+06	2.0	3974	25
14. CO+O ₂ =CO ₂ +O	2.53E+12	0.0	47693	25
15. H+O ₂ =OH+O	1.99E+14	0.0	16812	22
16. H+OH=O+H ₂	4.88E+03	2.8	3875	25
17. H+HO ₂ =O+H ₂ O	3.01E+13	0.0	1721	22
18. H+H ₂ O=H ₂ +OH	4.52E+08	1.6	18421	22
19. O+H(+M)=OH(+M)	8.68E+12	0.5	0	b
Low pressure limit:	4.71E+18	-1.0	0	25
20. O+HO ₂ =OH+O ₂	3.25E+13	0.0	0	22
21. O+H ₂ O=OH+OH	4.58E+09	1.3	17100	25
22. CO+O(+M)=CO ₂ (+M)	2.21E+14	0.0	10470	c
Low pressure limit:	6.17E+14	0.0	3001	25
23. CO+HO ₂ =CO ₂ +OH	1.51E+14	0.0	23648	25
24. C ₆ H ₅ OH+O ₂ =C ₆ H ₅ O+HO ₂	3.00E+14	0.0	38210	d
25. C ₆ H ₅ OH+HO ₂ =C ₆ H ₅ O+H ₂ O ₂	1.00E+12	0.0	10000	e
26. C ₆ H ₅ OH+OH=C ₆ H ₅ O+H ₂ O	3.00E+13	0.0	0	29
27. C ₆ H ₅ O+OH=C ₆ H ₅ OOH	1.00E+13	0.0	0	f
28. C ₆ H ₅ O+HO ₂ =C ₆ H ₅ O ₃ H	3.30E+14	0.0	0	g
29. C ₆ H ₅ O ₃ H=C ₆ H ₅ OO+OH	1.00E+16	0.0	44590	h
30. C ₆ H ₅ O+C ₆ H ₅ O=C ₁₂ H ₉ O ₂ H	1.00E+12	0.0	0	31
31. C ₁₂ H ₉ O ₂ H+HO ₂ =C ₁₂ H ₉ O ₂ +H ₂ O ₂	1.00E+12	0.0	5655	i
32. C ₁₂ H ₉ O ₂ H+OH=C ₁₂ H ₉ O ₂ +H ₂ O	3.00E+13	0.0	0	j
33. C ₁₂ H ₉ O ₂ H+O ₂ =C ₁₂ H ₉ O ₂ +HO ₂	3.00E+14	0.0	27000	k
34. C ₁₂ H ₉ O ₂ H+C ₆ H ₅ O=C ₁₂ H ₉ O ₂ +C ₆ H ₅ OH	1.00E+12	0.0	5655	l
35. C ₁₂ H ₁₀ O ₂ +O ₂ =C ₁₂ H ₉ O ₂ +HO ₂	5.00E+13	0.0	38210	k
36. C ₁₂ H ₁₀ O ₂ +HO ₂ =C ₁₂ H ₉ O ₂ +H ₂ O ₂	1.00E+12	0.0	10000	j
37. C ₁₂ H ₁₀ O ₂ +OH=C ₁₂ H ₉ O ₂ +H ₂ O	3.00E+13	0.0	0	j
38. C ₁₂ H ₁₀ O ₂ +C ₆ H ₅ O=C ₁₂ H ₉ O ₂ +C ₆ H ₅ OH	1.00E+12	0.0	10000	l
39. C ₆ H ₅ OO=C ₆ H ₅ O ₂	1.00E+14	0.0	15000	7
40. C ₆ H ₅ O ₂ +O ₂ =C ₆ H ₅ O ₄	2.40E+12	0.0	0	m
41. C ₅ H ₄ HO+CO=C ₆ H ₅ O ₂	1.51E+11	0.0	4800	n
42. C ₆ H ₅ O ₄ +C ₆ H ₅ OH=C ₆ H ₆ O ₄ +C ₆ H ₅ O	1.00E+12	0.0	6640	o
43. C ₆ H ₅ O ₄ +C ₁₂ H ₁₀ O ₂ =C ₆ H ₆ O ₄ +C ₁₂ H ₉ O ₂	1.00E+12	0.0	6640	o

Table I. *Continued*

44. C6H5O4+HO2=C6H6O4+O2	5.46E+10	0.0	-2640	<i>p</i>
45. C6H6O4=OH+C6H5O3*	1.00E+16	0.0	38600	<i>h</i>
46. C6H5O3*=CO2+C5H4HO	1.00E+13	0.0	10070	<i>q</i>
47. C5H4HO+O2=C4H4O2+HCO	5.42E+12	0.0	0	<i>r</i>
48. C4H4O2+O2=C4H3O2+HO2	5.00E+13	0.0	36442	<i>s</i>
49. C4H4O2+HO2=C4H3O2+H2O2	1.00E+12	0.0	10400	<i>t</i>
50. C4H4O2+OH=C4H3O2+H2O	4.15E+12	0.0	517	<i>u</i>
51. C4H3O2+O2=C4H3O4	2.40E+12	0.0	0	<i>m</i>
52. CHOCHCH+CO=C4H3O2	1.51E+11	0.0	4800	<i>n</i>
53. C4H3O4+C6H5OH=C4H4O4+C6H5O	1.00E+12	0.0	6640	<i>o</i>
54. C4H3O4+C12H10O2=C4H4O4+C12H9O2	1.00E+12	0.0	6640	<i>o</i>
55. C4H3O4+HO2=C4H4O4+O2	5.46E+10	0.0	-2640	<i>p</i>
56. C4H4O4=OH+C4H3O3	1.00E+16	0.0	38600	<i>h</i>
57. C4H3O3=CO2+CHOCHCH	1.00E+13	0.0	10070	<i>q</i>
58. CHOCHCH+O2=C2H2O2+HCO	5.42E+12	0.0	0	<i>r</i>
59. C2H2O4=CO+CO2+H2O	7.94E+14	0.0	29800	<i>v</i>
60. C2H2O4=CO2+OH+HCO	1.00E+16	0.0	38600	<i>w</i>
61. C2H2O2+O2=HCO+CO+HO2	3.00E+14	0.0	37400	<i>x</i>
62. C2H2O2+OH=HCO+CO+H2O	1.00E+13	0.0	0	<i>x</i>
63. C2H2O2+HO2=HCO+CO+H2O2	1.00E+12	0.0	10400	<i>t</i>
64. HCO+O2=CO+HO2	5.12E+13	0.0	1689	25
65. HCO+OH=H2O+CO	1.02E+14	0.0	0	22
66. C6H5O4=C6H5O4*	1.00E+11	0.0	6640	<i>y</i>
67. C4H3O4=C4H3O4*	1.00E+11	0.0	13640	<i>z</i>
68. C6H5OOH+HO2=C6H4OOH+H2O2	1.00E+12	0.0	5655	<i>i</i>
69. C6H5OOH+OH=C6H4OOH+H2O	3.00E+13	0.0	0	<i>j</i>
70. C6H5OOH+O2=C6H4OOH+HO2	3.00E+14	0.0	27000	<i>k</i>
71. C6H5OOH+C6H5O=C6H4OOH+C6H5OH	1.00E+12	0.0	5655	<i>l</i>
72. C6H4OOH+O2=C6H4O2+HO2	1.00E+12	0.0	0	<i>aa</i>
73. C6H4OHOH+O2=C6H4OOH+HO2	3.00E+14	0.0	38210	<i>j</i>
74. C6H4OHOH+HO2=C6H4OOH+H2O2	1.00E+12	0.0	10000	<i>j</i>
75. C6H4OHOH+OH=C6H4OOH+H2O	3.00E+13	0.0	0	<i>j</i>
76. C6H5OO+O2=C6H4O2+HO2	2.00E+11	0.0	2000	<i>ab</i>
77. C5H5O3+CO=C6H5O4*	1.51E+11	0.0	4800	<i>n</i>
78. C6H5O4*+O2=C6H5O6	2.40E+12	0.0	0	<i>m</i>
79. C6H5O6+C6H5OH=C6H6O6+C6H5O	1.00E+12	0.0	6640	<i>o</i>
80. C6H5O6+C12H10O2=C6H6O6+C12H9O2	1.00E+12	0.0	6640	<i>o</i>
81. C6H6O6=OH+C6H5O5*	1.00E+16	0.0	38600	<i>h</i>
82. C6H5O5*=CO2+C5H5O3	1.00E+13	0.0	10070	<i>q</i>
83. C5H5O3+O2=HCO+C4H4O4	5.42E+12	0.0	0	<i>r</i>
84. C3H3O3+CO=C4H3O4*	1.51E+11	0.0	4800	<i>n</i>
85. C4H3O4*+O2=C4H3O6	2.40E+12	0.0	0	<i>m</i>
86. C4H3O6+C6H5OH=C4H4O6+C6H5O	1.00E+12	0.0	6640	<i>o</i>
87. C4H3O6+C12H10O2=C4H4O6+C12H9O2	1.00E+12	0.0	6640	<i>o</i>
88. C4H4O6=OH+C4H3O5	1.00E+16	0.0	38600	<i>h</i>
89. C4H3O5=CO2+C3H3O3	1.00E+13	0.0	10070	<i>q</i>
90. C3H3O3+O2=HCO+C2H2O4	5.42E+12	0.0	0	<i>r</i>
91. C12H9O2+HO2=C12H10O4	3.30E+14	0.0	0	<i>b</i>
92. C12H10O4=OH+C12H9O3	1.00E+16	0.0	44000	<i>h</i>
93. C12H9O3=C6H4O2+C6H5O	1.00E+15	0.0	19000	<i>ac</i>
94. C6H4O2+OH=C6H4O3H	1.00E+13	0.0	0	<i>ad</i>
95. C6H4O3H=C6H4O3H*	1.00E+14	0.0	24730	<i>ae</i>
96. C6H4O3H*=CO+C5H5O2	1.00E+16	0.0	0	<i>af</i>

Continued on next page

Table I. Continued

97. $\text{CO} + \text{C}_4\text{H}_5\text{O} = \text{C}_5\text{H}_5\text{O}_2$	1.51E+11	0.0	4800	<i>n</i>
98. $\text{C}_5\text{H}_5\text{O}_2 + \text{O}_2 = \text{C}_5\text{H}_5\text{O}_4$	2.40E+12	0.0	0	<i>m</i>
99. $\text{C}_5\text{H}_5\text{O}_4 + \text{C}_6\text{H}_5\text{OH} = \text{C}_5\text{H}_6\text{O}_4 + \text{C}_6\text{H}_5\text{O}$	1.00E+12	0.0	6640	<i>o</i>
100. $\text{C}_5\text{H}_5\text{O}_4 + \text{C}_{12}\text{H}_{10}\text{O}_2 = \text{C}_5\text{H}_6\text{O}_4 + \text{C}_{12}\text{H}_9\text{O}_2$	1.00E+12	0.0	6640	<i>o</i>
101. $\text{C}_5\text{H}_5\text{O}_4 + \text{HO}_2 = \text{C}_5\text{H}_6\text{O}_4 + \text{O}_2$	5.46E+10	0.0	-2640	<i>p</i>
102. $\text{C}_5\text{H}_6\text{O}_4 = \text{OH} + \text{C}_5\text{H}_4\text{O}_3\text{H}$	1.00E+16	0.0	38600	<i>h</i>
103. $\text{C}_5\text{H}_4\text{O}_3\text{H} = \text{CO}_2 + \text{C}_4\text{H}_5\text{O}$	1.00E+13	0.0	10070	<i>q</i>
104. $\text{C}_4\text{H}_5\text{O} + \text{O}_2 = \text{HCO} + \text{C}_3\text{H}_4\text{O}_2$	5.42E+12	0.0	0	<i>r</i>
105. $\text{C}_3\text{H}_4\text{O}_2 + \text{O}_2 = \text{C}_3\text{H}_3\text{O}_2 + \text{HO}_2$	3.00E+14	0.0	36442	<i>k</i>
106. $\text{C}_3\text{H}_4\text{O}_2 + \text{OH} = \text{C}_3\text{H}_3\text{O}_2 + \text{H}_2\text{O}$	4.51E+12	0.0	517	<i>u</i>
107. $\text{C}_3\text{H}_4\text{O}_2 + \text{HO}_2 = \text{C}_3\text{H}_3\text{O}_2 + \text{H}_2\text{O}_2$	1.00E+12	0.0	10400	<i>t</i>
108. $\text{CO} + \text{C}_2\text{H}_3\text{O} = \text{C}_3\text{H}_3\text{O}_2$	1.51E+11	0.0	4800	<i>n</i>
109. $\text{C}_3\text{H}_3\text{O}_2 + \text{O}_2 = \text{C}_3\text{H}_3\text{O}_4$	2.40E+12	0.0	0	<i>m</i>
110. $\text{C}_3\text{H}_3\text{O}_4 + \text{C}_6\text{H}_5\text{OH} = \text{C}_3\text{H}_4\text{O}_4 + \text{C}_6\text{H}_5\text{O}$	1.00E+12	0.0	6640	<i>o</i>
111. $\text{C}_3\text{H}_3\text{O}_4 + \text{C}_{12}\text{H}_{10}\text{O}_2 = \text{C}_3\text{H}_4\text{O}_4 + \text{C}_{12}\text{H}_9\text{O}_2$	1.00E+12	0.0	6640	<i>o</i>
112. $\text{C}_3\text{H}_3\text{O}_4 + \text{HO}_2 = \text{C}_3\text{H}_4\text{O}_4 + \text{O}_2$	5.46E+10	0.0	-2640	<i>p</i>
113. $\text{C}_3\text{H}_4\text{O}_4 = \text{OH} + \text{C}_3\text{H}_2\text{O}_3\text{H}$	1.00E+16	0.0	38600	<i>h</i>
114. $\text{C}_3\text{H}_2\text{O}_3\text{H} = \text{CO}_2 + \text{C}_2\text{H}_3\text{O}$	1.00E+13	0.0	10070	<i>q</i>
115. $\text{C}_2\text{H}_3\text{O} + \text{O}_2 = \text{HCOOH} + \text{HCO}$	5.42E+12	0.0	0	<i>r</i>
116. $\text{HCOOH} + \text{O}_2 = \text{HOCO} + \text{HO}_2$	3.00E+14	0.0	39800	<i>k</i>
117. $\text{HCOOH} + \text{OH} = \text{HOCO} + \text{H}_2\text{O}$	2.00E+12	0.0	0	<i>ag</i>
118. $\text{HOCO} (+M) = \text{H} + \text{CO}_2 (+M)$	1.74E+12	0.3	32928	<i>35</i>
Low pressure limit:	2.29E+26	-3.0	35074	<i>35</i>
Kc:	0.123	-0.01	8700	<i>35</i>
119. $\text{HOCO} (+M) = \text{OH} + \text{CO} (+M)$	5.89E+12	0.53	33981	<i>35</i>
Low pressure limit:	2.19E+23	-1.89	35273	<i>35</i>
Kc:	7.41E+05	-1.32	34617	<i>35</i>
120. $\text{OH} + \text{CO} \Rightarrow \text{CO}_2 + \text{H}$	1.17E+07	1.354	-725	<i>35</i>
High pressure limit:	2.45E-03	3.684	-1234	<i>35</i>
121. $\text{HOCO} + \text{O}_2 = \text{HO}_2 + \text{CO}_2$	1.00E+12	0.0	0	<i>ah</i>

a Rate expressed as a sum of two exponentials (23).

b Hard spheres collision limit

c Interpolation based on values in Mallard et al. (26)

d E_a = Heat of reaction (= 36.9 kcal/mol calculated using THERM) + 1.31 kcal/mol (which is the activation energy for the reaction HO_2 + allyl radical = propene + O_2 . We assume the same E_a for the reverse of 24 since the allylic H and phenolic H bonds are about equally strong.). A factor = $3.00\text{E}+14$ (collision frequency), which has been used by Emdee et al. (27) for $\text{C}_6\text{H}_5\text{CH}_3 + \text{O}_2 = \text{C}_6\text{H}_5\text{CH}_2 + \text{HO}_2$.

e Same as for $\text{CH}_3\text{CHO} + \text{HO}_2$ (28). BDE = 87.1 kcal/mol for aldehydic H. BDE = 86.5 kcal/mol for phenolic H. E_a has been reduced by 40 cal/mol to reflect this.

f Recombination estimate

g Hard spheres collision limit. Same estimate used by Brezinsky et al. (30) for $\text{C}_6\text{H}_5\text{CH}_2 + \text{HO}_2$ recombination.

h E_a = Heat of reaction (THERM). A factor same as that used by Cavanagh et al. (28) for $\text{CH}_3\text{CO}_3\text{H}$ decomposition.

i A factor = same as for $\text{CH}_3\text{CHO} + \text{HO}_2$. E_a from Polanyi relation.

j Same as for the case of reaction with $\text{C}_6\text{H}_5\text{OH}$.

k E_a = Heat of reaction. A ~ collision frequency

l H abstractions by $\text{C}_6\text{H}_5\text{O}$ assumed to have the same rate parameters as those for abstraction by HO_2

m Same as for $\text{CH}_3\text{CO} + \text{O}_2$ (28)

n Same as for $\text{C}_2\text{H}_3 + \text{CO} = \text{C}_2\text{H}_3\text{CO}$ (25)

Table I. *Continued*

<i>o</i>	Same as for $\text{CH}_3\text{CO}_3 + \text{CH}_3\text{CHO} = \text{CH}_3\text{CO}_3\text{H} + \text{CH}_3\text{CO}$ (28)
<i>p</i>	Same as for $\text{CH}_3\text{CO}_3 + \text{HO}_2 = \text{CH}_3\text{CO}_3\text{H} + \text{O}_2$ (28)
<i>q</i>	E_a = Heat of reaction (5.27 kcal/mol) + 4.8 kcal/mol {which is the estimate for E_a for the reverse reaction based on the activation energy of $\text{C}_2\text{H}_3 + \text{CO}$ recombination estimated by Tsang and Hampson (25)}. A factor = same as that for CH_3OO decomposition.
<i>r</i>	Same as for $\text{C}_2\text{H}_3 + \text{O}_2 = \text{HCO} + \text{CH}_2\text{O}$ (22)
<i>s</i>	Same as for $\text{CH}_3\text{CHO} + \text{O}_2 = \text{CH}_3\text{CO} + \text{HO}_2$ (28)
<i>t</i>	Same as for $\text{CH}_3\text{CHO} + \text{HO}_2 = \text{CH}_3\text{CO} + \text{H}_2\text{O}_2$ (28)
<i>u</i>	Same as for $\text{CH}_3\text{CHO} + \text{OH} = \text{CH}_3\text{CO} + \text{H}_2\text{O}$ (28)
<i>v</i>	Same as for $(\text{COOH})_2 = \text{CO}_2 + \text{CO} + \text{H}_2\text{O}$ (32)
<i>w</i>	Cleavage of the weak O-O bond followed by β -scission of the unstable intermediate
<i>x</i>	Estimate for H abstraction followed by β -scission of the unstable intermediate
<i>y</i>	Internal abstraction. 9 centered transition state - no strain energy expected. A factor $\sim 1.00\text{E}+11$, since tightening of internal rotors is involved (21)
<i>z</i>	Internal abstraction - 7 centered TS (7 kcal/mol strain energy). A factor $\sim 1.00\text{E}+11$, since tightening of internal rotors is involved (21)
<i>aa</i>	Rate estimated to be same as for $\text{CH}_2\text{OH} + \text{O}_2 = \text{CH}_2\text{O} + \text{HO}_2$ (33)
<i>ab</i>	Estimated on the basis of $\text{C}_4\text{H}_9\text{O} + \text{O}_2 = \text{C}_3\text{H}_7\text{CHO} + \text{HO}_2$ (34)
<i>ac</i>	Estimate for β -scission of C-O bond. Since C-O is stronger than C-C, we use an E_a value higher than that used in reaction 38. The A factor is also higher since there are two fragments formed and hence an increase in entropy.
<i>ad</i>	Estimate for addition of OH across C-C bond of quinone.
<i>ae</i>	β -scission of C-C bond. E_a = heat of reaction. A factor as in reaction 38.
<i>af</i>	Unimolecular decomposition - slightly exothermic, hence $E_a \sim 0$
<i>ag</i>	H abstraction by OH. Bond strength of bond being broken ~ 89.5 kcal/mol, which is slightly stronger than aldehydic H. Rate of $\text{CH}_3\text{CHO} + \text{OH}$ slowed down slightly to reflect this.
<i>ah</i>	Estimate based on $\text{CH}_2\text{OH} + \text{O}_2 = \text{HCHO} + \text{HO}_2$

The equilibrium constant, K_c , can be calculated rigorously from the equilibrium constant, K_a , which is determined from free energies of formation of species, as

$$K_c = \frac{K_a}{\prod \phi_i^{v_i}} (\text{ZRT})^{-\sum v_i} \quad (5)$$

where T is the absolute temperature, R is the gas constant, v_i and ϕ_i are the stoichiometric coefficient and fugacity coefficient of species i , and Z is the compressibility factor of the reacting mixture. CHEMKIN uses the ideal gas law, which means $\phi_i = 1$ and $Z = 1$ in equation 5. At the conditions used in our experiments, supercritical water is not an ideal gas, so errors arise from using the ideal gas law. For example, at a typical set of initial experimental conditions ($[\phi\text{OH}] = 2.22 \times 10^{-4}$ M, $[\text{O}_2] = 8.55 \times 10^{-3}$ M, $[\text{H}_2\text{O}] = 5.78$ M, $T = 460^\circ\text{C}$, $P = 250$ atm), we used the Peng-Robinson equation of state (neglecting binary interaction parameters) to calculate fugacity coefficients for phenol, oxygen, and water as 0.43, 0.74, and 1.49 respectively. The compressibility factor used was 0.7. These values show that the uncertainty introduced into the reverse rate constants due to the ideal gas assumption should be less than an order of magnitude. We consider the uncertainty in many of the forward rate constants, which were estimated by analogy with similar reactions and with estimated thermochemical properties, to be about an order of magnitude. Moreover, there are very large uncertainties in estimating fugacity coefficients of free radicals (38), which constitute a majority of the species in the detailed mechanism. These considerations led us to use the ideal gas law and take the compressibility and species fugacity coefficients to all be equal to 1. Improving the

rate constant estimates and properly accounting for the non-ideal thermodynamics would clearly improve the model. Alternatively, experimental data at higher temperatures, where the ideal gas law is more closely followed, would facilitate validation of the model.

We considered pressure effects only for those reactions for which both high and low-pressure rate parameters were available in the literature. Other reactions are treated less rigorously. There are several unimolecular decompositions that are implicitly assumed to be at their high pressure limits as a first approximation. Some reactions that proceed via a bound complex, like the attack of O_2 on vinyl radicals to form an aldehyde and HCO, are assumed to be at their low pressure limits. Therefore, the estimates used for such reactions are upper limits. To estimate lower limits for the rates of such reactions, it was assumed that the bound adducts would be immediately stabilized by collisions. These adducts and the elementary reactions that form and destroy them were then explicitly accounted for in the detailed mechanism. The rate parameter estimates of Bozzelli and Dean (40) were used for these elementary reactions. Simulations showed no change in the model predictions for either phenol conversions or product yields. Given that the rate parameters of the unimolecular and chemically activated reactions are not available in the literature and had to be estimated, we elected to defer the more rigorous incorporation of pressure effects until we reach the next level of sophistication of the mechanistic model.

Results and Discussion

Model Validation. We performed simulations with the detailed mechanism of Table I using the initial conditions that were employed in our experiments (3). We considered temperatures between 420 and 480°C, a pressure of 250 atm, and initial phenol and oxygen concentrations between 3×10^{-5} and 3.9×10^{-4} M, and 1.6×10^{-3} and 9.9×10^{-3} M, respectively. For each set of initial conditions, we calculated the phenol conversion using the model. Figure 2 shows a parity plot that compares these predicted conversions with the conversions observed from experiments. The model consistently underpredicts phenol conversions at the lower temperatures of 420 and 440°C. Model predictions are clearly better at 460 and 480°C, but there is a great deal of scatter in the data. We also noted that the model underpredicts the phenol conversions obtained at low O_2 concentrations. This trend can clearly be seen in Figure 2 for the data at 460°C. For the low oxygen concentrations ($< 5 \times 10^{-3}$ M), the model predictions are always lower than the experimentally observed phenol conversions.

Using a nonlinear regression procedure detailed earlier (3) and the predicted conversions, we estimated the parameters in the global rate law for phenol disappearance. Table II compares the kinetics parameters, pseudo-first order rate constants, and their standard deviations obtained from the model and from experiments. The reaction order for phenol calculated from the model is close to that obtained from experiments, while the orders for oxygen and water are not. But qualitatively, the model does predict the correct effect of O_2 on phenol disappearance. Both the activation energy, E_a , and the pre-exponential factor, A , are significantly different from the experimental values, but they offset each other. Therefore, reaction rates and pseudo-first order rate constants predicted by the model are quite close at 460 and 480°C.

Figure 3 shows a plot of dimer ($C_{12}H_{10}O_2$) and gas ($CO + CO_2$) selectivities (defined as the fraction of the reacted carbon that forms a particular product cluster). The experimental selectivity profiles represent the fit of an empirical network model to experimental data as reported earlier (3). The trends in model predictions for product selectivities compare well with those observed experimentally. In short, the model does reasonably well in its qualitative predictions for product formation but

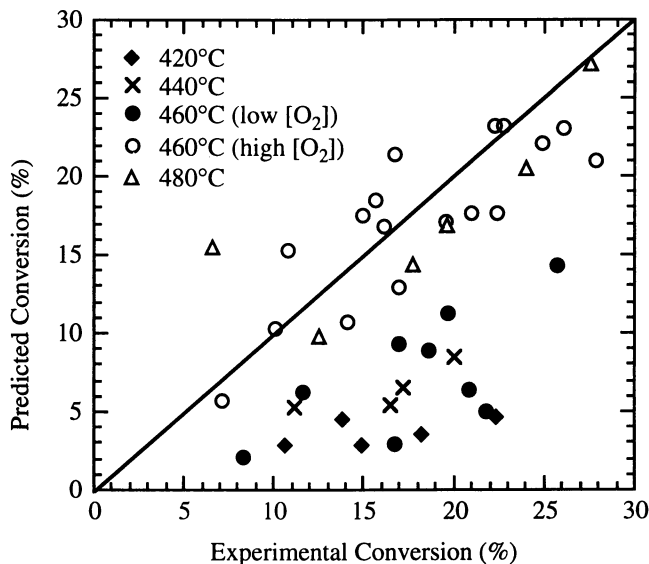


Figure 2. Parity plot of phenol conversions obtained from the model against experimental conversions.

Table II. Global kinetics for phenol disappearance in the form

$$\text{rate} = A \exp\left(-\frac{E_a}{RT}\right) [\phi\text{OH}]^a [\text{O}_2]^b [\text{H}_2\text{O}]^c$$

	Model	Experiment
a	1.09 ± 0.02	0.85 ± 0.04
b	1.23 ± 0.02	0.50 ± 0.05
c	-0.05 ± 0.02	0.42 ± 0.05
E_a (kcal/mol)	42.2 ± 0.5	12.4 ± 1.0
A ($\text{M}^{1-a-b-c}\text{s}^{-1}$)	$10^{14.95} \pm 0.19$	$10^{2.34} \pm 0.28$
$k_{420^\circ\text{C}}$ (s^{-1}) [†]	0.0039 ± 0.0010	0.0171 ± 0.0002
$k_{440^\circ\text{C}}$ (s^{-1})	0.0086 ± 0.0023	0.0225 ± 0.0045
$k_{460^\circ\text{C}}$ (s^{-1})	0.0206 ± 0.0095	0.0275 ± 0.0074
$k_{480^\circ\text{C}}$ (s^{-1})	0.0345 ± 0.0194	0.0321 ± 0.0138

[†] The pseudo-first order rate constants were evaluated using phenol conversions predicted by the model and measured for each of the experimental points. Thus, the effect of $[\text{O}_2]$ and $[\text{H}_2\text{O}]$ for both model predictions and experimental values of k is masked and manifests itself in the large standard deviations. These rate constants are meant to provide rough indicators of how well the model does at the four temperatures.

fails to provide accurate quantitative prediction of experimental results. Given the uncertainties in the various components of this initial model, any quantitative agreement should be viewed as being largely fortuitous.

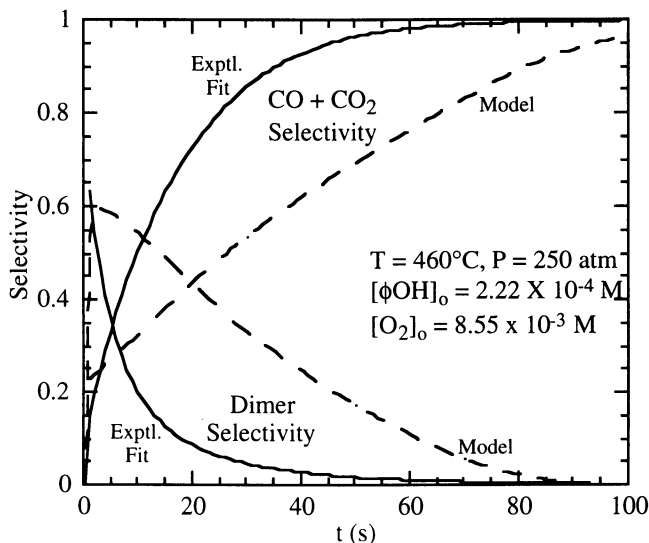


Figure 3. Selectivity profiles of dimers and carbon oxides: model predictions and experimental findings.

The CO/CO₂ ratios obtained from the simulations are much higher than those we have observed from experiments. For instance, for oxidations at 460°C the CO/CO₂ ratio from the model was between 1.1 and 1.2, whereas experiments consistently gave ratios less than 0.5. Elementary reaction models for SCWO of CO have also underpredicted CO conversions at 450 - 500°C (9,12). Thus the high CO/CO₂ ratios in our model for phenol might be a reflection of the inability of detailed chemical kinetics models to predict CO oxidation rates in supercritical water.

For SCWO of molecules like phenol, which yield stable radicals, chain propagation by oxygen addition is not favored. Radical recombination becomes dominant as both a termination process (dimerization) and as a necessary precursor (HO₂ addition) to chain-branching. Radical recombination is, however, much slower than a propagation step like O₂ addition to a radical that does not possess resonance-stabilization. This observation leads us to expect slower oxidation rates for molecules that yield stable radicals in the initiation step. This is consistent with the results of Rice et al. (39) who oxidized a large number of compounds including acetic acid, which is considered to be refractory, and reported that phenol proved to be the most difficult compound to destroy by SCWO. In the case of phenol SCWO, this stability of the phenoxy radical also leads to low levels of non-aromatic organic byproducts (aldehydes, in our mechanism). This is because these molecular intermediates, which upon H abstraction yield radicals that are not resonance-stabilized, can readily add O₂ and hence be consumed much faster than phenol. This scenario is fully consistent with our experimental results for phenol SCWO (3), which show dimers and gases to constitute a very large portion of the reaction products (See Figure 3).

Sensitivity Analysis. We performed a sensitivity analysis (20) on the detailed mechanism to determine the reactions that most strongly influenced the model results. The normalized sensitivity coefficient of a species *i* with respect to reaction *j* is defined as $\frac{\partial \ln X_i}{\partial \ln k_j}$ where *X_i* is the mole fraction of species *i* and *k_j* is the rate

coefficient of reaction j . Since the reactions are considered reversible, the sensitivity analysis actually corresponds to the net extent of reaction (i.e., forward minus reverse). An examination of the normalized sensitivity coefficients for phenol at $T = 460^\circ\text{C}$, $P = 250$ atm, $t = 10$ s, $[\phi\text{OH}]_0 = 2.22 \times 10^{-5}$ M, and $[\text{O}_2]_0 = 8.55 \times 10^{-3}$ M revealed that the sensitivity coefficients of all but two of the reactions had very low magnitudes (< 0.02). Reaction 29, $\text{C}_6\text{H}_5\text{O}_3\text{H} = \text{C}_6\text{H}_5\text{OO} + \text{OH}$, had the sensitivity coefficient with the largest magnitude ($= 0.26$) indicating that the calculated phenol concentration is most sensitive to this step. The sensitivity coefficient also has a negative sign indicating that the forward reaction results in the consumption of phenol. It is also noteworthy that this reaction can cause significant chain-branching, as it is a source of OH, an extremely reactive species.

The initiation step $\text{C}_6\text{H}_5\text{OH} + \text{O}_2 = \text{C}_6\text{H}_5\text{O} + \text{HO}_2$ (reaction 24) has the largest positive sensitivity coefficient ($= 0.17$). This indicates that an increase in the rate of the forward reaction would actually result in the formation of phenol. This seemingly counterintuitive result has its basis in the net reaction rates (i.e., forward minus reverse) of the individual reactions. Figure 4 shows the most important paths in the detailed mechanism at the same conditions used in the sensitivity analysis, based on net reaction rates. The net extent of reaction 24 is towards the left. An increase in its rate coefficient causes an increase in the rate of formation of phenol. But $\text{C}_6\text{H}_5\text{O}_3\text{H}$, whose decomposition causes degenerate chain-branching, is formed by addition of $\text{C}_6\text{H}_5\text{O}$ and HO_2 in reaction 28. Therefore, an increase in the net rate of reaction 24, which involves the same two radicals, comes at the expense of $\text{C}_6\text{H}_5\text{O}_3\text{H}$ formation and thus deters branching. In this sense, initiation and branching are in competition. This is the reason for both the large magnitude and the positive sign of the sensitivity coefficient for the initiation reaction.

The global activation energy of 42.7 kcal/mol is strongly influenced by the high activation energies (~ 44 kcal/mol) for the hydroperoxide decompositions. The overwhelming influence of degenerate chain branching is exemplified by the large rates for reactions 29, 56, and 81 in Table I, as determined by the reaction path

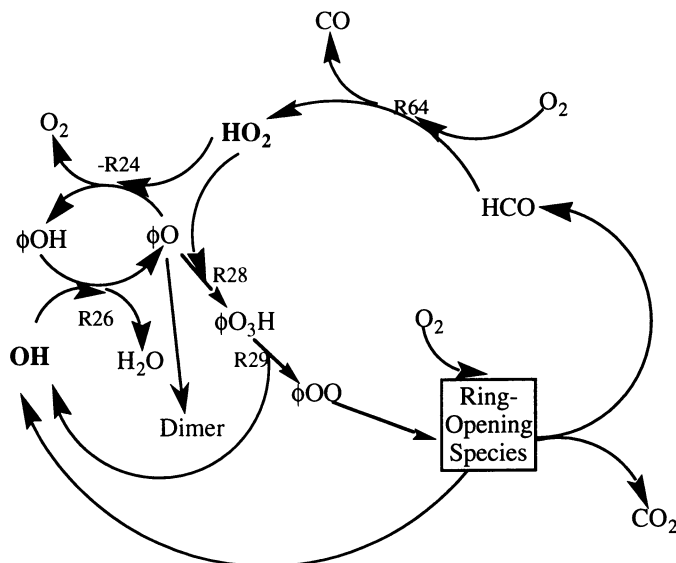


Figure 4. Most important reaction paths in detailed mechanism, based on net reaction rates of the elementary steps.

analysis. The large rates of O₂ addition steps required to form these hydroperoxides is the cause of the large global reaction order for oxygen. This suggests that the mechanistic model may be deficient in the important elementary processes for phenol consumption. Low activation energy steps involving radicals as opposed to unimolecular decompositions and O₂ additions should influence the phenol conversion to a greater extent for the global kinetics to be better predicted.

Summary and Conclusions

We have proposed a detailed free-radical mechanism for the supercritical water oxidation of phenol. It accounts for the consumption of phenol by the parallel paths of ring-opening and dimerization, the consumption of phenol dimers as the reaction progresses, and the formation of CO and CO₂ as final products of oxidation. We used the mechanism as a basis for a quantitative model and tested it against experimental phenol disappearance kinetics and dimer and carbon oxides yield profiles. The mechanism predicts the trends in product yields well but fails to predict accurately the influence of temperature and oxygen concentration on phenol disappearance. Degenerate chain-branching by decomposition of hydroperoxides is a key elementary process responsible for the consumption of phenol. These reactions merit more detailed focus by kinetics investigators.

This first attempt at mechanistic modeling of phenol oxidation in supercritical water posed several difficulties and necessitated a host of simplifying assumptions. We used unit species fugacity coefficients and took the compressibility to be equal to unity when calculating equilibrium constants. There are uncertainties in the kinetic parameters as most of these are estimated and not determined experimentally. Reliable kinetics data for some of the more sensitive reactions are required. Thermochemical properties of species were estimated by group additivity methods and have associated uncertainties. The relative abundance of the three different resonance structures of the phenoxy radical in supercritical water is not known *a priori*, which led us to consider the radical as a single species. Due to this constraint, the various isomer-specific forms of phenoxy radical coupling were approximated by a single form of coupling. Also, the alternative dimer decomposition paths were approximated by a single path since some of the other paths involve species whose thermodynamic properties cannot be estimated reliably by group additivity methods. Creative solutions to these problems that maintain the integrity of the chemistry are required to develop better quantitative models for the supercritical water oxidation of phenol.

Acknowledgments

We thank Prof. John Barker at the University of Michigan for helpful discussions that aided this modeling effort. Thanks are also due to Fran Rupley at Sandia National Labs for her assistance with SENKIN. This project has been supported by the EPA (R817857-01-O).

Literature Cited

1. Modell, M. In *Standard Handbook of Hazardous Waste Treatment and Disposal*; Freeman, H. M., Ed.; McGraw-Hill: New York, 1989; Sec 8.11.
2. Thornton, T. D.; Savage, P. E. *AIChE J.* **1992**, *38*, 321-327.
3. Gopalan, S.; Savage, P. E. *AIChE J.*, in press.
4. Li, R.; Thornton, T. D.; Savage, P. E.; *Environ. Sci. Technol.* **1992**, *26*, 2388-2395.
5. Thornton, T. D.; Savage, P. E. *J. Supercrit. Fluids* **1990**, *3*, 240-248.

6. Thornton, T. D.; LaDue, D. E.; Savage, P. E. *Environ. Sci. Technol.* **1991**, *25*, 1507-1510.
7. Gopalan, S.; Savage, P. E. *J. Phys. Chem.* **1994**, *98*, 12646-12652.
8. Holgate, H. R.; Tester, J. W. *Combust. Sci. and Tech.* **1993**, *88*, 369-397.
9. Holgate, H. R.; Tester, J. W. *J. Phys. Chem.* **1994**, *98*, 810-822.
10. Webley, P. A.; Tester, J. W. *ACS Symp. Ser.* **1989**, *406*, 259-275.
11. Webley, P. A.; Tester, J. W. *Energy & Fuels* **1991**, *5*, 411-419.
12. Brock, E. E.; Savage, P. E. *AIChE J.*, in press.
13. Boock, L. T.; Klein, M. T. *Ind. Eng. Chem. Res.* **1993**, *32*, 2464-2473.
14. Yang, H. H.; Eckert, C. A. *Ind. Eng. Chem. Res.* **1988**, *23*, 2009-2014.
15. Alfassi, Z. B.; Golden, D. M. *J. Am. Chem. Soc.* **1973**, *95*, 319-323.
16. Slagle, I. R.; Park, J. Y.; Heaven, M. C.; Gutman, D. *J. Am. Chem. Soc.* **1984**, *106*, 4356-4361.
17. Thornton, T. D.; Savage, P. E. *Ind. Eng. Chem. Res.* **1992**, *31*, 2451-2456.
18. Ritter, E. R.; Bozzelli, J. W. *Int. J. Chem. Kinet.* **1991**, *23*, 767-778.
19. Stein, S. E. *NIST Structures and Properties: Version 2.0* National Institute of Standards and Technology, Gaithersburg, MD, 1994.
20. Gopalan, S. Ph.D. Thesis, The University of Michigan, **1995**.
21. Benson, S. W. *Thermochemical Kinetics* Wiley Interscience: New York, 1976.
22. Baulch, D.L.; Cobos, C. J.; Cox, R. A.; Esser, C.; Frank, P.; Just, Th.; Kerr, J. A.; Pilling, M. J.; Troe, J.; Walker, R. W.; Warnatz, J. *J. Phys. Chem. Ref. Data* **1992**, *21*, 411-734.
23. Hippler, H.; Troe, J.; Willner, J. *J. Phys. Chem.* **1990**, *93*, 1755-1760.
24. Cobos, C. J.; Troe, J. *Chem. Phys. Lett.* **1985**, *113*, 419.
25. Tsang, W.; Hampson, R. F. *J. Phys. Chem. Ref. Data* **1986**, *15*, 1087-1279.
26. Mallard, W. G.; Westley, F.; Herron, J. T.; Hampson, R. F.; Frizzell, D. H. *NIST Chemical Kinetics Database: Version 5.0* National Institute of Standards and Technology, Gaithersburg, MD, 1993.
27. Emdee, J. L.; Brezinsky, K.; Glassman, I. *J. Phys. Chem.* **1992**, *96*, 2151-2161.
28. Cavanagh, J.; Cox, R. A.; Olson, G. *Combustion & Flame* **1990**, *82*, 15-39.
29. Bittker, D. A. *Combust. Sci. and Tech.* **1991**, *79*, 49-72.
30. Brezinsky, K.; Litzinger, T. A.; Glassman, I. *Int. J. Chem. Kinet.* **1984**, *16*, 1053-1074.
31. Born, J. G. P.; Louw, R.; Mulder, P. *Chemosphere* **1989**, *19*, 401-406.
32. Kakumoto, T.; Saito, K.; Imamura, A. *J. Phys. Chem.* **1987**, *91*, 2366-2371.
33. Tsang, W. *J. Phys. Chem. Ref. Data* **1987**, *16*, 471.
34. Heicklen, J. *Advances in Photochem.* **1988**, *14*, 177.
35. Larson, C. W.; Stewart, P. H.; Golden, D. M. *Int. J. Chem. Kinet.* **1988**, *20*, 27-40.
36. Kee, R. J.; Rupley, F. M.; Miller, J. A. *Chemkin-II: A Fortran Chemical Kinetics Package for the Analysis of Gas-Phase Chemical Kinetics* Sandia Report 89-8009, 1989.
37. Lutz, A. E.; Kee, R. J.; Miller, J. A. *SENKIN: A Fortran Program for Predicting Homogeneous Gas Phase Chemical Kinetics With Sensitivity Analysis* Sandia Report 87-8248, 1988.
38. Schmitt, R. G.; Butler, P. B.; Bergan-French, N. *CHEMKIN Real Gas: A FORTRAN package for analysis of Thermodynamic Properties and Chemical Kinetics in Nonideal Systems* University of Iowa, UMIE PBB 93-006, 1994.
39. Rice, S. F.; Steeper, R. R.; LaJeunesse, C. A. *Destruction of Representative Navy Wastes Using Supercritical Water Oxidation* Sandia Report SAND-94-8203, 1993.
40. Bozzelli, J. W.; Dean, A. M. *J. Phys. Chem.* **1993**, *97*, 4427-4441.

RECEIVED April 24, 1995

Chapter 15

Catalytic Supercritical Water Oxidation An Approach for Complete Destruction of Aromatic Compounds

Zhong-Yi Ding, Sudhir N. V. K. Aki, and Martin A. Abraham¹

Department of Chemical Engineering, University of Tulsa,
Tulsa, OK 74104–3189

Catalytic supercritical water oxidation has been investigated in a flow reactor at 390–460°C and 238 atm. $\text{MnO}_2/\text{CeO}_2$, $\text{V}_2\text{O}_5/\text{Al}_2\text{O}_3$, and $\text{Cr}_2\text{O}_3/\text{Al}_2\text{O}_3$ were used as catalysts. The addition of a heterogeneous catalyst during supercritical water oxidation of aromatic hydrocarbons is shown to promote conversion and improve selectivity to complete oxidation products when compared to conventional supercritical water oxidation. Significant increase of selectivity to CO_2 was observed on $\text{MnO}_2/\text{CeO}_2$ and $\text{V}_2\text{O}_5/\text{Al}_2\text{O}_3$. The catalysts chosen for this study have been determined to be mostly stable during supercritical water oxidation.

Introduction and Background

Wet oxidation, described as the reaction of oxygen with an organic reactant in the liquid phase at elevated temperature and pressure (but below the critical temperature), has been successfully demonstrated as a destruction method for many organic species. Increased destruction efficiency has been obtained by increasing the reaction temperature to that above the critical temperature of water, or through the addition of a catalyst. By operating slightly above the critical temperature of the mixture, some advantage is gained in that the reacting fluid is completely contained within a single, dense phase. Within the current paper, heterogeneous catalysis is discussed as a means to promote the oxidation of organic components in aqueous media near the critical temperature of water.

As evidence of one limitation of conventional SCWO, it has been reported that conversion of organic compounds to CO_2 may not be quantitative. For reaction of phenol, a large number of partial oxidation and condensation products [1],

¹Corresponding author

including such undesirable components as dibenzofuran and dibenzo-p-dioxin [2], are produced. The research group of Gloyna has reported in several papers [3, 4, 5] that acetic acid and ammonia are produced as stable intermediates in the oxidation reaction.

Oxidation of chlorophenol has been accomplished at 400°C and 240 atm and catalyzed with the homogeneous addition of manganese or copper [6]. Both catalysts accelerated the rate of the reaction, but apparently did not influence the product spectrum. Frisch & Gloyna [4] catalyzed the oxidation of acetic acid in supercritical water with the addition of $\text{CeO}_2/\text{MnO}_2$. High oxygen concentrations were used to maintain the catalyst in the oxide form. An increase in the destruction of acetic acid at 400°C and a residence time of 5 minutes from less than 40% to greater than 95% was observed through the addition of the catalyst. No information regarding the products of the reaction are reported.

Recently, we have reported on the catalytic oxidation of phenol in supercritical water [7]. Nearly quantitative conversion of the reactant was reported under essentially all reaction conditions. At high excess oxygen, and particularly using V_2O_5 catalyst, only very minor amounts of partial products were formed, and nearly complete conversion to CO_2 was obtained. MnO_2/CeO also showed good performance in promoting the formation of CO_2 , whereas $\text{Cr}_2\text{O}_3/\text{Al}_2\text{O}_3$ actually enhanced the formation of partial oxidation products. Results for the catalytic oxidation of phenol over $\text{Cr}_2\text{O}_3/\text{Al}_2\text{O}_3$ in supercritical water were recently reported [8]. The TOC reduction and phenol conversion were measured and found to be similar, prompting the authors to suggest that nearly complete selectivity to CO_2 was obtained. The results indicated higher conversion compared to homogeneous reaction experiments.

One major concern of adding a heterogeneous catalyst into the supercritical water oxidation environment is that the catalyst may not be stable. A potential catalyst can be selected based upon solubility data for the catalyst in high temperature, high pressure water. Quantitative data exists for the solubility of various metal oxides in water, and the solubility of inorganic compounds in subcritical and supercritical water was reviewed by Martynova [9]. The stability of the catalyst is not unlike the issue of reactor corrosion, which was found to be important during SCWO.

Within the current paper, results are reported for the catalytic oxidation of several aromatic compounds in supercritical water. Benzene, phenol, and 1,3-dichlorobenzene were investigated to determine the influence of substituent atoms on the aromatic ring. Catalysts, including $\text{Cr}_2\text{O}_3/\text{Al}_2\text{O}_3$, $\text{V}_2\text{O}_5/\text{Al}_2\text{O}_3$, and MnO_2/CeO , have been investigated for their ability to enhance the conversion of the reactant, promote the formation of CO_2 , and remain stable during supercritical water oxidation.

Experimental Section

The reactor system has been described previously [10]. As described in Figure 1, the apparatus consists of separate inlet systems for gas and liquid feeds, the main reactor unit along with pressure and temperature control equipment, and finally

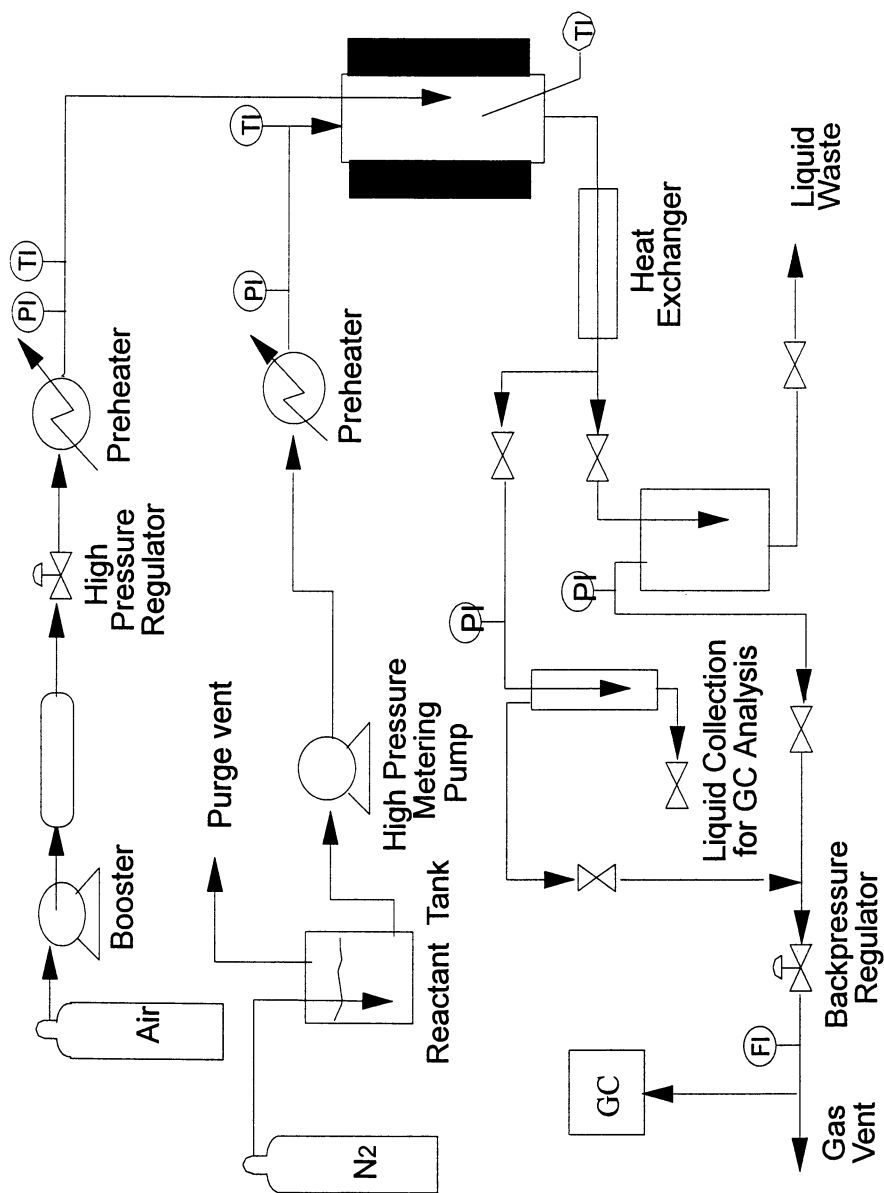


Figure 1: Schematic diagram of experimental apparatus.

product separation and analytical equipment. Feed gas is compressed from an air cylinder, fed through a pre-heater, and passed into the reactor at a point immediately above the catalyst layer. Water feed is controlled with an LDC Analytical 2396-89 high pressure metering pump, passes through a pre-heater, and then enters at the top of the reactor. Liquid reactants are fed to the system using an Eldex A-30-S high pressure metering pump. The reactant stream is mixed with the solvent at the top of the reactor, minimizing the effect of a hydrolysis reaction.

The reactor is an HiP MS-17 Microreactor, constructed of Hastelloy C-276 with an internal diameter of 1.25 cm and a length of 25 cm. The reactor is enclosed in a high temperature furnace, which serves to maintain the reaction temperature at the isothermal set point rather than to provide additional temperature increase. Inert α -alumina particles, crushed to a diameter of 1.5 mm, are used as the packing material. Catalyst is placed in a small layer within the bed just below the exit of the oxygen feed line. The particles are supported using a sintered Hastelloy disc.

The effluent exits the reactor, where it passes through a tube-in-tube heat exchanger and a high pressure gas-liquid separator. The gas then flows through a back pressure regulator (GO Inc. BP-66) to an on-line gas chromatograph (HP 5890A) for analysis. The liquid drains through the high pressure separator, which is emptied continuously. Liquid samples are collected for analysis in 20 mL sample cylinders, which are operated in parallel with the main separator. The liquid recovered in the sample cylinder exists as two phases. The organic phase volume is increased through the addition of a known amount of toluene, which also concentrates all of the organic products into the organic phase and serves as a quantification standard. The organic and aqueous phases are then analyzed using off-line gas chromatography.

Experiments were performed over a wide range of reaction conditions. Homogeneous experiments were performed by packing the reactor with inert α -alumina particles. For catalytic runs, 17.8 g of $\text{Cr}_2\text{O}_3/\text{Al}_2\text{O}_3$, 8.76 g of MnO_2/CeO , or 9.18 g of $\text{V}_2\text{O}_5/\text{Al}_2\text{O}_3$ were placed in a thin layer in the center of the reactor tube. All experiments were run at 238 atm, temperatures between 390 and 450°C, 0.5 - 30 s residence time, and 50 - 500% excess oxygen.

Two analytical methods were used for the quantification and identification of metal ions in the effluent liquid: Atomic Absorption Spectroscopy and UV/VIS Diode Array Spectroscopy. The UV/VIS Diode Array spectrophotometer (HP 8452A) was calibrated using prepared standard samples. The atomic absorption spectrometer (Perkin Elmer 2380) was used to confirm the UV analysis, and good agreement was obtained. Quantitative analysis was accomplished using a total response of $350 < \lambda < 370$ nm, the width of the λ_{max} peak identified from the calibration experiments. The samples were analyzed off-line using the UV spectrophotometer immediately after collection. Experiments were conducted at a given set of operating conditions until a steady state value for chromium ion in the effluent was obtained.

Table 1
Comparison of homogeneous and heterogeneous oxidation in SCW

	Phenol				Benzene				1,3-DCB			
	Homo	MnO ₂	V ₂ O ₅	Cr ₂ O ₃	Homo	MnO ₂	V ₂ O ₅	Cr ₂ O ₃	Homo	MnO ₂	V ₂ O ₅	Cr ₂ O ₃
Excess Oxygen (%)	300	300	300	300	200	300	300	400	300	300	200	400
Temperature (°C)	390	390	390	390	390	390	390	390	390	400	400	390
Concentration (mM)	6.07	4.75	4.77	8.18	12.13	7.50	7.50	6.21	8.95	8.40	15.32	6.2
Residence time (sec)	13.73	5.39	5.39	11.10	8.36	5.17	5.17	8.57	10.45	5.83	1.05	8.61
Conversion (%)	94.5	99.85	99.97	99.09	31.7	26.52	50.38	14.95	44.93	49.72	42	73.65
CO ₂ Yield (%)	27.63	63.98	63.11	66	3.40	12.77	29.89	0.88	1.64	8.20	19.17	1.1
PO Yield (%)	7.57	1.33	0.61	6.4		8.48	0.864	9.50	5.14	44.37	12.76	43.04
Metal Ion concentration in Effluent (ppm)	--	ND	10.71	10	--	ND	7.6	0.17	--	0.14	15.8	0.18

ND : Below the detectability level

Results and Discussion

The results are separated into two sections. First, the effectiveness of the catalyst is described through comparison of results from experiments performed under similar reaction conditions for all three catalysts investigated. Secondly, more detailed results are provided for the influence of concentration and temperature on the reactant conversion and the CO₂ selectivity.

Overview of Catalyst Performance

Phenol, benzene, and 1,3-dichlorobenzene were used as model compounds to investigate homogeneous and catalytic heterogeneous oxidation over MnO₂/CeO₂, V₂O₅/Al₂O₃, and Cr₂O₃/Al₂O₃ in supercritical water. CO₂ was the major product in all cases, however, additional products which remained in the liquid phase were observed in significant yield. These products included low molecular weight oxygenated hydrocarbons, which include acetic acid, formic acid, ethanol, methanol, and acetone, oxidized aromatic species, including catechol and hydroquinone, and dimerization products, such as biphenol and biphenyl. For the purpose of understanding the influence of the catalyst, these products are lumped together as partial oxidation products. Under no conditions was CO observed as a product. The yield of partial oxidation products and CO₂ were calculated on a carbon atom basis, and CO₂ selectivity was calculated on the basis of reactant converted.

Selected experimental results from homogeneous and heterogeneous oxidation of the model compounds studied are summarized in Table 1, in which the conversion, CO₂ yield, the yield of partial oxidation products, and metal ion concentration in the effluent are reported. Except for the Cr₂O₃/Al₂O₃ catalyst, which only increased CO₂ yield during phenol oxidation, the catalysts dramatically increased the CO₂ yield during oxidation of phenol, benzene, and 1,3-dichlorobenzene under operating conditions similar to conventional supercritical water oxidation. Among these selected aromatic compounds, phenol was the most easily converted compound during supercritical water oxidation, with nearly 100% conversion and high CO₂ yield under all reaction conditions. 1,3-DCB was the most refractory compound for complete oxidation in supercritical water.

One issue that is very important in the effectiveness of the catalyst is its stability in the harsh environment which is present during supercritical water oxidation. The concentration of metal ion in the effluent was monitored periodically using atomic absorption spectroscopy. The results are indicated in Table 1. It was observed that MnO₂/CeO₂ was the most stable catalyst in supercritical water; note that MnO₂/CeO₂ also gave very high activity for the conversion of the selected compounds as well as high selectivity to CO₂. V₂O₅/Al₂O₃, which also had a high activity for the conversion of aromatic compounds, was not stable under SCWO reaction conditions. Substantial vanadium ion was measured in the effluent, especially in the case of 1,3-DCB oxidation. It was postulated that the chloride product reacted with the catalyst to produce vanadium chloride which was soluble in the fluid phase and thereby extracted from the catalyst bed. Cr₂O₃/Al₂O₃ was generally stable, but not a particularly good oxidation catalyst. In the case of phenol oxidation, substantial

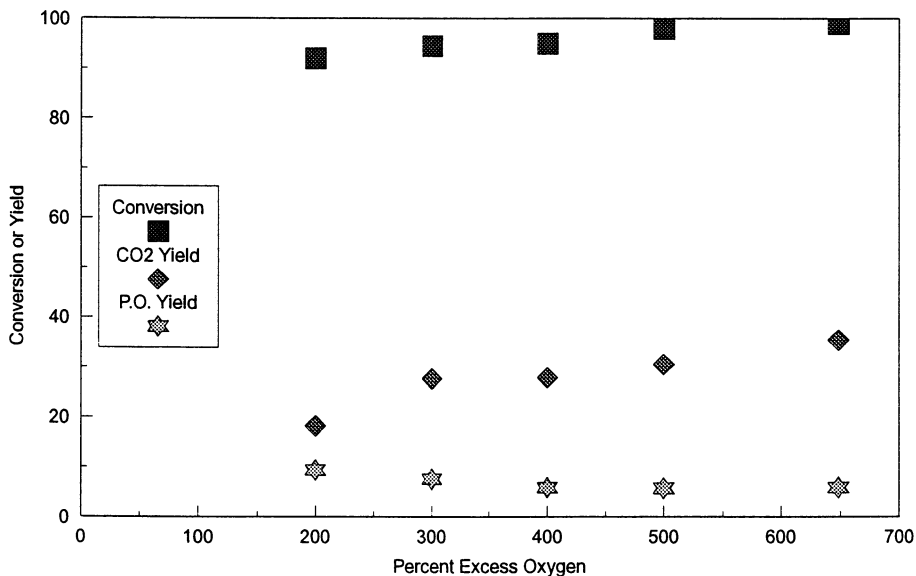


Figure 2a: Homogeneous oxidation of phenol in supercritical water at 390°C, 238 atm, $t \approx 13$ s, and $C_{\text{PhOH}} \approx 6$ mM.

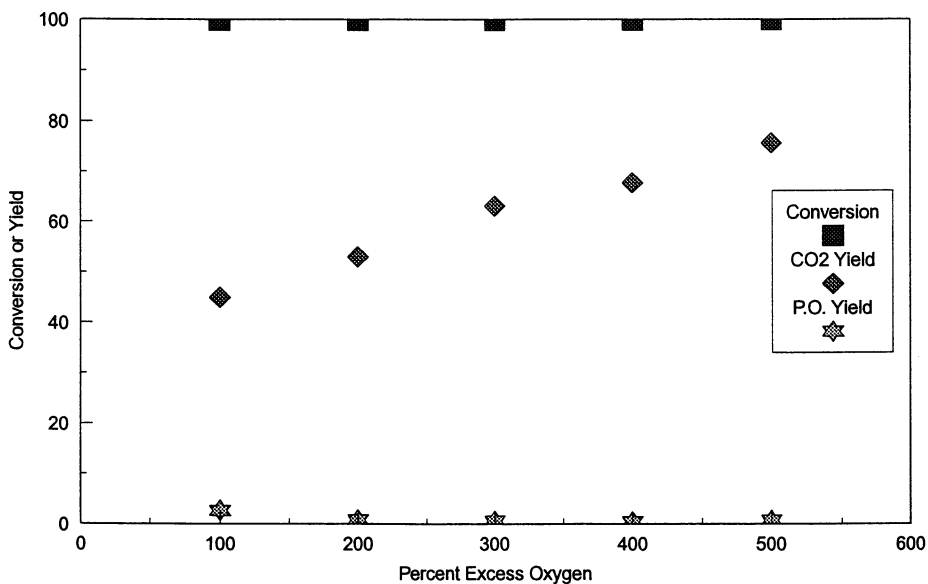


Figure 2b: Oxidation of phenol over 9.18 g V_2O_5 catalyst in SCW at 390°C, 238 atm, $t \approx 5.5$ s, and $C_{\text{PhOH}} \approx 5$ mM.

chromium was detected in the effluent. This is believed to be related to the high reactivity of phenol, as described in a related publication [11].

Effect of Concentration and Temperature

The oxidation of phenol was facile even under the mildest conditions investigated (390°C, no catalyst). Phenol conversion and product yields are reported for homogeneous SCWO as a function of excess oxygen concentration in Figure 2a. Greater than 90% conversion of phenol was noted even at 200% excess oxygen. As the oxygen concentration increased, the conversion and the yield of CO₂ both increased, whereas the yield of partial oxidation products decreased. However, even at 500% excess oxygen, the CO₂ remained below 50% while the yield of partial oxidation product remained greater than 5%.

A similar plot is reported in Figure 2b, for the oxidation of phenol over V₂O₅/Al₂O₃. In this case, phenol conversion was always approximately 100%. Partial oxidation products were observed only at the lowest oxygen concentration (100% excess), and then decreased to zero as the oxygen concentration increased. CO₂ yield, which was greater than 40% even at 100% excess oxygen, increased to nearly 80% at 500% excess oxygen. When comparing these results with those from the homogeneous oxidation, it is clear that V₂O₅/Al₂O₃ enhanced phenol conversion and CO₂ yield and simultaneously inhibited the formation of partial oxidation products.

Although greater than 90% conversion was obtained from phenol oxidation in supercritical water under all reaction conditions, the CO₂ selectivity was always below 1. Figure 3 provides a comparison of CO₂ selectivity from homogeneous supercritical water oxidation of phenol at 390°C, with approximately 6 mM of phenol concentration and 13 s residence time with catalytic supercritical water oxidation at approximately 5 mM concentration and 5.2 s residence time. As the oxygen concentration increased from 100 to 500% excess, CO₂ selectivity from homogeneous oxidation increased to approximately 0.4, whereas CO₂ selectivity from catalytic oxidation increased to 0.92 and 0.75 on MnO₂ and V₂O₅, respectively. Additional analysis of the liquid phase products further reveals a substantial decrease in both the quantity and variety of partial oxidation products formed during catalytic supercritical water oxidation when compared with homogeneous oxidation. Experimental evidence of this was provided in both Table 1 and Figure 2.

Benzene was much more difficult to oxidize than was phenol, under all experimental conditions. As indicated in Figure 4, for homogeneous supercritical water oxidation at 390°C, C_{benzene} ≈ 14 mM and τ ≈ 9 s, conversion decreased from approximately 50% at 40% excess oxygen to roughly 30% at 180% excess oxygen. A similar decrease in conversion was observed for oxidation over MnO₂/CeO₂, although in this case the residence time was approximately 5.2 s, and C_{benzene} ≈ 7.5 mM. The shorter residence time in the catalytic case represents the amount of catalyst which was packed into the reactor. For catalytic oxidation over V₂O₅/Al₂O₃ at conditions similar to that for the other catalysts, oxygen concentration showed little effect on the benzene conversion. Clearly, the V₂O₅/Al₂O₃ significantly enhanced the

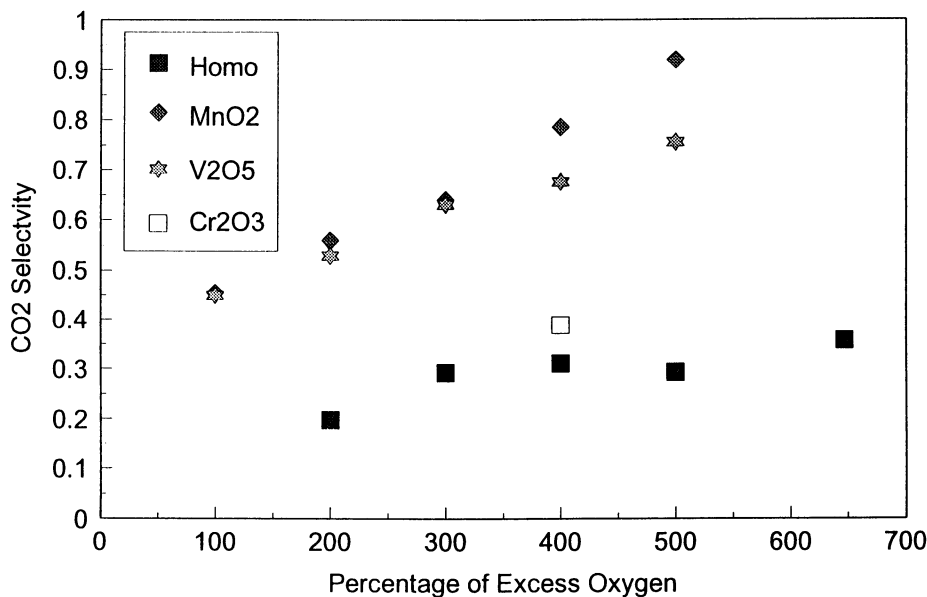


Figure 3: Comparison of catalyst performance against homogeneous oxidation for the selectivity to CO₂ during phenol oxidation as a function of oxygen concentration.

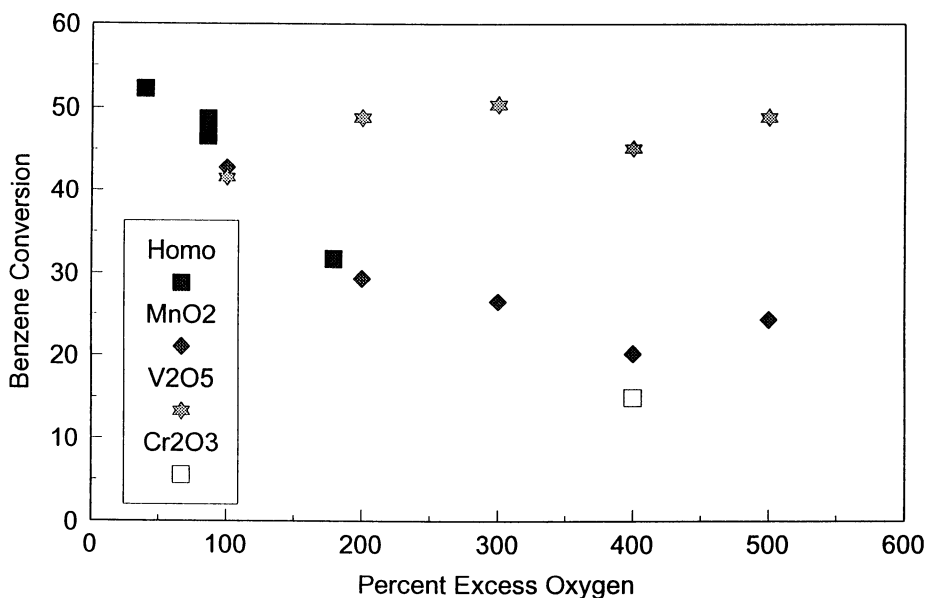


Figure 4: Comparison of catalyst performance against homogeneous oxidation for the conversion of benzene as a function of oxygen concentration.

conversion of benzene relative to the homogeneous oxidation, although the other catalysts appeared to have little effect.

Figure 5, however, indicates that the effect of oxygen concentration on the selectivity to CO₂ during benzene oxidation is unlike its effect on benzene conversion. When V₂O₅/Al₂O₃ or MnO₂/CeO₂ catalyst was present, the selectivity to CO₂ increased monotonically as the amount of excess oxygen increased. Very high selectivity to CO₂, approaching 1.0 on V₂O₅/Al₂O₃ at 500% excess oxygen, was obtained. A CO₂ selectivity below 0.4 would be expected at 400-500% excess oxygen from extrapolation of the homogeneous case. At 200% excess oxygen, the CO₂ selectivity was six times and three times greater on V₂O₅ and MnO₂, respectively, compared with that obtained from homogeneous oxidation.

Because of the low conversions obtained during benzene oxidation, additional data were obtained at higher reaction temperature. Results are reported in Figure 6, in which the effect of temperature on benzene conversion is compared for homogeneous SCWO (at $\tau \approx 13$ s) with that over the V₂O₅, MnO₂, and Cr₂O₃ catalysts (at $\tau \approx 6 - 9$ s). All experiments were performed at 238 atm and approximately 300% excess oxygen. Not unexpectedly, as the reaction temperature increased, the benzene conversion increased in all cases. Figure 6 compares the catalysts at constant loading (based on metal atom). It can be seen that the Cr₂O₃ was slightly effective in increasing the benzene conversion, followed by MnO₂ and V₂O₅ in order of increasing effectiveness. In fact, since the residence time was greatest for the homogeneous case, the enhancement due to the addition of the catalyst is even greater than that indicated by the figure.

Additional information regarding the effectiveness of the catalyst is indicated in Table II, which reports on the product selectivity for the homogeneous oxidation and the three catalysts, at the highest reaction temperature studied. The reported values are within experimental error of 100%, except for homogeneous oxidation, in which the production of partial oxidation products was not quantified and for the Cr₂O₃ catalyst, which produced substantial partial oxidation products. In this case, substantial error may result from the approximations which were involved in quantifying the numerous partial oxidation species which are produced. Note that

Table II
Summary of Benzene Oxidation Product Selectivity

	Homo- geneous	MnO ₂	V ₂ O ₅	Cr ₂ O ₃
Temperature (°C)	460	450	430	410
Conversion	30.6	74.99	68.04	19.03
CO ₂ Selectivity	5.72	98.85	101.18	12.98
Selectivity to partial oxidation products	N.Q.	4.23	0.96	114.08

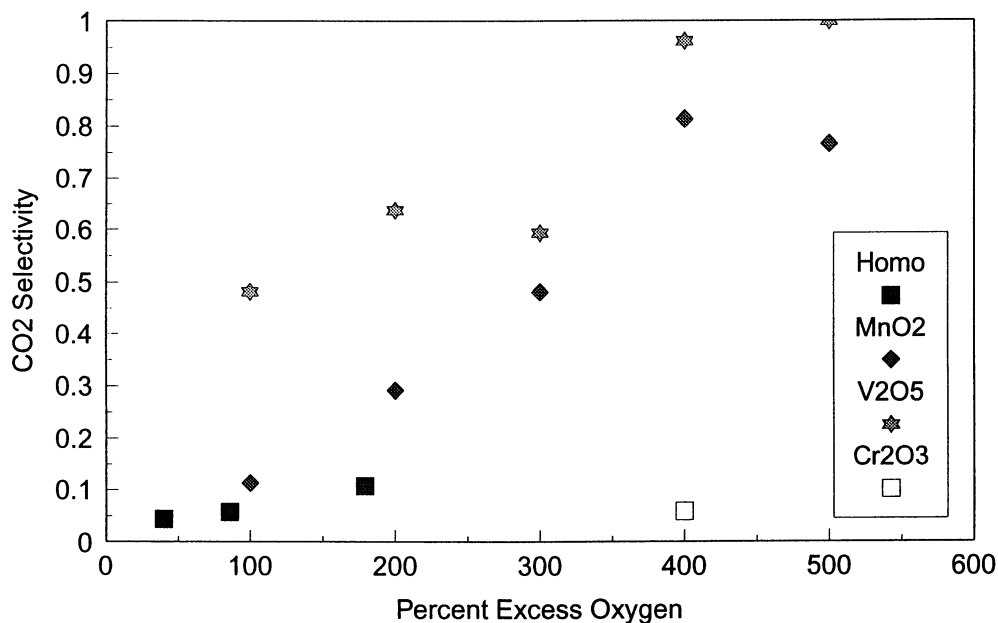


Figure 5: Comparison of catalyst performance against homogeneous oxidation for the selectivity to CO₂ during benzene oxidation as a function of oxygen concentration.

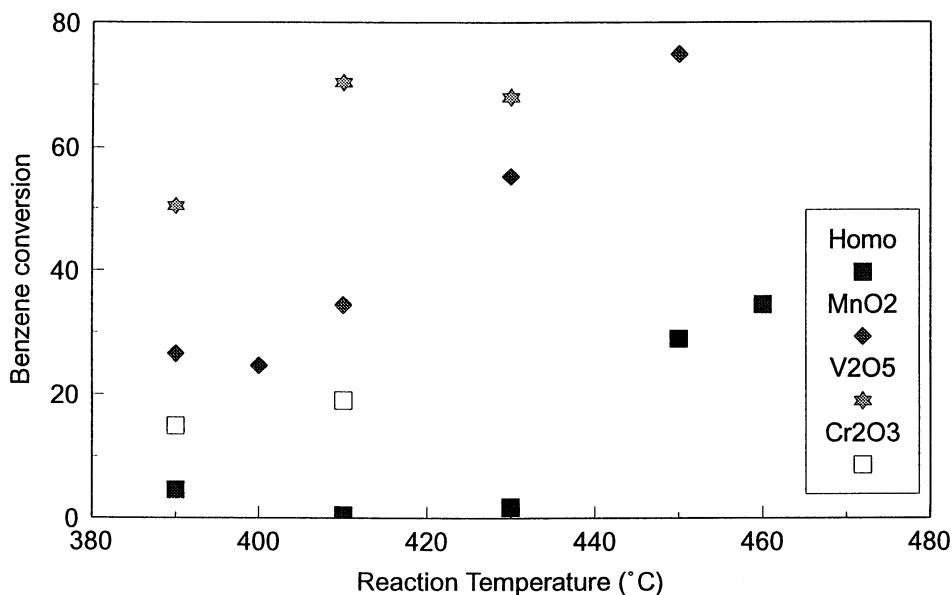


Figure 6: Comparison of catalyst performance against homogeneous oxidation for benzene conversion as a function of reaction temperature.

MnO_2 and V_2O_5 catalysts produced nearly quantitative yield of CO_2 , and gave low selectivity to partial oxidation products. On the other hand, high selectivity to partial oxidation products was observed with the Cr_2O_3 catalyst, with low selectivity to CO_2 .

Limited data were obtained on the catalytic oxidation of 1,3-DCB in supercritical water because the metal ion was eluted from the catalyst bed, which caused a substantial loss of catalyst activity. In the case of V_2O_5 catalyst, this loss of metal ion was tracked through an exponential decay in CO_2 selectivity from approximately 85% after 30 minutes on stream to less than 10% after 180 minutes on stream. The DCB conversion, however, remained relatively unchanged, and was little different than that obtained under homogeneous conditions. During the course of this run, the effluent had a strong blue color, and elemental analysis revealed the presence of high concentration of vanadium ion in the effluent. It was surmised that the vanadium catalyst had reacted with free chloride within the reactor to produce vanadium chloride, which was highly soluble in the fluid phase under reaction conditions.

The data in Table I reveals that none of the catalysts investigated substantially enhanced the conversion of DCB relative to homogeneous oxidation. However, this data, supplemented by the results reported in Figure 7, reveals that with the participation of MnO_2 or V_2O_5 , CO_2 selectivity was higher than that obtained during homogeneous oxidation. In addition, all catalysts appeared to enhance the formation of partial oxidation products over that obtained from homogeneous oxidation. Whereas MnO_2 increased the selectivity to both partial oxidation products and CO_2 , Cr_2O_3 enhanced the formation of partial oxidation products only.

Conclusions

Heterogeneously catalyzed oxidation in supercritical water has been demonstrated as an effective means of converting several organic species to non-hazardous products. The addition of MnO_2 or V_2O_5 catalyst increased significantly the selectivity to CO_2 . Under specific reaction conditions, nearly quantitative yield of CO_2 was obtained. This means catalytic supercritical water oxidation can give complete destruction at relatively mild operating conditions. This, in turn, may make supercritical water oxidation a more economical remediation technique for hazardous waste treatment.

Phenol, benzene, and 1,3-dichlorobenzene were used as pure component models of actual aqueous waste components. Phenol was the easiest species to destroy, giving nearly complete conversion under all reaction conditions, but low selectivity to CO_2 during homogeneous oxidation. The addition of MnO_2 or V_2O_5 catalyst increased the selectivity to CO_2 to greater than 70% at high excess oxygen. Benzene was more difficult to oxidize, although greater than 70% conversion could be obtained using MnO_2/CeO catalyst and 500% excess oxygen or through an increase in the reaction temperature to 450°C with either MnO_2 or V_2O_5 catalysts. Nearly quantitative yield of CO_2 was obtained under these reaction conditions. 1,3-DCB was the most difficult of the model compounds to oxidize; in addition, the

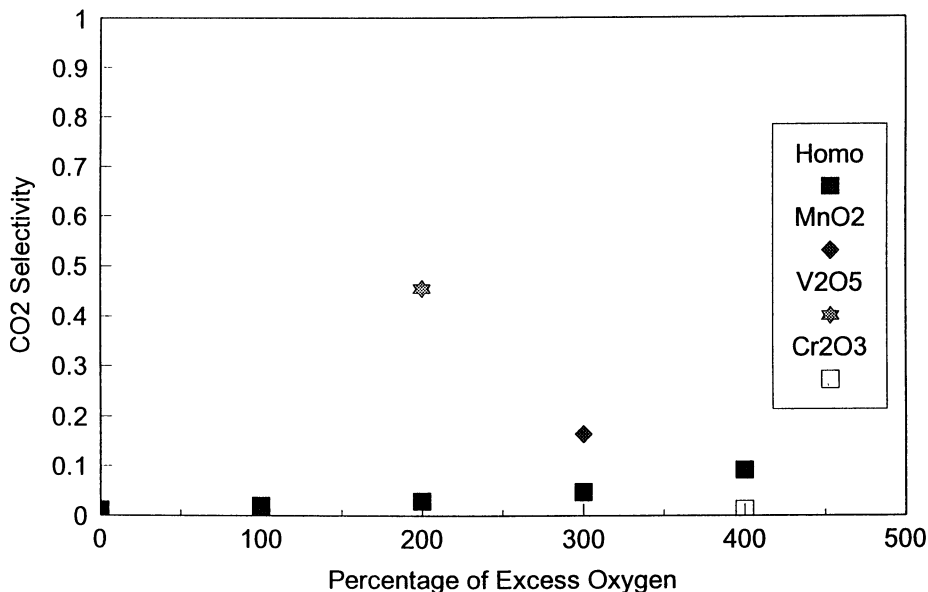


Figure 7: Comparison of catalyst performance against homogeneous oxidation for the selectivity to CO₂ during 1,3-DCB oxidation as a function of oxygen concentration.

oxidation products were found to react with the catalyst, leading to the formation of a metal chloride which was easily extracted by the fluid phase.

Acknowledgments

This work has been funded under a grant from the National Science Foundation, number CTS 8909940. Support for Mr. Ding has been provided by the NASA-JOVE program, under grant number NAG-8-1005. Additional support has been received from the University of Tulsa Office of Research and the Department of Chemical Engineering. The continued support of this research program is greatly appreciated.

Literature Cited

- [1] Thornton, T.D., Savage, P.E., "Kinetics of Phenol Oxidation in Supercritical Water", *AIChE J.*, **38**(3), 321-327, 1992
- [2] Thornton, T.D.; Savage, P.E., "Supercritical Water Oxidation of Phenol", AIChE Spring National Meeting, Orlando, FL, 1990
- [3] Lee, D.S., Gloyna, E.F. "Hydrolysis and Oxidation of Acetamide in Supercritical Water", *Environ. Sci. & Technol.*, **26**(8), 1587-1593, 1992.
- [4] Frisch, M. A., Gloyna, E.F. "Supercritical Water Oxidation of Acetic Acid Catalyzed by CeO₂/MnO₂", M.S. Thesis, University of Texas - Austin, 1992.
- [5] Li, L., Chen, P., Gloyna, E.F. "Kinetic Model for Wet Oxidation of Organic Compounds in Subcritical and Supercritical Water", in **Supercritical Fluid**

Engineering Science: Fundamentals and Applications, E. Kiran and J. Brennecke, eds., ACS Symposium Series 514, American Chemical Society, Washington, D.C., 305, 1993.

[6] Yang, H.H.; Eckert, C.A., "Homogeneous Catalysis in the Oxidation of p-Chlorophenol in Supercritical Water", *Ind. Eng. Chem. Res.*, **27**(11), 2009-2014, 1988

[7] Ding, Z. Y.; Abraham, M.A. "Catalytic Supercritical Water Oxidation: Phenol Conversion and CO₂ Yield", presented at the First International Symposium on Advanced Oxidation Processes for Air and Water Remediation, London, Ontario, Canada, June 29, 1994.

[8] Levec, J. "Catalytic Oxidation of Toxic Organics in Supercritical Water", *Appl Catal B - Environ*, **3**(2-3), 101, 1994.

[9] Martynova, O.I., "Some Problems of the solubility of involatile inorganic compounds in water vapor at high temperatures and pressures", *Russian Journal of Physical Chemistry*, **38**, (5), 587-592, 1964.

[10] Jin, L.; Ding, Z., Abraham, M.A.; "Catalytic Supercritical Water Oxidation of 1,4-Dichlorobenzene", *Chem. Eng. Sci.*, **47**(9-11), 2659, 1992.

[11] Aki, S.N.V.K., Abraham, M.A. "Dissolution of Cr₂O₃ Catalyst during Supercritical Water Oxidation", *AIChE J.*, submitted.

RECEIVED May 18, 1995

Chapter 16

In Situ Mitigation of Coke Buildup in Porous Catalysts with Supercritical Reaction Media

Effect of Feed Peroxides

Bala Subramaniam and Ashraf Jooma

Department of Chemical and Petroleum Engineering,
University of Kansas, 4006 Learned Hall, Lawrence, KS 66045-2223

For the Pt/ γ -Al₂O₃ catalyzed isomerization of 1-hexene ($P_C = 31.7$ bar; $T_C = 231^\circ\text{C}$), catalyst activity is severalfold higher and deactivation rates are severalfold lower in supercritical reaction media when compared to subcritical media. These improvements are due to the *in situ* extraction of coke-forming compounds from the catalyst by supercritical reaction media. To fully exploit the benefits of supercritical operation, it is essential to remove organic peroxides from the hexene feed. Otherwise, these peroxides promote the formation of hexene oligomers at reaction conditions. These oligomers, being major coke producers, accelerate catalyst deactivation. Therefore, removal of the peroxides by pretreatment with activated alumina leads to a further severalfold reduction in coke buildup, and concomitant improvements in catalyst activity and longevity.

Many industrially significant catalytic reactions such as isomerization, disproportionation of aromatics, and alkylation reactions on acid zeolites are characterized by catalyst deactivation due to coking. The mechanism of coke formation on acid catalysts has been reviewed in detail in several books and papers (1-4). Coking of acid catalysts is typically caused by side reactions that involve mainly acid-catalyzed polymerization and cyclization of olefins that produce higher-molecular-weight polynuclear compounds which undergo extensive dehydrogenation, aromatization and further polymerization (1). These products are generally termed as coke and have been characterized as either *consolidated* carbon deposits (that cannot be dissolved in organic solvents) or *mobile* deposits which are precursors of the consolidated deposits (2, 3). For example, in the case of reforming catalysts, the mobile deposits are typically polyaromatic hydrocarbons that can be extracted with the help of organic solvents.

0097-6156/95/0608-0246\$12.00/0
© 1995 American Chemical Society

Combating Catalyst Coking with Supercritical Reaction Media

Conceptually, catalyst deactivation by coking can be mitigated if the mobile coke compounds are desorbed from the catalyst before they can undergo transformation to consolidated carbon. However, the relatively low volatilities of the mobile coke compounds at gas phase (i.e., subcritical) reaction conditions results in the adsorption of these compounds on the catalysts leading to their progressive transformation to consolidated coke. The coked catalyst is typically regenerated by air oxidation of the coke exposing the catalyst to high temperatures (400-500°C), which often cause thermal degradation of the catalyst.

The prevention or mitigation of coke formation on catalysts continues to be the focus of active research. Supercritical media offer a unique combination of solvent and transport properties for the *in situ* extraction of coke-forming compounds from porous catalysts. Within the last decade, our research group at the University of Kansas has experimentally and theoretically investigated the coking and activity of porous catalysts in supercritical reaction mixtures. These studies, summarized elsewhere (5-7), employed 1-hexene isomerization on a Pt/ γ -Al₂O₃ reforming catalyst as the model reaction system. The isomerization was carried out at 281°C, which is about 1.1 T_c of 1-hexene. Hence, by varying the reactor pressure from 22 to 350 bars, we were able to investigate the catalytic isomerization in reaction mixtures ranging in densities from subcritical (0.2 ρ_c) to dense supercritical (2.2 ρ_c) values.

At a fixed space velocity (135 g hexene/h/g cat.), we found that in gas-like reaction mixtures, the catalyst deactivates rapidly due to accumulation of coke compounds in the catalyst. In near-critical reaction mixtures (1.2 ρ_c), however, the coke laydown decreased significantly due to the *in situ* extraction of coke-forming compounds, primarily hexene oligomers, from the catalyst pores. While coke laydown continued to decrease in dense supercritical reaction mixtures (1.7-2.2 ρ_c), the isomerization rates also decreased due to pore-diffusion limitations in the liquid-like media. These results are detailed elsewhere (7), and clearly show that near-critical reaction mixtures offer an *optimum combination* of solvent and transport properties that are better than either gas-phase or liquid-phase reaction media for maximizing the isomerization rates and for minimizing catalyst deactivation rates.

Deleterious Effects of Peroxides in Feed. Besides unreacted 1-hexene and product isomers, hexene oligomers (up to pentamers) were also detected in the reactor effluent (8). We found that these oligomers formed mostly in the fluid phase catalyzed by organic peroxides (about 700 ppm) present in the hexene feed. The oligomer formation steadily increased with pressure with the total amount being roughly 2 wt% of the effluent stream at the highest supercritical pressure investigated. These hexene oligomers are prolific coke producers (1, 8). Thus, the enhanced isomerization rates previously reported (7) at near-critical and supercritical conditions was in spite of increased oligomer formation (and therefore increased coke formation potential) at the higher pressures.

In this paper, we show that catalyst performance in near-critical and supercritical reaction mixtures is dramatically improved when the oligomer formation in the fluid phase is curtailed by removing the organic peroxides from the 1-hexene feed. An on-line alumina trap is used to virtually eliminate organic peroxides from the hexene feed. The resulting decrease in oligomer formation in conjunction with the continued *in situ* extraction of the coke-forming compounds by supercritical reaction mixtures are shown to significantly improve catalyst activity and longevity.

Experimental

Continuing our previous investigations (7, 8), the isomerization of 1-hexene over Pt/ γ -Al₂O₃ catalyst was investigated at 281°C (1.1 T_c) and at pressures yielding subcritical to supercritical conditions (0.2-2.2 ρ_c). Table I lists the operating

pressures and the corresponding reaction mixture densities estimated using the Peng-Robinson equation of state. As in the previous studies, a space velocity of roughly 135 g hexene/g cat./h was employed.

Table I. Operating pressures and reaction mixture densities: T = 281°C (1.1 T_c)

Pressure (bar)	Estimated Density (kg/m ³ x10 ⁻³)	Reduced density
21.7	0.050	0.21
35.5	0.101	0.42
52.7	0.204	0.85
70.0	0.287	1.20
139	0.412	1.72
222	0.475	1.98
277	0.502	2.09
346	0.528	2.20

Catalyst. One gram of 1/16" Pt/γ-Al₂O₃ (Engelhard E-302) reforming catalyst extrudates was used. The Pt loading on the catalyst is 0.6 wt%. The catalyst was first pretreated in flowing nitrogen at 100 sccm in a pretreatment reactor at 330°C for 18 hours, followed by hydrogen at the same flow rate and temperature for four hours. The pretreated catalyst was found to have a BET surface area of 175 m²/g, total pore volume of 0.44 ml/g and an average pore radius of roughly 50 Å.

Reactor Unit. Figure 1 shows a schematic of the high pressure experimental unit. This setup is essentially similar to the unit described previously (7), with improved data acquisition and process control instrumentation. The feed section consists of a liquid feed supply bottle connected to an HPLC pump (Waters' Associates #6000A) capable of delivering constant flow rates between 6 and 600 ml/h against pressure heads up to 400 bar. Either hydrogen or nitrogen gas (for catalyst pretreatment or system purging) is admitted to the experimental unit via a three-way solenoid valve (V1). Either gas or liquid feed is selected by opening valve V2 or V3 respectively.

The 1-hexene (Ethyl Corporation; Lot# PT060592) feed is pumped through a 30 cm long stainless steel tube (roughly 0.8 cm i.d.) containing 11.6 grams of dry activated neutral alumina to remove the peroxides. The feed is then passed through a high-pressure line filter fitted with a 10 μm frit, before flowing through a safety head equipped with a rupture disc rated to a burst pressure of 400 bar at 20°C. The safety head is directly connected to the building vent with a high-pressure hose.

Following the rupture disc, the feed enters the top of a vertically mounted stainless steel tubular reactor (15 ml capacity) and passes over a 3.5 cm long catalyst bed located approximately 10.5 cm from the bottom of the reactor. Thermocouples (J-type) are placed on each end of the catalyst bed to monitor and to provide feedback for PID control of the reactor temperature. The reactor pressure is controlled by means of an Autoclave Engineers' 30VRMM micrometering valve (C_v = 0.04). The micrometering valve is actuated via a microprocessor-controlled stepper motor which is part of the PID control loop for maintaining reactor pressure. A pressure transducer (PT1; 400 ± 1.9 bar) located upstream of the reactor provides feedback for the reactor pressure control loop. The nearly 14,000 steps from the fully-open to the fully-closed valve positions allow fine control of the reactor pressure within transducer precision. Sensitive pressure control is essential along a near-critical isotherm at which small changes in pressure around the critical pressure can lead to relatively large changes in density and transport properties.

Effluent and Catalyst Analyses. After passing through the micrometering valve, the reactor effluent is cooled in a heat exchanger. A manually controlled three-way valve (V7) is used to either sample the liquid effluent for off-line analysis or collect it

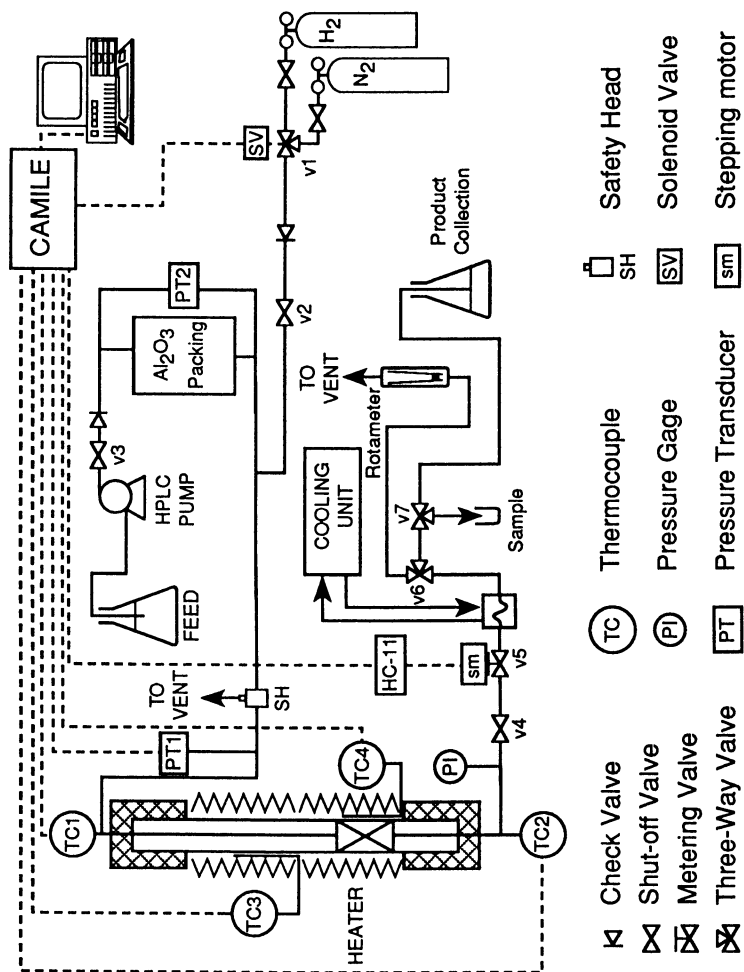


Figure 1. Schematic of high pressure catalytic reactor unit.

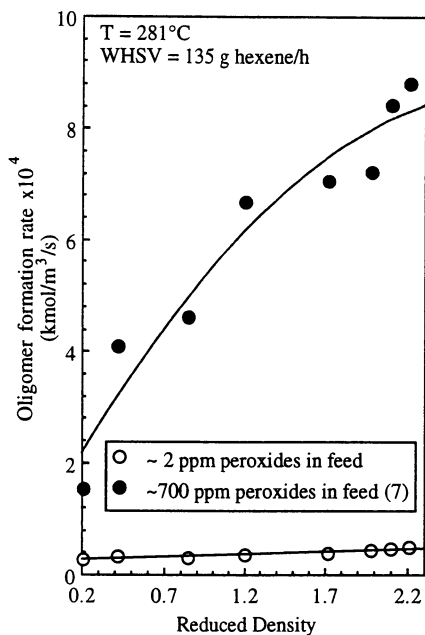


Figure 2. Effect of feed peroxides on fluid phase oligomer production rates.

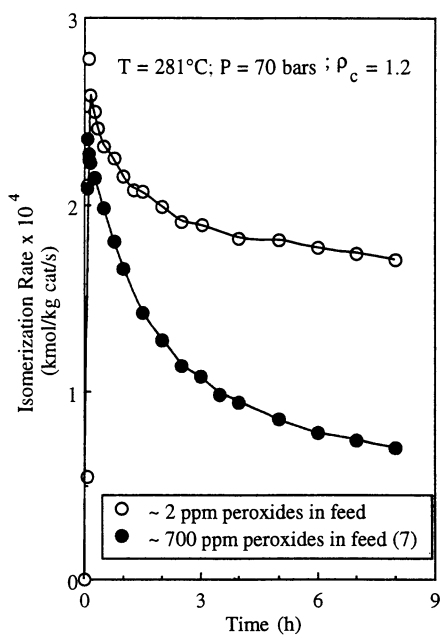


Figure 3. Effect of feed peroxides on isomerization rate histories.

for safe disposal. Whenever purge gas is used in the setup, a manually controlled three-way valve (V6) is used to direct the gas through a rotameter and to the vent. The reactor effluent was sampled at various times for off-line analysis of 1-hexene, its isomers and oligomers using an HP5890 GC/FID instrument. At the end of a run (typically lasting eight hours), the catalyst was removed and subjected to gravimetric analysis (to determine the amount of coke laydown) and micromeritics analysis (to determine the loss in surface area and in pore volume due to coking) with a Gemini 2000 Pore Volume and Surface Area analyzer.

Process Control and Safety Features. All the measurement and control devices in the reactor unit (viz., thermocouples, pressure transducers, stepping motor controls for driving the micrometering valves, solenoid valves and heaters) are interfaced with the Camile 2500 data acquisition and control unit. Programmed sequences developed for reactor startup, operation and shutdown enhance the ability to accurately repeat experimental procedures.

Several safety features have been incorporated into the reactor unit are as follows: (a) The reactor unit is shielded with 3/8" thick Plexiglas for physical protection of personnel and equipment; (b) The air space in the Plexiglas enclosure is kept continuously ventilated to the atmosphere through a roof vent equipped with a vacuum pump. Any accidental spills or leakage of reactants and products are therefore vented to the atmosphere; (c) The ability to stop or change flow streams and to shut off power to the heating elements by programmed sequences in the Camile 2500 data acquisition and control system greatly reduces the chance of thermal reactor runaway. Solid state relays have been installed in series with all the heaters to permit automatic shutdown if any of a number of emergency situations occurs. As an example, if reactor temperature exceeds the 'safe' operating temperature, the power to the heating elements is shut off and the feed introduction is continued to cool the reactor.

Results and Discussion

Peroxide Effect on Oligomer Production Rates. Figure 2 compares hexene oligomer production rates obtained using a hexene feed containing 700 ppm organic peroxides with those obtained using on-line alumina pretreatment of the hexene feed. Analysis by sodium thiosulfate titration following a contacting step with sodium iodide (O'Quinn, A., Ethyl Corporation, Baton Rouge, LA, personal communication, 1993) indicated that the alumina pretreatment reduced the peroxide content from 700 to 2 ppm, expressed as ppm oxygen. In both cases, oligomer formation was measured in the absence of the Pt/ γ -Al₂O₃ catalyst.

It is clear from Figure 2 that the peroxide reduction in the hexene feed results in an approximately fivefold decrease in the oligomer production rate at the lowest subcritical density (0.2 ρ_c) and an 18-fold decrease at the highest density (2.2 ρ_c). While the total oligomer production rate increased twofold over this density range in the case of the alumina-pretreated feed, the corresponding increase is fourfold when using untreated 1-hexene containing about 700 ppm peroxide.

As shown in Figure 3, reducing the oligomer formation in the fluid phase has a positive effect on catalyst performance. At a supercritical density of 1.20 ρ_c (70 bar, 281°C), the initial (10 min.) and end-of-run (8 hours) isomerization rates were about 20% and 250% higher respectively when the peroxide content is lowered. It can also be seen from Figure 3 that the catalyst deactivation rate (i.e., the decline of the isomerization rate with time) was more pronounced in the case of the higher peroxide feed.

Effect on Coke Laydown. The reduction in coke laydown with on-line alumina pretreatment of the hexene feed was observed in the subcritical as well as in the supercritical runs. Gravimetric measurements of the catalyst at the end of each run revealed that without alumina pretreatment, the coke laydown increased to a

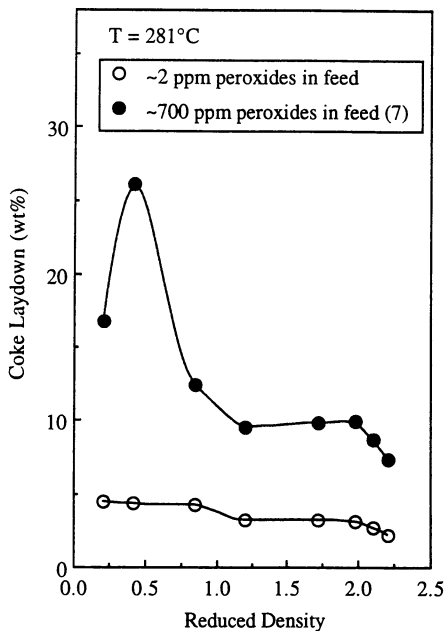


Figure 4. Effect of feed peroxides on coke laydown. (700 ppm data adapted with permission from ref. 7. Copyright 1994 Elsevier).

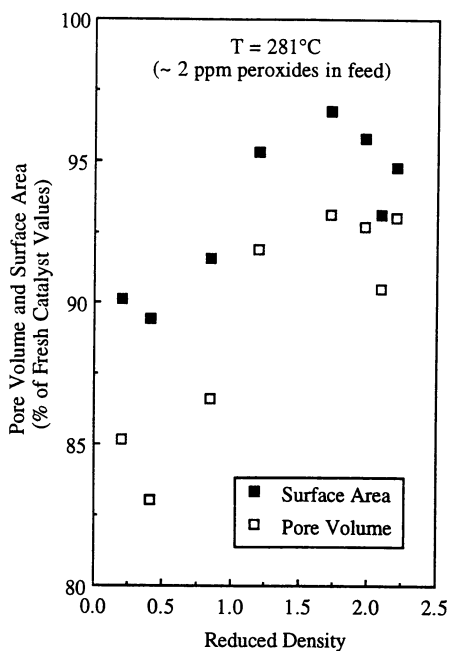


Figure 5. Effect of sub- and supercritical operation on pore accessibility.

maximum value of 26 wt% (based on the weight of the fresh, uncoked catalyst) at subcritical conditions and decreased to a minimum value of 7.3 wt% at supercritical conditions (Figure 4). In contrast, the maximum coke laydown when using on-line alumina pretreatment of the 1-hexene feed was only 4.5 wt%, even at subcritical conditions, and decreased to a minimum value of 2.1 wt % at supercritical conditions.

Micromeritics analysis (by nitrogen physisorption) revealed that more than 90% of the initial catalyst surface area and pore volume are accessible in catalysts exposed to supercritical reaction mixtures (Figure 5). In contrast, up to 70% of the pore volume and surface area are lost due to coking in catalysts exposed to subcritical reaction mixtures using hexene feed containing 700 ppm peroxides (7). These results provide clear evidence that the on-line alumina pretreatment of the 1-hexene feed significantly reduces coke laydown and improves pore accessibilities in subcritical and supercritical reaction mixtures.

Effect on Isomerization and Deactivation Rates. As seen in Figure 6, end-of-run (8 hours) isomerization rates in supercritical reaction mixtures were up to an order of magnitude higher in the case of the alumina-pretreated hexene feed when compared to the lowest rate obtained with the higher peroxide feed. In the former case, the end-of-run isomerization rates increased almost fourfold as the reaction mixture density is increased from subcritical ($0.2 \rho_c$) to supercritical ($1.7 \rho_c$) values. The corresponding increase was only 60% without peroxide removal. In both cases, the isomerization rates increase with isothermal increases in reaction mixture density from subcritical to supercritical values and eventually decrease with further increases in density in the supercritical region (Figure 6). The maximum in the isomerization rate occurs at about $1.7 \rho_c$ with peroxide reduction compared to roughly $1.2 \rho_c$ without peroxide reduction.

As shown previously (7, 9), the increase in the isomerization rates at near-critical conditions is due to the *in situ* extraction of coke-forming compounds. At supercritical densities, even though the coke laydown decreases slightly, the intrinsic pore diffusivities decrease more dramatically as liquid-like densities are approached. Consequently, pore diffusion rates become rate-determining, causing the isomerization rates to decrease with increases in pressure.

Besides the amount of coke laydown, the differences in the isomerization rate trends shown in Figure 6 are affected by both the chemical nature and the physical buildup (uniform vs. pore-mouth choking) of the coke formed in the pores. In general, we found that higher the average molecular weight of the oligomer mixture, denser the coke is (7, 8). Hence, in addition to the severalfold reduction in coke laydown, the coke formed with the lower peroxide feed should be less dense. Diffusion restrictions in the catalyst pores should therefore be correspondingly lower. The improved pore-accessibility may explain the higher rates *and* why the rate maximum (i.e., pore-diffusion limitations) occur at higher densities in the case of the reduced-peroxide feed.

As shown in Figure 7, alumina pretreatment of the feed results in up to a fivefold decrease in the overall deactivation rates (expressed as the % decrease in the isomerization rates between 10 min. and 8 hours) as the reaction mixture density is increased from 0.2 to $1.7 \rho_c$. In sharp contrast, the results obtained without alumina pretreatment of the feed indicate only a slight improvement in deactivation rates at supercritical conditions. Also, as seen in Figure 7, the minimum deactivation rates obtained with alumina pretreatment occurred around the same density range (1.7 - $2.0 \rho_c$) in which the isomerization rate reaches a maximum (Figure 6). These results clearly illustrate that the reduction of peroxides in the 1-hexene feed reduces catalyst deactivation rates, thereby improving isomerization rates. These improvements are especially significant (i.e., severalfold) at supercritical conditions.

Process Improvement and Potential Application Areas. During startup, the catalyst is inevitably exposed to subcritical reaction conditions which favor coke buildup. Also, the coke formation rate is highest initially, when the catalyst is most

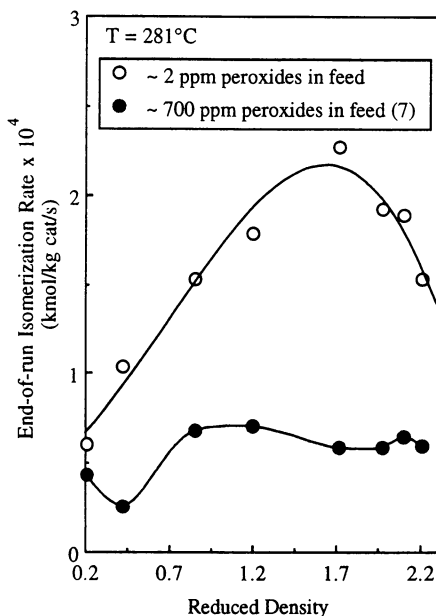


Figure 6. Effect of feed peroxides on end-of-run isomerization rates. (700 ppm data adapted with permission from ref. 7. Copyright 1994 Elsevier).

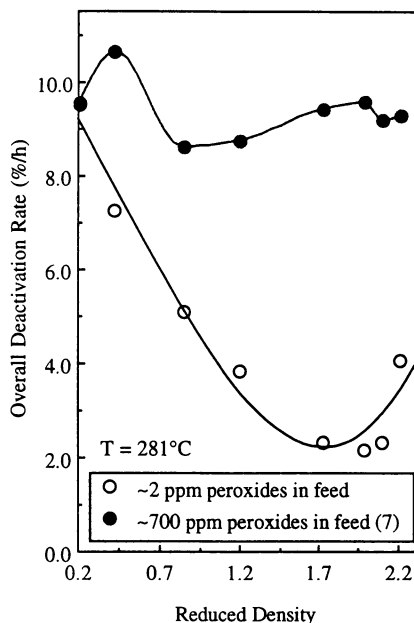


Figure 7. Effect of feed peroxides on catalyst deactivation rates. (700 ppm data adapted with permission from ref. 7. Copyright 1994 Elsevier).

active. To minimize exposure to subcritical reaction mixtures, the following startup procedure is used in all of our supercritical density experiments. With the reactor held at the operating temperature at 281°C, the 1-hexene feed is pumped into the 15 ml reactor at a high flow rate such that the critical density is reached or passed in two minutes. Even with this relatively fast reactor pressurization, the rapid initial deactivation rate could not be avoided (Figure 3).

Our recent studies indicate that dilution of the hexene feed with an inert cosolvent like *n*-pentane, so that the reaction mixture is at supercritical conditions, reduces coke precursor concentrations (and thereby the coke formation rates) while maintaining the *in situ* extraction of the coke-forming compounds (8). Consequently, catalyst deactivation rate is significantly reduced. We are currently investigating the addition of inert cosolvents such as *n*-pentane or *n*-hexane during reactor startup so that the catalyst is exposed to a supercritical reaction mixture when 1-hexene is introduced. This startup strategy could minimize or even eliminate catalyst deactivation during startup resulting in steady activity maintenance, when coke formation rates are balanced by the coke extraction rates.

The foregoing results are significant considering that many acid-catalyzed reactions such as isomerization and alkylation reactions involve olefinic feeds. Removal of the peroxides is essential to better exploit supercritical conditions for the *in situ* mitigation of coke buildup.

Conclusion

Organic peroxides form in olefinic feed stocks upon exposure to air. A few hundred parts per million of these impurities are sufficient to catalyze the formation of olefinic oligomers in the fluid phase. In the compressible region, the oligomer formation increases sensitively with pressure. These oligomers, being prolific coke precursors, cause extensive coking and accelerate catalyst deactivation. On-line adsorption of the peroxides by activated alumina results in almost total removal of the peroxides. For the Pt/ γ -Al₂O₃ catalyzed isomerization of 1-hexene, such pretreatment of the hexene feed significantly improves catalyst performance, especially in supercritical reaction mixtures. Coke laydown is reduced severalfold resulting in improved pore accessibilities, reduced deactivation rates, and enhanced isomerization rates.

Our results suggest that the supercritical decoking process can be further improved by using an inert cosolvent such as *n*-pentane (i.e., one that does not form coke on the catalyst) to fill up the reactor during startup so that the reaction mixture is supercritical when the olefinic feed is introduced. With such an improved process, it should be possible to mitigate coke buildup and, thereby, to obtain higher reaction rates with extended catalyst life in the case of industrially significant isomerization and alkylation reactions on porous catalysts. For alkylation reactions, a solid-acid catalyst with enhanced activity and longevity would be an environmentally-better alternative to conventional processes that employ extremely hazardous hydrofluoric and sulfuric acids as catalysts.

Acknowledgments. This material is based upon work supported partly by the National Science Foundation (under EPSCoR Grant No. OSR-925523). The USAID scholarship awarded to A.J. is gratefully acknowledged.

Literature Cited

1. Gates, B. C., *Catalytic Chemistry*, John Wiley, NY 1991.
2. Franck, J-P; Martino, G. P. In *Deactivation and Poisoning of Catalysts*; Oudar, J. and Wise, H., Eds.; *Chemical Industries*, Marcel Dekker Inc., New York and Basel, 1985, Vol. 20, pp. 216-219.
3. Guisnet, M.; Magnoux, P. In *Catalyst Deactivation 1994*: Delmon, B.; Froment, G. F., Eds.; *Studies in Surface Science and Catalysis*; Elsevier, Amsterdam, 1994, Vol. 88; pp. 53-68.

4. Butt, J. B.; Petersen, E. E. *Activation, Deactivation and Poisoning of Catalysts*, Academic Press, San Diego, CA, 1988; pp. 64-119.
5. McCoy, B. J.; Subramaniam, B. *AIChE J.*, **1995**, *41*, 317.
6. Savage, P. E.; Gopalan, S.; Mizan, T. I.; Martino, C. J.; Brock, E. E. *AIChE J.*, **1995**, *41*, 1500.
7. Ginosar, D. M.; Subramaniam, B. In *Catalyst Deactivation 1994*: Delmon, B.; Froment, G. F., Eds.; *Studies in Surface Science and Catalysis*; Elsevier, Amsterdam, 1994, Vol. 88; pp. 327-334.
8. Ginosar, D. M.; Subramaniam, B. *J. Catal.*, **1995**, *152*, 31.
9. Baptist-Nguyen, S.; Subramaniam, B. *AIChE J.*, **1992**, *38*, 1027.

RECEIVED May 31, 1995

Chapter 17

Supercritical-Fluid-Aided Preparation of Aerogels and Their Characterization

Sermin G. Sunol, Ozlem Keskin, Ozge Guney, and Aydin K. Sunol

Chemical Engineering Department, University of South Florida,
Tampa, FL 33620–5350

Gels of inorganic oxides (NiO/Al₂O₃ gels), prepared by the sol-gel method, are dried using supercritical solvent extraction and supercritical drying to obtain aerogel catalysts as porous powder. The supercritical extraction is carried out at several temperature and pressures of carbon dioxide. In supercritical drying of the solvent indigenous to the gel (alcohol), inert and solvating gases, (nitrogen and carbon dioxide) are used to pressurize the system to a value above the critical pressure of the fluid mixture. The effect of the solvent power of carbon dioxide is investigated at different temperatures. Gels are also dried in air and under vacuum in order to compare chemical and physical properties of xerogels with those of aerogels. Pore structure of the xerogel and aerogel catalysts is determined using scanning electron microscopy (SEM). Ni/Al ratio of the catalysts is determined using electron disperse spectroscopy (EDS).

Properties which need to be considered in catalyst design and their relation to catalyst behavior are depicted in Figure 1. Aerogels show great promise in catalytic applications, especially due to their unique morphological properties (high porosity and high surface area) as well as excellent chemical properties (high chemical activity) which can not be easily achieved with other types of catalysts (*J*). Therefore, it is worthwhile to investigate aerogel catalyst preparation.

In sol - gel process, metal alkoxide is dissolved in alcohol which can be readily removed from the gel matrix upon the formation. The gelation process involves hydrolysis and condensation reactions of metal alkoxides. Due to its unfavorable drying conditions, water is not used as a solvent, however, it is utilized during the hydrolysis reaction. If the solvent is evaporated slowly from the gel, a xerogel is obtained. During evaporation, large capillary forces are exerted as the liquid - vapor interface moves through the gel. These forces cause shrinkage of the pores within the gel. Removal of the solvent (alcohol) from the gel under supercritical conditions results in the formation of the aerogel. Since this drying procedure eliminates the liquid - vapor interface, aerogels are formed in the

0097–6156/95/0608–0258\$12.00/0
© 1995 American Chemical Society

absence of capillary forces. Aerogels retain the morphology of the original alcogel.

There are several methods developed for removing the solvent from the gel under supercritical conditions. The first one is the one suggested in the pioneering work by Kistler (2), in which the solvent is brought to supercritical conditions in an autoclave and evacuated under these conditions. In order to pressurize the autoclave to a pressure above the critical value for the alcohol, more alcohol is added to the autoclave (3). Supercritical conditions of the solvent are reached by supplying heat to the autoclave. After the system pressure reaches a preselected value which is above the critical, the temperature is raised at constant volume. Once the temperature is above its critical value, the supercritical fluid is vented out of the autoclave at constant temperature (4). The P-T behavior for this procedure is shown as route A-B (1) in Figure 2.

This method was later improved by van Lierop and co-workers (5). In this improved version of the method, vaporization of the solvent is completely suppressed by pressurizing the autoclave with an inert gas prior to heating while the subsequent heating is carried out batch at constant volume. Thus, the entire procedure is carried above the vapor-liquid interface of a Pressure-Temperature (P-T) diagram, shown as route A'-B (2) in Figure 2.

Different researchers have utilized solvent exchange prior to supercritical drying. In this method, the solvent (alcohol) was substituted with liquid Carbon Dioxide. This method was applied to the production of silica aerogel by Tewari et al. and Rangarajan et al. (6, 7).

In another method, developed by Jacobucci and co-workers (8), alcohol is removed by supercritical CO₂ extraction in a semi-continuous system.

In this present work, the objective is to develop a supercritical drying method which prepares aerogel catalysts with tunable physical and chemical properties. For this purpose, catalysts are prepared using different methods at various experimental conditions, and their characteristics like catalyst bulk density, pore structure and Ni/Al distribution are measured and compared with the ones of the xerogels.

Experimental

Gel Preparation. NiO/Al₂O₃ gels are prepared using the method suggested by Teichner and co-workers (3). Aluminum sec-Butylate is dissolved in sec-Butanol while Nickel Acetate is dissolved in Methanol separately. Water is added to the second mixture in near stoichiometric amounts necessary for the hydrolysis reactions. The two solutions are mixed and a precipitate of alumina is immediately formed. The only variable studied in the preparation of the gel is the amount of water used for the hydrolysis reaction. Excess water is used in the preparation of some gels in order to investigate the effect of excess water in drying of the gel. Gels are dried immediately after preparation, in order to eliminate the effect of aging.

Drying of Gel.

CO₂ Extraction of the Alcohol. In these semi-continuous experiments, CO₂ is passed through the extractor continuously at a constant temperature, pressure and flow

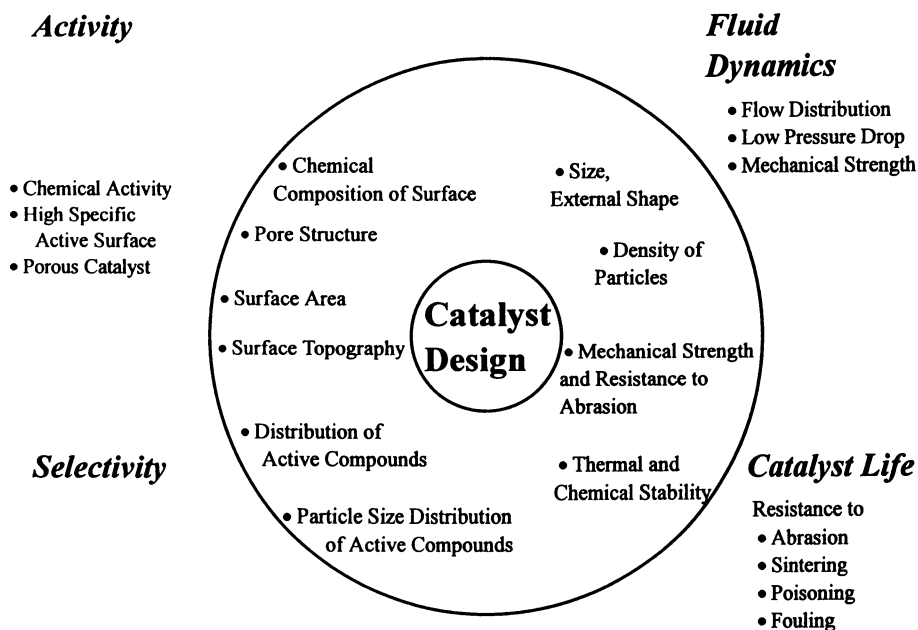


Figure 1. Design features of catalysts.

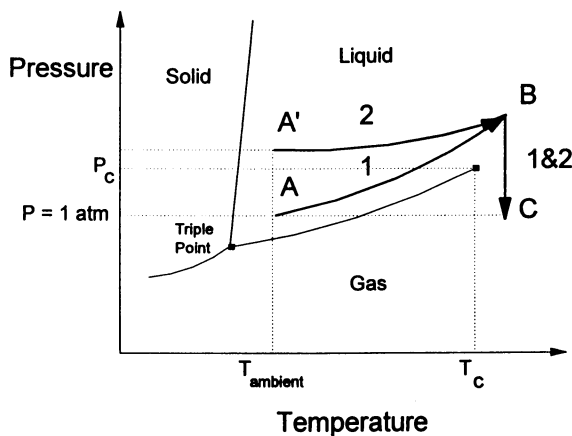


Figure 2. P-T diagram for supercritical drying.

rate in order to extract alcohols (butanol and methanol) from the gel. The experimental set-up is shown in Figure 3. CO₂ feed, from a gas tank, is compressed into a surge vessel which is enclosed at the same constant temperature environment as the extractor and the transfer lines up to the back pressure regulator. Flowing CO₂ is preheated in a coil and enters the extractor, that has the gel, from the bottom. The extractor has an I.D. of 0.562" and length of 12". The extractor outlet is connected to a back pressure regulator. CO₂-Alcohol mixture leaving the back pressure regulator bubbles through a sample collector, cooled with water, where alcohols are absorbed from the CO₂ which passes through a wet test meter as being vented.

Supercritical Drying of the Alcohols. In this second method, alcohols or CO₂-Alcohol mixtures are brought to a supercritical condition and the supercritical fluid is removed slowly from the gel. The experimental set-up for this system is shown in Figure 4. Prior to experiments, the reactor containing the gel is pressurized to 80 atmospheres. In cases where N₂ is used for pressurizing, high pressure feed gas is used directly in order for pressurization to the set pressure of 80 atmospheres. In experiments where the system is pressurized to 80 atmospheres with CO₂, CO₂ feed is compressed before it is fed to the drying vessel that contains the wet gel. The drying vessel has an I.D. of 0.562" and length of 6". After a predetermined pressure is reached, the sand bath heater housing the drying vessel is heated so that a temperature above the critical value of the alcohol mixture or CO₂-Alcohol mixture is reached. The heating rates used are 1°C/min (low heating rate), 10°C/min (high heating rate) and flash heating. The system is kept under these conditions for a specified time. The supercritical fluid is then vented out of the system keeping the temperature of the reactor constant. At the end of the experiment, the gel is swept with fresh CO₂ to remove remaining trace amounts of alcohol and water. The system is subsequently cooled and the aerogel catalyst is removed.

Air and Vacuum Drying of the Alcohols. Xerogels are prepared by air and vacuum drying. Air drying is performed at 110°C for 15 hours. Vacuum drying is performed at a pressure of 5 mmHg, at 60°C for 35 hours.

Analysis of Catalysts. Pore structure of the xerogel and aerogel catalysts are determined using scanning electron microscopy (SEM). Ni/Al ratio of the catalysts is determined using electron dispersive spectroscopy (EDS). Bulk densities of catalysts are determined gravimetrically, with a sample size of 10 ml.

Results and Discussion

Aerogel catalysts are obtained using different methods described above. Results are given and discussed separately for catalysts prepared using each method. An overview of the procedures is shown in Figure 5.

Aerogels Prepared by CO₂ Extraction of the Alcohols. Different aerogel catalysts are prepared using CO₂ extraction of the solvents (sec-butanol and methanol). Most important parameters which are expected to affect physical properties of the aerogels are

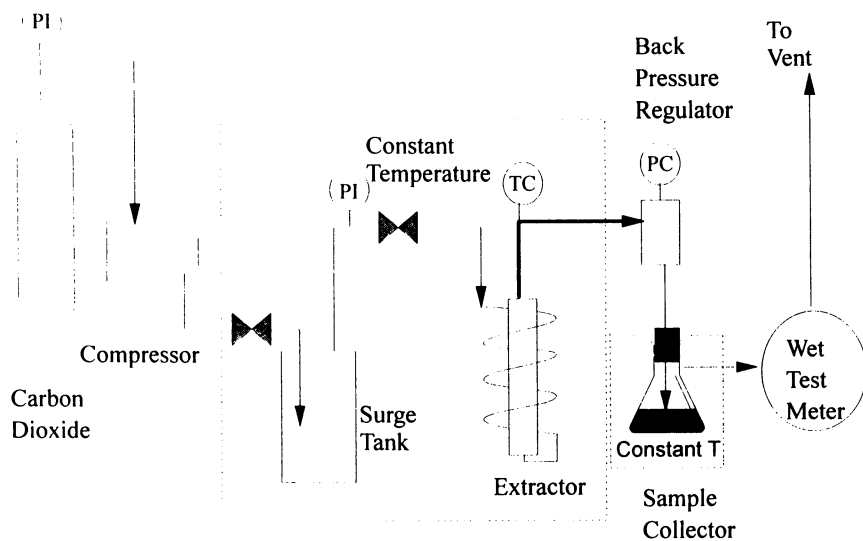


Figure 3. Experimental set-up for CO₂ extraction.

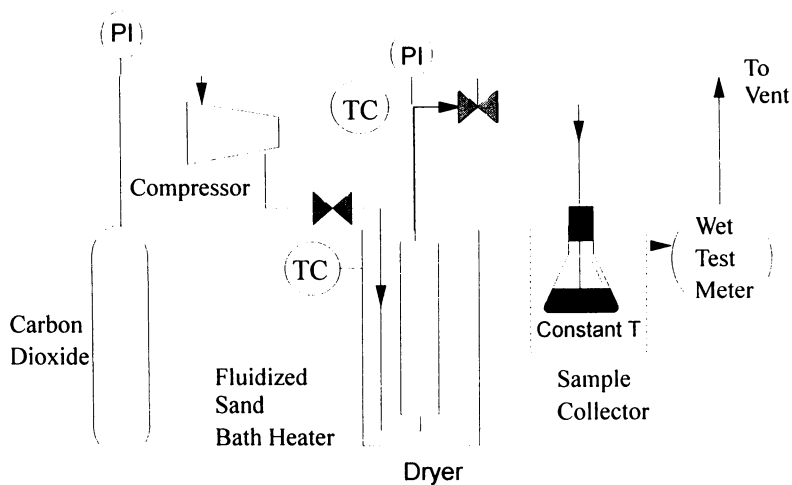


Figure 4. Experimental set-up for supercritical drying of alcohols.

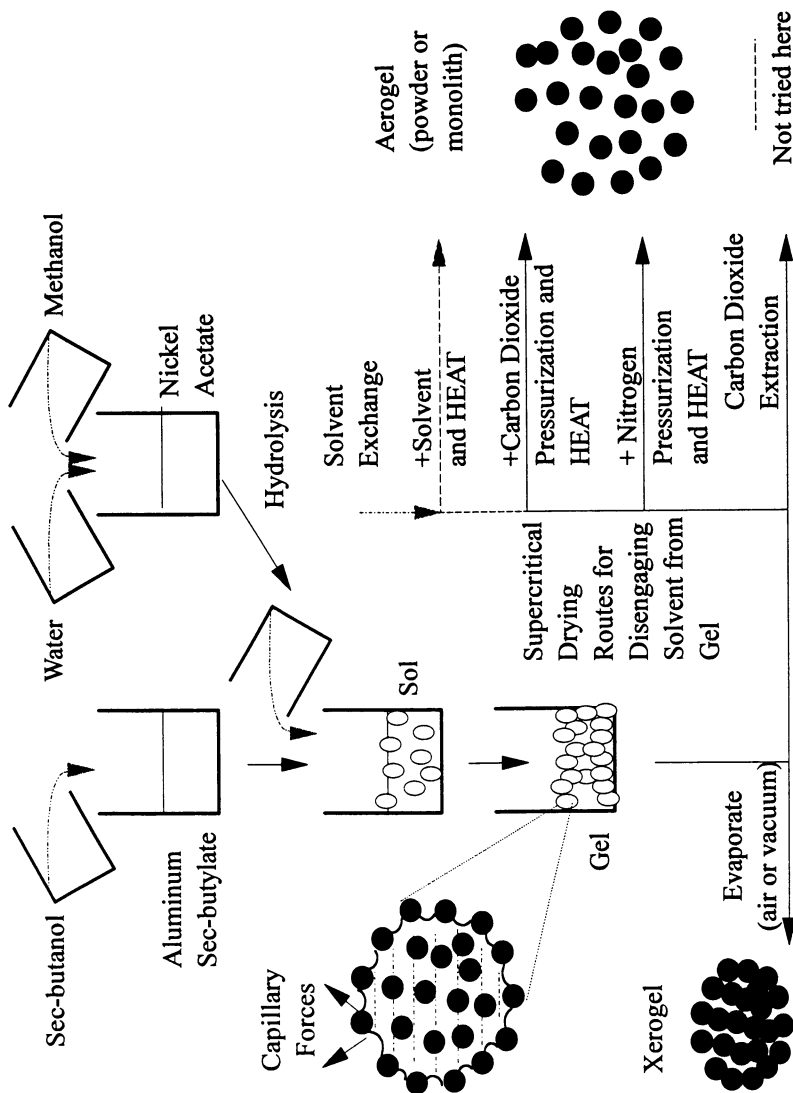


Figure 5. Procedure for aerogel and xerogel preparation.

temperature, pressure, time of extraction, amount of CO₂ used per gram of alcohol extracted, and flow rate of CO₂. In order to determine the effect of the amount of water used for the hydrolysis reaction during gel formation, Samples A20 and A21 are prepared using 100% excess water as opposed to 15% used in all other runs. (Table I).

Table I. Experimental Conditions and Densities of CO₂ Extracted Aerogels

Run No.	T (°C)	Extraction Time (min)	P (atm)	Amount of Wet Gels (g)	CO ₂ /Alcohol (l/g)	CO ₂ Flow Rate (l/min)	Aerogel Density (g/ml)
A5	45	120	100	24.5	5.3	2.8	0.083
A9	45	40	100	24.6	7.2	3.9	0.094
A14	45	40	100	8.4	24.1	4.3	0.112
A6	35	120	100	24.4	15.8	2.8	0.095
A7	35	40	100	8.5	7.9	1.4	0.082
A17	35	120	100	8.5	71.8	4.3	0.105
A10	40	80	80	16.4	32.4	5.8	0.070
A11	40	80	80	16.5	16.0	2.9	0.087
A12	40	80	120	16.4	25.4	4.5	0.091
A13	40	80	120	16.0	25.2	4.5	0.094
A16	40	80	100	16.4	24.7	4.4	0.095
A19	40	80	100	16.3	27.9	5.0	0.108
A20	40	80	100	17.0	25.3	4.5	0.098
A21	40	80	100	17.0	29.0	5.2	0.111

It is important to be able to produce aerogels with high surface area and porosity at low temperatures and pressures, using the minimum amount of CO₂. In order to have an idea about the porosity of the aerogels, their bulk densities are measured. Bulk densities of aerogels which are produced under different drying conditions are similar (Table I). Pore size distribution of the catalysts should be investigated to show the effect of drying conditions on the characteristics of the aerogels.

Aerogels Prepared by Supercritical Drying of the Alcohols. Fifteen different aerogel

catalysts are prepared using supercritical drying of butanol and methanol. Aerogel #B17 (Table II) is prepared according to the method suggested by van Lierop and co-workers. In preparation of the rest of the aerogels presented in Table II, CO₂ is used to pressurize the extractor prior to drying. There are two reasons for using CO₂ for pressurizing. The critical temperature of CO₂-alcohol mixture is less than that of alcohols. The other reason was to make use of the solvent power of CO₂ for dissolution of alcohols. In the experiments carried out with CO₂, the effect of temperature, the rate at which the reactor is heated to the peak temperature and the rate at which the supercritical fluid is vented out of the reactor are investigated. In all experiments, the initial pressure is adjusted and the pressure is allowed to increase as the temperature was raised. The possible effect of using excess water in hydrolysis on the properties of the aerogels is also investigated in this set of experiments (experiments #B11 and #B15).

Table II. Experimental Conditions and Densities of Supercritically Dried Aerogels

Run No.	Gas	Temperature (°C)	Heating Rate	Depressurizing Time (min)	% Excess Water	Aerogel Density (g/ml)
B17	N ₂	280	high	30	15	0.671
B3	CO ₂	170	low	30	15	0.140
B5	CO ₂	280	low	30	15	0.076
B6	CO ₂	170	high	30	15	0.080
B8	CO ₂	225	high	30	15	0.076
B10	CO ₂	225	high	30	15	0.077
B11	CO ₂	225	high	30	100	0.058
B12	CO ₂	225	high	60	15	0.105
B13	CO ₂	225	high	45	15	0.066
B15	CO ₂	225	high	30	100	0.085
B16	CO ₂	225	high	30	15	0.087
B18	CO ₂	170	flash	30	100	0.123

In experiments where the reactor is pressurized with CO₂, aerogels with densities similar to the ones obtained in the first set of experiments (CO₂ extraction of the alcohol) are obtained. Table II shows that at a temperature as low as 170°C, aerogels with low densities (~0.1 g/ml) are formed which indicates that the CO₂-Alcohol mixture forms a

supercritical fluid. Other experimental parameters such as heating rate, depressurizing rate, water content of the gel did not seem to affect the bulk density of the end product. On the other hand, the experiment, where the reactor is pressurized with N₂ prior to heating, shows that at a temperature as high as 280°C, supercritical fluid conditions could not be reached. The catalyst produced under these conditions is almost as dense as the air and vacuum dried xerogels. There was very limited number of experiments done with nitrogen and improvements over air and vacuum drying should be expected.

Comparison of Xerogels with Aerogels. Gels are dried under air and vacuum in order to compare properties of xerogels with those of the aerogels. Densities, and Ni/Al ratio (through EDS) of the xerogels are determined. Table III shows a comparison of the properties of the xerogels and aerogels. Standard deviations of the weight fractions of Nickel and Alumina for different particles of the same sample are shown in parentheses.

Table III. Comparison of the Properties of Xerogels and Aerogels

Catalyst Type / Run no.	Density (g/ml)	Ni / Al Ratio (wt/wt)
Air Dried Xerogel / D1	0.740	61.18 / 38.82
Air Dried Xerogel / D2	0.825	not determined
Vacuum Dried Xerogel / V1	1.165	59.00 / 41.00
Vacuum Dried Xerogel / V2	0.817	not determined
Aerogel / A5	0.083	41.62 / 58.38 (±0.65)
Aerogel / A9	0.094	43.12 / 56.89 (±1.08)
Aerogel / A14	0.112	43.13 / 56.87 (±3.99)
Aerogel / A16	0.095	46.51 / 53.49 (±0.11)
Aerogel / B5	0.076	38.20 / 61.80 (±0.52)
Aerogel / B6	0.080	35.35 / 64.65 (±7.91)
Aerogel / B8	0.076	39.23 / 60.77 (±4.48)

As can be seen from Table III, xerogels produced under air and vacuum conditions have similar densities while aerogels produced under supercritical extraction conditions, (and also under supercritical drying as can be seen also in Table II) are an order of magnitude less dense than the xerogels. The xerogels also have similar Ni/Al ratio. An other interesting feature of the aerogels is that they have a smaller Ni/Al ratio than the xerogels although the corresponding alcogels are prepared using the exact same procedure. This result is shown for both the CO₂ extracted and supercritically dried aerogels although standard deviation of the weight fractions for different particles of the same sample and

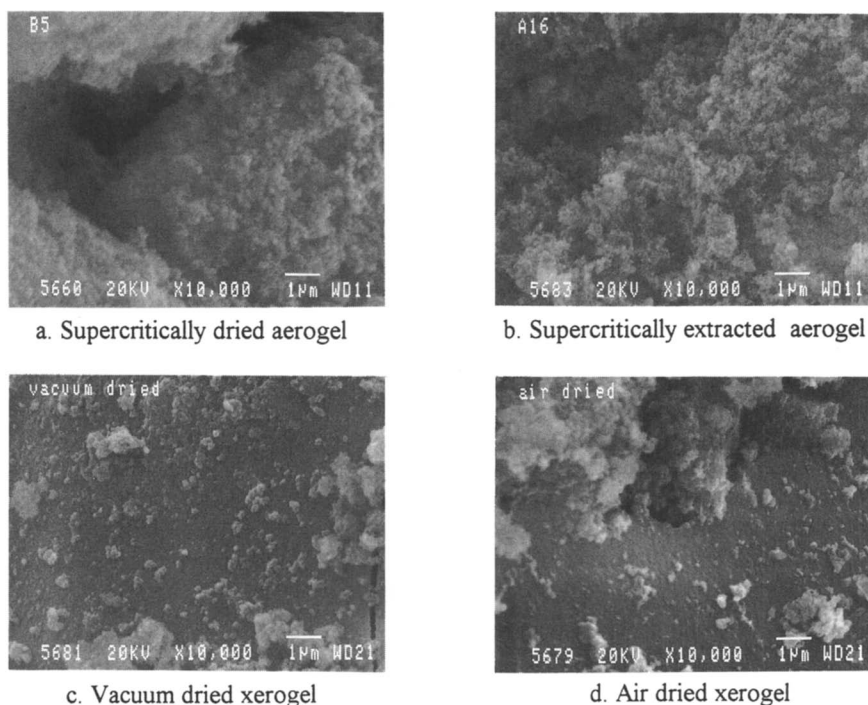


Figure 6. SEM image of xerogel and aerogel surfaces.

weight fractions for different samples show larger variation for the supercritically dried samples. Also, Nickel fraction is observed to be less for supercritically dried samples. However, further work is necessary to elucidate the Ni/Al distribution.

In order to compare the pore structure aerogels with xerogels qualitatively, SEM is used. Figures 6 and 7 show SEM pictures for two xerogels (D1 and V1) and two aerogels (A16 and B5), at different magnifications. Comparison of surfaces for xerogels and aerogels shows that aerogels have rougher surface. (e.g. Figure 6). Flat surfaces observed for xerogels could not be seen on any of the aerogels. This suggests that the aerogel is more porous than the xerogel, which is consistent with the results obtained for the bulk density. When xerogels and aerogels are imbedded into epoxy resin and the surfaces are polished, cross sections of the samples could be viewed, as seen in Figure 7. While 500 magnification shows single particles, pores can be seen at higher magnifications. The higher porosity of the aerogels seems to be due to the abundance of micro pores rather than macro pores.

Conclusions

NiO/Al₂O₃ aerogels in the form of porous powder can be prepared using supercritical CO₂ extraction at 35°C and at 100 atm within 40 minutes using CO₂ at a flow rate of 1.4 l/min. Results also show that a pressure of 80 atmospheres would be sufficient in order to obtain the aerogel at the 35°C and within 40 minutes.

A new method was introduced for drying the alcogels, where for the first time in literature, CO₂ is used in order to pressurize the reactor prior to the experiments. The use

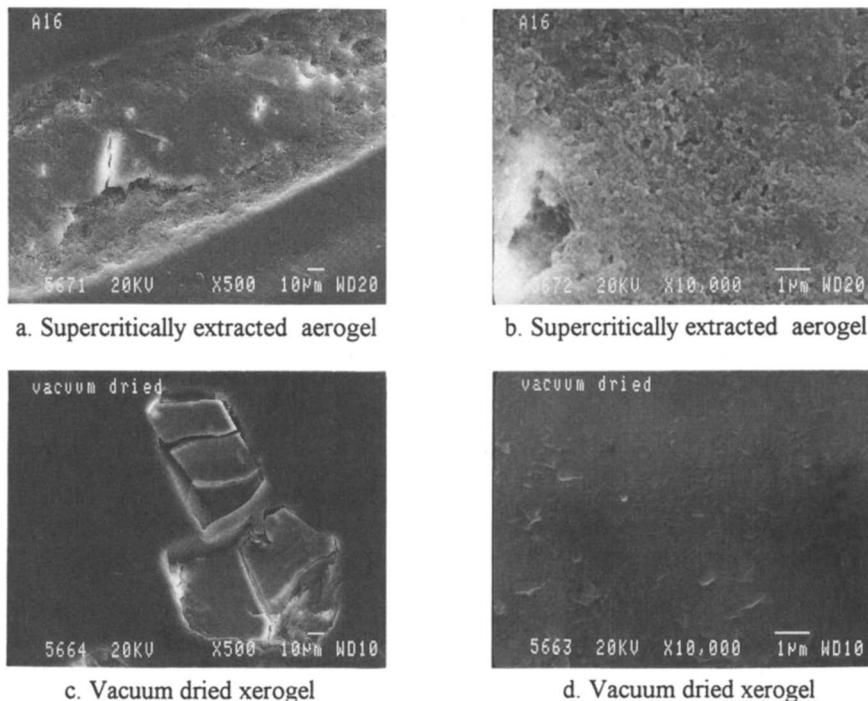


Figure 7. SEM image of the cross sections of xerogels and aerogels.

of CO_2 instead of an inert gas for this purpose is found to be extremely useful for carrying out the drying at lower temperatures. With the new method, aerogels are dried at temperatures which are 100°C or more lower than the critical temperature of the alcohols.

Acknowledgments

SGS would like to thank NATO for a Research Fellowship; SGS and OK appreciate leave provided by Bogazici University, and the authors acknowledge the Research and Creative Scholarship funds provided by the University of South Florida.

Literature Cited

1. Schneider, M. *Titania Based Aerogel Catalysts*, PhD Dissertation, ETH, Zurich, 1994.
2. Kistler, S.S. *J. Phys. Chem.* **1932**, *36*, 52.
3. Gardes, G.E.E.; Pajonk, G.M. and Teichner, S.J. *J. Catalysis* **1974**, *33*, 145.
4. Schmitt, W.J.; Grieger-Block, R.A. and Chapman, T.W. In *Chemical Engineering at Supercritical Conditions*; Paulaitis, M.E. et al. eds.; 1983, p 445-460.
5. Van Lierop, J.G.; Huizing, A.; Meerman, W.C.P.M. and Mulder, C.A.M. *J. of Non-Crystalline Solids* **1986**, *82*, 265.
6. Tewari, P.H.; Hunt, A.J. and Lofftus, K.D., *Mater. Lett.*, **1985**, *3*, 363.
7. Rangarajan, B.; Lira, C.T. *J. of Supercritical Fluids*, **1991**, *4*, 1.
8. Ayen, R.J.; Jacobucci, P.A. *Rev. Chem. Eng.* **1988**, *89*, 157.

RECEIVED July 18, 1995

Chapter 18

Measurement and Modeling of Supercritical Fluid Extraction from Polymeric Matrices

K. M. Dooley, D. Launey, J. M. Becnel, and T. L. Caines

Department of Chemical Engineering, Louisiana State University,
Baton Rouge, LA 70803-7303

Extraction of low-molecular weight solutes by supercritical fluids (SCFE) is often rate-limited by the interaction of the solute with a polymer. In typical applications, the effect of the SCF on the matrix through swelling is paramount. Both the equilibrium of the solute between polymer and SCF and its rate of mass transfer are affected by this polymer-solvent interaction. Experimental data for a situation where the SCF swells the polymer strongly (CO_2 /ethylbenzene/polystyrene) are presented; for this system the extractions are neither close to equilibrium nor are they completely diffusion-limited. This results in unusual variations in the amounts of ethylbenzene extracted versus temperature and pressure, in particular a much stronger dependence on temperature than on density. We found roughly a 10^6 -fold increase in the experimental ethylbenzene diffusivity in the polymer phase when SCF- CO_2 was present. A model used to estimate the solute's diffusivity in the swelled polymer is presented.

Introduction

Extraction of low-molecular weight solutes by supercritical fluids (SCFE) is often rate-limited by the interaction of the solute with a polymer. For example, in soil extractions the contaminants are often bound to organic polymers in the soil; these polymers are typically humic acids and polyphenols of molecular weights as high as 10,000. Also, polymer recycling is becoming more prevalent, and it is therefore necessary to open up new markets for recycled products. This will necessitate better purification methods for used polymers, and SCFE has shown promise in removing residual monomers, solvents, plasticizers and antioxidants from commercial polymers (1-5). In other polymer-related applications, SCFs can extract oligomers in the preparation of monodisperse polymers (6-7), and can separate mixed polyolefins by flotation, even those differing in density by only $\sim 10 \text{ kg/m}^3$ (8).

We have undertaken a fundamental study of the factors controlling SCFE

0097-6156/95/0608-0269\$12.00/0

© 1995 American Chemical Society

of trace contaminants from polymeric materials, which includes high organic-content soils. Phenomena of interest include (1) depression and broadening of the glass transition temperature (T_g) region by the SCF if it swells the polymer, (2) the often opposite effects of increased temperature on the solute diffusivity in the polymer (typically increases exponentially) and equilibrium solubility in the SCF (typically goes through a maximum), and (3) the significant effect an SCF can have on the solute diffusivity if the SCF strongly swells the polymer, which is often the case at high pressure.

Modeling Considerations for SCFE from Polymers

Because of these phenomena, extractions from polymers, or materials containing polymers such as high organic-content soils, show unusual rate-limited behavior that often cannot be predicted by simpler desorption models. Such models would include local equilibrium theory (LET), which assumes equilibrium at all times and all spatial positions between the SCF and the solid (9), and models based upon rate-limiting intraparticle diffusion to the solid surface at a constant diffusivity (5). More complex models with analytical solutions combining intraparticle diffusion, equilibrium at the solid surface, and interfacial mass transfer have been presented (10-11), but these are based on the assumption of a linear equilibrium relationship, which is sometimes a poor one where polymers are concerned.

The problems these unusual phenomena pose in the design of an SCFE unit can be understood by examining Figure 1, which is from previous work in our group (12). The data are for the extraction of DDT from a high organic-content soil (4.8 wt% total organics, 1000 mg/kg DDT). The SCF solvents are dry CO_2 , wet (~0.5 wt% water) CO_2 , and 5 wt% methanol/ CO_2 . With dry CO_2 the fraction of DDT which can be removed from the soil is fixed at ~60%, i.e., the rate of extraction approaches zero at this point. With 5 wt% methanol, however, extraction is rapid and goes to completion. Wet CO_2 exhibits a slower initial, but ultimately a faster extraction rate than does dry CO_2 .

These data can be interpreted as follows. Because methanol at this concentration does not greatly affect the solubility of DDT in SCF- CO_2 (13), the methanol/ CO_2 extraction data are more representative of an equilibrium solubility-controlled process. In other words, the methanol is enhancing the rate of mass transfer of DDT into the SCF, the non-methanol data are far from equilibrium, and so LET cannot apply to the non-methanol data. It can be seen that the times required to clean the soil using either dry or wet CO_2 are considerably in excess of times characteristic of LET. However, the wet CO_2 results suggest that water is a potentially effective cosolvent at longer times, when the soil has been depleted of most of its low molecular weight organic material. This is probably due to some polymer swelling by water.

Conversely, it is possible to accurately model the data of Tan and Liou (14) for the extraction of ethyl acetate from activated carbon by LET, using a Langmuir isotherm. This result suggests that the primary reason for the unusual

behavior in Figure 1 is the presence of the organic polymeric phase in the soil, which is not present in activated carbon or other simple adsorbents.

At first glance, the occurrence of phenomena (2)-(3) listed above would suggest extraction at as high an operating pressure as possible, and at a temperature much higher than is usually the case in SCFE. This operating strategy was essentially that adopted in a study of the extraction of plasticizers from polypropylene (5). However, aside from the economic impracticability of such a strategy, other results suggest lower temperature operation may be possible. In particular, the exact location of the modified T_g might be important in some extractions. Burgess and Jackson (3) observed maximum rates of extraction of CCl_4 from chlorinated polyisoprene using SCF-CO_2 at temperatures roughly the same as the modified T_g at any given pressure. These results suggest that depression of T_g through swelling by the SCF greatly affects either the solute equilibrium, or the solute's intraparticle diffusivity, or both. In our results we sometimes observed a similar phenomenon, in that as we approached the modified glass transition pressure at constant temperature the extraction rates were sometimes greater than was the case at higher pressures. But this was not universally true at all the temperatures we studied, and so does not represent a general principle.

Experimental Apparatus and Procedures

For the polymer extractions we used a bench-scale system (Figure 2) consisting of a cylindrical extraction cell (~6.4 mL) housed in a differential scanning calorimeter (DSC; Setaram C-80). The SCF entered the cell through a small tube just above the solid sample. An LC pump (Eldex) supplied the SCF-CO_2 , which was regulated by both a pressure controller (Dwyer Mercoind D) and a backpressure regulator (Tescom 26-1700). The effluent was sampled by a 16-port valve, then analyzed by GC (Varian 3400 with flame ionization). Therefore both the extraction rate and the enthalpy changes of the solid phase were measured.

A constant 1.0 mL/min liquid CO_2 feed rate was used to extract 3.0 wt% ethylbenzene (EB, Fisher, reagent) from thin circular disks of polystyrene (PS, Polyscience, MW = 20,000). The polymer was impregnated with EB in sealed tubes at 323 K for one day, under N_2 . The pellet geometry was controlled by die-molding 335 mg EB/PS (~4.3 mm thickness, 10.8 mm diameter, which was the cell i.d.). This geometry was deemed most appropriate for the extraction cell in order to maintain a controlled shape, because the disk could expand axially but not radially. Therefore its surface area for mass transfer remained roughly constant.

Results - Extraction of Ethylbenzene (EB) from Polystyrene (PS)

The DSC measurements during extraction showed that the exothermic dissolution of CO_2 into the polymer was rapid, followed by a long endotherm characterizing slow desorption of the solute ethylbenzene. These results showed that polymer swelling by SCF-CO_2 took place almost instantly considering the long time scale

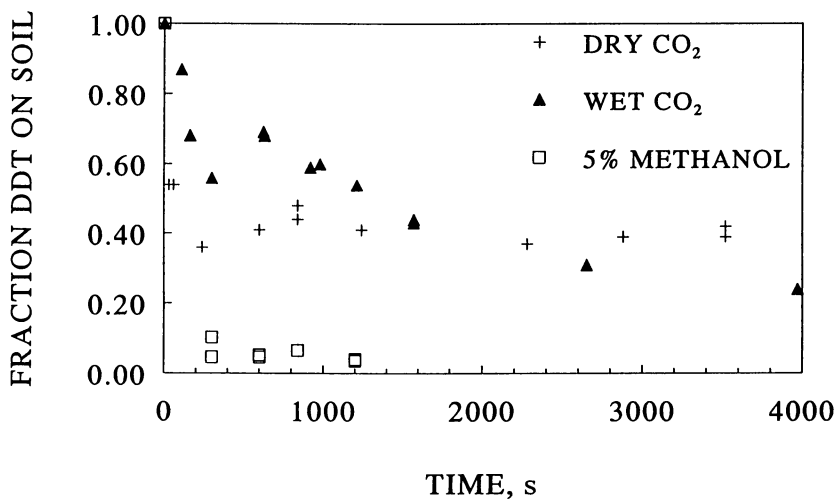


Figure 1. Extraction of DDT from soil (313 K, 10 MPa) using CO₂, H₂O-saturated CO₂, and 5 wt% methanol/CO₂. Reproduced with permission from ref. 12. Copyright ©1990, AIChE.

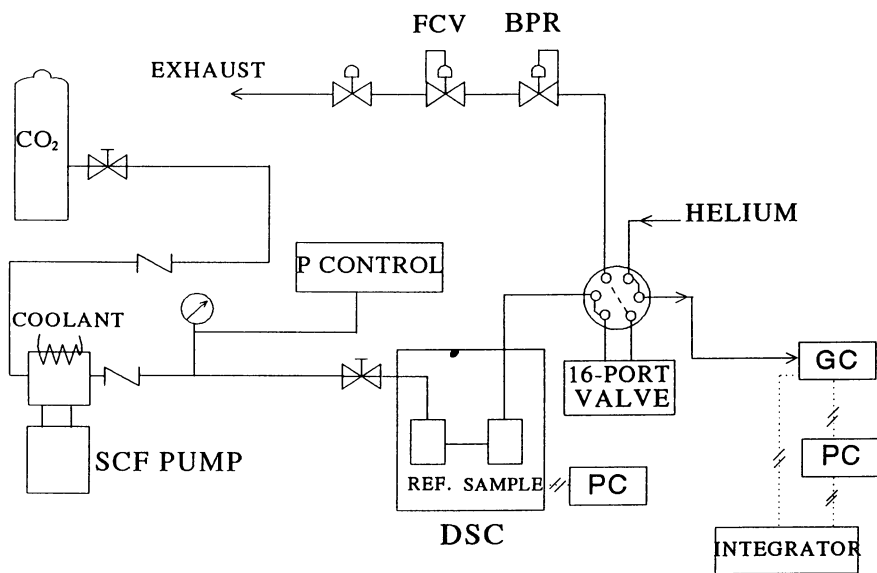


Figure 2. Apparatus for SCFE of polymers.

of the experiments. Post-experimental examination of the disks revealed swelling ratios of 2-4, but these examinations were by necessity conducted after depressurization, and so overestimate the extent of swelling. Nonetheless, these data combined with the DSC data suggest extensive, rapid swelling by CO₂; for example, a typical value for the integrated DSC exotherm in an extraction experiment was 300 J/g polymer (compare to a typical enthalpy of vaporization for CO₂ of 900 J/g CO₂).

Some of the near-critical and SCF-CO₂ extraction data for the 3 wt% EB/PS mixtures are presented in Figures 3 and 4. Data were taken at pressures of 6.9-11.8 MPa and temperatures of 308-363 K. These are plots of dimensionless EB concentration in the polymer, obtained through integration of the EB concentrations in the extract with respect to time. All of the EB concentration profiles showed a similar trend, indicating a rate of extraction which often tended to a limiting value at longer times. These results are consistent with a mass transfer model where the initial surface concentration was rapidly depleted, and then diffusion through the polymer phase was rate controlling.

Modeling the polymer phase as a semi-infinite slab (15) allowed estimation of the minimum initial diffusivities (D_s) of EB in the polymer. The slab geometry is possible because the polymer disk was exposed to the SCF only at its upper face. These are minimum D_s estimates because such a model assumes the maximum possible concentration driving force. The relevant formula for a diffusion-controlled process is:

$$Y = \sum_{n=0}^{\infty} \frac{8}{(2n+1)^2 \pi^2} \exp \left[\frac{-D_s (2n+1) \pi^2 t}{4L^2} \right] \quad (1)$$

where Y is the fraction of EB remaining in the polymer phase (q/q_0 , where q is the EB loading in wt EB/wt PS), L is the disk thickness, and D_s the diffusivity. These estimates are in Table I, from which it is evident that D_s for EB was greatly enhanced in the presence of SCF-CO₂. We note that, in the absence of CO₂, the binary diffusivities of EB in PS at below 373 K (the normal T_g) and solute concentrations of a few wt% are $< 10^{-16}$ m²/s (16).

These results show D_s increasing with pressure at 343 K. This might be explained solely in terms of enhanced swelling of the polymer by CO₂, because the solubility of SCF-CO₂ in pure PS increases with pressure in the range of these data (17-18). Although it is true that higher pressure (density) also enhances the solubility of EB in the SCF-CO₂, these data suggest that this is a secondary consideration; at 343 K, the highest initial rate of extraction occurred at a relatively low density, 252 kg/m³. However at the lower temperatures the data did not follow the simple pattern of the data at 343 K; here the maximum extraction rates were found at pressures closer to the glass transition pressure at the constant temperature, reminiscent of the results of Burgess and Jackson (3). Taken in their entirety, the results underscore the inadequacy of simple mass transfer models such as equation (1), and the necessity of combining a mass transfer model

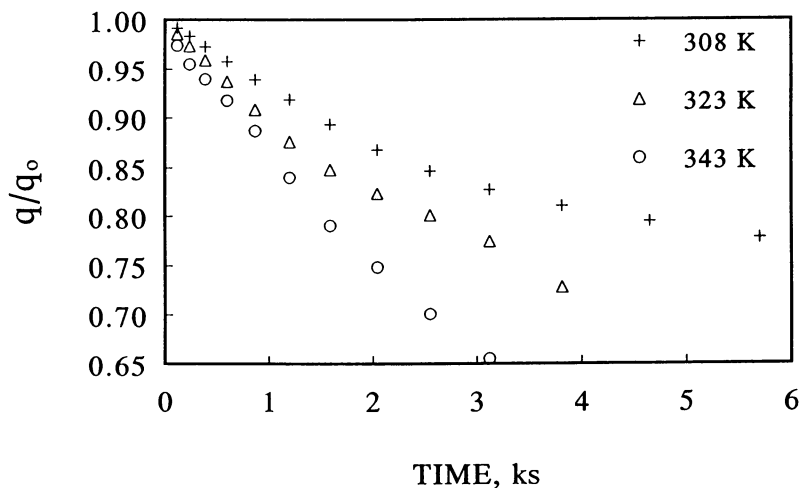


Figure 3. Relative amount of EB in polymer phase during SCFE at 10.4 MPa.

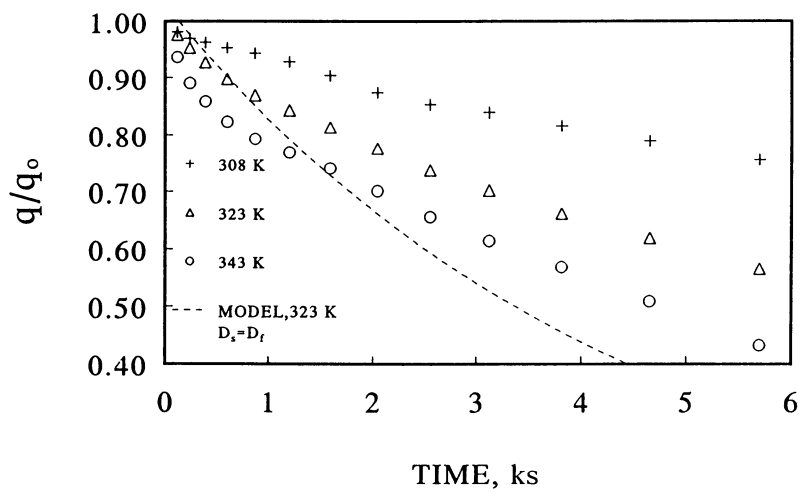


Figure 4. Relative amount of EB in polymer phase during SCFE at 8.4 MPa. Model curve for $D_s = D_r$.

Table I. Minimum D_s for Ethylbenzene in Polystyrene During SCFE

T, K	P, MPa	ρ_{CO_2} , kg/m ³	$(-dY/dt)_0^a$	$D_s \times 10^{10}$, m ² /s
308	7.0	220	1.89	1.7
323	7.0	171	13.9	13
343	7.0	143	11.7	11
308	8.4	577	9.66	9.1
323	8.4	265	18.8	14
343	8.4	185	19.7	15
308	10.4	721	7.04	6.4
323	10.4	440	6.72	6.2
343	10.4	252	20.3	18
363	9.1	176	15.3	13
323	11.8	568	13.5	16

^aInitial slope of EB concentration profile in polymer phase, (% extracted)/ks

developed specifically for polymers along with an accurate description of the ternary equilibria.

The extraction of EB by SCF-CO₂ from PS is a suitable model system because all three binary equilibria are well understood, and the binary diffusivities are available or can be readily estimated. Therefore we have a sound basis for interpreting the unusual phenomena observed with the ternary system at high pressure. In particular, we can estimate ternary equilibrium compositions using the equilibrium data for the three binaries and a suitable thermodynamic model. For this purpose we utilized the extended Flory-Huggins equation of state (EOS) for the polymer phase (19), and the Peng-Robinson cubic EOS for the fluid phase. The binary interaction parameters in the extended Flory-Huggins EOS were fitted from previous experimental data (17,20), or obtained from compilations of such parameters (21-22). The binary interaction parameters for CO₂-EB in the Peng-Robinson EOS were taken from the literature (20).

In Figure 5, the percentage of EB initially present which had been extracted by a characteristic time (the time at which the wt CO₂/wt polymer = 150) is plotted versus the calculated equilibrium solubility in the SCF, assuming

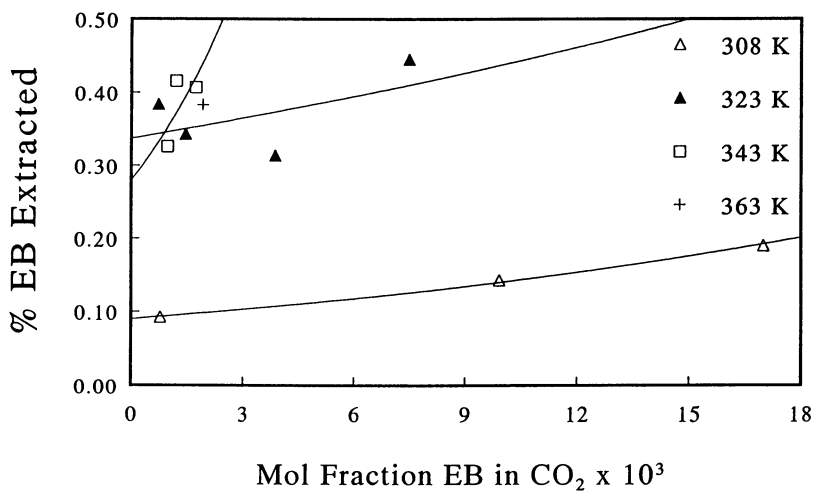


Figure 5. Relative amount of EB extracted (at wt CO₂/wt polymer = 150) vs. equilibrium solubility.

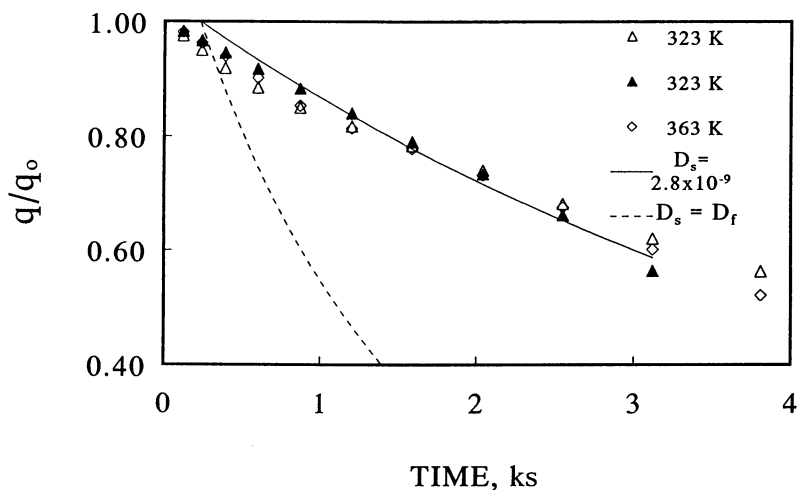


Figure 6. Relative amount of EB in polymer phase during SCFE. The pressure at 363 K was 9.1 MPa, and at 323 K was 11.8 MPa. The curves are model fits to the data at 323 K with the D_s values shown.

no PS in the SCF. This characteristic time was far enough into the run that swelling by CO₂ was complete, as indicated by the DSC data. If equilibrium between the two phases existed during the extractions, these solubilities would scale directly with the rates of extraction, and so we would expect to see all of the data lie on a single smooth curve; instead, the data appear as a family of curves (here shown as exponential for ease of visualization only). The pressure range (6.9–11.8 MPa) of the points is the same as for the extraction data; however, EB solubility rather than pressure or ρ_{SCF} is the abscissa because the purpose is to show that there is no relation between amount of EB extracted and its solubility in SCF-CO₂.

Because D_s for EB in pure PS is exponentially dependent on temperature in the region where the polymer is plastic, and because the observed rates of extraction were also temperature-dependent, we might conclude that CO₂ plasticized the polymer through swelling. This expectation was borne out by DSC measurements executed in a static mode. The normal T_g (at ambient pressure) of the PS was ~373 K, but we found that T_g was depressed to < 323 K in the presence of only 6.0 MPa of CO₂, and to lower values at higher pressures; these measurements are in agreement with previous work where T_g was measured volumetrically (17). The depressions in T_g were even greater when EB was present in the polymer. Therefore CO₂ swelling can be said to be the proximate cause both of the high rates of extraction we observed, and of the large values of the "minimum" D_s shown in Table I. However, because the rates still depended more on temperature than solubility (Figure 5), we know that they were still largely diffusion-controlled. For example, note that it was possible to have a high rate of EB extraction at 343 or 363 K, even though the predicted solubility in the SCF is relatively low. Further evidence for this conclusion is shown in Figure 6, where it is seen that it is possible to attain roughly the same extraction rate at a much lower CO₂ density (176 vs. 568 kg/m³), but higher temperature. Figure 6 also gives some idea of the replicability of the data by presenting results from two different runs at roughly the same temperature and pressure.

Extraction Model

The prediction of phase equilibria for the ternary system can be combined with mass balances on the fluid and polymer in the DSC cell, and with standard mass transfer equations for extraction from solid particles, in order to construct a model for the polymer extractions. The model can then be used to better estimate the true D_s values, by regression. The model used here was similar to that of Recasens et al. (10), except (1) we substituted the nonlinear equilibrium relationship based upon the extended Flory-Huggins and Peng-Robinson EOS for the linear equilibrium used in their work, and (2) we accounted for the change in polymer dimension as CO₂ dissolved in, and EB was removed from the polymer. Partial molar volumes for CO₂ dissolved in PS were computed from previous swelling data (17). For these reasons the equations had to be solved numerically.

The mass balances in terms of dimensionless variables are as follows:

$$\frac{dY}{dT} = \frac{K_p V_c}{F_o'} (X - X^*) \quad (2)$$

$$X = X^* \left(\frac{K_p V_c}{F_o'} \right) / \left[1 + \left(\frac{K_p V_c}{F_o'} \right) \right] \quad (3)$$

$$T = \left(\frac{F_o' t}{V_c} - \epsilon \right) / \Lambda \quad (4)$$

where X is the dimensionless solute concentration in the fluid phase (C/C_o^*), C_o^* is in equilibrium with q_o , X^* ($= C^*/C_o^*$) is in equilibrium with Y , T is dimensionless time, F_o' the SCF volumetric flow rate, V_c the cell volume, ϵ the void volume of the cell, Λ the partition ratio in fluid volume/total volume [$= (q_o W)/(MW_s C_o^* V_c)$], W the polymer weight, MW_s the molecular weight of the solute, and K_p the overall mass transfer coefficient from polymer to SCF, with units of inverse time. The linear driving force approximation for K_p can be derived for axial mass transfer from a disk by solving the parabolic intraparticle profile equations using the procedure of Liaw et al. (23). The result is:

$$K_p = \frac{(1 - \epsilon)}{L} \frac{3k_f}{3 + Bi} \quad (5)$$

where k_f is the fluid phase mass transfer coefficient and $Bi = k_f L/D_s$.

Transport properties were needed to predict k_f . The viscosity of pure CO_2 was obtained from a data compilation (24). The binary diffusivity of EB in SCF- CO_2 (D_f) was estimated by the procedure of Sun and Chen (25), which was able to reproduce experimental D_f data for benzene- CO_2 and mesitylene- CO_2 (26) with average relative deviation of 17%. For k_f itself, the correlation of Lim et al. (27), which combines natural and forced convection, was used. Other mass transfer correlations (all for spheres) gave similar results when an equivalent characteristic length for the disk [the ratio of six times volume to the exposed surface area] was used instead of sphere diameter. There are no published correlations of mass transfer from disks at SCF conditions. However, a sensitivity analysis revealed that at the conditions of this work the model was not sensitive to $\pm 50\%$ variations in k_f anyway.

This leaves D_s as the only adjustable parameter of the model. Some results obtained by setting $D_s = D_f$ are shown in Figures 4 and 6. Because the model is greatly sensitive to D_s at the conditions of this work, it is clear from these results that the actual D_s values are not far below those of the fluid phase. In Figure 6, adjusting D_s to $2.8 \times 10^{-9} \text{ m}^2/\text{s}$ gave a good fit to the data, as shown. This number is only 75% higher than the minimum D_s estimate given in Table I, which was

obtained assuming a fixed polymer volume and a maximum concentration driving force. The numbers we obtained from this model are also only about 0-1 orders of magnitude higher than measured (by a gravimetric technique) binary D_s values for CO_2 itself in PS at 298 K (18).

These modeling results, coupled to the present and many other past experimental results, suggest that SCFE from polymers is often a diffusion-driven process. The success of such a process hinges upon the ability of the SCF to swell the polymer, possibly plasticizing it, and thereby to increase the diffusivity of the solute in the polymer phase during extraction. However, at the same time the equilibria must not be adversely affected to the point where the solute's fugacity is much lower in the SCF-swelled polymer phase than in the binary solute/polymer mixture. This last consideration would restrict the range of cosolvents which might be useful in SCFE from polymers, probably to those which swelled the polymer, but not too strongly.

Conclusions

- (1) Swelling of a polymer by the SCF, and its effects on solute mass transfer, is of paramount importance in understanding and modeling the practical SCFE of a typical low molecular weight solute from a polymer.
- (2) The extraction rates for ethylbenzene from polystyrene using SCF- CO_2 more strongly depend on temperature than on SCF density, because they are primarily diffusion-controlled. Equilibrium solubility differences have only secondary effects on the rates of extraction (Figure 5).
- (3) There was at least a 10^6 -fold increase in the experimental ethylbenzene diffusivity in the polymer phase in the presence of SCF- CO_2 , according to two separate models used to describe the SCFE process.

Acknowledgment

We acknowledge the support of the Louisiana Educational Quality Support Fund through grant RD-B-06.

Literature Cited.

1. Allada, S.R. U.S. Patent 4,703,105 1987.
2. Shim, J.-J.; Johnston, K.P. *AIChE J.* **1989**, *35*, 1097.
3. Burgess, A.N.; Jackson, K. *J. Appl. Polym. Sci.* **1992**, *46*, 1395.
4. Koppers, St. *Chromatographia*, **1992**, *33*,434.
5. Cotton, N.J.; Bartle, K.D.; Clifford, A.A.; Dowle, C.J. *J. Appl. Polym. Sci.* **1993**, *88*, 1607.
6. Kumar, S.T.; Suter, U.W.; Reid, R.C. *Fluid Phase Equil.* **1986**, *29*, 373.
7. Daneshvar, M.; Gulari, E. *J. Supercrit. Fluids* **1992**, *5*, 143.

8. Super, M.S.; Enick, R.M.; Beckman, E.J. In *Emerging Technologies in Plastics Recycling*; Andrews, G.D. and Subramanian, P.M., Eds.; ACS Symposium Series No. 513; American Chemical Society, Washington, D.C., 1992; pp. 172-185.
9. Madras, G.; Thibaud, C.; Erkey, C.; Akgerman, A. *AIChE J* 1994, 40, 45.
10. Recasens, F.; McCoy, B.J.; Smith, J.M. *AIChE J.* 1989, 35, 951.
11. Srinivasan, M.P.; Smith, J.M.; McCoy, B.J. *Chem. Eng. Sci.* 1990, 45, 1885.
12. Dooley, K.M.; Ghonasgi, D.; Gambrell, R.P.; Knopf, F.C. *Env. Prog.* 1990, 9, 197.
13. Dooley, K.M.; Kao, C.-P.; Gambrell, R.P. and Knopf, F.C. *Ind. Eng. Chem. Research*, 1987, 26, 2058.
14. Tan, C.-S.; Liou, D.-C. *Ind. Eng. Chem. Res.* 1988, 27, 988.
15. Crank, J. *The Mathematics of Diffusion*; Oxford University Press: London, 1956, p.45.
16. Zielinski, J.M.; Duda, J.L. *AIChE J.* 1992, 38, 405.
17. Wissinger, R.G.; Paulaitis, M.E. *J. Polym. Sci. B: Polym. Phys.* 1987, 25, 2497.
18. Berens, A.R.; Huvard, G.S. In *Supercritical Fluid Science and Technology*; ACS Symposium Series No. 406; American Chemical Society, Washington, D.C., 1989; pp. 207-223.
19. Ruff, W.A.; Glover, C.J.; Watson, A.T.; Lau, W.R.; Holste, J.C. *AIChE J.* 1986, 32, 1954.
20. Mohamed, R.S.; Holder, G.D. *Fluid Phase Equil.* 1987, 32, 295.
21. Orwoll, R.A. *Rubber Chem. Technol.* 1977, 50, 451.
22. Errede, L.A. *J. Appl. Polym. Sci.* 1992, 45, 619.
23. Liaw, C.H.; Wang, J.S.P.; Greenkorn, R.A.; Chao, K.C. *AIChE J.* 1979, 25, 376.
24. Stephan, K.; Lucas, K. *Viscosity of Dense Fluids*; Plenum, New York, 1979.
25. Sun, C.K.; Chen, S.H. *AIChE J.* 1986, 32, 1367.
26. Swaid, I.; Schneider, G.M. *Ber. Bunsenges. Phys. Chem.* 1978, 83, 969.
27. Lim, G.B.; Holder, G.D.; Shah, Y.T. In *Supercritical Fluid Science and Technology*; ACS Symposium Series No. 406; American Chemical Society, Washington, D.C., 1989; pp. 380-395.

RECEIVED May 19, 1995

Chapter 19

Removal of Hazardous Contaminants from Soils by Supercritical Fluid Extraction

G. A. Montero, T. D. Giorgio, and K. B. Schnelle, Jr.

Department of Chemical Engineering, Vanderbilt University,
P.O. Box 1604, Station B, Nashville, TN 37235

Experimental data and a mathematical model are presented for the desorption of pure naphthalene and 1,2,4 trimethylbenzene from soil with supercritical CO₂ as solvent. The linear driving force concept was employed to incorporate intraparticle diffusion as well external mass transfer. The experimental data was approached as a concentration history of solute desorption at different flow rates. A simulation has been performed using an equilibrium desorption model where the rate of desorption is controlled by external and intraparticle mass transfer and solved using software. This model has been proved to be accurate in predicting the desorption profiles from organic contaminants over a range of operating conditions. From the experimental data, adsorption equilibrium constants and overall mass transfer coefficients are obtained using the model. The results indicate that external mass transfer was significant at very low flow rates, and intraparticle diffusion resistance was found to be significant for the particle size studied.

The objective of this investigation has been the study of the feasibility of supercritical fluid extraction (SFE) as a remediation technology for removal of hazardous organic contaminants from soil. The initial contamination levels of the two organic solutes studied (naphthalene/solid particles @ T = 298 K and 1,2,4 trimethylbenzene/liquid phase @ T = 298 K) were approximately 10000 mg/L and 50000 mg/L. The primary focus of the research was experimental extraction of organic hazardous waste from dry soil by supercritical carbon dioxide (SC-CO₂) as a function of operating parameters such as flow rate (Q_{CO₂}) and supercritical carbon dioxide density (ρ_{CO_2}).

An important aim of this research is to develop methodology for scale-up of laboratory supercritical fluid extraction (SFE) devices to a pilot-scale plant. Laboratory data necessary for scale-up, such as mass transfer coefficients, are

0097-6156/95/0608-0281\$12.00/0
© 1995 American Chemical Society

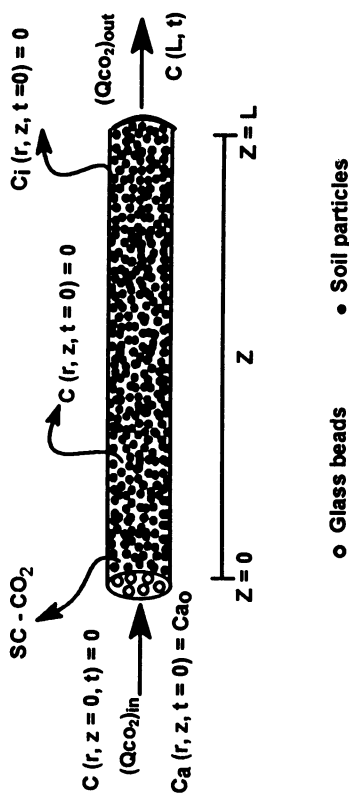


Figure 1. Solid packed-bed extraction cell schematic.

very limited. This study has been designed so that the experimental data can be used in the scale-up process and to perform a basic economic analysis of the process using the two organic solutes as model soil contaminants.

The attractive properties of supercritical fluid solvents are their ability to dissolve complex organic molecules, their pressure-dependent solvation power, and their advantageous transport properties. Advantages of using SFE as a clean-up process include the lack of solvent toxicity, the ability to recover the contaminant, possible economic benefits and the ability to remediate sites that can not be treated with current technology.

A simulation of the process was performed using a desorption model where the rate of desorption is controlled by external mass transfer and intraparticle resistances. The two-parameter (K and k_o) mathematical model, assumes that the adsorption-desorption process is very fast so that equilibrium is approached. The model agreed well with the experimental data for the higher superficial velocities. An additional aim of this investigation is to compare the experimental results with the known effectiveness of currently employed soil cleaning technologies.

Mathematical Model

Several recent publications discuss models for supercritical regeneration of granular activated carbon; Recasens et al. (1989) presented a model which incorporates the solid-SCF equilibrium and external mass transfer coefficient explicitly, assuming a parabolic concentration profile inside the particles. For all but very small values of time, Do and Rice (1986) showed a parabolic concentration profile in the pellet is an excellent approximation for equilibrium adsorption when time, $t > 0.05(\beta + \rho K)r_o^2/D_e$. Tomida and McCoy (1987) have shown that the assumption of a parabolic intraparticle concentration profile is a very good approximation for Thiele modulus ($\phi = r_o(\rho k/D_e)^{1/2}$) values less than 2 and a reasonable one for somewhat higher values of the Thiele modulus. Analytical solutions were developed from the model for the case where equilibrium desorption occurs and is controlled by the external and intraparticle mass transfer rates (Recasens, 1988). Figure 1 shows a schematic of the extraction cell defining the variables and initial conditions for the following equilibrium desorption model.

The solutions for the outlet concentration in the CO_2 stream with an initial concentration C_{a_0} in the soil are:

For $a \leq 1$ [$0 \leq t \leq$ (one residence time)]

$$\frac{C(L, t)}{C_{a_0}/K} = \frac{c}{b + c} [1 - \exp[-(b + c)a]] \quad (1)$$

For $a > 1$

$$\frac{C(L, t)}{C_{a_0}/K} = \frac{c}{b+c} \exp[-(b+c)a][\exp(b+c)-1] + \exp[-(b+c)(a-1)] * \sum_{m=0}^{\infty} (-1)^{m+1} \left(\frac{b}{c}\right)^m \frac{A_m(c)A_m[c(1-a)]}{(m!)^2} \quad (2)$$

and

$$a = \frac{tu}{L\alpha} \quad (3)$$

$$b = \frac{3k_o L \alpha}{r_o(\beta + \rho K)u} \quad (4)$$

$$c = \frac{3(1-\alpha)k_o L}{r_o u} \quad (5)$$

and A_m is related to the incomplete gamma function:

$$A_m(w) = \int_0^w \exp(-\tau) \tau^m d\tau \quad (6)$$

Experimental Section

Continuous-Flow Apparatus. Figure 2 is a schematic diagram of the experimental set-up for desorption experiments. Soil containing a known quantity of contaminant is placed in the extraction cell. Studies were performed assuming a packed bed of spherical soil particles with an initial loading of solute concentration C_{a_0} . The SC-CO₂ flows through the extraction cell removing the organic contaminant from the soil. The experiment continues until all of the contaminant is removed or the operating time becomes greater than about 600 minutes. The desorption profile of the organic can be calculated from this data. Details of the experimental set-up and procedures are provided elsewhere (Montero et al., 1995).

Materials. Linde "bone dry" and 99.0 % pure liquid carbon dioxide with dip tube in the cylinder was purchased from Air Products, Inc. The solid naphthalene particles, supplied by Kenova Chemical Company, was reagent grade of 99.9 % purity. The liquid 1,2,4 trimethylbenzene (TMB), supplied by Janssen

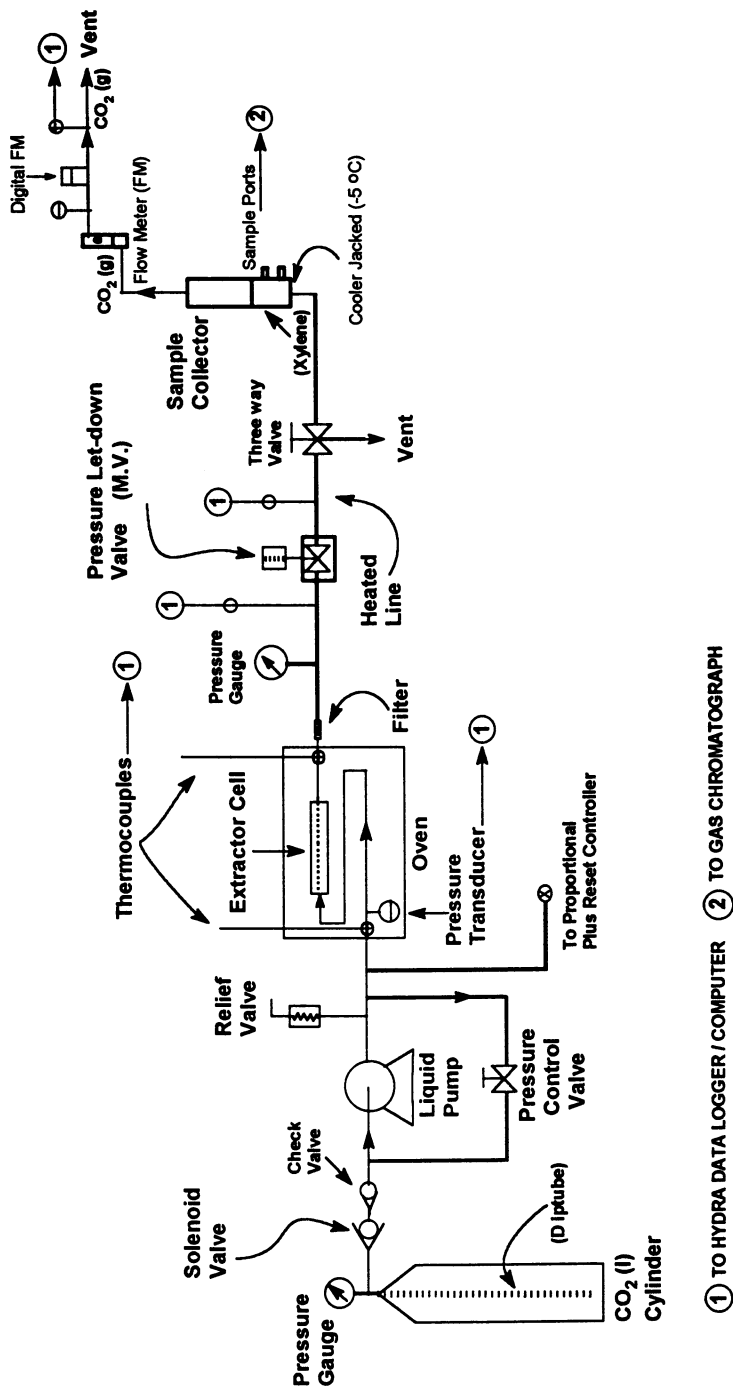


Figure 2. Actual schematic diagram of the experimental setup (SFE).

Chimica Company, was 98 % pure. The stated purity of naphthalene and 1,2,4 trimethylbenzene were verified by gas-chromatograph analysis and subsequently used without further purification.

Uncontaminated soil was obtained from a site at Argonne National Laboratory in Argonne, IL. Wet soil was first dried at 383 K in the oven overnight and then sieved to 12-14 mesh fraction (the average particle size is 0.13 cm), and finally stored in a sealed glass container. About 28 g of contaminated soil was packed in the extraction column which is 1.11 cm in diameter and 30.48 cm in length. Properties of the soil and the specifications of the packed bed are presented in Table I. The grain size analysis (ASTM D-422) and total organic content of the soil was done by Professional Service Industries, Inc. in Nashville, Tennessee.

All other chemicals were obtained commercially and were used without further purification.

Table I. Properties of the packed bed and soil.

Bed length, cm	28.58
Bed diameter, cm	1.10
Bed porosity	0.41
Particle diameter (12-14 mesh), cm	0.13
Soil composition, %	
Gravel	13.0
Sand	20.3
Fines (silts and clays)	66.7
Moisture content in soil as received, %	17.2
Total organic content in soil as received, %	3.0
Total organic content in soil after sieved, %	3.6

Preparing the Soil Matrix. Soil samples were spiked by making a slurry of the soil with an acetone solution of the required solute (naphthalene or 1,2,4 trimethylbenzene) in a covered glass pan, and allowing the solution to evaporate slowly (\approx 72 hours). To avoid evaporation of the contaminants, soils were subsequently stored in sealed glass containers. In order to determine the amount of solute left in the pan, it was rinsed with a small amount of acetone, which was analyzed by gas chromatography. The solute concentration was thus the total spike less the amount remaining in the glass shallow container. The experimental spiking procedure was found to be effective, as most of the solute was adsorbed in the solid particles. This technique enables uniform loading of the organic compounds on soil.

The soil samples were spiked at two levels. The initial contamination levels of naphthalene and 1,2,4 TMB were 10000 and 50000 \pm 500 mg/L by weight. Prior to supercritical extraction the solute concentration in the soil samples fed into the reactor was verified by conventional solvent extraction using xylene and gas chromatograph with a flame ionization detector prior the extraction. Gas chromatography of the extracted samples revealed no detectable acetone. For the highest supercritical density ($\rho_{\text{CO}_2} = 0.72 \text{ g/cm}^3$), the material balance closures were within 99.8 \pm 0.2% indicating that each extraction and measurement were performed accurately.

Results and Discussion

Figures 3 and 4 show the experimental rate of extraction and concentration histories of naphthalene ($C_{a_0} = 10000 \text{ mg/L}$), respectively, in the effluent at different flow rates. The points in Figure 3 for the solute extracted from soil represent our experimental data which showed scatter and indicated a significant effect of CO_2 flow rate. This plot was obtained from the accumulation of solute in xylene with respect to extraction time. Liquid samples (2 μl) were withdrawn from the sample ports, which are located on the sample collector as shown in Figure 2, every 10 minutes. The lines on Figure 3 represent a best fit curve to the experimental data. This best fit curve was used to describe the rate of extraction as a function of time which is then used to calculate the outlet concentration as a function of time with superficial velocity as a parameter and the bed pressure of 103 bar and temperature of 318 K (Figure 4).

The calculated outlet concentration increases steeply and then decreases gradually as shown in Figure 4. After a 30 minutes, zero flow, incubation period to the start of the specified CO_2 flow, the solute concentration increases rapidly. Naphthalene is desorbed almost completely within 460 min at the three highest superficial velocities. At the two lowest superficial velocities ($u = 1.87 \times 10^{-5} \text{ m/s}$ and $u = 3.74 \times 10^{-5} \text{ m/s}$) and at $P = 103 \text{ bar}$ and $T = 318 \text{ K}$ there is incomplete desorption in 460 min. This can be of a film transfer resistance at lower flow rates (Srinivasan et al., 1990), in which a significant reduction of the driving force concentration can be observed. Solute is transferred from the soil particles into the surrounding phase in an unsteady-state mass transfer process. From the beginning of the extraction, the solute concentration in the solid substrate decreases until mass transfer stops since concentration of solute in the particles is zero or approaches the equilibrium concentration at the interface. As seen from Figure 4, at the lowest velocity ($u = 1.87 \times 10^{-5} \text{ m/s}$) the initial outlet concentration approached to the equilibrium concentration of $7.9 \times 10^{-2} \text{ kgmol/m}^3$. However the final outlet concentration profile is much farther away from equilibrium. Furthermore, the results of Tan and Liou (1988), as explained by Recasens et al. (1989), also indicate that external mass transfer affects the rate of desorption at low flow rates which supports our conclusion.

Similar extraction results are obtained when the soil was contaminated with 1,2,4 trimethylbenzene ($C_{a_0} = 50000 \text{ mg/L}$) as seen in Figure 5. Also, at the two lowest superficial velocities, the initial outlet concentrations are close to the equilibrium concentration of 1,2,4 TMB in CO_2 ($C^* = 2.7 \times 10^{-1} \text{ kgmol/m}^3$) at $P = 121 \text{ bar}$ and $T = 308 \text{ K}$.

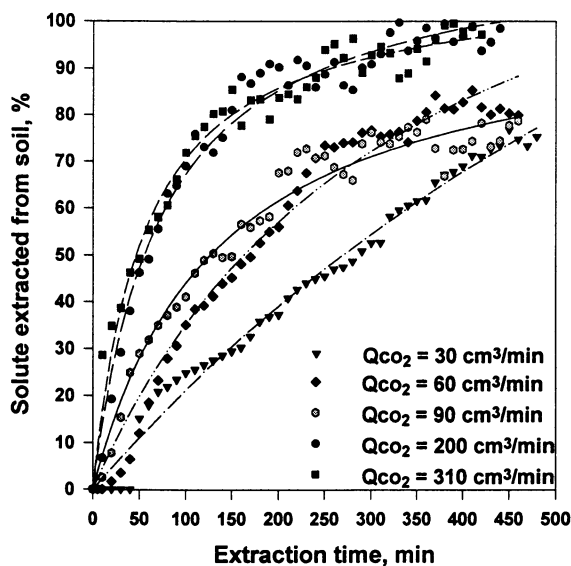


Figure 3. Effect of carbon dioxide flow rate (301 K; 1 bar) on the extraction of naphthalene from dry soil at $P = 103$ bar and $T = 318$ K.

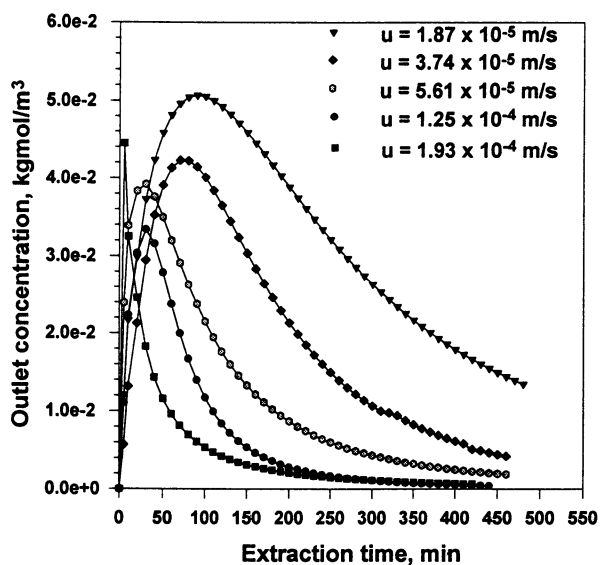


Figure 4. Outlet concentration histories for naphthalene from soil for varying CO_2 flow rates at $P = 103$ bar; $T = 318$ K and $C^* = 7.9 \times 10^{-2}$ kgmol/m^3 .

Figures 6 and 7 show naphthalene extractions and outlet concentration histories from dry soil at two different initial levels of contamination. Extraction at both concentration levels was controlled by a similar extraction mechanism which we believe to be the dissolution of the solute from porous particles of soil in a stream of supercritical carbon dioxide. Figure 6 shows that at $Q_{CO_2} = 60$ and $90 \text{ cm}^3/\text{min}$, the trends of the curves are almost a straight line (slope is constant) for the case of 50000 mg/L compared with the one at the lower concentration. At this high level of contamination there is enough solute in the soil to allow a significant period of constant rate of extraction. Figure 7 shows at both flow rates with an initial loading of 50000 mg/L the outlet concentration profile decays very slowly when compared to the concentration profile from the lower initial solute concentration. During the constant rate period steady state mass transfer is indicated. At the lower concentration (10000 mg/L) the constant rate periods are instantaneous (sharp fall as being due to a solute limit) and a desorption breakthrough for the all CO_2 flow rates are expected. It should be noted that for the higher loading level the initial outlet concentrations are far away from the equilibrium concentration ($C^* = 7.9 \times 10^{-2} \text{ kgmol/m}^3$) but they are still close to the initial value ($4.0 \times 10^{-2} \text{ kgmol/m}^3$) of the lower initial concentrations as shown in Figure 7.

Figure 8 presents the effect of supercritical carbon dioxide density (ρ_{CO_2}) on the rate and extent of naphthalene extraction from soil at the lower flow rate ($Q_{CO_2} = 310 \text{ cm}^3/\text{min}$). As expected, the most effective extraction was at the highest density ($\rho_{CO_2} = 0.72 \text{ g/cm}^3$). Increasing the supercritical density resulted in an increased rate of extraction, as well as greater eventual recoveries. Extractions of this lab-spiked soil showed that 100 % of the solute could be removed in approximately 420 min. Similar results have been shown in the contaminated soil with 1,2,4 TMB (100 % extracted), however the extraction time ($t \approx 320 \text{ min}$) was shorter compared with naphthalene ($t \approx 450 \text{ min}$) as shown in Figure 9. Theoretical data using a thermodynamic model indicates that the solubility of 1,2,4 TMB in CO_2 at $P = 121 \text{ bar}$ and $T = 308 \text{ K}$ is $Y^* = 0.1220$ compared with $Y^* = 0.0125$ of naphthalene in CO_2 . Thus, the high recoveries of 1,2,4 TMB using SC- CO_2 are due to the equilibrium solubility in the CO_2 .

The effect of methanol (5 wt %) used as entrainer or cosolvent is shown in Figure 10, under the same extraction conditions as used with pure SC- CO_2 ($P = 103 \text{ bar}$ and $T = 318 \text{ K}$ and $Q_{CO_2} = 310 \text{ cm}^3/\text{min}$ at STP). Extraction with cosolvent is more successful than with pure SC- CO_2 . Approximately 95% of the contaminant can be removed in 150 min or less. These results imply that for maximum extraction efficiency, a mixed solvent system should be used, where the entrainer or cosolvent is tailored to the soil type and solute being extracted. After the extraction, the soil samples exhibited a weight gain due to adsorption of a small fraction of the methanol by the soil.

Model Results

As a preliminary test, the data for supercritical fluid extraction of soil adsorbed with naphthalene have been modeled with the equilibrium desorption/mass

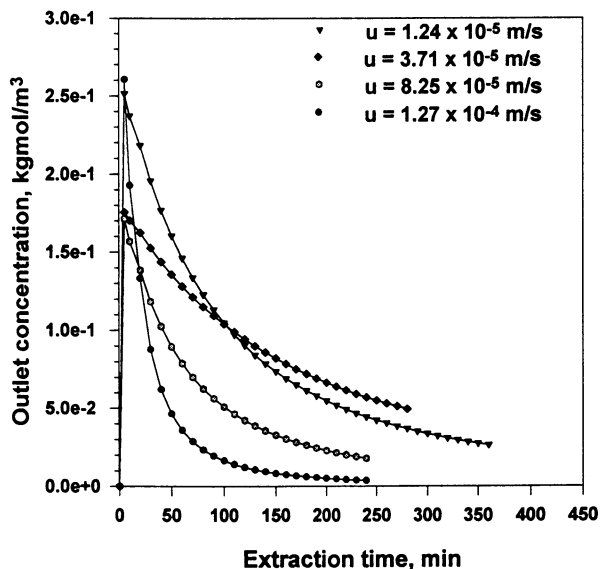


Figure 5. Outlet concentration histories for 1,2,4 trimethylbenzene from soil for varying CO_2 flow rates at $P = 121$ bar; $T = 308$ K and $C^* = 2.7 \times 10^{-1} \text{ kgmol/m}^3$.

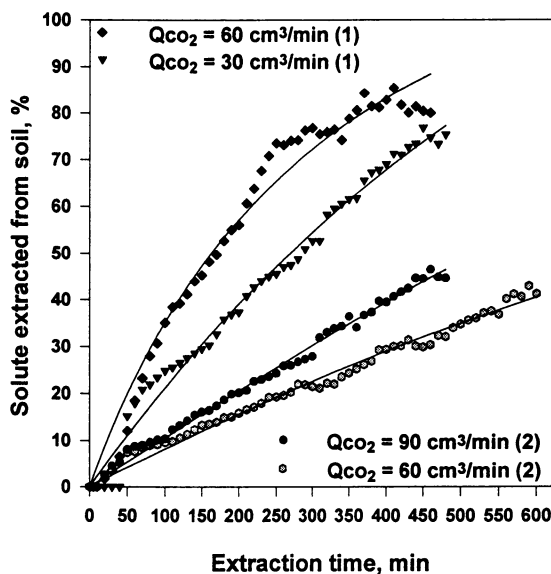


Figure 6. Effect of initial concentration and CO_2 flow rate on naphthalene from soil at $P = 103$ bar and $T = 318$ K. (1) $\text{Ca}_0 = 10000 \text{ mg/L}$ and (2) $\text{Ca}_0 = 50000 \text{ mg/L}$.

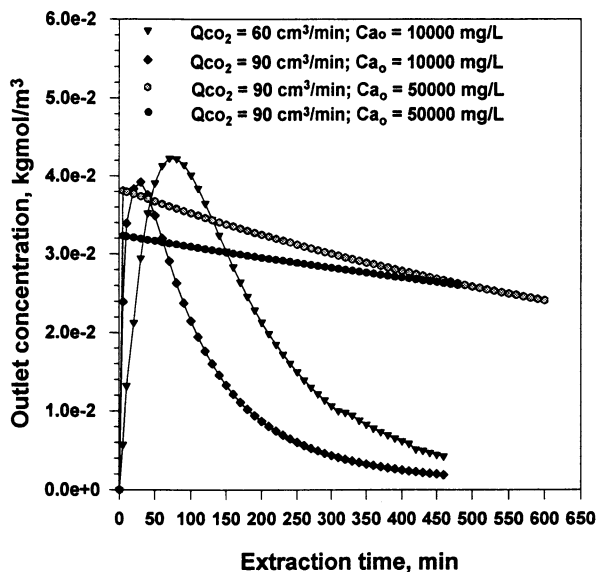


Figure 7. Outlet concentration histories for naphthalene from dry soil for varying initial concentration at $P = 103$ bar; $T = 318$ K & $C^* = 7.9 \times 10^{-2}$ kgmol/m^3 .

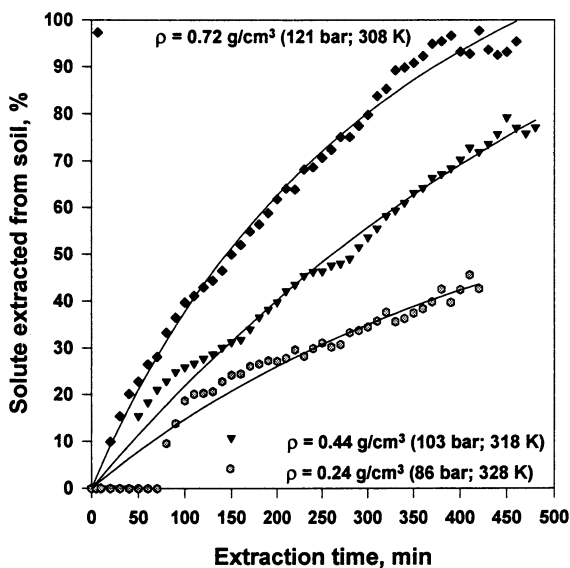


Figure 8. Effect of supercritical carbon dioxide density (ρ) on the extraction of naphthalene from dry soil at flow rate at $Q_{\text{CO}_2} = 30$ cm^3/min .

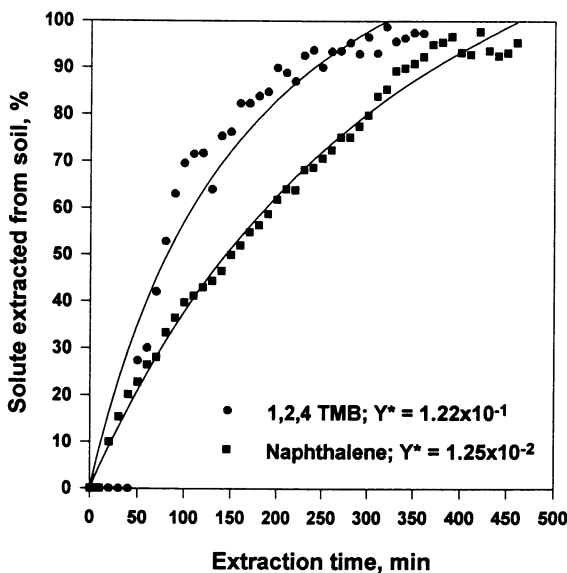


Figure 9. Effect of solubilities in supercritical solvent on the extraction of solutes from dry soil at $P = 121$ bar; $T = 308$ K and $Q_{CO_2} = 30$ cm³/min.

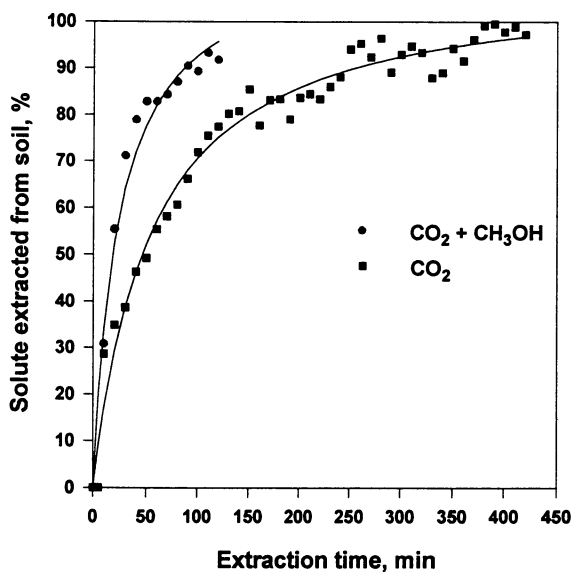


Figure 10. Effect of cosolvent in supercritical CO_2 on the extraction of naphthalene from dry soil at $Q_{CO_2} = 310$ cm³/min.

transfer equations (1 and 2). Optimal values for the overall mass transfer coefficient k_o and equilibrium constant K were obtained with the best fit between the experimental data points and the values predicted from the model. The approach to determine parameters from the experimental data was to approximate the external mass transfer coefficient (k_e) and intraparticle diffusivity (D_e) from empirical correlations. With these values as initial estimates, the experimental data were fitted to the concentration histories. The curves evaluated and displayed, using *MATHEMATICA*® software are shown in Figure 11. The experiments were at constant temperature and pressure. K , but not k_o , should be constant with respect to CO_2 flow rate.

Figure 11 shows that predicted and experimental concentration histories agree well with the equilibrium model for the effect of superficial velocity or Reynolds Number (N_{Re}). The range of N_{Re} is between 1.10 to 5.68. However, for the lowest N_{Re} these equilibrium model calculations did not agree with the experimental results for short times as shown in Figure 11. The model unsuccessfully fit the breakthrough front of the desorption profile but it is successful in fitting the elution tail. The basis for this disagreement is due to the assumption in the linear driving force model of a parabolic concentration profile in the solid particle. The initial concentration profile in the soil particles is presumably uniform and a parabolic profile can not be obtained until some solute extraction has taken place. It appears that the runs at the lowest superficial velocity did not have enough contact time to establish the parabolic concentration profile for equilibrium desorption. This also can be supported with the quantifiable criteria for assessing the suitability of this assumption which is provided by Do and Rice (1986). Consequently, for $u = 1.87 \times 10^{-5}$ m/s the criterion $t > 0.05(\beta + \rho K)r_o^2/D_e$ can estimate a time approximately equals 1.7×10^4 sec as the extraction time beyond which the linear driving force model should be accurate.

Table II shows the preliminary results of calculation and optimization. The values of k_e , k_o , and B_i are functions of superficial velocity (CO_2 flow rate). The slight variation of D_e , which is very sensitive quantity, does not significantly affect the equilibrium constant (K). A comparison between k_e and k_o shows a significantly different values ($k_e > k_o$) of up to two order of magnitude, which support the argument of intraparticle diffusion as well as external mass transfer as significantly affecting the extraction rate. Biot numbers were calculated using the equation $B_i = k_e r_o / D_e$. The B_i was used as the deciding factor to determine the effect of intraparticle resistance. When $B_i \gg 5$ intraparticle diffusion resistance is reported to dominate over the external mass transfer resistance (Srinivasan et al., 1989).

The optimal fitted values for the equilibrium constant (K) and the overall mass transfer coefficients (k_o) at the highest superficial velocity can be used as initial values for the calculation of the outlet concentration profile for a scaled-up extractor. Finally, the availability of these results will be useful in the evaluation of the economic feasibility of supercritical fluid extraction for a full scale soil remediation technology.

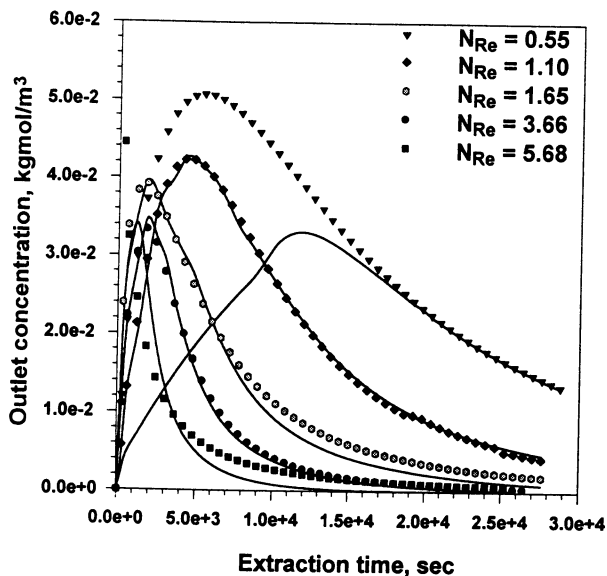


Figure 11. Comparison of simulated results with experimental data at $P = 103$ bar and $T = 318$ K. The continuous lines represent the model results.

Table II. Effect of CO_2 flow rate on adsorption equilibrium constants K and overall mass transfer coefficient k_o at $P = 103$ bar and $T = 318$ K.

u $\text{m/s} \times 10^{-4}$ Note 1	k_e $\text{m/s} \times 10^{-5}$ Note 2	K $\text{m}^3/\text{kg} \times 10^{-3}$ Note 3	k_o $\text{m/s} \times 10^{-7}$ Note 4	B_i Note 5	D_e $\text{m}^2/\text{s} \times 10^{-11}$ Note 6
0.1869	4.00	1.30	0.17	1504	1.73
0.3738	4.81	1.30	0.32	1691	1.85
0.5607	5.64	1.30	0.60	1860	1.91
1.2457	7.33	1.30	1.11	2383	2.00
1.9331	8.80	1.30	1.67	2637	2.17

Note 1: Superficial velocities, u , are at extractor $P = 103$ bar and $T = 318$ K.

Note 2: k_e calculated from the Wakao-Kaguei (1985) correlation.

Note 3: K obtained from optimized fit to experimental data.

Note 4: k_o final value calculated by using the linear driving force model which is defined as $k_o = 5 \cdot k_e / (5 + k_e \cdot r_o / D_e)$.

Note 5: B_i calculated from the equation $B_i = k_e \cdot r_o / D_e$. The initial effective diffusivity ($D_e = 2.8 \times 10^{-9} \text{ m}^2/\text{s}$) was taken to be ($D_e = \epsilon \cdot D_{ab} / \delta$).

Note 6: D_e obtained from optimized fit to experimental data.

Conclusions

The experimental procedures and the analysis for the dynamic process of supercritical fluid extraction from porous material have been successful. The extraction of contaminants from soil has several interesting features, some of which are of general applicability and some quite specific to remediation of soil. The conclusions can be summarized as follows:

- The highest extraction rate of naphthalene was at $P = 121$ bar and $T = 308$ K, due to the increased value of the supercritical fluid density (ρ_{CO_2}) at this experimental condition (Figure 8).
- The extraction efficiency was significantly improved when the mixed solvent system CO_2 - methanol was used at similar conditions with pure supercritical CO_2 .
- The overall mass transfer coefficient (linear driving force model) and the equilibrium constant were optimized to provide the best fit of the experimental data.
- The equilibrium model fit the breakthrough front of the desorption outlet concentration profile successfully for the range of Reynolds Numbers (N_{Re}) between 1.10 to 5.68 (Figure 11).
- The limitations of the equilibrium desorption model were apparent when optimization was attempted for the lowest superficial velocities due to the fact that a parabolic concentration profile is not established until some solute extraction has taken place ($t > 1.7 \times 10^4$ sec).
- The value of the Biot ($B_i \gg 5$) numbers indicate the presence of intraparticle diffusion resistance at higher flow rates.

Notation

- a = dimensionless time, equation 3
 $A_m(w)$ = incomplete gamma function, defined by equation 6
 B_i = biot number, dimensionless
 b = dimensionless group, defined by equation 4
 C = concentrations of adsorbate in bulk fluid, $kgmol/m^3$
 C_a = adsorbed solute concentration, $kgmol/kg$
 C_{a_0} = initial adsorbed solute concentration, $kgmol/kg$ of soil
 C_i = solute concentration in the pores, $kgmol/m^3$
 $C(L,t)$ = outlet concentration in the bed effluent, $kgmol/m^3$
 C^* = equilibrium concentration of solute in supercritical CO_2
 c = dimensionless group, defined by equation 5
 D_{ab} = binary diffusion coefficient (solvent-solute), m^2/s
 D_e = effective diffusivity in the porous particles, m^2/s

d_s	= diameter of sample, m
K	= adsorption equilibrium constant, m^3/kg
k_e	= external mass transfer coefficient, m/s
k_o	= overall mass transfer coefficient, m/s
k	= first-order adsorption rate constant, $m^3/kg\ s$
L	= bed length, m
m	= positive integers
N_{Re}	= modified Reynolds number ($N_{Re} = ud_s\rho/(1-\alpha)\mu$), dimensionless
P	= pressure, bar
r_o	= soil particle radius, m
T	= temperature, K
t	= extraction time, min or sec
u	= superficial velocity of fluid at T and P of bed, m/s
Y^*	= equilibrium mole fraction of solute in supercritical CO_2

Greek Letters

ϕ	= Thiele modulus ($\phi = r_o(\rho k/D_e)^{1/2}$)
α	= bed void fraction
β	= porosity of particles
δ	= tortuosity factor ($\delta = \beta D_{ab}/D_e$), dimensionless
μ	= viscosity of the fluid, $kg/m\ s$
ρ	= density of particles, kg/m^3
τ, w	= dummy variables, defined in equation 6

Acknowledgement

The authors gratefully acknowledge the financial support to Argonne National Laboratory, Environmental and Waste Management Program, under contract No. 30342403.

References

- Do, D. D., and R. G. Rice, "Validity of the Parabolic Profile Assumption in Adsorption Studies", *AIChE J.*, **32**, 149, 1986.
- Montero, G.A., K.B. Schnelle, Jr., and T.D. Giorgio, "Supercritical Fluid Extraction of Contaminated Soil", Presented at the 1993 ACS, I&EC Division 1993 Symposium: Emerging Technologies in Hazardous Waste V, Submitted for Publication to the *Journal of Environmental Science and Health*, 1995.
- Recasens, F., B. J. McCoy and J.M. Smith, "Desorption Processes: Supercritical Fluid Regeneration of Activated Carbon", *AIChE J.*, Vol. **35**, No.6, 951, June 1989.

Recasens, F., "Supercritical Fluid Regeneration of Spent Activated Carbon", Report on File at Department of Chemical Engineering, University of California, Davis, September 1988.

Srinivasan, M. P., J. M. Smith and B. J. McCoy, "Supercritical Fluid Desorption from Activated Carbon", *Chem. Eng. Sc.*, Vol. **45**, No.7, 1885-1895, 1990.

Tan, C. S. and D. C. Liou, "Desorption of Ethyl Acetate from Activated Carbon by Supercritical Carbon Dioxide", *Ind. Eng. Chem. Res.*, **27**, 988-992, 1988.

Tomida, T., and B. J. McCoy, "Polynomial Profile Approximation for Intraparticle Diffusion," *AIChE J.*, **33**, 1908, 1987.

Wakao, N., and S. Kaguei, "Heat and Mass Transfer in Packed Beds," Gordon and Breach, Sci. Publications, New York, 1982.

RECEIVED July 19, 1995

Chapter 20

Kinetic Model for the Supercritical Extraction of Contaminants from Soil

Ziyad G. Rahmé, Richard G. Zytner, and Warren H. Stiver¹

School of Engineering, University of Guelph, Guelph,
Ontario N1G 2W1, Canada

Supercritical carbon dioxide extraction is a novel technique for the remediation of soil contaminated with heavy organic chemicals. It has the potential to quickly and effectively remove the contaminants from soil, allowing for site redevelopment. Research on an analytical scale has proven its feasibility. However, there is limited information available on which to reasonably estimate the cost and timing involved in the application at a particular site.

This research paper presents three kinetic models for the supercritical extraction of contaminants from soil. The models consider the following factors affecting the breakthrough curve: axial dispersion, particle-to-fluid mass transfer coefficient, intraparticle diffusion and the equilibrium partition coefficient. The first three of these factors will affect the shape of a breakthrough curve while the latter will affect the breakthrough time. The models are solved using a Crank-Nicolson finite difference scheme.

The models have been applied to literature breakthrough data to determine parameter values necessary to fit the observations. As three values in the model affect breakthrough shape, many combinations successfully fit the experimental data. Comparing the parameters with independent correlations still leaves many combinations of plausible parameters that can fit the data. This points to a need for independent measures of the three kinetic parameters specifically for supercritical fluid - soil systems.

Soil contamination is a significant problem and results from waste sites and chemical spillage, intentional applications, and atmospheric deposition. It involves a wide range of contaminants from dioxins to explosives, from mercury to radioactive materials. The contamination threatens our air, water and food quality. Complete clean-up will be a slow and expensive exercise. Cairney estimated cleanup costs of in the billions

¹Corresponding author

of US dollars for each of the Netherlands, Germany and the US (1).

A recent survey indicates that excavation followed by landfill remains the most popular 'solution' (2). Some argue that this is not much of a solution at all. A number of alternative solutions are available or in various stages of development. Established alternatives include soil vapour extraction, bioremediation and soil washing. However, given the diversity of contaminants and sites, additional innovative technology development remains necessary. Supercritical Fluid Extraction (SFE) is one of the innovative technologies under development.

SFE is viewed as an on-site, ex-situ process in which the soil is excavated and transferred to a high pressure vessel for extraction of the contaminants from soil. SFE is part of a group of solvent extraction based approaches. However, it has a major benefit that solvent recovery is easily managed simply by depressurizing the fluid. Carbon dioxide is the fluid of choice owing to its benign character in the environment as a soil residue and as a result of its relatively low critical point.

Laitinen *et al.* (3) in a recent review of SFE for soil cleaning indicated that no work beyond the pilot-scale has been undertaken. To assist in the development and scale up of SFE it is necessary to understand the thermodynamics and the dynamics of the extraction process. The availability of these parameters will assist in the assessment of the economic feasibility of SFE for full scale soil remediation.

Akgerman and coworkers have made some significant progress on both the thermodynamics and kinetics using a laboratory system (4,5). In particular, Madras *et al.* (5) used a model incorporating three kinetic factors of axial dispersion, film mass transfer and intraparticle diffusion to describe the breakthrough curve from their packed soil columns. Each parameter was estimated from literature correlations based on systems other than the combination of supercritical fluids (SCFs) and soil. The agreement between their model predictions and experimental data is quite good. However, this agreement is not sufficient to validate the correlations used to predict the individual kinetic parameters. Valocchi (6) demonstrates that the shape of the breakthrough curve cannot distinguish between the three kinetic mechanisms, meaning that any one of the three mechanisms could be responsible for the observed shape of a breakthrough curve. Thus, a substantial error in one or more of the three parameters could exist and be compensated for by errors in the other parameters or be hidden if the parameter is not controlling in the laboratory setting. This has important implications for process scale up as each of the three mechanisms is affected differently by scale.

The objectives of this paper are to use kinetic models of the extraction process coupled with experimental observations of breakthrough behaviour to explore the rate controlling mechanisms of the overall process. Three models will be utilized that include different assumptions regarding which mechanism(s) control the overall process. The fitted kinetic parameters will be compared to independent correlations to assess the physical likelihood of the fitted values. This will allow an assessment of which mechanism(s) contribute significantly to the observed data as well to assess the applicability of correlations for process scale up.

Model Development

To model the process, the following initial assumptions were made: the system operation is isothermal and isobaric; CO₂ flow is at a constant velocity; the contaminant is initially sorbed homogeneously throughout the packed bed; initially, the solvent rapidly fills the intraparticle pores; equilibrium adsorption isotherm is linear; soil consists of single sized spheres that are uniformly distributed, and have a constant porosity; and, radial concentration gradients within the vessel are negligible, however, radial gradients within soil aggregates or particles are possible.

The models are all based on a differential mass balance describing transport of contaminant through a packed bed. The general form of the balance is given by Equation 1.

$$\frac{\partial C}{\partial t} = D_{ax} \frac{\partial^2 C}{\partial z^2} - u_i \frac{\partial C}{\partial z} - N_p \quad (1)$$

where N_p is a sink/source term. Equation 1 is subject to the following three boundary conditions.

$$\text{At } z=0, u_i(C - C_{in}) = D_{ax} \frac{\partial C}{\partial z} \quad (2)$$

$$\text{At } z=L, \frac{\partial C}{\partial z} = 0 \quad (3)$$

$$\text{At } t=0, C = C_{i0} \quad (4)$$

The particles making up the soil are viewed as porous spherical aggregates of finer grains in which chemicals are either sorbed to the soil or freely dissolved in the intraparticle pore fluid.

The desorption path of the contaminant follows four steps. First, the extract must be released from the sorbed state to the carbon dioxide. Second, the contaminant diffuses through the internal pores of the soil aggregates to the aggregate surface. Then, the contaminant diffuses through the external supercritical fluid film at the soil interface. Finally, the contaminant moves with the bulk fluid through the interparticle pores of the soil column.

Based on this desorption path, three models are presented. The models differ in which of the steps is considered to be controlling or significantly contributing to control of the overall rate of the extraction process. The first model considers the axial dispersion associated with the final step to be the only controlling factor and assumes that the internal and film diffusion is rapid. The second model includes both axial dispersion and film mass transfer as the controlling steps in the desorption process. Finally, the third model considers axial dispersion, film mass transfer and internal diffusion in the overall desorption process. For all three models the first

desorption step of the contaminant leaving the sorbed state is considered to be rapid and not rate limiting. For each of the three models only the sink/source term in Equation 1 is different.

Local Equilibrium with Axial Dispersion - Model Type I. The first type of the model assumes local equilibrium is valid. For this case, the concentration in the soil will be proportional to the concentration in the bulk supercritical fluid at all times and locations. The proportional constant will be the equilibria partition coefficient, K_a . The N_p term in Equation 1 is replaced as follows,

$$N_p = \frac{(1 - \epsilon)}{\epsilon} \rho_s K_a \frac{\partial C}{\partial t} \quad (5)$$

Therefore, substituting into Equation 1 and isolating the concentration-time derivative results in

$$\frac{\partial C}{\partial t} = \frac{D_{ax} \frac{\partial^2 C}{\partial z^2} - u_i \frac{\partial C}{\partial z}}{1 + \frac{(1-\epsilon)}{\epsilon} K_a \rho_s} \quad (6)$$

The only rate parameter controlling the desorption profile for the Type I model is axial dispersion.

Film Mass Transfer with Axial Dispersion - Model Type II. The Type II model incorporates a kinetic submodel to describe mass transfer through the film on the SCF side of the aggregate-fluid interface. In this case, the mass exchange rate with the packing is proportional to the driving force for transfer and is given by Equation 7.

$$N_p = \frac{3k_m(1-\epsilon)}{\epsilon R} \left(C - \frac{q}{K_a} \right) \quad (7)$$

In addition to the axial dispersion coefficient, a film mass transfer coefficient also controls the desorption profile.

Internal Soil Resistance with Axial Dispersion and Film Mass Transfer - Model Type III. The Type III model utilizes a kinetic submodel which has three steps controlling the desorption process. The model extends the Type II model to include a concentration gradient as a function of radial position in the aggregate as part of the rate limiting process. For this case, the expression for N_p is given by,

$$N_p = \frac{3(1-\epsilon)k_m}{\epsilon R} (C - C_a|_{r=R}) \quad (8)$$

In this model the packed bed equation must be coupled with an equation describing the profile within the soil aggregates. This latter equation is based on a differential mass balance of solute in the intraparticle pore region and is given as

$$\frac{\partial C_a}{\partial t} = \frac{D_e}{\eta + \rho_s K_a (1-\eta)} \frac{1}{r^2} \left(2r \frac{\partial C_a}{\partial r} + r^2 \frac{\partial^2 C_a}{\partial r^2} \right) \quad (9)$$

where

$$D_e = D_m \frac{\eta}{\tau} \quad (10)$$

The additional boundary conditions for Equation 9 are:

$$\text{At } t=0, C_a = C_{a0} = \frac{q}{K_a} \quad (11)$$

$$\text{At } r=0, \frac{\partial C_a}{\partial r} = 0 \quad (12)$$

$$\text{At } r=R, D_e \frac{\partial C_a}{\partial r} = k_m (C - C_a) \quad (13)$$

The rate parameters of concern are the axial dispersion coefficient, particle-to-fluid mass transfer coefficient and the effective diffusion coefficient. However, since the molecular diffusion coefficient and intraparticle porosity are fixed, the effective diffusion coefficient uncertainty is entirely in the tortuosity.

Model solution. All three models were solved using a Crank-Nicolson finite difference scheme (central difference in time and space). When the grid Peclet number exceeds two, the central difference scheme may diverge and lead to inaccurate solutions. Therefore, the convection terms in Equations 1 were discretized using the exponential scheme (7). In all of the numerical solutions presented here, mass closure was $100 \pm 1\%$.

For each of the models a single fitting parameter was used to fit the breakthrough front of the desorption profile. The region of the breakthrough curve used for the fitting corresponds to the experimental data between approximately 84% and 16% of the initial concentration, which represents the mean time plus one standard deviation. The spreading in this region of the breakthrough curve is

dependent on the contribution of axial dispersion, film mass transfer and intraparticle diffusion. The best fit for a given parameter was determined by producing the minimum mean squared error between the model and the experimental data.

Parameter Estimation

Two types of parameters have been estimated. One type is referred to as FIXED parameters based on the known operating conditions of the experiments and reliably estimated values of density, viscosity and partition coefficients. The second type is referred to as VARIABLE parameters which are the parameters associated with the kinetics of the extraction process.

Experimental results from two different sources are used in this paper. The first set of experimental data is provided in Erkey *et al.* (4) and will be referred as the Texas data. The second set of data is given in Kothandaraman *et al.* (8) and will be referred to as the Rutgers data. The Texas data contains desorption runs for two contaminants, naphthalene and phenanthrene, at three temperatures. The Rutgers data contains runs for phenanthrene and anthracene at one temperature. Table I summarizes the properties of the packed beds for these data sets.

Fixed Parameters. Table II summarizes the operating conditions used in the Rutgers and Texas experiments and calculated values of the fixed parameters.

The molecular diffusivities in supercritical carbon dioxide are derived from the following correlation (9).

$$D_m = \kappa * 10^{-5} \left(\frac{\mu * 10^6}{T} \right)^{-0.75} \quad (14)$$

For naphthalene a value of 19.49 for κ gave a average deviation with experimental data of $\pm 5.2\%$. The diffusivities for phenanthrene and anthracene can be determined from the value for naphthalene based on the ratio of the molar volumes raised to the 0.6 power (10). Thus, κ is 16.24 and 16.86 for phenanthrene and anthracene, respectively.

For the Texas data, the partition coefficients, or the adsorption equilibrium constants, were determined from the adsorption isotherms found in Erkey *et al.* (4). For the Rutgers data, Andrews *et al.* (11) reported non-linear adsorption isotherms for phenanthrene and anthracene. However, the models utilized in this work required a linear approximation of the adsorption constant, which was made using a moment analysis. A linear isotherm assumption was incorporated in the models of this paper based on the well established linear behaviour of hydrophobic organics in soil-water systems (12). The partition coefficients used for both the Texas and the Rutgers soil are presented in Table II.

Variable parameters. The rate parameters of concern are the axial dispersion coefficient (D_{ax}), the film mass transfer coefficient (k_m) and the tortuosity (τ). They are calculated using the correlations presented below.

Table I: Properties of the Packed Beds

	Bed Length (cm)	Bed Diameter (cm)	Bed Porosity (v/v)	Aggregate Diameter (μm)	Intraaggregate Porosity (v/v)	Particle Density ($\text{g}_{\text{soil}}/\text{cm}^3_{\text{soil}}$)
Texas	25.0	0.46	0.50	230	0.12	2.52
Rutgers	3.0	2.58	0.505	200*	0.018*	2.65

* assumed values based on a soil similar to the Rutgers soil

Table II: Fixed Parameter Data

Data	Chemical	T (K)	P (atm)	Interstitial velocity (cm/s)	Density [#] (g/cm^3)	Viscosity* (10^{-5} Pa s)	D_m^4 (10^{-4} cm^2/s)	Re	Sc	K_a ($\text{cm}^3/\text{g}_{\text{soil}}$)
Critical Point		304.136	72.8		0.468	2.56				
Texas	Naphthalene	308	100	0.74	0.718	6.11	1.17	10	7.3	0.17
		318	100	1.05	0.517	3.87	1.68	16	4.5	0.46
		328	100	1.61	0.341	2.69	2.26	24	3.5	2.26
	Phenanthrene	308	100	0.74	0.718	6.11	0.97	10	8.8	1.24
		318	100	0.99	0.517	3.87	1.40	15	5.3	3.06
		328	100	1.48	0.341	2.69	1.88	22	4.2	16.4
Rutgers	Phenanthrene	318	170	0.024	0.790	6.97	1.08	0.3	8.2	3.5
	Anthracene	318	170	0.024	0.790	6.97	0.94	0.3	9.4	6.0

Bender Equation of State (13) * Reichenberg correlation and Chapman-Enskog theory (14)

Axial dispersion. Tan and Liou (15) measured axial dispersion in experiments with supercritical fluids flowing through beds of glass beads. The following correlation had an accuracy of ± 8.5 based on their experimental observations.

$$D_{ax} = 0.085 u_i^{0.914} d_p^{0.388} \rho_r^{0.725} \mu_r^{0.676} \quad (15)$$

Freeze and Cherry (16) report that axial dispersion for the flow of water in soil can be represented by the following equation:

$$D_{ax} = \alpha u_s \quad (16)$$

where $\alpha = 0.01 - 2$ cm. Lower values of α are more likely for unconsolidated soil such as that found in re-packed soil columns.

Film mass transfer coefficient. The film mass transfer coefficients were calculated from the Lim *et al.* (17) correlation:

$$\frac{Sh}{(Sc Gr)^{1/4}} = 0.1813 \left(\frac{Re^{7/8} Sc^{1/3}}{Gr^{1/4}} \right) + 1.2149 \left[\left(\frac{Re^{3/2} Sc^{1/4}}{Gr^{3/4}} \right) - 0.01649 \right]^{1/3} \quad (17)$$

This correlation reproduced the Lim's experimental data with an average deviation of 12.2%. The experiments involved mass transfer from a packed bed of naphthalene balls into supercritical carbon dioxide. The mixture densities required to determine $\Delta\rho$ in the Grashof number were calculated using the Peng-Robinson equation-of-state. A conventional van der Waals mixing rule was used. The mixing parameters were taken from Pongsiri and Viswanath (18).

A second equation used in the calculation of film mass transfer coefficients was the Wakao and Kagueli (19) correlation:

$$Sh = 2 + 1.1 Sc^{1/3} Re^{0.6} \quad (18)$$

Internal Soil Resistance. The internal soil resistance is controlled by the effective diffusion coefficient within the soil aggregates. However, if the molecular diffusion coefficient and the aggregate porosity are known then the remaining variable parameter is the aggregate tortuosity. Chang (20) mathematically derived the following relationship between tortuosity and porosity,

$$\tau = 2 - \eta \quad (19)$$

Results and Discussion

Figures 1 to 3 indicate the degree of fit between the three model types and the observed experimental data. Each figure is representative of the fit possible by each model for all of the data. Although the fit was based on a least squares error for data from 16 and 84% of the initial concentration, the resulting fit typically matched from the beginning down to approximately 25% of the initial level. Beyond this point, in all but one case (Texas, naphthalene data at 35°C) the data began to tail in relation to the model.

If the results from the Type I, II and III models for a given run were to be plotted on the same figure, the three fitted curves would be virtually superimposed. This was observed in almost all cases. This observation is consistent with the work of Valocchi (6) in which several different models could fit the a breakthrough curve in the same way.

In an attempt to determine the most plausible model and to isolate the controlling mechanism behind the process, the curve fitted values were analyzed to assess whether they are physically plausible. The fitted values from each of the models are summarized in Table III. In addition, the values determined by the correlations are included for comparison.

Axial Dispersion - Model Type I. The axial dispersion parameters fitted to the data based on the model are approximately 4-20 times greater than those calculated from the Tan-Liou correlation and 7.5-55 times greater than those based on Freeze and Cherry's soil-water data. To decide whether this is sufficient evidence to reject the premise of model Type I that axial dispersion is the only controlling rate parameter, it is necessary to consider the certainty and applicability of the correlations.

The Tan and Liou (15) experiments were performed with spherical glass beads. On the other hand, soil particles can have shape factors ranging from 0.43 to 0.95 (21). This difference in sphericity can have a significant affect on axial dispersion. For water flow in soil, changing from glass spheres to like-grained sand has resulted in an increase of axial dispersion by between 35 and 700% (22). As well, the bed used in the Tan and Liou (15) experiments were uniform diameter glass beads. While a mean particle diameter is used for a packed bed of soil, in reality a substantial distribution of particle sizes exists. This can result in a substantially higher axial dispersion coefficients (22-24).

The Freeze and Cherry axial dispersion depends on the value of α . This value could be as much as 100 times larger than what was used in Table III which would directly increase the calculated value of the axial dispersion. It is uncertain if the axial dispersion of water and SCFs would be similar in the same system.

Caution should be taken in applying data from the soil-water domain. It is likely that soil-water experimental measurements of axial dispersion did not correct or account for intraparticle diffusion in their analysis. This could explain the typically higher axial dispersion coefficients in soil-water systems.

Overall, the fitted axial dispersion values exceed the available calculated values; however, once the uncertainty in the calculated values is reviewed the fitted values must be considered plausible.

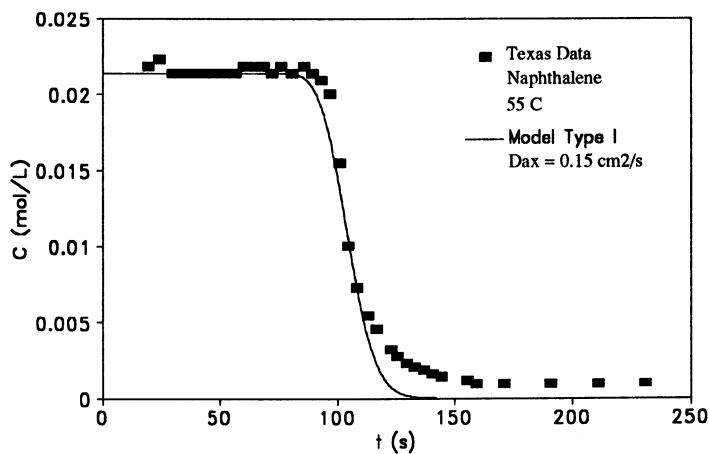


Figure 1: Illustration of Fit for Model Type I

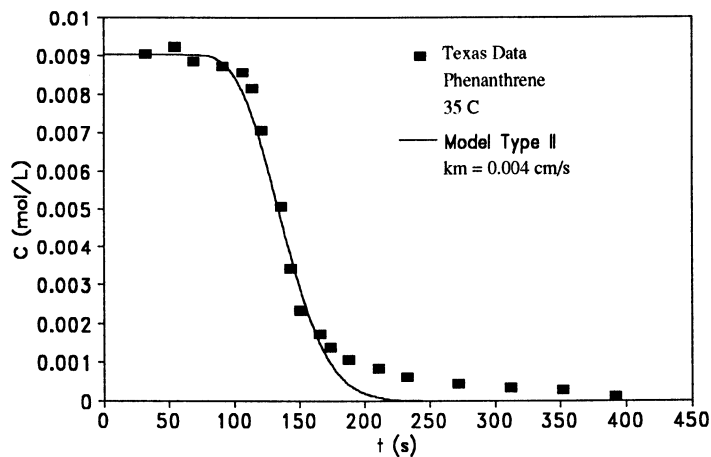


Figure 2: Illustration of Fit for Model Type II

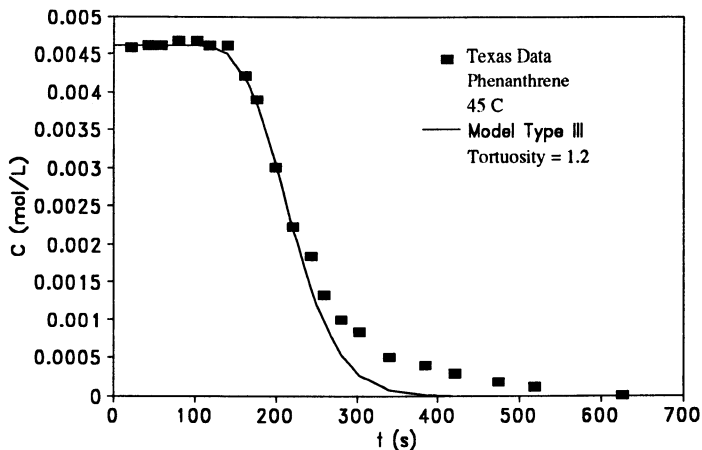


Figure 3: Illustration of Fit for Model Type III

Film Mass Transfer - Model Type II. For the Type II model, the computed mass transfer coefficients are, with the exception of the Texas naphthalene 55°C, approximately one order of magnitude lower than those predicted by the correlation. For this calculation the axial dispersion was assumed to be that calculated from Equation 15.

Once again, in order to determine the plausibility of the computed values of k_m , it is useful to examine the conditions for which the correlations are valid. The Lim *et al.* (17) experiments were conducted for Reynolds numbers ranging from 4 to 135 and Schmidt numbers ranging from 2 to 11. An examination of Table II indicates the Re and Sc numbers for Texas runs fall within this range. For the Wakao-Kaguei relationship, the lumped parameter $Sc^{1/3}Re^{0.6}$ for the Texas data once again falls within the range of validity of the correlation. As well, both correlations agree fairly closely, indicating the predicted mass transfer coefficient are within the right range. All these factors suggest that the fitted mass transfer coefficients are not plausible, assuming the Tan and Liou correlation for calculating axial dispersion is valid. However, neither correlation is derived from observations involving soils or SCF/soil systems.

A second approach to fitting the data with the Type II model was to assume the mass transfer correlation of Lim *et al.* (17) was valid and fit the curve by adjusting the value of the axial dispersion. This resulted in nearly identical axial dispersion values as in the Type I model and presented in Table III. Then, if the Lim correlated values are accurate, this would indicate that the particle-to-fluid mass transfer limitation has a negligible effect on the breakthrough curve and thus this limitation itself is negligible.

Table III: Model Results

Data	Chemical	Temp (°C)	Model Type I Axial Dispersion		Model Type II Film Mass Transfer		Model Type III Internal Resistance				
			D_{ax} (cm ² /s) Eq'n 15/16*	Ratio Fitted to Eq'n	k_m (10 ⁻² cm/s) Eq'n 17/18	Ratio Fitted to Eq'n	τ	Ratio			
									Fitted	Eq'n	Fitted
Texas	Naphthalene	35	0.13	0.037/0.007	3.5/19	0.3	6.0/5.3	0.05/0.06	2.4	1.9	1.3
		45	0.52	0.029/0.01	18/52	0.3	9.4/8.5	0.03/0.04	3.0	1.9	1.6
		55	0.15	0.025/0.02	6/7.5	12.	15./13.	0.8/0.93	n/a	1.9	-
Rutgers	Phenanthrene	35	0.37	0.037/0.007	10/53	0.4	5.4/4.7	0.07/0.09	0.8	1.9	0.42
		45	0.54	0.028/0.01	19/54	0.6	8.2/7.2	0.07/0.08	1.2	1.9	0.63
		55	0.45	0.023/0.02	20/23	1.0	12./11.	0.08/0.09	0.8	1.9	0.42
Rutgers	Phenanthrene	45	0.007	0.0018/0.0002	3.9/55	0.04	0.79/1.6	0.05/0.02	2.3	2.0	1.2
	Anthracene	45	0.04	0.0018/0.0002	6.1/55	0.03	0.72/1.4	0.04/0.02	3.0	2.0	1.5

* based on $\alpha=0.02$ cm

Internal Resistance - Model Type III. For the Type III model the axial dispersion from Equation 15 and the mass transfer coefficient from Equation 17 were assumed to apply. The value of the tortuosity in Equation 10 was used as the fitting parameter. The ratio of the fitted tortuosities to the Chang (20) values range from 0.4 to 1.6. This apparent agreement is encouraging. However, it should not be viewed as validation of the model and the independent correlations. To fully validate the model and correlations further studies are required including independent measures of the parameters for SC-CO₂/soil systems and measures of breakthrough curves for a wider range of conditions and soils.

It is necessary to recognize that the requirement to assume values for the particle diameter and the intraparticle porosity for the Rutgers data directly affects the fitted tortuosity. Other possible values for the diameter and porosity could result in the Rutgers tortuosity falling outside the 'correct' range. For example, if a particle diameter of 700 μm is assumed, the tortuosity for anthracene becomes 0.16. In essence because of the unknown values for the Rutgers experiments, the tortuosities derived from the Type III model can not be fairly evaluated.

Madras *et al.* (5) use the same system of equations, but a different solution technique, to model the Texas data. Their results are comparable to the results presented in this paper. The differences can be attributed to the use of different property estimation techniques and rate parameter correlations. Their model as well cannot satisfactorily predict the desorption tail for the extraction of contaminants from soil.

Tailing. Each model fails to predict the desorption tail, which is a major shortcoming. In the remediation of contaminated soils, the elution tail can have a large impact on economics. For the desorption of contaminants from activated carbon, for example, it is sufficient to regenerate the bed to within 5% of the initial concentration. The desorption tail in this case would not have to be considered. However, due to the low clean-up levels required in environmental applications, soil often needs to be remediated to under 0.1% of original levels. Therefore, the tail can have a large impact on the desorption process and needs to be understood.

Several mechanisms have been proposed to describe excessive tailing of the breakthrough curve, including: nonequilibrium, nonlinearity of the adsorption isotherm, nonsingularity, transformation reactions and aggregate size distribution (25,26). Further modelling research is necessary.

Summary

Three models incorporating axial dispersion, film mass transfer and intraaggregate diffusivity were applied to literature breakthrough data for the supercritical extraction of contaminants from soil. All three models fit the breakthrough front successfully.

Kinetic parameters were fitted and compared to independent correlations. The greatest consistency between the fitted parameters and the existing correlations occurred when the full Type III model was utilized. This should not be interpreted as validation of each of the existing correlations for two specific reasons. One, for the film mass transfer component the correlations suggest that it is the least contributing step. Thus, a substantial error in this correlation could exist and go

undetected by the experimental observations. Two, since the other two parameters are both contributing significantly, it is only the combination of the two parameters that has been validated. Consequently, given the apparent uncertainty in the available correlations, it is possible that significant errors prevailing in one parameter may be compensated for by errors in the other parameter(s).

As each of the three parameters are affected differently by the scale of the system, it is not sufficient to have only validated the combination of two parameters if the end goal is to use all three parameters for process scale up. The uncertainty associated with all of the independent correlations suggests direct measures of each individual parameter must be undertaken specifically for supercritical fluid - soil systems.

Nomenclature

C (C_{to})	= concentration of solute in bulk fluid (at time=0), mol/L ³ fluid
C_a (C_{ao})	= concentration of solute in intraparticle pores (at time=0), mol/L ³ fluid
C_{in}	= inlet concentration, mol/L ³ fluid
d_p	= particle diameter, L
D_m	= molecular diffusivity, L ² /T
D_{ax}	= axial dispersion coefficient, L ² /T
D_e	= effective intraparticle diffusivity, L ² /T
Gr	= Grashof number, $\rho g L^3 \Delta \rho / \mu^2$
k_m	= film mass transfer coefficient, L/T
K_a	= equilibrium partition coefficient, L ³ fluid/M
L	= bed length, L
N_p	= sink/source term, mol/L ³ T
q	= sorbate concentration, mol A/M
r	= radial distance in particle, L
R	= particle radius, L
Re	= Reynolds number, $u_s d_p \rho / \mu$
Sc	= Schmidt number, $\mu / (\rho D_m)$
Sh	= Sherwood number, $k_m d_p / D_m$
t	= time, T
T	= temperature
u_i, u_s	= interstitial, superficial velocity, L/T
z	= length along the packed bed, L
α, κ	= empirical constants
η	= intraparticle porosity, L ³ fluid/L ³ particle volume
ϵ	= bed void fraction, L ³ fluid/L ³ bed volume
ρ (ρ_f)	= fluid density (reduced), M/L ³ fluid
ρ_s	= particle density, M/L ³ soil
μ (μ_f)	= fluid viscosity (reduced), ML/T
τ	= tortuosity factor

Acknowledgments

This work has been funded by the Natural Sciences and Engineering Research Council of Canada and the Groundwater and Soil Remediation Program.

References

1. Cairney, T. in *Contaminated Land: Problems and Solutions*, Cairney, T., Ed., Chapman & Hall, **1993**, p1-7.
2. Parker, S. *Soils*, **1993**, March Issue, p41.
3. Laitinen, A.; Michaux, A.; Aaltonen, O. *Environ. Technol.*, **1994**, *15*, 715-727.
4. Erkey, C.; Madras, G.; Orejuela, M.; Akgerman, A. *Environ. Sci. Technol.*, **1993**, *27*, 1225-1231.
5. Madras, G.; Thibaud, C.; Erkey, C.; Akgerman, A. *AIChE J.*, **1994**, *40*, 777-785.
6. Valocchi, A.J. *Water Res. Res.*, **1985**, *21*, 808-820.
7. Patankar, S.V. *Numerical Heat Transfer and Fluid Flow*, McGraw-Hill Inc., New York, **1980**.
8. Kothandaraman, S.; Ahlert, R.C.; Venkataramani, E.S.; Andrews, A.T. *Environ. Prog.*, **1992**, *11*, 220-222.
9. Lamb, D.M.; Adamy, K.W.; Jonas, J. *J. Phys. Chem.*, **1989**, *93*, 5002-5005.
10. Sassiati, P.R.; Mourier, P.; Caude, M.H.; Rosset, R.H. *Anal. Chem.*, **1987**, *59*, 1164-1170.
11. Andrews, A.T.; Ahlert, R.C.; Kosson, D.S. *Environ. Prog.*, **1990**, *9*, 204-210.
12. Karickhoff, S.W. *Chemosphere*, **1981**, *10*, 833-846.
13. Knaff, G.; Schlunder, E.U. 1987 *Chem. Eng. Processing*, 21:151-162.
14. Reid, R.C.; Prausnitz, J.M.; Poling B.E. 1987 *The Properties of Gases and Liquids*, 4th edition, McGraw-Hill Inc., NY, p388-490.
15. Tan, C.-S.; Liou, D.-C. *Ind. Eng. Chem. Res.*, **1989**, *28*, 1246-1250.
16. Freeze, R.A.; Cherry, J.A. *Groundwater*, Prentice-Hall Inc., Englewood Cliffs, NJ, **1979**, p430.
17. Lim, G.-B.; Holder, G.D.; Shah, Y.T. *J. Supercritical Fluids*, **1990**, *3*, 186-197.
18. Pongsiri, N.; Viswanath, D.S. *Ind. Eng. Chem. Res.*, **1989**, *28*, 1918-1921.
19. Wakao, N.; Kaguei, S. *Heat and Mass Transfer in Packed Beds*, Gordon and Breach, NY, **1982**, p156-157.
20. Chang, H.C. *Chem. Eng. Communication*, **1982**, *15*, 83-91.
21. *Chemical Engineers Handbook*, 6th Ed., Perry, R.H.; Green, D. Eds.; McGraw-Hill Inc., NY, **1984**, p5-54.
22. Klotz, D.; Moser, H. *Isotope Techniques in Groundwater Hydrology*, International Atomic Energy Agency, Vienna, **1974**, Vol 2, pp 341-355.
23. Han, N.W.; Bhakta, J.; Carbonell, R.G. *AIChE J.*, **1985**, *31*, 277-288.
24. Rasmusson, A. *Chem. Eng. Sci.*, **1985**, *40*, 621-629.
25. Brusseau, M.L.; Rao, P.S.C. *Crit. Rev. Environ. Cont.*, **1989**, *19*, 33-99.
26. Fong, F.K.; Mulkey, L.A. *Water Res. Res.*, **1990**, *26*, 1291-1303.

RECEIVED June 20, 1995

Chapter 21

Corrosion and Chemical Agent Destruction Research on Supercritical Water Oxidation of Hazardous Military Wastes

Kevin W. Downey¹, Richard H. Snow², D. A. Hazlebeck¹,
and Adele J. Roberts¹

¹General Atomics, 3550 General Atomics Court, San Diego, CA 92121

²IIT Research Institute, 10 West 35th Street, Chicago, IL 60616

Supercritical water oxidation (SCWO) is a developing technology for the destruction of hazardous and nonhazardous wastes. General Atomics and its subcontractors are currently conducting two comprehensive research and demonstration programs geared toward the destruction of Department of Defense (DoD) wastes utilizing SCWO technology. Wastes of primary interest include chemical agents and solid propellants. Corrosion testing performed in support of these programs identified platinum and titanium as candidate reactor construction materials. Kinetics testing emphasized chemical agent destruction. Kinetics results for chemical agents show destruction and removal efficiencies for GB, VX, and mustard agents to be in excess of 99.9999%, limited only by detection capability.

Supercritical water oxidation (SCWO), also called hydrothermal oxidation (HTO), is a developing technology for the destruction of hazardous and nonhazardous wastes. SCWO destroys combustible materials using an oxidant in water at temperatures and pressures above the critical point of water, 374°C and 218 atm. General Atomics (GA) and its subcontractors are currently conducting two comprehensive research and demonstration programs geared toward the destruction of Department of Defense (DoD) hazardous wastes. The first program, performed for the Advanced Research Projects Agency (ARPA), involves the destruction of chemical agents, solid propellants, and other DoD hazardous wastes. The second program, performed for the U.S. Air Force, involves the destruction of Hazard Class 1.1 propellant removed from rocket motor casings.

Both the ARPA and Air Force programs required significant research efforts to provide sufficient data for pilot plant design. Numerous research areas

0097-6156/95/0608-0313\$12.00/0
© 1995 American Chemical Society

were investigated, including corrosion, kinetics, hydrolysis, catalysis, solids handling, and chemical agent destruction verification/kinetics (1-4). However, only the corrosion and chemical agent destruction data, generated under the ARPA program, are discussed herein. Corrosion testing investigated the corrosion resistance of various high nickel alloys, reactive metals, refractory metals, noble metals, and ceramics at temperatures of 350 to 550°C under the highly acidic conditions (pH=0) corresponding to SCWO of 5 wt% solutions of the chemical agents GB, VX, and mustard. Materials capable of withstanding these extremely aggressive conditions were identified. Chemical agent testing was performed at the facilities of IIT Research Institute (IITRI), a facility approved by the U.S. Army for the handling of chemical surety materials. Separate test programs were conducted for the chemical agents, GB, VX, and mustard.

Corrosion Testing.

Under supercritical conditions, the products that result from the oxidation of chemical agents are highly corrosive to a wide variety of materials. For example, the oxidation of GB agent yields hydrofluoric and phosphoric acids; the oxidation of VX agent yields sulfuric and phosphoric acids; and the oxidation of mustard agent yields sulfuric and hydrochloric acids. At desired pilot plant agent throughput rates, acid concentrations of several percent can be present, resulting in solutions with a pH of ~0.

In order to perform basic corrosion research using materials coupons, one must have a test rig capable of withstanding the corrosive environment for sufficient time to compile coupon data adequate for analysis and pilot plant design. Therefore, a partial solution to the corrosion problem was required during the test rig design and assembly stage because typical high strength materials such as Hastelloy C276 are grossly inadequate for even relatively short-term testing of highly acidic feeds. A literature search showed platinum to be a good materials candidate for many of the feeds in question, but the available data did not cover the supercritical regime (5-6). A platinum-lined reactor was designed and fabricated for testing candidate materials coupons at temperatures of 350, 450, and 550°C at a pressure of approximately 4000 psig. Numerous coupons could be suspended in an isothermal section of the reactor for extended periods of time. Exposure times ranged from 5 to 100 hr. The control system was designed to allow unattended overnight operation with automatic shutdown if temperature, pressure, or flow conditions outside of prescribed limits occurred. The corrosion test rig is shown in Fig. 1.

Table I shows the materials coupons studied during the test program. Most coupons were 3/8" square and approximately 65 mils thick. Table II shows the range of corrosive media tested. These test solutions corresponded to the composition expected following complete oxidation of 5 wt% chemical agent feeds. The H₂O₂ was present to provide oxygen, upon thermal decomposition, in the approximate concentration expected during later full-scale operations.

August 10, 2012 | <http://pubs.acs.org>
Publication Date: May 5, 1995 | doi: 10.1021/bk-1995-0608.ch021

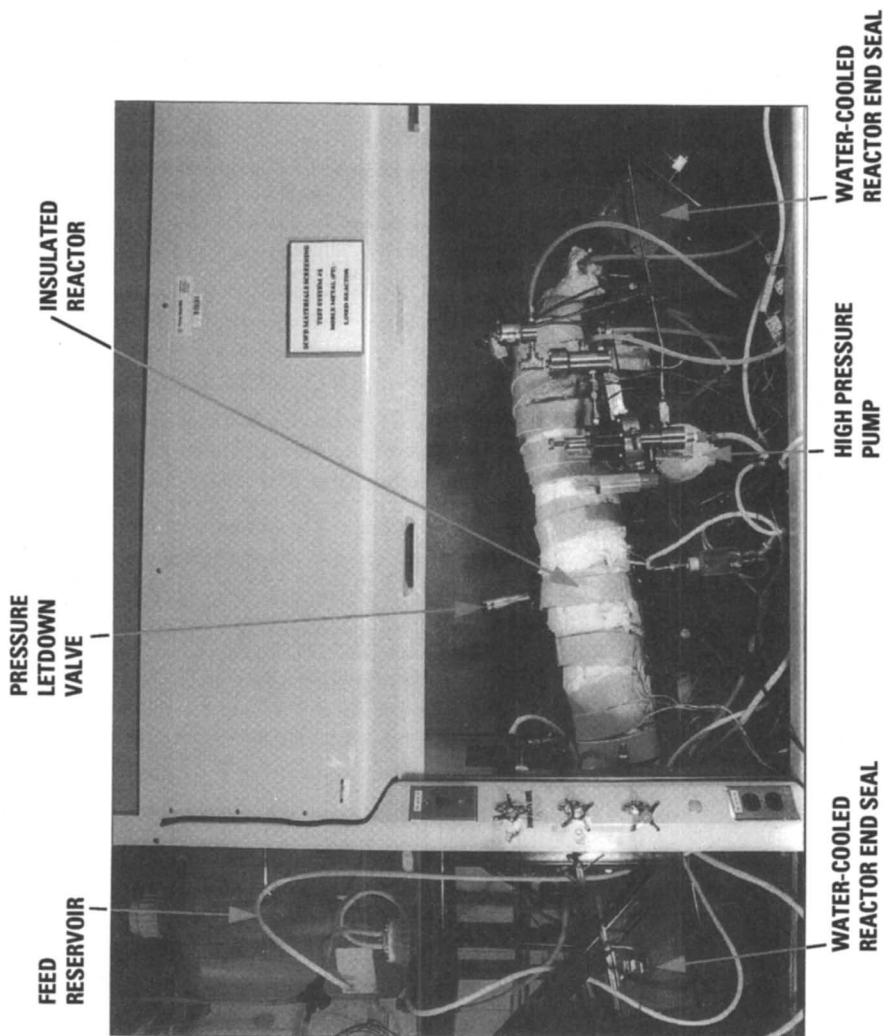


Figure 1. SCWO Corrosion Test Rig

TABLE I. MATERIALS INCLUDED IN CORROSION STUDIES

Category	Material
Nickel alloys	C22, C276, 625, 825, HR-160
Cobalt alloys	188
Reactive metals & alloys	Ti Gr 7, Ti-21S, Nb/55% Ti, Zr 704, Hf
Refractory metals	Mo Gr 361, Nb, Ta
Ceramics	Al ₂ O ₃ , Al ₂ O ₃ (sapphire), AlN, SiC, Si ₃ N ₄ , ZrO ₂ /9% Y ₂ O ₃
Noble metals & alloys	Pt, Pt/10% Rh, Pt/20% Ir
Other	PTFE

TABLE II. CORROSIVE CHEMICAL AGENT SIMULANT MEDIA

Test Simulant	Simulant Composition (wt%)	Temperature (°C)	Pressure (psi)	Time (hr)
GB agent, 5 wt%	0.7% HF, 3.5% H ₃ PO ₄ , 7.0% H ₂ O ₂	350, 450, 550	4000	0, 5, 20, and 65 or 90
VX agent, 5 wt%	1.8% H ₂ SO ₄ , 1.8% H ₃ PO ₄ , 7.0% H ₂ O ₂	350, 450, 550	4000	0, 5, 20, and 65 or 90
Mustard agent, 5 wt%	3.1% H ₂ SO ₄ , 2.3% HCl, 7.0% H ₂ O ₂	350, 450, 550	4000	0, 5, 20, and 65 or 90

A summary of the corrosion results is presented in Table III. All corrosion rates were determined from a combination of weight loss data and a visual inspection to confirm that weight loss calculations were reasonable. Additionally, microscopic inspections were performed for the most promising materials to look for signs of nonuniform corrosion. The data were compiled and presented in three broad classifications: (1) **Good** (<10 mil/yr corrosion rate) - candidate materials of construction showing excellent corrosion resistance, (2) **Moderate** (10-200 mil/yr corrosion rate) - potential materials of construction, and (3) **Poor** (>200 mil/yr corrosion rate) - clearly unacceptable materials of construction. These relatively broad categories were selected based on perceived limits of corrosion acceptability. For example, corrosion rates >200 mil/yr were deemed too great for these materials to be of practical use, while materials with corrosion rates of intermediate levels may be acceptable for some of our applications. Because of economics, expensive materials such as platinum compounds can only be used under conditions where corrosion is quite low.

The yearly corrosion rates used to categorize the materials coupons were calculated by extrapolating the rates observed during short-term testing to a yearly rate, assuming 24 hr/day, 365 day/yr exposure. Caution must be exercised in

TABLE III. CORROSION RESULTS SUMMARY

Material	HF and H ₃ PO ₄ (GB)			H ₂ SO ₄ and H ₃ PO ₄ (VX)			HCl and H ₂ SO ₄ (mustard)		
	350°C	450°C	550°C	350°C	450°C	550°C	350°C	450°C	550°C
Pt	O	O	O	O	O	O	◇	△	O
Pt/Ir	O	O	O	O	O	O	◇	△	O
Pt/Rh	O	O	O	O	O	O	◇	△	O
Hf	◇	◇	◇	△	△	△	◇	◇	◇
Ti	△	◇	△	O	◇	△	△	△	△
Timet 21S	O	◇	◇	O	◇	△	△	△	△
Zr 704	◇	◇	◇	△	△	△	◇	◇	N/A
Mo	◇	◇	◇	◇	◇	◇	◇	N/A	◇
Nb	△	△	◇	△	◇	◇	◇	◇	N/A
Nb/Ti	△	◇	◇	O	◇	△	△	△	△
Ta	O	◇	◇	O	O	◇	O	◇	N/A
Al ₂ O ₃	◇	◇	◇	△	◇	◇	◇	◇	△
AlN	◇	◇	◇	O	◇	△	◇	◇	◇
Sapphire	◇	◇	◇	△	△	△	◇	◇	△
Si ₃ N ₄	◇	◇	◇	◇	◇	◇	◇	◇	◇
SiC	◇	◇	◇	◇	◇	◇	◇	◇	◇
ZrO ₂	△	◇	◇	△	◇	△	◇	◇	△
C22	O	◇	◇	△	◇	◇	◇	◇	◇
Hast. C276	△	◇	◇	△	◇	◇	◇	◇	◇
Hayn. 188	△	◇	◇	△	◇	◇	◇	△	◇
HR-160	△	◇	◇	◇	◇	◇	◇	◇	◇
Inc. 825	O	◇	◇	△	◇	◇	◇	◇	◇
Inc. 625	O	◇	◇	△	◇	◇	◇	△	◇

- O - Good (<10 mil/yr corrosion rate)
 △ - Moderate (10-200 mil/yr corrosion rate)
 ◇ - Poor (>200 mil/yr corrosion rate)
 N/A - Not available

using these data since extrapolation from short-term data presents some risk. It is recommended that longer-term corrosion testing be performed.

For the nonchloride-containing feeds tested (GB and VX simulants containing HF, H₃PO₄, and/or H₂SO₄) platinum (and platinum alloyed with either iridium or rhodium) was found to be highly resistant to attack. It was clearly the best of all materials tested. Microscopic examination of platinum alloy coupons did not reveal any evidence of nonuniform modes of corrosion. High nickel alloys and ceramics showed poor resistance. Some refractory metals, e.g., titanium, showed reasonable resistance for some conditions, but not as good as platinum, especially over the entire range of test conditions and media.

During the 350°C testing of mustard agent simulant in the platinum-lined reactor, it became clear that a platinum-containing compound or complex was produced which was soluble in the subcritical fluid. High platinum losses

occurred in both the platinum coupons and the reactor liner. Upon further investigation, the platinum loss was found to be confined to temperatures below the supercritical transition region (at 350°C in our testing). At both 450 and 550°C, platinum was much more resistant to chloride attack.

Because of the high rate of platinum attack at the transition temperature with chloride feeds, the platinum-lined reactor was unsuitable for long-term testing of these feeds. A titanium-lined reactor was therefore constructed and used to perform mustard agent simulant testing. Titanium exhibited poor resistance to GB and VX simulants, especially with regard to fluoride attack. But, based on preliminary results, titanium appeared to exhibit reasonably good resistance to chloride/sulfur attack. Further testing confirmed the preliminary results, and titanium was found to be acceptable for chloride-containing feeds. Microscopic examination and microhardness testing of the titanium coupons did not reveal any evidence of nonuniform modes of corrosion or oxygen embrittlement. As with the GB and VX simulant feeds, high nickel alloys and ceramics showed very poor corrosion resistance when exposed to chloride-containing feeds.

Chemical Agent Testing.

The primary focus of the ARPA SCWO program, from both a research and design standpoint, was the processing of the nerve agents GB and VX, and the blister agent mustard. The safety requirements necessary for processing chemical agents dictated much of the pilot plant design, and the extremely corrosive conditions accompanying SCWO of chemical agents dictated the corrosion test conditions. To ensure a comprehensive, workable design, it was imperative that laboratory-scale SCWO testing of actual chemical agents be conducted. (None had been performed prior to this program.) Testing was performed at IITRI in discreet phases to provide sufficient time for changeover of equipment and agent monitors, validation of analytical techniques (7-9), and agent deliveries from the Army.

Agent testing was performed in a bench-scale test rig specifically designed for testing at IITRI. The rig was made as compact as possible to allow insertion into an IITRI agent test hood. The hood provided a ventilated, protected workspace for agent testing. The major features of the test rig included: (1) storage reservoirs for oxidant (H_2O_2) and water mixtures, (2) a high pressure pump, (3) an 8.5-ft long, 3/4" O.D., heated reactor lined with either platinum (for GB and VX testing) or titanium (for mustard testing), (4) slip-on heaters in three independently controlled temperature zones, (5) cooled reactor end fittings with O-ring seals, (6) pressure monitors at both ends of the reactor, (7) numerous external thermocouples positioned axially along the entire reactor length, (8) a pressure letdown valve to control the system operating pressure, (9) liquid effluent collectors, (10) a sealable, reinforced stainless steel enclosure capable of containing a worst-case system depressurization, and (11) a data acquisition and control system. Figure 2 shows a photograph of the rig inserted in the IITRI agent test hood. The agent feed pump, supplied by IITRI, is positioned to the far right

August 10, 2012 | <http://pubs.acs.org>
 Publication Date: May 5, 1995 | doi: 10.1021/bk-1995-0608.ch021

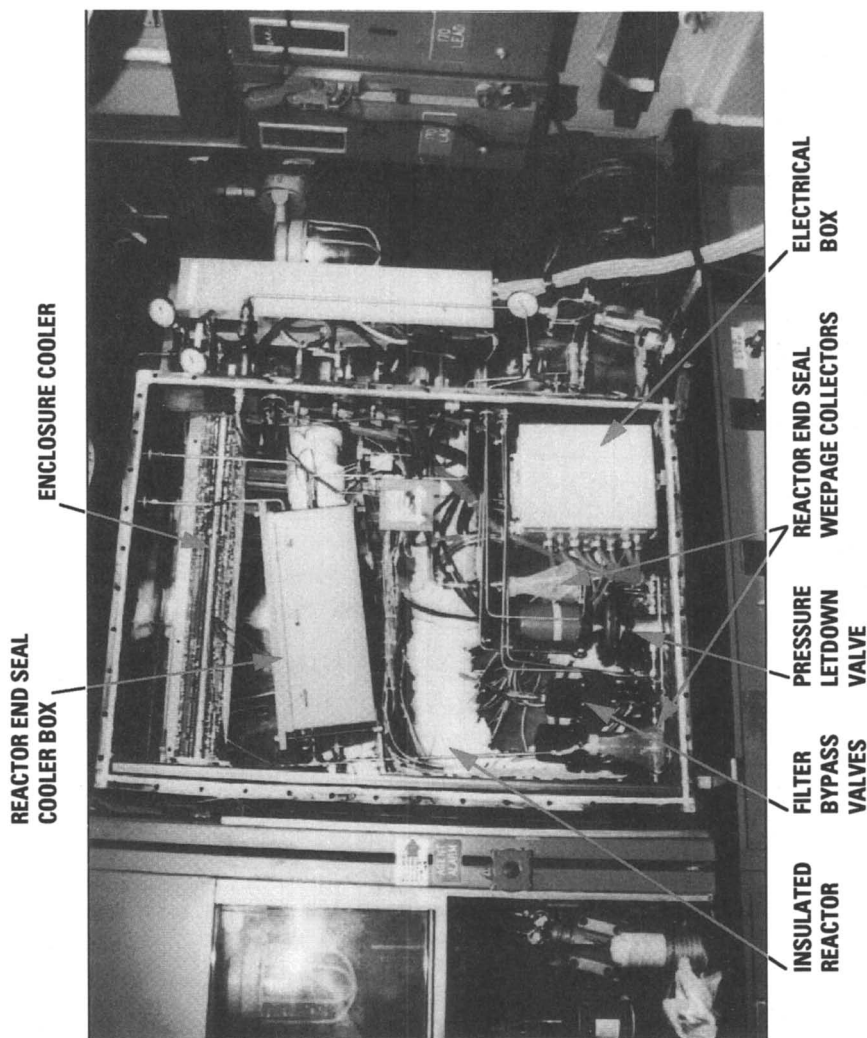


Figure 2. SCWO Chemical Agent Test Rig

of the test rig. The effluent collection and off-gas monitoring equipment were located in an adjacent hood.

Corrosion testing, discussed previously, identified platinum as the optimum material of construction for SCWO processing of GB and VX agents. A thin (0.010") platinum liner was contained within a Hastelloy C276 pressure-bearing tube. For processing of mustard agent, titanium was identified as the best material of construction, again as a thin liner within a Hastelloy C276 pressure bearing wall. A platinum-lined reactor was therefore used for the GB and VX test series. This reactor was removed and replaced with a titanium-lined reactor for the mustard agent test series.

The test rig data acquisition and control system consisted of an Apple Macintosh IICI computer coupled with National Instruments' data acquisition hardware. The software utilized was National Instruments' LabVIEW, a flexible, multipurpose, graphics-based data acquisition and control program. Inputs included 3 pressure and 29 temperature readouts. Outputs included pump actuation signals, back pressure control, and independent control of three reactor heating zones.

Prior to the start of agent testing, a test program was completed using chemical agent simulants in order to verify SCWO test rig capabilities. Tests were performed at temperatures of 450 to 550°C and flow rates of up to 100 ml/min. All tests were performed at a pressure of approximately 4000 psi. Agent simulants used were diethylmethylphosphonate (DEMP, GB and VX simulant), diisopropylethylamine (DIEA, VX simulant), and thiodiglycol (TDG, mustard simulant). Target simulant feed concentrations were 1 wt%.

GB Agent Testing. Following successful completion of the Preoperational Test for agent operations, an Army requirement, and the receipt of final Army approvals, GB agent testing commenced on May 10, 1993. All tests were performed at GB concentrations of approximately 1 wt% with 100% excess oxygen. Table IV presents the GB test matrix .

TABLE IV. GB AGENT TEST MATRIX

Test No.	Pressure (psig)	Temperature (°C)	Total Flow Rate (ml/min)	Residence Time (sec)	Test Duration (min)
1	4000	550	50.5	16	42
2	4000	450	39.4	29	15
3	4000	550	50.5	16	54
4	4000	450	43.4	26	71
5	4000	500	46.4	20	58

Gas and liquid samples were collected and analyzed throughout the test series. No agent was detected in any liquid samples, signifying a Destruction and Removal Efficiency (DRE) in excess of 99.99999%. [Higher DREs may have

August 10, 2012 | http://pubs.acs.org
Publication Date: May 5, 1995 | doi: 10.1021/bk-1995-0608.ch021

been achieved, but a DRE of 99.99999% is the maximum that can be measured given an influent agent concentration of 10,000 ppm (1 wt%) and the ~1 ppb detection limit for GB in liquid samples.] Additionally, no agent above the allowable exposure limit (AEL) was found in the gaseous effluent samples as analyzed on-line by a Minicams analyzer.

After the gaseous and liquid effluent samples were confirmed to be agent free, they were shipped to the Institute of Gas Technology (IGT) and the University of Texas Balcones Research Center (UTBRC), respectively, for further analysis. Gas samples were found to contain oxygen, nitrogen, argon, carbon dioxide, and trace amounts of methane. Liquid samples showed essentially quantitative conversion of the GB agent to complete oxidation products, i.e., HF and H₃PO₄. Small amounts (<400 ppm) of methyl phosphonic acid and acetone were detected in the 450°C samples, with significantly less detected in the 500 and 550°C samples. Table V shows the analytical results for the GB test series.

TABLE V. ANALYTICAL RESULTS FOR GB AGENT TESTING^(1,2)

Component	Unit of Measure	Reaction Temperature			
		450°C	500°C	550°C	
Liquid Analysis	Fluoride	ppm	1431	1719	1216
	Phosphate	ppm	6524	7785	5683
	MPA	ppm	122	83	48
	Acetone	ppm	385	106	<2
Gaseous Analysis	CO	vppm	BDL ⁽³⁾	BDL	BDL
	H ₂	vppm	BDL	BDL	BDL
	Methane	vppm		300	100

⁽¹⁾DRE of >99.99999% achieved for all test samples.

⁽²⁾Effluent data are averaged for multiple runs performed at the same temperature.

⁽³⁾Below detection limit.

VX Agent Testing. VX agent testing commenced on June 29, 1993. Six separate tests were performed, investigating temperatures of 450 to 550°C (see Table VI). As with the GB test series, all tests were performed at agent concentrations of approximately 1 wt% with 100% excess oxygen. Typically, four liquid and two gas samples were taken for each test. Additionally, 4-5 Minicams analyses of the gaseous effluent were performed during the course of testing. No agent was detected in any liquid samples, signifying a DRE in excess of 99.99999%. [Higher DREs may have been achieved, but a DRE of 99.99999% is the maximum that can be measured given an influent agent concentration of 10,000 ppm (1 wt%) and the ~1 ppb detection limit for VX in liquid samples.] No agent above the AEL for VX was detected during on-line Minicams analysis of the SCWO gaseous effluent.

TABLE VI. VX AGENT TEST MATRIX

Test No.	Pressure (psig)	Temperature (°C)	Total Flow Rate (ml/min)	Residence Time (sec)	Test Duration (min)
1	4000	500	50.5	18	68
2	4000	450	39.4	29	45
3	4000	500	50.5	18	93
4	4000	550	49.5	16	44
5	4000	450	39.4	29	56
6	4000	550	50.5	16	48

Gas and liquid samples were sent to IGT and UTBRC, respectively, for further analysis following verification by IITRI personnel of the absence of detectable agent. The VX agent was essentially quantitatively converted during testing to sulfuric and phosphoric acid. Small quantities of transformation products such as acetic acid and acetone were observed. Gas analyses showed the presence of N₂O and very low concentrations of NO_x and SO_x. The results of gas and liquid analyses are summarized in Table VII.

TABLE VII. ANALYTICAL RESULTS FOR VX AGENT TESTING^(1,2)

	Component	Unit of Measure	Reaction Temperature		
			450°C	500°C	550°C
Liquid Analysis	Acetate	ppm	83	446	160
	Phosphate	ppm	3507	3069	3862
	Sulfate	ppm	3474	3013	3812
	Acetone	ppm	22	3	7
	Ammonia	ppm	0	8	0
Gaseous Analysis	CO	vppm	BDL ⁽³⁾	BDL	BDL
	H ₂	vppm	BDL	BDL	BDL
	N ₂ O	vppm	3000	3500	3700
	NO _x	vppm	<2	<3	4
	SO _x	vppm	4	<4	2

⁽¹⁾DRE of >99.99999% achieved for all test samples.

⁽²⁾Effluent data are averaged for multiple runs performed at the same temperature.

⁽³⁾Below detection limit.

Mustard Agent Testing. Unlike GB and VX, mustard agent has a low solubility in water. GB and VX agents were mixed with the water/oxidizer solution in line just upstream of the reactor. They readily went into solution to yield a uniform, miscible solution. Because of its low solubility, mustard agent would yield a two-phase mixture upon feed to the SCWO reactor if fed in the same manner as the VX and GB agents. The two phase mixture could present operational and

performance difficulties in the compact test rig. Therefore, steps were taken to solubilize the mustard agent by hydrolyzing in hot water, thereby producing a safe, uniform feed for SCWO testing. A small test sample (2 g) was mixed with water in a 10 wt % solution and heated. The mixture initially showed distinct water and mustard agent phases, but after heating to 80-90°C for 7 minutes, it showed a single, clear, uniform phase. A hydrolysis apparatus was assembled to allow controlled hydrolysis of larger samples. The general procedure used during hydrolysis was: (1) load approximately 225 g of DI water and a Teflon stir bar into the hydrolysis vessel, (2) load approximately 25 g of mustard agent into a graduated feed cylinder, (3) heat the water to the desired temperature (at least 60°C) while stirring, (4) add 5-7 ml aliquots of mustard agent to the water and wait until signs of a separate mustard phase disappear, (5) when all agent has been added and solubilized, cool the solution and store for later SCWO use. The results of hydrolysis testing showed that mustard agent hydrolysis in water can be completed within approximately five minutes at 80 to 100°C, if suitably agitated. Hydrolysis at 60°C requires approximately 4 times longer.

Mustard agent testing began on April 5, 1994. Five separate tests were performed, investigating temperatures of 450 to 550°C (see Table VIII). As with the prior agent testing, all tests were performed at agent concentrations of approximately 1 wt% with 100% excess oxygen. Typically, four liquid and two gas samples were taken for each test. Additionally, multiple Minicams analyses of the gaseous effluent were performed during the course of testing.

TABLE VIII. MUSTARD AGENT TEST MATRIX

Test No.	Pressure (psig)	Temperature (°C)	Total Flow Rate (ml/min)	Residence Time (sec)	Test Duration (min)
1	4000	450	33.3	34	55
2	4000	450	31.3	37	55
3	4000	550	aborted	aborted	aborted
4	4000	500-525	30	34	92
5	4000	500	32.5	28	47
6	4000	500	31.5	29	47

No agent was detected in any liquid samples, signifying a DRE in excess of 99.9999%. [Higher DREs may have been achieved, but a DRE of 99.9999% is the maximum that can be measured given an influent agent concentration of 10,000 ppm (1 wt%) and the ~10 ppb detection limit for mustard agent in liquid samples.] Also, except for Run 3 & 4, where a system upset resulted in agent contamination of the effluent collection lines, no readings above the mustard agent AEL of 0.003 mg/m³ were detected. (During Run 3, an equipment malfunction necessitated test termination. Residual feed material was flushed at reduced pressure and temperature through the reactor into the effluent collection

lines, thus contaminating them. This was not discovered until after the start of Run 4.)

Gas and liquid samples were sent to IGT and UTBRC for further analysis. The results are listed below in Table IX. The data for runs performed at the same temperature have been combined and averaged. Low levels (≤ 600 ppm) of the intermediate transformation products acetic and formic acids were observed at 450°C, with less observed at 500°C, and none observed at $\sim 525^\circ\text{C}$. Relatively high concentrations of CO were observed at lower temperatures, decreasing to less than 2000 ppm at 525°C. Higher operating temperatures will even further reduce observed CO levels.

TABLE IX. ANALYTICAL RESULTS FOR MUSTARD AGENT TESTING^(1,2,3)

	Component	Unit of Measure	Reaction Temperature		
			450°C	500°C	525°C
Liquid Analysis	Acetate	ppm	597	47	<1
	Formate	ppm	211	16	<1
	Sulfate	ppm	6008	5336	3105
Gaseous Analysis	CO	mole%	14.5	1.4	0.17
	H ₂	vppm	3000	BDL ⁽⁴⁾	BDL
	C ₂ H ₄	vppm	700	BDL	BDL
	SO _x	vppm	2133	1098	2600

⁽¹⁾DRE of >99.9999% achieved for all test samples.

⁽²⁾Several unknown, nonagent peaks of ~ 50 -100 ppm each were detected.

⁽³⁾Effluent data are averaged for multiple runs performed at the same temperature.

⁽⁴⁾Below detection limit.

SO_x levels of 1000 to 2600 ppm were observed during testing. A major factor contributing to these relatively high levels is thought to be poor mixing/mass transport limitations caused by the low flow rates and short lengths of the test system. Even so, the sulfur present in the observed SO_x represented only about 2% of the available sulfur, the remaining having been fully converted to sulfate. The pilot plant reactor, designed to provide much better mixing and more flexibility in operational capabilities, should yield significantly lower SO_x levels.

Pilot Plant Reactor Design

The information and experiences collected during corrosion and chemical agent testing significantly influenced pilot plant reactor design. Figure 3 shows an isometric of the ARPA pilot plant reactor skid currently undergoing final assembly. (The high pressure/high temperature components were isolated on a

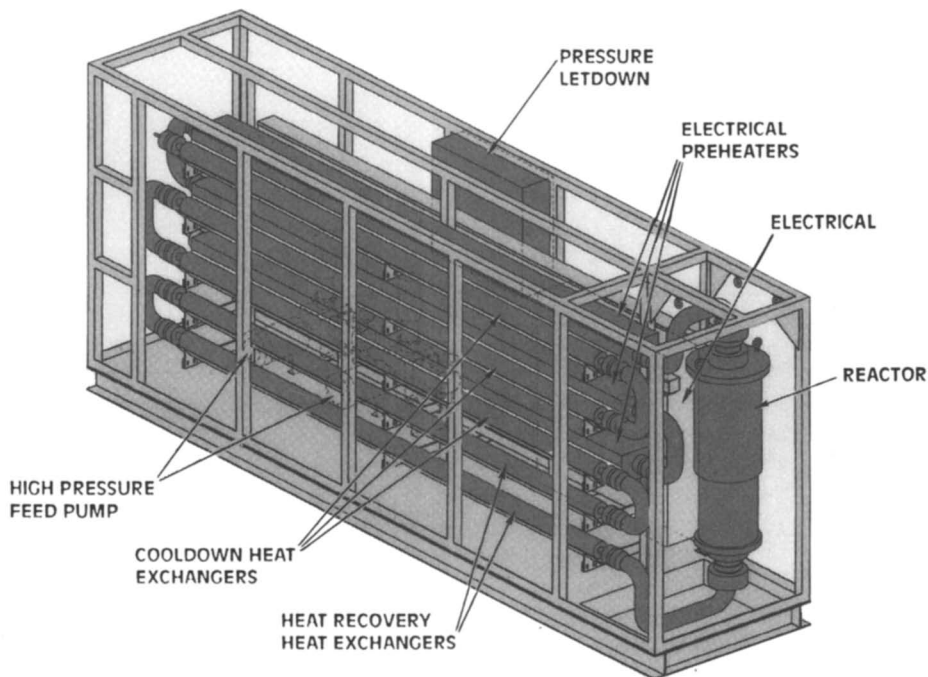


Figure 3. Pilot Plant Reactor Design

single skid for transportability and for personnel safety.) The major reactor skid components are: (1) a high pressure pump, (2) a lined preheat section, (3) a lined, large diameter, vertical, downflow section to ensure adequate residence time for complete hazardous waste destruction, (4) a lined heat recovery section to reduce preheat requirements, (5) a lined, water-cooled, cooldown section, and (6) a pressure letdown system. Two reactor systems are undergoing fabrication, one titanium lined for chlorinated feeds and one platinum lined for nonchlorinated feeds.

Conclusions/Highlights

- Based on the data observed to date, platinum and platinum alloys provide excellent corrosion resistance for non-chlorinated, highly acidic fluids such as those associated with the nerve agents GB and VX.
- Based on the data observed to date, titanium and titanium alloys provide good resistance to HCl-containing fluids such as those associated with mustard agent.
- Longer-term corrosion testing should be performed to validate the results observed during the short-term testing discussed herein.

- Destruction of the chemical agents GB, VX, and mustard using SCWO technology has been successfully demonstrated to 99.9999% or better. The low levels of products of incomplete combustion, e.g., acetic acid, observed during testing can be further reduced through operation at higher temperatures and/or longer residence times.
- Pilot plant construction is complete for the Air Force program and nearly complete for the ARPA program.

Literature Cited

1. Gloyna, E. F., Li, L., The University of Texas at Austin, *Batch Test Study*, work performed under contract to General Atomics, unpublished data.
2. Gloyna, E. F., Li, L., The University of Texas at Austin, *Catalysis Feasibility Testing for Application to SCWO*, work performed under contract to General Atomics, unpublished data.
3. Gloyna, E. F., Li, L., The University of Texas at Austin, *Continuous Flow Test Study*, work performed under contract to General Atomics, unpublished data.
4. Turner, M. D., *Supercritical Water Oxidation of Dimethylmethylphosphonate and Thiodiglycol*, Doctoral Dissertation, The University of Texas at Austin, December 1993.
5. Wise, E. M. In *The Corrosion Handbook*; Uhlig, H. H., Ed.; John Wiley & Sons: New York, New York, 1958; pp 299-312.
6. *Corrosion Resistance of Metal and Alloys*; LaQue, F. L.; Copson, H. R., Eds.; Reinhold Publishing Corporation, New York, 1965.
7. Taylor, K., IIT Research Institute, *Analysis of Gas Samples for GB*, unpublished data.
8. Taylor, K., IIT Research Institute, *Analysis of Gas Samples for VX*, unpublished data.
9. Taylor, K., IIT Research Institute, *Analysis of Gas Samples for HD*, unpublished data.

RECEIVED May 17, 1995

Chapter 22

Corrosion Studies in Supercritical Water Oxidation Systems

D. B. Mitton, J. C. Orzalli, and R. M. Latanision

H. H. Uhlig Corrosion Laboratory, Department of Materials Science
and Engineering, Massachusetts Institute of Technology,
77 Massachusetts Avenue, Cambridge, MA 02139

Supercritical water oxidation (SCWO) is a technology which can effectively destroy various civilian and military wastes, including nerve gas, by oxidation in water at high temperature and pressure. Although, as a technology SCWO can destroy such wastes, the process must be carried out in a reactor which will withstand not only the high temperature and pressure conditions but also a very corrosive environment. As process conditions are severe, corrosion could, ultimately, be the limiting factor in the useful application of this technique; nevertheless, little information relevant to degradation within such systems is available in the current literature. Results from laboratory and pilot-scale SCWO systems presently in operation indicate that wastage (accelerated general corrosion), pitting and stress corrosion cracking (SCC) are corrosion phenomena likely to be encountered in the various sections of SCWO systems. In order to increase our understanding of corrosion phenomena within such systems, systematic testing employing both exposure and electrochemical experiments will be carried out. Exposure samples are monitored for weight loss and subsequently examined to provide comprehensive information on both the rate and form of degradation. Additionally, in order to provide a fundamental understanding of degradation phenomena, an elevated temperature electrochemical facility has been constructed. This incorporates an Inconel-625 vessel designed to permit standard d.c. techniques as well as electrochemical impedance spectroscopy (EIS). Finally, results from the analysis of failures which have occurred within other SCWO systems have been employed to provide a more comprehensive understanding of potential failure modes.

The design and construction of the corrosion test facility at MIT is described in detail elsewhere (1). While the majority of the facility is constructed of Inconel 625, Hastelloy C-276 and stainless steel type 316 have been employed to a limited degree. The high nickel alloys are considered important for severe service applications (2); nevertheless, for conditions associated with SCWO, selective dissolution of Cr and Mo from Inconel-625 and severe selective dissolution of Cr, Mo and W from C-276

0097-6156/95/0608-0327\$12.00/0
© 1995 American Chemical Society

are reported (3). Solution analysis for Cr and Ni of the effluent from an Inconel-625 reactor carried out at Sandia National Laboratories suggested that non-chlorinated feeds produced little evidence of corrosion while chlorinated feeds resulted in relatively high amounts of metal in the effluent (4). When exposed at 580°C, Inconel 625 exhibits a general corrosion rate of about 80 mpy, SCC, and pitting for a feed stock of methylene chloride and isopropyl alcohol (neutralized with NaOH). For the same feed, but at the lower temperature of 380°C, Hastelloy C-276 exhibits similar localized phenomena; however, the rate of corrosion increases to approximately 480 mpy (5). As a result of the likelihood of significant corrosion damage to the system during experiments, the exposure vessel at MIT was designed with a thick wall to permit future machining. Additionally, to reduce the potential for severe corrosion within the preheater section, the water and corrosive delivery systems were separated until after the preheater. Thus, only that portion of the system after the preheater will be subjected to conditions which are both hot and corrosive.

Preliminary exposure studies were carried out to provide a base-line assessment of the materials of construction of the corrosion test facility. Short term exposure studies (96 or 24 hours) have been conducted in deionized water at 300, 400 and 500°C. The results are presented in detail (6) and in summary (1) elsewhere. All alloys were found to exhibit a weight gain, which, apparently, resulted from the formation of a relatively thick film. At the lowest temperature tested (300°C), both of the high-nickel alloys produced films and discrete raised regions, assumed to be reaction product caps on pits. There was some suggestion of a minor amount of intergranular corrosion for the stainless steel. At the highest temperature tested (500°C), there was an indication of crevice corrosion at the periphery of the washer for 316 stainless steel, and I-625 exhibited pitting. Even after only 24 hours at 400°C, pitting was observed for the I-625; however, neither the stainless steel nor the C-276 exhibit localized attack during this test.

The effect of exposure time in deionized water at 500°C has also been reported (7). Inconel-625 and Hastelloy C-276 exhibit a similar trend over the duration of the experiment (10 days), which may suggest the formation of a protective oxide. Conversely, the stainless steel initially revealed less weight gain (4 days); however, after 10 days exposure, this alloy exhibited a significantly larger gain in mass than either of the nickel alloys. This suggests the formation of a comparatively thick film on the stainless steel (at the longer exposure time), possibly indicative of non-protective (breakaway) oxidation. Additionally, after 4 days there was some indication of selective oxidation or deposition of Mo for the Inconel-625 sample. After 10 days, both the Inconel-625 and the Hastelloy C-276 coupons revealed localized phenomena. The relatively thick film development for the stainless steel alloy at the longer exposure time obscured the metallic surface and although discrete regions were seen on the coupons, these were not specifically correlated to any form of localized attack.

Results and Discussion.

Electrochemical Test Facility Design. While details of the original design of the corrosion test facility have been presented previously (1), the modified version is represented schematically by Figure 1. This figure shows the electrochemical equipment (1), which comprises a Schlumberger 1286 Electrochemical Interface (potentiostat) connected to a Schlumberger 1260 Impedance/Gain-Phase Analyzer. Electrochemical Impedance Spectroscopy (EIS) as well as d.c. techniques will be accomplished by employing software produced by Scribner Associates Inc.

The general electrochemical cell configuration (Figure 2(a)) has been presented elsewhere (1,7). One potential problem in conducting experiments at these temperatures and pressures involves the working electrode (WE) design. Details of the working electrode assembly which has been designed for tests at both sub- and

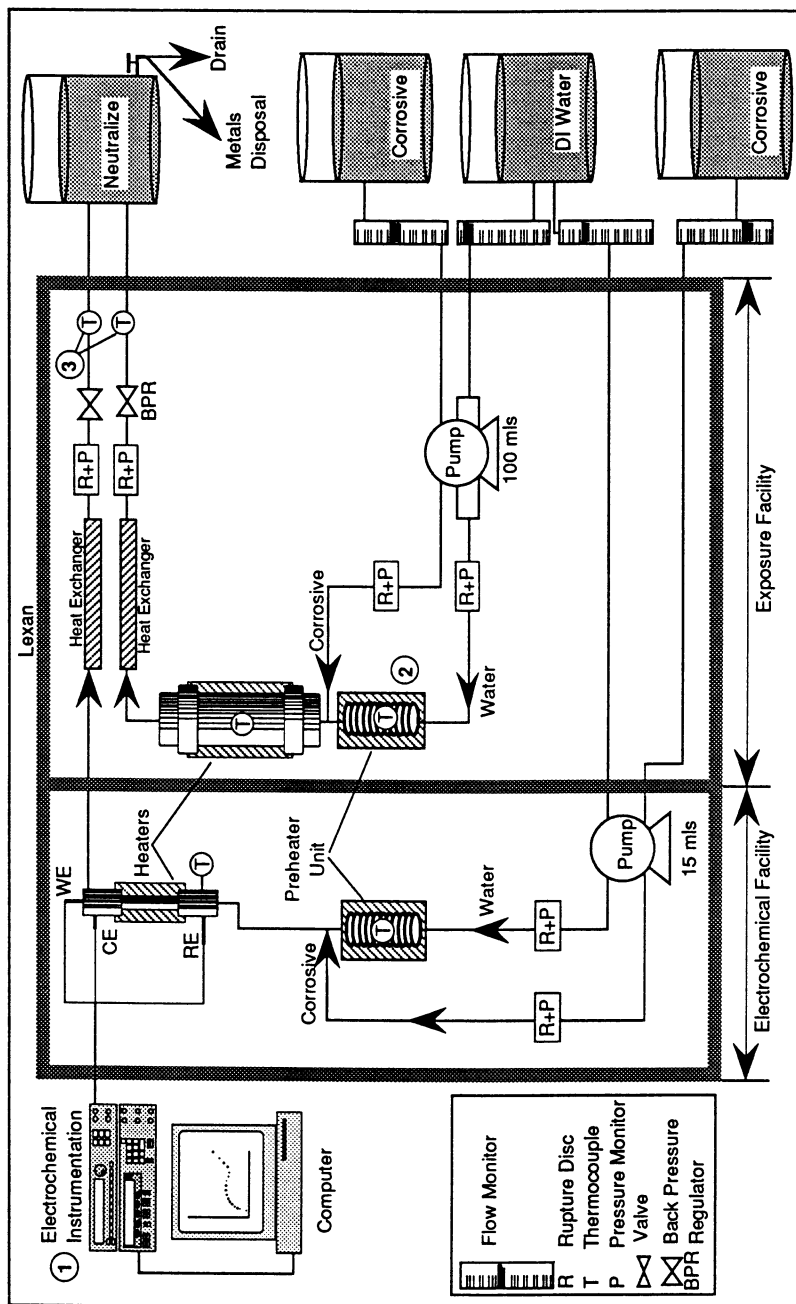


Figure 1. Schematic representation of the modified version of the corrosion test facility (Adapted from ref. 1.).

August 10, 2012 | http://pubs.acs.org
 Publication Date: May 5, 1995 | doi: 10.1021/bk-1995-0608.ch022

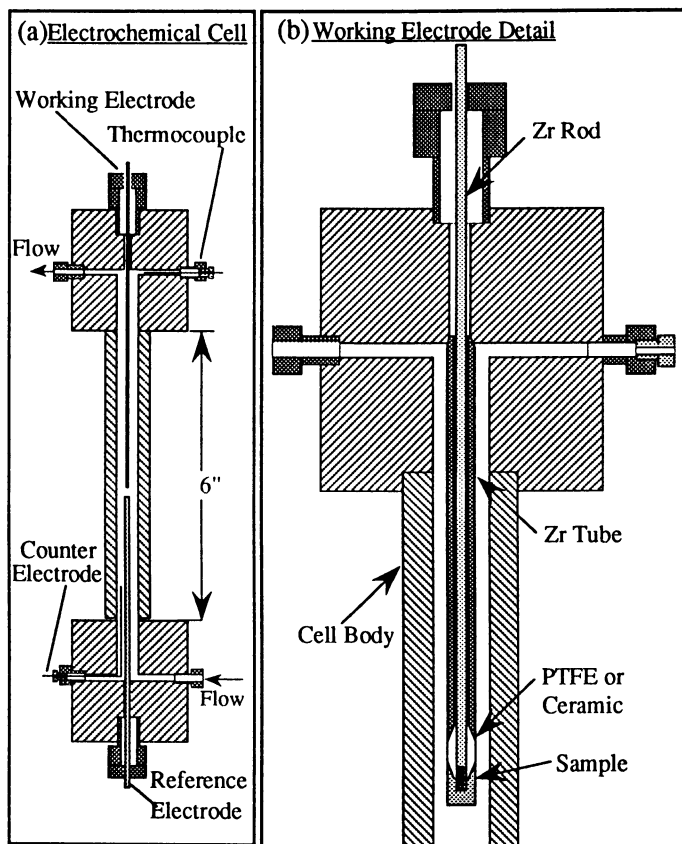


Figure 2. The general cell configuration, Figure 2 (a), (Adapted from ref. 1.) and details of the working electrode assembly, Figure 2 (b), which will be used for experiments at both sub and supercritical temperatures.

supercritical conditions are presented in Figure 2 (b) for the first time. As the cell is constructed from Inconel-625, it is necessary to electrically isolate the working electrode from the cell. This has been accomplished by the use of a thermally oxidized zirconium alloy. Added isolation is provided by using both Zr rod and tube. The connection between the sample and the Zr tube employs a PTFE seal at low operating temperatures; however, a ceramic seal is needed for work at supercritical temperatures.

Exposure Test Facility Design. After conducting a number of exposure tests, several design faults became obvious, and these have necessitated some modification to the facility (Figure 1). The preheater (2) was located too close to a portion of the Lexan shield, which melted. This region of Lexan was replaced and the preheater was insulated and relocated at a greater distance from the shield. The influent and effluent capacity has been increased and a thermocouple (3) has been added to the effluent lines. The latter will prevent a further escape of steam as a direct result of the lack of cooling water, which occurred during one experiment. If a temperature excursion occurs in the effluent line, the computer will now be able to shut the system down.

Preliminary Failure Analysis of Hastelloy C-276 Preheater Tubes. After almost ten years of essentially corrosion free service during experiments employing non-chlorinated organics, an axial through-wall rupture occurred in a Hastelloy C-276 preheater tube of a tubular plug-flow reactor (PFR) system schematically represented in Figure 3. This failure occurred approximately 104 hours after initiating tests with methylene chloride (CH_2Cl_2) (9). The rupture occurred near the top of the second sandbath, and although no thermocouple was located in this region, evidence indicates that the temperature was in the high subcritical range. The tube in the region of both the inlet (ambient temperature) and outlet (supercritical temperature) suffered near negligible corrosion (10). The penetration rate (based on 104 hours) as a function of position is presented in Figure 4. Penetration rates in this figure refer to the maximum cross section of wall which has been degraded both uniformly and at grain boundaries. As revealed in this figure, although the penetration rate is near negligible at the extremities of the tube, it is significant in the region of the through-wall failure. A second Hastelloy C-276 preheater was subsequently installed; however, this failed (within 20 cm of the location of the first failure) approximately 45 hours after initiating experiments with methylene chloride. For a wall thickness of 0.01 inches, the first and second failures represent penetration rates at the failure site of the order 850 - 2000 mils per year (mpy) (11). For comparison, approximately 20 mpy is considered to be acceptable from an engineering standpoint.

Due to the appearance of the rupture site, SCC must be considered as a potential failure mode (10). For nickel-base alloys, SCC is promoted by the following: elevated temperature ($T > 205^\circ\text{C}$), high Cl^- (% range), acidity ($\text{pH} < 4$), oxidizing conditions, H_2S , high stress and/or high strength materials (2). Virtually all of these factors were present during these experiments. A SEM micrograph of the cross-section of the failure site is presented in Figure 5. The sample was etched with a mixture of hydrochloric, acetic and nitric acids in the ratio 3:2:1 plus 2 drops of glycerol per 30 ml acid. The eventual through-wall failure is obviously intergranular in nature. Additionally, there is an indication in other regions in this micrograph that corrosion is enhanced at grain boundaries. Solution analysis for Cr and Ni from a subsequent failure within this system during tests employing methylene chloride revealed that the effluent was significantly enriched in nickel ($\text{Ni}/\text{Ni}+\text{Cr} = 97.6 - 98.6\%$) with respect to a nominal value ($\text{Ni}/\text{Ni}+\text{Cr} = 78.6\%$) in the alloy. Therefore, in addition to the possibility of SCC, both intergranular corrosion and selective dissolution or oxidation must be considered as contributory factors in the failure.

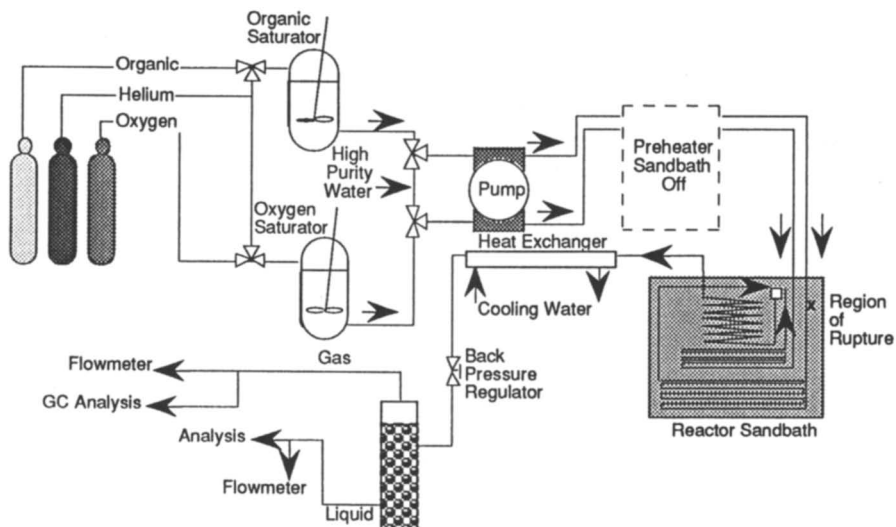


Figure 3. Schematic representation of the tubular plug-flow reactor (PFR) system employed at MIT to study kinetics in SCWO (Adapted from ref. 8).

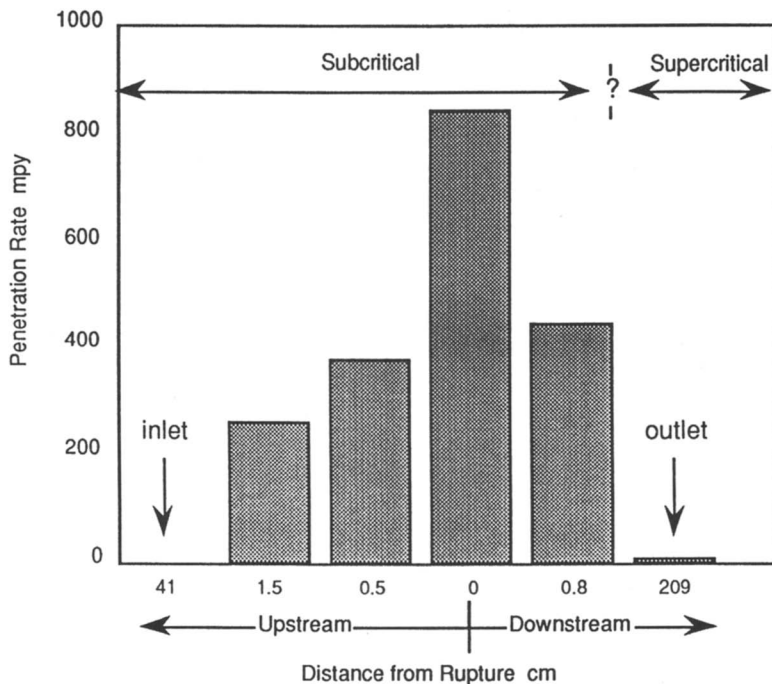


Figure 4. The penetration rate as a function of position of the a Hastelloy C-276 PFR preheater tube, which failed during experiments employing methylene chloride.



Figure 5. Cross-section of the a Hastelloy C-276 PFR preheater tube, which failed during experiments employing methylene chloride.

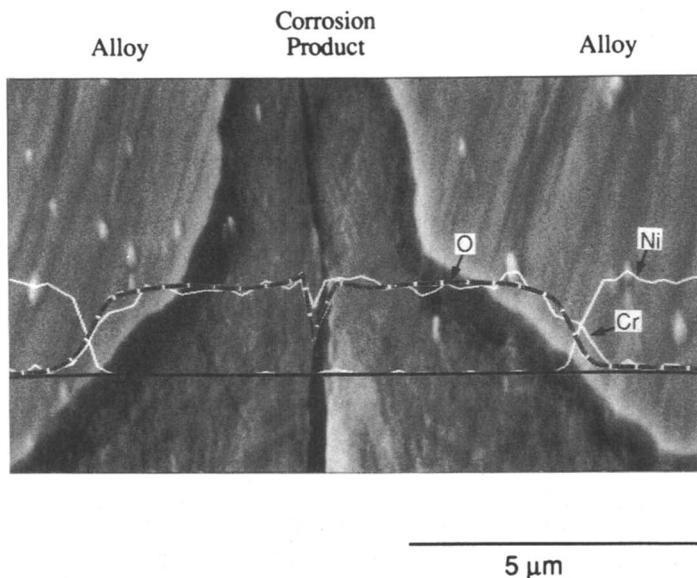


Figure 6. Auger line scan of the corrosion product from a Hastelloy C-276 PFR preheater tube, which failed during experiments employing methylene chloride. The corrosion product is apparently primarily a chromium oxide.

An Auger line scan is presented in Figure 6. This shows the relative amounts of Ni, Cr and oxygen in the metal and in the corrosion product. The dark solid horizontal line across the center of the micrograph shows the position of the scan. Both Ni and Cr levels are represented by white lines, which have been labelled, and the level of oxygen is depicted by a dashed line. In the alloy, as revealed by this scan, the oxygen intensity is negligible and the amount of nickel exceeds the chromium level. However, the relative intensity of these elements changes as the interface with the bulk corrosion product is reached. In the corrosion product, the chromium level is greater than that of nickel, and the oxygen values echo those of chromium. Thus, apparently, the bulk corrosion product is primarily a chromium oxide.

Although the Auger line scan indicates that the corrosion product is primarily a chromium oxide, the appearance of bands (Figures 7 (a) and 8 (a)) within this oxide suggests a more complex structure. The relative intensity of oxygen and the remaining major alloying constituents of Hastelloy C-276 (Ni, Mo, W, Fe) are presented as elemental maps in Figures 7 (b) and 8 (b). Each map corresponds to the SEM micrograph presented in the same figure, and the white dots reveal both the location and intensity of the element of interest. Chromium intensity is so high as to reveal essentially a solid white region, thus, it has been omitted from these figures. In Figure 7, the banded structure can only be seen in the oxygen element map. In Figure 8, at higher magnification, again the oxygen analysis reveals the only indication of varying intensities corresponding to a banded structure. At face value, this suggests a structure which is composed of a number of oxides of chromium. However, sample preparation requires mechanical polishing, which can result in smearing and, thus, obscure subtle differences in elemental composition of the corrosion product. During high temperature oxidation of similar alloys (12), both Cr and Ni oxides form and, therefore, it is anticipated that future work will indicate that the bands reflect oxides of various elements.

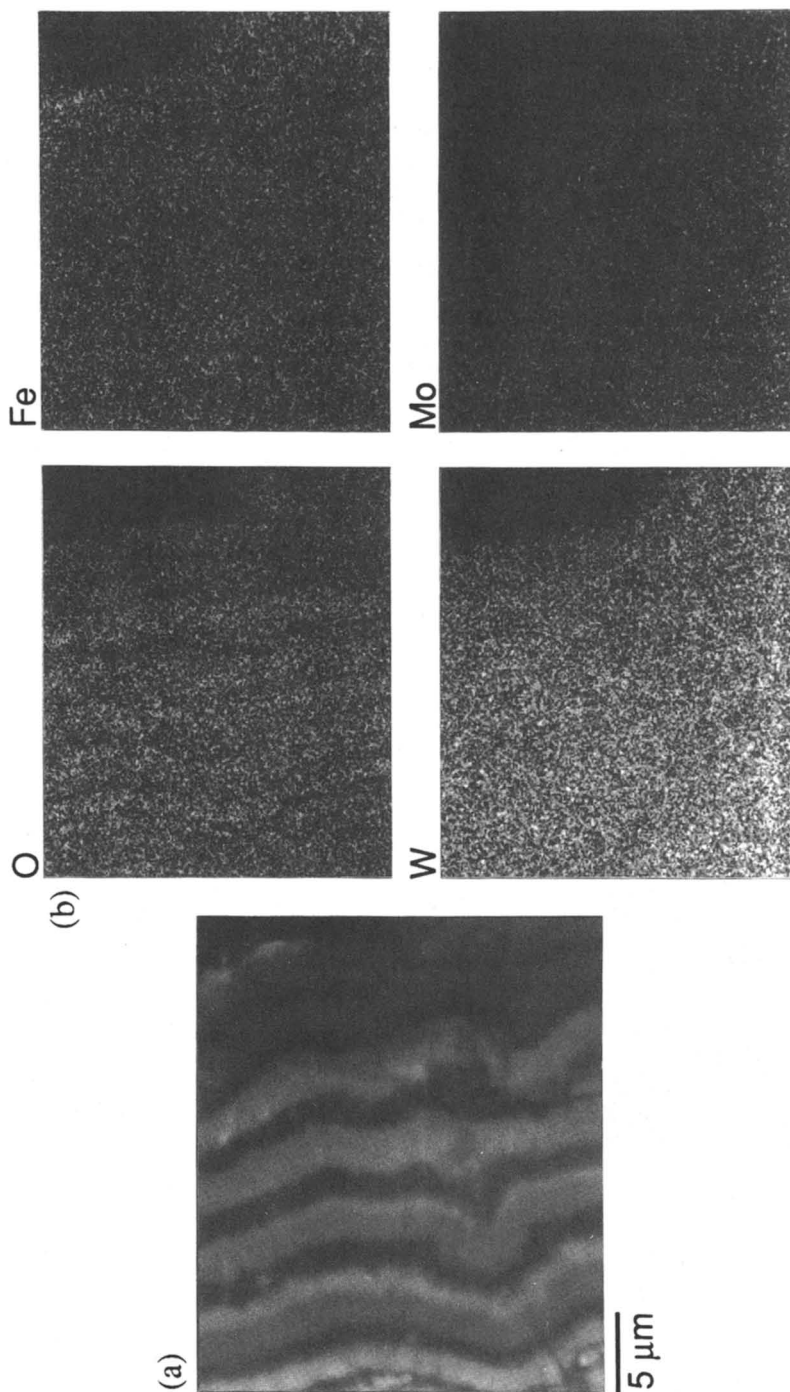


Figure 7. (a) A SEM micrograph and (b) elemental maps (O, Fe, W, Mo) of the corrosion product from a Hastelloy C-276 PFR preheater tube, which failed during experiments employing methylene chloride.

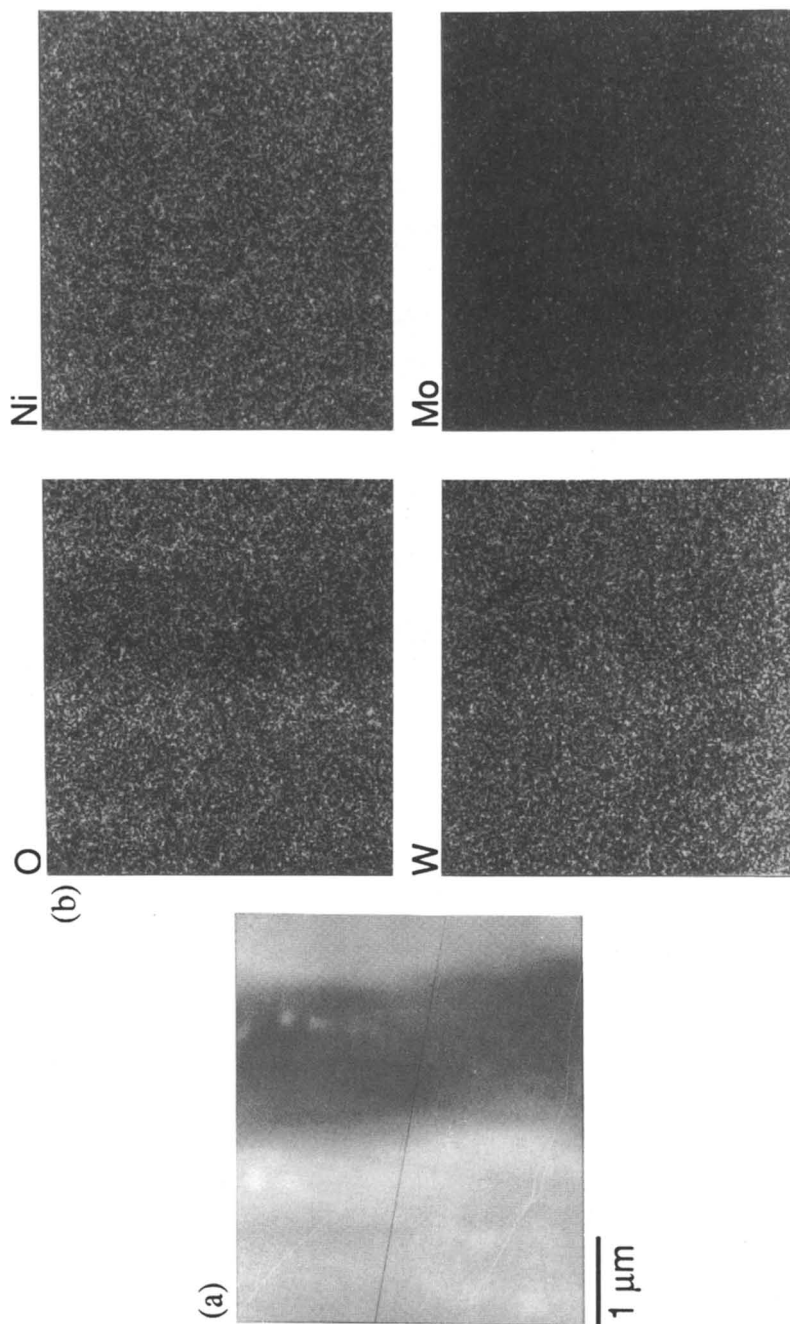


Figure 8. (a) A higher magnification SEM micrograph and (b) elemental maps of the corrosion product (O, Ni, W, Mo) from a Hastelloy C-276 PFR preheater tube, which failed during experiments employing methylene chloride.

Conclusions.

Penetration rates for Hastelloy C-276 preheater tubes exposed to methylene chloride are higher in the subcritical region than in the supercritical region. The corrosion product is primarily chromium oxide; however, there are also bands of different oxygen intensity within this oxide. Although SCC must be considered as a potential mode of failure for these tubes, there is enhanced corrosion at grain boundaries and some indication of selective dissolution. The extremely high penetration rates associated with these conditions confirm that corrosion will be a pivotal issue in the eventual commercialization of SCWO as a viable technique for the destruction of chlorinated organic waste.

Literature Cited.

1. Mitton, D.B.; Orzalli, J.C.; and Latanision, R.M., *Proc. 3rd Int. Symp. on Supercritical Fluids*; I.N.P.L.A.R: Strasbourg, France, 1994, Vol. 3, pp 43–48.
2. Asphahani, A.; *Metals Handbook 9th Edition*; ASM International: Metals Park, OH, 1987, Vol. 13., pp 641–655.
3. Bramlette, T.T.; Mills, B.E.; Hencken, K.R.; Brynildson, M.E.; Johnston, S.C.; Hruby, J.M.; Feemster, H.C.; Odegard, B.C.; and Modell, M., "Destruction of DOE/DP Surrogate Wastes with Supercritical Water Oxidation Technology"; Sandia National Laboratories, Livermore, CA, Sand 90-8229 1990.
4. Rice, S.F.; Steeper, R.R.; and LaJeunesse, C.A., "Destruction of Representative Navy Wastes Using Supercritical Water Oxidation"; Sandia National Laboratories, Livermore, CA, SAND94-8203 1993.
5. Latanision, R. M. and Shaw, R.W., Co-Chairs, "Corrosion in Supercritical Water Oxidation System - Workshop Summary"; Massachusetts Institute of Technology Energy Laboratory, MIT-EL 93-006 1993.
6. Orzalli, J.C., Master's Thesis, Massachusetts Institute of Technology 1994.
7. Mitton, D.B.; Orzalli, J.C.; and Latanision, R.M., *Proc. 12th ICPWS*, Orlando, Florida, 1994, in press.
8. Holgate, H.R.; and Tester, J.W., *Combustion Sci. and Tech.* **1993**, Vol. 88 pp. 369.
9. Mitton, D.B.; Latanision, R.M.; Orzalli, J.C.; Marrone, P.A.; Phenix, B.D.; Meyer, J.C.; and Tester, J.W., presented at the "University Research Initiative Meeting"; University of Delaware Newark, DE 1993, unpublished data.
10. Latanision, R.M., Willis Rodney Whitney Lecture presented at CORROSION 94, Baltimore MD 1994, in press.
11. Mitton, D.B.; Latanision, R.M.; Orzalli, J.C.; Marrone, P.A.; Phenix, B.D.; Meyer, J.C.; Lachance, R.; and Tester J.W., presented at the "University Research Initiative Meeting"; University of Texas at Austin, Austin, Texas 1994, unpublished data.
12. Shreir, L.L.; *Corrosion 2nd Ed*; Newnes-Butterworths: London, U.K., 1976, Vol. 1., pp 7:79–7:114.

RECEIVED May 24, 1995

Chapter 23

The Use of Rate Enhancers in Supercritical Water Oxidation

A. L. Bourhis¹, K. C. Swallow², G. T. Hong¹, and W. R. Killilea¹

¹MODAR, Inc., 14 Tech Circle, Natick, MA 01760

²Department of Chemistry, Merrimack College, 315 Turnpike Street,
North Andover, MA 01845

The initiation of supercritical water oxidation was dramatically enhanced when small amounts of strong oxidizing agents, such as H₂O₂ and HNO₃, were added to a simulated waste stream. Tests were performed in a 6.2 meter pipe reactor where oxidation was initiated by mixing the cold aqueous/organic feed with a hot supercritical water/oxidant stream. Without rate enhancers, an inlet mix temperature of 362 C resulted in the incomplete oxidation of isopropanol. When the feed contained 0.75, 1.5 and 3.0 wt% H₂O₂ oxidation was essentially completed at 5.1, 4.0 and 2.8 meters, respectively. When initiated at 380 C, without rate enhancers, isopropanol reacted completely in 5.6 meters. This length was reduced to ~ 2 meters when the feed contained 2.0 wt % HNO₃.

Supercritical water oxidation (SCWO) is an emerging waste treatment technology that takes advantage of the unique properties of water above its critical point (374 C and 221 bar). Organic destruction efficiencies in excess of 99.99% are routinely reported with efficiencies exceeding 99.9999% not uncommon (1). Successful commercialization will require that SCWO be a cost effective method of waste disposal. Small amounts of strong oxidizing agents can help to minimize capital and operating costs by initiating reaction at lower temperatures and/or reducing the required residence time.

Background

A large body of theoretical and experimental work exists (2,3) describing plug flow reactor (PFR) analysis, design and scale-up. Pipe reactor benefits include their well defined residence time distributions, turbulent mixing of reactants, ease of obtaining and applying kinetic data, efficient use of reactor volume and mechanical simplicity.

0097-6156/95/0608-0338\$12.00/0
© 1995 American Chemical Society

Pipe reactors do, however, have drawbacks(4). Their high surface-to-volume ratios lead to high levels of corrosion for waste streams containing or producing inorganic acids (e.g. HCl, H₂SO₄ and H₃PO₄). These acids cannot usually be neutralized since the salts generated are generally "sticky" (e.g. NaCl, Na₂SO₄, Na₃PO₄ and Na₂CO₃) and tend to plug the reactor. Due to the absence of back mixing in a PFR, the feed and oxidant must be heated to, or above, the critical point of water to initiate oxidation. Below the critical temperature, separate gas and liquid phases are generally present and reaction proceeds by the wet oxidation process (5). Wet oxidation typically requires tens of minutes or hours to achieve the same organic destruction that SCWO systems achieve in seconds.

There are two general methods of raising the reactant temperatures; indirect and direct heating. Indirect feed preheating, the most common method, involves transferring energy across a solid boundary to the waste feed stream. Regenerative heat exchange (e.g. feed/effluent heat exchangers, bayonet reactors, separate heat transfer fluid loops) and external heating (e.g. gas fired, resistive or radiant heating) are examples of indirect heating. Direct feed heating occurs when a cold (or partially preheated to < 250 C) aqueous waste stream is mixed with a hot (500 C to 650 C) SCW/oxidant stream to achieve an unreacted "mix" temperature at or above 374 C. This SCW is either recycled reactor effluent or a separate, indirectly heated water stream.

Regenerative heat exchange is especially amenable to treating low heating value feed streams, but it does have a number of drawbacks. Because the feed/effluent heat exchange surfaces experience the most corrosive environment in a SCWO system (6), the heat exchangers can cost several times more than the reactor itself. The feed heat exchanger is also susceptible to organic char and oxide/salt fouling.

By keeping the waste stream cold until it is injected into the reactor, direct feed heating avoids the highly corrosive 250 C to 400 C temperature range. Organic polymerization and charring are minimized. There are no feed heat exchange surfaces to foul. With the effluent no longer needed for regenerative heat exchange, corrosion can be further mitigated by quenching the effluent to below 300 C. In the case of a highly acidic effluent, the pH can be raised by quenching with a caustic solution. Salts generated by neutralization remain in solution.

Initiating oxidation by recycling the reactor effluent does, however, require either a high temperature canned pump or an eductor. Likewise, an indirectly heated SCW stream requires an additional water pump and heater. This clean SCW stream, however, does not have the processing problems associated with preheating waste feeds.

Figure 1 shows how the mix temperature of a simple cold water-hot water system varies as a function of the mass flow ratio. The cold water is assumed to be at 25 C and the hot water at 600 C. As the ratio of SCW to cold water is raised from zero to one, the mix temperature rapidly rises from 25 C to roughly the critical point. Because of the near-critical heat capacity spike, there is little change in temperature as the ratio is increased from 1 to ~ 2.5. Beyond 2.5 the temperature again increases with increasing SCW feed rates, asymptotically approaching 600 C.

Because higher heating value streams (~3500 J/g) can be treated, the reactor volume of a direct-heated system is the same as an equal capacity indirect-heated system, initiated at the same temperature. High initiation temperatures, needed for refractory compounds, normally would require large SCW flows. Beyond a certain point, the cost of providing this stream may outweigh the corrosion and processability benefits. The direct-heating method is most economical when initiation occurs near the critical point.

Regardless of the initiation method, liquid oxygen and compressed air are the most commonly used oxidants, both in experimental and in proposed commercial units. No dramatic differences have been reported for reaction rates between the two. Oxidation is generally believed to occur via free radical mechanisms (7-9). Most theoretical and experimental SCWO studies conclude that the global reaction rates tend to be first order in organic concentration and zero, or low fractional (< 1), order in oxygen concentration.

Oxidants other than dioxygen (from liquid oxygen or compressed air) have occasionally been used in conventional wet oxidation and SCWO studies. Welch and Siegwarth (10) describe the use of oxidants in a liquid phase, for example aqueous solutions of hydrogen peroxide, ozone, or inorganic oxides, and suggest that the free radical species formed by peroxide decomposition should lead to vigorous oxidation. Lee and Gloyna (11) compared the effectiveness of hydrogen peroxide and dioxygen in oxidizing acetic acid and 2,4 dichlorophenol at temperatures between 400 C and 500 C. For both compounds, the peroxide gave a higher degree of oxidation at comparable reactor conditions. In a subsequent article by Li, Chen and Gloyna (12), however, the claim is made that hydrogen peroxide and dioxygen give comparable reaction rates. Thus, the comparison between these two oxidants requires further study. Rofer et al. (13) have carried out SCWO on propellant materials which inherently contain some or all of the oxygen needed for the oxidation reactions. The perchlorate ion of ammonium perchlorate and the nitro moiety of nitromethane both proved to be effective oxidizers. Dell'Orco et al. (14) have also described the use of sodium nitrate as an oxidizing agent.

The inconsistent hydrogen peroxide results may be due to the method by which the oxidant is introduced to the system. Aqueous solutions of some oxidizing agents, hydrogen peroxide and ozone for example, are known to decompose irreversibly to less reactive dioxygen and water at temperatures well below the critical point of water. In much of the reported kinetic work, these oxidants are preheated to reactor conditions. The resulting oxidation rates may, therefore, be more indicative of those carried out with dioxygen. Nitric acid, in contrast, does not decompose irreversibly at SCWO conditions. Without a material to oxidize, nitric acid is recovered upon cooling and depressurizing the effluents to ambient conditions.

Alternative oxidants are considerably more expensive than either liquid oxygen or compressed air. Hydrogen peroxide and nitric acid are roughly 30 and 6 times more expensive than liquid oxygen, respectively.

Motivation of work

The choice of pipe reactor initiation method depends on the specific feed stream. Relatively clean, low heating value wastes are well suited to initiation by regenerative heat exchange and external heating. High heating value and corrosive waste streams are better suited to the direct injection initiation. Ideally, reaction would be initiated just above the critical temperature and the heat of reaction would quickly drive the temperature up to 500 C to 600 C, minimizing both corrosion and reactor size.

An experimental study is presented where low concentrations of strong oxidizing agents and organics are fed into a pipe reactor cold and rapidly brought to initiation conditions by direct contact with a combined supercritical water and air stream. The strong oxidizers, essentially intact at the reactor inlet, significantly enhance the initial organic destruction rate.

Apparatus

Figure 2 is a schematic of the MODAR bench unit as configured for use with a direct feed heated pipe reactor. Deionized water was pressurized to 234 bar and heated above the critical point. This water was mixed with air, which had also been pressurized and preheated. The combined, 500 C stream was introduced into the pipe reactor via the annulus of a co-annular nozzle. Air flows were chosen to provide stoichiometric excess oxidant; the effluent gas oxygen concentration varied between 2 and 5 volume percent.

Simulated waste feeds, deionized water and ~ 12 wt% organic, were pumped up to 234 bar separately. The feed stream was fed into the pipe reactor cold, via the insulated core of the co-annular nozzle. The 6.2 m insulated pipe reactor has a 0.925 cm I.D.. No external heaters were used. The core feed tube had a 0.635 cm O.D. and a 0.305 cm I.D.. The mix temperature at the pipe reactor inlet was controlled by varying the ratio of core to annular flow rates (typically 1:6 on a mass basis).

The main instrumentation used to assess the system performance was the set of thermocouples, consisting of three distinct groups; in-line, ribbon and bead. There were two in-line thermocouples, one located in the SCW/Air annulus of the nozzle, the other in the reactor exit (6.2 m). There were 6 ribbon thermocouples secured onto the surface of the pipe with graphite cement (Thermon). Finally, there were originally 16 bead thermocouples wired to the surface of the pipe. Of the three sets, the in-line and the ribbon thermocouples were the most accurate and were used to provide corrections for the more numerous bead thermocouples. The extent of reaction, along the length of the pipe reactor, was observed indirectly by measuring the temperature rise due to the exothermic nature of oxidation.

Reaction initiators were introduced by switching the cold feed water from deionized water to deionized water plus initiators. The initiator concentrations were varied between 0 and 3 weight percent of feed water flow. The oxygen available from the initiators never exceeded 5 percent of the stoichiometric requirement.

The effluent stream was first cooled to near ambient temperatures. The resulting two-phase flow was then letdown from 234 bar to 103 bar through a control valve. After separating the vapor and liquid, a back-pressure regulator was used to

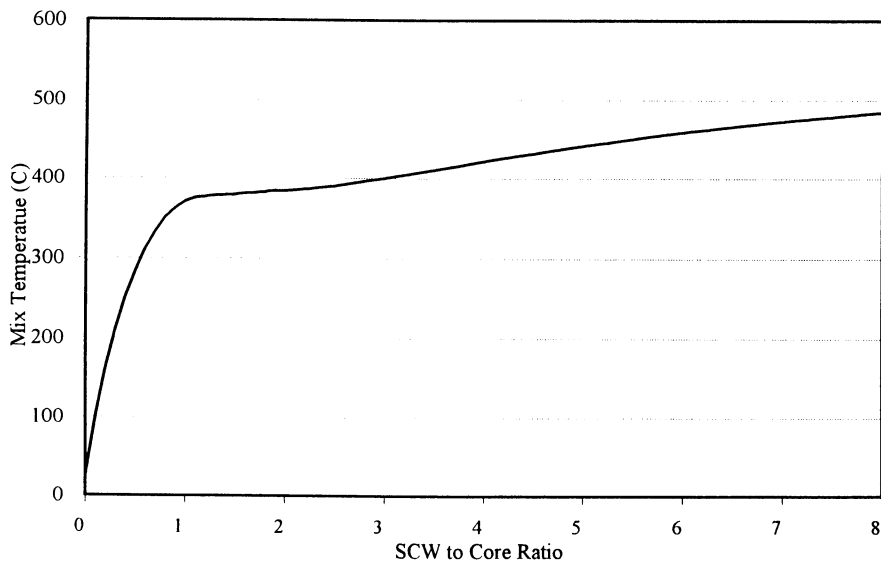


Figure 1. Mix temperature versus SCW to core ratio - SCW at 600°C and core at 25°C.

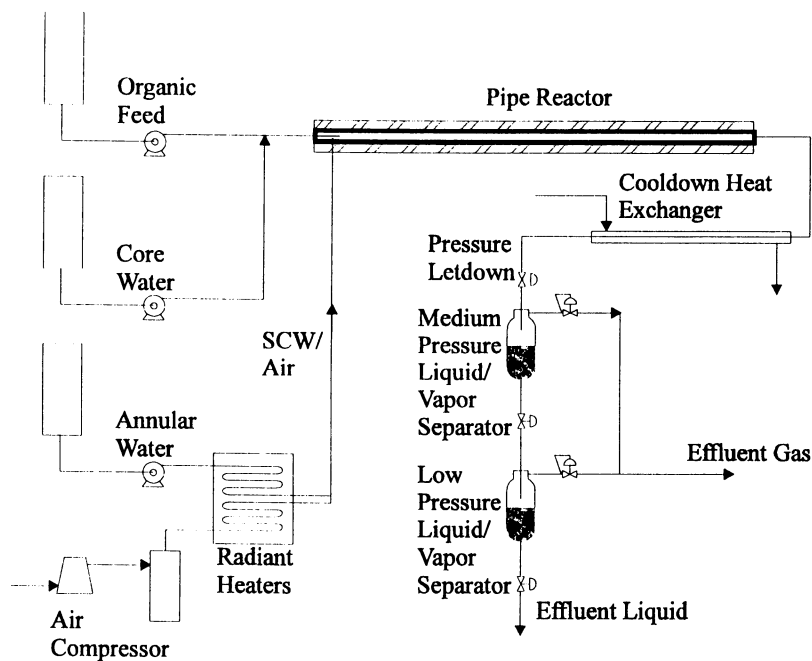


Figure 2. MODAR bench scale pipe reactor - configured for direct injection feed heating.

reduce the gas pressure to ambient. The liquid pressure was reduced to 4 bar by means of another control valve, leading to the evolution of CO₂. A second phase separation was carried out in a low pressure liquid-vapor separator. The gas streams from both separators were mixed before sampling or venting.

The flow rates ranged between 200 and 450 cc/min for SCW, 45 and 110 normal liters per minute (25 °C, 1 bar) for air, 15 and 55 cc/min for cold water and 3 and 15 cc/min for organics. The resulting residence times ranged between 3 and 6 seconds. Reynolds numbers near 25,000 insured fully turbulent flow.

Procedure

No direct measurements of organic concentration were made either in the reactor or system effluent. The extent of reaction was monitored solely by the axial temperature rise resulting from the exothermic heat of combustion. The assumption that the temperature profile accurately indicated the extent of reaction was supported by carbon monoxide (CO) levels in the effluent gas. Historically effluent gas CO levels below 10 ppm (volume basis) in the bench system correspond to 99.99% overall organic destruction efficiencies. During these experiments, every run that exhibited a temperature maximum over 500 °C had effluent CO levels below 10 ppm.

The tests were started by first feeding only SCW/Air to the reactor. Cold water was then fed through the core of the nozzle at flow rates equal to the combined water/fuel flows be used for the oxidation portion of the run. The resulting near nozzle temperature provided an estimate of the effective mix temperature. When the fuel flow was started, the cold water flow was reduced by an equal amount. The resulting temperature rise indicated the reactivity of a given organic compound for the apparent mix temperature. In the majority of the runs, two or more organic compounds were compared head-to-head (constant SCW/Air flow, cold feed flows and mix temperatures) by simply switching from one feed tank to another.

Results

Figure 3 shows the sensitivity of isopropanol oxidation to the apparent mix temperature. At mix temperatures above 400 °C, the isopropanol reacts completely in less than 1 m (1 sec). As the mix temperature is lowered towards the critical point, the temperature profiles take longer to develop until, finally, there is little or no oxidation in the reactor. The three profiles measured at the lowest mix temperature indicate the limits of resolving the mix temperature. Run 507d resulted in incomplete oxidation.

In Figure 4 ethanol oxidation is compared to isopropanol. The isopropanol base case is the same poorly initiating profile described in the previous figure (Run 507d). Two ethanol profiles are presented; one equi-molar and the other equi-enthalpic. In the equi-molar case the initial organic molar concentration is held constant, while in the equi-enthalpic case the overall heating value (J/g feed) is held constant. In both cases ethanol initiates more rapidly and reacts more completely than isopropanol. The dramatically faster reaction in the equi-enthalpic case is due to a combination of higher initial organic concentration and the "auto catalytic" effect of

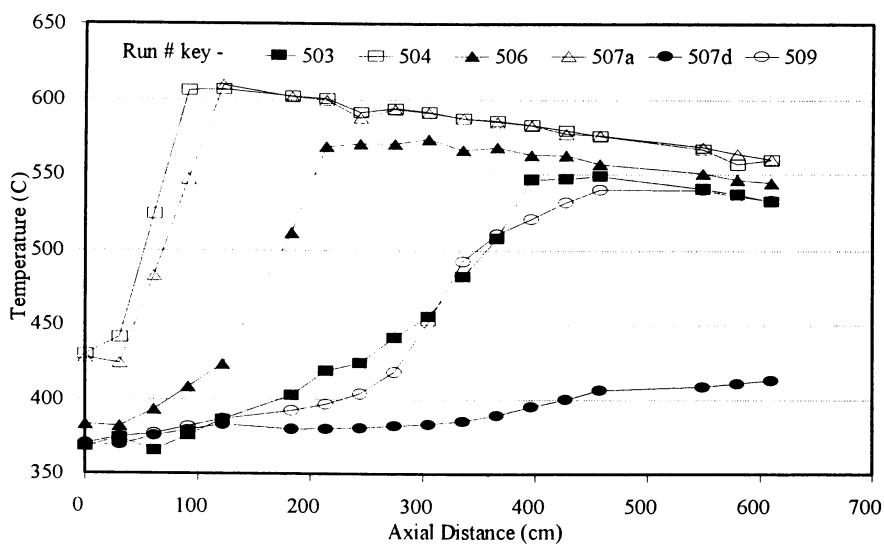


Figure 3. Sensitivity of isopropanol oxidation to mix temperature.

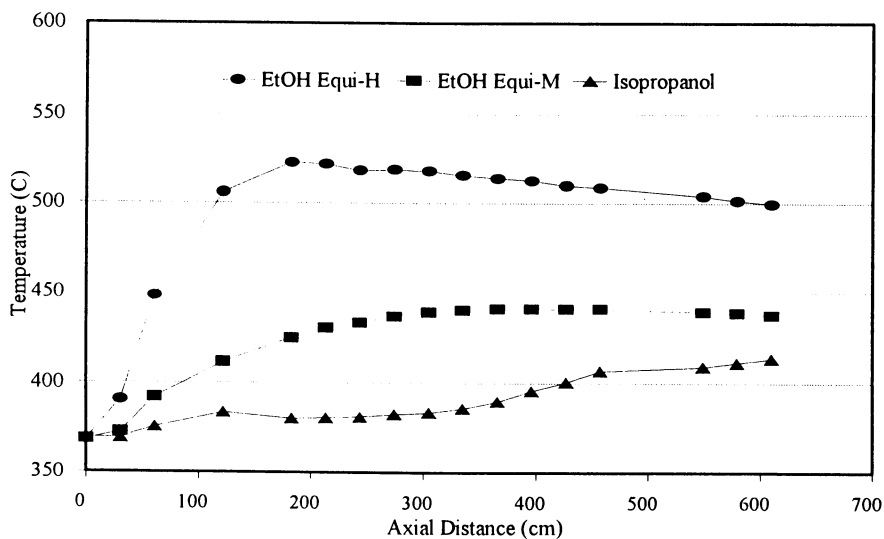


Figure 4. Comparison of ethanol oxidation to isopropanol oxidation.

the heat release as well as faster base kinetics. Even though the equi-molar case does not seem as dramatic an improvement as the equi-enthalpic case, it did result in essentially complete oxidation.

The reactivity of some organic compounds, relative to isopropanol, can be summarized as follows: both ethanol and methyl-ethyl-ketone are much more reactive, acetone is slightly less reactive, methanol is less reactive, acetic acid and toluene are much less reactive.

Even though the mix temperatures of all runs were at or above the critical temperature of water, finite mixing rates result in two phase flow at the reactor inlet. Liquid fuel and gaseous oxidant have to overcome mass transfer resistance in order to react. Liquid oxidants, in intimate contact with the organics, do not experience these resistances and initiate reaction closer to the nozzle.

The dramatic effect of H_2O_2 on isopropanol oxidation is shown in Figure 5. The base isopropanol case does not react completely. When the core water flow is switched to a 0.75 wt% H_2O_2 solution, the reaction reaches completion in roughly 5 m. As the concentration of H_2O_2 is increased to 3.0 wt%, the reaction rate increases. The improvement with increasing H_2O_2 concentration seems to display diminishing returns, suggesting that H_2O_2 is important only at the onset of the reaction. Once the reacting medium becomes homogeneous, oxidation by O_2 (which makes up 95% of the oxidant) dominates.

Figure 6 shows the effect of a 2 wt% HNO_3 solution on isopropanol oxidation. Although the different mix temperatures makes a direct comparison with H_2O_2 impossible, it is clear that HNO_3 also greatly increases the complete isopropanol oxidation rate. In this case, the residence time required to initiate isopropanol oxidation was cut by a factor of three. On an equivalent O_2 basis, 2 wt% HNO_3 corresponds to 2.7 wt% H_2O_2 .

Summary

Axial temperature profiles provide valuable insights into the design and optimization of SCWO pipe reactors. The relative reactivity of various compounds is easily determined by comparing temperature profiles for a fixed mix temperature and mass throughput. The sensitivity of reaction initiation to mix temperature, for a given compound, is revealed by varying the core to annular ratio while keeping the overall and organic throughputs constant.

The addition of small amounts of either hydrogen peroxide or nitric acid to the cold feed significantly enhanced the initial oxidation rates. These rate enhancers have the same effect as either raising the mix temperature or switching to a more reactive organic. The ability of the direct heating method to introduce these strong oxidizers into the reactor intact makes this initiation enhancement possible. The small quantities needed to effect this enhancement should allow this type of initiation to be economically viable for commercial SCWO pipe reactor applications.

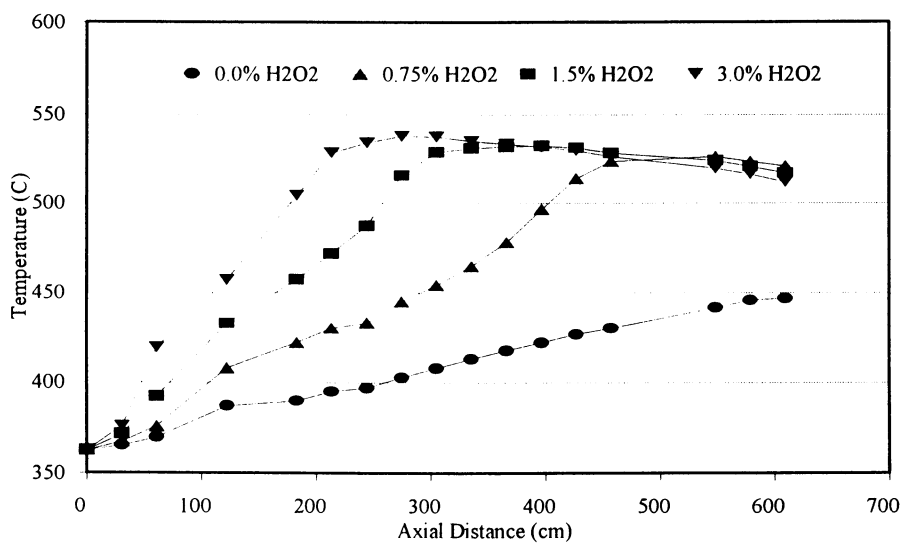


Figure 5. Enhancement of isopropanol oxidation by H₂O₂.

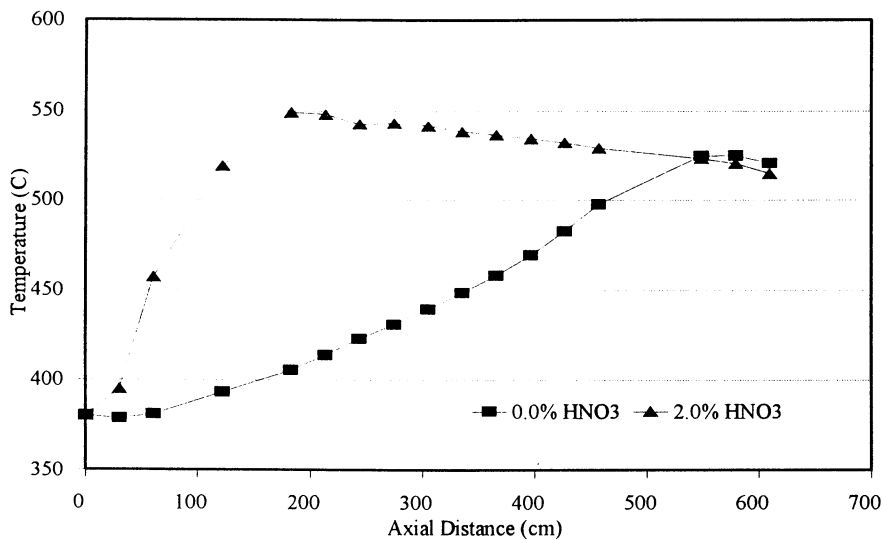


Figure 6. Enhancement of isopropanol oxidation by HNO₃.

Literature cited

- (1) Tester, J. W., et. al., "Supercritical Water Oxidation: A Review of Process Development and Fundamental Research", ACS Symposium Series 518, 1993.
- (2) Levenspiel, O., Chemical Reaction Engineering, Second Ed., John Wiley and Sons, Inc., 1972.
- (3) Smith, J. M., Chemical Engineering Kinetics, Third Edition, McGraw-Hill Book Co., 1981.
- (4) Zimmermann, F. J., "Waste Disposal", United States Patent No. 2,665,249, Jan. 5, 1954.
- (5) Barnes, C. M., "Evaluation of Tubular Reactor Designs for Supercritical Water Oxidation of U. S. Department of Energy Mixed Waste", Contract No. DE-AC07-94ID13223, Idaho National Engineering Laboratory, LITCO, Idaho Falls, ID, 1994.
- (6) Beller, J., K. Garcia and C. Shapiro, "Treatment of a Simulated Mixed Waste with Supercritical Water Oxidation", Contract No. DE-AC07-76ID01570, Idaho National Engineering Laboratory, LITCO, Idaho Falls, ID, 1993.
- (7) Helling, R. K., Oxidation Kinetics of Simple Compounds in Supercritical Water: Carbon Monoxide, Ammonia and Ethanol, Doctoral Thesis, Massachusetts Institute of Technology, Cambridge, MA, 1986.
- (8) Webley, P. A., Fundamental Oxidation Kinetics of Simple Compounds in Supercritical Water, Doctoral Thesis, Massachusetts Institute of Technology, Cambridge, MA, 1989.
- (9) Holgate, H. R., Oxidation Chemistry and Kinetics in Supercritical Water: Hydrogen, Carbon Monoxide and Glucose, Doctoral Thesis, Massachusetts Institute of Technology, Cambridge, MA., 1993.
- (10) Welch, J. F. and J. D. Siegwath, "Method for the Processing of Organic Compounds", United States Patent No. 4,861,497, Aug. 29, 1989.
- (11) Lee, D-S. and E. F. Gloyna, "Efficiency of H₂O₂ and O₂ in Supercritical Water Oxidation of 2,4-Dichlorophenol and Acetic Acid", The Journal of Supercritical Fluids, 1990, 3, 249-255.
- (12) Li, L., P. Chen and E. F. Gloyna, "Generalized Kinetic Model for Wet Oxidation of Organic Compounds", AIChE Journal, Vol. 37, No. 11, November 1991, pp. 1687- 1697.
- (13) Rofer, C. K., S. J. Buelow, R. B. Dyer and J. D. Wander, "Conversion of Hazardous Materials Using Supercritical Water Oxidation", United States Patent No. 5,133,877, July 28, 1992.
- (14) Dell'Orco, P.D., B.R. Foy, J.M. Robinson and S.J. Buelow, "Hydrothermal Reactions of Nitrate: Treatability of Hanford Tank Waste Constituents", Presented at the Summer National Meeting of the AIChE, Minneapolis, MN, August 1992.

RECEIVED May 19, 1995

Chapter 24

Simulation of a Concentric-Tube Reactor for Supercritical Water Oxidation

Peishi Chen¹, Lixiong Li, and Earnest F. Gloyna

Environmental and Water Resources Engineering, University of Texas,
Austin, TX 78712

To further enhance the development of the supercritical water oxidation (SCWO) process, a concentric-tube reactor model has been developed. Because of the heat generation and transfer processes within the reactor, both reaction kinetics and heat transfer rate factors are incorporated in the model. The simulation model treats the reactor as a number of segments, and each segment is assumed to be isothermal.

The model was validated by pilot-plant tests involving the destruction of acetic acid, phenol, and n-octanol. These tests were conducted in a pilot-scale SCWO facility that is equipped with a 6.1-meter long concentric-tube reactor and capable of treating waste water at a rate of 150 liter per hour. All simulation results, using pseudo-first-order kinetic models, agreed favorably with the pilot-plant data. The simulated reactor temperature profiles agreed well with the measured profiles.

The supercritical water oxidation process (SCWO) is an environmentally attractive method for the safe and economical treatment of toxic organic waste waters and sludges. The SCWO process is capable of destroying undesirable organic compounds, converting the waste into non-noxious materials, accomplishing this task within an essentially enclosed environment. The key unit in the SCWO process is the reactor that generally operates at temperatures and pressures ranging from 400°C to 650°C and 25 MPa to 35 MPa, respectively. The exothermic heat can be sufficient to sustain the reaction. It has also been demonstrated that byproducts such as reusable water, heat, and usable inorganic substances can be produced by the SCWO process.

After more than a decade of research and development, the process is now poised for potential wide-spread application (1), especially with the first commercial unit in operation.

To further enhance the development of the SCWO process for industrial-scale applications, it is necessary to understand the reactor performance and develop reliable

¹Current address: Philip Morris Research and Development, P.O. Box 26583,
Richmond, VA 23261

simulation models. For this purpose, a pilot-scale concentric-tube reactor was designed. In the present study, a concentric-tube reactor model has been developed. Because of the heat generation and transfer processes within the reactor, both reaction kinetics and heat transfer rate factors are incorporated in the model. Since isothermal conditions are usually difficult to obtain for the reactor as a whole and water properties are strong functions of temperature, the simulation model treats the reactor as a number of segments, and each segment is assumed to be isothermal. The residence time in each segment is determined by the properties of water, flow rate and volume of the segment.

The reactor simulation model was validated by a series of pilot-plant tests using acetic acid (a known rate-limiting SCWO reaction intermediate), phenol and n-octanol as representative organic compounds and oxygen as the oxidant.

Pilot-Scale SCWO Facility and Its Operation

Figure 1 shows a schematic of the 150 liter/hour (40 GPH) SCWO pilot plant. The major components in the plant included a concentric-tube reactor, a high-pressure diaphragm pump, two double-pipe heat exchangers, an electric heater, and an air driven oxygen booster.

The configuration of the specially designed concentric-tube reactor is shown in Figure 2. The reactor influent (oxygen was mixed with the feed prior to entering the reactor) flows downwards in the inner tube and returns upwards through the annular section between the inner and outer tubes. This configuration can provide a counter-current flow within the reactor. One of the advantages of the concentrated-tube reactor is that it permits heat exchange between the influent and effluent fluids, resulting in a more uniform temperature profile across the fluid pathway.

The reactor size was determined by the design capacity (150 liter/hour) and the destruction efficiency (99.99%) of selected organic compounds at 450°C. The length to diameter ratio was determined by the fluid velocity required to suspend particulates and to maintain the Reynolds number in the turbulent region. The overall dimensions of the outer tube were 8.89-cm O.D., 5.08-cm I.D., and 6.1-m long. The dimensions of the inner tube were 1.91-cm O.D., 0.17-cm wall thickness, and about 6.1-m long. The reactor was insulated with 5-cm thick Kaowool blanket and 8-cm fiber-glass casing. Thermocouples and sampling ports were installed at the reactor inlet, bottom, and outlet.

Prior to a typical pilot-plant test, an organic feed solution was prepared using deionized water. The feed stock was stirred continuously during each test. To initiate a test, deionized water was pumped through the system at a rate of about 90 liter/hour and a pressure of 24.8 ± 0.7 MPa. After the system pressure stabilized, the electric heater was turned on. The water temperature entering the reactor inlet was raised gradually to the desired level. After the desired operating conditions were established, the inlet to the feed pump was switched from water to the organic feed solution. Then pressurized oxygen was introduced. Oxygen concentration in all tests was greater than 120% stoichiometric oxygen demand. When the system reached a steady state, the samples were collected at the reactor inlet, bottom, and outlet. Organic and total organic carbon concentrations in these samples were measured. The accuracy of the

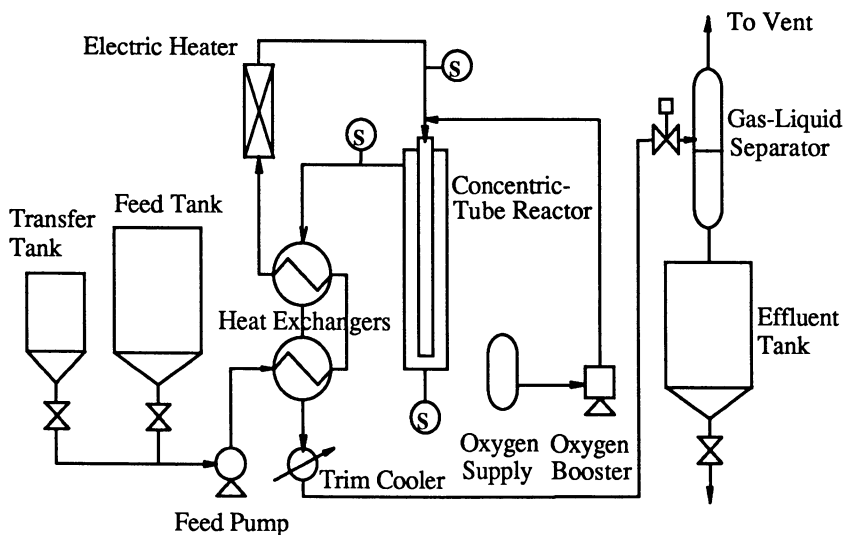


Figure 1. Process diagram of 150 liter/hour SCWO pilot plant

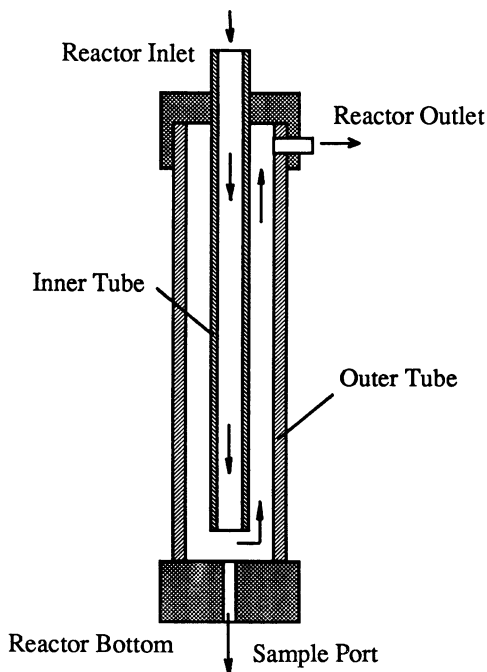


Figure 2. Schematic of the concentric-tube reactor

measurements was 50 mg/l for the acetic acid test samples and 5 mg/l for the phenol/octanol test samples. Process conditions, such as temperature, pressure, and oxygen flow rate were monitored and controlled by a Fisher-Porter DCU interfaced with a LOC-2000A console. Data were periodically downloaded to an IBM PC.

After the test was completed, the electric heater was turned off and the feed pump was switched back to deionized water to flush the system. As the reactor was being flushed, the flow of oxygen continued for an additional 15 minutes. The total washing sequence was completed in about 30 minutes (2).

Concentric-Tube Reactor Model

The concentric-tube reactor model developed to simulate the SCWO process is described as below. The total mass flow rate is G ,

$$G = G_w (1 + x_{in}). \quad (1)$$

where x_{in} is the initial mass fraction of the organic compound and G_w is the flow rate of pure water. When the organic concentration is low,

$$x_{in} = \frac{c_{in}}{\rho_w}$$

The feed solution heated by the electric heater enters the reactor with a temperature of T_{in} and a pressure of P_{in} , respectively. The differential equation that describes a plug flow reaction system with superimposed axial mixing can be written as,

$$u \frac{\partial x}{\partial z} = D_{eff} \frac{\partial^2 x}{\partial z^2} - R(T) \quad (2)$$

where $R(T)$ is the reaction term and u is the average fluid velocity. Under supercritical conditions, the average fluid velocity u can be approximated by the average water velocity. The effective diffusion coefficient D_{eff} is a lumped parameter incorporating the effects of non-flat velocity profile, fluctuation, and molecular diffusion (3). For a turbulent flow or low reaction rate, the diffusion term may be neglected.

The boundary condition at the reactor inlet, $z = 0$, was obtained from flux balances across the inlet plane.

$$u(x_{0+} - x_{in}) = D_{eff} \left. \frac{\partial x}{\partial z} \right|_{0+} \quad \text{at } z = 0 \quad (3)$$

At the reactor outlet, $z = 2L$, the boundary condition is assumed to be open, i.e., the reaction will continue after the fluid mixture leaves the reactor.

Since oxidation of a high organic concentration feed can release a large amount of heat and the concentric-tube reactor configuration permits heat transfer between the

fluids in the core and annular sections, heat transfer must be considered in the model. The heat transfer equation can be written as,

$$\frac{G_w}{A} \frac{\partial H}{\partial z} = k_{eff} \frac{\partial^2 T}{\partial z^2} + \rho_w R(T) \Delta H_R - \frac{\Sigma q}{A \partial z} \quad (4)$$

The axial thermal diffusion term is usually small as compared with the reaction heat and the heat loss, therefore, the first term of the right hand side can be neglected. Generally, for most organics, the reaction heat (ΔH_R) associated with complete oxidation is regarded as a constant of about 435 kJ/mol based on the COD (or TOC) destruction. Therefore, the reaction heat is 870 kJ/mol for acetic acid and 435 kJ/mol COD (or TOC) for the phenol/n-octanol mixture.

Since most of the SCWO reaction rate data reported in the literature yield acceptable correlation with pseudo-first-order kinetic models (4), the reaction rate term in equation 2 can be expressed as follows:

$$R(T) = -\frac{dx}{dt} = kx = k^0 \exp(-E/RT)x \quad (5)$$

For the phenol/n-octanol mixture, the reaction heat needs to be calculated based on the COD (or TOC) destruction and the generalized SCWO reaction model (4) should be used. The point selectivity, defined as the formation rate of acetic acid to that of carbon dioxide (the oxidation end product), characterizes the strength of the feed stream for the SCWO process. Generally, higher point selectivity means that the feed and the reaction intermediates contain higher level of short chain alcohol or carboxylic acids represented by acetic acid (4).

The solution of equation 2 can be obtained:

$$\frac{\partial x}{\partial z} = \frac{u}{2D_{eff}} (1-\beta)x \quad (6)$$

where

$$\beta = \sqrt{1 + \frac{4kd}{uPe}} \quad \text{and} \quad Pe = \frac{ud}{D_{eff}} \quad (7)$$

Because the parameters in the above equations and the properties of supercritical water are strong functions of temperature, these equations cannot be used directly over the entire length of the non-isothermal reactor. In this case, the reactor can be treated as a number (n) of pseudo-isothermal, equal length (l) segments. Thus, the solution to equation 2 for the first segment at the reactor inlet is

$$\frac{x_2}{x_1} = \frac{2 \exp\left(\frac{l}{2d} Pe_1 (1-\beta_1)\right)}{1+\beta_1} \quad (8)$$

The solution for other segments ($i = 2$ to n) are

$$\frac{x_{i+1}}{x_i} = \exp\left(\frac{l}{2d} Pe_i (1 - \beta_i)\right) \quad (9)$$

The Peclet number is a function of Reynolds number and Schmidt number given by Levenspiel (5,6) are as follows,

$$Pe^{-1} = (ReSc)^{-1} + \frac{ReSc}{192} \quad \text{for } Re < 2,100 \quad (10)$$

$$Pe^{-1} = 1.53 \times 10^{10} Re^{-2.8} + 0.83 Re^{-0.1} \quad \text{for } Re > 2,100 \quad (11)$$

The heat transferred from the core flow to the annular flow in each segment is determined by

$$q_i = h_i \pi d l_i (\bar{T}_i - \bar{T}_{n-i}) \quad (12)$$

where h_i is the overall heat transfer coefficient between the core and annular flows and

$$\bar{T}_i = \frac{T_i + T_{i+1}}{2} \quad (13)$$

The convective heat transfer coefficients for supercritical fluids may be determined by (7):

$$Nu = 1.86 \left(\frac{d}{L} Re Pr\right)^{0.33} \quad Re < 2,100 \quad (14)$$

$$Nu = 0.12 (Re^{0.67} - 125.) Pr^{0.33} \quad 2,100 < Re < 10,000 \quad (15)$$

$$Nu = 0.023 Re^{0.8} Pr^{0.33} \quad Re > 10,000 \quad (16)$$

For the annular flow, the surface heat loss term should be included in the Σq term, therefore, for each section,

$$\Sigma q_i = q_{k,i} + q_i = h_{k,i} \pi (d_o + 2\delta_o) l_i (\bar{T}_i - T_a) + q_i \quad (17)$$

where $h_{k,i}$ is the overall heat loss coefficient from the annular flow to air. The surface heat transfer coefficient includes the natural convection and radiant effects (7):

$$h_s = 5.72 \times 10^{-8} \left(\frac{T_s^4 - T_a^4}{T_s - T_a}\right) + 1.37 \left(\frac{T_s - T_a}{L}\right)^{0.25} \quad (18)$$

The residence time in each segment is determined by the density of water, flow rate and volume of the segment:

$$t_{r,i} = \frac{l}{u_i} = \frac{lA\rho_{w,i}}{G_w} \quad (19)$$

The computer program was written in FORTRAN and the solution method includes four major steps:

1. Calculate the concentration and temperature profiles and the residence time in the inner tube by assuming a temperature profile in the outer-tube;
2. Calculate the concentration and temperature profiles in the outer tube by using the calculated temperature profile in the inner-tube and the heat loss to the environment;
3. Compare the new outer-tube temperature profile to the assumed profile, if they are close enough, print the results;
4. Otherwise, repeat Steps 1 and 2 by assuming the new outer-tube temperature profiles.

Results and Discussion

Twenty pseudo-isothermal segments were used to obtain the computer calculation results in this study. The length of each segment is 61 cm. As shown in Table I, the kinetic parameters for the selected organic compounds are summarized. These parameters cover both the present model and those reported by others.

Table I. Kinetic Models for SCWO of Selected Organic Compounds

Compound	Parameters				Temperature (K)	Pressure (MPa)	Feed Conc. (g/L)	References
	k°	E	m	n				
Acetic Acid	9.82x10 ¹⁷	231	1	1	611-718	40-44	.525	[10]
Acetic Acid	2.55x10 ¹¹	172.7	1	0	611-718	40-44	.525	[10]
Acetic Acid*	2.63x10 ¹⁰	167.7	1	0	673-803	24-35	1.3-3.3	[1]
Acetic Acid	7.91x10 ¹⁰	174	1	0	660-713	25	4.1-20.5	[4] & this work
Phenol	2.61x10 ⁵	64	1	1	557-702	30-35	.1-.4	[10]
Phenol	3.03x10 ²	51.8	1	.5	573-693	19-28	.05-.33	[9]
Phenol	1.97x10 ³	60.8	1	0	677-715	25	.59-.74	[4] & this work
n-Octanol	1.39x10 ⁸	115.5	1	0	677-715	25	.24-.37	[4] & this work
Ph/Oct (TOC)	3.75x10 ⁴	78.9	1	0	677-715	25	.61-.81	this work

* H₂O₂ was used as the oxidant, while in all other cases O₂ was used
 Rate = k°exp(-E/RT) [C]^m[O₂]ⁿ.

The operating conditions, including temperature, pressure, and flow rate, and organic concentrations at the reactor inlet, bottom, and outlet are given in Tables II and III, respectively. The Reynolds number ranges from 3.5x10⁴ to 9.1x10⁴ for the core flow and 7.6x10³ to 2.0x10⁴ for the annular flow. Although the test data were the same as the earlier work of the authors (4), the present work considers the heat transfer effect and gives the reactor temperature profiles as well. Some kinetic

Table II. Reactor Model Results for SCWO of Acetic Acid

Test	<i>f</i>	<i>C_{in}</i>	<i>T_{in}</i>	<i>T_b</i> (F)		<i>T_{out}</i> (F)		<i>C_b</i> (g/l)		<i>C_{out}</i> (g/l)		<i>trb</i> (s)	<i>trout</i> (s)
	(lb/h)	(g/l)	(F)	model	data	model	data	model	data	model	data		
Hac-01	250	20.25	775	779	779	779				15.76	16.10		51.5
Hac-03	200	19.50	778	780	780	779		18.90	18.90	14.24	16.50	6.5	64.2
Hac-05	150	18.75	772	778	778	775		18.00	18.40	12.56	16.00	8.8	86.8
Hac-07	100	19.50	768	777	777	771		18.39	18.63	10.92	12.75	13.2	132.1
Hac-09	100	19.50	758	761	761	755				12.64	15.58		149.
Hac-11	150	20.50	759	761	761	758		19.88	18.90	15.23	14.55	9.8	97.9
Hac-13	200	19.40	759	761	761	758		18.97	14.40	15.53	12.25	7.4	73.4
Hac-15	250	20.25	759	760	760	759		19.88	19.00	16.97	15.00	5.9	58.8
Hac-17	257	20.50	802	820	820	839	820	19.45	17.75	10.41	6.30	4.3	40.8
Hac-19	254	19.63	735	730	730	729	728			17.31	17.50		91.4
Hac-21	200	21.12	734	729	729	728	727	20.78	20.75	17.97	17.84	11.8	120.6
Hac-23	145	20.50	739	730	730	728	726	20.05	20.25	16.46	16.56	15.7	162.3
Hac-25	240	20.25	780	790	790	793				14.56	15.61		50.5
Hac-27	140	20.25	777	792	792	794		19.16	19.38	11.08	12.25	8.8	85.3
Hac-29	140	20.25	776	791	791	793		19.18	19.33	11.30	11.49	8.8	86.
Hac-31	140	4.94	736	728	728	725	722	4.82	4.75	3.92	4.38	17.3	183.7
Hac-33	198	5.06	739	734	734	729	726			4.30	4.38		112.8
Hac-35	253	5.06	737	732	732	729	727			4.45	4.06		90.
Hac-37	249	4.31	758	750	750	746	741	4.24	4.19			6.5	
Hac-39	193	4.38	757	750	750	744	741	4.29	4.25			8.4	
Hac-41	160	4.62	850	819	819	804	797	4.21	4.38	2.19	3.25	6.8	69.7
Hac-43	122	4.25	860	814	814	795	793	3.78	4.13	1.77	0.33	9.1	93.8
Hac-45	140	5.06	844	816	816	800	795	4.58	4.50	2.29	2.62	7.8	80.8
Hac-47	113	4.75	833	800	800	783	784	4.34	4.50	2.32	2.25	10.3	107.2
Hac-49	150	4.75	834	804	804	789	787	4.41	4.38	2.63	3.50	7.6	79.
Hac-51	197	4.38	825	806	806	795	792	4.14	4.25	2.68	2.25	5.8	59.1
Hac-53	240	4.75	808	796	796	787	785	4.57	4.13	3.37	2.88	4.9	50.3
Hac-55	240	4.62	790	782	782	774	774			3.56	2.75		53.8
Hac-57	198	5.06	789	779	779	769	769			3.76	3.50		66.9
Hac-59	154	4.06	800	775	775	764	764	3.90	3.88	2.88	3.50	8.5	88.7
Hac-61	115	4.69	816	778	778	764	762			2.93	3.31		118.4
Hac-63	119	4.62	765	748	748	740	742	4.47	4.50			13.9	
Hac-65	151	4.75	768	750	750	743	740	4.62	4.38	3.72	3.75	10.7	112.7
Hac-67	220	4.70	840	823	823	812	801	4.38	4.28	2.53	1.11	4.9	49.6
Hac-69	220	4.70	840	828	828	817	806			2.37	.81		48.8

Table III. Reactor Model Results for SCWO of Octanol/Phenol Mixture

Test	<i>f</i>	<i>C_{in}</i>	<i>T_{in}</i>	<i>T_b</i> (F)		<i>T_{out}</i> (F)		<i>C_b</i> (g/l)		<i>C_{out}</i> (g/l)		<i>tr_b</i> (s)	<i>tr_{out}</i> (s)
	(lb/h)	(g/l)	(F)	model	data	model	data	model	data	model	data		
Oct-01	200	.232						.016	.025	0	0		
Ph-01	200	.587						.403	.401	.016	.089		
TOC-01	200	.68	843	825	825	808	802	.490	.530	.113	.185	5.3	54.6
Oct-03	170	.259						.012	.017	0	0		
Ph-03	170	.616						.396	.346	.010	.045		
TOC-03	170	.69	851	823	825	804	803	.473	.520	.104	.130	6.3	65.1
Oct-05	169	.268						.041	.044	0	0		
Ph-05	169	.616						.425	.379	.017	.068		
TOC-05	169	.69	793	781	781	770	773	.517	.480	.146	.285	7.5	77.6
Oct-07	132	.277						.025	.030	0	0		
Ph-07	132	.638						.397	.363	.007	.030		
TOC-07	132	.72	799	780	780	765	765	.501	.490	.133	.085	9.6	101.
Oct-09	100	.257						.010	.013	0	0		
Ph-09	100	.638						.339	.302	.002	.003		
TOC-09	100	.69	821	780	780	761	762	.429	.410	.112	.060	12.7	136.
Oct-11	100	.262						.020	.020	0	0		
Ph-11	100	.658						.362	.328	.001	.001		
TOC-11	100	.72	778	761	760	747	750	.469	.490	.131	.115	14.5	157.
Oct-13	130	.24						.032	.028	0	0		
Ph-13	130	.665						.420	.367	.007	.015		
TOC-13	130	.67	777	761	761	749	747	.479	.410	.136	.165	11.1	118.
Oct-15	173	.265						.060	.057	0	0		
Ph-15	173	.603						.427	.322	.020	.039		
TOC-15	173	.70	768	760	760	751	749	.543	.590	.164	.215	8.4	88.2
Oct-17	220	.318						.026	.011	0	0		
Ph-17	220	.636						.449	.339	.024	.083		
TOC-17	220	.67	846	828	828	813	807	.494	.430	.115	.120	4.8	49.0
Oct-19	169	.331						.016	.009	0	0		
Ph-19	169	.656						.423	.149	.011	.053		
TOC-19	169	.67	843	821	821	802	802	.461	.320	.102	.080	6.4	65.9
Oct-21	127	.366						.006	.007	0	0		
Ph-21	127	.649						.361	.206	.003	.018		
TOC-21	127	.80	860	820	820	796	796	.491	.570	.099	.070	8.5	89.1
Oct-23	100	.293						.002	.006	0	0		
Ph-23	100	.74						.349	.198	.001	.006		
TOC-23	100	.80	886	818	818	790	793	.432	.280	.085	.060	10.8	115.
Oct-25	127	.331						.015	.017	0	0		
Ph-25	127	.65						.383	.335	.005	.016		
TOC-25	127	.81	825	799	799	780	783	.531	.520	.127	.105	9.2	96.0
Oct-27	168	.345						.032	.026	0	0		
Ph-27	168	.705						.472	.390	.015	.015		
TOC-27	168	.78	817	800	800	785	786	.563	.570	.143	.115	6.8	71.4
Oct-29	215	.355						.057	.064	0	0		
Ph-29	215	.70						.512	.468	.035	.149		
TOC-29	215	.81	811	800	800	788	787	.627	.640	-	-	5.4	55.5
Oct-31	215	.324						.076	.078	0	0		
Ph-31	215	.772						.578	.600	.046	.216		
TOC-31	215	.78	789	780	780	770	768	.623	.640	-	-	5.9	61.1

parameters obtained from this work with the best fit to the test data confirms the results of the previous work (2). Acetic acid showed a relatively high activation energy of 174 kJ/mol. The activation energy values for phenol and n-octanol are 60.8 kJ/mol and 115.5 kJ/mol, respectively.

The heat transfer calculation for the phenol/n-octanol mixture was based on the TOC destruction. Using the generalized SCWO reaction model (4), The activation energy of the TOC destruction is 78.9 kJ/mol and the point selectivity is 0.33 with the best fit to the test data for the phenol/n-octanol mixture. The point selectivity value shows that the phenol/n-octanol mixture has medium strength for the SCWO process.

The calculated concentrations at the reactor bottom and exit, using the pseudo-first-order kinetic models, agreed favorably with the test data for all three compounds. The calculated exit reactor temperature agreed well with the test data, as shown in Figures 3-6. However, when the reactor exit temperature is greater than about 425°C (or about 800°F), the calculated exit temperature seems to be higher than the test data. The reasons are not clear, but it is possible that when the reactor temperature is high than 425°C, the oxidation becomes incomplete, therefore, the reaction heat may be less than the value used in the calculation.

The typical simulation results of the reactor concentration and temperature profiles for HAC-29 are shown in Figures 7 and 8. In Figure 8, the calculated temperature profile of the 0% HAC (i.e., there is no reaction heat) is also included to see the effect of the reaction heat. The typical simulation results of the reactor TOC concentration and temperature profiles for TOC-23, the phenol/n-octanol mixture feed, are shown in Figures 9 and 10. Figure 10 also includes the calculated temperature profile of the 0% TOC to see the effect of the reaction heat. The simulation results have shown that, due to the heat transfer between the fluids in the core and annular sections, the concentric-tube reactor configuration results in relatively smooth reactor temperature profiles and stable operating conditions in treating the feed solutions with higher and lower organic concentrations. This fact indicates that, the concentric-tube reactor has the flexibility to treat the waste waters with variable organic concentrations and effectively utilizes the reaction heat. Therefore, it will be beneficial to use the concentric-tube configuration in the reactor design for the future commercial SCWO units.

The developed reactor model will also be a useful tool for sensitivity studies, i.e., finding the most important input variables and most influential parameters. The information obtained from these studies will be useful to the future design and scale-up of the SCWO reactors. For example, in the present study, the Reynolds number ratio of the core flow to the annular flow is about 4.6. If the ratios were reduced to about 1, the reactor might have a better performance.

Conclusions

A concentric-tube reactor model was developed and it was proven to be effective in generating design data. Both reaction kinetics and heat transfer factors were incorporated in the model. The model was validated by pilot-plant tests involving SCWO of acetic acid, phenol, and n-octanol. Simulation results, using pseudo-first-order kinetic models, agreed favorably with the pilot-plant data for all three

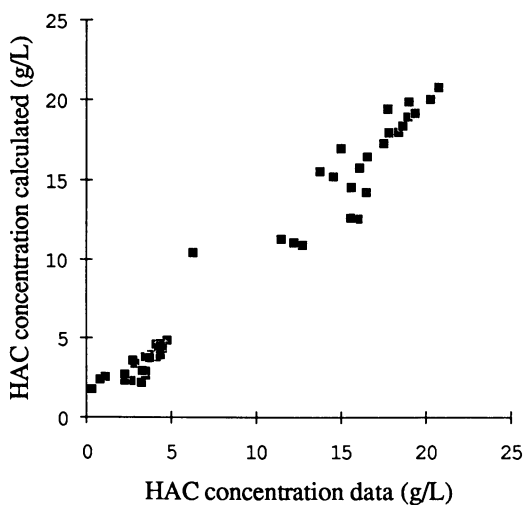


Figure 3. Comparison of model results with HAC-test data

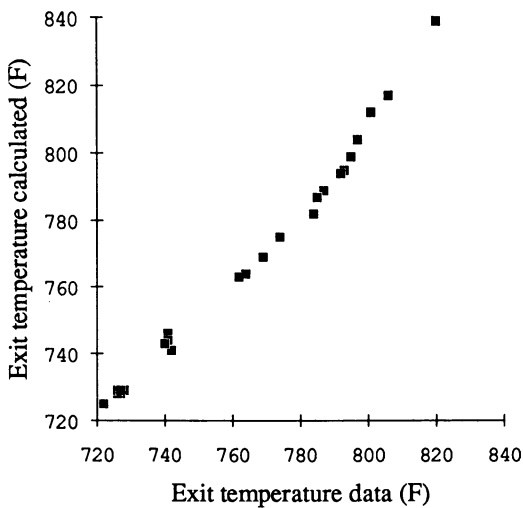


Figure 4. Comparison of model results with HAC-test data

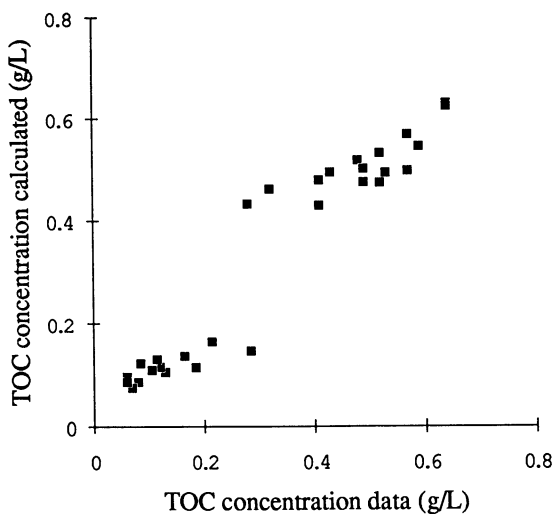


Figure 5. Comparison of model results with phenol/octanol-test data

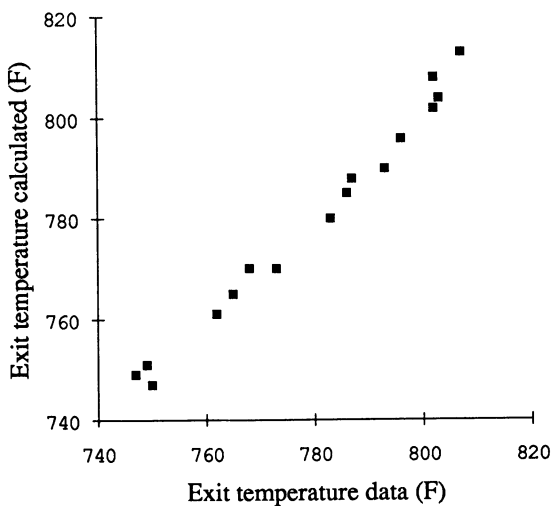


Figure 6. Comparison of model results with phenol/octanol-test data

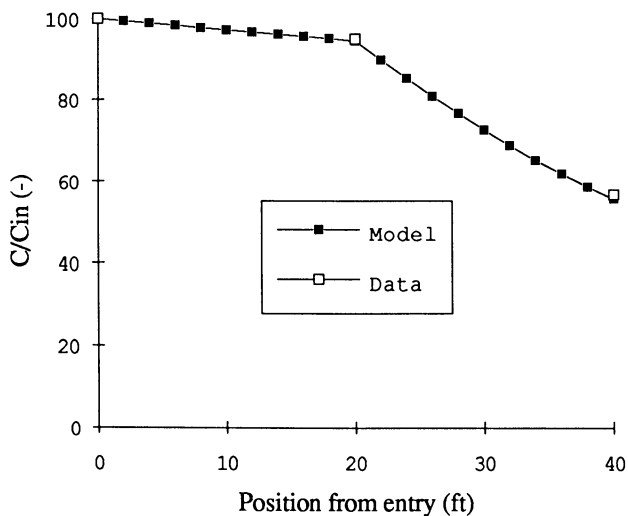


Figure 7. Reactor concentration profile (HAC-29, 2.03% HAC, 140 lb/h)

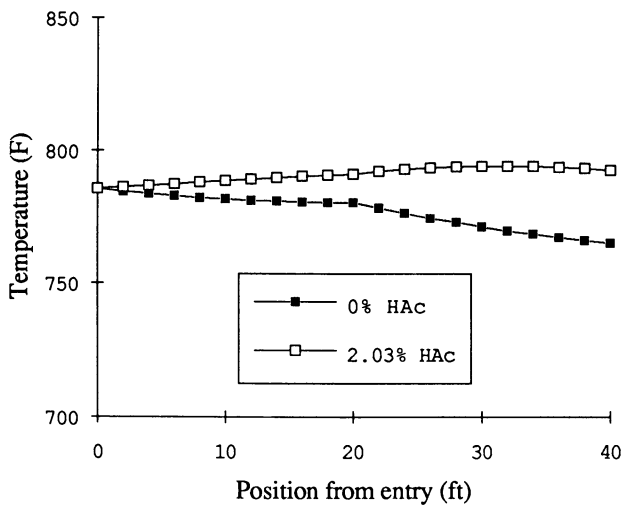


Figure 8. Reactor temperature profile (HAC-29, 2.03% HAC, 140 lb/h)

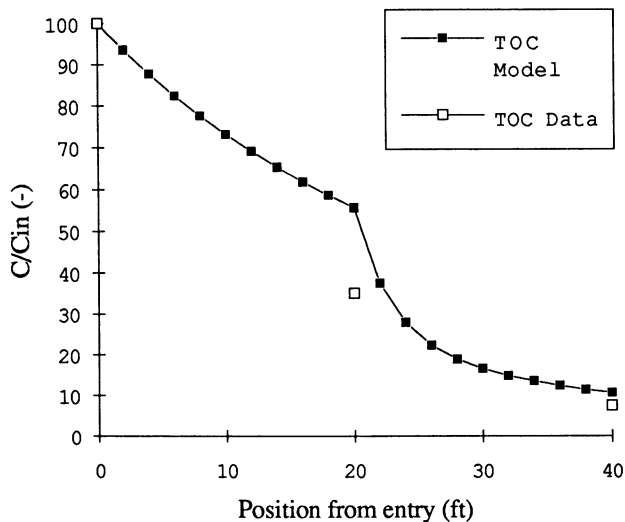


Figure 9. Reactor concentration profile (TOC-23, .074% TOC, 100 lb/h)

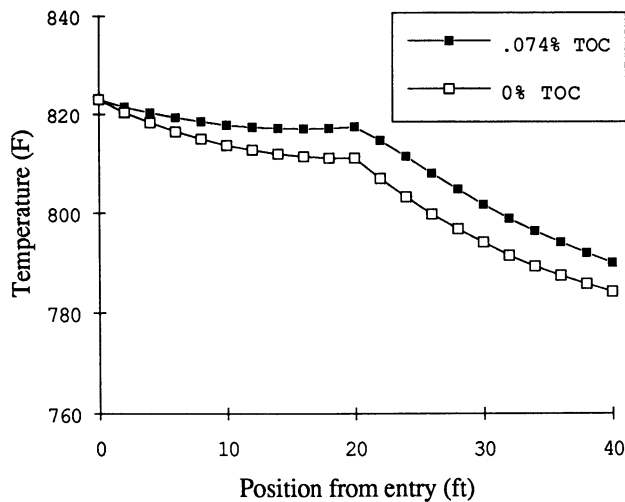


Figure 10. Reactor temperature profile (TOC-23, .074% TOC, 100 lb/h)

compounds. The simulated reactor temperature profiles agreed well with the measured profiles.

The kinetics of SCWO of the phenol/n-octanol mixture, based on TOC changes, followed the generalized SCWO reaction model, which shows an activation energy of 78.9 kJ/mol and a point selectivity α of about 0.33.

Due to the heat transfer between the fluids in the core and annular sections, the concentric-tube reactor configuration results in relatively smooth reactor temperature profiles and stable operating conditions in treating waste waters with variable organic concentrations.

Notation

A	cross section area (m^2)
C	concentration (g/l)
D_{eff}	effective axial diffusion coefficient (m^2/s)
d	equivalent tube diameter (m)
E	activation energy (kJ/mol)
G	mass flow rate (kg/s)
H	enthalpy of supercritical water (J/kg)
h	heat transfer coefficient ($W/m^2 K$)
k	reaction constant (1/s)
k_{eff}	thermal conductivity (W/m K)
L	reactor length (m)
l	pseudo-isothermal segment length, $=2L/n$ (m)
n	number of pseudo-isothermal segments
P	pressure (N/m^2)
q	heat flow rate (W)
Pr	Prandtl number (-)
R	gas constant (8.314 J/mol K)
$R(T)$	reaction rate term (kg/kg s)
Re	Reynolds number (-)
Sc	Schmidt number (-)
T	temperature (K)
t_r	residence time (s)
u	average velocity of the fluid (m/s)
x	mass fraction of the organic compounds (kg/kg)
z	axial coordinate (m)
ΔH	reaction heat (J/kg)
β	parameter, in equation 6
δ	tube wall thickness (m)
μ	viscosity (kg / m s)
ρ	density (kg/m^3)

Subscripts

a	air
b	reactor bottom

<i>i</i>	i-th segment, inner tube
<i>in</i>	reactor inlet
<i>ls</i>	heat loss
<i>o</i>	outer tube
<i>out</i>	reactor outlet
<i>R</i>	reaction
<i>s</i>	surface
<i>w</i>	water

Acknowledgment

Appreciation is extended to ECO Waste Technologies (Austin, Texas) for providing financial and technical assistance in the pilot-plant construction and operation. Also, this work is in part supported by the Separation Research Program and Bettie M. Smith Chair, The University of Texas at Austin.

Literature Cited

1. Rosasco, G. J. *Proceedings: Workshop on Federal Programs Involving Supercritical Water Oxidation*, NISTIR 4920, National Institute of Standards and Technology, September 1992.
2. Li, L.; Chen, P.; Gloyna, E. F. "Pilot-Plant Validation of Kinetic Models for Supercritical Water Oxidation", presented at Chemical Oxidation: Technology for the Nineties, Vanderbilt University, Nashville, TN, February 16-18, 1994.
3. Neuman, E. B. *Chemical Reactor Design*, John Wiley & Sons Inc, 1987.
4. Li, L.; Chen, P.; Gloyna, E. F. *AIChE J.* **1991**, *37* (11), 1687.
5. Levenspiel, O. *Ind. Eng. Chem.* **1958**, *50*, 343.
6. Levenspiel, O. *Chemical Reaction Engineering*, 2nd Ed., Wiley, New York, 1972.
7. Perry, R. H.; Chilton, C. H. *Chemical Engineer's Handbook*, 5th Ed., McGraw-Hill Book Company, 1972.
8. Wightman, T. J. *Studies in Supercritical Water Oxidation*, MS Thesis, University of California, Berkeley, 1981.
9. Lee, D.-S. *Supercritical Water Oxidation of Acetic Acetamide and Acetic Acid*, Ph.D. Dissertation, The University of Texas at Austin, 1990.
10. Thorton, T. D.; Savage, P. E. *AIChE J.* **1992**, *38* (3), 321.

RECEIVED May 19, 1995

Chapter 25

Release Mechanisms of Extractable Compounds from Plant Matrices During Supercritical Fluid Extraction

Mathematical Modeling

Ö. Hortaçsu, O. (Navaro) Aeskinazi, and U. Akman

Department of Chemical Engineering, Bogaziçi University, 80815 Bebek, Istanbul, Turkey

Two mathematical models: Cellular Permeable-Tube Arrays (CPTA) model and Serially-Interconnected Perfectly-Mixed Tanks (SI-PMTs) model were proposed in an attempt to explain the release mechanisms of extractable compounds from plant matrices during supercritical fluid extraction. Models enable phenomenological description of probable three-phase mass transfer taking place within plant cells. A complex chromatographic-type release is envisioned for the supercritical-fluid extraction of materials from plant matrices. A parametric sensitivity analysis is conducted on the SI-PMTs model.

Extraction of various natural compounds from plants is still an important and growing research area within the field of supercritical-fluid (SF) technology. Presently, in addition to the growing number of experimental studies both in extraction-process development and in physical-property determination areas, some mathematical modeling work on the extraction phenomena is appearing in the related literature (1,2). The mathematical models suggested for the purpose of defining the extraction phenomena from plant materials seem to consider the plant matrices as catalyst-like porous structures in/on which the extractable components are present. However, the mechanisms of transport even in the most complicated porous solid structures are quite simple when compared with the phenomena in the cellular plant structures. Thus, a more realistic modeling of the plant matrices would be beneficial for a better understanding of the extraction mechanisms from plant materials.

In contrast to a porous catalyst particle, the internal structure of which cannot be clearly defined, plant materials have structures which have definite characteristics depending upon the functions of the various parts of the plants. These structures in a simplified manner may be modeled as comprising of a cellular portion, an intercellular space, and a pore-like tubular section between the membranes of the adjacent cells (3).

Living plant cells, which are surrounded by membranes, contain other functional parts such as the nucleus, cytoplasm, vacuoles, etc. It is now well known that the

0097-6156/95/0608-0364\$12.00/0
© 1995 American Chemical Society

vacuoles play an important role in the plant cells and they are instrumental in storing the waste and toxic products as well as the useful materials such as oils, proteins, flavanoids, alkaloids and pigments, etc., which are mainly produced in the cytoplasm of the cell (4). In case of plants available for extraction however, the plant body is made up mostly of dead mature cells which are at least partially dehydrated. In these structures, it is expected that most of the materials aimed for recovery via supercritical-fluid extraction (SFE) are stored in the vacuoles which are bounded by the vacuolar membrane, which in turn is bounded by the cell membrane. In such cells, a reasonable assumption would be that the vacuolar volume and the cell volume are quite close quantities. In living cells, the interrelationships between a cell (with its vacuole, membranes, etc.) and its contents are very complicated. The different mobilities of dissolved substances in the cells remind us of a chromatogram, in which compounds are separated from one another by their solubility in a solvent and by the tenacity with which they adhere to another material such a filter paper or a column packing (3). Thus, a chromatographic-type behavior may be expected during the release of components from the cell during SFE.

The objective of this paper is to suggest the preliminary fundamentals of structured plant materials and the role of such structures during extractions using a solvent like supercritical carbon dioxide (SC-CO₂). Noting the above simple, but important, facts about the plant structures, we feel that the mathematical models suggested to explain the extraction phenomena from such matrices should contain elements which represent the facts as closely as possible. For this purpose, we have proposed two main types of models for SFE of materials from plant matrices constituting of mature dead cells. The first model is a Cellular Permeable-Tube Arrays (CPTA) model comprising of cells made up of tubes with permeable walls, which have boundaries to pore-like intercellular pathways and the latter is a Serially-Interconnected Perfectly-Mixed Tanks (SI-PMTs) model. Model equations are developed which enable the phenomenological description of probable three-phase mass-transfer taking place within the plant cells. A sensitivity analysis is conducted on the SI-PMTs model and the importance of each parameter in the model is investigated. The CPTA model is given as the basis of our ultimate aim.

Mathematical Modeling

Basic Assumptions. Plant materials most often used for extracting various substances via SFs could be classified into the following main groups: leafy materials, plant bulk, flowers, and seeds or fruits. It is well documented in literature that gaseous, liquid, and crystalline substances may be present in the plant cells and that these substances are quite mobile in the living plant structure (4). For example, gases may move at velocities near 50 m/hr in living plants, the plant materials in the solution form are quite mobile in the cytoplasm and diffusion of liquids and gases are possible through the cell membranes (3).

As already noted in almost all cases, when the plant material is ready for extraction, the cells it contains are dead, and in many or most instances, the plant material is at least partially dry. Besides, mostly in the seed-type plant materials a large percentage (up to 80% by weight) of the cell material may be composed of various

oils, proteins and sometimes alkaloids, whereas flavonoids and coloring materials may be the desired extractable materials in some of the leafy and flowery materials (5). For a first approximation, we will concern ourselves with oil-rich seed-type materials, which may still have some water (about 5-10%) in their cellular structure, and cells are taken as the smallest possible plant portion of independent entity. The extractable materials from the tubes may be picked up by SF via extraction (or dense-gas stripping) from the free liquid in the cells and/or via desorption from the cell walls. It will also be assumed that all of the extractable materials in the plant matrices are in the cells and not in the intercellular regions. It also seems to be very reasonable to presume that the extractable solutes in the plant matrices may exist both in an extractable liquid state and in an adsorbed state on the cell walls. A final point to note is that the models suggested below are for a single-solute system. Extension of these models to mixtures, some or all of which may be SF- extractable solutes is possible via proper thermodynamic modeling and will be dealt with in the future.

Cellular Permeable-Tube Arrays Model. The physical picture for the Cellular Permeable-Tube Arrays (CPTA) model, an idealized version of natural occurrences in plant structures, is depicted in Figure 1. Figure 1a shows a single cellular tube with a permeable membrane. Figure 1b depicts how the CPTA model may be used for a plant section which may be made up of tube arrays of differing geometry in the axial direction, each array having tubes of different lengths. Finally, in Figure 1c, a vertical cross-section of a cylindrical plant element representing the cellular and intercellular regions is shown.

When Figures 1a, 1b and 1c are compared with actual plant structures, it is evident that some degree of idealization of the structure has been made for the purpose of simpler mathematical formulation. At this point, it should be adequate to say that the actual plant structures may be determined under proper microscopic investigation, and the idealized structures may be assumed on this basis. The shape of the extracted body should also be defined for the purpose of proper mathematical formulation. Here, only as an example, a cylindrical-shaped plant structure is considered. As it is depicted in Figure 1b, plant material may initially be thought to be constituted of series of cylindrical sections of different lengths, each having a somewhat different internal structure. In this geometry each tube may be taken to represent a set of horizontally-connected plant cells, and the shaded spaces between the tubes could be taken as the intercellular regions as in plants. In plant structures made up of mature dead cells which have at least partially lost their water, it is reasonable to assume that the cell membranes and the intercellular spaces are present at minimum volumes, thus taking up only a very small portion of the total structure.

All the extractable materials are assumed to be in the cellular tubes in the form of free liquid in the cell and as adsorbed on the cell walls. In the permeable membrane (wall region), it is assumed that diffusion of the extracted solute and the solvent may simultaneously occur with the adsorption and/or desorption of the solute(s) on the membrane matrix. The intercellular spaces themselves have an axial solvent flow and they also receive flux from the neighboring cellular tubes.

The physical picture of the CPTA model as depicted in Figure 1, may be considered to have two distinct regions: the tubes making up the tubular array and the

intertubular (intercellular) regions. In the tubular array, each tube may be considered independently and the model equations given below are valid for each tube individually. This concept actually brings the flexibility to the model that all tubes in the array do not have to have the same characteristics, however, the assumption of geometrically identical tubes will bring important simplicities to the formulation and to the solution of the model. A tube of length L_T is considered to have a homogenous inner region of radius R_i , which is surrounded by a permeable wall of thickness $(R_o - R_i)$, as indicated in Figure 1 as w.

In the tubes two phases exist: namely the stationary liquid content of the cellular region which originally contains almost all the extractable solute species except for the already adsorbed on the cell walls, and the SF solvent phase which flows in the tubes picking up the solute species from this major source, as indicated in Figure 1 as L and G, respectively. Thus, the material balance equations have to be written for each phase.

For the solvent-phase region ($0 \leq r_T \leq R_i$), the concentration profile of a solute component $C_G(t, z_T, r_T)$, is governed by the following PDE and the initial and boundary conditions:

$$\frac{\partial C_G}{\partial t} = D_{Gz} \frac{\partial^2 C_G}{\partial z_T^2} - u_G \frac{\partial C_G}{\partial z_T} + D_{Gr} \left[\frac{1}{r_T} \frac{\partial}{\partial r_T} \left(r_T \frac{\partial C_G}{\partial r_T} \right) \right] + \frac{K_{OGL} a_{GL} (C_G^*(C_L) - C_G)}{\varepsilon_G} \quad (1)$$

$$C_G(0, z_T, r_T) = C_G^o(z_T, r_T) = C_G^o = 0, \quad C_G(t, 0, r_T) = C_p(t, z_p, r_p) - \left(\frac{D_{Gz}}{u_G} \right) \frac{\partial C_G}{\partial z_T} \Big|_{z_T=0} \quad (2)$$

$$\frac{\partial C_G(t, L_T, r_T)}{\partial z_T} = 0, \quad \frac{\partial C_G(t, z_T, 0)}{\partial r_T} = 0, \quad C_G(t, z_T, R_i) = C_w(t, z_T, R_i)$$

It is assumed that the possible mass-transfer of the solute species to the other parts of the plant matrix originates from the stationary liquid contents of the tubular cells. For the stationary liquid-phase region ($0 \leq r_T \leq R_i$), the concentration profile of a solute component $C_L(t, z_T, r_T)$, is governed by the following PDE and the initial and boundary conditions:

$$\frac{\partial C_L}{\partial t} = D_{Lz} \frac{\partial^2 C_L}{\partial z_T^2} + D_{Lr} \left[\frac{1}{r_T} \frac{\partial}{\partial r_T} \left(r_T \frac{\partial C_L}{\partial r_T} \right) \right] - \frac{K_{OGL} a_{GL} (C_G^*(C_L) - C_G)}{\varepsilon_L} \quad (3)$$

$$C_L(0, z_T, r_T) = C_L^o(z_T, r_T) = C_L^o, \quad \frac{\partial C_L(t, z_T, 0)}{\partial z_T} = 0, \quad \frac{\partial C_L(t, z_T, R_i)}{\partial r_T} = 0,$$

$$-D_{Lz} \frac{\partial C_L(t, 0, r_T)}{\partial z_T} = K_{LP} \left[C_p^* \{ C_L(t, 0, r_T) \} - C_p(t, z_p, r_p) \right], \quad (4)$$

$$D_{Lz} \frac{\partial C_L(t, L_T, r_T)}{\partial z_T} = K_{LP} \left[C_p^* \{ C_L(t, L_T, r_T) \} - C_p(t, z_p, r_p) \right]$$

Now we look at the permeable tube-wall region. All solute brought into this region is picked up by the solvent flowing within the inner region of the tube. As the solvent diffuses through the permeable tube-wall, either solute is adsorbed on the wall surfaces or is desorbed from the wall surfaces depending upon the level of saturation of the solvent phase. Therefore, in the tube wall region ($R_i \leq r_T \leq R_o$), the concentration profile of a solute component $C_W(t, z_T, r_T)$, is governed by the following PDE and the initial and boundary conditions:

$$\frac{\partial C_W}{\partial t} = D_{Wz} \frac{\partial^2 C_W}{\partial z_T^2} + D_{Wr} \left[\frac{1}{r_T} \frac{\partial}{\partial r_T} \left(r_T \frac{\partial C_W}{\partial r_T} \right) \right] - \left(\frac{1 - \varepsilon_W}{\varepsilon_W} \right) \frac{\partial \bar{q}_W}{\partial t} \quad (5)$$

$$C_W(0, z_T, r_T) = C_W^o(z_T, r_T) = C_W^o, \quad C_W(t, 0, r_T) = C_p(t, z_p, r_p),$$

$$C_W(t, L_T, r_T) = C_p(t, z_p, r_p), \quad C_W(t, z_T, R_i) = C_G(t, z_T, R_i), \quad (6)$$

$$C_W(t, z_T, R_o) = C_p(t, z_p, r_p)$$

The solute uptake $\bar{q}_W(t, z_T, r_T)$, of the wall surfaces within the wall region ($R_i \leq r_T \leq R_o$), is governed by the following implicit PDE and its initial condition:

$$\frac{\partial \bar{q}_W}{\partial t} = K_{AW} a_{AW} \left[q_W^* \{ C_W(t, z_T, r_T) \} - \bar{q}_W \right] \quad (7)$$

$$\bar{q}_W(0, z_T, r_T) = \bar{q}_W^o(z_T, r_T) = q_W^o \quad (8)$$

The driving force ($q_W^* - \bar{q}_W$) will become positive for adsorption and negative for desorption.

The second group of equations, as noted earlier, deal with the intertubular region which is the hatched region in Figure 1c. In this region initially no extractable solute is assumed to be present, and the solvent is assumed to be in bulk flow. However, as the extraction proceeds, solute is carried into this region from the permeable walls of the adjoining tubes. In real plant structures, some portion of this intertubular region is bounded by the cylindrical tubes forming closed triangular-shaped regions (as shown in Figure 1c by the small hatched regions surrounded by three tubes of triangular layout). However, difficulties associated with mathematical modeling of the boundary conditions between cylindrical tubes and triangular-shaped intertubular duct, forces one to treat all the hatched regions in Figure 1c as homogenous (i.e., tube-pitch is somewhat greater than $2R_o$). Therefore, here, the intertubular region will be considered as a cylindrical annular region with radius equal to the approximate radius of the bundle of tubes (R_p). Also, it will be envisioned that the plant pellets or the pellet-like plant cuts with radii R_p and length L_p contains randomly-distributed cellular tubes (that may have different lengths L_T and radii R_o)

as shown in Figure 1b. From this point of view, the concentration profile of a solute component $C_p(t, z_p, r_p)$ within a pellet-shaped intertubular region ($0 \leq r_p \leq R_p$) is governed by the following PDE and the initial and boundary conditions:

$$\frac{\partial C_p}{\partial t} = D_{pz} \frac{\partial^2 C_p}{\partial z_p^2} - u_p \frac{\partial C_p}{\partial r_p} + D_{pr} \left[\frac{1}{r_p} \frac{\partial}{\partial r_p} \left(r_p \frac{\partial C_p}{\partial r_p} \right) \right] + K_{PT} a_{PT} [\bar{C}_w(t, z_p, r_p) - C_p(t, z_p, r_p)] \quad (9)$$

$$C_p(0, z_p, r_p) = C_p^0(z_p, r_p) = C_p^0 = 0, \quad C_p(t, 0, r_p) = C_b(t, z, r) - \left(\frac{D_{pz}}{u_p} \right) \frac{\partial C_p}{\partial z_p} \Big|_{z_p=0} = 0 \quad (10)$$

$$\frac{\partial C_p(t, L_p, r_p)}{\partial z_p} = 0, \quad \frac{\partial C_p(t, z_p, 0)}{\partial r_p} = 0, \quad C_p(t, z_p, R_p) = C_b(t, z, r)$$

where, $\bar{C}_w(t, z_p, r_p) = \frac{1}{L_T} \int_0^{L_T} C_w(t, z_T, R_o) dz_T$ is the surface-area averaged wall-region concentration from of the tubes. A similar volume-averaging technique may be used to obtain $\bar{C}_p(t, z, r)$, time-rate-of-change of which may be incorporated to the standard component-continuity equation for the bulk solvent $C_b(t, z, r)$ within the fixed-bed-type extractor ($(0 \leq z \leq L, 0 \leq r \leq R)$).

The CPTA model equations derived from the basic principles of conservation of mass describe the phase aggregates and mass-transfer paths under supercritical conditions quite realistically. The set of PDE's representing the four physically distinct regions (dense-gas solvent, stationary liquid, wall, and duct) given by equations 1-10, could be solved numerically via the "method of lines" technique.

Serially-Interconnected Perfectly Mixed Tanks Model. With a lesser degree of accuracy and completeness as compared to the CPTA model, the natural release phenomena occurring during supercritical extraction from plant matrices could also be modeled as perfectly mixed tanks (PMTs), which are serially connected to each other, permitting partial bypass of the solvent phase. Initially, the PMTs are assumed to contain most of the extractable solute in a free-liquid state, while the extractable solute could also be adsorbed on the tank (cell) walls. At this point it may be beneficial to consider just one of the tanks as in Figure 2, noting that the same type of mechanisms prevail in all of them.

Figure 2 shows the pictorial representation of the constituents of a PMT (which may represent one plant cell or a group of cells), where solute is accessible to both liquid and vapor phases. The extractable component may also be present in an adsorbed state on the walls of the PMT. The solvent assuming that it is not saturated with the solute, may pick up the solute from the liquid phase, and from the cell walls. The availability of extractable materials in these phases, and the competing mass-transfer mechanisms of extraction (dense-gas stripping) from the liquid and desorption

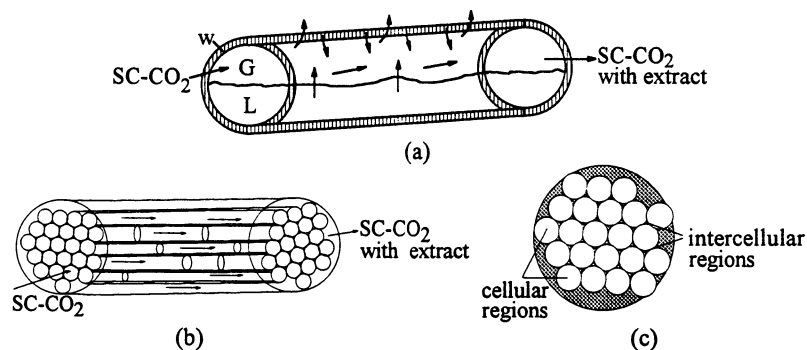


Figure 1. Idealized cellular plant structure for Cellular Permeable-Tube Arrays Model: (a) transport phenomena in a cellular tube (b) a bundle of cellular tubes representing the plant material (c) cross-section of the tube bundle illustrating the intertubular ducts.

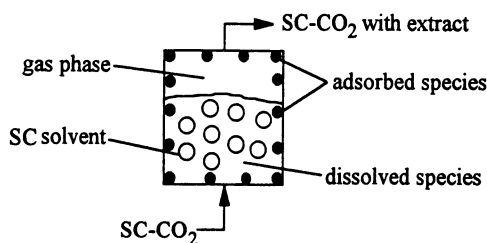


Figure 2. A single plant cell represented as a PMT with extraction and sorption.

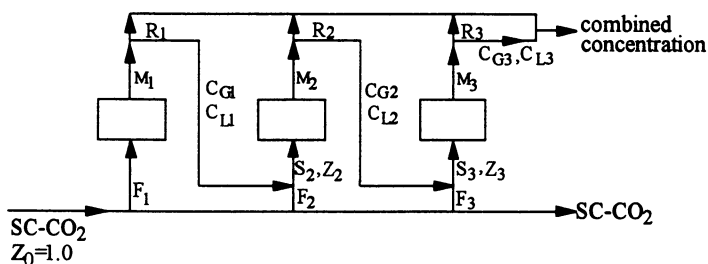


Figure 3. Serially-Interconnected PMTs representing model plant structures.

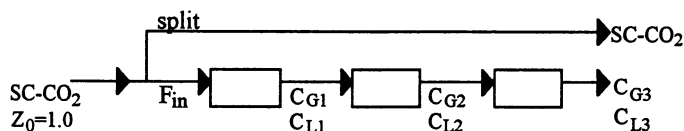


Figure 4. Serially-Interconnected PMTs representing simplified model plant structures.

from the walls, determine the exit concentration of the extractable components in the solvent phase. As time goes on, it is expected that the fraction of the volume occupied by the liquid will decrease. This process will go on until the PMT in question is fully depleted of all extractable component(s). At this point we have to note that the solvent stream leaving the PMT may or may not have reached the saturation concentration of the extractable solute component. This depends on various factors such as the residence time of the solvent in the PMT, the interfacial mass transfer rates, the availability of the extractable compounds, etc.

The Serially-Interconnected PMTs, (SI-PMTs) model could be represented as in Figure 3 (by considering three stages for the sake of simplicity), where the solvent is pure SC-CO₂. The CO₂ containing streams entering a PMT may consist of a combination of stream types. It is evident from Figure 3 that the transport between the PMTs is quite flexible and the solvent phase may enter each cell directly as fresh feed or, after it exits from a previous cell. A special case of Figure 3, where the fresh solvent streams F₂ and F₃, and the fraction of the exit streams from each cell R₁, R₂, and R₃ are taken zero, is shown in Figure 4.

In the very simplified phenomena envisioned above, it should be understood that the solution thermodynamics in the liquid phase, the mass transfer from the liquid phase to the SF solvent, the adsorption/desorption thermodynamics on the cell walls, and the permeation of both the solvent and the extractable materials from the cell walls (membranes) play an important role in the overall extraction process. Once out of a PMT, the solvent with its contents may leave the extracted body in its present form, or partially re-enter another PMT (refer to Figure 3)

The model equations representing stage n in Figure 3 are given as:

Mass balance for the solute over the solvent phase:

$$\frac{dC_{G(n)}}{dt} = K_{OGL} a_{GL} (C_{G(n)}^* - C_{G(n)}) - K_{SG}^p a_{SG} (q_{G(n)}^* - \bar{q}_{G(n)}) + \left(\frac{S_{(n)} Z_{(n)}}{V_G} \right) - \left(\frac{M_{(n)} C_{G(n)}}{V_G} \right) \quad (11)$$

Mass balance for the stationary liquid phase:

$$\frac{dC_{L(n)}}{dt} = -\frac{V_G}{V_L} K_{OGL} a_{GL} (C_{G(n)}^* - C_{G(n)}) - K_{SL}^p a_{SL} (q_{L(n)}^* - \bar{q}_{L(n)}) \quad (12)$$

Mass balance for the solute over the cell walls in contact with the gas phase:

$$\frac{d\bar{q}_{G(n)}}{dt} = K_{SG}^p a_{SG} (q_{G(n)}^* - \bar{q}_{G(n)}) \quad (13)$$

Mass balance for the solute over the cell walls in contact with the liquid phase:

$$\frac{d\bar{q}_{L(n)}}{dt} = K_{SL}^p a_{SL} (q_{L(n)}^* - \bar{q}_{L(n)}) \quad (14)$$

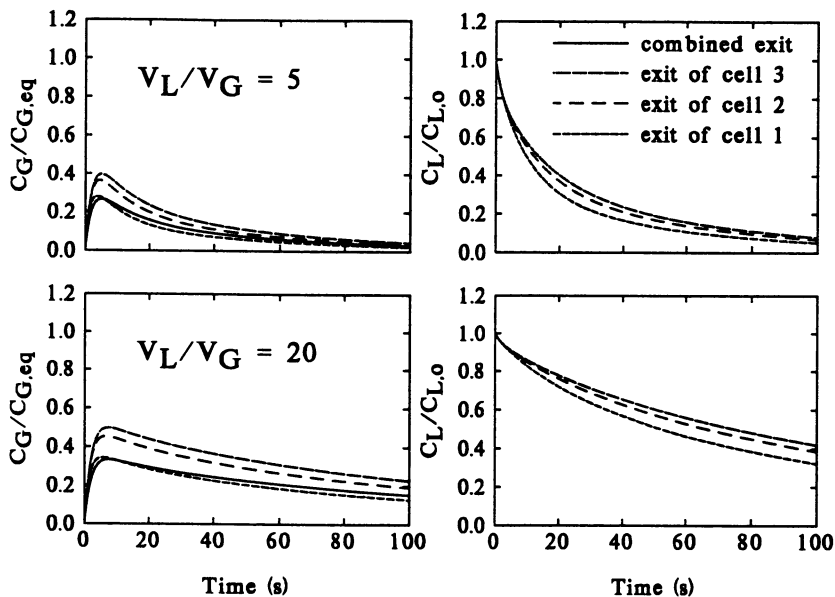


Figure 5. Effect of V_L/V_G ratio on gas and liquid concentrations at fixed split ratio of 0.6 and feed flowrate of $1.0 \text{ cm}^3/\text{s}$ (refer to Figure 3).

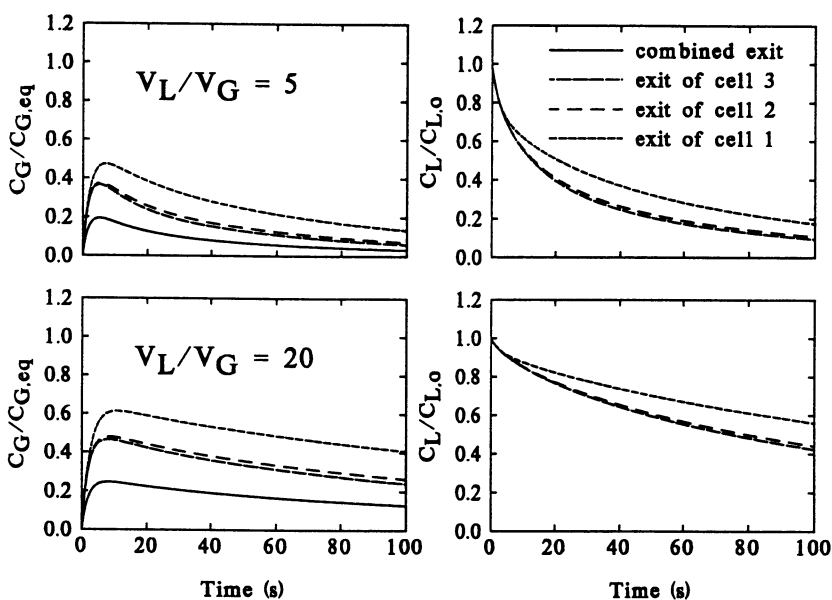


Figure 6. Effect of V_L/V_G ratio on gas and liquid concentrations at fixed split ratio of 0.9 and at fixed inlet flowrate of $0.1 \text{ cm}^3/\text{s}$ to the system (refer to Figure 3).

$$\text{where, } Z_{(n)} = \frac{((R_{(n)} C_{G(n)}) + (F_{(n)} Z_0))}{S_{(n)}}; \quad S_1 = F_1; \quad Z_1 = Z_0 \quad (15)$$

In the above equations the overall volume of the PMT is constant and $V = V_L + V_G$. In the above model, as a first approximation the V_L / V_G ratio may be assumed to be constant. A fundamental and detailed model showing the time variations of these ratios is not warranted at this time, since in reality it is not easy to accept that a clear separation between the vapor and liquid phases actually exist in cells. It is may be more acceptable to assume a homogeneous dispersed medium for the cell contents during extraction.

Sensitivity Analysis for SI-PMTs Model. The behavior of the SI-PMTs model was obtained by integrating the set of ODE's numerically. Base values for all model parameters were taken from the literature related to supercritical fluids (6). To help clearly discriminate among the results, the base parameter values were slightly altered. The pictorial representation of the SI-PMTs model (Figures 3 and 4) designates two possible passages of the SF solvent containing the extractable species throughout the plant matrix. The solvent and its contents once out of the cell walls, may either combine with the fresh solvent stream before entering a different cell (Figure 3) or may directly penetrate another cell (Figure 4). But, in both cases it is assumed that at least a fraction of the fresh solvent will be involved in the extraction process, as indicated through a split stream.

Considering Figure 3, a sensitivity analysis is done to investigate the effect of V_L / V_G ratio and fresh solvent feed flowrate in the SI-PMTs model, as shown in Figures 5-7. Dealing with the fixed split ratio case, at a higher V_L / V_G ratios the initial solute concentration in the liquid phase will be higher, hence requiring a longer period of time for extraction to extinction, as seen in both Figures 5 and 6. Furthermore, at a higher V_L / V_G ratio, the difference in gas concentrations between cell 1 and cells 2 and 3 is more, since the exit solvent phase is closer to saturation, as shown in Figure 6. The effect of feed flowrate on gas and liquid concentrations at fixed inlet flowrate is shown in Figure 7. At low fresh solvent flowrates, it is impossible to differentiate among the cell exit concentrations for both gas and liquid phases. At 1.0 cm^3/s feed flowrate, this difference among the cells is very clear; whereas at high solvent flowrates due to the access of fresh solvent to cells 2 and 3, a dilution occurs in the gas concentration profiles, as seen in Figure 7.

Considering Figure 4, the results obtained from the SI-PMTs model for various SC-CO₂ extraction conditions are shown in Figures 8 and 9, in which only the exit concentrations of cell 3 are plotted. Figure 8 accounts for the case of fixed-split condition at increasing flowrates of the fresh solvent ranging from 0.05 to 10.0 cm^3/s , where V_L / V_G ratio in each PMT is taken to be 5. It is obvious that increasing the flowrate of the fresh solvent will also increase the inlet flowrate of pure SF solvent entering the system at fixed-split ratio of 0.8, hence causing a dilution in the solute concentration in both phases. Figure 9 accounts for the case of fixed inlet flowrate of 0.01 cm^3/s at fresh solvent flowrates of 2.0 and 10.0 cm^3/s , where V_L / V_G ratio in each PMT is taken to be 5. It is observed that exactly the same concentration profiles

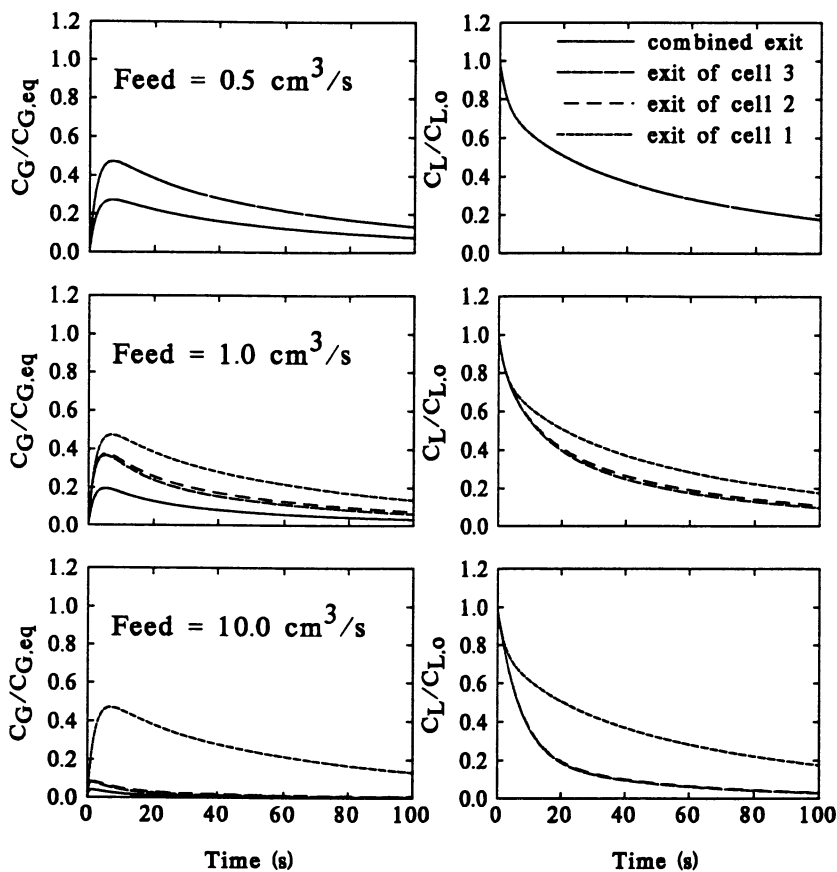


Figure 7. Effect of feed flowrate on gas and liquid concentrations at fixed split ratio of 0.6 and $V_L/V_G = 5$ (refer Figure 3).

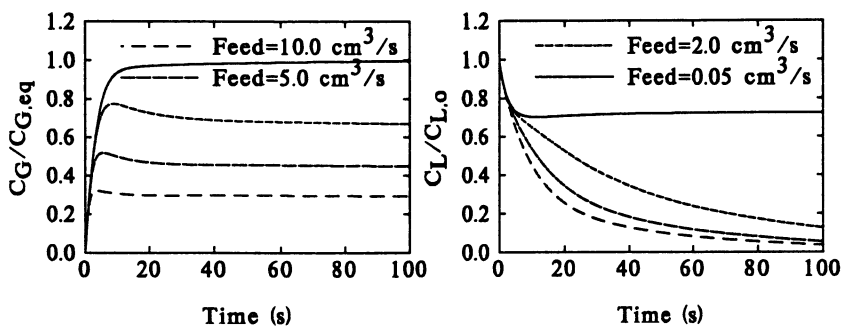


Figure 8. Exit concentration of cell 3 at fixed split ratio of 0.8 and $V_L/V_G = 5$ (refer to Figure 4).

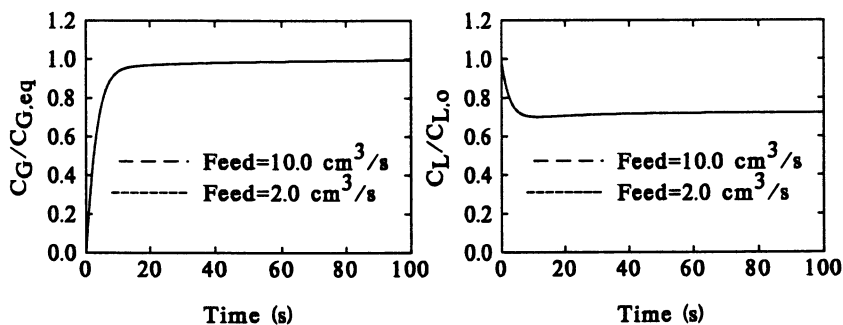


Figure 9. Exit concentration of cell 3 at fixed inlet flowrate of 0.01 cm³/s to the system and $V_L/V_G = 5$ (refer to Figure 4).

are obtained for both flowrates. This is an indicative of the phenomena that increasing the flowrate of the SF solvent does not at all increase the amount of material extracted. The data reported by Özer et al. (7), also clearly shows that only a fraction of the SC fluid solvent diffuses into the cellular structure of the plant material, the rest simply bypasses. This observation indicates that external-mass transfer resistances may not always control the extraction. If the external mass-transfer resistances were controlling, increasing the interparticle solvent velocity would have an effect on the external mass-transfer resistance, and hence, would have proportionally increased the mass-transfer rate (extraction yield per mass of solvent used).

Conclusion

Two mathematical models: Cellular Permeable-Tube Arrays (CPTA) model and Serially-Interconnected Perfectly-Mixed Tanks (SI-PMTs) model were proposed in an attempt to explain the release mechanisms of extractable compounds from plant matrices during supercritical extraction by SC-CO₂. In this work, the extraction of desirable compounds from the plant matrix in the presence of SC-CO₂ is believed to take place in a manner which is a very close to the CPTA model, which is a more detailed representation of the phenomena modeled as SI-PMTs. The CPTA model describes the extraction phenomena by taking into consideration the inherent plant structures along with characteristics of the plant materials more realistically. The predicted extraction behavior of the simple SI-PMTs model (with three stages) showed directional coincidence with available experimental data. The model equations derived are valid for a single component system, but could easily be extended to a multicomponent system, via thermodynamic modeling.

Legend of Symbols

a_{AW}	interfacial area for sorption in the wall region
a_{GL}	gas/liquid interfacial area for extraction
a_{SG}	gas/solid interfacial area for sorption
a_{SL}	gas/solid interfacial area for sorption
a_{PT}	interfacial area for tube-to-pellet region mass transfer
C_b	bulk solvent-phase concentration of solute within fixed-bed-type extractor
C_G	concentration of solute in the solvent-phase region
C_G^o	initial concentration of solute in the solvent-phase region
$C_G^*(C_L)$	gas-phase concentration of solute in equilibrium with liquid-phase concentration
C_L	concentration of solute in the liquid-phase region
C_L^o	initial concentration of solute in the liquid-phase region
C_p	concentration of solute in the pellet-like intertubular region
C_p^o	initial concentration of solute in the pellet-like intertubular region

$C_p^*(C_L)$	concentration of solute in the pellet-like intertubular-region at equilibrium with solute concentration in the liquid-phase at the tube ends
C_W	concentration of solute in the wall region
C_W^o	initial concentration of solute in the wall region
\bar{C}_W	surface-area averaged wall-region concentration of solute
$C_{G(n)}^*$	gas-phase concentration of solute in equilibrium with liquid-phase concentration in the n^{th} cell
$C_{G(n)}$	gas-phase concentration of solute in the n^{th} cell
$C_{L(n)}$	liquid-phase concentration of solute in the n^{th} cell
D_{Gz}, D_{Gr}	gas-phase axial and radial dispersion coefficients
D_{Lz}, D_{Lr}	liquid-phase axial and radial dispersion coefficients
D_{pz}, D_{pr}	axial and radial dispersion coefficients in the intertubular region
D_{Wz}, D_{Wr}	axial and radial dispersion coefficients in the permeable wall region
$F_{(n)}$	inlet flowrate of fresh solvent to n^{th} cell
K_{AW}	mass-transfer coefficient for sorption in the wall-region
K_{LP}	mass-transfer coefficient for liquid/intertubular-region mass transfer
K_{PT}	mass-transfer coefficient for tube-to-pellet region mass transfer
K_{OGL}	overall gas/liquid mass-transfer coefficient
K_{SG}^p	solid/gas mass-transfer coefficient
K_{SL}^p	solid/liquid mass-transfer coefficient
L_p	pellet-like intertubular region length
L_T	tube length
$M_{(n)}$	outlet flowrate from n^{th} cell
$\bar{q}_{G(n)}$	average adsorbed-phase concentration from gas-phase in the n^{th} cell
$\bar{q}_{L(n)}$	average adsorbed-phase concentration from liquid-phase in the n^{th} cell
$q_{G(n)}^*$	equilibrium loading from gas-phase
$q_{L(n)}^*$	equilibrium loading from liquid-phase
\bar{q}_W	average adsorbed-phase concentration of the solute per volume of the wall region
\bar{q}_W^o	average initial loading of solute within the wall region
$q_W^*(C_W)$	adsorbed-phase concentration of solute in the wall region at equilibrium with solute concentration
$R_{(n)}$	fraction of the outlet flowrate of n^{th} cell
R_i	inner radius of tubes
R_o	outer radius of tubes
R_p	radius of the pellet-shaped intertubular region
S	total flowrate of the inlet stream entering the n^{th} cell
$S_{(n)}$	total inlet flowrate to n^{th} cell

t	time
u_G	interstitial gas-phase velocity
u_p	interstitial velocity of solvent within the pellet region (extratubular region)
V_L	liquid volume
V_G	gas volume
z, r	axial and radial coordinates for the fixed-bed-type extractor
z_p, r_p	axial and radial coordinates within the pellet region
z_T, r_T	axial and radial coordinates within the solvent-phase region
$Z_{(n)}$	mole fraction of solute in gas-phase entering n^{th} cell
Z_0	feed concentration
ε_G	volumetric holdup of gas-phase per volume of tube based on R_0
ε_L	volumetric holdup of liquid-phase per volume of tube based on R_0
ε_W	volume of void space within the wall region per volume of tube based on R_0 , such that $\varepsilon_T = \varepsilon_G + \varepsilon_L + \varepsilon_W$, ε_T is the volume of total void space of the tube per unit volume of tube

Acknowledgments

The authors would like to thank Prof. Amable Hortaçsu of the Department of Chemical Engineering, Boğaziçi University, for her help and suggestions in the formulation of the CPTA Model. Financial support of the Turkish State Planning Organization, (DPT), (Project: 91K120480), and of the Boğaziçi University Research Foundation (Project: 94A0525) are gratefully acknowledged.

Literature Cited

- (1) Madras, G.; Thibaud, C.; Erkey, C.; Akgerman, A. *AIChE J.*, **1994**, *40*, pp.777
- (2) Goto, M.; Sato, M.; Hirose, T. *J.Chem.Eng.Japan*, **1993**, *26*, pp.401
- (3) *Plant Biology Today: Advances and Challenges*; Jensen, W. A.; Kavaljian, L. G., Eds.; 2nd. Ed., Wadsworth Pub. Co., Inc., Belmont, Ca. 1967
- (4) *Plant Vacuoles*; Marin, B., Ed.; NATO ASI Series 134; Plenum Press: New York, NY, 1987
- (5) Strasburger, E.; Noll, F.; Schenck, H.; Schimper, W. In *Strasburger's Textbook of Botany*; Translated by, Bell, P. R.; Coombe, D. E., New English Edition, Longman Inc. New York, NY, 1976
- (6) Akman, U., "Simultaneous Extraction and Sorption Under Supercritical Conditions", Ph.D. Dissertation, University of South Florida, 1991
- (7) Özer, E. Ö.; Effects of Process Variables on Yield and Composition of Spearmint Oil Extracted under Supercritical Fluid Conditions", MS Thesis, Boğaziçi University, 1993

RECEIVED May 31, 1995

Chapter 26

Supercritical Fluid Processing in the Pulp and Paper and the Forest Products Industries

Erdogan Kiran

Department of Chemical Engineering, University of Maine,
Orono, ME 04469-5737

The application areas of supercritical fluids in the pulp and paper and the forest products industries are reviewed. In particular, use of supercritical fluids in delignification, waste treatment, chemical conversion, recycling, and impregnation are discussed. Specific results on high pressure delignification of wood with acetic acid-water-supercritical carbon dioxide mixtures are presented. Chemical changes as well as morphological changes in the cell wall structure are discussed. A new approach for direct impregnation of wood with high molecular weight polymers is presented. Specific results for impregnation of red spruce with polyethylene are discussed in terms of miscibility and phase separation conditions for the polymer solutions and their viscosities in near and supercritical fluids.

The *supercritical fluid state* refers to a special state of ordinary fluids which is reached when the temperature and the pressure are increased beyond some critical values. In this state, the distinction between a liquid and a gas disappears, and many properties such as density, viscosity, and diffusivity become readily adjustable. A wide range of properties from *gas-like* to *liquid-like* become accessible by simple manipulations of pressure and temperature without entering the two-phase region of the fluid. Depending upon the pressure or density, different solvent characteristics become accessible by the same fluid. Such adjustable properties make supercritical fluids very attractive as process fluids or reaction media for many industrial applications (1-3). A particularly important case is the pulp and paper and the forest products industries which constitute the focus of the present paper.

0097-6156/95/0608-0380\$12.50/0
© 1995 American Chemical Society

At the University of Maine, we maintain a broad perspective for high-pressure processing and utilization of supercritical fluids in this particular industry. We are evaluating these fluids for applications involving both chemical transformations and physicochemical modifications of wood. The ultimate objective is to provide alternative processing schemes for improved utilization of wood and fiber resources while minimizing adverse environmental impact.

The present paper is structured in three parts. Part I provides a brief review of wood structure to demonstrate why supercritical fluids are important for this industry and how they can be used. Part II is devoted to topics of relevance to the pulp and paper industry with specific discussions on delignification, mill effluent treatment, chemical conversion and recycling. Part III is devoted to wood modification and preservation and presents a new methodology for direct impregnation of wood with high molecular weight polymers and additives.

Part I. Wood Structure and Rational for Use of Supercritical Fluids

In order to appreciate why supercritical fluids are of great interest in processing of wood, it is important to review the chemical composition and ultrastructure of wood.

Chemically, wood consists of cellulose (40-45 % by weight of wood), hemicelluloses (20-30 %), lignin (20-30 %), extractives (2-4%), and inorganic matter (less than 1%) (4, 5). The relative amounts of these constituents vary with wood species. Cellulose, hemicelluloses and lignin are all polymeric in nature. More specifically, cellulose is a linear polysaccharide involving 1-4 glucosidic linkages. It is highly crystalline. Hemicelluloses are also polysaccharides, but unlike cellulose, they are of lower molecular weight, involve heterogeneous building blocks (containing both pentose and hexose sugars) and are amorphous in nature. Lignin is a non-linear non-crystalline aromatic polymer network consisting of phenyl propane units joined by carbon-carbon or carbon-oxygen linkages. Extractives are the low molecular weight compounds of various types which are readily extractable from wood by water or organic solvents. Within this group, there are the aliphatic compounds (such as fats and waxes), terpenes and terpenoids (such as volatile oil turpentine and resin acids diterpenes), and phenolic compounds (such as tannins and flavonoids). Alkali and earth alkali carbonates are the major ash components of wood, reflecting the inorganic matter.

Physically, wood is a porous material composed of elongated hollow cells (fibers). Typical cell dimensions for a softwood tracheid are 3 mm length, 0.03 mm width and 3 μm cell wall thickness. The cells are held together by an intercellular substance. This is known as middle lamella which contains mostly lignin and pectic substances. The cell wall displays a layered structure and contains different amounts of cellulose, hemicelluloses and lignin. Even though the middle lamella has the highest lignin concentration, the majority of lignin (about 70-80%) is located in the cell walls (4, 5). Another feature of the cell walls is that there are openings known as

pits or pit holes which permit connectivity (for fluid transport) between adjacent cells.

From a practical perspective wood is a versatile composite natural material. It serves as a source for chemicals, fuel, and specialty products. It is the primary source for pulp and paper products, and is used directly or in modified forms as structural or specialty materials. Depending upon the end-product of interest, the processing of wood (and lignocellulosic materials in general) involve either chemical transformations or physicochemical modifications.

Examples of chemical transformations include (a) specific extractions to produce wood-based chemicals, (b) specific reactions and extractions to produce cellulose or pulp suitable for papermaking, or for preparation of cellulose derivatives, (c) specific treatment to facilitate digestibility by biological agents, (d) specific reactions and extractions to produce lignocellulosic matrices with altered microstructure and porosity, and (e) specific reactions for controlled gasification, liquefaction, or char formation.

Examples of physicochemical modifications include treatment for improved properties such as (a) dimensional stability and weathering characteristics, (b) resistance to biodegradation, (c) resistance to chemicals or other environmental factors such as photodegradation, (e) fire resistance, (f) mechanical strength, and (g) uniformity or consistency of properties and predictability of behavior.

Whatever the mode of transformation, accessibility of wood components with either the reactants, the extraction fluids, or the modifying chemicals is a central factor. The interactive fluids or chemicals must be able to enter the cell lumens and the cell walls. For example, for effective delignification, which is key to pulping and bleaching operations, reactants must diffuse into the middle lamella region and into the cell walls to react with lignin, and the products must then diffuse out of the cell wall into the bulk fluid phase.

Selectivity of the transformations is another important consideration. For example, in delignification processes, it is highly desirable to achieve lignin removal with minimal damage to the cellulosic fractions. In wood treatment processes, it is important to achieve uniformity of additive distribution without causing cell collapse during the impregnation stage.

Another central issue which is common to all industrial operations is the minimization of the negative impact, if any, of a given process on the environment, in particular on the air and water quality. For example, there is a great demand for environmentally benign, sulfur and chlorine-free pulping and bleaching processes in the pulp and paper industry. Equally important is the minimization of the toxic effluents from sites where wood is treated with chemicals such as pentachlorophenol for preservation against biodeterioration.

With these considerations in mind, suitability of supercritical fluids for processing of wood and lignocellulosic materials can be better appreciated. Low viscosities of supercritical fluids improve penetration. Liquid-like densities improve dissolution. Pressure and temperature, or more generally the density, and the fluid composition become adjustable tuning parameters for selectivity. In this context, composition of the process fluid mixtures is used as a tuning parameter to (a) lower

operational temperatures, (b) reduce the amount of less desirable solvent, (c) improve selectivity, (d) introduce reactivity, and (e) facilitate overall processing.

Primary application areas for supercritical fluids in the pulp and paper and the forest products industries include:

- (a) selective extraction of wood based chemicals,
- (b) unconventional pulping and bleaching processes,
- (c) unconventional bioconversion processes for fuels and chemicals,
- (d) recovery from waste streams,
- (e) toxic materials removal or destruction,
- (f) improved swelling and impregnation with chemicals or additives,
- (g) modifications of wood or wood fibers as materials, and
- (h) recycling.

which are at different stages of development.

From a historical perspective, earlier studies on the use of supercritical fluids with lignocellulosic materials were essentially devoted to extraction of low molecular weight substances from plant materials (6-9) and liquefaction and gasification of wood (10-13). Specific examples include extraction of tall oil and turpentine from wood with supercritical carbon dioxide (7), extraction of resins and waxes from wood bark with supercritical carbon dioxide or propane (9), extraction of wood with organic solvents such as supercritical acetone, tetrahydrofuran, dioxane, and toluene as an alternative to distillation (10), complete liquefaction of cellulose in supercritical acetone (11), and liquefaction of wood in supercritical methanol (13).

In recent years, other possibilities for novel processing of wood and lignocellulosics with supercritical fluids are being explored (14-39). These include extraction, delignification and pulping in pure fluids such as carbon dioxide, butane, ammonia, amines and alcohols, as well as binary and ternary mixtures such as alcohol-carbon dioxide, amine-nitrous oxide, alcohol-carbon dioxide-water, acetic acid-water-carbon dioxide (16-22); fractionation of commercial lignins such as the kraft lignin with binary mixtures of ethanol and carbon dioxide (21), degradative extraction of lignin with alcohols such as methanol (23), butanol and isopropanol (24), delignification with ammonia (25) and dioxane (26), liquefaction of wood and cellulose in supercritical water (27, 28), treatment of pulp mill sludges by supercritical water oxidation (29-31), non-catalytic conversion of cellulose in supercritical water (28), physical changes in wood after extraction with supercritical carbon dioxide (32-35), and incorporation of monomers such as methylmethacrylate (36) and wood preservatives (37) from supercritical carbon dioxide streams. Some recent activity on extractions are devoted to specific compounds such as extraction of taxol with carbon dioxide and carbon dioxide-ethanol mixtures (38), and extraction of tropolones from Western red cedar wood with carbon dioxide (39). Taxol which is a diterpene alkaloid, is of interest because it is used as an anti-cancer drug. Tropolones are of interest because of toxicity to fungi and insects and are the basis for the well known resistance of Western red cedar wood to bacterial decay.

Part II. Supercritical Fluid Processing in the Pulp and Paper Industry

Conventional Delignification and Pulping. The majority of the chemical pulp in the world is produced by the Kraft process. It involves three basic steps, namely cooking (pulping), washing and chemicals recovery. Delignification is achieved under alkaline conditions using an aqueous solution of sodium hydroxide and sodium sulfide as the cooking chemicals (4, 5). Cooking conditions of around 170 °C and 1 MPa for 2 to 4 hours are typical. The pulp produced is washed, bleached if necessary, and used in manufacturing a wide variety of paper grades. In the recovery cycle, the effluents from the digester which contains the dissolved lignin and other components of wood are first combined with the effluents from the washing steps. The combined stream (referred to as black liquor) is then concentrated in multiple effect evaporators and burned in a special furnace to recover heat and further processed to recover the inorganic cooking chemicals. The Kraft recovery cycle is complex and is highly capital and energy intensive. Furthermore, it is a bottle-neck in the process since the energy and the chemicals balance of the mill are intimately linked to the recovery cycle which puts limitations on the mill capacity and the operational flexibility. The Kraft process is versatile in processing of both softwood and hardwood species and produces high quality pulp. However, because of the use of sulfur based chemicals, it leads to air pollution with emissions of malodorous substances such as mercaptans and other reduced sulfur compounds, and because of the chlorine-based bleaching sequences employed to achieve desired levels of brightness, it leads to additional environmental problems with formation of chlorinated lignin fragments causing water pollution.

There is a continual search to overcome the problems associated with the Kraft process. Among the various approaches, delignification processes using organic solvents are at an advanced stage (40-42). The Allcell process which is based on aqueous ethanol has been advanced to a semi-commercial state in Canada. The process uses a 50/50 mixture of ethanol and water at 195 °C as the pulping liquor at 2.7 MPa. Even though pulps comparable to Kraft pulp are reported to be produced, the process is usable primarily with hardwood species (such as aspen). Processing of softwood species (such as spruce and pine) is a general problem with conventional solvent-pulping processes. Current practice is to employ a two-stage pulping scheme in which the first stage is extraction with ethanol or methanol in water (about 50/50 mixture) at elevated temperatures (190 °C) which is then followed by the second stage cooking at somewhat lower temperatures (around 170 °C) with aqueous alkali (sodium hydroxide at around 20 % concentration). The Organocell process which is semi-commercial in Germany is an alkaline methanol pulping process based on this methodology. Even though the process is sulfur-free and applicable to both softwood and hardwood species, the conventional Kraft recovery process is still required because of the use of alkali. Another solvent-pulping process which is being developed in Germany is the acetosolv process. Delignification is achieved with a mixture of acetic acid (93 % by volume) and water (6.8% by volume) in the presence of an acid catalyst (0.2 % hydrochloric acid) at the reflux temperature of the mixture

at 108 °C and 0.1 MPa. Without the acid catalyst, pulping of softwood species is difficult with this pulping process also.

High Pressure and Supercritical Delignification. Supercritical delignification and pulping is a more recent research activity (14, 16-22, 25, 26). The majority of the systematic work in this area has been conducted in our laboratory (16-22). The approach is to solubilize low molecular weight extractives and the high molecular weight lignin in an extractor/reactor operated at high pressures and then recover them after the extraction stage by reducing the dissolving power of the fluid through pressure reductions. It is envisioned that the eventual process may involve multiple pressure reduction stages to separate a range of wood based chemicals as well as lignin, depending on their solubility thresholds.

Even though supercritical pulping is far from commercialization, it is important to highlight the drive and motivations for research and development. The following factors are especially important:

(1) Corresponding to pulping, washing and spent liquor recovery stages in the Kraft pulping process, supercritical fluid pulping will also involve three basic steps, namely extraction, separation by pressure reduction and recompression / recycling of the process fluid. However, the possibility of replacing the washers, multiple effect evaporators, recovery furnace, lime kiln, and caustisizer units that constitute the spent liquor treatment in the Kraft process by simply a phase separation unit is very attractive. Not only the plant land-size requirements can be drastically reduced, but also the recovery bottle-neck which causes the pulp and paper mills to be built with excess capacity (in anticipation that pulp productivity may increase in the future) may be removed.

(2) The possibility of isolation of the wood-based chemicals in solvent-free fractionated forms will facilitate separations and permit their use as chemical feedstocks, or fuels to generate steam and electricity. Since the precipitated fragments will not contain the inorganic chemicals encountered in the conventional pulping operations, they will be of greater value as raw materials or low-ash fuel. In the Kraft process, inorganics constitute about 20 % of the Kraft black liquor solids. In the absence of such inorganic loadings, precipitated fragments can be burned in ordinary steam generators (power boilers) and eliminate the need for capital-intensive recovery boilers. Kraft recovery furnaces recover only 60% of the potential heat value of fuel as compared to over 80% for a conventional power boiler (43). Therefore, if the fragments are used as fuel, greater heat generation would be possible due to higher efficiency of power boilers.

(3) Because of higher diffusivities and lower viscosities of supercritical fluids, cell-walls of wood can be penetrated and the dissolved fragments can be removed faster compared to conventional pulping processes. As a result, along with an increased production capacity which may reduce the digester size, more uniform delignification may be achieved leading to higher yields of screened pulp. Furthermore, a separate wood impregnation stage prior to pulping may not be needed.

(4) By using non-sulfur, non-chlorine chemicals, and minimizing the effluent streams, adverse effects on the environment may be greatly reduced.

Our approach is indeed to work with non-sulfur, non-chlorine chemicals and use binary or ternary fluid mixtures in which one of the components has special

reactivity and / or selectivity towards lignin. This is because lignin is a crosslinked network polymer which cannot be dissolved in any known solvent without fragmentation. Other fluid components include a fluid with low critical temperature which can lower operational temperatures while maintaining supercritical conditions, and may also act as the carrier fluid or post-extraction washing (or flushing) fluid. Operation at relatively low temperatures is desirable to prevent thermal degradation of cellulose and hemicelluloses. Water is also considered as a component since it arises naturally from the moisture content of wood.

Investigations on different wood species and model compounds representing wood based polymers in selected supercritical fluids conducted in our laboratory have shown that extraction efficiencies can be modulated using fluid mixtures (17, 18, 22). Extracted lignins can indeed be separated from the solvent phase and collected as essentially solvent-free solids by reducing the fluid pressure after the extraction stage, which as stated above is of great importance for simplifying recovery cycle.

Among recent activity in our laboratory is the delignification of red spruce using ethanol-water-carbon dioxide and acetic acid-water-carbon dioxide mixtures. Effect of solvent composition, temperature, pressure and extraction times have been evaluated (21, 22). Acetic acid containing systems have proved to be particularly interesting and are discussed below.

The critical temperatures and pressures are 304.1 K and 7.38 MPa for carbon dioxide, 592.71 K and 5.786 MPa for acetic acid, and 647.3 K and 22.12 MPa for water. Binary mixtures of acetic acid and water are known to show a continuous critical line between the critical points of the pure components - critical temperatures are in between, while the critical pressures for the mixtures pass through a maximum around 17 MPa (44). For the carbon dioxide water mixtures, the critical line is not continuous and critical pressures increase very rapidly with addition of carbon dioxide to water (45). Ternary mixtures are known to display three phase regions (46).

In these fluid mixtures, carbon dioxide is the component with the low critical temperature, while acetic acid or acetic acid - water mixtures function as the active delignifying agent. As already mentioned above in connection with the acetosolv pulping process, acetic acid can be an effective pulping chemical, but under normal conditions requires the use of either an acid catalyst such as HCl or high temperatures (around 220 °C) without which softwood species are difficult to pulp.

Table I is a comparison of the delignification efficiency of red spruce (a softwood) with acetic acid-water binary mixtures at low (1.4 MPa) and high (25 MPa) pressures (22). The extractions were carried out at 180 °C for 3 hr. No catalysts were added to the system. Selective delignification, at levels greater than 90%, were achievable at high pressures with mixtures containing 73 to 41 mole % acetic acid. Outside this range, selectivity is greatly reduced even at high pressures. Comparing the results at 25 MPa to 1.4 MPa shows that at all compositions delignification is very much increased with application of pressure, while leading to still respectable pulp yields around 50 %. Table II shows more explicitly the effect of pressure on delignification with the mixture containing 73 mole % acetic acid which has been

found to be most selective for lignin. With this mixture, high degree of delignifications are achieved even by about 7 MPa pressure. Indeed, the IR spectra shown in Figure 1 shows that the characteristic lignin peak at 1510 cm^{-1} is essentially absent in the wood after extractions at pressures above 3.4 MPa.

Table I. Delignification of red spruce with acetic acid / water binary mixtures (180 °C and 3 hr extraction; solvent-to-wood ratio of 5/1)

Solvent composition Acetic acid (mole %)	% Delignification ^a		% Pulp Yield ^b	
	1.4 MPa	25 MPa	1.4 MPa	25 MPa
100	47	59	79	71
73	26	93	75	51
41	38	91	65	48
3	0	12	75	56

^aBased on the total lignin in the initial bone-dry wood prior to extraction

^bFraction of wood remaining after extraction

Table II. Delignification of red spruce with acetic acid / water binary mixture (73 mole % acetic acid, 180 °C, 3 hr extraction; solvent-to-wood ratio of 5/1)

Extraction Pressure (MPa)	% delignification	% pulp yield
1.4	26	75
3.4	63	60
6.8	82	60
13.7	89	53
25	93	51

Figure 2 compares the electron micrographs of red spruce wood before and after extraction at different pressures with the acetic acid/water mixture containing 73 mole % acetic acid. They are shown at two levels of magnification which demonstrate the changes both in the overall appearance of the cell walls and the changes that take place in the middle lamella region between the cells. The removal of lignin from the middle lamella leads to the separation of the adjacent cell walls, and the removal from the cell wall leads to the loss of rigidity in the cell walls both of which are visible in these micrographs. After extractions at 13.7 MPa, cell wall integrity appears to be lost indicating removal of essentially all lignin not only from the middle lamella but also from the cell wall at and above these pressures. This is in concert with the high delignification levels shown in Table II at these pressures.

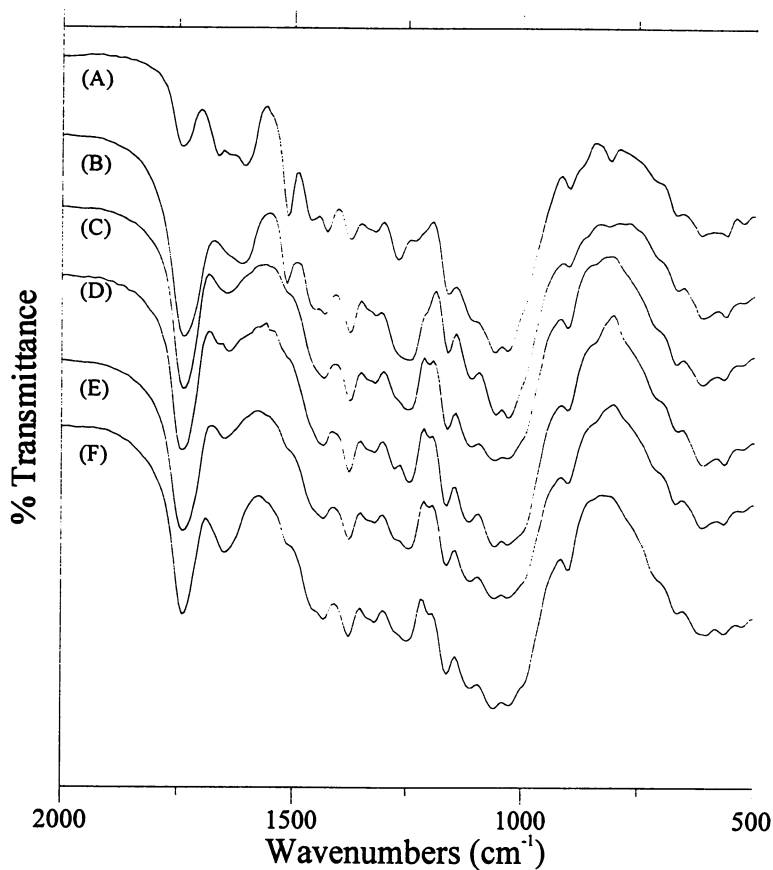


Figure 1. IR spectra of red spruce before (A) and after 3 hr extraction at 180 °C with acetic acid-water mixtures containing 73 mole % acetic acid at 1.4 (B), 3.4 (C), 6.8 (D), 13.7 (E) and 25 (F) MPa pressure.

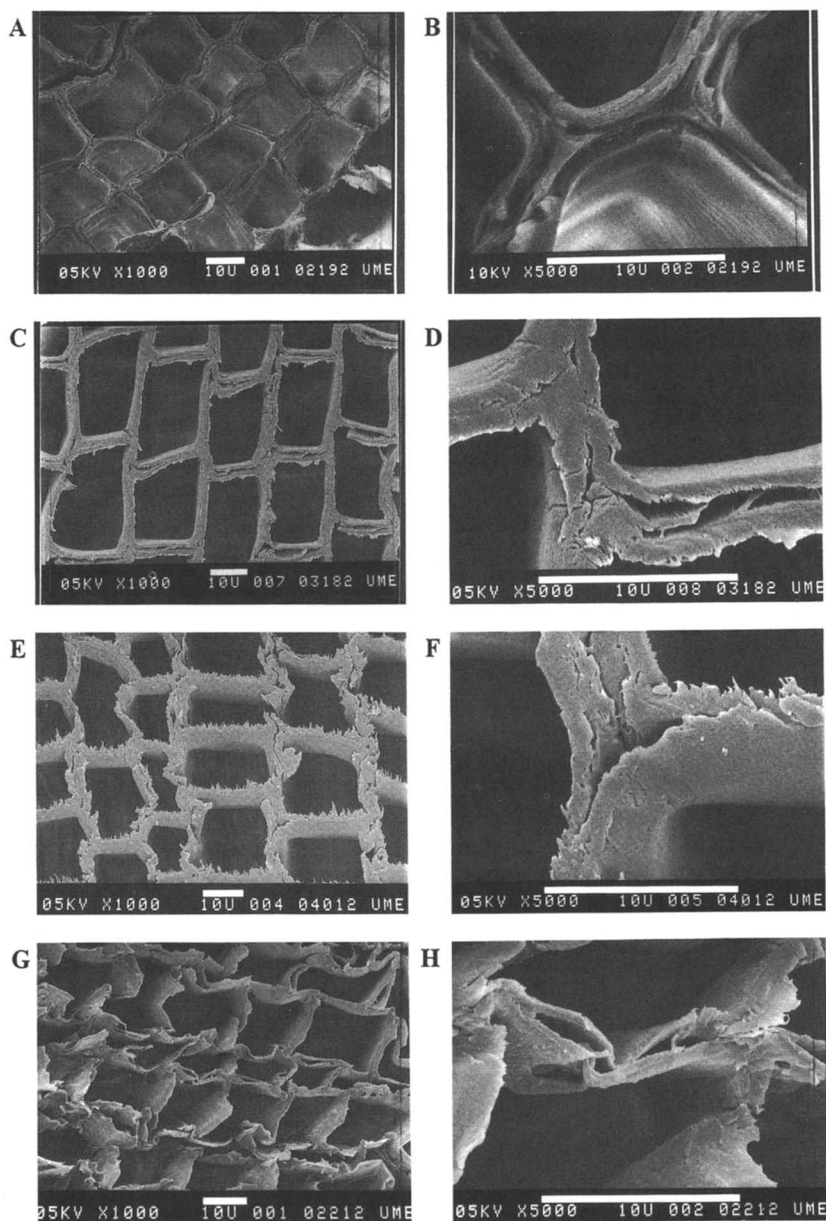


Figure 2. SEM micrographs of red spruce before (A, B), and after extractions with acetic acid-water mixtures containing 73 mole % acetic acid at 3.4 MPa (C, D), 13.7 MPa (E, F) and 25 MPa (G, H) at a magnification of 1000 (A, C, E, G) and 5000 (B, D, F, H).

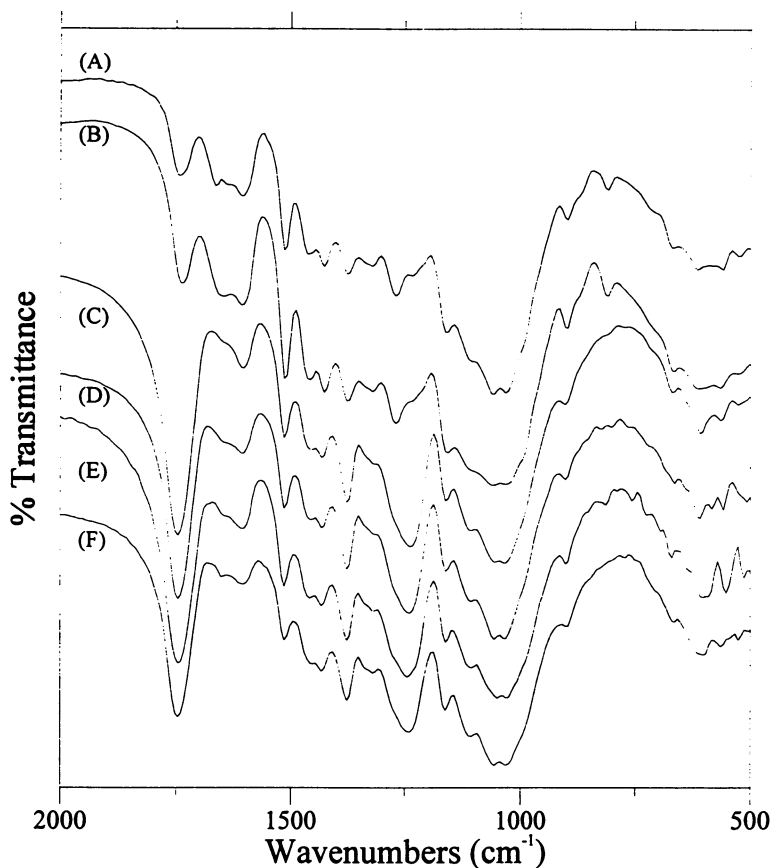


Figure 3. IR spectra of red spruce before (A) and after extractions with ternary mixtures of carbon dioxide, acetic acid and water containing 100 (B), 81.6 (C), 52 (D), 11(E) and 0.0 (F) mole % carbon dioxide and while maintaining a constant mole ratio of 73/27 for the acetic acid-water fraction.

For this system, we have also evaluated the effect of extraction time and temperature. Delignification level reaches 75 % within 1 hour at 180 °C at 25 MPa. Cell wall softening becomes more apparent at extraction times of 2 hour or greater. If temperature is lowered below 150 °C, delignification is observed to be dramatically reduced. At 120 °C, delignification after 3 hr extraction is only around 20 %. This reflects the significance of being above the glass transition temperature of lignin in conducting the extractions. Softening temperature of lignin is in the range from 160-185 °C [5].

Clearly mixtures of acetic acid and water are not supercritical at the conditions evaluated. We have introduced supercritical carbon dioxide to this delignification mixture and evaluated the lignin extraction process. Table III shows the results. These experiments represent the case where the internal acetic acid / water ratio is maintained at 73/27 mole ratio in all mixtures while different amounts of carbon dioxide were introduced and extractions were carried out at 25 MPa for 3 hr at 180 °C. (The phase information for these mixtures have not yet been documented, however it is likely that the mixtures were in a one-phase miscible (liquid) region). As shown in the table, in the presence of carbon dioxide delignification level decreases. The IR analysis of the wood after extractions shown in Figure 3 confirm these by the appearance of the 1510 cm⁻¹ lignin band at CO₂ additions greater than about 10 %. This is because of the carbonic acid formation with water which causes hydrolysis of hemicellulose and cellulose fractions and thereby lowers the overall selectivity of the extraction for lignin.

Table III. Delignification of red spruce with acetic acid / water / carbon dioxide ternary mixtures (acetic acid / water mole ratio of 73/27, 180 °C, 3 hr extraction; solvent-to-wood ratio of 5/1)

Solvent composition (mol % CO ₂)	% delignification	% pulp yield
0	93	51
11	89	57
52	49	72
81.6	13	83

Due to the presence of water in wood, delignification fluids which are not only sulfur and chlorine -free, but can also tolerate water are preferred. Water and most organic solvents having high critical temperatures put restrictions on operation at supercritical conditions. So far only nitrous oxide and carbon dioxide have been explored to any extent as low critical temperature supercritical components introduced into the extraction fluid mixtures. Even though cellulose and hemicellulose hydrolysis in near and supercritical fluids is by itself very intriguing,

for pulping operations carbon dioxide addition levels cannot be chosen freely. Nonetheless, it is important to note that even at low additions, carbon dioxide introduces the option for process flexibility in terms of removal of acetic acid or alcohols from the extracted wood. After extractions, passing only carbon dioxide through the reactor helps remove the residual solvent. Current research on delignification fluid mixtures is being directed to other low T_c fluids (other than carbon dioxide) to minimize hydrolysis.

Supercritical Fluid Processing of Waste Streams. Supercritical fluids are being explored for processing of waste streams with different objectives. These include disposal of mill sludges for environmental remediation, recovery of by products from conventional pulp mill effluents, and waste paper recycling.

Treatment of Mill Effluents. Because of the environmental concerns, considerable activity recently has been devoted to supercritical water oxidation processes that are aimed at disposal of pulp mill sludges and destruction of specific compounds such as dioxins which forms in chlorine-based bleaching processes (29-31). Supercritical water oxidation processes are carried out at temperatures above the critical point of water (374 °C and 22 MPa). Supercritical water is a very good solvent for organic materials as well as gases, and at high pressures, oxidation without char formation becomes possible. Organic materials are converted to carbon dioxide and inorganic acids. Nitrogen containing organic compounds are converted to nitrogen gas or nitrous oxide. Recent studies report essentially total destruction of dioxins and organic halides in pulp mill sludges at 500-650 °C at around 25 MPa. Supercritical water oxidation is indeed a viable alternative to incineration of waste which is essentially free of harmful emission and / or discharge.

Chemical Conversion of Cellulosic Wastes. Supercritical and near-critical water in the absence of oxygen is recently being explored for chemical conversion of biomass or waste cellulosic materials (28, 47, 48). Glucose yields of about 71 % have been reported at 488 K, 34.5 MPa and 0.05% sulfuric acid (47). More recently, at 673 K and 37 MPa over a 10 minute reaction time, complete liquefaction of cellulose has been reported in the absence of any added acid catalyst (28, 48). The decomposition products include sugars such as glucose and fructose. Hydrolysis rates much faster than comparable acid catalyzed reactions are indicated. At 40 MPa, and 653 K over a residence time of 25 msec, 75 % glucose yields have been reported (48).

Paper Recycling. A novel supercritical fluid methodology is under development in our laboratory for recycling of paper and paper products. New opportunities exist for cleaning, separation and recovery of secondary fiber from wastes.

Part III. Supercritical Fluid Processing in the Forest Products Industries

An especially important area of activity in the forest products industries is the modification of wood and wood fibers for production of advanced lignocellulosic composite materials. Many of the desirable properties such as dimensional stability, resistance to chemicals or degradation, and improved physical strength characteristics are achievable through incorporation of polymers and/or special additives into the wood matrix and the fiber cell walls.

The traditional method of incorporating a polymer into the wood matrix invariably involves impregnating the wood with either oligomers (in the case of phenol-formaldehyde modifications) or monomers (in the case of vinyl polymer modifications) followed by post-curing by radiation or catalyst-heat processes (49-54). Direct impregnation with a polymer is difficult due to the difficulty in finding suitable solvents for each polymer, and the high viscosities of polymer solutions in ordinary organic solvents. One exception is perhaps the bulking of wood with polyethylene glycol (which is water soluble up to a molecular weight of about 6000).

As part of a research program supported by the USDA, we have been exploring the possibilities for direct impregnation and in-situ precipitation or coprecipitation of polymers and/or additives from supercritical fluid solutions in the wood matrix. Opportunities exist to prepare advanced composites, with essentially any polymer or additive directly incorporated into the wood matrix. Incorporation of special additives are important for a number of end uses including fire retardancy, UV stability, or resistance to biodeterioration.

Supercritical Impregnation of Wood with Polymers and Additives. As an example, in the following sections, we present some results of direct impregnation of red spruce with polyethylene. Polyethylene is especially difficult to dissolve in ordinary solvents and there is much interest in the production of composites of polyethylene with lignocellulosic materials. Currently, such composites with polyolefins are produced primarily by melt blending of lignocellulosic fibers with the polymer [55-61]. These procedures are not adaptable for direct incorporation into wood. They are also limited by resin processing temperatures, since above 200 °C degradation of cellulose is enhanced. The possibility of impregnating wood using solutions of polyethylene and other polymers and additives in near- and supercritical fluids has been recently demonstrated in our laboratory. The methodology is based on fundamental measurements on miscibility, viscosity and phase separation conditions of polymers and additives in high pressure fluids.

Miscibility and Phase Separation. A fundamental task in impregnation studies is the identification of the pressure and temperature conditions for miscibility and phase separation for a given solvent / polymer system.

Studies on formation, modification and processing of polymers is a major focus area at the University of Maine (62). We have already published an extensive data base for the phase boundaries for polyethylene and other polymers in a wide

range of pure fluids and binary fluid mixtures at near and supercritical conditions (62-66). Figure 4 shows a pressure-temperature (P-T) diagram for polyethylene in n-pentane for different molecular weight samples. These are determined using a variable-volume view-cell which can be operated at pressures up to 1000 bar and 200 °C. It involves loading the cell with a known amount of polymer and the solvent and then adjusting the temperature and pressure until complete miscibility is achieved. Then, at any given temperature, changing the internal volume of the cell permits scanning a wide range of pressures without changing the solvent composition and helps determine the miscibility and phase separation conditions. Phase separation and complete miscibility are observable through two sapphire windows mounted on the cell.

The region above each curve corresponds to the one-phase regions; below is the phase-separated region. Pentane, which is not a solvent for polyethylene at ambient conditions, when pressurized, becomes an effective solvent. In general, the required pressure for miscibility and phase separation (demixing) depends on the nature of the polymer, type of the fluid, temperature, and the molecular weight and concentration of the polymer (62). For example, in n-butane, polyethylene dissolves less readily and requires much higher pressures for complete miscibility. Solutions of polyethylene in n-alkanes show lower critical solution temperatures (LCST), and the pressures required to achieve complete miscibility increase with increasing temperatures. In binary fluids containing carbon dioxide, the pressures for miscibility increase, and at high carbon dioxide additions, the behavior shifts to that of UCST (upper critical solution temperature), and demixing pressures decrease with increasing temperature.

Impregnations can thus be carried out by exposing the wood sample to be treated to the solution at conditions corresponding to complete miscibility regions for the polymer and the solvent, followed by pressure reduction which would induce phase separation and in-situ precipitation of the polymer from the solvent. In systems displaying LCST, precipitation of polymer can also be achieved at constant pressure by increasing the temperature. There is a high degree of flexibility in the operating temperatures and pressures using both the impregnation and phase separation stages.

Viscosity. For effective impregnations, information on the conditions leading to favorable transport properties, especially viscosity, is as important as the information on miscibility and phase separation for polymer solutions. In fact, high viscosity of polymer solutions has in the past prevented direct impregnation of wood with high molecular weight polymers from ordinary solvents.

Measurement of viscosities of polymer solutions at high pressures in near and supercritical fluids is another focus area at the University of Maine (67-70). Viscosities are being determined as a function of polymer concentration, molecular weight, solvent type, pressure, temperature and solution density. Figure 5 shows the viscosity of polyethylene ($M_w = 15,520$) solutions (1% by weight) in n-pentane at three different temperatures in the pressure range from 25 to 55 MPa. These measurements were conducted in a special high-pressure falling cylinder type viscometer that has been developed in our laboratory [67-68]. It consists of a

variable-volume cell to which a fall-tube is attached. Viscosities are determined by measuring the fall time of the sinker located in the fall tube.

Even though viscosities of these solutions increase with pressure, it is important to note that the viscosities shown in Figure 5 are less than 0.25 mPa.s. (1 mPa. s = 1 cp). Even for polyethylene samples of high molecular weight (i.e., $M_w = 420,000$) solution viscosities remain below 0.6 mPa.s over the same pressure/temperature interval. These viscosity levels are much lower than the viscosity of ordinary water which is 1 mPa.s. Clearly, low viscosities are important for impregnation of matrices from such solutions.

Impregnation Studies. Impregnation experiments were conducted using red spruce samples in the variable volume view-cell at pressures in the range from about 20 MPa to 50 MPa at different temperatures (at or below 150 °C) from homogeneous solutions in n-pentane and n-butane. The impregnation conditions were all above the critical pressure of the solvents, but the temperatures were near-critical for n-pentane and near-critical and supercritical for n-butane. Impregnation times ranging from 4 to 48 hours were tested.

These studies all showed that treatment of the wood species using homogeneous solutions of polymers in near and supercritical fluids results in impregnation with the polymer, and that upon reduction of the pressure, in-situ precipitation is achieved. Varying degrees of penetration and different morphologies ranging from lamellar crystals to almost spherical particles, or sponge-like morphologies have been obtained depending upon the details of the impregnation and the subsequent phase separation steps.

Figures 6 and 7 show the electron microscopic pictures of wood species impregnated with polyethylene from solutions in n-pentane at 25 MPa and 140 °C and in n-butane at 50 MPa and 150 °C, respectively. In Figure 6, the presence of polyethylene in the pit holes is easily identifiable. At high magnification, the lamellar crystalline structure of the deposited polyethylene (from n-pentane) is noted. The micrographs in Figure 7 show that after impregnations from n-butane solutions, the cell interiors (lumens) are essentially all filled with almost spherical polyethylene particles. At higher magnification these spherical particles are seen to be fused together.

Further details including results on other polymer/solute/solvent systems along with information on polymer distributions across the cell walls will be presented in a future publication.

Concluding Comments

Supercritical fluid processing in the pulp and paper and forest products industries is indeed of much interest for a diversity of applications ranging from chemical modifications to physical alterations. The present paper has focused primarily on delignification and impregnation studies both of which have far reaching industrial

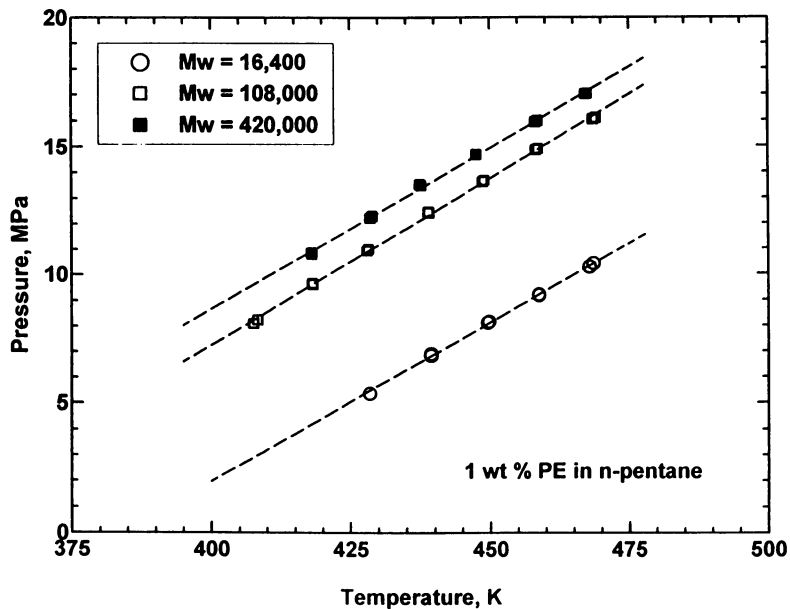


Figure 4. Variation of the demixing pressures with temperature for polyethylene in n-pentane.

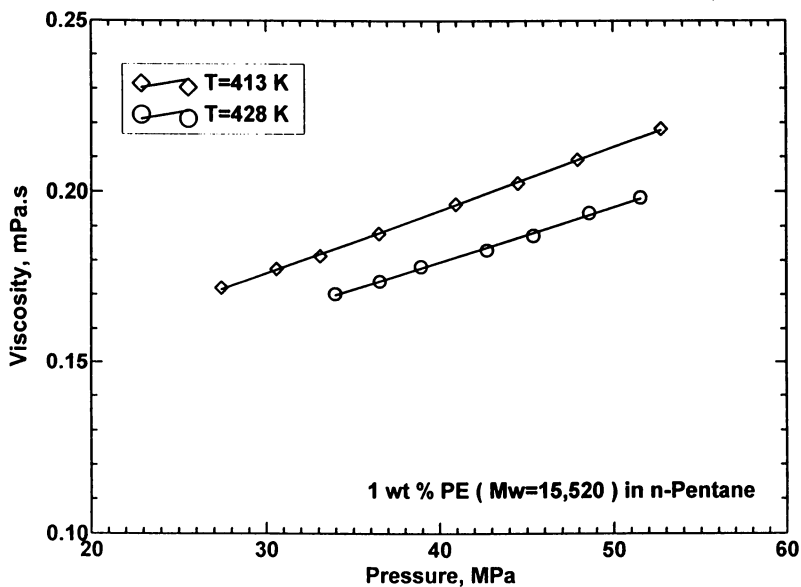


Figure 5. Variation of viscosity with pressure for solutions of polyethylene in n-pentane.

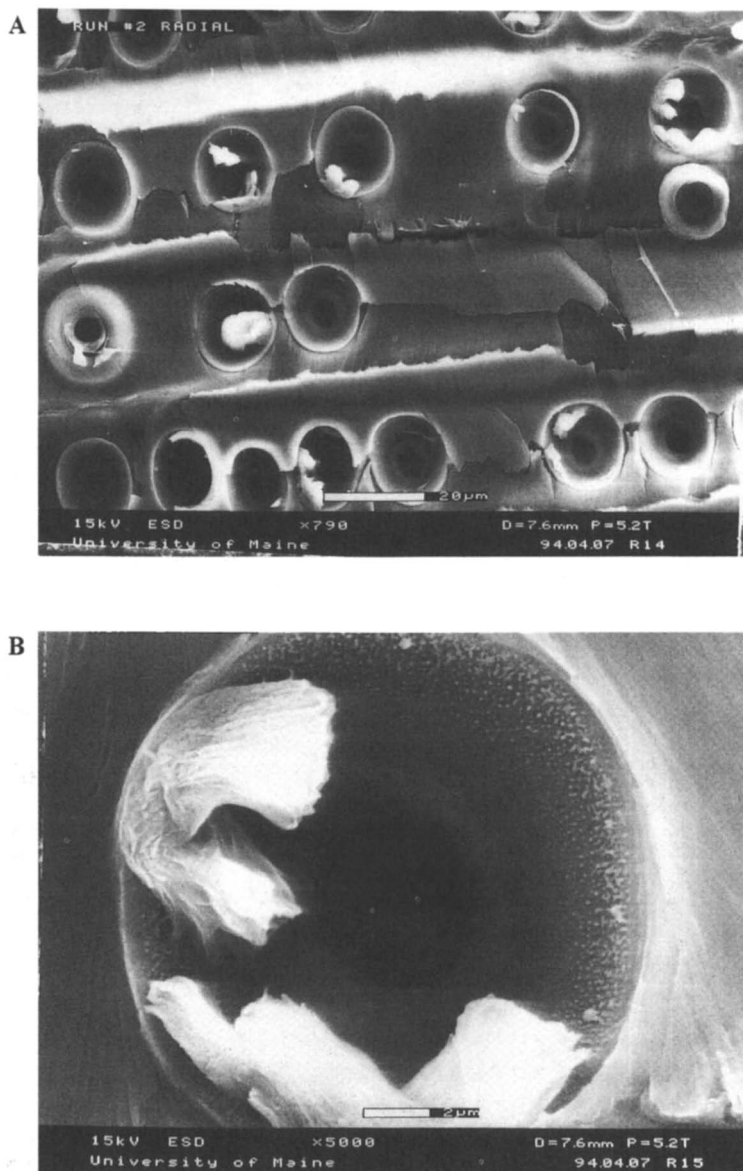


Figure 6. SEM micrographs of red spruce impregnated with polyethylene from n-pentane solutions at low (A) and high (B) magnifications showing crystallization in the pit holes. The higher magnification is a picture of the pit hole at the top right.

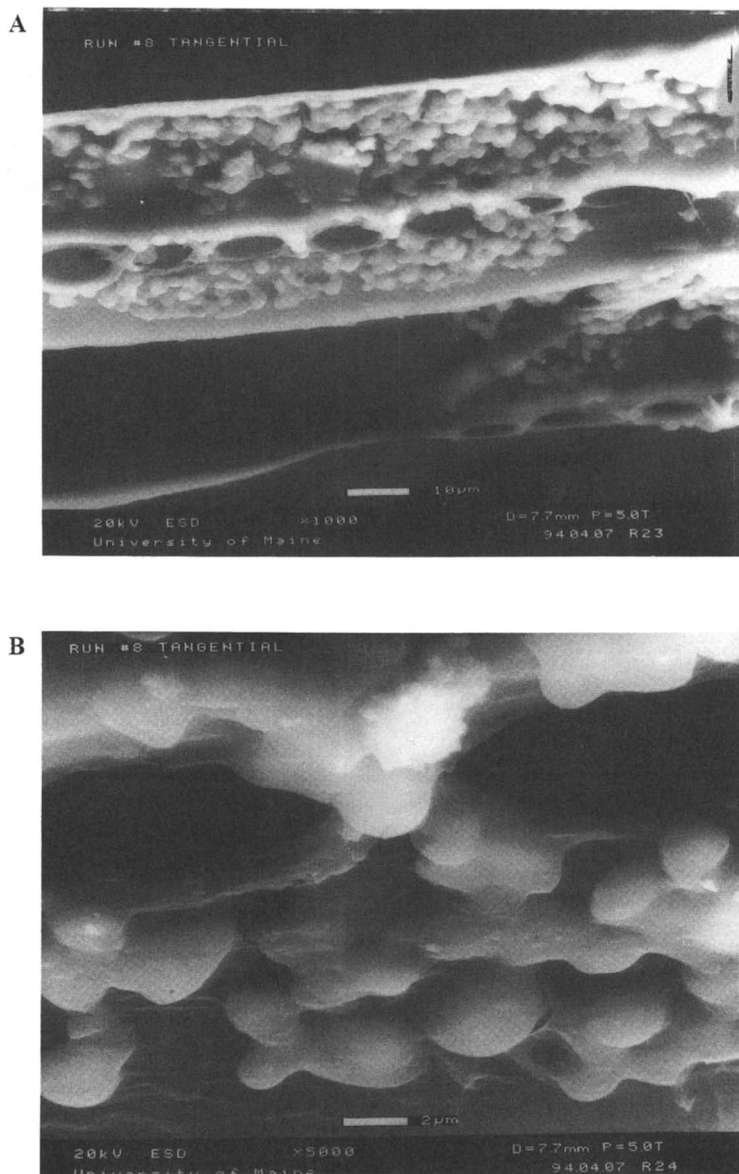


Figure 7. SEM micrographs of red spruce impregnated with polyethylene from n-butane solutions at low (A) and high (B) magnifications showing crystallization and loading in the lumens.

implications. This is the first report on direct impregnation and incorporation of commercially available high molecular weight polymers into the microporous wood matrix. This methodology is opening up a new field of activity. Among other applications not discussed in the present paper, but under exploration in our laboratory are the modulation of porosity and pore size distribution with controlled extractions, post processing of previously treated wood based materials, recycling, and conversion of cellulose to cellulose derivatives.

Acknowledgments

This chapter is based on research activities that has been supported by USDA, NSF, and the Supercritical Fluids Program (SFEST) at the University of Maine. I thank my former and current graduate students and research associates (H. Balkan, Y. Xiong, K. Malki, Z. Gokmenoglu) for their contributions.

Literature Cited

1. *Supercritical Fluids. Fundamentals for Application*, Kiran, E.; Levelt Sengers, J. M. H., Eds.; Kluwer Academic Publishers: Dordrecht, 1994.
2. McHugh, M. A.; Krukoni, V. *Supercritical Fluid Extraction*, 2nd Ed., Butterworth: Boston, 1994.
3. *Extraction of Natural Products Using Near-Critical Solvents*, King, M. B.; Bott, T. R., Eds., Chapman & Hall: New York, 1993.
4. Sjostrom, E. *Wood Chemistry-Fundamentals and Applications*; Academic Press: New York, 1981.
5. Fengel, D.; Wegener, G. *Wood Chemistry, Ultrastructure, Reactions*; Walter de Gruyter & Co.: London, 1983.
6. Hubert, P.; Vitzthum, O.G. *Angew. Chem. Int. Ed. Eng.* **1978**, 17, 731.
7. Froment, H. A. *US Patent* 4,308,200, 1981.
8. Amer, G. I. *US Patent* 4,422,966, 1983.
9. McDonald, E.C.; Howard, J.; Bennett, B. *Fluid Phase Equilibria*, **1983**, 10, 337.
10. Calimli, A.; Olcay, A. *Holzforshung*, **1978**, 32, 7.
11. Koell, P.; Bronstrup, A.; Metzger, J. V. *Holzforshung*, **1979**, 33, 112.
12. Torul, O.; Olcay, A. *Holzforshung*, **1984**, 38, 221.
13. Labrecque, R.; Kallaguine, S.; Grandmaison, J. L. *Ind. Eng. Chem. Prod. Res. Dev.* **1984**, 23, 177.
14. Beer, R.; Peter, S. in *Supercritical Fluid Technology*, Penninger, J. M. L.; Radosz, M.; McHugh, M. A.; Krukoni, V. J., Eds.; Elsevier: New York, 1985; p. 385.
15. VicRoy, J. R.; Converse, A. D. in *Supercritical Fluid Technology*, Penninger, J. M. L.; Radosz, M.; McHugh, M. A.; Krukoni, V. J., Eds.; Elsevier: New York, 1985; p. 397.
16. Kiran, E. *Tappi J.*, **1987**, 70(11), 23.
17. Li, L.; Kiran, E. *Ind. Eng. Chem. Res.* **1988**, 27, 1301.
18. Li, L.; Kiran, E. *Tappi J.*, **1989**, 72(4), 183.

19. Li, L.; Kiran, E. in *Lignin: Properties and Materials*, Glasser, W.G.; Sarkanen, S., Eds., ACS Symposium Series 397, ACS: Washington, DC, 1989.
20. Li, L.; Kiran, E. in *Supercritical Fluid Science and Technology*, Johnston, K. P.; Penninger, J. M. L., Eds., ACS Symposium Series 406, ACS: Washington, DC, 1989.
21. Balkan, H., Ph. D. Thesis, University of Maine, 1993.
22. Kiran, E.; Balkan, H. *J. Supercrit. Fluids*, **1994**, *7*, 75.
23. Poirier, M. G.; Ahmed, A.; Grandmaison, J. L.; Kaliaguine, S. C. F. *Ind. Eng. Chem. Res.* **1987**, *26*, 1738.
24. Goto, M.; Smith, J. M.; McCoy, B. J. *Ind. Eng. Chem. Res.*, **1990**, *29*, 282.
25. Bludworth, J.; Knopf, F. C. *J. Supercrit. Fluids*, **1993**, *6*, 249.
26. Machado, A. S. R.; Sardinha, R. M. A.; de Azevedo, E. G.; da Ponte, M. N. *J. Supercrit. Fluids*, **1994**, *7*, 87.
27. West, M. A. B.; Gray, M. R. *Can. J. Chem. Eng.*, **1987**, *65*, 645.
28. Adschiri, T.; Hirose, S.; Malaluan, R.; Arai, K. *J. Chem. Eng. Japan*, **1993**, *26*, 6.
29. Modell, M., *Final Report, DOE Grant DE-FG05-90CE40914*, 1990.
30. Modell, M.; Larson, J.; Sobczynski, S. F. *Tappi J.* **1992**, *75* (6), 195.
31. Blaney, C. A.; Li, L.; Gloyna, E.; Hossain, S. U. Paper presented at the AIChE Annual Meeting, San Francisco, CA, 1994; Paper 252e.
32. Ritter, D. C.; Campbell, A. G. *Biotechnology & Bioengineering Symposium*, **1986**, *17*, 179.
33. Weimer, P. J.; Chou, Y. C. T.; Weston, W. M.; Chase, D. B. Paper presented at the 8th Symposium on Biotechnology for Fuels and Chemicals, Tennessee, May 13-16, 1986.
34. Campbell, A. G.; Ritter, D. C. *Wood & Fiber Sci.*, **1991**, *23*, 98.
35. Smith, S. M.; Sahle-Demessie, E.; Morrell, J. J.; Levien, K. L.; Ng, H. *Wood and Fiber Sci.*, **1993**, *25*, 119.
36. Ward, D.; Sunol, A.; Curcio, R. *Proc. 2nd. Int. Symp. Supercritical Fluids, Boston, MA, 1991*; pp.364.
37. Sahle-Demessie, E.; Levien, K. L. paper presented at the AIChE Annual Meeting, San Francisco, CA, November, 1994.
38. Vandana, V.; Teja, A. S.; Zalkov, L. H., paper presented at the AIChE Annual Meeting, San Francisco, 1994; Paper 122d.
39. Ohira, T.; Terauchi, F.; Yatagi, M. *Holzforschung*, **1994**, *48*, 308.
40. Aziz, S.; Sarkanen, K. *Tappi J.*, **1989**, *72* (3), 169.
41. Stockburger, P. *Tappi J.*, **1993**, *76* (6), 71.
42. McDonough, T. J. *Tappi J.*, **1993**, *76* (8), 186.
43. deHaas, G. G.; Lang, C. J. *Tappi*, **1974**, *57* (5), 127.
44. Brunner, E. *J. Chem. Thermodyn.* **1987**, *19*, 823.
45. Hicks, C. P.; Young, C. L. *Chem. Rev.*, **1975**, *75*, 119.
46. Panagiotopoulos, A. Z.; Willson, R. C.; Reid, R. C. *J. Chem. Eng. Data*, **1988**, *33*, 321.
47. Mok, W. S. L.; Antal, M. J. *Ind. Eng. Chem. Res.* **1992**, *31*, 94.
48. Adschiri, T.; Malaluan, R.; Takeda, N.; Arai, K. *Proc. 3rd. Int. Symp. Supercritical Fluids, Strasbourg, France, October 1994*.

49. Meyer, J. A. in *Wood Technology: Chemical Aspects*, Goldstein, I. S., Ed., ACS Symposium Series 43, ACS: Washington, DC, 1977.
50. Walters, C. S. in *Wood its Structure and Properties*, Wangaard, F. F., Ed., Pennsylvania State University, 1981.
51. Meyer, J. A. in *Chemistry of Solid Wood*, Rowell, R., Ed., ACS Advances in Chemistry Series 207, ACS: Washington, DC, 1984.
52. Schneider, M. H. *Wood & Fiber Sci.* **1994**, 26, 142.
53. Kumar, S. *Wood & Fiber Sci.* **1994**, 26, 270.
54. Mathias, L. J.; Lee, S.; Wright, J. R.; Warren, C. *J. Appl. Polym. Sci.*, **1991**, 42, 55.
55. Sapiuha, S.; Allard, P.; Zang, Y. H. *J. Appl. Poly. Sci.*, **1990**, 41, 2039.
56. Felix, J. M.; Gatenholm, P. *J. Appl. Polym. Sci.*, **1991**, 42, 609.
57. Woodhams, R. T.; Law, S.; Balatincez, J. J. in *Wood Adhesives 1990*, Forest Products Research Society, 1991, pp.177-182.
58. Freischmidt, G.; Michell, A. J.; Lewis, M. J.; Vanderhoek, N. *Polymer International*, **1991**, 24, 113.
59. *Emerging Technologies for Materials and Chemicals from Biomass*, Rowell, R. M.; Schultz, T. P.; Narayan, R., Eds., ACS Symposium Series 476, ACS: Washington, DC, 1992.
60. Raj, R. G.; Kokta, B. V. in *Viscoelasticity of Biomaterials*, Glasser, W.; Hatakeyama, H., Eds, ACS Symposium Series 489, ACS: Washington, D.C., 1992; pp. 99-117.
61. Gatenholm, P.; Felix, J. M. in *New Advances in Polyolefins*, Chung, T. C., Ed., Plenum: New York, 1993; pp. 237-244.
62. Kiran, E. in *Supercritical Fluids-Fundamentals for Application*, Kiran, E.; Levelt Sengers, J. M. H., Eds., Kluwer Academic Publishers: Dordrecht, 1994; pp. 541-588.
63. Kiran, E.; Zhuang, W. *Polymer*, 1992, 33, 5259.
64. Kiran, E.; Zhuang, W.; Sen, Y. L. *J. Appl. Polym. Sci.*, **1993**, 47, 895.
65. Xiong, Y.; Kiran, E. *J. Appl. Polym. Sci.*, **1994**, 53, 1179.
66. Kiran, E.; Xiong, Y. *Proc. 3rd. Int. Symp. Supercritical Fluids*, Strasbourg, France, 17-19 October, 1994; Volume 3, pp. 271-276.
67. Kiran, E.; Sen, Y. L. *Int. J. Thermophysics*, 1992, 13, 411.
68. Sen, Y. L.; Kiran, E. *J. Supercritical Fluids*, **1990**, 3, 91.
69. Kiran, E.; Sen, Y. L. in *Supercritical Fluid Engineering Science*, Kiran, E.; Brennecke, J. F., Eds., ACS Symposium Series 514, ACS: Washington, D.C., 1993; p. 104.
70. Kiran, E.; Gokmenoglu, Z., *12 th Int. Symp. on Thermophysical Properties*, June 19-24, Boulder, Colorado, 1994.

RECEIVED May 25, 1995

Chapter 27

Phase Behavior of Binary and Ternary Mixtures of Wood Preservatives in Supercritical CO₂ with Cosolvents

A. Hassan¹, K. L. Levien¹, and J. J. Morrell²

¹Department of Chemical Engineering, Oregon State University,
103 Gleeson Hall, Corvallis, OR 97331-2702

²Department of Forest Products, Oregon State University,
105 Forestry Research Lab, Corvallis, OR 97333

Experimental measurements of supercritical phase equilibria for CO₂, cosolvent and three systemic organic biocides were performed in support of research in the use of supercritical fluids in the preservation of wood. The critical loci of binary (biocide and CO₂) and ternary (biocide, CO₂ and cosolvent) mixtures were determined experimentally. Two or three fluid phase equilibria were studied in a view cell system and compositions of the coexisting phases were calculated using a stoichiometric technique from measured volumes. Biocide concentrations ranged up to 2 wt% when methanol or acetone was used as a cosolvent at levels up to 5 wt%. Results of this study will be used to set operating conditions which ensure a single phase in a vessel used for wood treatment.

Supercritical Fluids and Wood Preservation

The critical point for a pure substance or a mixture defines the temperature and pressure at which the vapor and liquid phases existing in equilibrium have identical properties and become indistinguishable. This critical point represents the upper endpoint of the vapor-liquid curve on the *P-V* phase diagram of a pure substance. Critical properties and phase behavior of mixtures are important because of the increased industrial significance of high-pressure processes and because of fundamental interest in the intermolecular energies of fluids (1). Knowledge of mixture critical properties is important in petroleum and natural gas engineering, and for the design of chemical reactors and high pressure extraction and separation equipment (2). PVT properties of mixtures in the critical region are necessary for the economic assessment of new processes utilizing supercritical fluids (SCFs). Determination of phase boundaries can be used to estimate appropriate operating conditions for supercritical fluid extraction. Phase boundaries are used to identify regions of retrograde behavior, i.e. where a temperature increase or pressure decrease leads to an increase in the amount of liquid

0097-6156/95/0608-0402\$12.00/0

© 1995 American Chemical Society

phase. Applications of the work reported in this paper are in the impregnation of wood with biocides.

Telephone and electric power poles are exposed in environments conducive to biodeterioration and must be protected against fungal attack. In conventional treatments of wood, preservatives are dissolved in liquids and the solution is then forced into the wood structure by pressure (up to 200 psia/1.38 MPa). However, since in some species liquid preservatives penetrate only a short distance into the wood, only the surface and the outer layer of the wood becomes protected from biodeterioration. Cracks or checks in the wood then permit fungi to attack the unprotected interior of the wood. The average life of poles treated by these conventional methods is 30 to 40 years. Efforts are currently being made to impregnate wood with preservatives using SCF technology. This approach has the potential to prolong the useful life of a pole with less impact to the environment. Complete penetration with newer biocides can be achieved and the treatment process would be designed to efficiently recycle biocide.

Solubilities of biocides in SCFs can be much higher than those in gases. In SCF wood treatment, the biocide is dissolved in supercritical CO₂ (sometimes a mixture of CO₂ and a cosolvent) and then contacted with the wood. The supercritical solution moves through the pores of the wood to the interior of the wood. When conditions are changed appropriately, the biocide can be precipitated within the wood, while the CO₂ or CO₂/cosolvent gas flows out of the wood structure. Several biocides have been deposited deeply within the wood through this method and were found to be more uniformly distributed than conventional treatment processes (3). Since the wood can be completely impregnated with biocide, it should resist fungal attack even if checks develop. Because treatment process experiments and treated wood analyses are very time consuming, fundamental information about the phase behavior of CO₂, cosolvent and biocide mixtures would be very useful.

Methods

To measure the critical point of mixtures, Gurdial et al. (4) used a constant volume sight gauge equipped with a stirrer as a static equilibrium device. Temperature and pressure in the cell were measured and controlled. The final total mass of CO₂ present in the cell was determined by venting the gas through a wet-test meter. In the studies reported in this paper, a cell similar to that used by Gurdial et al. was used. Mixing was obtained by mechanically shaking the cell instead of using a stirrer and heating tapes with insulation were used in place of a water bath. A digital flow meter and a totalizer were used in place of a wet-test meter.

Analysis of the compositions of phases in equilibrium can be done by direct or indirect methods. In direct methods, compositions are measured by sampling each phase and analyzing the samples usually by a GC or another chromatographic method with a suitable detector. Because of the pressure drop during sampling, partial condensation, re-evaporation, and adsorption can introduce significant errors. In a sampling method there is the possibility of preferentially sampling the more volatile components when operating at elevated pressures. In addition, it is difficult to sample phases that are nearly critical because the sampling procedure itself can cause large

disturbances to equilibrium conditions. Knobler and Scott (5) have described an indirect stoichiometric method for determining the compositions of equilibrium phases provided the system potentials (e.g., temperature, pressure, and number of phases) are fixed. The analysis requires that the overall mixture composition (i.e., the total number of moles of each component) and the measured volumes for each of the coexisting phases be known. The limitation with this method is that the number of phases coexisting in the equilibrium cell must be equal to or greater than the number of components. For example, for a three component system forming three equilibrium phases at constant temperature and pressure, a mole balance for each component, j , can be written as:

$$C_j^{L1} V_i^{L1} + C_j^{L2} V_i^{L2} + C_j^G V_i^G = n_{j,i}$$

C_j^α is an unknown molar concentration of component j in the α phase, V_i^α is the measured volume of α phase in experiment i , and $n_{j,i}$ is the total number of moles of component j in experiment i . This mole balance is a linear relationship of three measured independent variables (the phase volumes) and one known dependent variable ($n_{j,i}$). The molar concentrations are the coefficients of this linear expression and can be determined from a linear least-squares fit of experimental data (linearly independent sets of phase volumes and $n_{j,i}$) (6). For three component systems, at least three experiments at the same temperature and pressure but with different amounts of one or more components of the mixture are necessary. As more experimental sets of data are used, the accuracy of the parameter estimation is expected to improve.

A schematic of the apparatus used is shown in Figure 1. A high pressure optical cell (Jerguson model 12-T-40) was used to observe the phase behavior of mixtures. The cell had two tempered Borosilicate windows which allowed observation of about 70% of the volume of the cell. The windows were 4 5/8" (11.75 cm) wide and located along the centerline of the 8 1/4" (21 cm) long view cell. The cell body was made of carbon steel and fluid contact parts were made of 316 stainless steel. The cell had a volume of 40 cm³, weighed 15 kg and had a maximum operating pressure of 33 MPa at 90 °C. Because of the large mass of the cell, cell cooling by conduction was a very slow process and only three experiments could be performed per day. A J type thermocouple (Omega model JMTSS-062-U-12) was fitted to the cell, and the cell was heated using a heating tape (Omega model FWH171-060). The thermocouple and the heater were connected to a temperature controller (Omega CN9000A) which controlled and displayed the temperature inside the cell. The precision of the temperature measurement was 0.1 °C and temperature fluctuations in the cell after mixing at equilibrium were less than 0.1 °C. The temperature controller was calibrated before and after each set of experiments. A precision pressure transducer/indicator (Heise Gauge model 901A) was used to determine the pressure inside the cell within ± 1 psia (0.007 MPa). Observed pressure fluctuations at equilibrium in the cell were less than 1 psia.

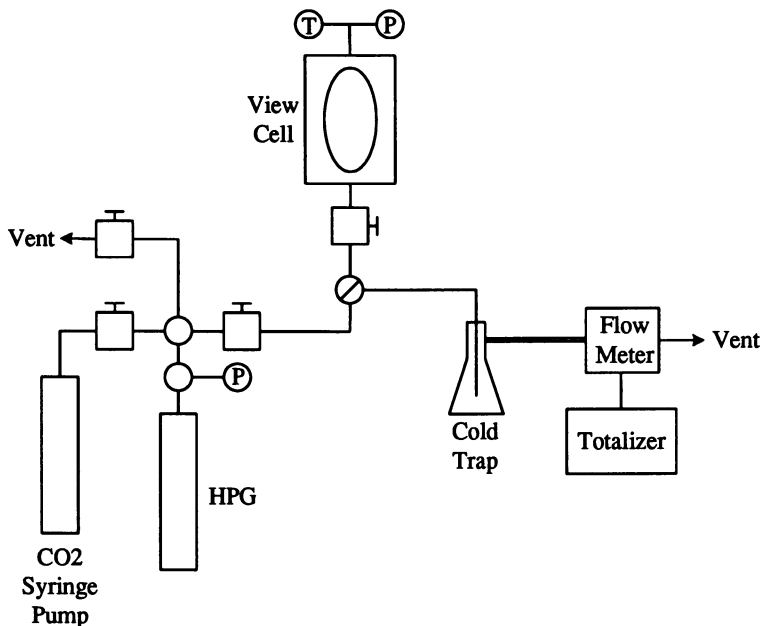


Figure 1. Schematic diagram of experimental apparatus.

A manual high pressure generator (HPG) (HiP model 87-6-5, screw pump) and a syringe pump (ISCO model 260D) were used to feed CO₂ to the cell. All wetted parts of the HPG were of 316 stainless steel or 17-4PH stainless steel. The syringe pump was used to feed the initial loading of the CO₂, while the HPG was used to slowly add any further CO₂ to keep all phase boundaries visible. A cathetometer (Eberbach model 5100) was used to observe phase behavior and measure phase volumes at equilibrium. The meniscus height was calibrated to fluid volume by adding known amounts of water into the cell with a pipet and measuring the meniscus height with the cathetometer. Because of the differences in curvature of the meniscus when using water or supercritical fluids, an average level was used rather than the lowest point of the interface. Errors in measuring the cell volume were expected to be less than 0.05 cm³. A cold trap containing dry ice and acetone was used to separate CO₂ from other components of the mixture. A turbine flow meter (McMillian Co. model 310-3) was used to indicate the instantaneous flow rate of CO₂ while a flow totalizer (Kessler-Ellis Products co., model INT96TBL1A) was connected to the flow meter and used to determine the cumulative volume of CO₂ exhausted.

Procedures

Carbon dioxide was obtained from Industrial Welding Supply at a purity of 99.9 wt%. Methanol and acetone were purchased from Mallinckrodt Chemicals with purities of 99.9 wt% and 99.7 wt%, respectively. 2-(thiocyanomethylthio) benzothiazole (TCMTB) was supplied by Buckman Laboratories, Inc. at 99.6 wt% purity, propiconazole by Janssen Pharmaceutica N. V. at 88 wt% purity, and tebuconazole by Mobay Corporation at 95 wt% purity. All of the chemicals were used without further purification. Table I contains the molecular structures of these biocides.

Table I: Biocide Structures

Biocide	Mol. Mass	Molecular Structure
Tebuconazole	308	
TCMTB	238	
Propiconazole	342	

For measurements of T_c and P_c of mixtures, the thermocouple at the top of the optical cell was first removed and the lines and the cell were flushed with CO_2 to remove air. Desired amounts of biocide, cosolvent, or a cosolvent/biocide mixture were then added using a graduated pipet to the cell through its top. The thermocouple was then reinstalled and CO_2 was added. First the gas filled the cell and then the liquid/gas meniscus rose in the cell as the pressure increased with additional CO_2 . As the temperature was increased, the meniscus level was maintained near the middle of the window by further addition of CO_2 . On reaching the critical point, the meniscus disappeared. At this point, mixing the cell contents created an opaque fluid and fluid motion was easily observed as opalescence. Observations were made repeatedly for both increasing and decreasing temperature paths, to ensure accuracy of the final values of temperature and pressure. All reported data are for decreasing temperature, since the absolute rate of change was smaller during cooling. After the critical point of the mixture was observed, the fluid was expanded to the cold trap to separate the components. The CO_2 was then sent to the flow meter and flow totalizer. Using the known initial amount of the liquid and the total amount of the gas, the composition at the critical point of the mixture was calculated.

For phase equilibria at subcritical conditions, the top thermocouple in the cell was removed and the lines and the cell were flushed with CO_2 to remove air. Known amounts of a biocide, a cosolvent, or a cosolvent/biocide mixture were added. The thermocouple was reinstalled and the heater was turned on. CO_2 was fed to the cell to increase pressure to the desired value at which two or three phases were observed. After CO_2 was added to the cell, the line to the cell was disconnected and the cell was shaken mechanically to ensure proper mixing. Equilibrium was established when the pressure, temperature and the meniscus level were stable. Equilibrium was usually observed after one hour, but measurements were made only after at least three hours. The meniscus level was then measured using a cathetometer and the volume of each phase was determined. The cell contents were then expanded to the cold trap to capture the liquid solution and measure the gas with the flow meter and totalizer. The same procedure was repeated several times at a constant temperature and pressure, but with different initial amounts of the components. Each time the meniscus levels were different and the corresponding volumes of the phases were recorded. Compositions of the phases were calculated from the phase volumes and the total amount of each component. After each experiment, the cell was rinsed and cleaned.

Results

Critical point measurements. The accuracy and reliability of the methods described above were assessed by measurements of the binary system of methanol in CO_2 . Figure 2 presents the critical pressure data for CO_2 /methanol mixtures obtained in this study along with the data of Gurdial et al. (4). Figure 3 similarly presents data for critical temperatures. In both cases the critical property was found to increase with increasing methanol content. The measurements were done at less than 8 mole% of methanol and for this range the two sets of data agree within about 3%, except for P_c at the upper limit of methanol concentration. In this work, the purities of CO_2 and methanol were slightly higher than used by Gurdial et al. (99.9 wt % versus 99.8).

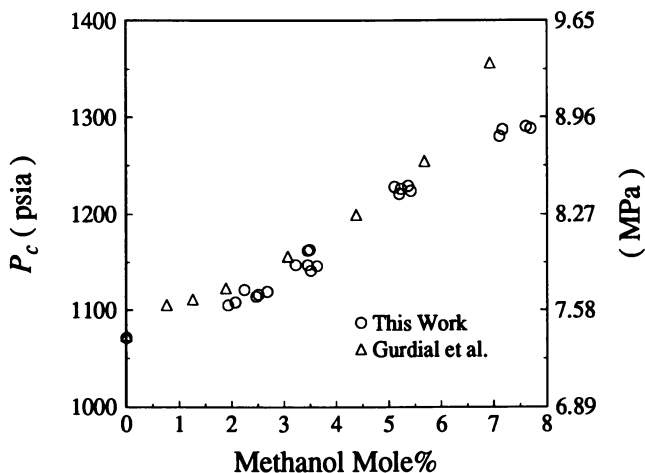


Figure 2. Critical pressures of binary mixtures of CO_2 and methanol.

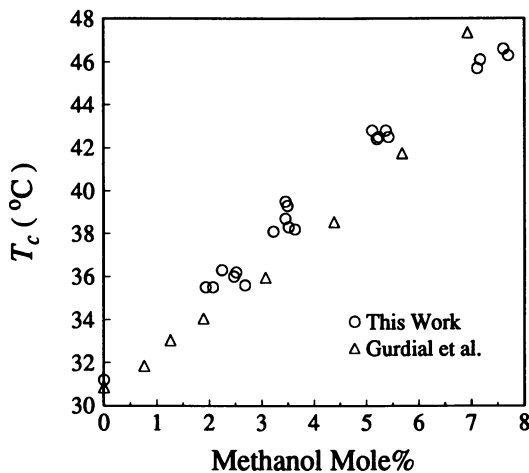


Figure 3. Critical temperatures of binary mixtures of CO_2 and methanol.

Brunner (1) also presented data for T_c and P_c of CO_2 /methanol mixtures, but without composition data for the two phases. Figure 4 is a plot of P_c versus T_c data from this work, Gurdial et al. (4) and Brunner (1). From the plot the results of this work can be seen to be closer to those of Brunner (CO_2 at 99.95 wt%, methanol at 99.9 wt%) than to Gurdial et al., possibly because of the purities of the CO_2 and methanol used.

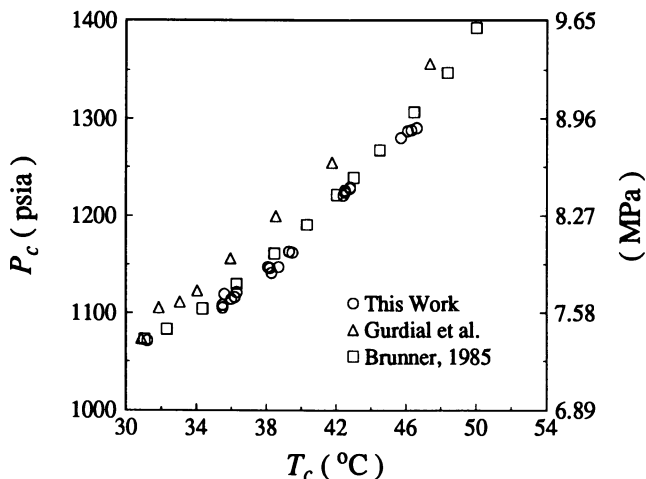


Figure 4. Critical pressures and temperatures of binary mixtures of CO_2 and methanol.

The critical point of binary mixtures of CO_2 /propiconazole for less than 1 wt% of propiconazole was studied. As the amount of propiconazole was increased, the critical pressure and temperature of the mixture also increased, as shown in Figures 5 and 6 respectively. For mixtures containing more than 1 wt% propiconazole, a small amount of a third fluid phase was observed.

Ternary systems exhibit a critical surface in the four dimensional T - P - x_1 - x_2 space which makes the phase behavior even more complicated than for binary mixtures when the components are dissimilar. The critical parameters of ternary mixtures of CO_2 /acetone/TCMTB were studied for the two phase region, where acetone content was less than 4 wt% and TCMTB content was less than 2 wt%. The critical temperature of TCMTB (405.48 $^{\circ}\text{C}$) was estimated (7) to be higher than that of CO_2 or acetone, while its critical pressure (2.89 MPa) was estimated to be lower than that of CO_2 or acetone.

The effect of acetone content on critical pressures of CO_2 /acetone/TCMTB mixtures is shown in Figure 7 for three levels of TCMTB (0, 0.24 and 0.95 wt%). For each TCMTB level, the points represent a critical curve on the critical surface of the ternary mixture. As the composition of acetone was increased in this range, the critical pressure of the mixture also increased. Critical pressures of the mixtures were only slightly affected by the presence of TCMTB.

Figure 8 presents the critical temperatures of CO_2 /acetone/TCMTB mixtures at several levels of acetone for a TCMTB level of 0, 0.24 or 0.95 wt%. For a constant composition of TCMTB, higher acetone composition yielded a higher critical temperature. The critical temperature also was only slightly affected by the presence of TCMTB.

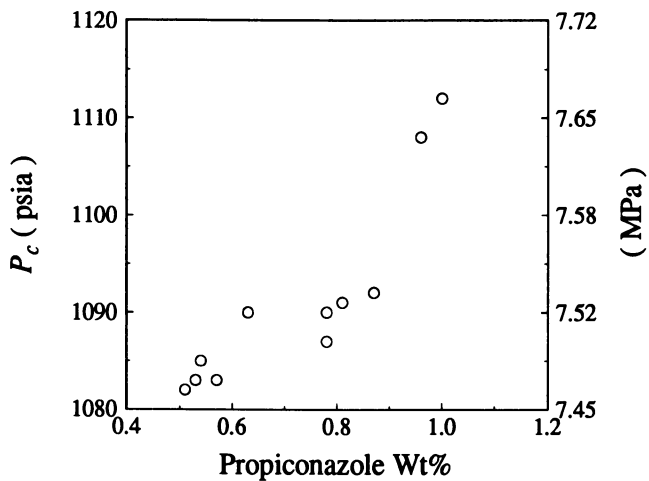


Figure 5. Critical pressures of binary mixtures of CO_2 and propiconazole.

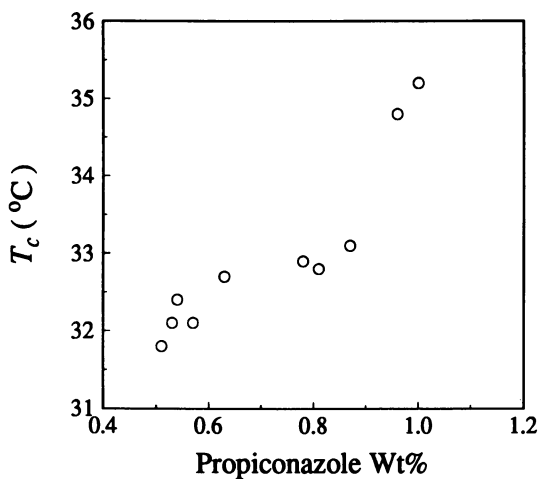


Figure 6. Critical temperatures of binary mixtures of CO_2 and propiconazole.

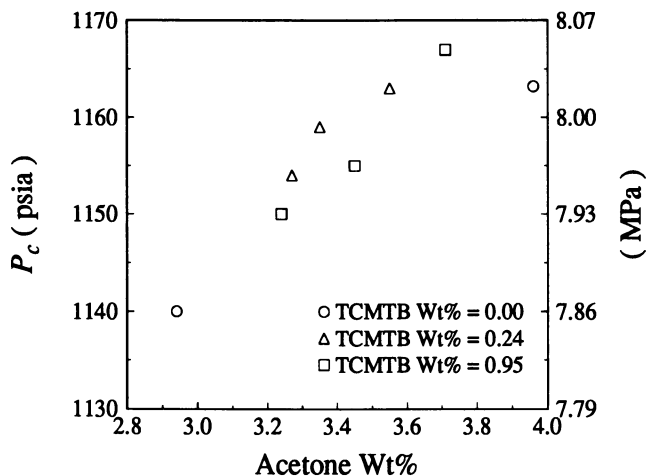


Figure 7. Critical pressures of ternary mixtures of CO_2 , acetone, and TCMTB.

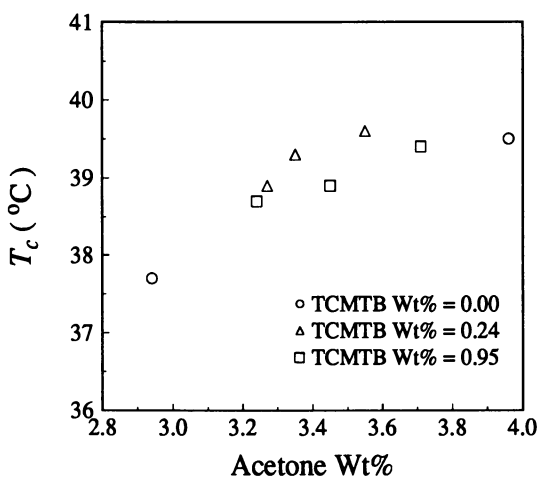


Figure 8. Critical temperatures of ternary mixtures of CO_2 , acetone, and TCMTB.

Critical behavior was also investigated for ternary mixtures of CO₂/methanol/tebuconazole in the two fluid phase region. In this study, transitions from two to a single fluid phase were studied in the region where methanol was less than 5 wt% and tebuconazole was less than 2 wt% of the total. At constant tebuconazole content, the critical temperature and pressure both increased as methanol increased. The critical temperature of tebuconazole (606.46 °C) was estimated (7) to be more than that of CO₂ or methanol while its critical pressure (1.83 MPa) was estimated to be less than that of CO₂ or methanol. If the amount of tebuconazole exceeded 2 wt%, a third fluid phase was observed at the bottom of the cell.

The effect of methanol content on critical pressures in CO₂/methanol/tebuconazole mixtures is shown in Figure 9 at a constant total tebuconazole content of either 0 or 0.44 wt%. The critical pressure of the mixture increased as the amount of methanol was increased and was slightly higher in the presence of tebuconazole.

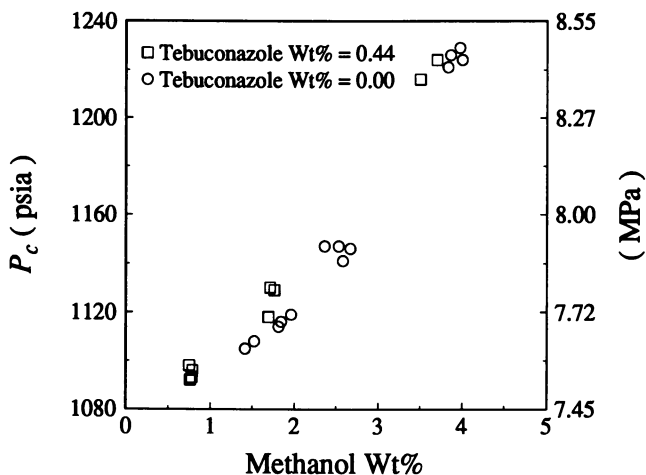


Figure 9. Critical pressures of ternary mixtures of CO₂, methanol, and tebuconazole.

Figure 10 presents critical temperature data for the CO₂/methanol/tebuconazole mixture versus methanol content of the mixture. For a constant composition of tebuconazole, as the methanol composition was increased, the critical temperature of the mixture increased. There was little effect of the presence of tebuconazole on the critical temperature at this level of biocide.

Phase composition measurements. Many investigators have reported phase behavior of mixtures of simple cosolvents and CO₂ at subcritical conditions. To check the accuracy and reliability of the stoichiometric method, phase compositions of binary systems of CO₂/methanol were measured at 25 °C. Figure 11 presents results obtained by this method and data from two previous reports (8,9). For the pressures studied here (above 5 MPa), the gas phase mole fraction of CO₂ was always at or above 0.99, as found previously (8,9).

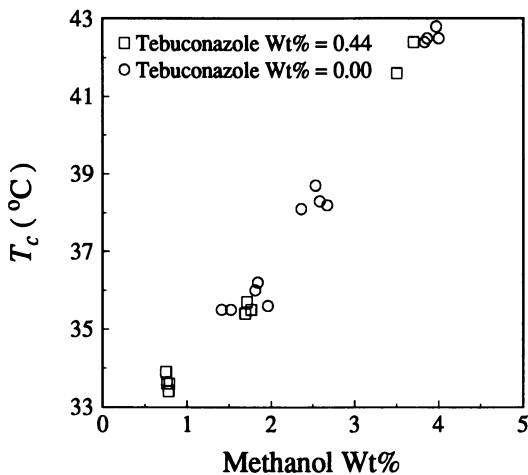


Figure 10. Critical temperatures of ternary mixtures of CO_2 , methanol, and tebuconazole.

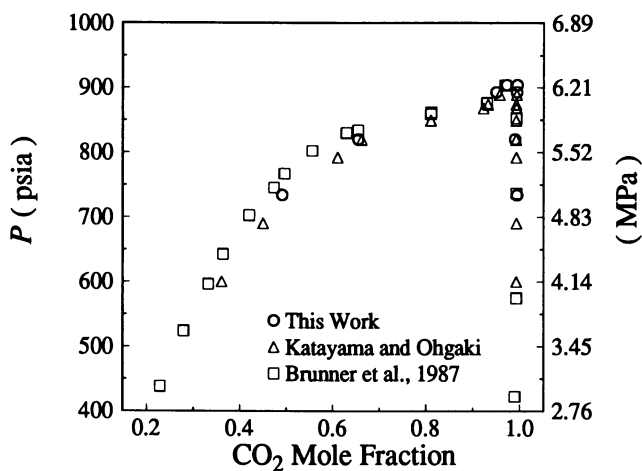


Figure 11. Vapor-liquid equilibria for CO_2 and methanol mixtures at 25 °C.

Since the results of this work corresponded to published data, the stoichiometric method was chosen to study the phase behavior of near critical mixtures.

Compositions of the phases in gas-liquid-liquid equilibrium were determined for CO₂/acetone/TCMTB mixtures at 35 °C and 766 psia (5.28 MPa). Mole fractions for the corresponding phases (top=G, middle=L2 and bottom=L1) were as shown in Table II. These results were based on five independent experiments performed at the same temperature and pressure, but with different overall compositions.

Table II: Liquid-liquid-gas Equilibrium Compositions for CO₂/acetone/TCMTB Mixtures at 35 °C and 766 psia (5.28 MPa)

Phase	x_{CO_2}	x_{acetone}	x_{TCMTB}
G	0.645	0.165	0.190
L2	0.614	0.337	0.049
L1	0.727	0.145	0.128

In summary, the compositions obtained for CO₂/methanol mixtures using a static view cell with a stoichiometric analysis method were in good agreement with those obtained from direct sampling methods. The techniques described here have been applied to phase equilibria in the near critical region in the development of wood preservation technology.

Acknowledgment

Some of the equipment used for this study was purchased with the support of the Electric Power Research Institute.

Literature Cited

1. Brunner, E. J. *Chem. Thermodynamics* **1985**, *17*, 671-679.
2. Ohgaki, K.; Katayama, T. *J. Chem. Eng. Data* **1975**, *20*(3), 264-267.
3. Morrell, J.J.; Levien, K.L.; Sahle-Demessie, E; Kumar, S.; Smith, S.; Barnes, H.M. "Treatment of Wood Using Supercritical Fluid Processes," 14th Annual Meeting of the Canadian Wood Preservation Association, Vancouver, B.C., Nov. 2-4, 1993.
4. Gurdial, G. S.; Foster, N.R.; Yun, S. L. J.; Tilly, K. D. In *Supercritical Fluid Engineering Science*; Kiran, E.; Brenneke, J.F. Eds.; ACS Symposium Series 514; American Chemical Society: Washington, DC, 1993; 34-45.
5. Knobler, C. M.; Scott, R. L. *Journal of Chem. Phys.* **1980**, *73*, 5390-5391.
6. DiAndreth, J. R.; Ritter, J. M.; Paulaitis, M. E. *Ind. Eng. Chem. Res.* **1987**, *26*(2), 337-343.
7. *Perry's Chemical Engineers' Handbook*, 6th ed., Perry, R. H.; Green, D., Eds.; McGraw Hill: New York, NY, 1984.
8. Katayama, T.; Ohgaki, K. *J. Chem. Eng. of Japan* **1975**, *8*(2), 89-92.
9. Brunner, E.; Hultenschmidt, W.; Schlichtharle, G. J.; *Chem. Thermodynamics* **1987**, *19*, 273-291.

RECEIVED June 26, 1995

Chapter 28

Impregnation of Wood with Biocides Using Supercritical Fluid Carriers

E. Sahle-Demessie^{1,3}, K. L. Levien¹, and J. J. Morrell²

¹Department of Chemical Engineering, Oregon State University,
103 Gleeson Hall, Corvallis, OR 97331-2702

²Department of Forest Products, Oregon State University,
105 Forestry Research Lab, Corvallis, OR 97333

The use of supercritical fluids (SCFs) to deliver biocides into wood is a promising technique for preservation. Data are presented from recent SCF impregnation studies of Douglas-fir heartwood for two of the commercially available biocides tested: PCP (*pentachlorophenol*) and TCMTB (*2-(thiocyanomethylthio) benzothiazole*). The final spatial distribution of a biocide within the wood was strongly affected by treatment pressure, period of treatment, and the size of the wood piece. A simple rate model to predict the distribution was developed based on compressible flow through porous media and rapid precipitation kinetics. Simulations indicated that maximum deposition occurs at the surface and that higher treatment pressure yields higher deposition at all locations, which agreed qualitatively with data. The sensitivity of the model to a single constant which depended on measurable wood and supercritical fluid properties was also shown.

Impregnation of a semi-porous solid, e.g. wood, with polymers, preservatives, fire retardants or silicon compounds greatly improves their basic properties (1) and overcomes service limitations (2). Most conventional techniques used for impregnation of porous solids use viscous fluids and suspensions that may not flow properly through semi-porous solids, resulting in uneven distribution or shallow penetration. Properties such as low viscosity, high diffusivity and adjustable solvent characteristics and the absence of an air-liquid interface should make SCFs good candidates for complete impregnation of semi-porous solids. SCFs can also remove extractives that encrust the flow passage (pit membrane) and increase wood permeability and treatability (3).

The concept of employing supercritical fluids to preserve refractory wood species was first proposed in a Japanese patent (4). Kayihan (5) claimed the use of pure and modified supercritical carbon dioxide (SC-CO₂) for perfusion of a porous solid with chemicals by demonstrating the deposition of a blue dye within small wood

³Current address: Risk Reduction Engineering Laboratory, U.S. Environmental Protection Agency, Mail Stop 489, Cincinnati, OH 45268

0097-6156/95/0608-0415\$12.00/0

© 1995 American Chemical Society

dowels. The use of SCFs to impregnate wood with monomers to create new composite materials has also been reported (6,7). Other impregnation processes which used supercritical fluids include the densification of ceramics (8) and the dyeing of synthetic textiles in SC-CO₂ (9).

SCF deposition within a porous or semi-porous media conceptually involves several phenomena: solubility, compressible flow through porous media, homogeneous/heterogeneous crystallization and adsorption/desorption. Although some of these have been individually studied, a quantitative understanding of their simultaneous effects on total deposition, and more importantly the spatial distribution of the deposited material, has not been fully developed. Previous efforts by others to develop a model for total retention have been reported (10). The experiments and modeling study reported here were part of an on-going study of the use of supercritical fluids in the preservation of wood. The objective of this work was to experimentally identify major factors which influence the distribution as well as total amount of biocide retained in the wood. A simple model was to be formulated which could be used to predict biocide distribution as well as total retention for further process development.

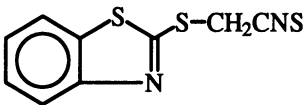
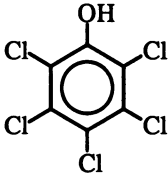
Experiments

Materials. The biocides reported here were: TCMTB (2-(*thiocyanomethylthio*)*benzothiazole*) from Buckman Laboratories, Inc. and PCP (*pentachlorophenol*) from Sigma Chemical Company. The chemical structures of these biocides are shown in Table I. Small Douglas-fir heartwood (*Pseudotsuge menziesii* (Mirb.) Franco) cylindrical dowels (13 mm diameter, 40 mm length) were used in bench-scale experiments, while larger blocks (100 mm length, square sides of 38, 25 or 19 mm) were used in pilot-scale studies. The surface of the wood was carefully smoothed to avoid blocking of the pores. The two ends of the dowels and four of the six sides of the blocks were sealed by double coating with epoxy resin to minimize longitudinal flow. Wood dowels and blocks were conditioned to a 12% moisture content prior to treatment.

Impregnation Process. A simplified description of the SCF impregnation process is that the pressure in a treatment vessel, which contains a wood piece and a supercritical solution of biocide, is first increased to a specified value called the treatment pressure. This pressure is then maintained for a specific amount of time, called the treatment period, after which the system is vented, which causes the pressure in the vessel and within the wood to drop. Conceptually, since the solubility of the biocide in the fluid phase is orders of magnitude smaller at subcritical conditions, the biocide leaves the fluid phase while still within the wood, thus resulting in impregnation. Impregnation experiments were done on wood pieces using bench-scale and pilot-scale equipment.

The bench-scale equipment was based on an ISCO 2000 Series dual pump system. A single wooden dowel and a suitable biocide were initially loaded in a small treatment vessel (15 mm i.d., 56 mm length) in a system similar to that used by others for a supercritical solubility study (11). Temperature and pressure within the treatment vessel were measured and could be independently adjusted to ensure the contents were significantly above the critical values for carbon dioxide.

Table I: Biocide Structures

Biocide	Mol. Mass	Molecular Structure
TCMTB	238	
PCP	266	

The pilot-scale equipment was a modified Newport Scientific, Inc. extraction system which included three separate vessels: a saturator, a treatment vessel and a separator, as shown in Figure 1. Carbon dioxide flowed from a commercial cylinder with a dip-tube through a 5 μ m filter at about 60 bar to a compressor (Newport, 46-133320-2, capacity of 690 bars and 50 cm³/min). Cosolvent was added using a metering duplex pump (LDC Analytical, 2396-57, flow rate = 0.48 to 9.7 cm³/min). The CO₂ / cosolvent mixture flowed into the saturator vessel (65 mm i.d., 254 mm length), where the supercritical solution was formed. This solution then flowed through heated tubing into the treatment vessel (65 mm i.d., 533 mm length), which was equipped with four hand-operated valves that could be used to change the direction of flow through the vessel. The fluid leaving the treatment vessel was expanded across a micrometering valve and the majority of solute was collected in a separator vessel (38 mm i.d., 267 mm length). A second separation operation was then accomplished in a cold trap at atmospheric pressure. Finally the gas stream passed through a flow meter (McMillan Co., 310-3) at atmospheric pressure and its temperature was measured. The total volume of this vent gas at known temperature and pressure was determined using a flow totalizer (Kessler-Ellis Co., INT-69) connected to the flow meter. Temperature and pressure readings from all the pilot-scale vessels and the flow meter readings were recorded using a personal computer for data acquisition.

Retention Analysis. Qualitative methods to visually detect PCP or TCMTB in wood were used in preliminary tests. Qualitative analyses for PCP were determined by cutting the dowels in half and spraying the cut transverse face with penta-check or chrome azurol S. (12). Qualitative analyses for TCMTB were performed by spraying

zinc powder on the cut cross section of treated blocks, followed by application of dilute hydrochloric acid (13). A bright red color was indicative of TCMTB.

Both total retention for a wood piece and retention at a particular location in the piece were quantitatively measured for the two biocides (both in kg/m^3). Blocks from pilot-scale impregnation with TCMTB were analyzed by removing plugs, grinding slices of the plugs to pass a 20 mesh screen, and then extracting with methanol for 3 hours at 60°C in a sonicator bath. The extract was analyzed using high performance liquid chromatography (Shimadzu Model LC-6A) to determine retentions at selected depths (14). Dowels from bench-scale impregnation using PCP were separated into two regions: the "inner core" consisted of the material from the center to approximately 3 mm radius, while the "outer shell" was material from 3 to 6.5 mm from the center. The samples were ground to pass a 20 mesh screen and analyzed using an x-ray fluorescence analyzer (ASOMA 8620, ASOMA Instruments, Austin, TX).

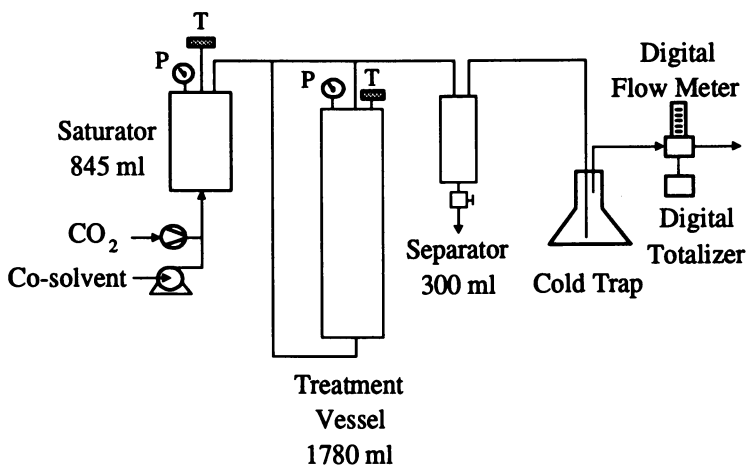


Figure 1. Schematic diagram of the pilot-scale impregnation system.

Experimental Results

The effects of treatment pressure, treatment period and size of block were examined in pilot-scale blocks treated with TCMTB. The effects of cosolvents were examined by measuring differences between inner and outer regions of bench-scale dowels treated with PCP. PCP was used since it had been previously found that cosolvents could significantly increase PCP solubility in SC-CO₂ (15).

Effect of Pressure and Treatment Period on Deposition. Douglas-fir heartwood blocks (38 x 38 x 100 mm) were treated using SC-CO₂ and with 2.7 mol% acetone as cosolvent at 50°C in the pilot-scale equipment and were visually found to be impregnated with TCMTB at all depths within the block. For a treatment period of 30

minutes, when the treatment pressure was changed from 140 to 270 bar, the retention near the center of the block increased by a factor of seven (Figure 2A). This increase was similar to the four-fold increase in solubility of TCMTB in SC-CO₂ found previously for the same pressure change (15). Higher pressures apparently enhanced biocide solubility and created a greater driving force for bulk flow into the wood, which resulted in higher and more uniform distribution of biocide. Longer treatment periods also increased TCMTB retention, as shown in Figure 2B. For example, retentions at the four selected depths increased an average of 75% when the treatment period was extended from 15 to 60 minutes at 250 bar.

Influence of Specimen Size. In order to examine the effect of wood sample size, three different sizes of blocks (19, 25 or 38 mm square sides, length of 100 mm in all cases) were treated in a single charge at 50°C and 248 bar for 60 minutes. Average retentions at selected depths are shown in Figure 3. The high measured retentions near the surface may have been influenced by surface deposition. Inner distributions were nearly uniform for the two smaller blocks. However, there was a significant concentration change with depth, even near the center in the largest blocks. This may have been due to the smaller surface-to-volume ratio or to a nonuniform effective permeability (16,17) in the largest blocks.

Effects of Cosolvents on Biocide Distribution. Cosolvents can significantly increase biocide solubility and thus improve the potential for delivering effective biocide levels into wood. Five cosolvents at 3.5 mol% in SC-CO₂ were used with PCP at four sets of operating conditions: 207 or 248 bar at 60 or 80°C. Retentions in the inner core and outer shell of 5 replicate bench-scale dowels were measured at each operating condition. The range of retentions and average achieved for each cosolvent are shown in Table II. As expected, the retention in the outer shell was much higher. Dimethylformamide (DMF) and dimethyl sulfoxide (DMSO) are polar solvents and seemed to cause the wood to swell, which may have resulted in high retentions. An effect of cosolvent use for impregnation was also noted by Kayihan (5). He observed uniform color of C.I. Solvent Blue 35 dye throughout the cross section of yellow birch dowels (4.8 mm diameter and 20 mm length) after using SC-CO₂ with 3.95 % acetone as the cosolvent, even though he found no visible dye deposited in such dowels when pure SC-CO₂ was used. The amount of cosolvent can also affect the total deposition. For example, an increase of methanol from 2 to 6 mol% resulted in an increase in total PCP retention in Douglas-fir dowels from 3.5 to 6.5 kg/m³ (15).

Model of the Impregnation Process and a Simplification

The model is based on compressible flow through a one-dimensional slab with thickness δ . At elapsed time (t) equal to zero and later, the slab is exposed on both surfaces to a saturated supercritical solution of biocide. The vessel pressure is increased from atmospheric at a rate of 24.9 bar/min. until the specified treatment pressure is reached. After a specified treatment period, t_{tr} , the vessel pressure is decreased back to its original value at 50 bar/min. These rates are similar to those used in pilot-scale experiments.

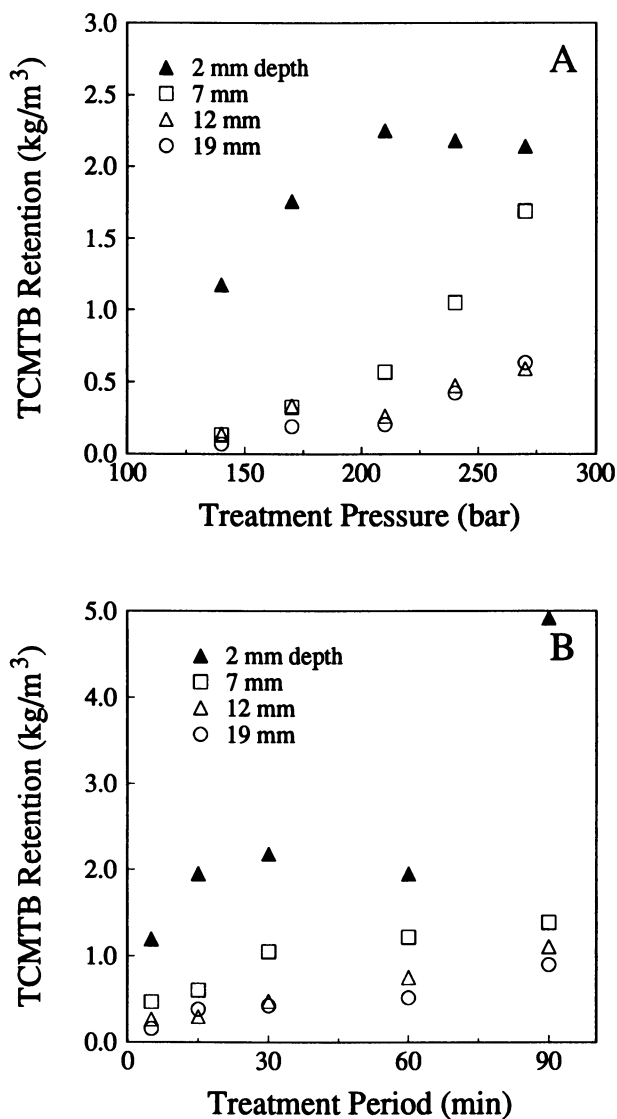


Figure 2. TCMTB retention at selected depths in 38x38x100 mm Douglas-fir blocks after treatment at 50°C for: A) Selected treatment pressures at constant treatment period of 30 minutes and B) Selected treatment periods for a constant treatment pressure of 250 bar.

The venting rate is constrained to avoid potential collapse of the wood. The stress level at which wood cell flattening occurs is about 400 bar/cm² for softwoods (18,19).

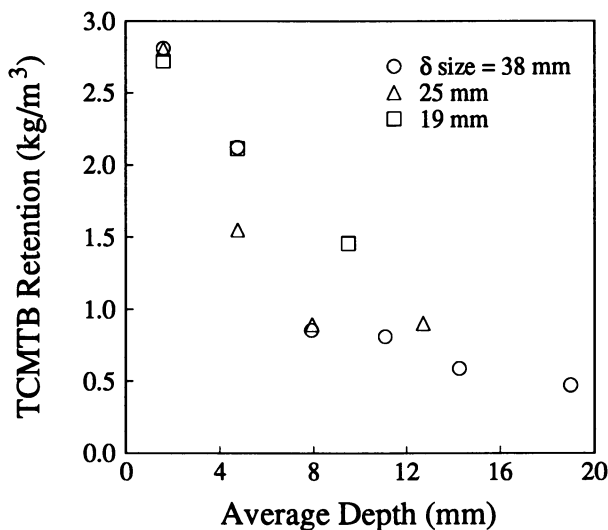


Figure 3. Retentions of TCMTB at selected depths in Douglas-fir blocks of 100 mm length and selected square side sizes: 38, 25 or 19 mm.

Table II: Ranges of Retentions of PCP in Douglas-fir Dowels Treated with SC-CO₂ and Cosolvent at Four Combinations of Temperature and Pressure

Cosolvent @ 3.5 mol%	Retention, kg/m ³	
	Inner Core Range	Outer Shell Range
Acetone	0.95 - 1.49 (1.26) = avg.	0.46 - 13.9 (4.45)
Ethanol	1.39 - 1.92 (1.71)	1.20 - 11.1 (6.16)
Methanol	1.00 - 1.47 (1.26)	14.4 - 28.9 (21.55)
DMF	0.16 - 0.46 (0.31)	21.1 - 34.8 (27.95)
DMSO	2.38 - 2.91 (2.65)	16.0 - 32.0 (24.0)

The simple deposition model was intended to give the spatial distribution of deposited biocide as a function of time. As a first approximation, the following simplifications were made:

- 1) The wood piece has one-dimensional uniform slab geometry. Experimental wood blocks had four of the six ends sealed - including the ends cut perpendicular to the longitudinal growth direction.
- 2) Wood porosity and permeability are uniform and constant. Since two of the sides of the experimental wood pieces which were end-sealed were in the longitudinal direction of growth, this means that the radial and tangential growth directions, which made up the two non-sealed sides, have similar permeability. The volume fraction of the precipitated biocide was small compared to the void volume of the wood and the wood did not swell.
- 3) The wood piece is isothermal and pressure at the surface of the piece is equal to vessel pressure.
- 4) Viscous flow is the dominant mechanism for fluid transport.
- 5) The fluid within the wood during venting is in equilibrium with deposited biocide.

Total Mass Balance. Equations of continuity and motion for flow of a pure isothermal fluid through a porous medium can be developed from the basic equation of continuity and Darcy's law. For flow of a real compressible gas through a homogenous porous medium, changes of normalized pressure in time and space satisfy (20):

$$\frac{\partial P}{\partial t} + PZ \frac{\partial Z^{-1}}{\partial t} = \frac{\zeta}{\mu_R} \left[\frac{\partial^2 P^2}{\partial x^2} + \frac{\partial P^2}{\partial x} \left(Z \frac{\partial Z^{-1}}{\partial x} + \mu \frac{\partial \mu^{-1}}{\partial x} \right) \right] \quad (1)$$

$$\text{where } P = \frac{p}{p_o} \quad \text{and} \quad \zeta = \frac{K p_o}{\epsilon \mu_c} \quad (2)$$

The local pressure is p , p_o is the initial pressure (atmospheric) used for normalization, and ζ is a flow parameter similar to diffusivity and expressed in units of m^2/s . The critical viscosity of the fluid is μ_c , μ_R is the reduced viscosity defined as the ratio μ/μ_c , and Z is the compressibility of the fluid. K is the permeability of the porous medium and ϵ is its porosity. Dimensionless time (τ) and dimensionless distance (X) are defined as:

$$\tau = \left(\frac{\zeta}{\delta^2} \right) t = \Omega \cdot t \quad \text{and} \quad X = \frac{x}{\delta} \quad (3)$$

where Ω , the dynamic flow coefficient, is equal to ζ/δ^2 and can be considered to be the inverse of a characteristic time. Using dimensionless time and distance variables, equation 1 becomes:

$$\frac{\partial P}{\partial \tau} + PZ \frac{\partial Z^{-1}}{\partial \tau} = \frac{1}{\mu_R} \left[\frac{\partial^2 P^2}{\partial X^2} + \frac{\partial P^2}{\partial X} \left(Z \frac{\partial Z^{-1}}{\partial X} + \mu \frac{\partial \mu^{-1}}{\partial X} \right) \right] \quad (4)$$

Initially, at $\tau = 0$, $P = 1$ at all locations. The boundary conditions at $X = 0$ and $X = 1$ are that p is equal to the vessel pressure at all times. Since most biocides have low solubility in pure SC-CO₂ (less than 10^{-3} mole fraction), model fluid properties were assumed to be those of carbon dioxide. The modified Benedict-Webb-Rubin equation of state (21) was used to estimate compressibility. Viscosity was estimated based on the method of Jossi et al. (22).

Fundamental Solute Balance Equation. As an SCF solution flows through a porous medium, deposition of the solute on the interior porous surface results in retention. A balance on the mass of solute within the porous medium per volume of porous medium can be written as (23):

$$\varepsilon \frac{\partial w_2}{\partial t} + \frac{\partial(w_2 u)}{\partial x} + \varepsilon' \frac{\partial w_{2s}}{\partial t} = 0 \quad (5)$$

where w_2 is the mass of solute per volume of fluid, u is the superficial velocity of the fluid through the porous medium, w_{2s} is the mass of solute deposited per unit area within the porous medium, and ε' is the specific area, i.e. the surface area of pores per unit volume of porous medium. The term $\partial w_{2s} / \partial t$ in equation 5 represents the rate of deposition of solute onto the surface of the porous medium at position x and time t due to precipitation, reaction or adsorption. This local net deposition rate (per unit surface area) can be expressed as (24,25):

$$\frac{\partial w_{2s}}{\partial t} = \kappa_1 \exp\left(\frac{-\kappa_2}{(\log S)^2}\right) + \kappa_3 w_2 \quad (6)$$

where $S = w/w^*$ is the supersaturation with w^* as the saturated concentration. The constants κ_1 , κ_2 and κ_3 depend on the properties of the solvent, solute and the porous medium. The first term on the right-hand side represents precipitation. The second term accounts for first-order adsorption or reaction between the solute and the porous surface, however more complicated kinetics could be treated. The second term may be important in wood preservation because interactions of a biocide with the wood during conventional treatment with liquids can affect biocide distribution (26). The solute concentration (w_2) can be related to the SCF mass density (ρ_m) by (27):

$$\ln w_2 = n \ln \rho_m + \frac{a}{T} + b \quad (7)$$

where the constants a and b are related to the heat of solvation and molecular weight.

Simplified Solute Balance and Retention Calculation. Although the model developed above includes the important rates of phenomena involved in the impregnation process, methods do not exist to predict the parameters ε' , κ_1 , κ_2 and κ_3 . However, an assumption based on a limiting case allows the solution of a simplified model of the impregnation process. From solutions of equation 4 during venting, the rate of pressure drop at a point in the wood was calculated to be greater than the rate of pressure drop at a point in the flowing fluid (15). When the second term of equation 5 is negligible,

as a first approximation, the amount of deposited biocide can be calculated from the amount present in the fluid at the beginning of venting and the amount remaining in the saturated solution within the wood at any later time. The amount of biocide in the fluid within the wood (R^* in gm) in a volume of wood with L length, W width and (x_f-x_i) thickness at time t can be calculated from the biocide solubility f_s (mass biocide per mass solvent) when no supersaturation is assumed.

$$R^*(t) = \int_{x=x_i}^{x=x_f} \rho_m(x,t) f_s(x,t) \epsilon L W dx \quad (8)$$

Numerical solutions of the simplified model were obtained by first solving equation 4 using finite differences, then using those results to calculate SCF mass density and solute concentration from equation 7. Current retention in the fluid was then calculated from equation 8, and finally local deposition amounts were calculated as the biocide lost from the fluid since the beginning of the venting.

Performance of Simplified Model. In equations 2 and 3, the wood permeability, porosity, and thickness combine with the fluid critical viscosity and the initial pressure to produce the single model parameter Ω . For a treatment pressure of 250 bar at 50°C, the effects of treatment period on simulated total average retentions of TCMTB for selected values of Ω are shown in Figure 4. The solubility of TCMTB in pure SC-CO₂ at 50°C for various pressures was included by specifying n to be 9.129 and the term $a/T + b$ to be -3.314 in equation 7 (15). The maximum retention level shown in Figure 4 occurs when the treatment period is long enough to allow the saturated fluid to completely fill the wood before venting begins. The retention levels shown for a treatment period of zero minutes reflect impregnation during the initial pressurization period to reach treatment pressure. Final simulated distributions of TCMTB after a 30 minute treatment period at selected pressures from 140 to 250 bar are shown in Figure 5 for Ω equal to 10^{-4} s^{-1} . At higher treatment pressure, the retention at every location was larger and the distribution was more uniform. For example, a change from 200 bar to 250 bar resulted in an increase in the amount of TCMTB at the center from zero to more than one-third the value at the surface. For the same operating conditions, lower Ω values resulted in larger gradients near the surface.

Results obtained from the simplified model were compared with data collected for TCMTB treatment of Douglas-fir heartwood blocks using SC-CO₂ with 2.7 mol% acetone for 30 minutes at pressures between 140 and 270 bar. These experiments were not designed to obtain estimates of model parameters, but simply to obtain a variety of final distributions. Measured local retentions in a 38 mm square block at four depths are shown in Figure 6 along with model results for reasonable values of Ω based on previously measured wood properties (3). Measured retentions near the block surface were probably higher because of some surface deposition. Although simulated retentions were not based on fitted parameters, they showed reasonable behavior when compared with the data.

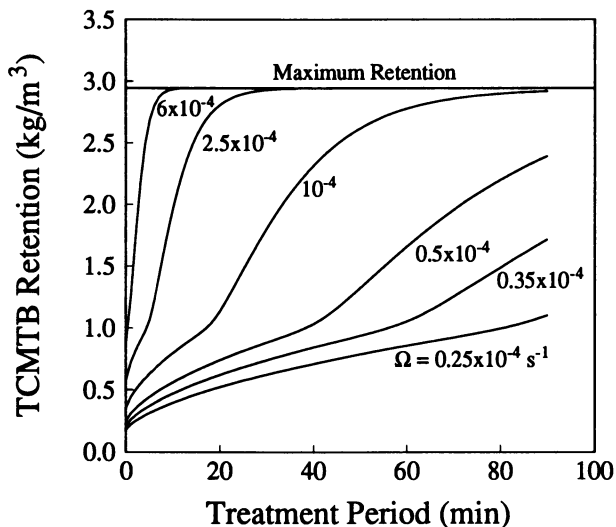


Figure 4. Simulated retentions of TCMTB in Douglas-fir blocks for selected values of Ω .

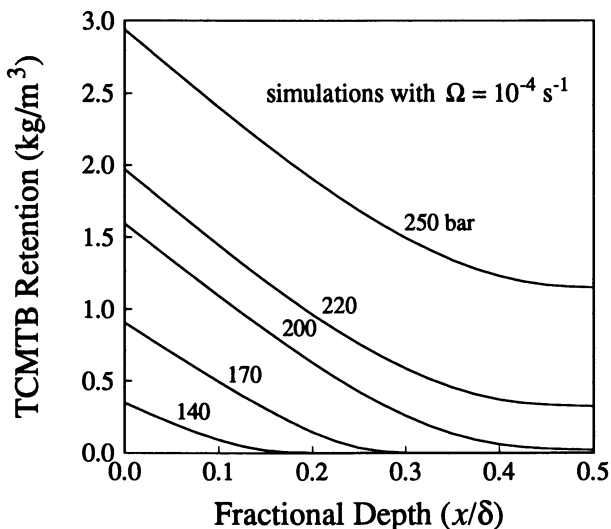


Figure 5. Simulated final distributions of TCMTB in Douglas-fir blocks treated for 30 minutes at 50°C at selected pressures from 140 to 250 bar.

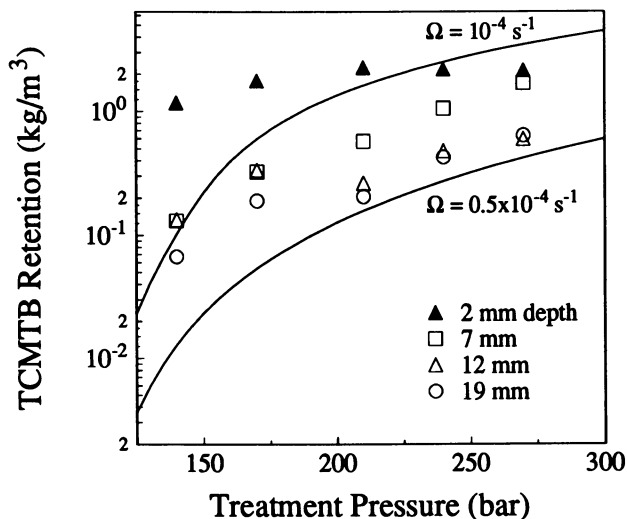


Figure 6. Simulated and measured TCMTB retentions at selected depths in Douglas-fir blocks treated for 30 minutes at 140 to 270 bar.

Final measured distributions of TCMTB in Douglas-fir blocks (19, 25 or 38 mm square sides, 100 mm length) treated at 250 bar for 30 minutes at 50°C are compared with simulation results for Ω values of 10^{-4} , 1.2×10^{-4} and 1.5×10^{-4} in Figure 7. Since this range of Ω values is reasonable, based on values of the wood porosity and permeability, the qualitative agreement to data indicates the modeling approach merits further development. These data clearly show that distribution can be affected by choice of operating variables and that modeling efforts are potentially useful in the study and design of supercritical wood impregnation processes.

Conclusions

Longer experimental treatment periods resulted in more uniform distributions with TCMTB and higher treatment pressure resulted in higher retention at all positions within wood blocks treated with TCMTB. Cosolvents had significant effects on total average retention of PCP in small dowels. A simplified model of the dynamics of the wood impregnation with a biocide using a supercritical fluid was developed which was based on macroscopic flow dynamics. The key features of this dynamic model include solvent and solute properties as functions of temperature and pressure and specification of the operating vessel pressure as a function of time. Additional experimental work is necessary, however, to identify model parameters which would allow important effects such as crystallization kinetics and biocide adsorption or reaction with wood to be included in an improved model.

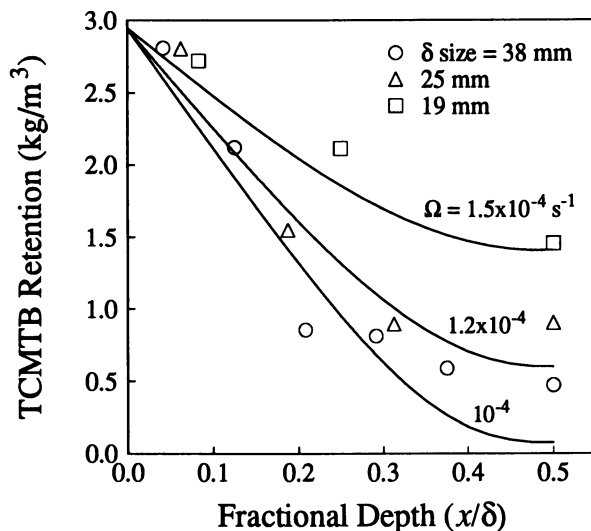


Figure 7. Simulated and measured TCMTB retentions in 19, 25 or 38 mm Douglas-fir blocks treated for 30 minutes at 250 bar and 50°C.

Acknowledgment

Some of the equipment used for this study was purchased with the support of the Electric Power Research Institute.

Literature Cited

1. Mott, W. E.; Rotariu, G. J. In *Impregnated Fibrous Materials*; Study Group on Impregnated Fibrous Materials meeting in Bangkok, Thailand; International Atomic Energy Agency: Vienna, 1967.
2. Bodig, J.; Jayne, B. A. *Mechanics of Wood and Wood Composites*, Van Nostrand Reinhold: New York, 1982.
3. Sahle-Demessie, E.; Hassan, A.; Levien, K. L.; Morrell, J. J. *Wood Fiber Sci.*, in press.
4. Ito, N. T.; Someya, T.; Taniguchi, M.; Inamura, H. Japanese Patent 59-1013111, 1984.
5. Kayihan, F. U.S. Patent 5 094 892, 1992.
6. Ward, D.; Dinatelli, T.; Sunol, A. K. Presented at the AIChE Spring National Meeting, Orlando, FL, March 1990; paper 66b.
7. Sunol, A. K. U.S. Patent 4 992 308, 1991.
8. Berneburg, P. L.; Forest, V.; Krukoni, V. J. U.S. Patent 4 552 786, 1985.
9. Saus, W.; Knittle, D.; Schollmeyer, E. *Textile Research J.*, **1993**, 63(3), 135-142.
10. Ward, D. MS Thesis, University of South Florida, 1989.

11. Ting, S. S. T.; Tomasko, D. L.; Macnaughton, S. J.; Foster, N. R. *Ind. Eng. Chem. Res.* **1993**, *32*, 1482-1487.
12. American Wood Preservers' Association (AWPA) *A Standard Method for Determining Penetration of Preservatives and Fire Retardants*; Standard A3-94, AWPA: Woodstock, MD, 1993.
13. Ferlazzo, D. E.; Kennedy, M.J. *A Reliable Spot Test for TCMTB in Wood*, International Research Group on Wood Preservation, 1992, IRG/WP Document No. 2391-92.
14. Daniels, C. R.; Swan, E. P. *J. of Chromatographic Science* **1987**, *25(1)*, 43-45.
15. Sahle-Demessie, E. Ph.D. Thesis, Oregon State University, 1994.
16. Bramhall, G. *Wood Sci. and Techno.* **1971**, *5*, 21-134.
17. Siau, J. F. *Transport Processes in Wood*; Springer-Verlag: Berlin, 1984.
18. Kunesh, R. H. *Forest Products J.* **1968**, *18(1)*, 65-72.
19. Dietz, A. G., Schaffer, E. L.; Gromala, D. S. *Wood As a Structural Material*, USDA Forest Products Laboratories, University of Wisconsin-Extension: Madison, WI, 1980.
20. Bear, J.; Buchline, J. M. *Modelling and Applications of Transport Phenomena in Porous Media*; Kluwer Academic Publishers: Dordrecht, 1991.
21. Ely, J. F.; *Proc. 65th Gas Proc. Assoc.*, 1986, 185-192.
22. Jossi, J. A.; Stiel, L. I.; Thodos, G. *AIChE J.* **1962**, *8*, 59.
23. Bel'kov, V. M. *Kolloidny Zhurnal* **1989**, *51*, 968-972.
24. Mullin, J. W. *Crystallization*; 2nd ed.; CRC Press: Boston, MA, 1972.
25. Song, L.; Elimelech, M. *J. Colloids and Surfaces* **1993**, *11(3)*, 104-111.
26. Nicholas, D. D.; Preston, A. F. *Interaction of Preservatives With Wood*, In *Advances in Chemistry*, 207; American Chemical Society: Washington, DC, 1984.
27. Chrastil, J. *J. Phys. Chem.*, **1982**, *86*, 3016-3021.

RECEIVED June 26, 1995

Chapter 29

Supercritical Extraction of Paclitaxel Using CO₂ and CO₂–Ethanol Mixtures

Vishnu Vandana and Aryn S. Teja¹

School of Chemical Engineering, Georgia Institute of Technology,
Atlanta, GA 30332–0100

Taxol is an exceptionally promising cancer therapeutic agent with an unusually broad spectrum of antileukemic and tumor inhibiting activity. To date, slow growing yew trees are the major source of this compound. New separation methods are therefore of interest for its extraction from the plant material. The extraction of taxol from the bark of *Taxus brevifolia* using supercritical carbon dioxide with and without ethanol as a co-solvent was studied in this work. The extractions were performed at 319 K and 331 K and at pressures ranging from 10 to 38 MPa. The addition of co-solvent significantly increased the rate of extraction of taxol. Furthermore, supercritical extraction was found to be more selective than conventional liquid ethanol extraction and could remove a significant amount of the taxol present in the bark.

Taxol is an alkaloid currently in phase III clinical trials for the treatment of ovarian cancer. It is found in trees of the *Taxus* species and was first isolated from the bark of *Taxus brevifolia* by Wani et al. in 1971 [1]. Its chemical structure shown in Figure 1. Isolation of the drug from the bark of several *Taxus* species has been reported by a number of researchers [2, 3, 4], although there is some concern about the natural supply of taxol.

Total and partial synthesis of the drug are being studied in several laboratories [5, 6, 7, 8, 9, 10]. Total synthesis of taxol has been achieved from simple starting materials by Holton et al. and Nicolaou et al. [11, 12, 13, 14]. However, the yields obtained in these syntheses are small and total synthesis

¹Corresponding author

NOTE: Paclitaxel is the generic name for Taxol, which is now a registered trademark.

0097–6156/95/0608–0429\$12.00/0

© 1995 American Chemical Society

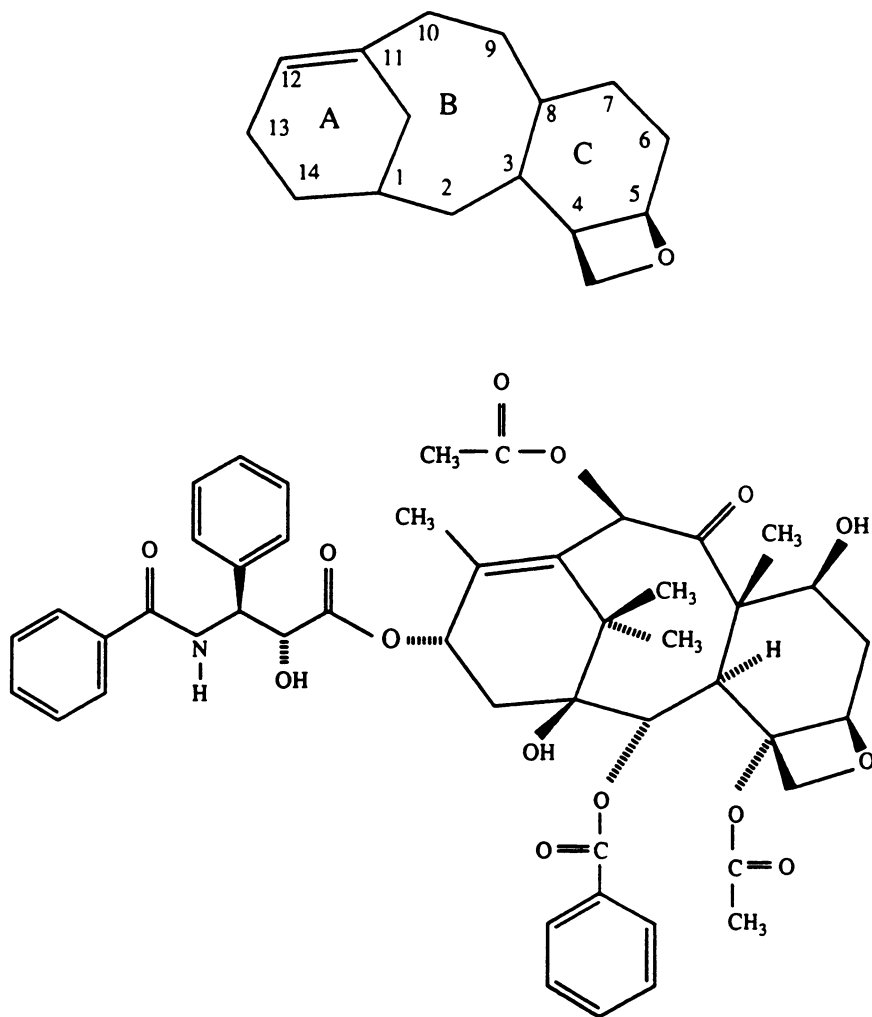


Figure 1. Structure of Taxol.

is unlikely to provide the required quantity of taxol in the near future. Partial synthesis from precursors such as baccatin III and 10-deacetylbaccatin III is a more practical solution to the supply problem, and has been achieved by Dennis et. al [15]. However, this approach will require more efficient isolation and extraction methods for the precursors.

Production from tissue culture is another alternative that is being pursued [16]. However, it is difficult to establish long term micro cultures of conifers due to the difficult juvenile tissue, production of detrimental secondary metabolites and recalcitrance of this group of plants to form in-vitro cultures. Though shoot cultures are difficult to establish, long term maintenance of callus and cell cultures is being established and effects of various parameters such as plant growth regulators, vitamins and minerals on growth rate, production of secondary metabolites, rate of production of taxol, and formation of other taxanes, are being studied. Genetic engineering of taxol is also being investigated. Transferring the enzyme system to a faster growing species or to a yeast or a bacterium is being considered [17]. However, the apparent difficulty in executing this method is the bioactivity of the product towards eukaryotic tubulin. The other obstacle is the absence of information on the biosynthetic pathway.

One of the major sources of taxol is material from the trees of the *Taxus* species. Since the amount of taxol present in the trees is small ($\sim 0.01\%$), it is important to develop an effective separation process for its extraction. Current production methods are estimated to extract only half the amount of taxol that is present in the tree. In this study, a new supercritical based separation process has been developed to extract and isolate taxol and related taxanes from the bark and needles of the *Taxus brevifolia*.

Supercritical extraction offers a number of advantages over more conventional separation techniques in biochemical and biotechnology applications. The solvents (*e.g.*, carbon dioxide) used are physiologically inert thus avoiding toxicity and environmental problems. Since the density of a supercritical fluid is a strong function of temperature and pressure, separation of the solute and solvent can be achieved with small changes in temperature or pressure. Also, addition of a small amount of co-solvent generally increases the solvent power and selectivity of the solute in the supercritical phase. Finally, supercritical extraction can be combined with other post extraction processes to yield hybrid separation processes. Because of these advantages, the use of

supercritical fluids in the recovery of taxol and precursors was studied in this work.

Experimental

Reagents and Materials. Coleman grade carbon dioxide of minimum purity 99.99 % was obtained from Matheson Gas Products. HPLC grade Methanol and Water and reagent grade (99.99 %) Toluene and Ethanol were purchased from J. T. Baker Incorporated. Acetic acid with a purity of 99.99 % was obtained from Fischer Scientific Incorporated. The taxane standard kit consisting of taxol, cephalomannine, 10-deacetylbaaccatin III, baccatin III, 7-epi 10-deacetyltaxol, and 10-deacetyltaxol was obtained from the Drug Synthesis and Chemistry Branch, Development Therapeutics Program, Division of Cancer treatment, National Cancer Institute (Bethesda, MD). The C₁₈ reverse phase column was purchased from Alltech Associates Inc. Supercritical extracts were filtered using nylon 66 membranes 13 mm in diameter and 0.45 micron pore size, purchased from Alltech Associates Inc. Dry bark of *Taxus brevifolia* from Connolly/Eller Cottage Grove, Oregon. The bark was ground before use and the same source of ground tree bark was used in all the experiments. All substances were used without further purification.

Apparatus. An ISCO SFE 2-10 Extractor system was used to perform supercritical extractions of taxol from the bark of *Taxus brevifolia*. The system employed two ISCO syringe pumps (Model 260 D) to pump liquid carbon dioxide and the co-solvent (ethanol) into the extractor. A Buchler micro-rotary evaporator from Fischer Scientific Inc. was used to evaporate the solvents from the supercritical extracts. The extracts were analyzed using an LDC Analytical HPLC system. The HPLC system was equipped with a constaMetric 4100 quaternary solvent delivery pump, a membrane degasser and a spectroMonitor 5000 photo-diode array detector. The HPLC system was also equipped with a 486DX IBM PC/AT computer containing the LCTalk 2-channel analog data acquisition system for automated analysis.

A vortex mixer purchased from Thermolyne Corporation (model M16715) was used to mix the extracts before filtering. A wet test meter purchased from Precision Scientific Inc. (model 63111, D-3B) was used to measure the gas volumes of carbon dioxide. The system pressure and temperature were monitored by a pressure gauge purchased from Heise (model 8400) and a Leeds and Northrup thermistor respectively. A standard platinum resistance thermometer (SPRT) was used to calibrate the thermistor.

Experimental Procedure. A schematic diagram of the apparatus used in this work is shown in Figure 2. Liquid carbon dioxide from a cylinder equipped with an eductor tube was pumped using an ISCO syringe pump while a second ISCO syringe pump was used to pump ethanol when needed. The syringe pump used to pump carbon dioxide was equipped with a cooling jacket to ensure that carbon dioxide remained in the liquid phase while being pumped into the extractor. Absolute ethanol was stored in a reservoir connected to the other syringe pump. A common pump controller unit was used to set the ethanol concentration and the system pressure. The supercritical fluid mixture then passed through static mixers into the extractor which was maintained at a constant temperature. A thermistor was used to record the temperature of the experiments.

Extractions of taxol from the bark were performed using carbon dioxide as the supercritical fluid with and without ethanol as a co-solvent. During each experiment, carbon dioxide and ethanol were pumped through a coil and static mixers placed to ensure that the CO₂ + ethanol mixtures were homogeneous and at bath temperature prior to contacting the ground *Taxus brevifolia* bark. Approximately 3.5 grams of ground bark was placed in a high pressure cell (cartridge) of 10 mL internal volume. Filters, 5 microns in diameter, were placed in the cartridge at the exit ports to prevent any bark from being carried out with the supercritical fluid. The loaded supercritical fluid was depressurized across a heated capillary tubing into a collection vessel placed in an ice bath. The depressurized fluid was then passed through a second collection vessel (in experiments involving a co-solvent) placed in a dry ice/ethanol bath. The gaseous carbon dioxide was then passed through the wet test meter (Fischer Scientific Inc., model 63111,D-3B) for flow totalization. Flowrates were kept at approximately 0.3-0.4 mL/min to allow sufficient residence time for the solvent to contact the bark.

The soluble bark extract, as well as some of the ethanol (if present), were precipitated and collected in the first collection vessel. The collection vessel incorporated a cold finger with the exit arm of the trap packed with glass wool to prevent the precipitated material from being carried out of the trap. A U-tube packed with glass wool served as an additional trap for any remaining ethanol, leaving practically pure carbon dioxide to pass through the wet test meter.

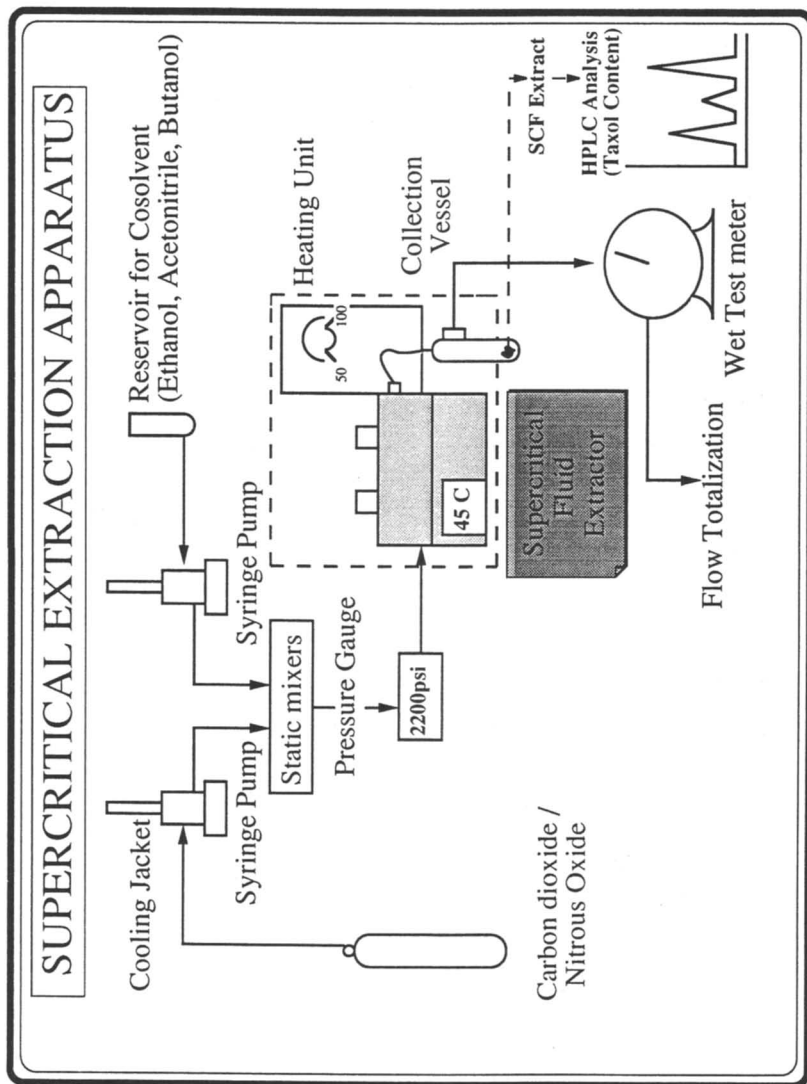


Figure 2. Experimental Apparatus.

The pressure was controlled by the pump controller unit and measured with a Heise pressure gauge (model 8400). The Heise gauge was calibrated against a Budenberg dead weight tester. The uncertainty in the measurement of system pressure was found to be ± 0.046 MPa. The temperature was monitored by a Leeds and Northrup thermistor in the extractor, and a thermocouple inserted inside the extractor was used to control the temperature of the extractor. The thermistor was calibrated against a standard platinum resistance thermometer (model number: R800-3 2.5Ω , Serial Number: RS90Y-11) traceable to NIST. The uncertainty in the measurement of system temperature was estimated to be ± 0.5 K. The volume of carbon dioxide was determined using the wet test meter which was factory calibrated with a stated accuracy of ± 0.5 %. Blank experiments were performed to calibrate the solvent delivery system and the co-solvent composition was found to be accurate within ± 0.5 mole %. The amount of ethanol was determined gravimetrically by weighing the collection vessels before and after the experiment. A Sartorius balance was used for the gravimetric analysis and had an accuracy of ± 0.0005 g. Since the total weight of bark extract was small, it was neglected in determining the weight of ethanol collected. The amount of dried bark extract was also determined gravimetrically as follows. At the end of the extraction run, the contents of the first collection vessel, extracted bark material, flush solvent, and co-solvent (if used), were transferred to a distillation flask. 5-10 mL of toluene were then used to flush the collection vessel and the liquid was also transferred to the flask. The flush solvent and co-solvent ethanol were then evaporated under reduced pressure in a rotary evaporator. The bark extract was dissolved in approximately 5 mL of toluene and transferred into a preweighed vial; and the toluene was again evaporated by rotary evaporator. A slow stream of nitrogen was passed over the bark extract to ensure that all the toluene was removed. The vial was then weighed to determine the total weight of bark extract.

The amount of taxol present in the bark extract was determined by HPLC analysis of the methanol soluble portion of the extract. The HPLC samples were prepared and analyzed in the following manner. A known amount of methanol was first added to the dried bark extract. The solution was sonicated and mixed in a vortex mixer to ensure that the soluble components had dissolved. The solution was then filtered and the methanol soluble portion was analyzed by HPLC. The solution was separated on a 250 mm C_{18} Alltech

Table I: Extraction of Taxol from *Taxus brevifolia* Using Supercritical Carbon Dioxide and Carbon Dioxide + Ethanol Mixtures

T (K)	P (MPa)	Mass Bark in Cell (g)	Mass Taxol in Bark (mg)	Moles CO ₂	Mole % Ethanol	Mass Taxol in Extract (mg)	Mass Extract (g)
319.7	13.67	3.4085	0.5454	6.9619	0	0.0021	0.0100
318.5	20.67	3.5968	0.5755	7.1960	0	0.0025	0.0055
318.9	27.59	3.5746	0.5719	6.0154	0	0.0078	0.0021
319.3	34.39	3.5773	0.5724	6.3740	0	0.0021	0.0289
av:319.1							
320.4	10.29	3.4460	0.5514	3.6253	6.1	0.0665	0.1122
320.2	13.75	3.5923	0.5748	3.3908	5.0	0.0377	0.0673
320.0	20.63	3.6762	0.5882	3.9933	5.5	0.0721	0.0705
319.9	27.37	3.4936	0.5590	3.4673	5.1	0.0746	0.0915
319.9	34.18	3.6516	0.5843	3.1254	5.6	0.1410	0.1408
319.8	38.20	3.7699	0.6032	3.3769	4.9	0.1670	0.1285
av:320.0					av:5.4		
319.7	10.33	3.5876	0.5740	3.3465	11.0	0.1210	0.0586
319.8	13.78	3.4301	0.5488	4.9237	9.8	0.0784	0.4083
319.9	20.37	3.1699	0.5072	3.7093	10.0	0.1210	0.0726
319.7	27.12	3.6723	0.5876	3.6687	11.1	0.2200	0.1318
319.6	34.34	3.5411	0.5666	4.9789	10.0	0.3020	0.4865
319.3	37.74	3.4988	0.5598	3.5089	11.1	0.2590	0.1427
av:319.7					av:10.5		
330.6	13.71	3.8346	0.6135	3.2005	4.6	0.0693	0.0822
330.5	20.74	3.7293	0.5967	4.4236	5.1	0.0509	0.1157
330.5	27.64	3.5530	0.5685	3.3603	4.5	0.0951	0.2279
331.0	34.30	3.9139	0.6262	3.7439	4.9	0.0858	0.1269
331.6	38.10	3.6255	0.5801	3.7015	4.7	0.1150	0.0965
av:330.8					av:4.9		
330.8	10.65	3.8197	0.6112	3.2593	10.4	0.1470	0.2669
330.7	14.07	3.7333	0.5973	5.5343	11.0	0.1300	0.0506
330.7	20.80	3.7819	0.6051	3.8924	9.8	0.1570	0.0681
331.2	27.62	3.5230	0.5637	4.4458	11.1	0.1620	0.0629
330.8	34.28	3.7584	0.6013	3.3728	11.0	0.2440	0.0648
330.8	37.95	3.7523	0.6004	3.7390	9.4	0.2470	0.0584
av:330.8					av:10.5		

reverse phase column using a shallow gradient of mobile phase which varied from 58.5:41.5 methanol-water to 61.5:38.5 methanol-water for 25 minutes. The mobile phase flowrate was maintained at ~ 1.45 ml/min. The absorption at 227 nm was monitored and the datafiles containing the chromatograms were stored on disk for future reference. The amount of taxol present in the bark was quantified by comparing the response of the peak area of taxol in the extract sample to the peak area of taxol from a standard solution of taxol in methanol. The injection volumes were $20 \mu\text{L}$ for each extract and standard solution.

Results and Discussion

Table I shows the results of extractions using supercritical carbon dioxide and carbon dioxide + ethanol mixtures at 319 K and 331 K. All the experiments were performed with ground bark of *Taxus brevifolia*, with an average particle size less than 0.495 mm in diameter. As expected, the amount of taxol extracted is small and increased with an increase in pressure. Addition of ethanol as a co-solvent led to an increase in the amount of taxol present in the extracts as shown in Table I. In our previous studies [18], it was observed that the concentration of taxol in the extract decreased with extraction time and became quite small after 3.5 - 4.0 moles of carbon dioxide had passed through the bed. Therefore, 3.2 - 5.5 moles of carbon dioxide + ethanol mixtures were used in the extractions carried out in this study. Figure 3 shows a plot of moles of taxol extracted by 4 moles of carbon dioxide as a function of pressure at 318 K. It can be seen that the amount of taxol extracted increases with an increase in pressure and with the the addition of co-solvent. The selectivity and extractability of taxol improved with the addition of ethanol. A plot of solubility enhancement (E) = $y_{\text{ternary}}/y_{\text{binary}}$ is shown in Figure 4 which shows solubility enhancements of 5-20 fold.

The supercritical extracts obtained using carbon dioxide contained small amounts of taxol and were spiked with the taxol standard to quantify the total amount of taxol extracted. However, with the addition of ethanol, samples could be directly injected on to the HPLC columns. A comparison of the amount of taxol extracted shows that almost 50 % of taxol present in the bark was extracted using approximately 4 moles of supercritical carbon dioxide at the highest co-solvent composition of ~ 10.5 mole % ethanol, whereas only 9 % was extracted without the use of a co-solvent. The composition of taxol in the supercritical extracts using carbon dioxide + ethanol mixtures varied from 0.05 to 0.5 mass %, an increase of approximately 5-50 fold from that

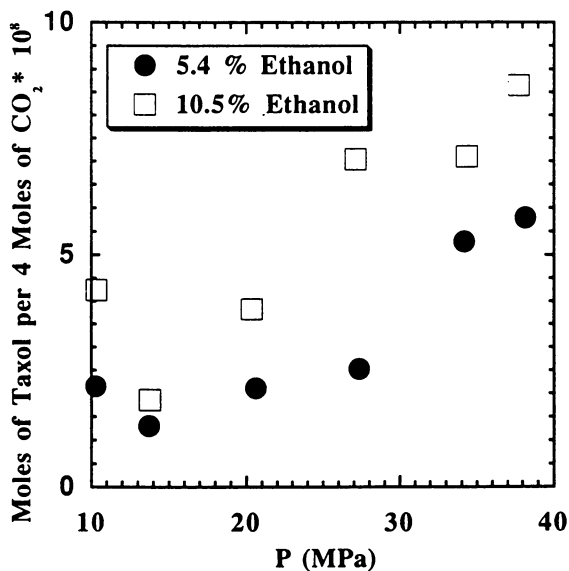


Figure 3. Moles of Taxol Extracted per 4 Moles of Carbon Dioxide as a Function of Pressure (the results are normalized to show the trends).

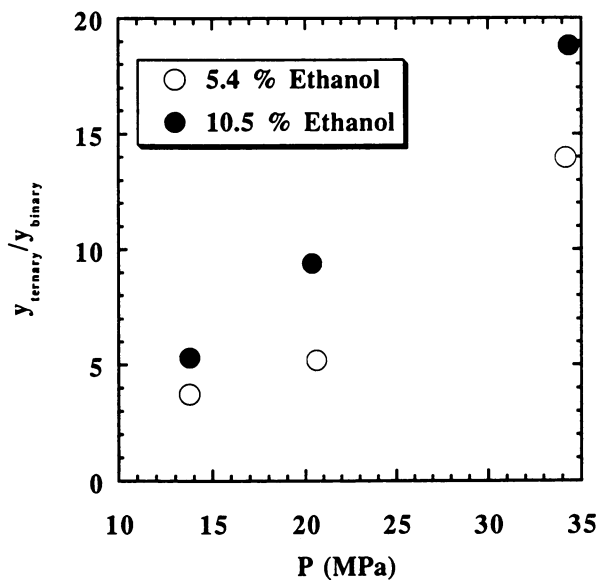


Figure 4. Solubility Enhancement.

seen in the bark. All the calculations to determine the taxol content in the extracts were based on total taxol content of 0.016 % in the bark obtained by an exhaustive liquid ethanol extraction of the bark [19].

The HPLC analysis of the supercritical extracts involved a time-optimized method incorporating a gradient elution of the mobile phase. Figure 5 shows the results obtained when a standard solution of pure taxol was injected on the C₁₈ column; taxol is shown to elute at about 19.0 minutes. Figure 6 shows the results when a standard solution containing taxol and related taxanes was injected on the column using the same mobile phase; there is clear baseline separation of all the taxanes. Two of the more polar taxanes, 10-deacetylbaccatin III and baccatin III elute at the beginning of the run. These two compounds are found in the leaves of the *Taxus* species and have been used as starting materials to partially synthesize taxol. This represents an excellent solution to the supply problem as the leaves are renewable and taxol can be obtained without depleting the yew population. Cephalomannine, which elutes at 17.27 minutes is very similar in structure to taxol but does not have any tumor-inhibitory activity. Since it elutes very closely to taxol, it generally creates a problem in the separation of taxol. With the method chosen in this study, we have been able to eliminate the problem as can be seen clearly in the chromatogram. The other two compounds, 10-deacetyltaxol and 7-epi 10-deacetyltaxol, are decomposition products which need to be identified to ensure that taxol has not decomposed during the extraction process. Figure 7 shows a typical chromatogram of the supercritical extracts. A lot of polar material elutes at the beginning of the run, but a clear baseline separation of taxol and related taxanes is observed.

Addition of ethanol as a co-solvent alters the components present in the supercritical extracts. When supercritical extractions were performed using carbon dioxide, the extracts consisted of predominantly non-polar components. With the addition of ethanol, the extracts included both non-polar and some polar components. Liquid ethanol extracts of the plant material consisted predominantly of polar material. This can be seen clearly in the HPLC analysis of the extracts using a mobile phase starting with 50:50 methanol-water for the first five minutes and a gradient to 100 % methanol in the next five minutes, followed by 100 % methanol in the last 10 minutes. Figure 8 illustrates the composition of the supercritical extracts (with and without a co-solvent) and the liquid ethanol extracts on a C₁₈ reverse phase column. The more polar

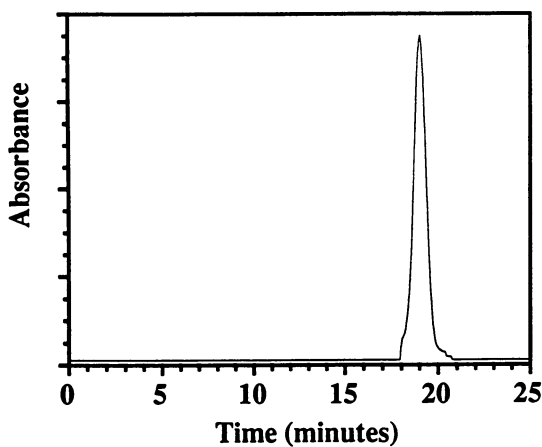


Figure 5. Chromatogram of a Standard of Pure taxol on a C_{18} Reverse Phase Column.

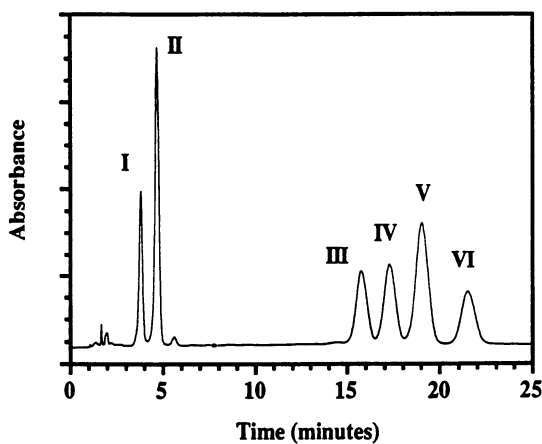


Figure 6. Chromatogram of a Mixture of 10-deacetylbaaccatin III (I), bac-catin III (II), 10-deacetyltaxol (III), cephalomannine (IV), taxol (V), and 7-epi-10-deacetyltaxol (VI) on a C_{18} Reverse Phase Column.

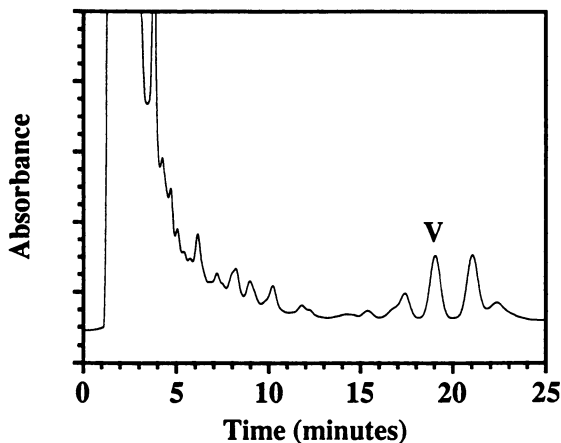


Figure 7. Chromatogram of a Supercritical Extract on a C_{18} Reverse Phase Column. Taxol Peak is Labelled as (V).

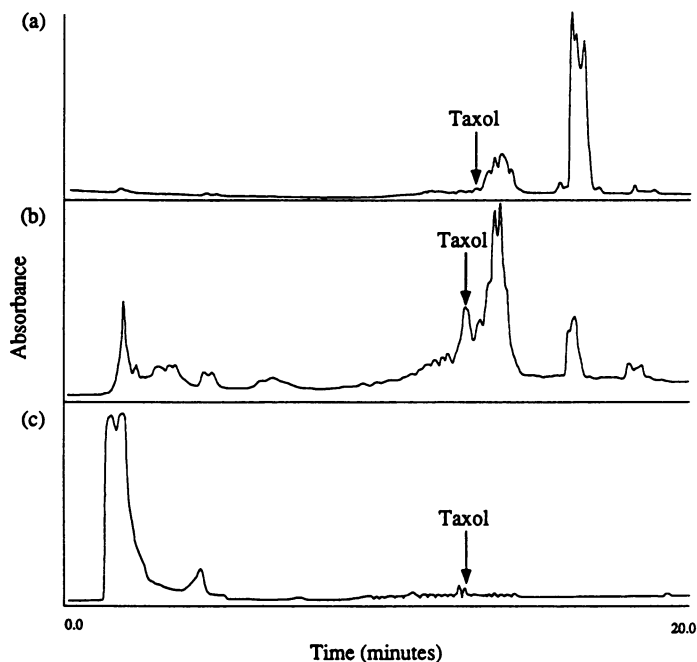


Figure 8. Comparison of the Composition of the Extracts Depicted in the Chromatograms on a C_{18} Reverse phase Column a: Supercritical Extract Using CO_2 Without Co-solvent, b: Supercritical Extract Using CO_2 With Ethanol as a Co-solvent, c: Liquid Ethanol Extract.

material elutes at the beginning of the run, followed by the less polar material when 100 % methanol is used as the mobile phase towards the end of the run. Taxol elutes at 12.8 minutes in this case.

Conclusions

Supercritical fluid carbon dioxide and carbon dioxide + ethanol mixtures were used to extract taxol from the bark of *Taxus brevifolia*. The carbon dioxide + ethanol mixtures proved to be better solvents in extracting the drug from the plant material than carbon dioxide alone. Addition of ethanol led to an increase in selectivity and extractability of taxol. This study shows that supercritical fluid extraction can be used as a valuable step in the extraction of taxol.

Acknowledgments

The authors would like to thank Dr. Gordon Cragg and the National Cancer Institute for supplying the bark of *Taxus brevifolia*; Dr. K. Snader and the Drug Synthesis and Chemistry Branch, Development Therapeutics Program, Division of Cancer treatment, National Cancer Institute (Bethesda, MD) for supplying the taxanes standards kit; and Dr. H. M. Deutsch for his help and suggestions in the HPLC method development.

Literature Cited

- [1] Wani, M. C.; Taylor, H. L.; Wall, M. E.; Coggon, P.; and McPhail, A. T. *J. Am. Chem. Soc.*, **1971**, 93, 2325.
- [2] McLaughlin, J. L.; Miller, R. W.; Powell, R. G.; and Smith, Jr., C. R. *J. Nat. Prod.*, **1981** 44, 312.
- [3] Miller, R. W.; Powell, R. G.; and Smith, C. R. *J. Org. Chem.*, **1981**, 46, 1469.
- [4] Stasko, M. W.; Witherup, K. M.; Ghiorzi, T. J.; McCloud, T. G.; Look, S. A.; Muschik, G. M.; and Issaq, H. J. *J. Liq. Chrom.*, **1989**, 12, 2133.
- [5] Wender, P. A.; and Muccario, T. P. *J. Am. Chem. Soc.*, **1992**, 114,5878.
- [6] Deng, L. and Jacobsen, E. N. *J. Org. Chem.*, **1992**, 57, 4320.
- [7] Queneau, Y.; Krol, W. J.; Bornmann, W. G.; and S. J. Danishefsky, S. J. *J. Org. Chem.*, **1992**, 57, 4043.
- [8] Magee, T. V.; Bornmann, W. G.; Richard, C. A.; and Danishefsky, S. J. *J. Org. Chem.*, **1992**, 57, 3274.
- [9] Benchikh Le-Hocine, M.; Do Khac Duc; Fetizon, M.; Guir, F.; Guo, Y.; and Prange, T. *Tetrahedron Lett.*, **1992**, 33, 1443.

- [10] Denis, J. N.; Correa, A.; and Greene, A. E. *J. Org. Chem.*, **1991**, 56, 6939.
- [11] Holton, R. A.; Somoza, C.; Kim, H-B.; Liang, F.; Biediger, R. J.; Boatman, P. D.; Shindo, M.; Smith, C. C.; Kim, S.; Nadizadeh, H.; Suzuki, Y.; Tao, C.; Vu, P.; Tang, S.; Zhang, P.; Murthi, K. K.; Gentile, L. N.; and Liu, J. H. *J. Am. Chem. Soc.*, **1994**, 116, 1597.
- [12] Holton, R. A.; Kim, H-B.; Somoza, C.; Liang, F.; Biediger, R. J.; Boatman, P. D.; Shindo, M.; Smith, C. C.; Kim, S.; Nadizadeh, H.; Suzuki, Y.; Tao, C.; Vu, P.; Tang, S.; Zhang, P.; Murthi, K. K.; Gentile, L. N.; and Liu, J. H. *J. Am. Chem. Soc.*, **1994**, 116, 1599.
- [13] Nicolaou, K. C.; Yang, Z.; Liu, J. J.; Ueno, H.; Nantermet, P. G.; Guy, R. K.; Clairborne, C. F.; Renaud, J.; Couladouros, E. A.; Paulvannan, K.; and Sorensen, E. J. *Nature*, **1994**, 367, 630.
- [14] Nicolaou, K. C.; Clairborne, C. F.; Nantermet, P. G.; Couladouros, E. A.; and Sorensen, E. J. *J. Am. Chem. Soc.*, **1994**, 116, 1591.
- [15] Denis, J. N.; Greene, A. E.; Guenard, D.; Gueritte-Voegelein, F.; Mangatlal, L.; and Potier, P. *J. Am. Chem. Soc.*, **1988**, 110, 5917.
- [16] Christen, A. A.; Bland, J.; and Gibson, D. M. *Proc. Am. Assoc. Cancer Res.*, **1989**, 30, 2252.
- [17] Towers, G. H. N. *Workshop on Taxol and Taxus: Current and Future Perspectives*, **1990**, June.
- [18] Vandana, V.; and Teja, A. S. *Submitted to Biotech. & Bioeng.*, **1994**.
- [19] Jennings, D. W.; Deutsch, H. M.; Zalkow, L. H.; and Teja, A. S. *J. Supercrit. Fluids.*, **1992**, 5, 1.

RECEIVED July 24, 1995

Chapter 30

Supercritical Water Oxidation of Pulp and Paper Mill Sludge as an Alternative to Incineration

Carol A. Blaney¹, Lixiong Li², Earnest F. Gloyna², and Shafi U. Hossain¹

¹Long Range Research and Development, Kimberly-Clark Corporation,
1400 Holcomb Bridge Road, 400-4, Roswell, GA 30076

²Environmental and Water Resources Engineering and Separation
Research Programs, J. J. Pickle Research Campus, University of Texas,
Austin, TX 78758

This paper summarizes recent research by Kimberly-Clark Corporation and The University of Texas at Austin in a new technology referred to as "Supercritical Water Oxidation" (SCWO), an emission-free and discharge-free alternative to incineration, to treat wastes such as pulp and paper mill sludges. SCWO has been shown to be an effective method to treat pulp and paper mill sludge, converting it to usable by-products of clean water (for reuse in paper mill), carbon dioxide gas, and dioxin-free ash (mostly CaCO₃, which can be used as paper filler or cement aggregate). The majority of all organics are destroyed, including polychlorinated biphenyls and 99+ % of chlorinated organics such as dioxins and dibenzofurans. Economic studies indicate that a commercial SCWO process can compete on a cost basis with fluidized bed incineration. A new reactor design is discussed which avoids the problem of corrosion.

The present work relates to the technical feasibility of the process termed "Supercritical Water Oxidation" in oxidizing pulp and paper mill sludge in water under supercritical conditions in order to destroy all organic material, including all trace chlorinated organics such as polychlorinated biphenyls (PCBs), dioxins (PCDDs) and dibenzofurans (PCDFs). In the context of this report, pulp and paper mill sludge refers to that portion of the papermaking process waste stream that contains cellulosic fibrous fines and debris, inorganic materials such as fillers and clay, and small amounts of residual pulping and/or deinking chemicals, in an aqueous medium.

Responsible solid waste stream management, of which industrial wastes such as pulp and paper mill sludge constitute a significant part (approximately 70 million bone dry tons per year of pulp and paper mill sludge is generated worldwide), is becoming a regular theme of modern society. Until recently, landfill has been the disposal method of choice for solid wastes such as paper mill sludge due to economic appeal. However, recent legislative trends indicate that in the future, landfill sites may become harder to obtain and more expensive to maintain, especially for solid wastes containing real or perceived toxic materials. Increased attention has thus begun to be placed on alternative methods of

0097-6156/95/0608-0444\$12.00/0
© 1995 American Chemical Society

waste disposal such as recycling, waste reduction at the source, various forms of conventional incineration, bioremediation, and most recently SCWO.

Incineration. In the case of paper mill sludge disposal, conventional incineration is commonly thought to be a feasible alternative to landfill, but as presently practiced, incineration may bring with it potential problems, specifically the issue of releasing reportedly toxic compounds such as PCDDs and PCDFs, whose structures are shown in Figure 1, into the environment via the incinerator off-gas emissions and/or fly ash. Since rotary kiln and fluidized bed incinerators are inherently open systems (open to the atmosphere), there is always a potential for fugitive emissions. It has been reported in the literature that conventional incineration may not always destroy these chlorinated organic compounds, and in fact, under certain conditions incineration systems may actually generate more of these compounds [1].

For example, as described by Acharya et al. [1], as long as the minimum required temperature of 871°C for the complete combustion of organics is maintained, the rate-limiting step in incinerators is often the diffusion of oxygen to carbon monoxide intermediates to form carbon dioxide. Hence the reaction is mixing limited. Often incinerators do not obtain adequate mixing, and thus organics and chlorinated organics present in the feed may not be completely oxidized.

Another potential problem with incinerators is the possible formation of PCDDs, referred to in the literature as "de novo formation of dioxins", and is defined as follows: "dioxin formation from the pyrolysis of a variety of chemically unrelated precursors including naturally occurring precursors together with a chlorine donor" [1]. Likely precursors include, for example, 2,4,5-trichlorophenol, halogenated aliphatics, benzene in the presence of AlCl_3 , short chain alkanes with HCl, residual carbon with catalyst, and even CO_2 plus catalyst in the presence of chlorine compounds (although to a lesser extent), all of which can and often do occur in incinerator fly ash.

Vogg et al. [2] found for incinerators that, in the presence of air, the optimum temperature for PCDD formation from precursors (such as those listed above) was between 250 and 350°C, and for PCDF formation was between 250 and 400°C. These temperatures can often occur in waste incinerators, principally in the energy recovery boilers and the partial quench associated with certain systems.

Further experiments by Vogg et al. [2] confirm that both oxygen and water vapor concentrations affect the formation of PCDDs in incinerators. For example, at 300°C, oxygen concentrations over one mole percent exacerbated PCDD and PCDF formation dramatically. And in experiments where moisture was present, predominantly tetra-, penta-, and hexachloro isomers of PCDDs and PCDFs were formed – whereas in dry experiments the more highly chlorinated isomers (e.g. octa-) of PCDDs and PCDFs tended to be formed instead.

Other factors affecting dioxin formation in incinerators are: 1) the presence of residual carbon and inorganic chlorides such as NaCl on the fly ash, 2) the presence of HCl, SO_2 and Cl_2 , and 3) the presence of catalysts (e.g. CuCl, alkali and alkaline earth chlorides, alkali halides and alkaline halide salts). To prevent dioxin formation in the boiler, it was suggested by Acharya et al. [1] to "Use a two-stage incinerator utilizing a turbulent high-temperature oxidative secondary combustor operating with 2 seconds minimum retention time, followed by a rapid full quench to adiabatic saturation (no boiler)." This implies no heat would be recovered, and the system would be energy intensive (requiring fuel).

Supercritical Water Oxidation (SCWO). The largest known commercial SCWO unit is 5 gallons per minute capacity (Huntsman Chemical unit at Austin Research Laboratories, Austin, Texas, constructed by Eco Waste Technologies). Although this size is still very small, the new and emerging technology of SCWO offers definite environmental benefits over incineration, and will possibly mature into being cost-

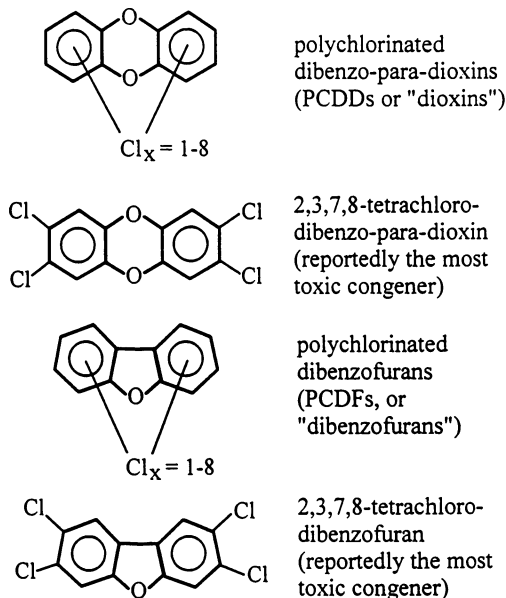


Figure 1. Chemical structure of PCDDs and PCDFs.

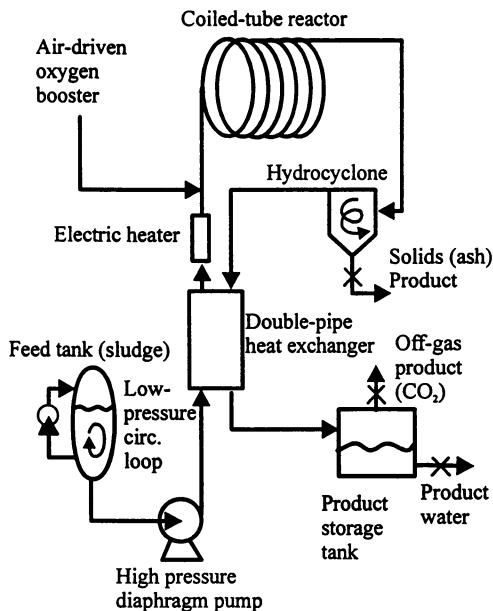


Figure 2. Pilot plant schematic diagram.

comparable to 'standard' incineration ('standard' incineration here implies minimal pollution control equipment).

In a SCWO process environment, the chemical oxidation takes place in a dense water vapor-type medium. Typically the supercritical water mixture's densities are around 0.3 g/cc, and around two-thirds of the hydrogen bonds are destroyed. Under these conditions the supercritical water acts as a powerful organic solvent which penetrates into polymeric networks, surrounding organic moieties. The oxidation reaction is generally complete in less than about a minute if temperatures are in the range of 500 to 600°C.

The application of SCWO to treat pulp or paper mill sludge would comprise bringing the aqueous sludge slurry to conditions near or above the critical point of water ($T_c=374^\circ\text{C}$, $P_c=218\text{ atm} = 3204\text{ psi}$) in the presence of an oxygen donor such as air or hydrogen peroxide. Typical temperatures are around 500°C, and typical pressures are 230 atm (3400 psi). Products are clean water (may contain HCl), clean ash (e.g. deinking sludge would produce predominantly calcium carbonate ash with residual metals if present) and clean vapor containing the carbon dioxide product and any residual oxygen, along with water vapor. Any nitrogen-containing organic material will produce nitrogen gas (N_2) or N_2O ; little or virtually no NO_x is formed due to the low temperatures [3].

SCWO is inherently a closed system, so there is less risk of fugitive emissions. If the pressure containment is breached, runaway reactions are not a threat because a complete loss of pressure halts the oxidation reaction. The exothermic heat of reaction may be used to preheat the feed sludge as well as to generate low-pressure steam for process usage. Clean product water can be neutralized and used as process water in the mill. Carbon dioxide may be collected and sold. Ash by-product could be used as a cement extender or sold as calcium carbonate. (Note: unlike the fly ash from conventional incinerators which contains unoxidized carbon which may include PCDDs, PCDFs, PCBs, and so forth, the by-product ash obtained from SCWO has been found in this research to be substantially free of these organics.)

At this point in the discussion, the interested reader may refer to any textbook or review paper on supercritical fluids for a discussion of the theory and properties of supercritical water [4,5,6,7].

Experimental Section

The University of Texas at Austin currently owns and operates one of the largest known SCWO pilot facilities (40 gallons per hour capacity, continuous flow system). Kimberly-Clark Corporation has performed numerous experiments at this facility and has shown that paper mill sludges can be converted (oxidized) to clean water, clean calcium carbonate ash, and clean gas (carbon dioxide and residual oxygen). Experiments were performed on deinking (recycled) sludge. Results for virgin sludges are reported elsewhere by Hossain and Blaney [8].

The effect of temperature on paper mill sludge conversion was investigated, holding pressure and flowrates constant. Test conditions included pressures of 245 atm (3600 psi), flowrates of 20 gallons per hour, and two reaction temperatures of 450 and 500°C. The overall organic destruction was quantified in terms of total organic carbon (TOC). The thoroughness of destruction of trace chlorinated organics was quantified by measuring the trace quantities of PCDDs, PCDFs, and PCBs before and after SCWO, using gas chromatography and high-resolution mass spectrometry [9].

Pilot Plant. A schematic diagram of the 40 gallon/hour SCWO pilot plant at the University of Texas is shown in Figure 2.

Table I. Composition of Feed Sludge and Product Ash¹

	<i>Feed Sludge</i> ²	<i>Expt. A Product Ash</i> ³	<i>Expt. B Product Ash</i> ³
TOC	440,000 PPM	3400 PPM	<100 PPM
2,3,7,8-TCDD	3.99 ppt	<0.325 ppt*(DE>99%)	<0.23 ppt*(DE>99%)
total TCDD	6.41 ppt	18 ppt	1.5 ppt
total PeCDD	<2.46 ppt*	<2.5 ppt*	<0.81 ppt*
total HxCDD	15.36 ppt	<1.23 ppt*	<0.445 ppt*
total HpCDD	33.81 ppt	5.25 ppt	<0.64 ppt*
<u>OCDD</u>	<u>470.70 ppt</u>	<u><7 ppt*</u>	<u>1.6 ppt</u>
total PCDD	530 ppt	23.3 ppt (DE>96%)	3.1 ppt(DE>96%)
2,3,7,8-TCDF	35.09 ppt	2.85 ppt(DE>99%)	<0.505 ppt *(DE>99%)
total TCDF	72.42 ppt	63.5 ppt	7 ppt
total PeCDF	9.37 ppt	<1.05 ppt*	<0.275 ppt*
total HxCDF	<2.97 ppt*	<0.8 ppt*	<0.34 ppt*
total HpCDF	12.06 ppt	<1.19 ppt*	<0.22 ppt*
<u>OCDF</u>	<u>15.19 ppt</u>	<u><1.5 ppt*</u>	<u><0.53 ppt*</u>
total PCDF	144 ppt	66.4 ppt(DE>96%)	7 ppt(DE>96%)
mono-chlor- biphenyl	<0.32 ppb*	46.5 ppb	<0.2 ppb*
Di-Chl-Bp	8.65 ppb	20.5 ppb	<0.2 ppb*
Tri-Chl-Bp	<1.51 ppb*	<0.945 ppb*	<0.2 ppb*
Tetra-Chl-Bp	<0.65 ppb*	<0.4 ppb*	<0.4 ppb*
Penta-Chl-Bp	<0.69 ppb*	<0.4 ppb*	<0.4 ppb*
Hexa-Chl-Bp	<0.65 ppb*	<0.4 ppb*	<0.4 ppb*
Hepta-Chl-Bp	<1.29 ppb*	<0.8 ppb*	<0.8 ppb*
Octa-Chl-Bp	<1.29 ppb*	<0.8 ppb*	<0.8 ppb*
Nona-Chl-Bp	<3.23 ppb*	<2 ppb*	<2 ppb*
<u>Deca-Chl-Bp</u>	<u><3.23 ppb*</u>	<u><2 ppb*</u>	<u><2 ppb*</u>
Total PCBs	8.65 ppb	67 ppb(PCBs formed)	<DL*(DE>90%)

¹All data reported on dry basis²Average of 4 analyses³Average of 2 analyses

*Below detection limit

TCDD = tetrachlorodibenzo-para-dioxin
PeCDD=pentachlorodibenzo-para-dioxin
HxCDD=hexachlorodibenzo-para-dioxin
HpCDD=heptachlorodibenzo-para-dioxin
PCDD=polychlorinated dibenzo-para-dioxin
PCDF=polychlorinated dibenzofuran, etc.

The major components in the pilot plant consisted of a high-pressure diaphragm pump, a number of double-pipe heat exchangers, an electric heater, a coiled-tube reactor, an air-driven oxygen booster, and a hydrocyclone. The heat exchange between the feed and reactor effluent allowed the recovery of some thermal energy, giving a reduction of electrical power input required to maintain the process. The oxygen flowrate, electrical power input to the heater, and process pressure and temperature were controlled and monitored by a computer work station. The feed flowrate was controlled by manually adjusting the stroke length dial at the pump head and was monitored by the computer. The reactor volume was 13.08 liters. The pilot plant was made available to The University of Texas by a grant from Eco Waste Technologies, Inc., Austin, Texas.

Feed Preparation. Aqueous deinking sludge was collected at a "recycled" paper mill before biological treatment, and was about 5 to 7 percent solids, the solids portion being 30 percent inorganic (clays, fillers) and 70 percent organic (cellulosic fiber fines, residual pulping and deinking chemicals, and trace chlorinated organics). The pH was about 5.7, and total chlorides about 1.1 mg/L. This sludge was diluted to 2.5 percent solids, and this diluted mixture is termed the 'feed sludge'. In Experiment B, a small amount of methanol was added to the feed holding tank and blended evenly throughout the feed sludge in an attempt to increase its heating value. By blending the methanol evenly throughout the feed sludge, upsets in the heating value of the feed stream were minimized, in an effort to prevent any hot spots from forming in the reactor.

Table I contains feed sludge (not including the added methanol) values for total organic carbon (TOC), PCDDs, PCDFs, and PCBs on a dry basis.

Experimental Procedure. Feed sludge at 2.5% consistency was brought to conditions above the critical point of water. This was achieved by first pressurizing the sludge to approximately 245 atm (3600 psig) using a high-pressure diaphragm pump, and then heating it using electrical heaters to reach the desired average reaction temperature. Pure oxygen was introduced into the stream at this point via an air-driven oxygen booster, upon entering the plug-flow type reactor. The oxygen booster system used in the pilot plant was provided by Haskel, Inc. (Burbank, CA).

The system was assembled and cleaned for pure oxygen service. The University of Texas routinely follows the NASA design guide for high pressure oxygen systems [10]. In addition, all personnel in the laboratory were required to attend a video training class to learn how to safely handle high pressure oxygen. This video was prepared by NASA [11].

A number of double-pipe heat exchangers allowed recovery of some thermal energy, reducing the amount of electrical power input required to maintain the process. (Note: Due to poor insulation, much of the heat of reaction was lost to the surrounding air, hence the need for electrical heaters.) The reactor residence time at these conditions was about 50 seconds. Flowrates were 20 gallons per hour. Reactor temperature profiles are shown in Figure 3 for Experiment A, averaging about 450°C, and Experiment B, averaging about 500°C. No hot spots were observed.

Experiment A. Average reactor temperature was maintained at approximately 450°C, all other variables as described above.

Experiment B. Average reactor temperature was maintained at approximately 500°C. To maintain the reactor temperature at 500°C, which was above the electric heater capacity at the given feed flowrate, 2 wt% methanol was mixed with the feed (in the feed

hold tank) as an auxiliary fuel, and its added heat of combustion provided the necessary additional heat to bring the average temperature to 500°C. Since methanol is very easily oxidized to carbon dioxide and water at SCWO conditions, it is assumed by the authors that adding this small amount of methanol would only minimally affect the product mix.

Sample Analyses. Feed, product water and product ash from both Experiment A and Experiment B were analyzed within two weeks of the trials. Kimberly-Clark testing included all congeners of PCDDs, PCDFs, and PCBs; Total Organic Carbon (TOC); percent solids, and metals analyses. These tests were subcontracted to a well-known independent laboratory [12] which utilized gas chromatography and high-resolution mass spectrometry for trace chlorinated organics analyses [9]. In addition, The University of Texas performed numerous tests on the aqueous phase for suspended solids, total chemical oxygen demand, acetic acid, ammonia, chlorides, and pH. Tests on the solid (ash) phase included volatile solids and the Toxicity Characterization Leaching Procedure [13].

Results and Discussion

Data for the product streams are shown in Table I adjacent to the feed data. Values of PCDDs, PCDFs, and PCBs in the product water were less than one percent of that in the product solids (ash) so these data were not included. For both experiments the majority of the PCDDs and PCDFs were destroyed.

In Experiment B, at 500°C, the oxidation appears to be approaching completion, as the TOC in the solids was under the detection limit of 100 ppm, and virtually all of the PCDDs and PCDFs were destroyed. Destruction Efficiencies (DEs) of 2,3,7,8- TCDD and 2,3,7,8-TCDF (widely accepted as the most toxic congeners) were over 99%, and DEs of total PCDDs and PCDFs were over 96%. Over 90% of the PCBs were destroyed.

In Experiment A, the DEs for PCDDs and PCDFs were roughly the same for Experiment A as for Experiment B (>99%). However, at the lower temperature of 450°C in Experiment A, the data indicate that PCBs were *formed* (ppb levels) rather than destroyed, and the TOC in the product ash was still at 3400 ppm (from 440,000 ppm in the feed solids). This unexpected finding was clearly significant with respect to the quantification limits of the analytical procedures. Unfortunately, the high cost of the pilot runs and analytical procedures (many tens of thousands of dollars) prohibited repeating of these experiments. Although there is no known prior literature with this result, it isn't unreasonable to expect that, like conventional incineration, SCWO has certain windows in which unwanted chlorinated organics may be formed. Future testing will be needed to confirm and expand upon these findings. Although at first glance it may appear that some TCDDs were formed in Experiment A, this is in fact not the case, as can be shown by performing a complete mass balance and taking into account that the 18 ppt total TCDD in the product ash is based on inorganic only (dry basis), whereas the 6.41 ppt total TCDD in the feed solids is based on a mixture of inorganic plus organic (also dry basis). Sample calculations of DEs and mass balances are described elsewhere by Hossain and Blaney [8].

Leaching Tests. The solid residues (ash) derived from the SCWO tests were characterized by the Toxicity Characteristic Leaching Procedure [13]. Concentrations of the metals in the leachate from the ash were lower than the regulatory levels set by the EPA. Most heavy metals including As, Cd, Cr, Hg, Ni, Pb, Se, Tl, and V were nonleachable (below the detection limit of 0.0005 mg/g solid).

Conclusions

Supercritical water oxidation at temperatures of 500°C, pressures of 245 atm (3600 psi), and a residence time of about 50 seconds, was shown to be effective in destroying over 99 percent of the most toxic dioxin-type congeners, 2,3,7,8-TCDD and 2,3,7,8-TCDF, over 96 percent of the total PCDDs and PCDFs, and over 90 percent of the PCBs. However, at a lower temperature of 450°C (other conditions remaining constant), destruction of chlorinated organics was not as thorough, and PCBs appear to have been formed rather than destroyed.

In conclusion, the results show that under the right conditions, SCWO is an effective method to treat pulp and paper mill sludge, substantially destroying the most toxic PCDD/PCDF congeners and with the potential to minimize emissions, discharges, and other pollution or waste products. Although PCB destruction was observed to be somewhat less efficient (at just over 90 percent DEs), the authors surmise that the rate limiting step is mass-transfer related, and that rates of destruction of PCBs will be significantly greater in a commercial-scale reactor which has inherently better mixing from increased turbulence.

Economics

Two independent economic analyses were made, one by Kimberly-Clark Corporation, and another by Professor Charles Eckert at Georgia Institute of Technology Chemical Engineering Department in a report prepared for Kimberly-Clark. Both independent cost analyses were "venture guidance appraisals" involving the development of conceptual process designs and process simulations. The two cost estimates compared surprisingly well. Each compared the costs of landfill, incineration, and SCWO. Results indicate that both SCWO and incineration become economically preferred where transportation-plus-landfill tipping fees exceed about \$30 to \$40 per wet ton of sludge (dewatered to 50% solids), for a 100 bone dry ton per day sludge treatment facility.

When comparing the economics of a 'standard' fluidized bed incinerator with *minimal pollution control devices* to a SCWO system operating at 500°C and 245 atm (3600 psig) with 10 percent solids feed, costs appear to be roughly 25% higher for SCWO, although several process modifications, if proven viable, would bring SCWO costs at or below those of "standard" incineration. These SCWO process modifications include operating at lower pressures (e.g. under 135 atm = 2000 psi, as taught by Hong [14]), thickening the feed sludge to 12 or more percent solids, and obtaining \$60/ton credit for calcium carbonate ash, all of which are clearly within the range of possibility.

If pollution control equipment, e.g. an activated carbon bed to treat off gases, is added to an incinerator to reduce risks of fugitive emissions in an attempt to make the incineration process more environmentally comparable to SCWO, the cost of incineration will increase roughly 40 to 45%, making SCWO more attractive. Table II summarizes approximate treatment costs per bone dry ton of sludge for the various treatment options discussed above.

New Reactor Design

Efficient containment of high pressure, high temperature, corrosive reactions such as SCWO reactions, has become a major concern in commercialization of SCWO systems. A current problem with existing SCWO reactor designs is that they all require materials which will, over a substantial period of time, withstand pressures of 135-270 atm (2000-

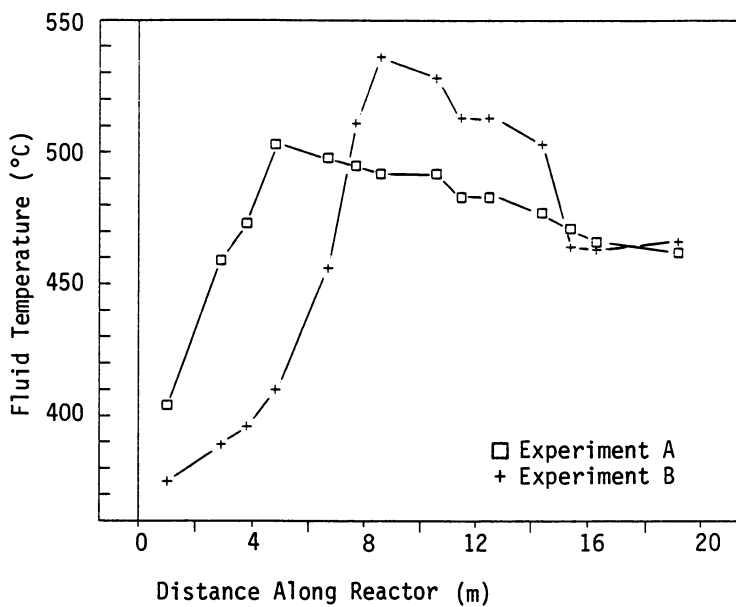


Figure 3. SCWO reactor temperature profile.

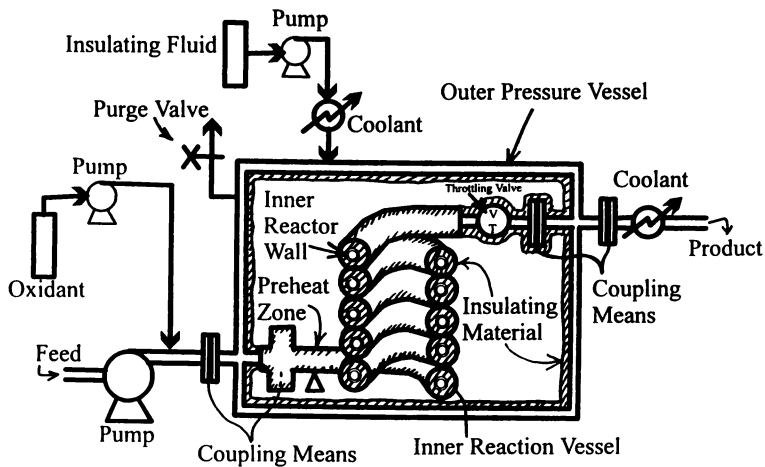


Figure 4. Kimberly-Clark patent-pending reactor design.

4000 psi), temperatures of 450–600°C, and corrosive conditions. No known materials exist which will handle all of these conditions simultaneously.

Metal alloys tend to embrittle (de-anneal), as well as experience creep, when exposed to high temperatures such as those encountered in SCWO reactions. This, coupled with the likelihood of corrosion-induced pitting or crazing on the surface of the metal alloy due to the corrosive nature of some SCWO reactions, demands that an alternative solution be found to contain both the high pressures and high temperatures of the SCWO reaction.

Certain ceramics and glasses are resistant to corrosion, but do not possess the mechanical strength to contain the high pressures typical of SCWO reactions. Some exotic metals and metal alloys are also corrosion-resistant, but may embrittle and/or creep at high temperatures under strain, or be cost-prohibitive to use on a commercial basis [15].

A Kimberly-Clark patent-pending reactor design, shown conceptually in Figure 4, offers an improved method to handle the problem of high pressure, high temperature, corrosive reactions. In general, it consists of a carbon steel pressure vessel containing an inner reactor made of a high-temperature, corrosion-resistant material, such as ceramic. The pressure vessel is maintained at a substantially lower temperature than the inner reactor via an insulating fluid that fills the space between the pressure vessel and the inner reactor, along with solid insulation and cooling means. The pressure vessel contains the high pressure so that the inner reactor does not experience a large pressure drop across its walls, thus permitting it to be constructed of ceramic or other high-temperature materials that do not hold up well under high stress loadings. By keeping the pressure vessel wall cool, it can contain the high pressure without risking loss of ductility.

Recommendations

The determining factors which might make SCWO an attractive sludge treatment technology for pulp and paper mills are listed below:

1. If landfill costs become prohibitively expensive, or if the landfill of paper mill sludge becomes no longer permissible in certain areas.
2. If legislation makes incineration prohibitively expensive (due to pollution control equipment requirements), or if the building of new incinerators becomes prohibited in certain areas (as it now is in Texas, for example [16]).
3. If the production of sludge in pulp and paper mills cannot be completely eliminated, or if no use is found for the sludge in a saleable by-product.
4. If a SCWO reactor design, such as the one depicted in Figure 4, is proven effective over sufficiently long periods.

In addition, the following experiments are recommended to answer pertinent questions regarding the commercial feasibility of SCWO to treat specific mill sludge:

- a. Determine the maximum "consistency" (e.g. % solids) of sludge which can be pumped up to reaction pressure. (By pumping more solids and less water, the reactor size can be decreased, improving economics. Some pump manufacturers claim their pumps can handle slurries containing up to 20% solids.) Determine the effect that higher consistencies have on reactor conditions.
- b. Optimize reaction conditions (temperature, pressure, residence times, mixing) to optimize plant economics while insuring maximum destruction efficiencies.
- c. Determine preheat conditions to insure against char formation. (Char is more difficult to oxidize than less-polymerized carbon-based moieties such as cellulose or polyaromatic hydrocarbons, for example.)
- d. Characterize product ash for utilization in specific by-products (cement filler, paper filler, etc.).

Table II. Capital* and Operating Costs

<u>Sludge Treatment Option:</u>	<u>\$/Bone dry ton:**</u>
1. Dewater to 50% solids plus landfill	\$113 to 353
2. Dewater to 50% solids plus fluidized bed incineration, with activated carbon bed to treat off-gas, ash to landfill	\$129 to 198
3. Gravity settle to 10% solids plus SCWO: - oxidant: pure oxygen - pressure: 245 psi (3600 psi) - temperature: 500°C - residence time: 50 sec, - ash to landfill	\$187 to 215
4. Same as 3, with process modifications/enhancements: - pump feed at 12% solids - pressure < 135 atm (2000 psi) - obtain credit for clean ash	\$120 to 140

*10 year straight line depreciation

** Landfill tipping fees tend to vary widely from location to location, causing a broad spread in minimum and maximum sludge treatment costs (due to landfill of sludge or ash). In this economic analysis, tipping fees were estimated to range from 30 to 150 \$/(wet)ton. Fees can run higher in populated areas.

Literature Cited

- [1] Acharya, P.; DeCicco, S. G.; and Novak, R. G. *J. Air Waste Manage. Assoc.*, vol 41, no. 12, pp. 1605- 1615.
- [2] Vogg, H.; Metzger, M.; Stieglitz, L.; (Karlsruhe Nuclear Research Center), "Recent Findings on the Formation and Decomposition of PCDD/PCDF in Solid Municipal Waste Incineration," Presented at the seminar: "Emissions of Trace Organics from Municipal Solid Waste Incinerators", Copenhagen, January 1987.
- [3] Killilea, W. R.; Swallow, K. C.; Hong, G. T. "The Fate of Nitrogen in Supercritical-Water Oxidation", *J. of Supercrit. Fluids*, vol 5, pp. 72-78, 1992.
- [4] McHugh, M.; Krukonis, V. *Supercritical Fluid Extraction, Principles and Practice*, 2nd ed., Butterworths: Boston, MS, 1994.
- [5] Gloyna, E.F.; Li, L.; "Supercritical Water Oxidation: An Engineering Update", *Waste Management*, vol 13(5-7), pp. 379-394, 1993.
- [6] Shaw, R.W.; Brill, T. B.; Clissord, A. A.; Eckert, C. A.; and E.U. Franck, E. U. "Supercritical Water -- A Medium for Chemistry", Special Report in *Chemical and Engineering News*, Dec. 23, 1991.
- [7] Testor, J.W., Holgate, H. R.; Armellini, F. J.; Webley, P. A.; Killilea, W. R.; Hong, G. T.; Barner, H. E. in *"Supercritical Water Oxidation Technology: A Review of Process Development and Fundamental Research"*, D. W. Tedder and F. G. Pohland, Eds; American Chemical Society Symposium Series 518, Emerging Technologies for Hazardous Waste Management III; American Chemical Society: Washington, DC, 1992, Chapter 3.
- [8] Hossain, S.U.; Blaney, C.A.; US Patent No. 5,075,017, "Method for Removing Polychlorinated Dibenzodioxins and Polychlorinated Dibenzofurans From Paper Mill Sludge", Dec. 24, 1991.
- [9] EPA method 1613a for trace analysis of PCDDs and PCDFs; EPA method 680 for analysis of PCBs.
- [10] NASA Reference Publication 1113.
- [11] Stradling, J. "A Review of the Hazards, Safety Aspects, Design Concepts, and Contamination Control Considerations Relating to the Safe Use of Liquid and Gaseous Oxygen", prepared by Jack Stradling at the NASA White Sands Test Facility, March 21, 1989.
- [12] Alta Analytical Lab, 5070 Robert J. Mathews, Suite 2, El Dorado Hills, CA 95630; EPA Method 1613A.
- [13] Toxicity Characterization Leaching Procedure, EPA method 1311.
- [14] Hong, G. T.; U.S. Patent no. 5,106,513, "Process For Oxidation of Materials in Water at Supercritical Temperatures and Subcritical Pressures", April 21, 1992.
- [15] *Chemical Engineer's Handbook*; Perry, R. H.; Chilton, C. H., Eds; 5th ed., McGraw-Hill Book Co: New York, NY, 1963. Table 23-3, pp. 23-16.
- [16] The Governor of Texas recently initiated a two-year moratorium on all new incinerator permits. Source: Eco Waste Technologies, Austin, Texas, 1992, private conversation.

RECEIVED May 31, 1995

Author Index

- Abraham, Martin A., 234
Aeskinazi, O. (Navaro), 366
Aki, Sudhir N. V. K., 234
Akman, U., 366
Alessi, P., 128
Balbuena, Perla B., 77
Becnel, J. M., 271
Blaney, Carol A., 446
Bourhis, A. L., 340
Brennecke, Joan F., 158
Buelow, S., 181
Caines, T. L., 271
Chateaufneuf, John E., 158
Chen, Peishi, 350
Chester, Thomas L., 93
Chialvo, A. A., 34,65
Cochran, H. D., 65
Coniglio, Lucie, 142
Connery, Karen A., 158
Cortesi, A., 128
Cummings, P. T., 34,65
Dell'Orco, P., 181
Dillow, Angela K., 168
DiNaro, Joanna L., 199
Ding, Zhong-Yi, 234
Dooley, K. M., 271
Dorsey, John G., 93
Downey, Kevin W., 315
Eckert, Charles A., 168
Ely, J., 181
Foster, Neil R., 1,128
Foy, B., 181
Fulton, J. L., 111
Gani, Rafiqul, 142
Giorgio, T. D., 283
Gloyna, Earnest F., 350,446
Gopalan, Sudhama, 219
Guney, Ozge, 260
Hassan, A., 404
Hazlebeck, D. A., 315
Hong, G. T., 340
Hortaçsu, Ö., 366
Hossain, Shafi U., 446
Hutchenson, Keith W., 1
Innis, David P., 93
Johnston, Keith P., 77
Jooma, Ashraf, 248
Kalyuzhnyi, Yu. V., 34
Keskin, Ozlem, 260
Kikic, I., 128
Killilea, W. R., 340
Kiran, Erdogan, 382
Knudsen, Kim, 142
Knutson, Barbara L., 168
Lachance, Russell P., 199
Latanision, R. M., 329
Launey, D., 271
Le, L., 181
Levien, K. L., 404,417
Li, Lixiong, 350,446
Liotta, Charles L., 168
Macnaughton, S. J., 128
Marrone, Philip A., 199
Mesmer, R. E., 65
Meyer, Jerry C., 199
Mitton, D. B., 329
Mizan, Tahmid I., 47
Montero, G. A., 283
Morrell, J. J., 404,417
Orzalli, J. C., 329
Page, Steven H., 93
Patterson, K., 181
Peters, William A., 199
Phenix, Brian D., 199
Rahmé, Ziyad G., 300
Roberts, Adele J., 315
Rossky, Peter J., 77
Sahle-Demessie, E., 417
Savage, Phillip E., 47,219
Schnelle, K. B., Jr., 283
Simonson, J. M., 65
Snow, Richard H., 315

- Stiver, Warren H., 300
 Subramaniam, Bala, 248
 Sunol, Aydin K., 260
 Sunol, Sermin G., 260
 Swallow, K. C., 199,340
 Teja, Aryn S., 431
 Tester, Jefferson W., 199
 Vandana, Vishnu, 431
- Wilmanns, E., 181
 Xiang, Tao, 77
 Zhang, J., 111
 Zhang, Jianwei, 158
 Ziegler, James W., 93
 Ziff, Robert M., 47
 Zytner, Richard G., 300

Affiliation Index

- Bogaziçi University, 366
 DuPont Central Research and Development, 1
 General Atomics, 315
 Georgia Institute of Technology, 168,431
 IIT Research Institute, 315
 Kimberly-Clark Corporation, 446
 Los Alamos National Laboratory, 181
 Louisiana State University, 271
 MODAR, Inc., 340
 Massachusetts Institute of Technology, 199,329
 Merrimack College, 199,340
 National Institute of Standards and Technology, 93
 Oak Ridge National Laboratory, 34,65
 Oregon State University, 404,417
- Pacific Northwest Laboratory, 111
 Procter & Gamble Company, 93
 Technical University of Denmark, 142
 Università di Trieste, 128
 University of Cincinnati, 93
 University of Guelph, 300
 University of Kansas, 248
 University of Maine—Orono, 382
 University of Michigan, 47,219
 University of New South Wales, 1,128
 University of Notre Dame, 158
 University of Pau, 142
 University of South Florida, 260
 University of Tennessee—Knoxville, 34,65
 University of Texas—Austin, 77,350,446
 University of Tulsa, 234
 Vanderbilt University, 283

Subject Index

- A·
- Additives, impregnation of wood, 393–396
 Aerogels, supercritical-fluid-aided preparation and characterization, 258–268
 Air and vacuum drying of alcohol, 261,263f,266–268
 Ambient to supercritical conditions, solvation in water, 77–90
- Aqueous Na⁺/Cl⁻ at supercritical state condition
 association constants, 67–69
 association process, 66
 equilibrium constants, 67–69
 experimental results, 71,73–74
 experimental description, 66
 hydrogen-bonding calculation, 67
 intermolecular potential, 66–67
 simulation, 66–67,69–74

- Stiver, Warren H., 300
 Subramaniam, Bala, 248
 Sunol, Aydin K., 260
 Sunol, Sermin G., 260
 Swallow, K. C., 199,340
 Teja, Aryn S., 431
 Tester, Jefferson W., 199
 Vandana, Vishnu, 431
- Wilmanns, E., 181
 Xiang, Tao, 77
 Zhang, J., 111
 Zhang, Jianwei, 158
 Ziegler, James W., 93
 Ziff, Robert M., 47
 Zytner, Richard G., 300

Affiliation Index

- Bogaziçi University, 366
 DuPont Central Research and Development, 1
 General Atomics, 315
 Georgia Institute of Technology, 168,431
 IIT Research Institute, 315
 Kimberly-Clark Corporation, 446
 Los Alamos National Laboratory, 181
 Louisiana State University, 271
 MODAR, Inc., 340
 Massachusetts Institute of Technology, 199,329
 Merrimack College, 199,340
 National Institute of Standards and Technology, 93
 Oak Ridge National Laboratory, 34,65
 Oregon State University, 404,417
- Pacific Northwest Laboratory, 111
 Procter & Gamble Company, 93
 Technical University of Denmark, 142
 Università di Trieste, 128
 University of Cincinnati, 93
 University of Guelph, 300
 University of Kansas, 248
 University of Maine—Orono, 382
 University of Michigan, 47,219
 University of New South Wales, 1,128
 University of Notre Dame, 158
 University of Pau, 142
 University of South Florida, 260
 University of Tennessee—Knoxville, 34,65
 University of Texas—Austin, 77,350,446
 University of Tulsa, 234
 Vanderbilt University, 283

Subject Index

- A·
- Additives, impregnation of wood, 393–396
 Aerogels, supercritical-fluid-aided preparation and characterization, 258–268
 Air and vacuum drying of alcohol, 261,263f,266–268
 Ambient to supercritical conditions, solvation in water, 77–90
- Aqueous Na⁺/Cl⁻ at supercritical state condition
 association constants, 67–69
 association process, 66
 equilibrium constants, 67–69
 experimental results, 71,73–74
 experimental description, 66
 hydrogen-bonding calculation, 67
 intermolecular potential, 66–67
 simulation, 66–67,69–74

Aromatic compounds, destroyed by catalytic supercritical water oxidation, 232–244

Axial dispersion, estimation, 305

B

Benzene, destruction using catalytic supercritical water oxidation, 232–244

Benzhydryl cation with tetramethylethylene and with triethylamine, 157–194

Binary mixtures

containing carbon dioxide, supercritical fluid flow injection method for mapping liquid–vapor critical loci, 93–109

wood preservatives in supercritical carbon dioxide with cosolvents, phase behavior, 402–414

Biocides in supercritical fluids, impregnation of wood, 415–427
solubilities, 403

C

C_3H_8 – H_2O –isopropyl alcohol system, phase equilibria, 147–149

Carbon dioxide

supercritical, phase behavior of binary and ternary mixtures of wood preservatives, 402–414

supercritical extraction of taxol, 429–442
use as modifier, 93

Carbon dioxide binary mixtures

phase equilibria, 149–151
supercritical fluid flow injection method for mapping liquid–vapor critical loci, 93–109

Carbon dioxide–ethanol mixtures, supercritical extraction of taxol, 429–442

Carbon dioxide extraction of alcohols, 259,261–264

Carbon dioxide–solvent binary mixtures, 93–95

Catalyst(s)

design features, 258,260f
porous, in situ mitigation of coke buildup with supercritical reaction media, 246–255

Catalytic supercritical water oxidation to destroy aromatic compounds, 232–244
catalyst performance, 236f,237,239
experimental system, 233–235
oxygen concentration, 238–242
previous studies, 233
product selectivity, 241,243,244f
temperature, 241,242f

Cellular permeable tube arrays model to explain release mechanisms of extractable compounds, 366–369

assumptions, 366

idealized cellular plant structure, 366,370f

intertubular region, 368–369

permeable tube wall region, 368

regions, 366–367

solvent-phase region, 367

stationary liquid–phase region, 367

Chemical agent testing, supercritical water oxidation of hazardous military wastes, 318–324

Chemical conversion of cellulosic wastes, supercritical fluid processing, 392

Chemistry and catalysis in supercritical fluid media, selected examples of innovations, 20–23

Chlorinated organic compounds, disposal and cleanup techniques, 198

Cluster size distribution, hydrogen bonding in supercritical water, 60–63

CO_2 – CH_3OH – H_2O system, phase equilibria, 146–148f

Coke buildup in porous catalysts with supercritical reaction media, in situ mitigation, 246–255

Coking of acid catalysts, cause, 246

Compressed fluid antisolvents, use in separations and materials formation, 25–26

Computer simulation, solvation in water from ambient to supercritical conditions, 78–83

Concentric tube reactor, simulation for supercritical water oxidation, 348–363
experimental description, 348–349
experimental vs. calculated exit reactor temperature, 357–359f
kinetic parameters, 355

- Concentric tube reactor, simulation for supercritical water oxidation—*Continued*
octanol–phenol mixtures, 357,361f
operating conditions and results
acetic acid, 354–355,357
octanol–phenol mixture, 354,356–357
pilot-scale facility, 349–351
reactor model, 351–354
temperature profiles, acetic acid, 357,360f
- Contaminants, soil
hazardous, removal by supercritical fluid extraction, 281–296
kinetic model for supercritical extraction, 298–311
- Conventional delignification and pulping, description, 384–385
- Corrosion studies in supercritical water oxidation systems, 327–337
electrochemical test facility design, 328–331
exposure test facility design, 331
failure analysis of Hastelloy C–276 preheater tubes, 331–336
previous studies, 328
test facility, 327–328
- Corrosion testing, supercritical water oxidation of hazardous military wastes, 313–318
- Cosolute, role in solubility measurement and technology, 7–12
- Cosolvent(s)
effects of solvent property, 167
phase behavior of binary and ternary mixtures of wood preservatives in supercritical carbon dioxide, 402–414
predictive and experimental methods for choice in supercritical fluid extraction of pesticides, 126–138
applicability of method to ternary liquid systems, 127–129
CO₂–cosolvent–lindane solubility, 136–137
CO₂–lindane solubility, 134–135
cosolvent effect for lindane, 133,134f,136
experimental description, 127,129
Henry's constant, 131,134
previous studies, 126–127
- Cosolvent(s)—*Continued*
predictive and experimental methods for choice in supercritical fluid extraction of pesticides—*Continued*
solubility measurement procedure, 130
solubility of lindane, 132–134
role in solubility measurement and technology, 11,13–16
supercritical extraction of taxol using CO₂ and CO₂–ethanol mixtures, 437–449
- Cosolvent effect, definition, 133
- Critical loci of binary mixtures containing carbon dioxide, supercritical fluid flow injection method for mapping, 93–109
- Critical point for pure substance or mixture, function, 402
- Critical pressures, phase behavior of binary and ternary mixtures of wood preservatives in supercritical CO₂ with cosolvents, 407–412
- Critical temperatures, phase behavior of binary and ternary mixtures of wood preservatives in supercritical CO₂ with cosolvents, 407–413
- CrO₃/Al₂O₃, supercritical water oxidation, 232–244
- Cycloadditions in SCF media, 23
- D
- Density-dependent local composition model, phase equilibria predictions, 142
- Density-induced structural changes in microemulsions formed in near- and supercritical solvents, 111–124
electrical conductivity in didodecyltrimethylammonium–propane microemulsion, 114–116f
experimental description, 112–113
L- α -lecithin
FTIR spectroscopy, 117–119
viscosity, 115–119
solubility of ethylene in sodium dodecyl sulfate aqueous systems, 117,120–124
- 1,3-Dichlorobenzene, destruction using catalytic supercritical water oxidation, 232–244

Didodecyldimethylammonium bromide–propane microemulsion, electrical conductivity, 114–116f
 Diels–Alder reaction in supercritical propane, kinetics, 166–176
 Dimer energies, hydrogen bonding in supercritical water, 51–54,56
 2,3-Dimethyl-1,3-butadiene–maleic anhydride reaction, kinetics, 166–176
 Direct feed heating, description, 339

E

Electrical conductivity, didodecyldimethylammonium bromide–propane microemulsion, 114–116f
 Enantioselective synthesis in SCF media, 23
 Enthalpic solute induced effect, 37
 Entropic solute induced effect, 37,39
 Enzymatic reactions in SCF media, 23
 Equations of state, for correlation and prediction of phase equilibria of mixtures with supercritical compounds, 140–154
 Equilibrium constant, calculation, 225
 Ethanol, role in supercritical extraction of taxol, 429–442
 Ethylbenzene, extraction from polystyrene, 271,273–277
 Ethylene, solubility in sodium dodecyl sulfate aqueous systems, 117,120–124
 Experimental methods, cosolvent choice in supercritical fluid extraction of pesticides, 126–137
 Extractable compounds from plant matrices
 mathematical modeling of release mechanisms during supercritical fluid extraction, 364–376
 Extraction
 natural compounds from plants, use of supercritical fluid technology, 364
 soil contaminants, supercritical, kinetic model, 298–310

F

Feed concentration, role in methylene chloride oxidation and hydrolysis in supercritical water, 203–208
 Feed peroxides, in situ mitigation of coke buildup in porous catalysts with supercritical reaction media, 246–255
 Film mass transfer coefficient, estimation, 305
 Film mass transfer with axial dispersion model
 development, 301
 fit, 307–309
 Flow injection method for mapping liquid–vapor critical loci of binary mixtures containing carbon dioxide, 93–109
 Fluid structure, relationship to hydrogen bonding in supercritical water, 57–59f
 Fluorescence spectroscopy, solvation in water from ambient to supercritical conditions, 86f,87
 Forest products industry
 supercritical fluid processing, 380–399
 use of supercritical fluids, 28

G

Gas antisolvent process, separations and materials formation, 25–26
 Gas solubility at near-critical conditions, molecular-based approach, 34–45
 GB agent, supercritical water oxidation of hazardous military wastes, 320–321

H

H₂O₂, effect of isopropyl alcohol oxidation, 345,346f
 Hastelloy C–276 preheater tubes, failure analysis, 331–336
 Hazardous contaminant removal from soil by supercritical fluid extraction, 298–311
 advantages, 283
 apparatus, 284,285f

- Hazardous contaminant removal from soil
 by supercritical fluid extraction—
Continued
 experimental description, 281–287
 mathematical model, 282–284
 model results, 289,293–294
 naphthalene
 CO₂ flow rate, 287,288*f*
 contamination level, 289,290*f*,291*f*
 cosolvent in supercritical CO₂ vs.
 extraction, 289,292*f*
 solubilities in supercritical CO₂ vs.
 extraction, 289,292*f*
 supercritical CO₂ density vs. extraction,
 289,291*f*
 1,2,4-trimethylbenzene
 CO₂ flow rate vs. outlet concentration,
 287,290*f*
 solubilities in supercritical CO₂ vs.
 extraction, 289,292*f*
 Hazardous military wastes, supercritical
 water oxidation, 313–325
 Henry's constant
 cosolvents in lindane, 134
 measurement procedure, 131
 temperature dependence, 38–40
 Heterogeneous catalysis in SCF media, 21–22
 High-pressure delignification, 385–392
 HNO₃, effect of isopropyl alcohol oxidation,
 345,346*f*
 Homogeneous catalysis in SCF media, 21
 HV thermodynamic model, phase equilibria
 predictions, 145–152
 Hydration of solutes, effect of temperature, 79
 Hydrogen bonding
 between pair of molecules, determination
 criteria, 48–49
 ambient liquid water, 47
 supercritical aqueous solutions, 65–74
 supercritical water, molecular dynamics,
 47–63
 Hydrolysis, methylene chloride in
 supercritical water, 197–213
 Hydrothermal oxidation, organic com-
 pounds by nitrate and nitrite, 179–196
 Hydrothermal processing of wastes,
 destruction of organic components, 179
- I
 Impregnation of wood with biocides, use of
 supercritical fluid carriers, 415–427
 In situ mitigation of coke buildup in
 porous catalysts with supercritical
 reaction media
 analytical procedure, 248,251
 application areas, 255
 catalyst, 248
 deleterious effect of peroxides in feed, 247
 experimental conditions, 247–248
 peroxide effect
 coke laydown, 251–253
 deactivation rates, 253
 isomerization rates, 253,254*f*
 oligomer production rates, 250*f*,251
 previous studies, 247
 process control, 251
 process improvement, 253,255
 safety features, 251
 Incineration, supercritical water oxidation
 as an alternative, 444–454
 Indirect feed preheating, description, 339
 Intermolecular interactions in supercritical
 fluids studied with pulse radiolysis,
 156–164
 Internal soil resistance
 estimation, 305
 with axial dispersion and film mass
 transfer model
 development, 301–302
 fit, 308–310
 Ion pairing, supercritical aqueous
 solutions, 65–74
 Ionic reactions in SCF media, 23
- K
 Kinetic model for supercritical extraction
 of soil contaminants, 298–311
 degree of fit, 301–302,312
 development
 assumptions, 300
 film mass transfer with axial model,
 307–309

Kinetic model for supercritical extraction of soil contaminants—*Continued*
development—*Continued*

internal soil resistance with axial dispersion and film mass transfer model, 301–302

local equilibrium with axial dispersion model, 301

transport of contaminant through packed bed, 300–301

experimental objective, 299

parameter estimation

fixed parameters, 303,304*t*

properties of packed beds, 303,304*t*

variable parameters, 305

previous studies, 299

Kinetics of Diels–Alder reaction in supercritical propane, 166–177

apparatus, 168–170

cosolvent effect, 174–176

data analysis procedure, 170–171

degree of association of reactants in activated complex, 175

density, 172*f*,173,175

estimated activation volumes, 173

experimental description, 167–168,170
pressure, 171–173

previous studies, 167

reaction, 167–168

Krichevskii's parameter, use in gas solubility description, 35

L

Linear combination of Vidal and Michelsen model

description, 143

phase equilibria predictions, 145–152

L- α -Lecithin

FTIR spectroscopy, 117–119

viscosity, 115–117

Lindane, effect of cosolvent on solubility, 126–137

Liquid–vapor critical loci of binary mixtures containing carbon dioxide, supercritical fluid flow injection method for mapping, 93–109

Local composition model of Schwartzentruber, Galivel-Solastiouk, and Renon, phase equilibria predictions, 142

Local equilibrium with axial dispersion model

development, 301

fit, 306,307*f*,309*t*

M

Maleic anhydride–2,3-dimethyl-1,3-butadiene reaction, kinetics, 166–176

Mapping liquid–vapor critical loci of binary mixtures containing carbon dioxide by supercritical fluid flow injection method, 93–109

Materials formation and separations with compressed fluid antisolvents, 25,26

Mathematical modeling of release mechanisms of extractable compounds from plant matrices during supercritical fluid extraction, 364–377

assumptions, 365–366

cellular permeable tube arrays model, 366–370

experimental objective, 365

sensitivity analysis, 372–376

serially interconnected perfectly mixed tanks model, 369–371,373

Matrices, polymeric, supercritical fluid extraction, 269–279

Mean spherical approximation, use in two-component hard core Yukawa fluid, 41

Measurement, supercritical fluid extraction from polymeric matrices, 269–279

Methylene chloride oxidation and hydrolysis in supercritical water corrosion, 211,213

experiment(s), 201–203

experimental description, 198–201

feed concentration, 203–208

oxidation reaction steps, 212,213*f*

previous studies, 198–199

products detected, 205,207–211

- Methylene chloride oxidation and hydrolysis in supercritical water—
Continued
reaction extent in organic feed preheater coil, 205
residence time, 203–206
temperature, 203,204*f*,207–211
- MHV1 and MHV2 thermodynamic models, phase equilibria predictions, 145–152
- Microemulsions formed in near- and supercritical solvents, density-induced structural changes, 112–124
- Military wastes, hazardous, supercritical water oxidation, 313–325
- Mill effluent treatment, supercritical fluid processing, 392
- Mitigation of coke buildup in porous catalysts with supercritical reaction media, in situ. *See* In situ mitigation of coke buildup in porous catalysts with supercritical reaction media
- $\text{MNO}_2/\text{CeO}_2$, supercritical water oxidation, 232–244
- Modeling, supercritical fluid extraction from polymeric matrices, 269–279
- Molecular-based approach to gas solubility at near-critical conditions, 34–45
experimental description, 35–36
future work, 45
integral equation calculations, 40–45
solvation process mechanism, 35
temperature dependence of Henry's constant and solute distribution factor, 38–40
theory, 36–38
- Molecular dynamics of hydrogen bonding in supercritical water, 47–64
cluster size distribution, 60–63*f*
degree of hydrogen bonding, 53,55,57
dimer energies, 51–54,56
experimental description, 49
fluid structure–hydrogen bonding relationship, 57–59*f*
hydrogen-bond persistence times, 61,63*f*
orientational correlation–hydrogen-bonding relationship, 57,60
simulation procedure, 49–51
- Mustard agent testing, supercritical water oxidation of hazardous military wastes, 322–324
- N
- Near-critical conditions, molecular-based approach to gas solubility, 34–45
- Near-critical properties of dilute aqueous electrolyte solutions, determination problems, 65–66
- Near-critical solvents, density-induced structural changes in microemulsions, 111–124
- Nitrate, hydrothermal oxidation of organics, 179–195
- Nitrite, hydrothermal oxidation of organics, 179–195
- O
- Organic components
destruction by hydrothermal processing, 179
hydrothermal oxidation by nitrate and nitrite, 179–195
use of wet oxidation for destruction, 232
- Organic wastes
destruction using supercritical water oxidation, 197–198
oxidative destruction, 24
- Oriental correlation, relationship to hydrogen bonding in supercritical water, 57,60
- Ostwald's coefficient, use in gas solubility description, 35
- Oxidation
hydrothermal, organic compounds by nitrate and nitrite, 179–196
methylene chloride in supercritical water, 197–213
phenol in supercritical water, 217–230
- Oxygen concentration, role in catalytic supercritical water oxidation, 238–242

P

Paclitaxel

- extraction from trees, 431
- structure, 429,430f
- supercritical extraction using CO₂ and CO₂-ethanol mixtures, 429-442
- synthesis methods, 429,431

Paper and pulp industry, supercritical fluid processing, 380-399

Paper and pulp mill sludge, supercritical water oxidation, 444-454

Paper recycling, supercritical fluid processing, 392

Parameter estimation, kinetic model for supercritical extraction of soil contaminants, 303-305

Peng-Robinson equation of state, cosolvent choice methods in supercritical fluid extraction of pesticides, 126-137

Peroxides, feed, in situ mitigation of coke buildup in porous catalysts with supercritical reaction media, 246-255

Persistence times, hydrogen bonding in supercritical water, 61,63f

Pesticides, choice of cosolvent in supercritical fluid extraction, 126-137

Phase behavior of binary and ternary mixtures of wood preservatives in supercritical carbon dioxide with cosolvents, 402-414

apparatus, 404-405

critical pressures

- acetone content effect, 409,411f
- CO₂-methanol mixtures, 407-409
- CO₂-propiconazole mixtures, 409-410
- methanol content effect, 412

critical temperatures

- acetone content effect, 409,411f
- CO₂-methanol mixtures, 407-409
- CO₂-propiconazole mixtures, 409-410
- methanol content, 412,413f

experimental procedure, 403-404,406

importance, 402-403

phase composition measurements, 412,414

Phase composition, phase behavior of binary and ternary mixtures of wood preservatives in supercritical CO₂ with cosolvents, 412,414

Phase equilibria, mixtures with supercritical compounds, correlation and prediction for a class of equations of state, 140-152

C₃H₈-H₂O-isopropyl alcohol system, 147-149CO₂-CH₃OH-H₂O system, 146,147-148f

computational procedure, 144-145

experimental description, 141

mixtures, 144

models compared for mixtures, 145-146

recommendations, 152

thermodynamics models, 141-143

Phase equilibrium data, inadequacies, 93

Phase-transfer catalysis in SCF media, 22

Phenol

destruction using catalytic

supercritical water oxidation, 232-244

oxidation in supercritical water, 217-230

experimental description, 217-218

future work, 230

kinetic modeling, 220-226

mechanism development, 219-220

model validation, 226-228

previous studies, 217-218

sensitivity analysis, 228-230

Pipe reactors, use of rate enhancers in

supercritical water oxidation, 339-346

Plant materials, structure modeling, 364

Plant matrices, mathematical modeling of

release mechanisms of extractable

compounds during supercritical fluid

extraction, 364-376

Polymer(s), impregnation of wood,

393-396

Polymeric matrices, supercritical fluid

extraction, 269-279

Polymerizations in SCF media, 23

Polystyrene, ethylbenzene extraction,

271,273-277

Porous catalysts, in situ mitigation of

coke buildup with supercritical

reaction media, 246-255

- Predictive methods, cosolvent choice in supercritical fluid extraction of pesticides, 126–137
- Pressure, role in supercritical extraction of taxol using CO₂ and CO₂ dioxide–ethanol mixtures, 436–438*f*
- Pressure, effect on ionic reactions in supercritical fluids, 156–164
- Propane, supercritical, kinetics of Diels–Alder reaction, 166–176
- Pulp and paper industry, supercritical fluid processing, 380–399
- Pulp and paper mill sludge
definition, 444
disposal methods, 444–447
supercritical water oxidation, 444–454
- Pulse radiolysis to study intermolecular interactions and reactivity in supercritical fluids, 156–164
- R**
- Random–nonrandom model, *See* Density-dependent local composition model
- Rapid expansion of supercritical solutions (RESS), description, 26–28
- Rate enhancers in supercritical water oxidation, 338–346
ethanol vs. isopropyl alcohol oxidation, 343–346
experimental description, 341–343
initiation, 340
isopropyl alcohol oxidation sensitivity to mix temperature, 343,344*f*
mix temperature vs. supercritical water to core ratio, 339,342*f*
oxidants, 340
reactant temperature raising methods, 339
- Reactivity in supercritical fluids studied with pulse radiolysis, 156–164
- Release mechanisms of extractable compounds from plant matrices during supercritical fluid extraction, mathematical modeling, 364–376
- Remediation of contaminated soils, use of supercritical fluid extraction, 126
- Removal, hazardous contaminants from soil by supercritical fluid extraction, 281–294
- Residence time, role in methylene chloride oxidation and hydrolysis in supercritical water, 203–205,206*f*
- S**
- Selective oxidations in SCF media, 22–23
- Sensitivity
model of phenol oxidation in supercritical water, 228–230
serially interconnected perfectly mixed tanks model of release mechanisms of extractable compounds, 372–376
- Separations
with compressed fluid antisolvents, 25–26
with supercritical solvent prediction of phase equilibria, 140
- Serially interconnected perfectly mixed tanks model of release mechanisms of extractable compounds
constituents of perfectly mixed tanks, 369–371
mass balance equation, 371,373
representation, 370*f*,371
sensitivity analysis, 372–376
- Simulation, solvation in water from ambient to supercritical conditions, 77–90
- Sludge, supercritical waster oxidation, 444–454
- Soil
removal of hazardous contaminants by supercritical fluid extraction, 281–294
kinetic model for supercritical extraction of contaminants, 298–310
- Sol–gel process
description, 258–259
solvent removal methods, 259,260*f*
- Solubility
effect of solvent, 126–139
ethylene in sodium dodecyl sulfate aqueous systems, 117,120–124
measurement procedure, 130

- Solubility measurement and technology
 correlation of data, 13,17–20
 effects of cosolute, 7–12
 effects of cosolvent, 11,13–16
 precision and accuracy, 2–7
- Solute distribution factor
 temperature dependence, 38–40
 use in gas solubility description, 35
- Solute-induced effects, 39–40
- Solvation
 supercritical aqueous solutions, 65–74
 water from ambient to supercritical conditions, 77–91
 computer simulation, 79–81
 experimental description, 77–78
 fluorescence spectroscopy, pyrene in water, 86f,87
 previous studies, 77
 structural results from molecular dynamics simulations, 87–90f
 UV–visible spectroscopy, 83–86
- Solvents, effect on ionic reactions in supercritical fluids
 experimental procedure, 157–159
- Ph_2CH^+ reaction
 with tetramethylethylene, 159–162f
 with triethylamine, 161,163–164
 previous studies, 156–157
 reactions schemes, 157
- Solvent replacement in SCF media, 20–21
- Spectroscopy, solvation in water from ambient to supercritical conditions, 77–90
- Stress corrosion cracking, role in supercritical water oxidation systems, 327–336
- Structural changes in microemulsions formed in near- and supercritical solvents, density-induced, 111–124
- Supercritical aqueous solutions, solvation, hydrogen bonding, and ion pairing, 65–74
- Supercritical carbon dioxide, phase behavior of binary and ternary mixtures of wood preservatives with cosolvents, 402–414
- Supercritical compound mixtures for class of equations of state, phase equilibria, 140–154
- Supercritical drying
 alcohols, description, 261–266
 removal of solvent from gel, 259
- Supercritical extraction
 paclitaxel using CO_2 and CO_2 -ethanol mixtures, 429–442
 advantages, 431–432
 apparatus, 432
 effect of cosolvent, 437–439,441–442
 experimental procedure, 432–435,437
 HPLC analysis, 439–441f
 pressure, 436–438f
 temperature, 436t,437
 soil contaminants, kinetic model, 298–310
- Supercritical fluid(s)
 advantages as solvents for reactions and separations, 166
 factors affecting reaction rates, 156–157
 polymer-related applications, 269
 property manipulations, 380
- Supercritical-fluid-aided preparation of aerogels, 258–268
 air and vacuum drying of alcohol
 comparison of xerogels with aerogels, 266–268
 procedure, 261,263f
 CO_2 extraction of alcohols
 procedure, 259,261–263f
 results, 261,264t
 experimental procedure, 259,261
 supercritical drying of alcohols, 261–266
- Supercritical fluid carriers for wood impregnation with biocides, 415–427
- Supercritical fluid extraction
 description, 299
 from polymeric matrices, 269–279
 apparatus, 271,272f
 ethylbenzene extraction from polystyrene, 271,273–277
 experimental description, 269–271
 extraction model, 277
 modeling considerations, 270–272f
 rate-limiting reaction, 269

- Supercritical fluid extraction—*Continued*
hazardous contaminants from soil, 281–294
mathematical modeling of release mechanisms of extractable compounds from plant matrices, 364–376
of pesticides, cosolvent choice, 126–137
release mechanisms of extractable compounds from plant matrices, 364–377
remediation of contaminated soil, 126
- Supercritical fluid flow injection method for mapping liquid–vapor critical loci of binary mixtures containing carbon dioxide, 93–109
apparatus, 99–100
calibration procedure, 101
column length, 97,99
comparison of CO₂–toluene and –methanol data, 103,105*f*,107
critical loci, 106*f*,107,108–109*t*
dynamic liquid film formation and removal, 96097,98*f*
experimental materials, 99
flame ionization detector temperature, 97,98*f*
peak height vs. pressure, 101–104*f*
phase separation, 95–97*f*
procedure, 95
- Supercritical fluid processing in pulp and paper and forest products industries, 380–399
applications, 383
conventional delignification and pulping, 384–385
future work, 399
high-pressure and supercritical delignification, 385–392
impregnation of wood with polymers and additives
miscibility and phase separation, 393–394,396*f*
studies, 395,397–398*f*
viscosity, 394–396*f*
previous studies, 383
rationale for use, 382–383
waste streams, 392
wood structure, 381–382
- Supercritical fluid science and technology applications, 1–2
chemistry and catalysis in supercritical fluid media, 20–23
commercialization, 1
extraction of natural compounds from plants, 364
forest products industry, 28
RESS process, 26–28
separations and materials formation compressed with fluid antisolvents, 25–26
solubility measurement and technology
correlation of data, 13,17–20
cosolute, 7–12
cosolvent, 11,13–16
precision and accuracy, 2–7
supercritical water oxidation, 24
- Supercritical mixture density, calculation, 133
- Supercritical propane, kinetics of Diels–Alder reaction, 166–176
- Supercritical reaction media, in situ mitigation of coke buildup in porous catalysts, 246–255
- Supercritical solvents, density-induced structural changes in microemulsions, 111–124
- Supercritical water advantages as medium for chemical processes, 47
methylene chloride oxidation and hydrolysis, 197–213
molecular dynamics of hydrogen bonding, 47–63
phenol oxidation, 217–230
- Supercritical water oxidation advantages for organic compound destruction, 348
catalytic, to destroy aromatic compounds, 232–244
concentric tube reactor simulation, 348–361
corrosion studies, 327–336
description, 24,179
for waste treatment, 217,338

Supercritical water oxidation—*Continued*

- hazardous military wastes
 - chemical agent testing, 318–324
 - corrosion testing, 314–318
 - pilot plant reactor design, 324–325
- limitation, 232–233
- organics by nitrate and nitrite
 - analytical procedure, 185
 - apparatuses, 180–181
 - bench-scale reactor procedure, 181–184
 - concentrations of constituents, 180,181*t*
 - experimental description, 180
 - kinetics, 192–194*f*
 - nitrogen–organic reaction pathways, 191–192
 - pressure, 193,195
 - previous studies, 180
 - reaction intermediate production and disappearance, 188–191,194
 - reactions of simple mixtures, 185–189
 - small pilot-scale reactor procedure, 185
- procedure, 197–198
- process, 313
- pulp and paper mill sludge, 444–454
 - chlorinated organics levels, 448*t*,450
 - economics, 451,454*t*
 - experimental procedure, 447–450,452*f*
 - leaching tests, 450
 - new reactor design, 451–453
 - pilot plant, 446*f*,447,449
 - recommendations, 453
 - rate enhancers, 338–346

T

- Taxol, *See* Paclitaxel
- Telephone and electric power poles,
 - impregnation of wood with preservatives using supercritical fluid technology, 403
- Temperature, role
 - catalytic supercritical water oxidation, 241,242*f*
 - Henry's constant and solute distribution factor, 38–40
 - hydration of solutes, 79
 - methylene chloride oxidation and hydrolysis in supercritical water, 203–204,207–211

- Temperature, role—*Continued*
 - supercritical extraction of taxol using CO₂ and CO₂–ethanol mixtures, 436*t*,437
- Ternary mixtures of wood preservatives in supercritical carbon dioxide with cosolvents, phase behavior, 402–414
- Thermodynamic models, phase equilibria of mixtures with supercritical compounds, 141–143
- Two-component hard core Yukawa fluid, molecular-based approach to gas solubility, 40–45

U

- UV–visible spectroscopy, solvation in water from ambient to supercritical conditions, 82–85

V

- V₂O₅/Al₂O₃, supercritical water oxidation, 232–244
- Vacuum and air drying of alcohol,
 - description, 261,263*f*,266–268
- Validation, model of phenol oxidation in supercritical water, 226–228
- Vapor–liquid equilibria, prediction methods, 127
- vdW thermodynamic model
 - description, 141–142
 - phase equilibria predictions, 145–152
- Volumetric solute induced effect, 36,39
- VX agent, supercritical water oxidation of hazardous military wastes, 321–322

W

- Waste streams, supercritical fluid processing, 392
- Waste treatment, use of supercritical water oxidation, 217
- Water, solvation from ambient to supercritical conditions, 77–90
- Water–pentanol, phase equilibria, 149,150*f*
- Water–water interactions, simple point charge model description, 66
- Wet air oxidation, description, 179

Wet oxidation, use for destruction of organic species, 232

Wong-Sandler model, 143,145-152

Wood

chemical transformations, 382

impregnation with biocides using supercritical fluid carriers advantages, 415

conventional technologies, 415

cosolvent, effect on biocide

distribution, 419,421*f*

development, 415-416

experimental procedure, 416-418

fundamental solute balance, 423

future work, 426

model, 419-427

performance, 424-427

pressure, effect on deposition, 418-420*f*

Wood—*Continued*

impregnation with biocides using

supercritical fluid carriers—*Continued*

previous studies, 416

simplified solute balance and

retention calculation, 423-424

specimen size, 419,421*f*

total mass balance, 422-423

treatment period effect on deposition, 418-420*f*

physicochemical modifications, 382

rationale for use of supercritical

fluids, 382-383

structure, 381-382

Wood preservatives, phase behavior of

binary and ternary mixtures in

supercritical CO₂ with cosolvents,

402-414

Production: Amie Jackowski & Charlotte McNaughton

Indexing: Deborah H. Steiner

Acquisition: Michelle D. Althuis

Printed and bound by Maple Press, York, PA